Lecture Notes in Electrical Engineering 563

Jiadong Sun
Changfeng Yang
Yuanxi Yang *Editors*

China Satellite Navigation Conference (CSNC) 2019 Proceedings

Volume II

Springer

Lecture Notes in Electrical Engineering

Volume 563

Series Editors

The book series *Lecture Notes in Electrical Engineering* (LNEE) publishes the latest developments in Electrical Engineering - quickly, informally and in high quality. While original research reported in proceedings and monographs has traditionally formed the core of LNEE, we also encourage authors to submit books devoted to supporting student education and professional training in the various fields and applications areas of electrical engineering. The series cover classical and emerging topics concerning:

- Communication Engineering, Information Theory and Networks
- Electronics Engineering and Microelectronics
- Signal, Image and Speech Processing
- Wireless and Mobile Communication
- Circuits and Systems
- Energy Systems, Power Electronics and Electrical Machines
- Electro-optical Engineering
- Instrumentation Engineering
- Avionics Engineering
- Control Systems
- Internet-of-Things and Cybersecurity
- Biomedical Devices, MEMS and NEMS

For general information about this book series, comments or suggestions, please contact leontina.dicecco@springer.com.

To submit a proposal or request further information, please contact the Publishing Editor in your country:

China

Jasmine Dou, Associate Editor (jasmine.dou@springer.com)

India

Swati Meherishi, Executive Editor (swati.meherishi@springer.com)

Aninda Bose, Senior Editor (aninda.bose@springer.com)

Japan

Takeyuki Yonezawa, Editorial Director (takeyuki.yonezawa@springer.com)

South Korea

Smith (Ahram) Chae, Editor (smith.chae@springer.com)

Southeast Asia

Ramesh Nath Premnath, Editor (ramesh.premnath@springer.com)

USA, Canada:

Michael Luby, Senior Editor (michael.luby@springer.com)

All other Countries:

Leontina Di Cecco, Senior Editor (leontina.dicecco@springer.com)

Christoph Baumann, Executive Editor (christoph.baumann@springer.com)

**** Indexing: The books of this series are submitted to ISI Proceedings, EI-Compendex, SCOPUS, MetaPress, Web of Science and Springerlink ****

More information about this series at http://www.springer.com/series/7818

Jiadong Sun · Changfeng Yang ·
Yuanxi Yang
Editors

China Satellite Navigation Conference (CSNC) 2019 Proceedings

Volume II

Springer

Editors
Jiadong Sun
China Aerospace Science and Technology Corporation
Chinese Academy of Sciences
Beijing, China

Changfeng Yang
China Satellite Navigation Engineering Center
Beijing, China

Yuanxi Yang
State Key Laboratory of Geo-information Engineering
Xi'an Research Institute of Surveying and Mapping
Xi'an, Shaanxi, China

ISSN 1876-1100 ISSN 1876-1119 (electronic)
Lecture Notes in Electrical Engineering
ISBN 978-981-13-7758-7 ISBN 978-981-13-7759-4 (eBook)
https://doi.org/10.1007/978-981-13-7759-4

This Springer imprint is published by the registered company Springer Nature Singapore Pte Ltd.
The registered company address is: 152 Beach Road, #21-01/04 Gateway East, Singapore 189721, Singapore

Preface

BeiDou Navigation Satellite System (BDS) is China's global navigation satellite system which has been developed independently. BDS is similar in principle to global positioning system (GPS) and compatible with other global navigation satellite systems (GNSS) worldwide. BDS will provide highly reliable and precise positioning, navigation and timing (PNT) services as well as short-message communication for all users under all-weather, all-time and worldwide conditions.

China Satellite Navigation Conference (CSNC) is an open platform for academic exchanges in the field of satellite navigation. It aims to encourage technological innovation, accelerate GNSS engineering and boost the development of the satellite navigation industry in China and in the world.

The 10th China Satellite Navigation Conference (CSNC2019) is held during May 22–25, 2019, Beijing, China. The theme of CSNC2019 is "Navigation, 10 Years and Beyond", including technical seminars, academic exchanges, forums, exhibitions and lectures. The main topics are as follows:

Conference Topics

S01 Satellite Navigation Applications
S02 Navigation and Location-based Service
S03 Satellite Navigation Signal and Signal Processing
S04 Satellite Orbit and System Error Processing
S05 Spatial Frames and Precise Positioning
S06 Time Primary Standard and Precision Time Service
S07 Satellite Navigation Augmentation Technology
S08 Test and Assessment Technology
S09 User Terminal Technology
S10 PNT System and Multi-source Fusion Navigation
S11 Anti-interference and Anti-spoofing Technology
S12 Policies, Regulations, Standards and Intellectual Properties

The proceedings (Lecture Notes in Electrical Engineering) has 114 papers in 12 topics of the conference, which were selected through a strict peer review process from 371 papers presented at CSNC2019. In addition, another 156 papers were selected as the electronic proceedings of CSNC2018, which are also indexed by "China Proceedings of Conferences Full-text Database (CPCD)" of CNKI and Wan Fang Data.

We thank the contribution of each author and extend our gratitude to 251 referees and 53 session chairmen who are listed as members of editorial board. The assistance of CNSC2019's organizing committees and the Springer editorial office is highly appreciated.

Editorial Board

Topic: S01: Satellite Navigation Applications

Chairman

Qin Zhang	Chang'an University, Shaanxi, China

Vice-chairmen

Shuanggen Jin	Shanghai Astronomical Observatory, Chinese Academy of Sciences, Shanghai, China
Geyang Li	Qianxun Spatial Intelligence Inc., Beijing, China
Dangwei Wang	Beijing UniStrong Science & Technology Co., Ltd., Shaanxi, China
Xiaolin Meng	University of Nottingham, Nottingham, England

Topic: S02: Navigation and Location-Based Service

Chairman

Yamin Dang	Chinese Academy of Surveying and Mapping, Beijing, China

Vice-chairmen

Baoguo Yu	The 54th Research Institute of China Electronics Technology Group Corporation, Hebei, China

Qun Ding	The 20th Research Institute of China Electronics Technology Group Corporation, Shaanxi, China
Kefei Zhang	RMIT University, Melbourne, Australia

Topic: S03: Satellite Navigation Signal and Signal Processing

Chairman

Xiaochun Lu	National Time Service Center, Chinese Academy of Sciences, Shaanxi, China

Vice-chairmen

Yanhong Kou	Beihang University, Beijing, China
Zheng Yao	Tsinghua University, Beijing, China
Tianxing Chu	Texas A&M University-Corpus Christi, Corpus Christi, Texas, USA

Topic: S04: Satellite Orbit and System Error Processing

Chairman

Xiaogong Hu	Shanghai Astronomical Observatory, Chinese Academy of Sciences, Shanghai, China

Vice-chairmen

Geshi Tang	Beijing Aerospace Control Center, Beijing, China
Rongzhi Zhang	Xi'an Satellite Control Center, Shaanxi, China
Maorong Ge	Geo Forschungs Zentrum (GFZ), Potsdam, Germany

Topic: S05: Spatial Frames and Precise Positioning

Chairman

Qile Zhao	Wuhan University, Hubei, China

Vice-chairmen

Jianwen Li	The PLA Information Engineering University, Henan, China
Shuli Song	Shanghai Astronomical Observatory, Chinese Academy of Sciences, Shanghai, China
Yanming Feng	Queensland University of Technology, Brisbane, Australia

Topic: S06: Time Primary Standard and Precision Time Service

Chairman

Lianshan Gao	The 203th Research Institute of China Aerospace Science and Industry Corporation, Beijing, China

Vice-chairmen

Chunhao Han	Beijing Satellite Navigation Center, Beijing, China
Xiaohui Li	National Time Service Center, Chinese Academy of Sciences, Shaanxi, China
Aimin Zhang	National Institute of Metrology, Beijing, China
Zhiheng Jiang	International Bureau of Weights and Measures (BIPM), Paris, France

Topic: S07: Satellite Navigation Augmentation Technology

Chairman

Rui Li	Beihang University, Beijing, China

Vice-chairmen

Jinping Chen	Beijing Satellite Navigation Center, Beijing, China
Shaojun Feng	Imperial College London Qianxun Positioning Network, Co., Ltd., Shanghai, China
Dun Wang	Space Star Aerospace Technology Applications Co., Ltd., Heilongjiang, China
Liwen Dai	John Deere, Torrance CA, USA

Topic: S08: Test and Assessment Technology

Chairman

Xiaolin Jia	Xi'an Research Institute of Surveying and Mapping, Shaanxi, China

Vice-chairmen

Jianping Cao	Air Force Equipment Institute, Beijing, China
Jun Yang	National University of Defense Technology, Hunan, China
Dexiang Ming	Changsha Technology Research Institute of BeiDou Industry Safety, Hunan, China
Yang Gao	University of Calgary, Alberta, Canada

Topic: S09: User Terminal Technology

Chairman

Mingquan Lu	Tsinghua University, Beijing, China

Vice-chairmen

Wenjun Zhao	Beijing Satellite Navigation Center, Beijing, China
Baowang Lian	Northwestern Polytechnic University, Shaanxi, China
Ying Xu	Academy of Opto-Electronics, Chinese Academy of Sciences, Beijing, China
Sang Jeong Lee	Chungnam National University, Daejeon, South Korea

Topic: S10: PNT System and Multi-source Fusion Navigation

Chairman

Zhongliang Deng	Beijing University of Posts and Telecommunications, Beijing, China

Vice-chairmen

Hong Yuan	Academy of Opto-Electronics, Chinese Academy of Sciences, Beijing, China
Yongbin Zhou	National University of Defense Technology, Hunan, China
Jinling Wang	University of New South Wales, Australia

Topic: S11: Anti-interference and Anti-spoofing Technology

Chairman

Hong Li	Tsinghua University, Beijing, China

Vice-chairmen

Wei Wang	The 20th Research Institute of China Electronics Technology Group Corporation Shaanxi, China
Feixue Wang	National University of Defense Technology, Hunan, China
Xuebin Zhuang	The First Research and Development Center of China Aerospace Science and Technology Corporation Ltd., Beijing, China

Topic: S12: Policies, Regulations, Standards and Intellectual Properties

Chairman

Junlin Yang	Beihang University, Beijing, China

Vice-chairmen

Daiping Zhang	China Defense Science and Technology Information Center, Beijing, China
Yonggang Wei	China Academy of Aerospace Standardization and Product Assurance, Beijing, China
Huiying Li	Electronic Intellectual Property Center, Ministry of Industry and Information Technology, PRC, Beijing, China

Scientific Committee

Chairman

Jiadong Sun	China Aerospace Science and Technology Corporation, Beijing, China

Vice-chairmen

Rongjun Shen	China Satellite Navigation System Committee, Beijing, China
Jisheng Li	China Satellite Navigation System Committee, Beijing, China
Qisheng Sui	China Satellite Navigation System Committee, Beijing, China
Changfeng Yang	China Satellite Navigation System Committee, Beijing, China
Zuhong Li	China Academy of Space Technology, Beijing, China
Shusen Tan	Beijing Satellite Navigation Center, Beijing, China

Executive Chairmen

Jingnan Liu	Wuhan University, Hubei, China
Yuanxi Yang	China National Administration of GNSS and Applications, Beijing, China

Executive Members

Organizing Committee

Directors

Deputy Directors

Jiaqing Ma	China Satellite Navigation Office, Beijing, China
Guangzhi Jiang	Beijing Municipal Bureau of Economy and Information Technology, Beijing, China
Xianwei Zhi	Beijing Shunyi District People's Government, Beijing, China

Secretary-General

Haitao Wu	Satellite Navigation Headquarters, Chinese Academy of Sciences, Beijing, China

Deputy Secretary-General

Weina Hao	Satellite Navigation Headquarters, Chinese Academy of Sciences, Beijing, China
Wenhai Jiao	China Satellite Navigation Engineering Center, Beijing, China
Jing You	Beijing Municipal Bureau of Economy and Information Technology, Beijing, China
Xiongjing Lan	Beijing Shunyi District Economic and Information Commission, Beijing, China

Committee Members

Qun Ding	The 20th Research Institute of China Electronics Technology Group Corporation, Shaanxi, China
Qiang Ma	Beijing Airport Economic Core Area Management Committee, Beijing, China
Ze Wang	Beijing Shunxin Holding Group Co., Ltd., Beijing, China
Chunsheng Wang	Haidian Investment Promotion Bureau, Beijing, China
Li Wang	International Cooperation Research Center, China Satellite Navigation Office, Beijing, China
Bo Wang	Academic Exchange Center, China Satellite Navigation Office, Beijing, China

Contents

Satellite Orbit and System Error Processing

Calculating the Mean Orbit Elements of Navigation Satellites Using Hilbert-Huang Transformation

Nan Ye[1(✉)], Haiyue Li[2], Wendong Zhong[2], Yufan He[2], and Yu Ren[2]

[1] State Key Laboratory of Astronautic Dynamic, Xi'an Satellite Control Center, Xi'an, China
nl_l024@163.com
[2] State Key Laboratory of Astronautic Dynamic, Xi'an, China

Abstract. When the navigation satellite GEO performs a station keeping, high-precision orbit elements are required. The analytical solution can hardly meet the high-precision requirement while the spectrum analysis method based on Fourier analysis theory has limitations. The Hilbert-Huang transform theory decomposes the signal adaptively into a finite number of intrinsic modes and residual signals that characterize the trend of the signal through empirical mode decomposition. It is strong adaptable and frequency sensitive, so that it can give spectral analysis to the oscular orbit ephemeris sequence effectively. By analyzing the data of Beidou 3G01 satellite positioned on November 9th, 2018, a clear time-varying frequency and a set of mean orbit elements that characterize the mean motion are obtained.

Keywords: GEO · HHT · EMD · Orbit element

1 Introduction

The Beidou-3 project is a global satellite navigation system independently built by China, including three geosynchronous orbit GEO satellites. Due to the influence of the orbit motion, the geosynchronous satellites have long-term, long-period, medium-long and short terms. In order to maintain the fixed position, the satellite needs to overcome long-term and long-period perturbation. This raises a high demand for the identification and separation of periodic motion. When the geosynchronous orbit satellites perform position maintenance (especially for colocation control), in order to eliminate the coupling effect of the positioning target, the short term perturbation needs to be separated from the satellite ephemeris [1]. In order to improve the accuracy of navigation calculations and reduce the computational load of on-board computers, it is also necessary to accurately compress the satellite oscular ephemeris. The mean orbit elements and quasi-mean elements using analytical methods are important method for separating the short terms of the periodic perturbation motion of geosynchronous satellites. In 1959, Kozai used the idea of averaging in nonlinear analytical mechanics to propose the mean orbit element for the perturbation motion of satellites in the Earth's non-spherical gravitational field [2]. The mean elements method can be used to construct the small

J. Sun et al. (Eds.): CSNC 2019, LNEE 563, pp. 3–15, 2019.
https://doi.org/10.1007/978-981-13-7759-4_1

deviation perturbation form solution of the satellite perturbation equation, which plays an important role in the satellite orbit determination and quantitative analysis of satellite motion [3]. The analysis method has several problems. The form of the power series will be very complicated when the solution order is high. The coherence of the solution also makes it difficult to identify and separate the periodicity of the perturbation motion. It is also difficult to accurately separate the satellite short term perturbation caused by Three-body gravity and solar radiation pressure. Only the lunar gravity causes the eccentricity to be half-month short-term term of about 0.00005. With the development of dynamic model and computer technology, the orbit accuracy of geosynchronous satellites has reached centimetres [4]. At the same time, the theory and method of time-frequency signal analysis such as wavelet analysis have also made great progress. From the perspective of engineering application, this paper uses the numerical calculation method to identify and separate the periodic perturbation information of the satellite precise ephemeris, and obtain the high-precision mean orbit elements.

2 Mean Orbit Elements Calculation

2.1 Analytical Method

The mean orbit elements method was firstly applied by Kozai [1] to the analytical solution of the earth satellite under the influence of the perturbation of the earth's non-spherical gravitational force (mainly with harmonics j2, j3 and j4). The mean elements can represent the sum of the zero-order term, the first-order long-term change term, the second-order long-term change term, and even the higher-order long-term change term. The mean elements including only the second-order long-term change term is constructed as follows:

$$
\begin{cases}
\bar{\sigma}(t) = \bar{\sigma}^{(0)}(t) + \sigma_1(t-t_0) + \sigma_2(t-t_0) + \cdots \\
\bar{\boldsymbol{\sigma}}^{(0)}(t) = [a_0 \quad e_0 \quad i_0 \quad \Omega_0 \quad \omega_0 \quad M_0 + n_0(t-t_0)]^T \\
\boldsymbol{\sigma}_1(t-t_0) = \left[0 \quad 0 \quad 0 \quad -\frac{A_2}{\bar{p}^2}\bar{n}\cos\bar{i}(t-t_0) \quad \frac{A_2}{\bar{p}^2}\bar{n}\left(2-\frac{5}{2}\sin^2\bar{i}\right)(t-t_0) \quad \frac{A_2}{\bar{p}^2}\bar{n}\left(1-\frac{3}{2}\sin^2\bar{i}\right)\sqrt{1-\bar{e}^2}(t-t_0)\right]^T \\
\Omega_2(t-t_0) = -\frac{\bar{n}\cos\bar{i}}{\bar{p}^4}\left[A_4\left(\left(\frac{6}{7}+\frac{9}{7}\bar{e}^2\right)-\sin^2\bar{i}\left(\frac{3}{2}+\frac{9}{4}\bar{e}^2\right)\right)+A_2^2\left(\left(\frac{3}{2}+\frac{1}{6}\bar{e}^2+\sqrt{1-\bar{e}^2}\right)-\sin^2\bar{i}\left(\frac{5}{3}-\frac{5}{24}\bar{e}^2+\frac{3}{2}\sqrt{1-\bar{e}^2}\right)\right)\right] \\
\omega_2(t-t_0) = \frac{A_4}{\bar{p}^4}\bar{n}\left[\left(\frac{12}{7}+\frac{27}{14}\bar{e}^2\right)-\sin^2\bar{i}\left(\frac{94}{14}+\frac{27}{4}\bar{e}^2\right)+\sin^4\bar{i}\left(\frac{21}{4}+\frac{81}{16}\bar{e}^2\right)\right]+ \\
\qquad \frac{A_2^2}{\bar{p}^4}\bar{n}\left[\left(4+\frac{7}{12}\bar{e}^2+2\sqrt{1-\bar{e}^2}\right)-\sin^2\bar{i}\left(\frac{103}{12}+\frac{3}{8}e^2+\frac{11}{2}\sqrt{1-\bar{e}^2}\right)+\sin^4\bar{i}\left(\frac{215}{48}-\frac{15}{32}\bar{e}^2+\frac{15}{4}\sqrt{1-\bar{e}^2}\right)\right] \\
M_2(t-t_0) = \frac{A_2^2}{\bar{p}^4}\bar{n}\sqrt{1-\bar{e}^2}\left\{\left[\frac{1}{2}\left(1-\frac{3}{2}\sin^2\bar{i}\right)^2\sqrt{1-\bar{e}^2}+\left(\frac{5}{2}+\frac{10}{3}\bar{e}^2\right)-\left(\frac{19}{3}+\frac{26}{3}e^2\right)\sin^2\bar{i}+\left(\frac{233}{48}+\frac{103}{12}\bar{e}^2\right)\sin^4\bar{i}+\right.\right. \\
\qquad \left.\left.\frac{\bar{e}^4}{1-\bar{e}^2}\left(\frac{35}{12}-\frac{35}{4}\sin^2\bar{i}+\frac{315}{32}\sin^4\bar{i}\right)\right]+\left(\frac{A_4}{A_2^2}\right)\bar{e}^2\left(\frac{9}{14}-\frac{35}{14}\sin^2 i+\frac{45}{16}\sin^4\bar{i}\right)\right\} \\
\bar{n} = \bar{a}^{-3/2},\ \bar{p} = \bar{a}(1-\bar{e}^2),\ A_2 = \frac{3}{2}J_2,\ A_3 = -J_3,\ A_4 = -\frac{35}{8}J_4
\end{cases}
\tag{2.1}
$$

Liu et al. proposed the concept of quasi-mean elements [5]. The quasi-mean elements only separated the short term of the perturbation solution. The difference is that the quasi-mean elements also includes a first-order long-period term, a second-order long-period term, and even a higher-order long-period term, that is,

$$\begin{aligned}\bar{\sigma}(t) &= \bar{\sigma}^{(0)}(t) + (\sigma_1(t-t_0) + \sigma_2(t-t_0) + \cdots) \\ &+ \left(\sigma_L^{(1)}(t-t_0) + \sigma_L^{(2)}(t-t_0) + \cdots\right)\end{aligned}. \tag{2.2}$$

Since the formula of the mean elements containing only the second-order long-term term is already quite complicated, the analytical expression is not given here. It should be pointed out that the long-period term of the eccentricity e and the orbital inclination i is not 0, although. The first-order long-period term of a $a_L^{(1)}(t-t_0) = 0$, but its second-order long-period term $a_L^{(2)}(t-t_0)$ is not 0. Therefore, the six mean orbit elements contain periodic variation terms, and these periodic variation terms cannot be eliminated by polynomial fitting.

The advantage of the analytic method is that the physical meaning is clear, and it can be converted between the oscular elements and mean elements. However, the high-order term structure is complex, the rounding error is large, and the analytical solution for the dissipative perturbation is low, the conversion accuracy too low to meet the needs of high-precision numerical calculation.

2.2 Harmonic Decomposition

Determining the coefficients in the expansion is a classic time domain fitting problem when the long-term term order and the periodic term frequency are known. For the orbit elements of any epoch time, there is:

$$f(t) \approx \sum_{k=0}^{m} a_k \Phi_k(t) = \Phi^T(t) P,\ t \in \left[t_0, t_f\right]. \tag{2.3}$$

$\Phi(t) = \begin{pmatrix} \Phi_0(t) \\ \vdots \\ \Phi_m(t) \end{pmatrix}$ is basis function column vector. $P = \begin{pmatrix} a_0 \\ \vdots \\ a_m \end{pmatrix}$ is coefficient vector corresponding to the basis function.

The orbit elements at time series $t_i \in \left[t_0, t_f\right],\ i = 1, 2, \cdots, n$ Can be described as:

$$\begin{pmatrix} \Phi^T(t_1) \\ \vdots \\ \Phi^T(t_n) \end{pmatrix} P = \begin{pmatrix} f(t_1) \\ \vdots \\ f(t_n) \end{pmatrix} \tag{2.4}$$

The above equations are generally over determined equations, and the least squares solution is:

$$\hat{P} = \left(\Phi^T \Phi\right)^{-1} \Phi^T f, \tag{2.5}$$

where $f = \begin{pmatrix} f(t_1) \\ \vdots \\ f(t_n) \end{pmatrix}$, $\Phi = \begin{pmatrix} \Phi^T(t_1) \\ \vdots \\ \Phi^T(t_n) \end{pmatrix}$.

When the long-period term is decomposed by the ephemeris signal with a short time, the conditional number of the regular matrix will be very large, close to the ill-conditioned matrix, and the more stable coefficient matrix singular value decomposition algorithm is often used in practical.

The limitation of the harmonic decomposition method is that the basis function frequency is fixed and cannot adapt to the processing of time-varying signals. However, there is a frequency coupling phenomenon in the fine perturbation modelling, and the actual perturbation period is not fixed. This method is also subject to the incompleteness of rounding error and perturbation modelling, and the adaptability is not strong.

2.3 Hilbert-Huang Transformation

In 1996, American Chinese Norden. Huang et al. created a time-frequency analysis method for Hilbert-Huang Transformation (HHT) for the concept of instantaneous frequency [6, 7]. The method proposes the concept of Intrinsic Mode Functions (IMF) and the method of decomposing arbitrary signals into intrinsic mode functions—Empirical Mode Decomposition (EMD), which establishes the instantaneous frequency as a basic variable that characterizes the alternating signal, and a time-frequency analysis method in which IMF signal is the basic time domain signal.

Since the orbital perturbation cannot be fully modelled and the perturbation frequency is coupled, the unmodelled periodic components cannot be completely separated using a finite fixed basis function. Regardless of the physical constraints, the Fourier decomposition will bring false periodic signals and false frequency phenomena. Limited by the uncertainty of Heisenberg, the time-frequency analysis method based on Fourier analysis theory cannot describe the transformation of frequency with time. The perturbation orbit is a typical nonlinear non-stationary time series. The HHT theory adaptively decomposes the orbital signal into a finite number of IMFs and residual signals that characterize the trend of the signal through EMD. It has strong adaptive performance and sensitive frequency detection. By performing a HHT on the sequence of oscular orbit element, the mean orbit elements that characterize the motion can be obtained.

The characteristic of HHT is that it does not directly perform Hilbert transform on the signal, but first studies the reasonable definition of the IMF signal, and uses EMD method to decompose the signal into IMFs, and calculates each component separately by the definition of instantaneous frequency. HHT not only utilizes the reasonable definition of instantaneous frequency, but also consistent with the multi-component result recognition of the signal, which can more accurately reflect the physical characteristics of the system.

3 Analysis of Algorithms

3.1 Dynamic Perturbation

Due to the J_{22} term of the ellipsoid of the Earth's equatorial plane, that is, the triaxiality of the Earth, the stationary orbiting satellite at the nominal longitude λ receives an additional tangential gravitational acceleration. The tangential acceleration will cause the semi-major axis of the geostationary orbit to change, which will cause the orbital flat motion to be inconsistent with the angular velocity of the Earth's rotation, causing the satellite to deviate from the nominal fixed-point longitude. The perturbation equation for the semi-major axis of the stationary orbit caused by the non-spherical perturbation of the Earth is:

$$\begin{aligned} \frac{da}{dt} &= -\frac{2}{3}\frac{a_c}{n_c}\cdot\Gamma_\lambda \\ \Gamma_\lambda &= -3n_c^2\left\{\begin{array}{l} -6J_{22}\left(\frac{R_e}{a_c}\right)^2\sin 2(\lambda-\lambda_{22}) \\ \quad +\frac{3}{2}J_{31}\left(\frac{R_e}{a_c}\right)^3\sin(\lambda-\lambda_{31}) \\ \quad -45J_{33}\left(\frac{R_e}{a_c}\right)^3\sin 3(\lambda-\lambda_{33}) \end{array}\right\} \end{aligned} \tag{3.1}$$

Where a_c is the semi-major axis of the geostationary orbit. n_c is the angular velocity of the earth's rotation. J_{nm} and λ_{nm} are the Earth's gravitational field association Legendre polynomial coefficient and geographic longitude, respectively. E is the satellite longitude of the satellite.

Sun and moon perturbation does not produce long-period perturbations on the semi-major axis of the stationary orbit. The half-long axis change rate of the orbit in one circle is zero, but a short period is generated for the semi-major axis of the orbit, and the period is half a solar day. The amplitude of the short term change rate is related to the elevation angle of the sun and the moon to the celestial equator and the phase of the sun and the moon. The short term oscillation of the semi-major axis of the sun and moon perturbation orbit is expressed as:

$$\frac{da}{dt} = -3a_s\frac{n_k^2}{n_e}\cos^2\delta_k\sin 2\lambda_k \tag{3.2}$$

Where $a_s = 42164.2$ km is the semi-major axis of the stationary orbit under the two-body problem. n_k is the angular velocity of the third body (day, month) around the center of the earth, n_e is the angular velocity of the earth's rotation, δ_k is the vertical angle of the third body, and λ_k is the difference between the right ascension of the satellite and the third body.

The short term perturbation of the semi-major axis of the stationary orbit caused by the sun's light pressure, is a period of one day. The amplitude of the semi-major axis caused by light pressure is greatest when the sun is at the vernal equinox or the equinox. The specific expression is:

$$\frac{da}{dt} = \frac{2}{n} C_R \left(\frac{S}{m}\right) P_0 \cos\delta_s \sin(l - \alpha_s) \tag{3.3}$$

Where n is the orbital angular velocity, C_R is the optical pressure coefficient, $\frac{S}{m}$ is the area to mass ratio, P_0 is the solar radiation pressure per unit area, (α_s, δ_s) is the solar right ascension declination, and l is the satellite mean right ascension.

Similarly, it modeled by the perturbation potential, to establish and eccentricity perturbed inclination motion equation is as follows:

$$\begin{aligned} \frac{de}{dt} &= \frac{1-e^2}{na^2e}\frac{\partial R}{\partial M} - \frac{\sqrt{1-e^2}}{na^2e}\frac{\partial R}{\partial \omega} \\ \frac{di}{dt} &= \frac{\cot i}{na^2\sqrt{1-e^2}}\frac{\partial R}{\partial \omega} - \frac{\csc i}{na^2\sqrt{1-e^2}}\frac{\partial R}{\partial \Omega} \end{aligned} \tag{3.4}$$

The effects of the perturbation on the long-term, long-period, medium and short period and short-term caused by the number of orbits are organized as follows (Table 1):

Table 1. The perturbation effects on orbit elements

	Cycle/frequency	Perturbation source	Semi-major axis	Eccentricity vector	Inclination vector
Long term	Constant term	Two-body perturbation	√	√	√
	first degree term	Sun and moon gravity			√
Long period	Year/n_s	Solar gravity		√	√
	Half year/$2n_s$				√
	Quarter/$3n_s$				√
Medium and short period	Mouth/n_m	Lunar gravity		√	√
	Half mouth/$2n_m$				√
	Ten days/$3n_m$				√
Short period	Day/n_e	Earth's non-spherical perturbation/sun and moon gravity/solar pressure perturbation	√	√	√
	Half day/$2n_e$		√	√	√

Where $n_s = 0.0172$, $n_m = 0.23$, $n_e = 6.283$ (radian/day), the eccentricity vector is defined as $\vec{e} = e\cos(\Omega + \omega) + \mathrm{j}e\sin(\Omega + \omega)$, and the inclination vector is defined as $i = i\cos(\Omega) + \mathrm{j}\,i\sin(\Omega)$.

3.2 Empirical Mode Decomposition

The intrinsic mode function IMF defined in the HHT transform is a type of signal that satisfies the physical interpretation of a single component signal [8]. At each moment, there is only a single frequency component, which is the instantaneous frequency in the physical sense. The IMF component must satisfy the following two conditions: one is that the number of extreme points and the number of zero crossings are the same or at most one, and the other is that the upper and lower envelopes are locally symmetric about the time axis.

The empirical mode decomposition EMD method assumes that any signal is composed of different IMFs [9]. The method steps are: first finding the maximum value and the minimum value of the signal $x(t)$, and obtaining the upper envelope $U_x(t)$ and the lower envelope $L_x(t)$ of the signal by cubic spline fitting, and calculating the mean value of the upper and lower envelopes:

$$m_1(t) = \frac{U_x(t) + L_x(t)}{2} \tag{3.5}$$

Subtracting this mean $m_1(t)$ from the original signal x(t) signal yields the first component $h_1(t)$, i.e.: $h_1(t) = h_1(t) - m_1(t)$ Check whether $h_1(t)$ is the two conditions that satisfy the IMF component. If it is not satisfied, perform the re-screening, that is, calculate the mean line $m_1(t)$ through the upper and lower envelopes of $h_1(t)$, and obtain a new component. Repeat the above process k times:

$$h_{1k}(t) = h_{1(k-1)}(t) - m_{1k}(t) \tag{3.6}$$

Until $h_{1k}(t)$ satisfies the condition of the IMF component, the $h_{1k}(t)$ obtained at this time is taken as the first IMF component $C_1 = h_{1k}(t)$, which contains the local high frequency portion of the original signal $x(t)$.

Subtracting C_1 from the original signal $x(t)$ yields the residual signal $r_1(t)$:

$$r_1(t) = x(t) - C_1 \tag{3.7}$$

The residual signal is subjected to screening as described above to obtain more IMF until the final IMF is separated. The final residual signal $r_n(t)$ is a constant or constant trend change, which is the long-term trend of the number of mean orbital element in this scenario.

At this point, the signal $x(t)$ is decomposed into the sum of n IMFs and residual signal $r_n(t)$: $x(t) = \sum_{1}^{n} C_i(t) + r_n(t)$.

3.3 HHT Perform

The mathematical basis of the Hilbert Transform (HT), proposed by the German mathematician Hilbert, is an important tool in signal analysis [10, 11]. Perform a Hilbert transform on each IMF with the expression:

$$\overline{C_i}(t) = C_i(t) * \frac{1}{\pi t} = \frac{1}{\pi} P \int_{-\infty}^{+\infty} \frac{C_i(\tau)}{t-\tau} d\tau, \tag{3.8}$$

where P is the Cauchy principal value. The HT can be understood as the IMF passing a linear time-invariant system with a unit impulse response of $\frac{1}{\pi t}$.

Constructing an analytical signal:

$$z_i(t) = C_i(t) + j\overline{C_i}(t) = a_i(t)e^{j\phi_i(t)} \tag{3.9}$$

where $a_i(t) = \sqrt{C_i^2(t) + \overline{C}_i^2(t)}$ is the amplitude and $\phi_i(t) = \arctan(\overline{C_i}(t)/C_i(t))$ is the phase. The instantaneous frequency of each IMF is defined as $\omega_i(t) = \frac{d\phi_i(t)}{dt}$, then the signal can be expressed as:

$$x(\mathrm{t}) = \mathrm{Re}\sum_{i=1}^{n} a_i(\mathrm{t})\mathrm{e}^{j\int \omega_i(\mathrm{t})\mathrm{dt}} + r_n(\mathrm{t}) \tag{3.10}$$

The signal amplitude can be expressed as a function of time t and instantaneous frequency $\omega_i(t)$, so called the Hilbert spectrum. Due to the introduction of instantaneous frequency, the limitation of Fourier variation is broken, so that HHT transform can be applied to the processing of nonlinear systems and non-stationary signals.

4 Calculation Results

The Beidou-3 satellite project is a global satellite navigation system independently built by China, including five GEO satellites pointing at 60°, 80°, 110°, 140° and 160° east longitude. Beidou 3G01 is the first geostationary orbit satellite of the Beidou-3 project. It was launched at the Xichang Satellite Launch Center on November 1, 2018, Beijing time and was successfully positioned on November 9th, Beijing time. It can provide large-capacity short message service, and satellite-based enhancement services for civil aviation users. In this paper, 3 months numerical predicted oscular orbit of Beidou3G01 is analyzed.

4.1 EMD Decomposition

HHT is a repetitive cycle decomposition process. In theory, the decomposition ends when the signal margin cannot be decomposed into more IMFs. However, the last few IMF amplitudes are often too small to lose physical meaning, but if the conditions are too loose, the useful signal components may be lost. Since the evolution of the orbit affected by perturbation is a deterministic nonlinear process, the frequency components of main perturbation can be estimated. Therefore, the number of iterations of the decomposition termination is consistent with the main perturbation period of Sect. 3.1, which has a clear physical meaning. The EMD decomposition of the semi-major axis and the eccentricity vector is shown in figure, where the eccentricity vector is processed as a complex signal (Figs. 1, 2 and 3):

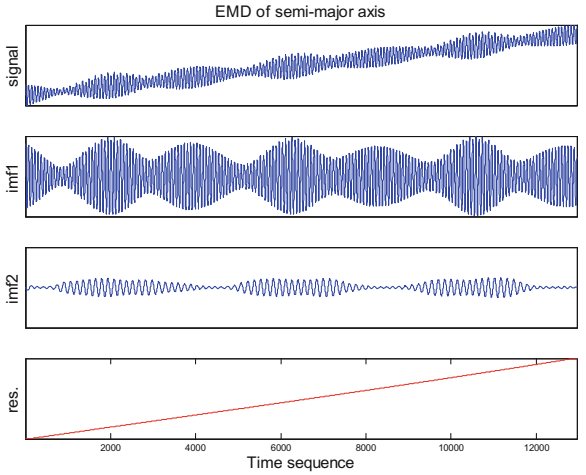

Fig. 1. EMD decomposition of semi-major axis

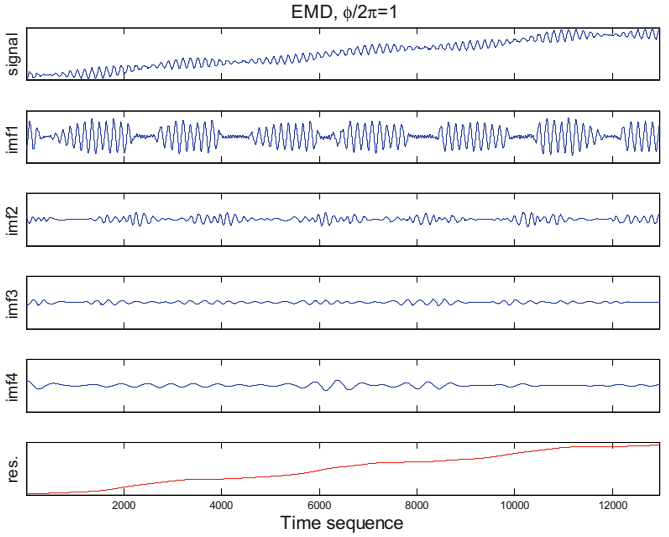

Fig. 2. EMD decomposition for real part of eccentricity vector

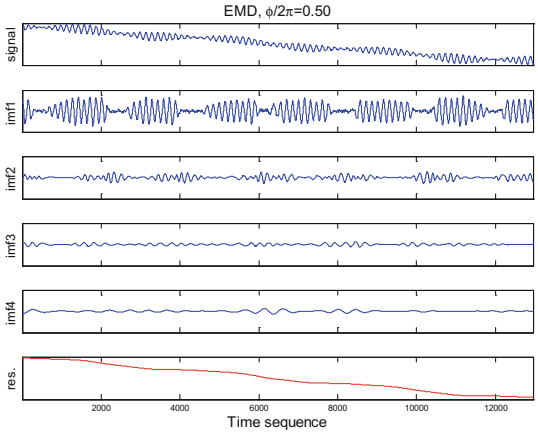

Fig. 3. EMD decomposition for imaginary part of eccentricity vector

It can be seen from the figure that the semi-major axis EMD decomposes 2 IMFs, corresponding to the daily and half-day periods of the semi-major axis perturbation evolution. The eccentricity vector decomposes 4 IMFs, corresponding to the year, month, day, and half-day periods of the eccentricity vector perturbation evolution.

4.2 Frequency Analysis

Decomposition semi-major axis as an example, perform HT to 2 IMF signals, the instantaneous frequency of the information changes over time, as shown (Fig. 4):

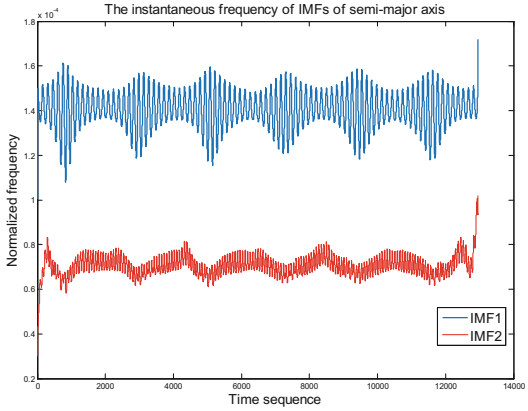

Fig. 4. Instantaneous frequency of IMFs of semi-major axis

As it can be seen from the figure, since the coupling perturbation period and other factors, the two frequencies obtained from IMF component are not constant but varies with time. HHF visually shows this change. The blue component IMF1 frequency is approximately twice the red component IMF2, corresponding to the semi-major axis perturbation day period term and half-day period term, respectively, and the physical meaning is clear.

4.3 Mean Orbit Elements Evolution

Apply the analytical method and the HHT methods respectively to the semi-major axis (topical), eccentricity and inclination vector time series. The comparison results of the mean orbit elements shown below (Figs. 5, 6 and 7).

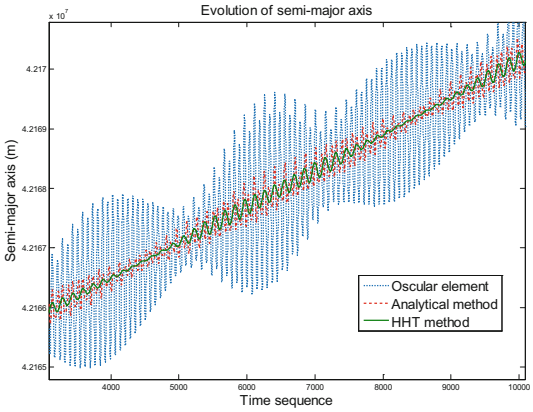

Fig. 5. Semi-major axis evolution

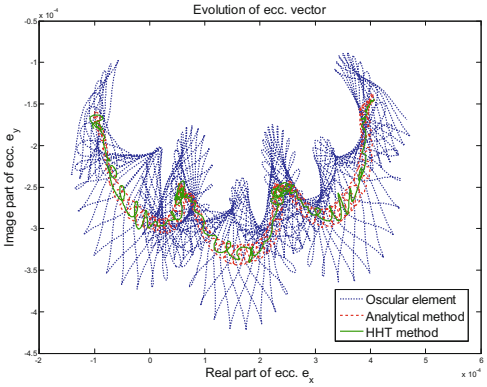

Fig. 6. Eccentricity vector evolution

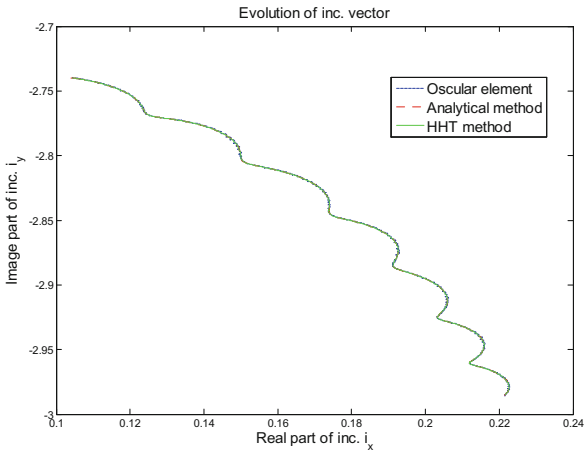

Fig. 7. Inclination vector evolution

It can be seen from the figure that the mean semi-major axis and the mean eccentricity vector solved by the HHT method have significantly reduced jitter, and the stability and accuracy are better than the analytical method. Due to the inclination of the trend vector is much greater than perturbation fluctuations, it shows rarely difference between the two methods.

5 Conclusions

For the deficiencies of the analytical method and the Fourier spectrum analysis method, the Hilbert-Huang transform is introduced. Under the premise that no preset basis function needed, the HHT transform adaptively decomposes the oscular orbit elements ephemeris data into multiple IMF components and residual trend information. The instantaneous frequency information with time is obtained after perform HT to separated IMF component, which is consistent with the perturbation analysis result. The mean semi-major axis and the mean eccentricity vector solved by the HHT method have significantly reduced jitter, and the stability and accuracy are better than the analytical method. However, the inclination vector is less obvious because its perturbation fluctuation is far weak than trend.

The instantaneous frequency fluctuations of the separated IMF signals reflect the error portion of the perturbation period coupling and modelling and real perturbation, including the influence of the lunar high-order gravitational field and the lunar orbital eccentricity. The HHT decomposition termination condition problem, the influence of the fitting method used in searching the IMF, and the endpoint problem causing the inaccurate frequency estimation [12], etc., can be further explored.

References

1. Li H, Gao Y, Yu P et al (2009) Research on co-location control strategy of geostationary orbit. J Astronaut 30(3):967–973
2. Kozai Y (1959) The motion of a close earth satellite. Astron J 64:367
3. Brouwer D (1959) Solution of the problem of artificial satellite theory without drag. Astron J 64:378
4. Liu C, Li F (2018) Perturbation analysis method for Influence of satellite orbit error on positioning accuracy. Astron Res Technol 15(1):40–45
5. Liu L (1975) An artificial earth satellite perturbation calculation method. Astron J 16(1): 5–80
6. Huang NE, Shen Z, Long SR et al (1971) The empirical mode decomposition and the Hilbert spectrum for nonlinear and non-stationary time series analysis. Proc Roy Soc Lond A: Math Phys Eng Sci 1998(454):903–995
7. Huang NE, Wu MLC, Long SR et al (2003) A confidence limit for the empirical mode decomposition and Hilbert spectral analysis. Proc Roy Soc Lond A: Math Phys Eng Sci 459 (2037):2317–2345
8. Rilling G, Flandrin P, Goncalves P (2003) On empirical mode decomposition and its algorithms. In: IEEE-EURASIP workshop on nonlinear signal and image processing. NSIP 2003, Grado (I), vol 3, pp 8–11
9. Huang NE (2000) New method for nonlinear and nonstationary time series analysis: empirical mode decomposition and Hilbert spectral analysis. In: Wavelet applications VII, vol 4056. International Society for Optics and Photonics, pp 197–210
10. Feldman M, Seibold S (1999) Damage diagnosis of rotors: application of Hilbert transform and multihypothesis testing. J Vib Control 5(3):421–442
11. Feldman M (1997) Non-linear free vibration identification via the Hilbert transform. J Sound Vib 208(3):475–489
12. Chen Z, Zheng S (2003) Analysis of edge effect of EMD signal analysis method. Data Acquis Process 18(1):114–118

GNSS Orbit Prediction with Enhanced Solar Radiation Pressure Model

Bingbing Duan(✉) and Urs Hugentobler

Technical University of Munich, Arcisstr 21, 80333 Munich, Germany
{bingbing.duan,urs.hugentobler}@tum.de

Abstract. To serve real-time users, orbit prediction is in most cases used to provide real-time GNSS (Global Navigation Satellite System) orbit products. With precise Solar Radiation Pressure (SRP) model and sufficient ground tracking stations in orbit determination, the IGS (International GNSS Service) states that the officially published GPS Ultra-rapid (IGU) orbit products are prepared with 1D mean RMS of 5 cm. However, for the new emerging satellites the prevailing Empirical CODE Orbit Models (ECOM, ECOM2) are not always good enough, especially if the spacecraft is a stretched body satellite. In our former study, we showed that the use of an a priori box-wing (BW) model by taking our adjusted optical parameters enhanced the ECOM model and resulted in the best results for Galileo, BeiDou-2 GEO, BeiDou-3e and QZS-1 satellite orbits. In this contribution, we test the performances of ECOM, ECOM+BW, ECOM2 and ECOM2+BW models in orbit prediction. Daily precise orbits by using individual SRP models are taken as observed orbits. Consistencies between 3-h predicted orbits and precise orbits for individual SRP models are evaluated. Results show that the pure ECOM2 model performs in general better than the pure ECOM model for the stretch body satellites. The ECOM+BW model results in the best predictions for Galileo, BeiDou-2 GEO and QZS-1 satellites, for which the improvement of 3D RMS is about 10%, 50% and 60% respectively over the pure ECOM model. BeiDou-2 IGSO, MEO and BeiDou-3e predictions do not benefit much from the a priori box-wing model.

Keywords: GNSS · Solar Radiation Pressure · Orbit prediction · Box-wing

1 Introduction

The IGS began providing GPS Ultra-rapid (IGU) orbit products in November 2000, originally with updates every 12 h. Then, in April 2004 the update cycle was reduced to every 6 h (at 00:00, 06:00, 12:00, 18:00 UTC) (Choi et al. 2013). Each IGU is composed of 24-h observed orbits together with 24-h propagated orbits, and the start-stop epochs continuously shift by 6 h with each update. 1D mean RMS of the first 6-h prediction is about 5 cm for GPS and 8 cm for GLONASS, which can satisfy high accuracy real-time applications fairly well (Hadas and Bosy 2015).

Apart from the fully developed GPS and GLONASS systems, the European Galileo satellite navigation system, the Chinese BeiDou satellite navigation system (BDS) and the Japanese Quasi Zenith Satellite System (QZSS) are all advancing towards their

J. Sun et al. (Eds.): CSNC 2019, LNEE 563, pp. 16–23, 2019.
https://doi.org/10.1007/978-981-13-7759-4_2

global or regional services. As stated by the European Global Navigation Satellite Systems Agency (www.gsc-europa.eu) there are totally 24 Galileo satellites in space by the end of October 2018. The latest 4 Galileo satellites are still under commissioning whose signals are not yet available. BDS consists of three types of constellations: Geostationary Orbit (GEO), Inclined Geosynchronous Orbit (IGSO) and Medium Earth Orbit (MEO) satellites. By evaluating the performance of BeiDou-3 experimental (BeiDou-3e) satellites, the next generation BeiDou-3 is proposed to aggregate 3 GEO satellites, 3 IGSO satellites and 24 MEO satellites (Zhao et al. 2018). QZSS is a regional satellite navigation system developed by the Japan Aerospace Exploration Agency (JAXA). With the launches of QZS-4 in October 2017, there are now 4 QZSS satellites (QZS-1, QZS-2, QZS-3, QZS-4) in orbit.

To enhance the Multi-GNSS service, the IGS initiated the Multi-GNSS Experiment (MGEX) in August 2011. Montenbruck et al. (2017) summarized the achievements of Multi-GNSS orbits by a cross-comparison between individual analysis centres over half a year in 2016. Results show that the RMS values of Galileo, BeiDou-2 and QZSS orbits are not as good as for GPS and GLONASS orbits. The German Research Centre for Geosciences (GFZ) started to provide Ultra-rapid Multi-GNSS products since November 2015 with update every 3 h (Deng et al. 2016). Similar as post-processing orbits, BeiDou-2 GEO and QZS-1 predictions show worse accuracy than other satellites. In addition to the insufficient number and distribution of tracking stations the imperfect SRP model also limits the quality of the orbit products.

Technical University of Munich (TUM), one of the Multi-GNSS Experiment (MGEX) analysis centers has estimated the optical parameters of Galileo, BDS, and QZSS satellites based on the physical processes from SRP to accelerations (Duan et al. 2018a). We proved that combined with an a priori box-wing model based on our adjusted parameters the ECOM model results in the best orbits for all the new emerging satellites except for BeiDou-2 IGSO and BeiDou-2 MEO satellites. Based on this background, we test also the performance of the ECOM and ECOM2 model as well as their combination with the a priori box-wing model in orbit prediction.

2 Performance of Our Daily Adjusted Orbits

We have tested the performance of ECOM models and their combination with an a priori box-wing model that based on our estimated optical parameters at TUM.

- 5-parameter ECOM model
- 5-parameter ECOM+BW model
- 9-parameter ECOM2 model
- 9-parameter ECOM2+BW model.

We use a network of 80 tracking stations, in which all stations track Galileo and BeiDou-2 observations while 40 stations track QZS-1 observations. Data period starts from day 180 to day 365 in year 2017. Bernese software 5.3 (Dach et al. 2007) is modified to support the estimation. Setting and model options are listed in Table 1. Phase center offset (PCO) and variation (PCV) corrections follow the IGS14 ANTEX. Earth albedo is considered for all the satellites, but antenna thrust is not yet taken into

account. Station related parameters are all fixed on the daily GPS Precise Point Positioning solutions using the CODE products while estimating system bias for each station. Optical and other box-wing parameters of all the GNSS satellites are taken from Duan et al. (2018a).

Table 1. Settings and model options in orbit determination

Items	Value
Observations	Undifferenced ionosphere-free
Data arc	1 day
Sampling	5 min
Elevation cutoff	5°
PCO/PCV	IGS14 ANTEX
SRP model	ECOM w/o BW, ECOM2 w/o BW
Earth albedo	Considered (Rodriguez-Solano et al. 2012)
Antenna thrust	Not considered
Station coordinate/Troposphere	Fixed on GPS PPP solutions (CODE)
Receiver clock	Fixed on GPS PPP solutions (CODE)
Satellite clock	Estimated
Receiver system bias	Estimated

BeiDou-2 IGSO, BeiDou-2 MEO and QZS-1 satellites take two different attitude modes depending on the elevation of the Sun above the orbital plane (β). When the absolute value of β is greater equal than 4° BeiDou-2 IGSO and MEO satellites take yaw-steering (YS) mode while switching to orbit normal (ON) mode in case of the absolute value of β smaller than 4° (Dai et al. 2015). Ishijima et al. (2009) introduced that QZS-1 used a YS mode for most of its mission and switched to ON mode when the absolute value of β is smaller than 20°. In the latest IGS workshop 2018 that was held in Wuhan, China, we presented the standard derivation (STD) of Satellite Laser Ranging (SLR) residuals for all the estimated satellite orbits, as shown in Table 2 (Duan et al. 2018b).

Table 2. STD of SLR residuals for all the satellites (cm)

	ECOM	ECOM+BW	ECOM2	ECOM2+BW
Galileo	8.2	4.2	5.4	5.2
BeiDou-2 GEO	21.2	17.7	18.3	17.2
BeiDou-2 IGSO (YS)	10.0	10.8	14.1	16.4
BeiDou-2 IGSO (ON)	12.3	12.3	15.9	16.5
BeiDou-2 MEO (YS)	12.2	13.1	15.3	16.5
BeiDou-2 MEO (ON)	16.4	17.4	20.0	21.4
BeiDou-3e	14.7	12.5	18.2	12.7
QZS-1 (YS)	19.9	4.8	8.2	7.4
QZS-1 (ON)	33.7	10.5	28.2	19.3

The pure ECOM2 model performs better than the pure ECOM model for Galileo, BeiDou-2 GEO and QZS-1 orbits. Combined with the a priori box-wing model the ECOM model results in the best orbits for all the satellites except for BeiDou-2 IGSO and Beidou-2 MEO. The reason might be that SRP acceleration varies periodically if a satellite has asymmetric body dimensions. The higher Fourier series in the ECOM2 model compensate such periodical accelerations better than the ECOM model. However, deficiencies of the ECOM2 model occur when the QZS-1 satellite takes ON mode. We also find that the ECOM2+BW results are not as good as for ECOM+BW, which might indicate that once the periodical accelerations have been correctly modeled it is not necessary to estimate additional higher Fourier series in the Sun-satellite direction.

3 Evaluation of GNSS Orbit Predictions

Choi et al. (2013) showed how the accuracy of predicted orbits varied with the observed arc length for GPS satellites. Apart from that, the quality of the observed orbit itself also plays an essential role in precise orbit prediction (Lutz et al. 2016). However, since we use different SRP models in orbit determination the observed orbits are not identical in accuracy. Hence, in this contribution we do not evaluate the absolute accuracy of the predicted orbits. Only comparisons between the predicted orbits and the corresponding precise orbits are taken to investigate the consistencies of the predictions by using different SRP models. The observed arc length is 24 h, and the predicted arc length is 3 h. Data period starts from day 330 in year 2017 to day 060 in year 2018 for BeiDou-3e satellites while starts from day 200 to day 300 in year 2017 for all the other satellites.

RMS values of Galileo, BDS and QZS-1 predictions are discussed one after the other. Maneuver days of all the satellites are excluded from our analysis. All the Galileo satellites are constantly in YS mode, the averaged RMS of all the Galileo satellites over 100 days are shown in Table 3. The 3-h predicted Galileo orbits agree with the estimated orbits fairly well in all the four cases. The ECOM+BW model results in the best RMS values in all the three components. The improvements of 3D RMS are about 10% and 5% over the pure ECOM and ECOM2 models.

Table 3. Mean RMS of Galileo 3-h predicted orbits (unit: cm)

Solution	Radial	Along-track	Cross-track	3D
ECOM	2.5	5.8	3.4	7.2
ECOM+BW	2.2	5.3	2.4	6.2
ECOM2	2.7	5.5	2.6	6.7
ECOM2+BW	2.7	5.4	2.5	6.6

For BeiDou-2 GEO satellites the C-band telecommunication antenna contributes to the z-area, which makes them more like stretch body satellites. The RMS values are

shown in Table 4. Obviously, BeiDou-2 GEO orbit predictions benefit much from the a priori box-wing model. The ECOM+BW model results in the best predictions, which marks notable improvements of about 50% and 30% over the pure ECOM and ECOM2 models. However, the use of the a priori box-wing model do not help the ECOM2 model for BeiDou-2 GEO satellite in orbit prediction.

Table 4. Mean RMS of BeiDou-2 GEO 3-h predicted orbits (unit: cm)

Solution	Radial	Along-track	Cross-track	3D
ECOM	43.3	80.9	3.9	91.8
ECOM+BW	28.4	38.4	5.9	48.1
ECOM2	38.0	52.8	4.2	65.2
ECOM2+BW	37.3	54.8	6.0	66.6

BeiDou-2 IGSO and MEO satellites take two attitudes according to the β angle. Figure 1 shows the daily 3D RMS of 3-h predicted orbits of BeiDou-2 IGSO satellite C09. Predictions in the ON mode exhibit larger RMSs than those in the YS mode, and the ECOM2 model shows worse performance than the ECOM model in the ON mode. The averaged RMSs of all the BeiDou-2 IGSO and MEO satellites are shown in Table 5. The ECOM+BW model shows the best orbit predictions despite the improvement over the pure ECOM model is small. RMSs of the ECOM2 model in the ON mode are two times larger than those of the ECOM model. Thus, it is not recommended to use ECOM2 model for the IGSO and MEO satellite orbit prediction, especially in the ON mode.

Table 5. Mean RMS of BeiDou-2 IGSO and MEO 3-h predicted orbits (unit: cm)

Solution	Radial		Along-track		Cross-track		3D	
	YS	ON	YS	ON	YS	ON	YS	ON
ECOM	5.9	16.3	8.6	28.4	5.8	4.1	11.9	33.0
ECOM+BW	5.8	15.9	7.4	28.0	5.3	3.8	10.8	32.4
ECOM2	6.4	37.1	7.4	41.9	6.4	4.1	11.7	56.1
ECOM2+BW	6.7	34.3	7.6	38.1	6.0	3.7	11.7	51.4

BeiDou-3e satellites do not use ON mode but experience midnight and noon maneuvers when $|\beta| < 3°$. In our experiment, only around 20 stations track BeiDou-3e observations. The averaged RMSs of all the 5 BeiDou-3e 3-h predicted orbits are shown in Table 6. The ECOM models are in general slightly better than the ECOM2 models. The use of the a priori box-wing model does not enhance the ECOM model while the ECOM2 model benefits from the a priori box-wing model. If in the future more stations track BeiDou-3e observations we can get more precise results.

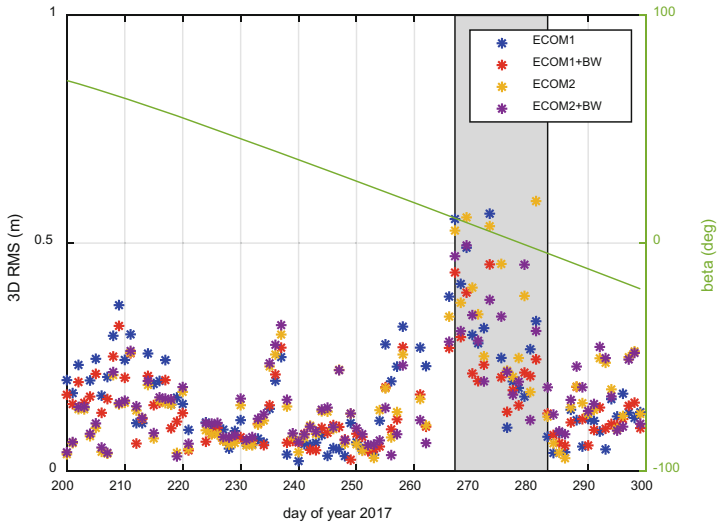

Fig. 1. Daily 3D RMS of 3-h predicted orbits of satellite C09. The β angle is indicated by a solid green line and the ON mode period is indicated in grey.

Table 6. Mean RMS of BeiDou-3 3-h predicted orbits (unit: cm)

Solution	Radial	Along-track	Cross-track	3D
ECOM	8.7	23.0	9.7	26.5
ECOM+BW	8.7	23.0	9.4	26.3
ECOM2	11.8	24.2	11.0	29.1
ECOM2+BW	8.7	23.6	10.4	27.2

QZS-1 satellite takes both YS and ON modes. Figure 2 illustrates the daily 3D RMSs of QZS-1 3-h predicted orbits for the four types of SRP models covering both the YS and ON mode periods. The pure ECOM model show clear larger scatter RMS values than the other SRP models. Use of the a priori box-wing model reduces such deficiency fairly well and results in the best predictions both in YS and ON modes. The averaged RMSs of QZS-1 3-h predicted orbits are shown in Table 7. The pure ECOM2 model reduces the 3D RMS of overall 30% over the pure ECOM model. Combined with the a priori box-wing model the ECOM models results in the best QZS-1 orbit predictions. The improvements are about 40% and 60% over the pure ECOM2 model and ECOM model.

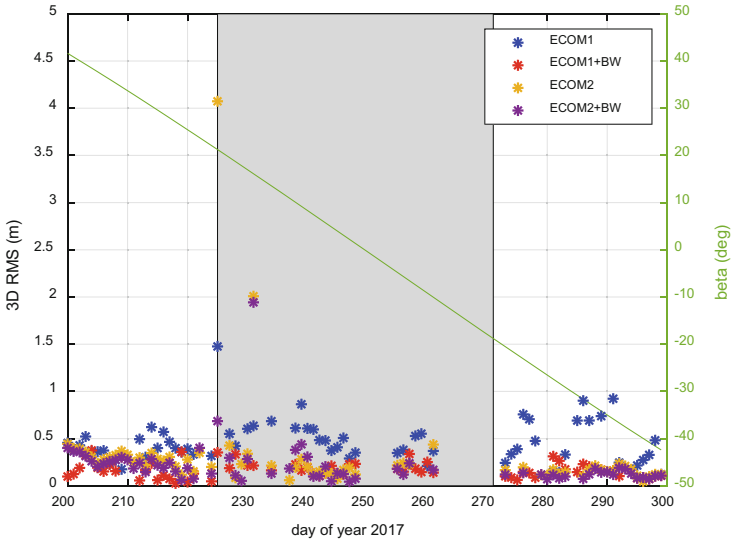

Fig. 2. Daily 3D RMS of 3-h predicted orbits of QZS-1 satellite. The β angle is indicated by a solid green line and the ON mode period is indicated in grey.

Table 7. Mean RMS of QZS-1 3-h predicted orbits (unit: cm)

Solution	Radial		Along-track		Cross-track		3D	
	YS	ON	YS	ON	YS	ON	YS	ON
ECOM	23.0	27.4	19.1	38.7	12.1	4.1	32.2	47.6
ECOM+BW	6.5	11.7	8.1	13.8	4.0	2.1	11.1	18.2
ECOM2	17.9	20.1	14.6	14.3	6.3	6.7	24.0	25.5
ECOM2+BW	9.1	17.9	11.5	14.1	4.8	5.0	15.5	23.3

4 Summary and Conclusion

Solar radiation pressure is the dominant non-gravitational perturbation for GNSS satellites. Without a precise surface model, the ECOM and ECOM2 models are in most cases used in orbit determination and orbit prediction. However, for the new emerging satellites, for instance Galileo, BDS and QZSS satellites the prevailing ECOM models are not good enough, especially if the spacecraft is a stretch body satellite or is maintaining ON mode.

By taking the adjusted box-wing parameters from our former study as well as the performances of individual SRP models in orbit determination, we aims at developing an optimal SRP model for GNSS orbit prediction. ECOM, ECOM+BW, ECOM2 and ECOM2+BW models are tested in orbit prediction by taking the daily orbits as observed orbits. The corresponding daily precise orbits are employed to evaluate the consistency of predicted orbits by using individual SRP models.

Results show that combined with the a priori box-wing model the ECOM model results in the best orbit predictions for Galileo, BeiDou-2 GEO and QZS-1 orbits. The improvement is about 10%, 50% and 60% over the pure ECOM model respectively. BeiDou-2 IGSO, BeiDou-2 MEO and BeiDou-3e orbit predictions do not benefit much from the a priori box-wing model. Furthermore, the pure ECOM2 model shows better performance than the pure ECOM model if the spacecraft is a stretch body satellite, and the use of the a priori box-wing model enhance both ECOM and ECOM2 models if a satellite is in ON mode. Thus, we would like to recommend using ECOM+BW model for GNSS orbit prediction.

Acknowledgments. This research is based on the analysis of Multi-GNSS observations provided by the IGS MGEX. The effort of all the agencies and organizations as well as all the data centers is acknowledged.

References

Choi KK, Ray J, Griffiths J, Bae T-S (2013) Evaluation of GPS orbit prediction strategies for the IGS Ultra-rapid products. GPS Solutions 17:403–412

Dach R, Hugentobler U, Fridez P, Meindl M (2007) Bernese GPS software version 5.0. Astronomical Institute, University of Bern

Dai X, Ge M, Lou Y, Shi C, Wickert J, Schuh H (2015) Estimating the yaw-attitude of BDS IGSO and MEO satellites. J Geodesy 89:1005–1018

Deng Z, Fritsche M, Uhlemann M, Wickert J, Schuh H (2016) Reprocessing of GFZ multi-GNSS product GBM. In: Proceedings of IGS workshop, Sydney, Australia, pp 8–12

Duan B, Hugentobler U, Selmke I (2018a) The adjusted optical properties for Galileo/BeiDou-2/QZS-1 satellites and initial results on BeiDou-3e and QZS-2 satellites. Adv Space Res (in press). https://doi.org/10.1016/j.asr.2018.11.007

Duan B, Hugentobler U, Selmke I (2018b) The adjusted optical properties of GNSS satellites and applications in precise orbit determination and prediction. In: Proceedings of IGS workshop, Wuhan, China, pp 29–30

Hadas T, Bosy J (2015) IGS RTS precise orbits and clocks verification and quality degradation over time. GPS Solutions 19:93–105

Ishijima Y, Inaba N, Matsumoto A, Terada K, Yonechi H, Ebisutani H, Ukawa S, Okamoto T (2009) Design and development of the first Quasi-Zenith satellite attitude and orbit control system. In: Aerospace conference. IEEE, pp 1–8

Lutz S, Beutler G, Schaer S, Dach R, Jäggi A (2016) CODE's new ultra-rapid orbit and ERP products for the IGS. GPS Solutions 20:239–250

Montenbruck O, Steigenberger P, Prange L, Deng Z, Zhao Q, Perosanz F, Romero I, Noll C, Stürze A, Weber G (2017) The Multi-GNSS Experiment (MGEX) of the International GNSS Service (IGS)–achievements, prospects and challenges. Adv Space Res 59:1671–1697

Rodriguez-Solano C, Hugentobler U, Steigenberger P, Lutz S (2012) Impact of Earth radiation pressure on GPS position estimates. J Geodesy 86:309–317

Zhao Q, Wang C, Guo J, Wang B, Liu J (2018) Precise orbit and clock determination for BeiDou-3 experimental satellites with yaw attitude analysis. GPS Solutions 22:4

A Method for Improving the Short-Term Prediction Model for ERP Based on Long-Term Observations

Chao Hu[1,2], Qianxin Wang[1,2,3(✉)], Zhiwen Wang[4], and Ya Mao[1,2]

[1] NASG Key Laboratory of Land Environment and Disaster Monitoring, China University of Mining and Technology, Xuzhou 221116, China
wqx@cumt.edu.cn
[2] School of Environment Science and Spatial Informatics, China University of Mining and Technology, Xuzhou 221116, China
[3] Mathematical and Geospatial Sciences, RMIT University, Melbourne 3001, Australia
[4] CCCC First Harbor Consultants Co., LTD., Tianjin 300222, China

Abstract. Earth Rotation Parameter (ERP) is one of the most important parameters in the area of positioning and navigation, autonomous orbit determination and Earth reference framework. However, due to the restriction of timeliness of data processing, the predicted ERPs are taken into the relevant applications to meet the requirements of real-time or near real-time users. Therefore, given the disadvantages of short-term prediction models for ERPs, such as model mismatch, over parametrization and divergence with time, this study proposed a method for improving the short-term prediction model for ERP based on long-term observations. Firstly, the optimal length of observations was analyzed for the Least Square (*LS*) prediction model based on the Akaike Information Criterion (*AIC*). It is found that one year of ERP observations is the optimal data sets to establish the prediction model. Then, two constraints models based on *LS*, called (Constraint *LS*) *CLS* and (Enhanced *CLS*) *ECLS*, were discussed to decrease the errors in prediction models, which takes the correlation factors and residuals of prediction model into consideration. The results indicated that the prediction errors of ERP can be significantly decreased for short-term prediction, which improved the accuracy of ERP prediction with 50% for polar motions (PM), and 20% for UT1-UTC. Moreover, considering the divergence of predicted ERP along with the increasing of time and separate prediction of each parameters in ERP of Auto Regressive model (*AR*), a Multivariable Regression model (*MAR*) was introduced to correct the residuals of predicted ERP, which combined the PM, and UT1-UTC with LOD into prediction models. And the accuracy of predicted ERP can be improved at least 20% compared with *AR* model. Finally, according to data experiments, the improved short-term prediction model was analyzed based on different observations. It is suggested that our method can improve the short-term prediction in cases that long-term ERP observations are available.

Keywords: Earth Rotation Parameter (ERP) · Akaike Information Criterion (*AIC*) · Short-term prediction · Least Square (*LS*) · Auto regression model · Long-term observations

J. Sun et al. (Eds.): CSNC 2019, LNEE 563, pp. 24–38, 2019.
https://doi.org/10.1007/978-981-13-7759-4_3

1 Introduction

Earth Rotation Parameter (ERP) is one of important inputs of Earth reference framework, precise orbit determination and positioning and navigation, which contains polar motions (PM) and UT1-UTC [1]. It was determined based on the observations from very long baseline interferometry (VLBI), lunar laser ranging (LLR), satellite laser range (SLR), GPS and Doppler orbitography by radio positioning integrated on satellite (DORIS). Due to the characteristics of different technologies, IERS produces EOP (including precession and nutation) with different accuracies, lengths and periods. However, the timeliness of the estimated ERP with different technologies cannot meet the requirement of real-time or near-real time applications [2], which is updated with observed and predicted parts. According to IERS C04, the accuracy of ERP in direction of PM and UT1-UTC are better than 100 uas and 10 us respectively. Moreover, the accuracy of predicted ERP by IERS reaches up to 0.150 mas and 0.053 ms in PM and UT1-UTC, respectively [1], which imposes a significant impact on the predicted orbit of GNSS Analysis Centre (AC). In addition, the accuracies of ultra-short-term for <10 days, short-term for <30 days, and medium-term for <500 days are 3.0 mas, 8.2 mas, 50 mas and 1.2 mas, 3.8 mas, 30 mas for PMX and PMY, respectively [2]. However, the short-term predicted ERP cannot meet the requirements of autonomous orbit determination, Earth reference framework maintained [3] and the applications of real-time or near real-time users [1]. Therefore, to improve the accuracy of predicted ERP, it is necessary to refine and improve the prediction model of ERP [4, 5].

The prediction models of ERP are adopted by IERS mainly include spectral analysis and least squares extrapolation [6–8], wavelets and fuzzy inference systems, Kalman filter (AAM forecast: NCEP) [9, 10], neural networks and auto regressive prediction (*AR*). For the predicted ERPs, ACs mainly predict ERPs on the basis of a continuous piecewise linear function [1]. In general, the prediction models of ERP can be divided into two parts, called linear and nonlinear prediction model. For the linear prediction models, it includes *AR*, Auto Covariance (*AC*), and Least Squares (*LS*). And the nonlinear prediction models contain Artificial Neural Networks (*ANN*), and Wavelet Decomposition (*WD*) etc. Meanwhile, scholars tried to refine the prediction models. Schuh et al. studied the prediction system of ERP based on Back Propagation Neural Network (*BPNN*) [11]; Xu et al. took the Kalman filter to correct the *AR* model, which was combined with *LS* model to build the *LS*+*AR*+Kalman prediction model [12]. Zhang combined the General Regression Neural Network (*GRNN*) with *LS* to predict LOD [13]. However, the prediction algorithms of IERS should be continuously improved because the prediction accuracy for even a few days in the future is worse than observation accuracy [2, 14]. The prediction errors of ERP are consisted of observations errors and model errors, in which prediction models are influenced by different types and lengths of observations. Therefore, it is suggested a reliable prediction model for different observations should be adopted to acquire accurate predicted ERP.

In the theory of model selection, the Akaike Information Criterion (*AIC*) is a simple and widely used model selection method, which gives an optimal index to evaluate the model based on the accuracy and complexity [15–17]. Based on the *AIC*, Felus et al. compared the accuracy of coordinate transformation models (translation, similarity,

affine transformation, and mapping) in special area [18]; Lehmann et al. used the *AIC* to select the error models and detect the gross [19]. Since the 1960s and the later period of continuous improvement of geodesic technology, ERP has accumulated more than 50 years of long-term observations, which provides a steady and reliable data to study the predicted ERP. It should be noticed that *LS* and *LS+AR* are commonly used into short-term ERP prediction. So, this study tries to improve the *LS* and *LS+AR* models for ERP prediction based on the analyses of *AIC*.

This study is about the high-accuracy short-term prediction of ERP based on long-term ERP observations. Section 2 introduces the theory of *AIC*, and tests the optimal lengths of observations for *LS* prediction model; Sect. 3 proposes two improved prediction models based the constrain conditions; Sect. 4 improves the *AR* model with Multivariable regression model (*MAR*); Sect. 5 analyzes the ERP prediction models based on lots of experiments.

2 The Principle of *AIC*

AIC is closely related to the important concept in statistics-Fisher likelihood theory. Meanwhile, *AIC* is also closely related to theory-*KL* information [20] and was first proposed to estimate *KL* information [16], which is used to express the loss of one probability distribution, or the relative values of information loss when using a model to describe data [21]. *AIC* actually gives a kind of asymptotic, relative and mean estimation of *KL* information. Assume that the distribution of the observations is normal, the value of *AIC* is defined by

$$AIC = n\ \log(\hat{\sigma}^2) + 2k \tag{1}$$

Where n is the number of observations, k is the number of parameters, $\hat{\sigma}$ is the mean square error. In the right side of Eq. (1), the first and second terms denote the goodness and complexity of models, respectively [22]. Thus, the preferred model is the one with the minimum *AIC* value. However, when we have deficient number of observations, i.e., the ratio between n and k is small, the reliability of *AIC* is low. Thus, a refined *AIC* called *AICc* is employed. The value of *AICc* can be given as

$$AICc = n\ \log(\hat{\sigma}^2) + 2k(n/(n-k-1)) \tag{2}$$

Likewise, the smaller the value is, the more rational model is. In the prediction models of ERP, predicted ERP is fitted and extrapolated based on the known values of ERP by *LS* model. The model of *LS* can be divided into linear and trend parts, in which the function of PM can be presented as

$$\begin{aligned} P(t) = a + bt + C_1 \cos(\frac{2\pi t}{P_{SA}}) + C_2 \sin(\frac{2\pi t}{P_{SA}}) + D_1 \cos(\frac{2\pi t}{P_A}) \\ + D_2 \sin(\frac{2\pi t}{P_A}) + E_1 \cos(\frac{2\pi t}{P_S}) + E_2 \sin(\frac{2\pi t}{P_S}) \end{aligned} \tag{3}$$

Where $P(t)$ represents the values at t-th epoch; a and b are the coefficients of the constant term and trend terms, respectively; C_1 and C_2 are the semi-annual coefficients; D_1 and D_2 are the coefficients of annual period terms; E_1 and E_2 are the Chandler wobble parameters; P_{SA}, P_A and P_S are the constants for semi-annual, annual and 1.183 years in Eq. (3). Moreover, the model for UT1-UTC is

$$f(t) = a_0 + a_1 t + B_1 \cos(\frac{2\pi t}{P_1}) + B_2 \sin(\frac{2\pi t}{P_1}) + C_1 \cos(\frac{2\pi t}{P_2}) + C_2 \sin(\frac{2\pi t}{P_2}) + D_1 \cos(\frac{2\pi t}{P_3}) + D_2 \sin(\frac{2\pi t}{P_3}) + E_1 \cos(\frac{2\pi t}{P_4}) + E_2 \sin(\frac{2\pi t}{P_4}) + F_1 \cos(\frac{2\pi t}{P_5}) + F_2 \sin(\frac{2\pi t}{P_5}) \tag{4}$$

In Eq. (4), t is the time of UTC; P_1, P_2, P_3, P_4 and P_5 are 18.6, 9.3, 1, 0.5 and 1/3 years of *LS* model. The parameters in Eqs. (3) and (4) can be estimated by *LS*. Take the estimation of PM as an example

$$\hat{X} = (B^T B)^{-1} B^T L \tag{5}$$

In Eq. (5), $X = [\,a \quad b \quad C_1 \quad C_2 \quad D_1 \quad D_2 \quad E_1 \quad E_2\,]$, $L = [\,\hat{X}(t_1) \quad \hat{X}(t_2) \quad \cdots \quad \hat{X}(t_n)]$.

$$B = \begin{bmatrix} 1 & t_1 & \cos(\frac{2\pi t_1}{P_{SA}}) & \sin(\frac{2\pi t_1}{P_{SA}}) & \cos(\frac{2\pi t_1}{P_A}) & \sin(\frac{2\pi t_1}{P_A}) & \cos(\frac{2\pi t_1}{P_S}) & \sin(\frac{2\pi t_1}{P_S}) \\ 1 & t_2 & \cos(\frac{2\pi t_2}{P_{SA}}) & \sin(\frac{2\pi t_2}{P_{SA}}) & \cos(\frac{2\pi t_2}{P_A}) & \sin(\frac{2\pi t_2}{P_A}) & \cos(\frac{2\pi t_2}{P_S}) & \sin(\frac{2\pi t_2}{P_S}) \\ \vdots & \vdots & \vdots & \vdots & \vdots & \vdots & \vdots & \vdots \\ 1 & t_n & \cos(\frac{2\pi t_n}{P_{SA}}) & \sin(\frac{2\pi t_n}{P_{SA}}) & \cos(\frac{2\pi t_n}{P_A}) & \sin(\frac{2\pi t_n}{P_A}) & \cos(\frac{2\pi t_n}{P_S}) & \sin(\frac{2\pi t_n}{P_S}) \end{bmatrix} \tag{6}$$

It should be noted that the results of predicted ERP are influenced by the prediction model, which has a high correlation with the length of observations. Therefore, to investigate the impacts of observations on *LS* prediction model, *AIC* values are taken to select the optimal length of observations. In experiments, prediction models of PM choose 0.5, 1, 3, 6 and 9 years of observations to estimate the parameters of *LS* model. Similarly, 0.5, 1, 3, 9, 12 and 17 years of observations are adopted to solve the coefficients of UT1-UTC prediction models. Moreover, the 30-day predictions of ERP are outputted from the January, 1, 2010. To reduce the errors in observations, IERS08 C04 is downloaded as the observations. Mean Absolute Error (*MAE*) is calculated as the accuracy index of predicted ERP.

$$MAE_i = \frac{1}{M} \sum_{j=1}^{M} \left| \varepsilon_{i,j} \right| \tag{7}$$

Where i is the total days of predictions; M is the times of predictions; $\varepsilon_{i,j}$ is the residuals. In Table 1, the *AIC* values of ERP prediction models (*LS*) based on different lengths of ERP observations are calculated out, in which the observations with one year is the minimum in *AIC* values. It can be concluded that one year observation of *LS*

prediction model is optimal. Meanwhile, the *MAE* values of different lengths of observations are showed in Fig. 1. The accuracy of short-term predicted ERP with one year observations is better than others.

Table 1. The *AIC* values for different lengths of ERP observations

Length (years)	0.5	1	3	6	9	12	17
AIC (PM)	234.381	163.957	324.483	431.318	417.904	–	–
AIC (UT1-UTC)	234.631	163.054	322.011	425.604	406.058	389.689	412.562

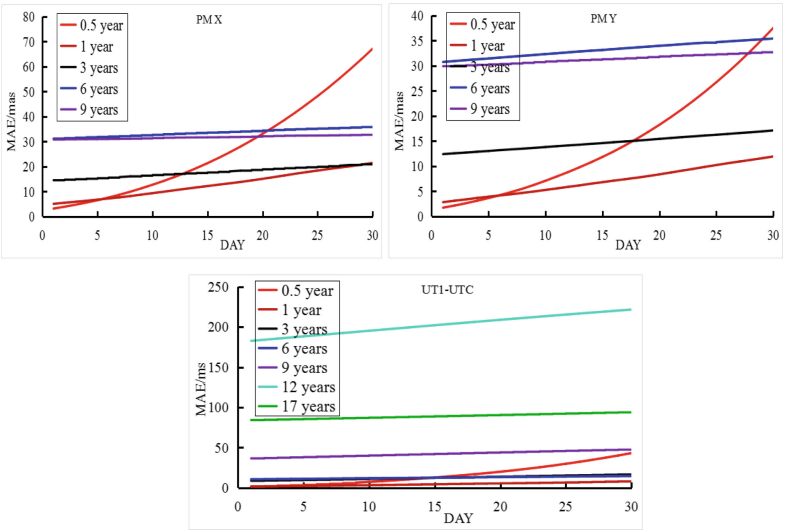

Fig. 1. The *MAE* values for different lengths of observations of prediction models

In Table 1, the *AIC* values of PM are the averages of PMX and PMY. For different lengths of ERP observations, it is found that the accuracy of predicted ERP becomes worse with the increasing of time. To refine the prediction models, the following sections will discuss the improved method for *LS* model.

3 Improved *LS* Models for ERP Prediction

Based on the Fig. 1, it can be found the accuracy of short-term ERP prediction did not reach to the optimal with the optimal lengths of observations. To access the results of predicted ERP, the fitting precision is analyzed by *AICc* values based on one year observations. In Table 2, the *AICc* values are listed out with the intervals of two months for the direction of PMX.

Table 2. *AICc* values of different data segments during one year observations for PMX with *LS*

Segments (months)	0–2	2–4	4–6	6–8	8–10	10–12
AICc (PMX)	158.3	182.2	234.1	102.8	114.7	273.1

From the results of Table 2, the *AICc* values are presented as the maximum between October to December, which indicts the *LS* model can not fit the corresponding segment, called the end effect of *LS*. Therefore, to reduce the residuals of fitting in the end of segment, this study proposes an improved *LS* model called *CLS* (*LS* with constraints). The *CLS* takes the end of ERP observation (the beginning point of prediction) into consideration, which fixes the observations of the end on the *LS* model to make the beginning point of prediction as the real values. To describe the *CLS* clearly, Fig. 2 gives the residuals of extrapolation before and after imposing constraints on the *LS* for the direction of PMX. It can be seen that the errors of extrapolation of *LS* are reduced after the constraints. Moreover, the errors of *CLS* increase from zero as the constraints.

Meanwhile, to verify the *CLS* model, the *LS* and *CLS* are taken into the ERP prediction. Similarly, 30-day of predicted ERP is outputted from the January, 1, 2010. The details of results can be found in Table 3 and Fig. 3. It can be concluded as follows: (1) for PMX and PMY, *CLS* can improve the accuracy with more than 50% for ultra-short-term prediction; (2) for 30-day of prediction, the improvement of *CLS* reaches to 30% than for *LS*; (3) for UT1-UTC, the accuracy of prediction for short-term ERP can improve by 20%.

The ERP prediction based on *CLS* can improve the accuracy of short-term ERP prediction based on *LS*. However, the predicted ERP of 30 days are beyond 14 mas and 6 us in PM and UT1-UTC, respectively, which are behind the requirements of users and should be corrected with refined model. Given the symmetry between the end point and the beginning point of the ERP observations, the ERP errors of prediction are increased from the left of the observations, which is equally to the prediction from the right point of observations based the constraints on the beginning point of observations. Therefore, the correlation factors between the prediction from the right and left points are investigated. Based on the correlation of prediction with two points, the short-term predicted ERP can be corrected by the corresponding prediction with right side.

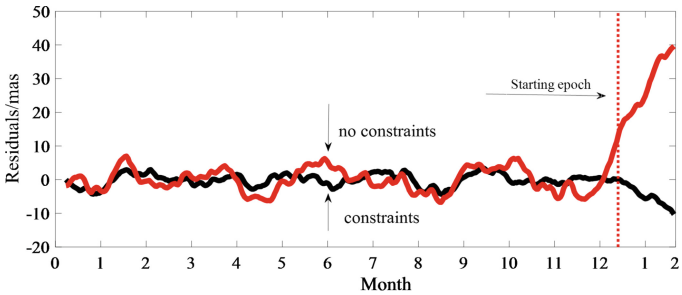

Fig. 2. The residuals of predicted ERP before and after constraints

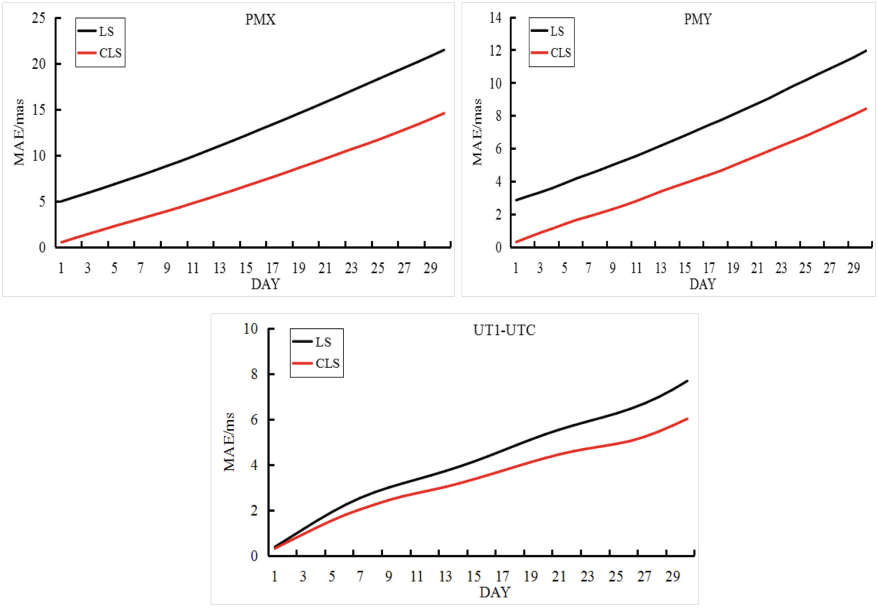

Fig. 3. Comparison of ERP prediction of *LS* and *CLS*

To verify the correlation of predicted ERP between the direction of right and left, the following experiments based on PM are conducted: One year of observations are selected to predict 5-year of ERP from the January, 1, 2010. The correlation factors between the extrapolation from right and left sides are calculated as discussed in [1]. The results of correlation factors are showed in the Fig. 4, in which most of the numbers are beyond 0.5, such as the direction of PMX and PMY with 67% and 74%, respectively. Therefore, it demonstrates that the significant correlation of the residuals for the prediction ERP based on two sides.

Table 3. Statistics of predicted ERP by *CLS* and *LS*

Day	MAE								
	PMX/mas			PMY/mas			UT1-UTC/ms		
	Models			Models			Models		
	CLS	*LS*	Improvements (%)	*CLS*	*LS*	Improvements (%)	*CLS*	*LS*	Improvements (%)
1	0.51	4.97	89.753	0.29	2.84	89.50	0.32	1.55	78.93
5	2.26	6.83	66.878	1.38	3.87	64.24	1.57	2.35	33.15
10	4.33	9.33	53.591	2.54	5.27	51.80	2.59	3.39	23.36
15	6.64	12.16	45.384	3.89	6.78	42.68	3.52	4.43	20.52
20	9.11	15.14	39.830	5.26	8.40	37.40	4.55	5.47	16.78
25	11.66	18.27	36.187	6.75	10.15	33.50	5.24	6.66	21.37
30	14.55	21.44	32.140	8.41	11.94	29.55	6.54	8.19	20.11

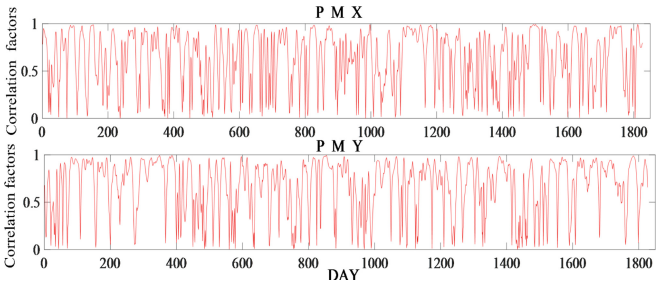

Fig. 4. The correlation factors of predicted PM on both sides

To further describe the residuals differences between extrapolation with two sides, one year of predicted PMX based on *CLS* with constraints in two sides are tested. Meanwhile, the slope of residuals for two directions prediction of PMX are extracted out in Fig. 5, in which no significant differences between the residuals of two sides are found.

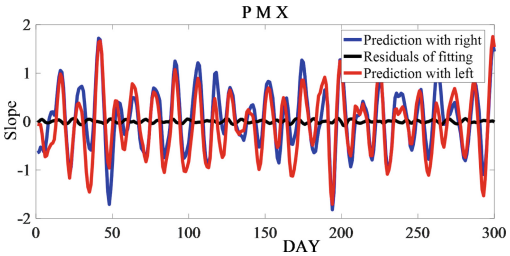

Fig. 5. The slope of residuals different prediction

As mentioned above, the significant correlation between the extrapolation in two directions can be established for *LS* prediction model. Therefore, an improved *CLS* model called *ECLS* is proposed to compensate prediction errors of ERP. The details of *ECLS* are listed in Fig. 6.

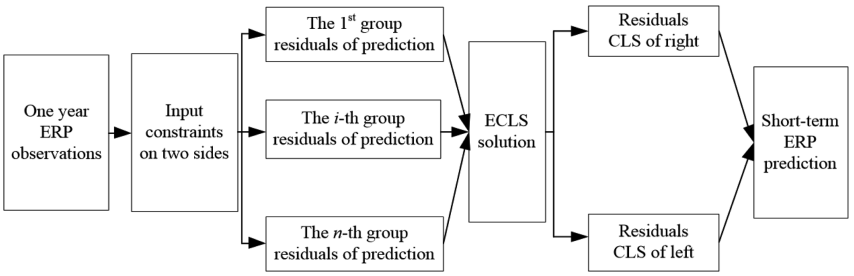

Fig. 6. The flowchart of *ECLS* prediction model

From the Fig. 6, the main idea of *ECLS* prediction model can be summarized as: firstly, the *CLS* is used to predict ERP; then, the coefficients of prediction ERP correction based on the left side are estimated with the observations of ERP; finally, the correction parameters are taken into the extrapolated ERP of the right side. The correction model of *ECLS* and it corresponding parameters estimation can be acquired as

$$\begin{cases} \hat{Y}_k = Y_k^{'} + \Delta\varphi_k \\ \Delta\varphi_k = A_k + B_k \Delta\phi_k \end{cases} \tag{8}$$

Where k is the k-th predicted day; $\hat{Y}_k$ is the predicted values by *ECLS*; $Y_k^{'}$ is extracted based on *CLS*; $\Delta\varphi_k$ is the correction values; $\Delta\phi_k$ is the residuals of predicted ERP by left side; A_k and B_k are the coefficients of fitting function.

Furthermore, to verify the *ECLS* model in short-term ERP prediction, 30-day of predicted ERP based on *ECLS* and *CLS* is outputted in Fig. 7 and Table 4.

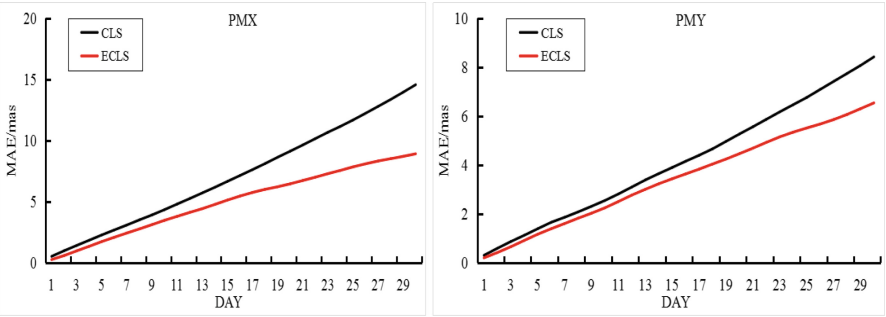

Fig. 7. The predicted ERP (PM) based on *CLS* and *ECLS* models

In Fig. 7, the results of UT1-UTC are not showed, which were listed in the Table 4. It is found that 1-day prediction of ERP with the highest improvement. Moreover, comparing with *CLS* model, it is suggested that *ECLS* can improve the accuracy of predicted ERP. The improvements of PMX are better than PMY based on *ECLS*.

Table 4. The results of predicted ERP based on *CLS* and *ECLS*

Day	MAE								
	PMX/mas			PMY/mas			UT1-UTC/ms		
	Models			Models			Models		
	ECLS	*CLS*	Improvements (%)	*ECLS*	*CLS*	Improvement (%)	*ECLS*	*CLS*	Improvement (%)
1	0.24	0.51	107.21	0.19	0.29	53.80	0.14	0.32	131.79
5	1.72	2.26	31.50	1.16	1.38	19.33	1.30	1.57	20.88
10	3.46	4.33	25.19	2.24	2.54	13.36	2.03	2.59	27.42
15	5.11	6.64	29.92	3.43	3.89	13.41	3.15	3.52	11.73
20	6.44	9.11	41.43	4.45	5.26	18.06	3.93	4.55	15.62
25	7.82	11.66	48.98	5.50	6.75	22.65	4.05	5.24	29.39
30	8.90	14.55	63.51	6.53	8.41	28.80	4.62	6.54	41.41

4 *ECLS+MAR* Prediction Model

According to the *ECLS* and *CLS*, the accuracy of short-term predicted ERP can be improved in term of *LS* model. However, it can be noted that the errors of predicted ERP are increased with the increasing of time. To reduce the accumulation errors of prediction ERP, *AR* model was used to correct the residuals of prediction. Due to the fact that the predicted ERP was divided into single direction to process in traditional *AR* model, the accuracy of predicted ERP correction is limited by the ignoring of correlation between each parameters. According to related researches [2, 23], it is found that the correlation between PMY and PMX, and UT1-UTC and LOD is obviously, which should be taken into consideration in ERP prediction to improve the accuracy. Therefore, this study proposes a *MAR* model to improve the *AR* based on *ECLS* discussed in the last section. The main idea of *MAR* model is to find the correlated parameters between the random component of residuals for multivariable, which takes the correlation factor into consideration to improve the precision of parameter solutions. The *MAR* can be expressed as

$$\begin{cases} x_t^1 = a_{11}^1 x_{t-1}^1 + \cdots + a_{1p}^1 x_{t-p}^1 + a_{11}^2 x_{t-1}^2 + \cdots + a_{1p}^2 x_{t-p}^2 + \cdots + a_{11}^n x_{t-1}^n + \cdots + a_{1p}^n x_{t-p}^n + e_t^1 \\ \qquad\qquad \vdots \\ x_t^i = a_{i1}^1 x_{i-1}^1 + \cdots + a_{ip}^1 x_{i-p}^1 + a_{i1}^2 x_{t-1}^2 + \cdots + a_{ip}^2 x_{t-p}^2 + \cdots + a_{i1}^n x_{t-1}^n + \cdots + a_{ip}^n x_{t-p}^n + e_t^i \\ \qquad\qquad \vdots \\ x_t^n = a_{n1}^1 x_{n-1}^1 + \cdots + a_{np}^1 x_{n-p}^1 + a_{n1}^2 x_{t-1}^2 + \cdots + a_{np}^2 x_{t-p}^2 + \cdots + a_{n1}^n x_{t-1}^n + \cdots + a_{np}^n x_{t-p}^n + e_t^n \end{cases} \tag{9}$$

In Eq. (9), x_t^i represents the i-th parameter in time t; a_{np}^n is the coefficient of the p-th step of n-th parameter; e_t^n is the white noise. The Eq. (10) can be simplified as

$$\boldsymbol{X}_t = \boldsymbol{A}(1)\boldsymbol{X}_{t-1} + \boldsymbol{A}(2)\boldsymbol{X}_{t-2} + \cdots + \boldsymbol{A}(p)\boldsymbol{X}_{t-p} + \boldsymbol{e}_t \tag{10}$$

Where, $\boldsymbol{A}(p) = \begin{bmatrix} a_{1p}^1 & a_{1p}^2 & \cdots & a_{1p}^n \\ \vdots & \vdots & \ddots & \vdots \\ a_{np}^1 & a_{np}^2 & \cdots & a_{np}^n \end{bmatrix}$, $\boldsymbol{X}_t = \begin{bmatrix} x_t^1 & x_t^2 & \cdots & x_t^n \end{bmatrix}^T$, $\boldsymbol{e}_t = \begin{bmatrix} e_t^1 & e_t^2 & \cdots & e_t^n \end{bmatrix}^T$.

The coefficients of Eq. (10) can be estimated by *LS*. To verify the *MAR* model, the residuals of ERP fitting function are analyzed based on the correlation. Furthermore, the optimal order of *MAR* model is selected by *AIC*. Steps of *ECLS+MAR* in prediction of PM and UT1-UTC are summarized in the Figs. 8 and 9, respectively.

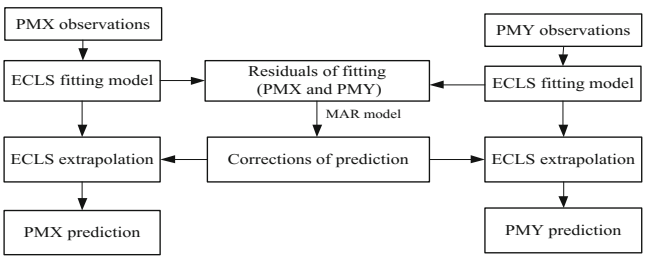

Fig. 8. The flowchart of *ECLS+MAR* for prediction of PM

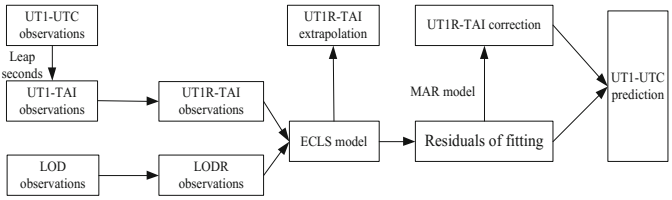

Fig. 9. The flowchart of *ECLS+MAR* for prediction of UT1-UTC

The main steps of experiments are as follows: firstly, The residuals of fitting for PMX, PMY, UT1-UTC and LOD with six years observations by *ECLS* are calculated out; secondly, the correlation factors between PMX and PMY, and UT1-UTC and LOD are analyzed as the Sect. 3. The Fig. 10 lists the correlation factors for PM and UT1-UTC, in which the numbers beyond 0.5 reach up to 81.92% for PM, and 58.95% for UT1-UTC and LOD. Meanwhile, Table 5 gives the *AIC* values for different order of *MAR* model.

The accuracy of short-term predicted ERP is tested based on *ECLS+MAR*. The 30-day of predicted ERP is outputted by both *ECLS+AR* and *ECLS+MAR*. The corresponding results are showed in Fig. 11 and Table 6. It is suggested that the accuracy of predicted ERP for ultra-short-term or short-term is better by *ECLS+AR*. Moreover, the PMY is improved with more significant than for PMX. In addition, UT1-UTC can be improved with at least 20% in experiments.

Table 5. The *AIC* values for different order of *MAR* model

Order	1	2	3	4	5	6	7	8
AIC (PM)	273.1	382.0	234.2	103.1	115.5	158.2	164.3	201.1
AIC (UT1-UTC)	18.1	17.2	13.1	9.0	10.1	18.4	16.2	18.9

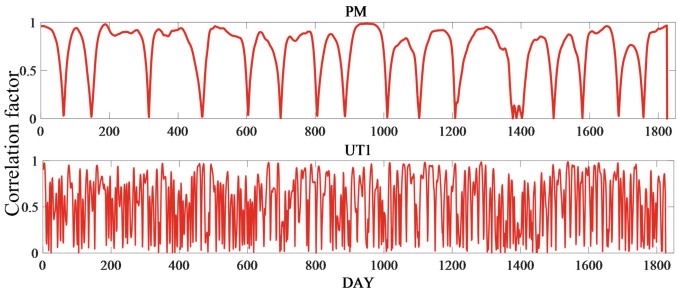

Fig. 10. Correlation factors of residuals for PM and UT1-UTC

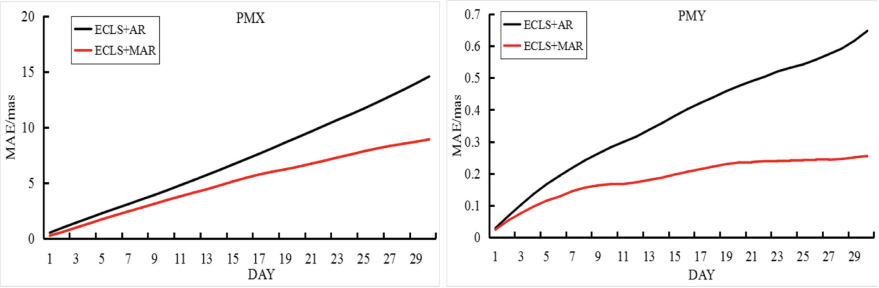

Fig. 11. The results of predicted ERP (PM) by *ECLS+AR* and *ECLS+MAR*

Table 6. The accuracy of predicted ERP based on *ECLS+MAR* and *ECLS+AR*

Day	MAE								
	PMX/mas			PMY/mas			UT1-UTC/ms		
	Models			Models			Models		
	ECLS +MAR	*ECLS +AR*	Improvement (%)	*ECLS +MAR*	*ECLS +AR*	Improvement (%)	*ECLS +MAR*	*ECLS +AR*	Improvement (%)
1	0.24	0.27	8.36	0.16	0.19	13.28	0.027	0.03	28.07
5	1.49	1.69	11.87	1.05	1.19	12.11	0.301	0.41	27.88
10	3.08	3.65	15.54	1.84	2.18	15.34	0.860	1.15	25.546
15	4.54	5.56	18.39	2.54	3.48	27.11	1.493	2.05	27.49
20	5.78	7.66	24.48	3.23	4.95	34.64	2.175	2.99	27.34
25	6.98	9.83	28.93	4.02	6.52	38.34	2.917	3.98	26.86
30	8.06	12.16	33.69	4.58	8.32	44.92	3.624	4.74	23.55

5 Experiments and Analyses

This study mainly improves the short-term ERP prediction based on *LS* and *AR* models. The improved models called *CLS*, *ECLS* and *ECLS+MAR* are proposed in short-term ERP prediction. Based on the experiments, it is found that the improved models can significantly enhance the accuracy of predicted ERP.

To further explain the accuracy improvements of improved short-term ERP prediction models, the results of EOP_PCC [24] predictions are taken into the experiments to compare the ERP accuracy. The EOP_PCC includes more than 20 groups of ERP predictions from eight countries. In Figs. 12 and 13, the prediction models are distinguished by different colors, in which the corresponding *CLS*, *ECLS* and *ECLS+MAR* are also listed.

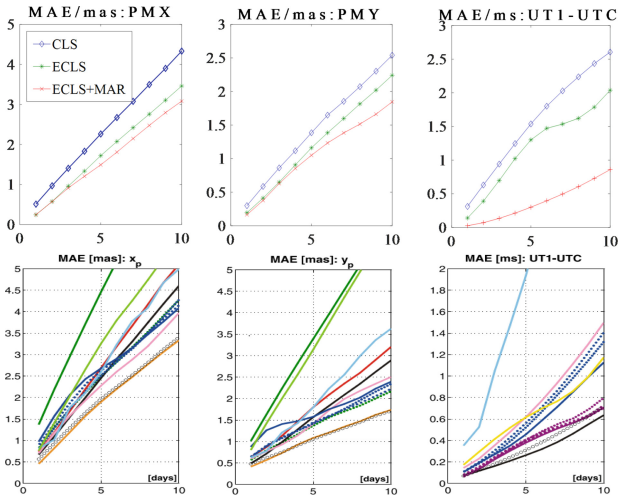

Fig. 12. The ultra-short-term prediction based on EOP_PCC and improved methods

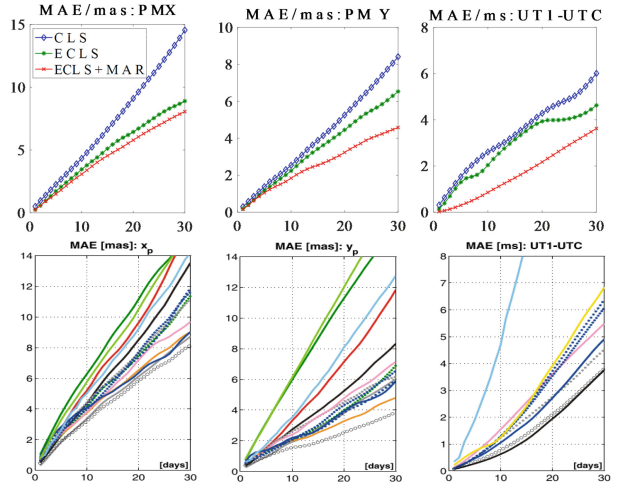

Fig. 13. The short-term prediction based on EOP_PCC and improved methods

From the results of ultra short-term prediction, we can conclude: for PMX, *ECLS+MAR* with higher accuracy than EOP_PCC, which is similar to *ECLS*. Moreover, the *CLS* model is better than six groups in EOP_PCC; for PMY, *ECLS+MAR* has similar results of the highest accuracy model in EOP_PCC; for UT1-UTC, EOP_PCC is better than improved models proposed in this study; for the results of short-term prediction, for PMX and PMY, there are no differences for ultra-short-term results. However, for the UT1-UTC, *ECLS+MAR* is better than EOP_PCC. According to the comparison with the EOP_PCC, it is suggested that *ECLS+MAR* can acquire the same accuracy of ultra-short-term and short-term prediction as the EOP_PCC.

6 Conclusions and Prospects

Due to the facts that the important parameters of short-term prediction ERP in real-time or near real-time applications, high-accuracy prediction of ERP is discussed. In this study, given the drawbacks of *LS* and *LS+AR* models for short-term ERP prediction, the improved models called *CLS*, *ECLS* and *ECLS+MAR* are proposed to predict short-term ERP. The *AIC* values are selected to assess the prediction models and chose the optimal lengths of observations for prediction models. According to the corresponding experiments, it is showed that the proposed improved models are better than *LS* and *LS+AR* model, which can significantly improve the accuracy of short-term predicted ERP.

However, to extract the advantages of each prediction models, a combined model should be adopted in ERP prediction to achieve the adaptive algorithm. The follow-up researches will discuss the combined models to further improve the ERP prediction. Moreover, the improved models are based on the mathematics methods, which cannot represent the real values with high accuracy. A model from physical method also should be paid more attentions.

Acknowledgments. The author appreciates the International GNSS Monitoring and Assessment Service (iGMAS) for the data and products. This work was supported by the Jiangsu Dual Creative Teams Program Project Awarded in 2017, the National Natural Science Foundation of China (Grant Nos: 41404033 and 41874039), Jiangsu Natural Science Foundation (Grant No. BK20181361), and Postgraduate Research & Practice Innovation Program of Jiangsu Province (Grant No. SJCX18_0668).

References

1. Wang Q, Hu C, Xu T et al (2017) Impacts of Earth rotation parameters on GNSS ultra-rapid orbit prediction: derivation and real-time correction. Adv Space Res 60(12):2855–2870
2. Wu F, Deng K, Chang G et al (2018) The application of a combination of weighted least-squares and autoregressive methods in predictions of polar motion parameters. Acta Geod Geoph 2018:1–11
3. Liu W (2009) Impact of extrapolating orbit and reference frame transformation on precision orbit determination of navigation satellite. Master thesis, Nation University of defense technology, Changsha, China
4. Gambis D, Luzum B (2011) Earth rotation monitoring, UT1 determination and prediction. Metrologia 48(4):S165
5. Lei Y, Guo M, Hu D et al (2017) Short-term prediction of UT1-UTC by combination of the grey model and neural networks. Adv Space Res 59(6):524–531
6. Akulenko L, Kumakshev S, Markov Yu (2002) Motion of the Earth's pole. Dokl Phys 47:78–84
7. Akulenko L, Kumakshev S, Markov Yu et al (2002) A model for the polar motion of the deformable Earth adequate for astrometric data. Astron Rep 46:74–82
8. Akulenko L, Kumakshev S, Markov Yu et al (2002) Forecasting the polar motions of the deformable Earth. Astron Rep 46:858–866
9. Freedman A, Steppe J, Dickey J et al (1994) The short-term prediction of universal time and length of day using atmospheric angular momentum. J Geophys Res 99:6981–6996

10. Gross R, Eubanks T, Steppe J et al (1998) A Kalman filter-based approach to combining independent Earth orientation series. J Geodesy 72:215–235
11. Schuh H, Ulrich M, Egger D et al (2002) Prediction of Earth orientation parameters by artificial neural networks. J Geodesy 76(5):247–258
12. Xu X, Zhou Y, Liao X (2012) Short-term earth orientation parameters predictions by combination of the least-squares, AR model and Kalman filter. J Geodyn 62(8):83–86
13. Zhang X (2011) Prediction of Length of Day Based on Artificial Neural Networks. Central South University, Changsha
14. Kosek W (2010) Causes of prediction errors of pole coordinates data. In: Proceedings of the 6th Orlov's conference, "The study of the Earth as a planet by methods of geophysics, geodesy and astronomy", 22–24 June 2009. MAO NAS of Ukraine, Kiev, Ukraine, pp 96–103
15. Akaike H (1973) Information theory and an extension of the maximum likelihood principle. In: Second international symposium on information theory. Akademiai Kiado, Budapest, pp 267–281
16. Akaike H (1974) A new look at the statistical model identification. IEEE Trans Autom Control 19(6):716–723
17. Akaike H (1981) Likelihood of a model and information criteria. J Econometrics 16(1):3–14
18. Felus Y, Felus M (2009) On choosing the right coordinate transformation method. In: Proceedings of FIG working week 2009: surveyors key role in accelerated development. Eilat, Israel, 3–8 May 2009
19. Lehmann R, Lösler M (2016) Multiple outlier detection: hypothesis tests versus model selection by information criteria. J Surv Eng 142(4):04016017
20. Kullback S, Leibler R (1951) On information and sufficiency. Ann Math Stat 22(1):79–86
21. Cover T, Thomas J (2012) Elements of Information Theory. Wiley, New York
22. Burnham K, Anderson D (2004) Multimodel inference: understanding AIC and BIC in model selection. Soc Methods Res 33:261–304
23. Xu G (2007) GPS-Theory, Algorithms and Applications. Springer, New York
24. Kalarus M, Schuh H, Kosek W et al (2010) Achievements of the earth orientation parameters prediction comparison campaign. J Geodesy 84(10):587–596

An Improved Method for BDS Inter-frequency Clock Bias Estimation

Yize Zhang[1,2,3(✉)], Nobuaki Kubo[1], Junping Chen[2,3], Hu Wang[4], and Jiexian Wang[5]

[1] Tokyo University of Marine Science and Technology, Tokyo, Japan
zhyize@163.com
[2] Shanghai Key Laboratory of Space Navigation and Positioning Techniques, Shanghai, China
[3] Shanghai Astronomical Observatory, Chinese Academy of Science, Shanghai, China
[4] Chinese Academy of Surveying and Mapping, Beijing, China
[5] College of Surveying and Geo-Informatics, Tongji University, Shanghai, China

Abstract. Inter-frequency clock bias (IFCB) should be considered when performing triple-frequency GNSS precise point positioning (PPP). Traditional approach of IFCB estimation is by averaging IFCB of all stations. However, this method doesn't consider the variation of receiver IFCB, so the averaged receiver IFCB is lumped into satellite IFCB. If the receiver IFCB can't eliminate by averaging when station number is limited, this method is not theoretical compactness. In this paper, we propose a more compactness IFCB estimation method based on network solution. In this method, the satellite and receiver IFCB are estimated together under a constraint of satellite IFCB. To validate this method, we select a 60-days global MGEX data and estimate the BDS IFCB between B1B2 and B1B3. Results show that BDS IFCB is within 10 cm and the RMS for all satellites are within 3 cm, while for receiver IFCB, it has a similar periodic performance as satellite. After correcting IFCB in kinematic PPP using B1B3 combination, statistical results among 13 MGEX stations show about 0.5 cm improvement in horizontal and vertical comparing with uncorrected IFCB PPP solution.

Keywords: Inter-frequency clock bias · Epoch difference · Network solution · Precise point positioning

1 Introduction

With the development and modernization of GNSS systems, triple frequency signal is now available. The existing GPS Block IIF and the ongoing Block III satellites provide L5 signal besides of L1 and L2 frequency[1]. Galileo, BDS and QZSS all provide triple or even four frequency signals at the beginning of system design. With the redundant

[1] https://www.gps.gov/systems/gps/space/.

J. Sun et al. (Eds.): CSNC 2019, LNEE 563, pp. 39–48, 2019.
https://doi.org/10.1007/978-981-13-7759-4_4

information of triple frequency, precise point positioning (PPP) users could benefit in positioning accuracy and convergence performance (Geng and Bock 2013; Mohamed 2015; Cao et al. 2018).

Conventional IGS precise clock solution is based on L1/L2 ionosphere-free combination. When performing SPP (single point positioning) or PPP in other frequency or other frequency combinations, one should consider the signal delay difference on code, namely timing group delay (TGD) or differential code bias (DCB) (Ge et al. 2017; Montenbruck et al. 2018).

However, Montenbruck found that there also exists inter-frequency clock bias (IFCB) between L1/L2 and L1/L5 for GPS (Montenbruck et al. 2012; Li et al. 2013a). For BDS, researches also prove the existence of IFCB between B1/B2 and B1/B3 (Li et al. 2013b; Pan et al. 2016). For both GPS and BDS, IFCB exhibits periodic characteristic with a notable period of 24 h, which makes it possible to predict IFCB change according to pre-day estimation of IFCB (Li et al. 2016; Pan et al. 2018).

However, traditional method to estimate IFCB is based on single station IFCB solution of all visible satellites and then combined by weighted averaging of all tracked stations for each satellite. In this approach, receiver IFCB is assumed as a constant value and could be eliminated after epoch difference. Li proves that the contribution of receiver IFCB can be ignored (Li et al. 2012). However, this may attribute to the stability averaged receiver IFCB of all tracked stations, while it can't proves the assumption of constancy in receiver IFCB. When few stations are tracked for one satellite, averaged receiver IFCB may be not stable and satellite IFCB would absorb the residual of averaged receiver IFCB. For the estimation of BDS IFCB, MEO satellite would show noisier comparing with GEO and IGSO satellites (Pan et al. 2018), which may attribute to the unstable of averaged receiver IFCB when not enough stations are tracked.

Although IFCB estimation is fully discussed by many researchers, there are not many works on demonstration and effects of IFCB correction in PPP, especially for BDS. Pan investigates the BDS triple frequency PPP performance after correcting IFCB (Pan et al. 2018). However, only one station of one day is used so that the conclusion is not convincing.

In this paper, we propose an improved method to estimate both satellite and receiver IFCB change based on network solution. 55 MGEX station are selected to assess the long term variation of IFCB for BDS, together with IFCB for stations. The estimated BDS IFCB is then corrected in PPP of B1B3 combination to evaluate their effects in PPP.

2 IFCB Estimation

2.1 Traditional Approach of IFCB Estimation

Tradition approach to estimate IFCB is proposed by Montenbruck (Montenbruck et al. 2012). For carrier phase observation of triple frequency in the case of BDS, one can form two ionosphere-free (IF) combinations. The geometry range, troposphere delay and some station depended displacement errors can be removed by subtracting these two ionosphere-free combinations:

$$\mathrm{DIF}(B_1, B_1, B_3) = IF(B_1, B_2) - IF(B_1, B_3) = IFCB^s - IFCB_r + dN \tag{1}$$

where dN is the differenced ambiguity between B1B2 and B1B3 IF combination, $IFCB^s$ and $IFCB_r$ stand for IFCB between B1B2 and B1B3 ionosphere combination on satellite and receiver, respectively.

If no cycle slip occurs between two adjacent epochs, dN could eliminated by epoch differencing. The epoch differenced observation in Eq. (1) could express as:

$$\Delta\mathrm{DIF}(B_1, B_1, B_3) = \Delta IFCB^s - \Delta IFCB_r \tag{2}$$

where Δ is the symbol of epoch differencing.

In traditional method, receiver IFCB is assumed as a constant value and thus $\Delta IFCB_r$ in Eq. (2) becomes zero. So IFCB on satellite is easy to estimate at each station.

For one specific satellite, if it is tracked by n stations, the integrated epoch differenced IFCB could be calculated by weighted averaging of all tracked stations:

$$\Delta IFCB^s = \left(\sum\nolimits_{r=1}^{n} (\Delta IFCB_r^s \cdot w_r) / \sum\nolimits_{r=1}^{n} w_r\right) \tag{3}$$

where w_r is the weight contribution at station r.

After we get epoch differenced IFCB, the accumulated IFCB could be calculated by simple sum up of $\Delta IFCB^s$:

$$IFCB^s(t) = \sum\nolimits_{i=1}^{t} \Delta IFCB^s(i) \tag{4}$$

where $IFCB^s(t)$ is the IFCB at epoch t.

What should be pointed out is that the IFCB at first epoch is assumed as zero, which is obvious not true. Therefore the estimated IFCB in this approach contains a constant bias on each satellite. However, for PPP float ambiguity solution, the constant bias of IFCB would be absorbed by ambiguity. Therefore it would not affect PPP result.

2.2 Improved IFCB Estimation Based on Network Solution

As mentioned in previous sub-section, the IFCB on receiver is assumed as a stable value and is eliminated after epoch difference. However, there is no evidence proving the stability of this value. If IFCB on receiver is not a constant value, then the traditional approach is not theoretical compactness, even receiver IFCB may be very small after station averaging. In other words, the averaged receiver IFCB may not be ignored when there are not many stations tracking one satellite. Results prove that in traditional approach, when satellite average weight is low for one satellite, the estimated IFCB may exhibit higher noise (Pan et al. 2018)

To full consider the variation of receiver IFCB, we propose an improved method based on network solution.

In the improved approach, receiver IFCB is not regarded as a constant value in Eq. (2). Therefore $\Delta IFCB_r$ is not zero and should also estimate together with $\Delta IFCB^s$,

which is impossible to estimate within a single station. Fortunately, $\Delta IFCB_r$ is same for all satellite at the same station, so we can solve the epoch differenced satellite and receiver IFCB base on a network solution.

For all stations and all satellites, we can form the network observation as:

$$\begin{bmatrix} 1 & 0 & \cdots & -1 & 0 & \cdots \\ 1 & 0 & \cdots & 0 & -1 & \cdots \\ \vdots & \vdots & \ddots & \vdots & \vdots & \vdots \\ 0 & 1 & \cdots & -1 & 0 & \cdots \\ 0 & 1 & \cdots & 0 & -1 & \cdots \\ \vdots & \vdots & \cdots & \vdots & \vdots & \vdots \end{bmatrix} \begin{bmatrix} \Delta \mathrm{IFCB}^1 \\ \Delta \mathrm{IFCB}^2 \\ \vdots \\ \Delta \mathrm{IFCB}_1 \\ \Delta \mathrm{IFCB}_2 \\ \vdots \end{bmatrix} = \begin{bmatrix} \Delta \mathrm{DIF}_1^1 \\ \Delta \mathrm{DIF}_1^2 \\ \vdots \\ \Delta \mathrm{DIF}_2^1 \\ \Delta \mathrm{DIF}_2^2 \\ \vdots \end{bmatrix} \tag{5}$$

For the solution of Eq. (5), the normal equation is rank defected as there is no defined datum. To overcome this problem, we define the averaged epoch differenced IFCB for all satellite is zero. Then by using Least Square or Kalman Filter, one can estimate the epoch differenced IFCB for all satellite and receiver.

After epoch differenced IFCB is estimated, we can use Eq. (4) to get IFCB at each epoch.

3 Experiment Setup

To validate the proposed approach, 55 MEGX stations that can track triple frequency signal of BDS are selected, which are shown in Fig. 1. To assess the long term performance IFCB for BDS, we choose 60-days of data from day of year (DOY) 180∼239 in 2017.

For estimation of BDS IFCB, we assume the averaged epoch differenced BDS IFCB is zero in the improved approach.

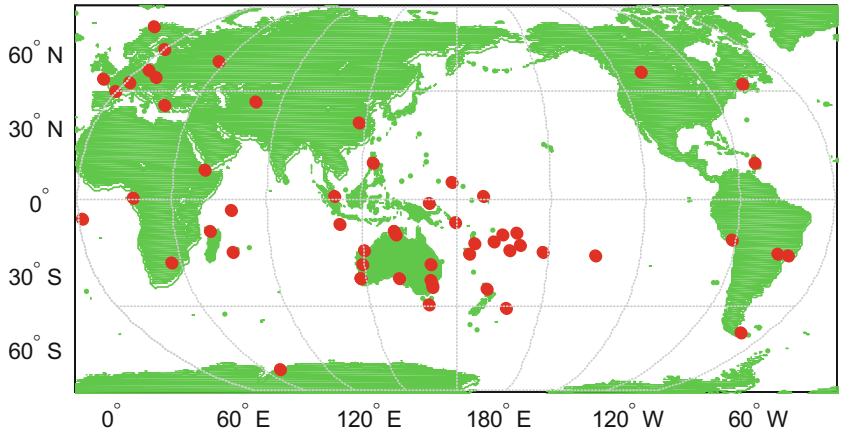

Fig. 1. 55 Selected MGEX stations for the estimation of BDS IFCB

4 IFCB Results and Analysis

4.1 BDS IFCB and Station IFCB

By using the proposed IFCB estimation approach, we can get the IFCB variation of BDS satellites. Figures 2, 3 and 4 shows the long term variation of IFCB C03, C04, C08, C09, C11, C12, which represents GEO, IGSO and MEO satellites, respectively.

From the figures we can obviously see that the daily BDS IFCB change is always within 10 cm and it shows a quite good periodic characteristic of 24 h. Comparing our result with previous result using traditional method (Pan et al. 2018), we can know that the magnitude is similar but the IFCB noise for MEO satellite is similar with GEO and IGSO satellites, which shows much smaller noise than precious research (Pan et al. 2018). This may attribute to that in the improved approach, the IFCB of one satellite doesn't affect by tracked station number as it is connected with receiver and other satellite IFCB.

Table 1 also summarize the RMS of BDS IFCB, it can be seem that the RMS is within 3 cm for all BDS satellites, which is comparable with other results (Pan et al. 2018).

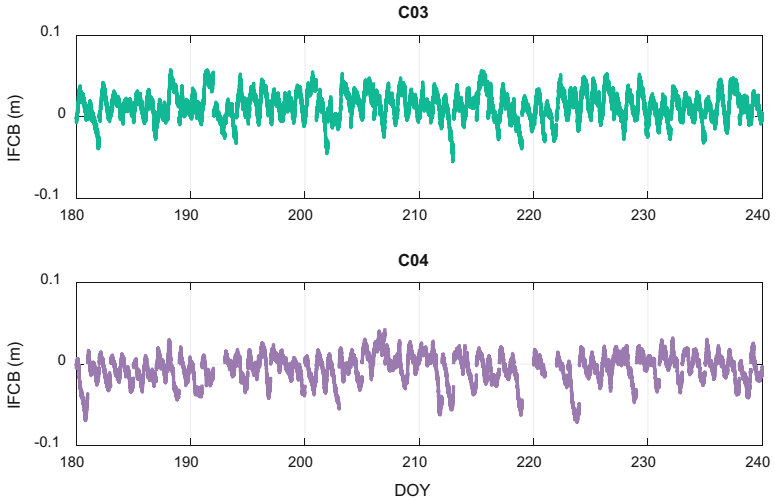

Fig. 2. Long term variation of IFCB for BDS GEO satellites (C03/C04, DOY180 ~ DOY239)

In the improved approach, station IFCB can also derived. Figure 5 shows the estimated station IFCB at station CUT0 and DARW. We can see that IFCB is actually not stable and it also has a periodic characteristic of 24 h, which proves that the assumption of stability for receiver IFCB is not true.

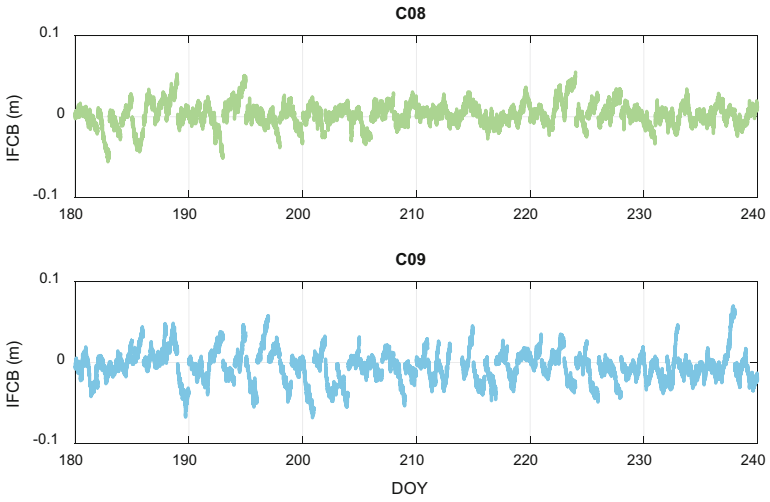

Fig. 3. Long term variation of IFCB for BDS IGSO satellites (C08/C09, DOY180～DOY239)

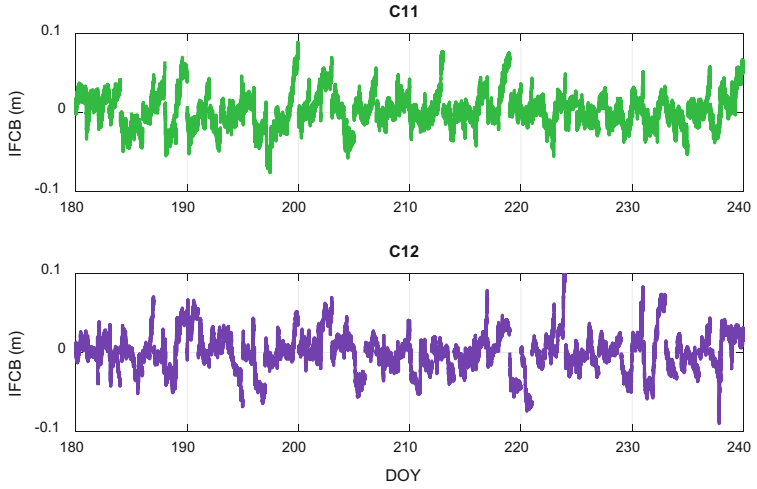

Fig. 4. Long term variation of IFCB for BDS MEO satellites (C11/C12, DOY180～DOY239)

4.2 Effect of IFCB on PPP

To evaluate the estimated IFCB, we perform kinematic PPP solution using B1B3 ionosphere-free combination by correcting and not correcting IFCB. To have a better understanding and comparison of B1B3 based PPP, traditional B1B2 ionosphere-free based kinematic PPP solution is also calculated. 13 MGEX stations on DOY 201, 2017 are selected and statistical RMS of kinematic PPP are presented in Table 2. The convergence period of kinematic PPP is set as 30 min therefore the first 30 min PPP error is not included in the statistical RMS.

Table 1. RMS of BDS IFCB (DOY180～DOY239)

PRN	RMS(m)	PRN	RMS(m)
C01	0.016	C08	0.015
C02	0.018	C09	0.020
C03	0.021	C10	0.019
C04	0.019	C11	0.022
C05	0.026	C12	0.024
C06	0.024	C13	0.019
C07	0.015	C14	0.023

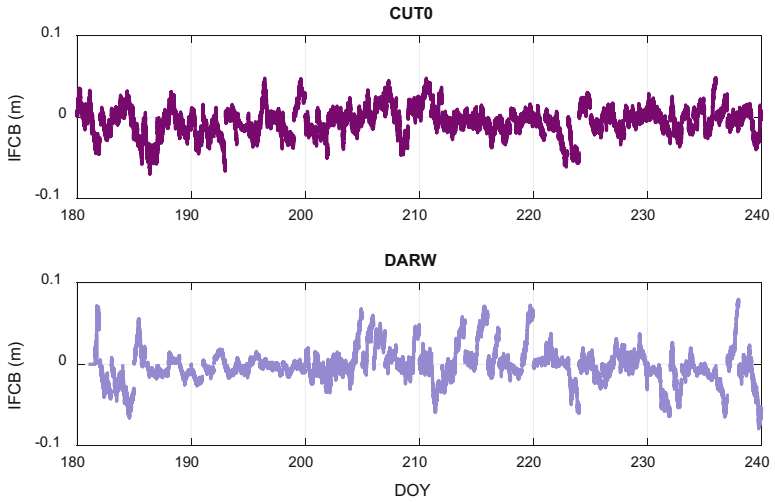

Fig. 5. Long term variation of IFCB at station CUT0 and DARW (DOY180～DOY239)

We can see that the mean accuracy of B1B3 PPP after IFCB correction is 0.081 m in horizontal and 0.121 m in vertical, while it is 0.087 in horizontal and 0.126 in vertical, which indicates a slight improvement of about 0.5 cm in horizontal and vertical, respectively. However, both solutions in B1B3 are worse than traditional B1B2 based PPP solution. The improvement after IFCB correction is not so obvious, which may due to the reason that the estimated RMS of IFCB is only within 3 cm, and when cycle slip occurs on a satellite, the ambiguity solution would re-initialize so that the mean value of IFCB would absorbed into ambiguity.

To take a detailed view of PPP performance after IFCB correction, we select result at station of XMIS as example, the B1B3 based kinematic PPP with and without IFCB correction is shown in Fig. 6. We can clearly see the improvement of PPP performance after IFCB correction. Figure 7 shows the histogram of positioning residuals for carrier phase. With more positioning residuals gather in the center of zero, it proves slightly better performance after IFCB correction.

Table 2. Kinematic PPP performance of B1B2 and B1B3 combination (H means horizontal and V means vertical)

Station	B1B3 IFCB uncorrected		B1B3 IFCB corrected		B1B2	
	H (m)	V (m)	H (m)	V (m)	H (m)	V (m)
CEDU	0.045	0.099	0.057	0.084	0.045	0.090
CUT0	0.050	0.082	0.030	0.079	0.029	0.062
DARW	0.051	0.074	0.036	0.082	0.041	0.064
KARR	0.034	0.058	0.030	0.070	0.028	0.054
KAT1	0.053	0.092	0.062	0.081	0.053	0.062
KITG	0.353	0.287	0.336	0.266	0.236	0.155
MCHL	0.089	0.125	0.096	0.125	0.098	0.110
MRO1	0.033	0.060	0.035	0.056	0.028	0.045
PNGM	0.055	0.122	0.055	0.141	0.051	0.122
SIN1	0.052	0.109	0.048	0.102	0.039	0.104
STR1	0.102	0.189	0.095	0.190	0.126	0.168
STR2	0.141	0.191	0.133	0.190	0.109	0.166
XMIS	0.076	0.143	0.066	0.132	0.051	0.110
Mean	0.087	0.126	0.081	0.121	0.072	0.101

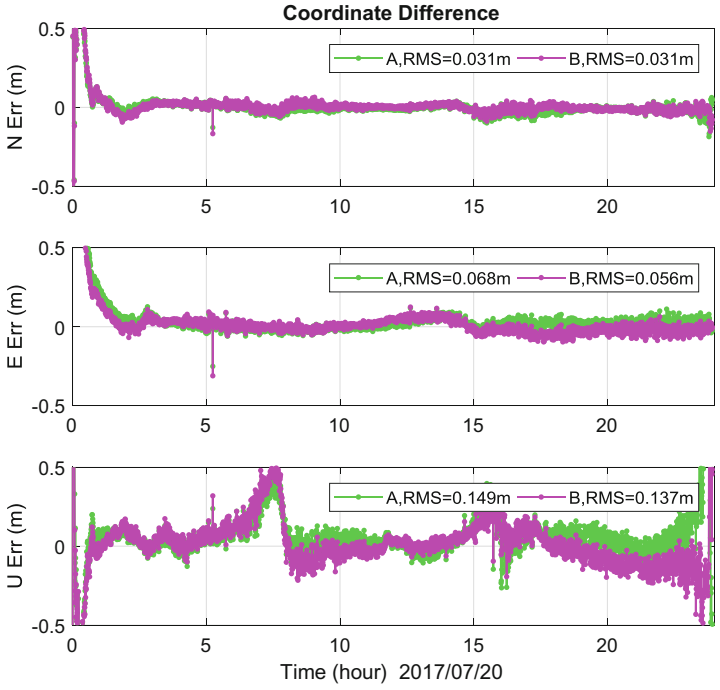

Fig. 6. Kinematic PPP performance with and without IFCB correction at station of XMIS (A means IFCB uncorrected and B means IFCB corrected)

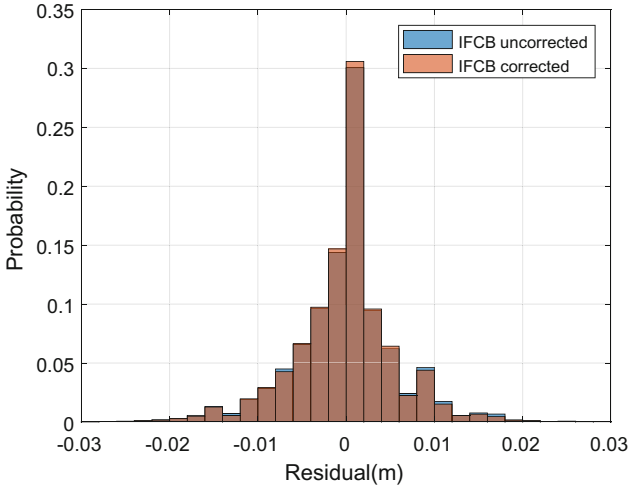

Fig. 7. Histogram of positioning residuals of carrier phase with and without IFCB correction at station of XMIS

5 Conclusions

In this paper, we propose an improved IFCB estimation approach based on network solution. In this method, the satellite and station IFCB are estimated together under the zero mean constraint epoch differenced satellite IFCB. To validate this method, 60-days of global MGEX data are used to estimate BDS IFCB between B1B2 and B1B3. Results show that:

(1) BDS IFCB is within 10 cm and the RMS for all satellites are within 3 cm with a periodic characteristic, and the estimated IFCB based on network solution have a smaller noise compared with traditional method.
(2) For station IFCB, it has a similar periodic performance as satellite.
(3) After correcting IFCB in kinematic PPP in B1B3 combination, statistical results among 13 MGEX stations show about 0.5 cm improvement in horizontal and vertical comparing with uncorrected IFCB PPP solution.

This method could apply in the estimation of other GNSS system and the new BDS-3 satellite.

Acknowledgement. This work is support by the National Natural Science Foundation of China (No. 41874042) and the Opening Project of Shanghai Key Laboratory of Space Navigation and Positioning Techniques (No. KFKT_201706).

References

Cao X, Li J, Zhang S et al (2018) Uncombined precise point positioning with triple-frequency GNSS signals. Adv Space Res, S0273117718302515

Ge Y, Zhou F, Sun B et al (2017) The impact of satellite time group delay and inter-frequency differential code bias corrections on multi-GNSS combined positioning. Sensors 17(3):602

Geng J, Bock Y (2013) Erratum to: triple-frequency GPS precise point positioning with rapid ambiguity resolution. J Geodesy 87(5):449–460

Li H, Wu B, Zhou X (2013a) Fast estimation and analysis of the inter-frequency clock bias for the Block IIF satellites. GPS Solutions 17(3):347–355

Li H, Chen Y, Wu B et al (2013b) Modeling and initial assessment of the inter-frequency clock bias for COMPASS GEO satellites. Adv Space Res 51(12):2277–2284

Li H, Li B, Xiao G, Wang J, Xu T (2016) Improved method for estimating the inter-frequency satellite clock bias of triple-frequency GPS. GPS Solut 20:751–760

Li HJ, Zhou XH, Wu B et al (2012) Estimation of the inter-frequency clock bias for the satellites of PRN25 and PRN01. Sci China: Phys Mech Astron 55(11):2186–2193

Mohamed E (2015) Precise point positioning using triple-frequency GPS measurements. J Navig 68(3):13

Montenbruck O, Hugentobler U, Dach R, Steigenberger P, Hauschild A (2012) Apparent clock variations of the Block IIF-1 (SVN62) GPS satellite. GPS Solut 16:303–313

Montenbruck O, Steigenberger P, Hauschild A (2018) Multi-GNSS signal-in-space range error assessment – methodology and results. Adv Space Res, S0273117718302813

Pan L, Zhang X, Liu J et al (2016) Analysis and correction of the inter-frequency clock bias for BeiDou satellites. In: China Satellite Navigation Conference (CSNC) 2016 Proceedings: Volume II. Springer Singapore

Pan L, Zhang X, Li X et al (2018) GPS inter-frequency clock bias modeling and prediction for real-time precise point positioning. GPS Solut 22(3):76

A Tightly Combined BDS and GPS Method for RTK Positioning with Triple-Frequency Widelane Combinations

He Wen[1], Shuguo Pan[1(✉)], Wang Gao[1], and Qing Zhao[2]

[1] School of Instrument Science and Engineering, Southeast University, Nanjing 210096, China
psg@seu.edu.cn
[2] School of Transportation, Southeast University, Nanjing 210096, China

Abstract. Processing the differential inter-system biases (DISBs) correctly is critical for multi-GNSS fusion positioning. A pivot satellite can be selected for RTK positioning if we can process DISBs correctly, which is the so-called tightly combination between systems. Due to the different frequencies of GPS and BDS, DISB cannot be calibrated in advance. In this paper, a tightly combined BDS/GPS method for RTK positioning model is proposed. A zero baseline is selected to verify the near time-constant characteristic of DISB. In addition, aiming at the limitation of traditional MW combination that the fixed success rate of WL ambiguity is greatly affected by pseudorange noise and has long convergence time, we could use the triple-frequency data to fix a long-wavelength EWL ambiguity. Then assists in solving WL ambiguity. The results show that the fractional part of phase DISB with WL combination is rather stable. Under the medium baseline, the fixed success rate of WL ambiguity floating point solution fraction within 0.2 cycles is 100%, and WL ambiguity can be fixed correctly in the first epoch. Compared with the classical differencing model, the inter-system differencing model can effectively improve the positioning accuracy and reliability, especially for severely obstructed environment. In the normal observation environment, the positioning accuracy can reach 2–3 cm in horizontal and 5 cm in vertical under the medium baseline. When the number of available satellites is seven, the positioning accuracy can be increased by more than 20%.

Keywords: BDS · GPS · Differential inter-system bias (DISB) · Medium baseline · RTK · EWL/WL ambiguity resolution

1 Introduction

With the development of the information age, the demand for accurate location information is increasing, so multi-GNSS combined positioning become an inevitable trend. Multi-GNSS differential positioning has two models. The classical differencing model [1] requires different pivot satellite for each system. The performance of GPS/BDS/GLONASS combined RTK positioning for middle-long baseline was investigated by Gao et al. [2]. In addition, if DISBs are processed correctly and only

J. Sun et al. (Eds.): CSNC 2019, LNEE 563, pp. 49–61, 2019.
https://doi.org/10.1007/978-981-13-7759-4_5

one satellite is selected as the pivot satellite, which is the so-called tight tightly combination between systems [3]. For the overlapping frequencies between two systems (e.g., GPS L1 and Galileo E1), the time-varying characteristics of DISB are analyzed by Odijk et al. [4], and can be calibrated in advance. What's more, GPS/Galileo inter-system bias and drift are evaluated by Gioia et al. using different types of receivers: two mass market and two professional receivers, and three different approaches are considered for the inter-system bias determination. From their experiments, it emerges that the inter-system bias is very stable. In addition, Liu et al. proposed that the Inter-System Bias (ISB) could help to maximize the redundancy of the positioning model, and can improve the performance of multi-GNSS positioning [5]. Moreover, Inter-system differencing model based on single frequency was proposed by Gao et al. [6], which can improve the positioning accuracy and reliability under the short baseline. Tian et al. [7] presented a new method by means of particle filter to estimate ISBs in real time without any a priori information based on the fact that the accuracy of a given ISB value can be qualified by the related fixing RATIO. This method can be carried out epoch by epoch to provide precise ISB in real time. In obstructed environments, if a system has only one satellite available, using the classical differencing model, the satellite cannot be used, but it still can be used with the inter-system differencing model.

At present, we usually solve L1 or L2 ambiguity for RTK positioning. For medium or long baselines, influenced by factors such as base station distance and atmospheric error, the success rate of ambiguity resolution is low in a short time, and the initialization time is very long [8], which lead to the reliability of the positioning results cannot be guaranteed. In order to improve the success rate of ambiguity resolution, and shorten the initialization time, MW combination can be used to fix the ambiguity of double difference wide lane observations. Then, L1 observation equation is adopted to fix the ambiguity of L1 double difference observations. In addition, Three-frequency data is used to form a series of WL or EWL combinations with long wavelengths, which can effectively reduce the atmospheric error and observation noise and can improve the success rate of fixed ambiguity [9–12].

Although many studies have been focused on the DISB with single frequency under zero/short-baseline experiments, the effect of DISB with WL combination under medium baseline conditions remains to be further studied. The rest of this paper is organized as follows: In Sect. 2, the EWL/WL Ambiguity resolution model and the inter-system model of BDS and GPS with WL combination are introduced. In Sect. 3, the results of EWL/WL ambiguity resolution are analyzed under the medium baseline. In Sect. 4, the stability of DISB with WL combination between BDS and GPS is analyzed with zero baseline. In Sect. 5, we mainly test the improvement of the inter-system differencing model in BDS+GPS WL combination RTK with normal and simulated obstructed environments under the medium baseline. Some conclusions will be given in Sect. 6.

2 Methods

2.1 EWL/WL Ambiguity Resolution Model

Considering the influence of troposphere and ionosphere, the DD observation equations for GPS or BDS can be expressed as

$$\begin{aligned}\Delta\nabla\phi^{s}_{(i,j,k)} &= \Delta\nabla\rho^{s} + \Delta\nabla T - \eta_{(i,j,k)}\Delta\nabla I + \lambda_{(i,j,k)}\Delta\nabla N_{(i,j,k)} + \Delta\varepsilon^{s}_{\phi_{(i,j,k)}} \\ \Delta\nabla P^{s}_{[\alpha,\beta,\gamma]} &= (\alpha+\beta+\gamma)(\Delta\nabla\rho^{s} + \Delta\nabla T) + \eta_{[\alpha,\beta,\gamma]}\Delta\nabla I + \Delta e^{s}_{P_{[\alpha,\beta,\gamma]}}\end{aligned} \tag{1}$$

where

$$\begin{aligned}\Delta\nabla\phi_{(i,j,k)} &= \frac{i\cdot f_1\cdot\Delta\nabla\phi_1 + j\cdot f_2\cdot\Delta\nabla\phi_2 + k\cdot f_3\cdot\Delta\nabla\phi_3}{i\cdot f_1 + j\cdot f_2 + k\cdot f_3},\ \Delta\nabla P_{[\alpha,\beta,\gamma]} \\ &= \alpha\cdot\Delta\nabla P_1 + \beta\cdot\Delta\nabla P_2 + \gamma\cdot\Delta\nabla P_3\end{aligned} \tag{2}$$

where ϕ is the carrier observation and P is the pseudorange observation; $\Delta\nabla$ represents the double-differential operator; the superscript s is the index of satellites; i, j, k are the arbitrary integer; α, β, γ and η are the arbitrary real number; f_1, f_2, f_3 are the frequency of different frequency points; ρ is the distance between satellite and receiver; T and I denote tropospheric delay and ionospheric delay respectively; λ is the wavelength; N is the integer phase ambiguity; ε and e are the measurement noise for carrier phase and pseudorange observations, respectively. In Eq. (1), combining the triple-frequency carrier observations, a series of WL and EWL combinations with longer wavelengths can be constructed. In this paper, the selected EWL combination is (0, −1, 1), and the WL combination is (1, −1, 0). In addition, compared with WL, EWL has longer wavelength, so the EWL ambiguity is more easily fixed.

Based on the geometry-free and ionosphere-free model (GIF) using carrier and pseudorange combination [13], the EWL ambiguity resolution equation can be obtained as

$$\Delta\nabla N_{(0,-1,1)} = \frac{\Delta\nabla\phi_{(0,-1,1)} - \Delta\nabla P_{[0,1,1]}}{\lambda_{(0,-1,1)}} - \frac{\Delta\nabla\varepsilon_{\phi_{(0,-1,1)}} - \Delta\nabla e_{P_{[0,1,1]}}}{\lambda_{(0,-1,1)}} \tag{3}$$

In the above equation, the accuracy of the ambiguity resolution is significantly affected by the pseudorange noise, and the pseudorange noise is difficult to obtain accurately [9]. So in practical applications, the EWL ambiguity resolution [15] can be obtained as

$$\Delta\nabla N_{(0,-1,1)} = \frac{\Delta\nabla\phi_{(0,-1,1)} - \Delta\nabla P_{[0,1,1]}}{\lambda_{(0,-1,1)}} \tag{4}$$

In Eq. (4), the ionospheric delay and geometric correlation error can also be eliminated. The experimental part of this paper verifies that the above model can

reliably fix the EWL ambiguity in single epoch. Taking advantage of this advantage, TCAR method [14] with step-by-step fixed thinking can be adopted. Namely, we can take the observation with fixed EWL ambiguity as a high-precision observation. The EWL observation and WL observation are composed of geometry-free model to assist in solving the WL ambiguity. The solution equation can be obtained as

$$\Delta\nabla N_{(1,-1,0)} = \frac{1}{\lambda_{(1,-1,0)}}[\Delta\nabla\phi_{(1,-1,0)} - \Delta\nabla\phi_{(0,-1,1)} - (\eta_{(0,-1,1)} - \eta_{(1,-1,0)})\Delta\nabla I + \lambda_{(0,-1,1)}\Delta\nabla N_{(0,-1,1)}] \quad (5)$$

In Eq. (5), the TCAR method eliminates troposphere error and orbit error and so on, and avoid the effects of pseudorange noise. However, it is affected by ionospheric delay. The ionospheric delay (unit: meter) influence coefficient can be obtained as

$$\frac{(\eta_{(0,-1,1)} - \eta_{(1,-1,0)})}{\lambda_{(1,-1,0)}} = -0.352 \quad (6)$$

In Eq. (6), we can see that the influence coefficient of ambiguity solution by ionospheric delay is −0.352, and the sensitivity is small. So the ionospheric delay can be ignored for medium baselines. Therefore, when the carrier observation accuracy is well, the WL ambiguity could be accurately fixed.

2.2 Inter-system Model of BDS and GPS with WL Combination

For a short or medium baseline, assuming differential atmospheric delays to be absent. Then the between-receiver SD carrier observation equation with WL combination for GPS can be expressed as

$$\Delta\phi^q_{WL,G} = \Delta\rho^q_G + \Delta dT + \lambda^G_{WL}\Delta\delta^G_{WL} + \lambda^G_{WL}\Delta N^q_{WL,G} + \Delta\varepsilon^q_{WL,G} \quad (7)$$

Similarly, the between-receiver SD carrier observation equation with WL combination for BDS can be expressed as

$$\Delta\phi^s_{WL,C} = \Delta\rho^s_C + \Delta dT + \lambda^C_{WL}\Delta\delta^C_{WL} + \lambda^C_{WL}\Delta N^s_{WL,C} + \Delta\varepsilon^s_{WL,C} \quad (8)$$

where, Δ represents the station-difference operator; G and C represent GPS and BDS system respectively; the superscript q and s are the index of GPS and BDS satellites respectively; δ denote the phase hardware delay; The meaning of other characters is as described above.

Afterward, we need to select a system as pivot system. Because BDS system has more satellites to broadcast triple-frequency data than GPS system, so in this paper, we

can select BDS system as pivot system. According to Eq. (7), the DD carrier observation equation with WL combination for BDS can be expressed as

$$\Delta\nabla\phi_{WL,C}^{1_C s} = \Delta\phi_{WL,C}^{s} - \Delta\phi_{WL,C}^{1_C} = \Delta\nabla\rho^{1_C s} + \lambda_{WL}^{C}\Delta\nabla N_{WL,C}^{1_C s} + \Delta\nabla\varepsilon_{WL,C}^{1_C s} \tag{9}$$

where, 1_C denotes pivot satellite for BDS.

According to Eqs. (7) and (8), The inter-system DD carrier observation equation with WL combination between GPS and BDS can be obtained as

$$\Delta\nabla\phi_{WL,CG}^{1_C q} = \Delta\phi_{WL,G}^{q} - \Delta\phi_{WL,C}^{1_C} = \Delta\nabla\rho^{1_C q} + \lambda_{WL}^{G}\Delta N_{WL,G}^{q} - \lambda_{WL}^{C}\Delta N_{WL,C}^{1_C} + \lambda_{WL}^{G}\Delta\delta_{WL}^{CG} + \Delta\nabla\varepsilon_{WL,CG}^{1_C q} \tag{10}$$

where

$$\delta_{WL}^{CG} = \delta_{WL}^{G} - \frac{\lambda_{WL}^{C}}{\lambda_{WL}^{G}}\delta_{WL}^{C} \tag{11}$$

In Eq. (11), Due to $\lambda_{WL}^{G} \neq \lambda_{WL}^{C}$, SD ambiguities cannot be combined into intra-system DD ambiguities. Also, the Eq. (10) is rank-defective. So the Eq. (10) need be processed. Firstly, we need to select a pivot satellite for GPS. Afterward, the above equation can be reparameterized as

$$\begin{aligned}\lambda_{WL}^{G}\Delta N_{WL,G}^{q} - \lambda_{WL}^{C}\Delta N_{WL,C}^{1_C} &= \lambda_{WL}^{G}\Delta N_{WL,G}^{q} - \lambda_{WL}^{G}\Delta N_{WL,G}^{1_G} + \lambda_{WL}^{G}\Delta N_{WL,G}^{1_G} - \lambda_{WL}^{C}\Delta N_{WL,C}^{1_C} \\ &= \lambda_{WL}^{G}\Delta\nabla N_{WL,G}^{1_G q} + \lambda_{WL}^{G}\Delta N_{WL,G}^{1_G} - \lambda_{WL}^{C}\Delta N_{WL,C}^{1_C}\end{aligned} \tag{12}$$

where, 1_G denotes pivot satellite for GPS. Lastly, we need to merge some parameters, the final equation can be obtained as

$$\Delta\nabla\phi_{WL,CG}^{1_C q} = \Delta\nabla\rho^{1_G q} + \lambda_{WL}^{G}(\Delta\nabla N_{WL,G}^{1_G q} + \Delta\bar{\delta}_{WL}^{CG}) \tag{13}$$

where

$$\Delta\bar{\delta}_{WL}^{CG} = \Delta\nabla N_{WL,CG}^{1_C 1_G} + (1 - \frac{\lambda_{WL}^{C}}{\lambda_{WL}^{G}})\Delta N_{WL,C}^{1_C} + \Delta\delta_{WL}^{CG} \tag{14}$$

From the Eq. (14), we can see that the new phase DISB parameter includes the DD ambiguity between pivot satellite of GPS and pivot satellite of BDS, the SD ambiguity of pivot satellite of BDS and the original new phase DISB parameter. So the integral part of phase DISB parameter and integer ambiguity cannot be separated. When we analyze the time-varying characteristics of DISB parameter, due to the integer ambiguity remains unchanged, we can analyze the fractional part of DISB. If pivot satellite of BDS changes, the fractional part of DISB is affected. So when the pivot satellite of BDS changes from 1_C to 2_C, the corresponding strategy can be expressed as

$$\Delta\tilde{\delta}_{WL}^{CG} = \Delta\bar{\delta}_{WL}^{CG} - (1 - \frac{\lambda_{WL}^{C}}{\lambda_{WL}^{G}})\Delta\nabla N^{ref} = \Delta\delta_{WL}^{CG} + \Delta\nabla N_{WL,CG}^{2_C 1_G} + (1 - \frac{\lambda_{WL}^{C}}{\lambda_{WL}^{G}})\Delta N_{WL,C}^{1_C} \quad (15)$$

where

$$\begin{gathered}\Delta\bar{\delta}_{WL}^{CG} = \Delta\delta_{WL}^{CG} + \Delta\nabla N_{WL,CG}^{2_C 1_G} + (1 - \frac{\lambda_{WL}^{C}}{\lambda_{WL}^{G}})\Delta N_{WL,C}^{2_C} \\ \Delta\nabla N^{ref} = \Delta\nabla N_{WL,CG}^{1_C 2_C}\end{gathered} \quad (16)$$

where, $\Delta\bar{\delta}_{WL}^{CG}$ and $\Delta\tilde{\delta}_{WL}^{CG}$ denote DISB parameters before and after conversion respectively. $\Delta\nabla N^{ref}$ represents the DD ambiguity between pivot satellites before and after conversion.

In real-time estimation with multi-epochs, whether the pivot satellite of GPS or BDS changes from epoch to epoch, the phase DISB parameter in the filter also needs to be transformed correspondingly. When the pivot satellite of BDS changes from 1_C to 2_C, the phase DISB parameter can be transformed as follows

$$\Delta\bar{\delta}_{WL}^{CG}(t_2) = \Delta\bar{\delta}_{WL}^{CG}(t_1) - \frac{\lambda_{WL}^{C}}{\lambda_{WL}^{G}} N_{WL,C}^{1_C 2_C} = \delta_{WL}^{CG} + N_{WL}^{2_C 1_G} + (1 - \frac{\lambda_{WL}^{C}}{\lambda_{WL}^{G}})N_{WL,C}^{2_C} \quad (17)$$

where

$$\Delta\bar{\delta}_{WL}^{CG}(t_1) = \Delta\delta_{WL}^{CG} + \Delta\nabla N_{WL}^{1_C 1_G} + (1 - \frac{\lambda_{WL}^{C}}{\lambda_{WL}^{G}})\Delta N_{WL,C}^{1_C} \quad (18)$$

where, t_1 and t_2 represent the two consecutive epochs.

Similarly, when the pivot satellite of GPS changes from 1_G to 2_G, the phase DISB parameter can be transformed as follows

$$\Delta\bar{\delta}_{WL}^{CG}(t_2) = \Delta\bar{\delta}_{WL}^{CG}(t_1) + \Delta\nabla N_{WL,G}^{1_G 2_G} = \Delta\delta_{WL}^{CG} + \Delta N_{WL}^{1_C 2_G} + (1 - \frac{\lambda_{WL}^{C}}{\lambda_{WL}^{G}})\Delta N_{WL}^{1_C} \quad (19)$$

Through the above conversion, continuous RTK positioning can be ensured. In the single-epoch model, the inter-system differencing model have the same performance with the classical differencing model. However, in the multi-epoch model, the inter-system differencing model has more redundant observations than classical differencing model. Therefore we can believe that the inter-system differencing model will have better positioning performance, especially in the severely obstructed environment.

3 Results of EWL/WL Ambiguity Resolution

In order to test the success rate of WL ambiguity resolution for medium baseline, in this paper, the baseline with length of 22.4 km is selected for experiment. The baseline information is shown in Table 1. The data were collected on DOY 150, 2018 with the sampling interval of 30 s.

Table 1. Baseline used in the experiment of EWL/WL ambiguity resolution

Baseline	Baseline length	Data length	Sampling interval	Receiver type	Collection location
CUT0-PERT	22.4 km	One day (DOY 150, 2018)	30 s	Trimble NETR9	Perth Australia

Using the model shown in Eq. (4), the fraction of EWL ambiguity floating solution can be obtained as follows

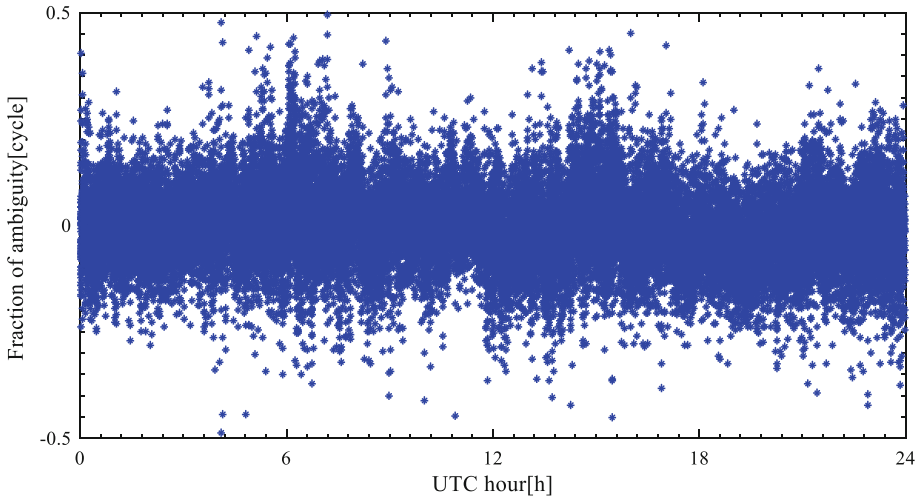

Fig. 1. The fraction of EWL ambiguity floating solution

From Fig. 1, we can see that the fraction of EWL ambiguity floating solution is basically distributed in the range of −0.2 to 0.2 cycles. The percentage of the fraction of EWL ambiguity floating solution in different fractional intervals is shown in Table 2. In addition, According to statistics, the accuracy rate of the EWL ambiguity resolution in single epoch is 100%, which verifies the reliability of model of the WL ambiguity resolution in single epoch shown in Eq. (4).

Afterward, according to Eq. (5), the WL ambiguity can be solved. The fraction of WL ambiguity floating solution can be obtained as follows (Fig. 2)

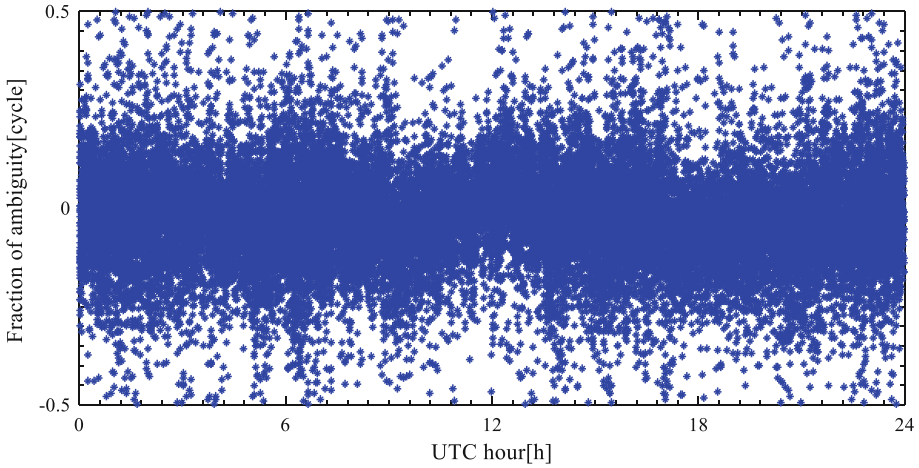

Fig. 2. The fraction of WL ambiguity floating solution

The percentage of the fraction of WL ambiguity floating solution in different fractional intervals is shown in Table 2. In order to further improve the fixed success rate of WL ambiguity, multi-epoch averaging filtering can be adopted. The fraction of WL ambiguity floating solution after filtering can be obtained as follows

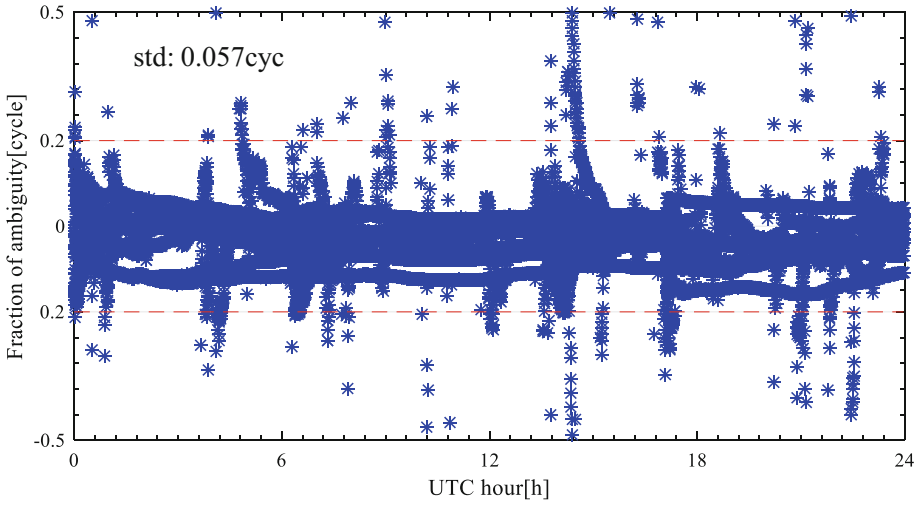

Fig. 3. The fraction of WL ambiguity floating solution after filtering

From Fig. 3, we can see that the fraction of WL ambiguity floating solution after filtering is basically distributed in the range of −0.2 to 0.2 cycles. The standard deviation is 0.057cyc. The percentage of the fraction of WL ambiguity floating solution after filtering in different fractional intervals is shown in Table 2. What's more, in order

to ensure the accuracy of coordinate calculation, the WL ambiguity bias threshold is set to 0.2 cycles. According to statistics, the fixed success rate of WL ambiguity floating point solution fraction within 0.2 cycles is 100%.

Table 2. The percentage of the fraction of ambiguity floating solution in different fractional intervals

Fractional interval (cycle)	The percentage of the fraction of ambiguity floating solution (%)		
	EWL ambiguity of single epoch	WL ambiguity of single epoch	WL ambiguity after filtering
−0.1–0.1	74.83	62.76	87.03
−0.2–0.2	96.92	89.80	99.36
−0.3–0.3	99.65	97.30	99.76
−0.4–0.4	99.97	99.26	99.89
−0.5–0.5	100	100	100

4 Stability Analysis of BDS-GPS DISB with WL Combination

In order to eliminate the influence of atmospheric error and multipath error, in this paper, the zero baseline CUT2-CUT0 is selected to verify the near time-constant characteristic of DISB parameter. The estimated phase DISB with WL combination result is shown in Fig. 4.

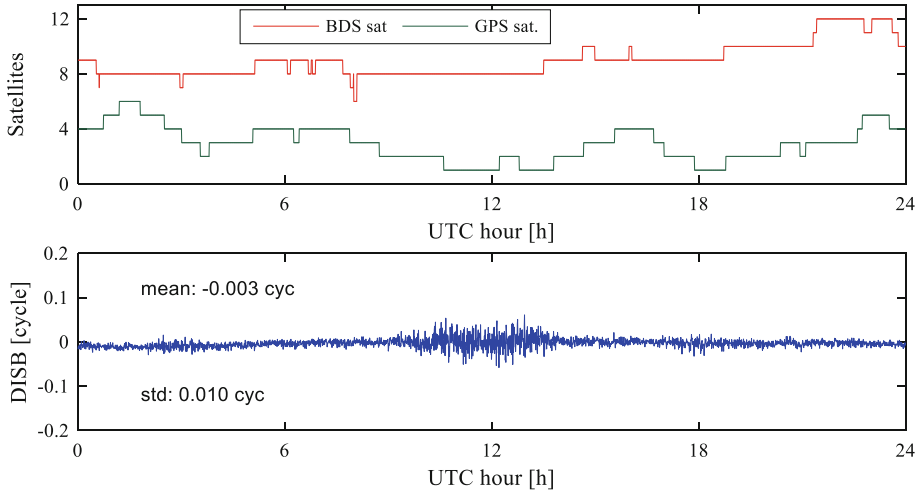

Fig. 4. Number of satellites and the estimated phase DISB with WL combination result

From Fig. 4, we can see that the DISB with WL combination is basically unchanged in one day. Because there are few GPS satellites capable of transmitting three-frequency signals, only one GPS satellite with triple-frequency data can be received in many epochs. At around 12 o'clock, the DISB fluctuated because there was only one GPS satellite with triple-frequency data during this time. The mean of the solution result is −0.003cyc and the standard deviation is 0.010cyc. Therefore, we can adopt the DISB real-time estimation in the medium baseline experiment.

5 Experiments of Medium-Baseline RTK Positioning

In the medium baseline experiment, we still select the baseline CUT0-PERT. Detailed information for the baseline is as described above. Under normal observation, the cut-off elevation angle threshold is set to 15° in the experiment. The positioning results of the inter-system differencing model and the classical differencing model are shown in Fig. 5.

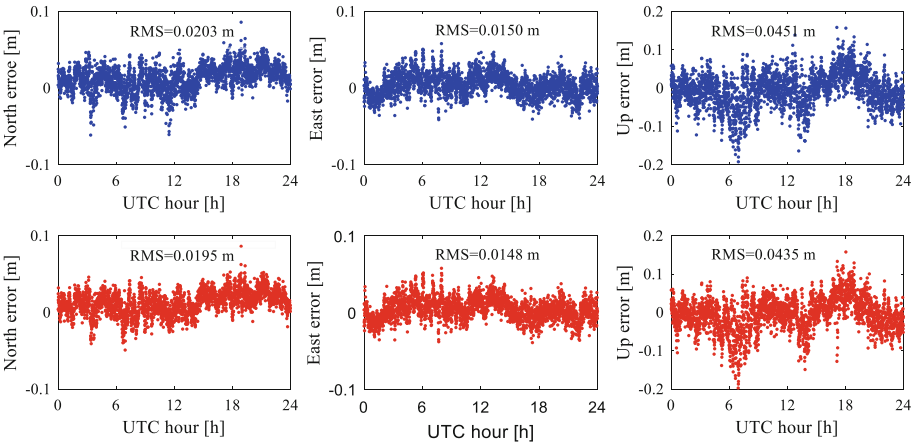

Fig. 5. The positioning results of the inter-system differencing model (red dots) and the classical differencing model (blue dots) in N/E/U directions

From Fig. 5, we can see that comparing with the classical differencing model, the inter-system differencing model has less improvement in positioning accuracy. In the N, E, and U directions, the positioning errors are 1.95 cm, 1.48 cm, and 4.35 cm, respectively. In order to further test the positioning performance of the inter-system differencing model in the medium baseline, we need to simulate obstructed environment. In this paper, the obstructed mode is to select 7–11 satellites in descending order of elevation angles. For the different visible satellites, the positioning results of the inter-system differencing and classical differencing model are shown in Table 3.

Table 3. The positioning results of the inter-system differencing and classical differencing model

Visible satellites	RMS of positioning errors (cm)						Improvement (%)		
	Classical differencing			Inter-system differencing					
	N	E	U	N	E	U	N	E	U
7	3.04	2.54	11.8	2.35	2.09	9.65	22.9	17.8	18.2
8	2.38	1.93	7.89	2.13	1.75	6.78	10.5	9.4	14.1
9	2.27	1.77	6.88	2.08	1.68	6.29	8.4	5.1	8.5
10	2.16	1.64	5.84	2.02	1.61	5.53	6.1	2.0	5.3
11	2.08	1.57	5.21	1.97	1.54	4.97	5.2	1.9	4.6
All	2.03	1.50	4.51	1.95	1.48	4.35	3.8	1.6	3.6

From Table 3, we can see that the inter-system differencing model has better performance than the classical differencing model. As the number of visible satellites decreases, the improvement of positioning accuracy becomes more and more significant. When the number of visible satellites is seven, the positioning results of the inter-system differencing model and the classical differencing model are shown in Fig. 6.

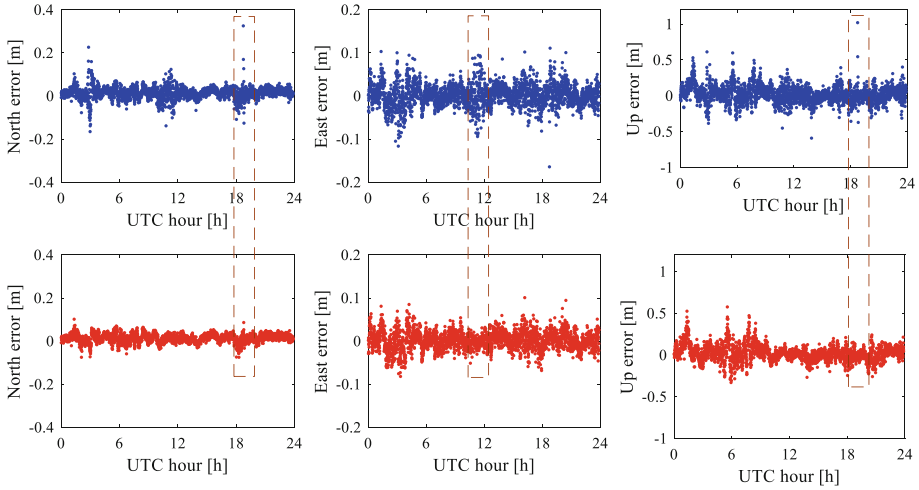

Fig. 6. The positioning results of the inter-system differencing model (red dots) and the classical differencing model (blue dots) with seven available satellites in N/E/U directions

When the number of satellites is seven, the positioning accuracy of classical differencing model is significantly improved compared to classical differencing model, and the parts with obvious improvement in accuracy have been marked in the Fig. 6.

It is worth noting that in the case of severe occlusion, when there is only one GPS satellite, if we use the classical differencing model, the GPS satellite is unavailable.

However, the GPS satellite is available when using the inter-system differencing model, which is the advantage of the inter-system differencing model to use more satellites and improve the geometry of the satellites.

6 Conclusions

In this paper, we propose a tightly combined BDS and GPS method for RTK positioning with triple-frequency WL combinations. Firstly, the triple-frequency data is used to fix EWL ambiguity and the fixed success rate in single epoch is 100%. Then we can use fixed EWL ambiguity to assists in solving WL ambiguity, which avoids the effects of pseudorange noise. Experiments show that the WL ambiguity resolution results can ensure accuracy and reliability under the medium baseline, and the ambiguity can be correctly fixed in the first epoch. In addition, the DISB results based on zero baseline shows that the phase DISB with WL combination is rather stable over time, which means that it can be estimated in real time to get lots of redundant observations. A medium baseline of 22.4 km was tested with DISB estimation to verify the proposed model. The results show that in the normal observation environment, compared with the classical differencing model, the inter-system differencing model has less improvement in positioning accuracy. Under the medium baseline, the positioning accuracy can reach 2–3 cm in horizontal and 5 cm in vertical. In the obstructed environment, the positioning accuracy of the inter-system differencing model is significantly improved compared to the classical differencing model. When the number of available satellites is seven, the positioning accuracy can be increased by more than 20%. In this paper, the influence of ionospheric delay is neglected in the WL ambiguity resolution under the medium baseline, but we need to use atmospheric error model for the long baseline circumstances. It should be noted that the above conclusions are obtained from same receiver types. The characteristics of DISBs for different receiver types need to be further studied. This is also the focus of our next research.

Acknowledgments. This work is partially supported by the National Natural Science Foundation of China (Grant No. 41774027, 41574026), the Primary Research & Development Plan of Jiangsu Province (Grant No. BE2016176), the National Key Technologies R&D Program (Grant No. 2016YFB0502101) and the Six Talent Peaks Project in Jiangsu Province (Grant No. 2015-WLW-002). The authors gratefully acknowledge GNSS Research Centre of Curtin University and the Multi-GNSS Experiment and Pilot Project (MGEX) for providing the multi-GNSS data. We appreciate anonymous reviewers for their valuable comments and improvements to this manuscript.

References

1. Odolinski R, Teunissen P, Odijk D (2014) Combined GPS+ BDS+ Galileo+ QZSS for long baseline RTK positioning. In: 27th International technical meeting of the satellite division of the institute of navigation, ION GNSS 2014, vol 3. Institute of Navigation, pp 2326–2340
2. Gao W, Gao C, Pan S (2017) A method of GPS/BDS/GLONASS combined RTK positioning for middle-long baseline with partial ambiguity resolution. Surv Rev 49 (354):212–220

3. Paziewski J, Wielgosz P (2015) Accounting for Galileo–GPS inter-system biases in precise satellite positioning. J Geodesy 89(1):81–93
4. Odijk D, Teunissen PJG (2013) Characterization of between-receiver GPS-Galileo inter-system biases and their effect on mixed ambiguity resolution. GPS Solutions 17(4):521–533
5. Liu H, Shu B, Xu L et al (2017) Accounting for inter-system bias in DGNSS positioning with GPS/GLONASS/BDS/Galileo. J Navig 70(4):686–698
6. Gao W, Gao C, Pan S et al (2017) Inter-system differencing between GPS and BDS for medium-baseline RTK positioning. Remote Sens 9(9):948
7. Tian Y, Ge M, Neitzel F et al (2017) Particle filter-based estimation of inter-system phase bias for real-time integer ambiguity resolution. GPS Solutions 21(3):949–961
8. Pan SG, Wang Q, Ke FY et al (2009) Method for integer ambiguity resolution in GPS network RTK. J Southeast Univ (Engl Ed) 25(4):491–495
9. Wang GAO, Chengfa GO, Shuguo PAN et al (2015) Single-epoch positioning method in network RTK with BDS triple-frequency widelane combinations. Acta Geodaet Cartogr Sin 44(6):641–648
10. Li B, Shen Y, Feng Y (2009) Long-range real-time precise navigation with three frequency GNSS. Geomat Inf Sci Wuhan Univ 34:782–786
11. Li B, Shen Y, Zhou Z (2009) A new method for medium and long range three frequency GNSS rapid ambiguity resolution. Acta Geodaet Cartogr Sin 38(4):296–301
12. Li J (2011) Research on the algorithms of GNSS triple frequency precise positioning. Information Engineering University, Zhengzhou
13. Wang K, Rothacher M (2013) Ambiguity resolution for triple-frequency geometry-free and ionosphere-free combination tested with real data. J Geodesy 87(6):539–553
14. Jung J, Enge P, Pervan B (2000) Optimization of cascade integer resolution with three civil GPS frequencies. In: ION GPS, vol 2200
15. Feng Y (2008) GNSS three carrier ambiguity resolution using ionosphere-reduced virtual signals. J Geodesy 82(12):847–862

A Hierarchical Planning Method for the Inter-satellite Links Network of Navigation Satellite Constellations

Yaoyao Yu(✉), Yin Hao, Jianfang Wei, and Hefang Zheng

The 6th Research Institute of China Electronics Corporation, Changping, Beijing, China
yuyoyo2014@hotmail.com

Abstract. Given the communication features of STDMA among inter-satellite links, this the-sis proposed a hierarchical planning method for the inter-satellite links network of navigation constellation. First, we hierarchized the satellite networks in accordance with their visible relationships, and interlinked them hierarchically on the basis of STDMA. Second, we comprehensively analyzed the costs of hop, time-delay and load on the stability of inter-satellite links, and therefore designed an improved A* algorithm suitable for multi-level satellite networks. At last, we simulated our method under constellation models. The results of simulations revealed that the time-delay among links was less than 5 s on average, mean hops were less than 2 counts, and on-board load converged, which met the requirements of QoS communication.

Keywords: Inter-satellite links · Network layer · A* algorithm · QoS communication index

1 Foreword

Navigation satellite links are used for specific data exchange and bidirectional ranging between navigation satellites. The communication is realized through inter-satellite link, which solves the problem of ground global station distribution limit, realizes the indirect retransmission of the information between the satellite and the earth, improves the communication performance of navigation system, and effectively reduces the operational costs and operational risks of the satellite navigation system. The relative measurement between the satellites is realized through inter-satellite link, the observation data and relative observation clock difference between the satellites are obtained. The accuracy of satellites orbit determination and the performance of service of navigation system are improved.

The 2nd reference proposes a routing backup strategy based on fault-tolerant mechanism of satellite network, though satisfying the Qos of network, only analysed the delay. The 3rd reference proposed a scheme for two-tier satellite networks with inter-satellite links, and accomplished a dynamic routing strategy suitable for this scheme, in which sub-networks delay minimization strategy based on Floyd algorithm is adopted, but the simulation implementation method is not mentioned. The 4th

J. Sun et al. (Eds.): CSNC 2019, LNEE 563, pp. 62–70, 2019.
https://doi.org/10.1007/978-981-13-7759-4_6

reference improved the virtual topology strategy in the design of satellite network routing algorithm and introduced heuristic methods to meet user's QoS requirements, including end-to-end delay, time delay fluctuation, link utilization and bandwidth.

At present, the research on routing strategy in satellite communication scenarios is premature worldwide. In this paper, a heuristic routing algorithm for hierarchical satellite networks is designed by analyzing the effects of hop cost, delay cost and load cost on service satisfaction, expect to enrich and improve domestic inter-satellite link system of satellite navigation system.

2 Time Slot Planning Techniques

2.1 Multilayer Link Network Partition Based on Visual Analysis

According to the visible relationship between the satellites or between the satellite and the earth, the link network is divided into layers.

Step 1: Set Ka station on the ground and S station collection of GKa and GS, satellite collection SAT;
Step 2: According to the visible relationship between the satellites and the earth, acquire the domestic satellite collection Sa_{tin}. In particular, the domestic satellite of the S station may also be the domestic satellite of Ka station simultaneously;
Step 3: According to the visible relationship between the satellites, further stratifies Ka and S's offshore satellite Sat_{out}. Get $Sat_{out}L1$, $Sat_{out}L2$, …$Sat_{out}Ln$, denotes one-hop visible offshore satellites collection, two-hop visible offshore satellites collection and n-hop visible offshore satellites collection respectively. In particular, the outer offshore satellites of the Ka station may also be an offshore satellite or a domestic satellite in the inner layer of an overseas S station.

By multi-layering link network, on the one hand, the S station can be introduced to do unified planning. On the other hand, through further stratification of foreign satellites, it can help judge the merits and demerits of the visible relations between offshore satellites. For the less visible offshore satellites (outer offshore satellites), priority needs to be given to ensuring the construction of their satellites and paths on the ground. Such hierarchical processing is particularly critical when there are fewer satellite-earth resources.

2.2 Time Slot Planning

In the process of time slot planning, the impact of digital constraint on chain construction planning is mainly considered. It can be divided into two categories according to its digital transmission direction, the upstream tasks and downstream tasks. For the ascending task, the "earth station to domestic satellite to overseas satellite" channel should be established as far as possible, while for the descending task, the "foreign satellite to domestic satellite to earth station" channel should be established as far as possible. The specific construction of the chain is shown in Fig. 1.

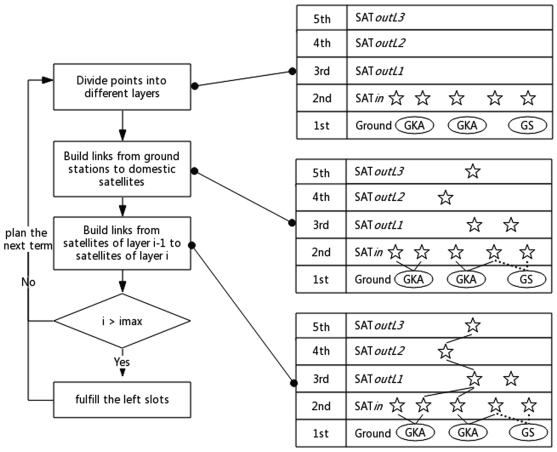

Fig. 1. Time slot planning process

2.3 Time Slot Planning Based on Load Balancing

The nature of load balancing is using the possible existence of different transmission path in the network and transferring the data through sufficient residual capacity of nodes. Load balancing algorithm is used to alleviate the existing and potential risks of local congestion, to adapt to the dynamic change of network load, to reduce loss as much as possible and to increase the network throughput to provide better QoS guarantee for the task.

Therefore, the "chain construction times" attribute is added for each node to measure the data flow load of the node indirectly. When there are multiple candidate stars for chain construction, the satellite with the least number of chain construction times is selected for chain construction. The time-gap planning processes based on load balancing are as follows:

Step 1: Construct Ka links between the satellite and the earth. In accordance with the above principle, access satellites and ground stations are subgrouped according to the load of stations and the load of access to satellites. Given priority to the chain construction between the satellite and the earth with few loads, so that "even construction chain" can be ensured. in order to balance the difference of data transmission rate between the satellite accessed which is taken as the interstellar junction between the satellite and the earth, the maximum chain construction per minute is set. In particular, because S station and satellite communication do not use STDMA system, S channel is only marked.

Step 2: The chain construction of satellites in different layers. Starting from the layer of domestic satellites, standby time slots are followed by the adjacent outer satellites in order, and the order of chain construction of satellites in different layers is "Sat_{in} to $Sat_{out}L1$ to $Sat_{out}L2$ to $Sat_{out}Ln$". In the process of wheel constructing chain, the satellite priority chain with fewer chains is constructed.

Step 3: Supplement the chain with free time slots. From the perspective of the homogeneity of the chain construction, the supplementary chain is preferred to select the satellite with fewer times of construction in the current planning cycle for the chain construction. If the current planning cycle is the last planning cycle, the planning is completed; if not, the time gap planning of the next planning cycle is returned to Step 1.

3 Routing Design Scheme

The core idea of A* [5] routing planning in a highly dynamic network is to perform static processing on a highly dynamic network constructed by time slots. A* searching algorithm with heuristic method is adopted to generate path evaluation from multiple dimensions such as path delay, hop number, node load, etc., to complete the point-to-point multipath search.

3.1 Evaluation Model

A* searching algorithm is a kind of heuristic search algorithm, whose cost function is generally expressed as:

$$f(n) = g(n) + h(n) \tag{4.1}$$

Where, $f(n)$ is the valuation function of the path passing through node n in the state space, g(n) is the actual cost from the initial node to node n in the state space, $h(n)$ is the budget cost from node n to target node, and $h(n)$ plays a key role in the evaluation function, which determines the efficiency of A* algorithm.

(a) **Selection of Actual Cost g(n)**

The actual cost needs to take the path consumption such as path hop, transmission delay and node load into account. The cost function from the starting point to node n is defined as follows:

$$g(n) = \omega 1 \times turnCost(n) + \omega 2 \times delayCost(n) + \omega 3 \times loadCost(n) \tag{4.2}$$

Where, $turnCost(n)$ represents the actual jump cost from the starting point to node n, $delayCost(n)$ represents the average delayCost from the starting point to node n, and $loadCost(n)$ represents the average loadCost from the starting point to node n. Based on the numerical tolerance of each cost and normalization, the theoretical values of corresponding coefficients are obtained, $\omega 1 = 0.5$, $\omega 2 = 0.17$, $\omega 3 = 0.33$.

As shown in Fig. 2 on the left, take data sent from $Sat_{out}L2(5)$ to GKA as an example. In the case of no load, only the number of hops and time delay are used as evaluation indexes. It can be seen that data is forwarded through $Sat_{out}L1(4)$ in all five links, and there is a forwarding bottleneck, which makes SatoutL1(4) memory occupied too high and leads to data congestion.

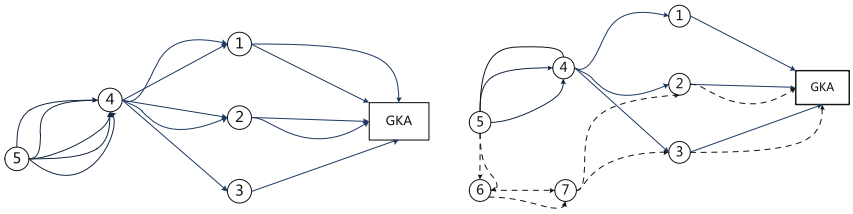

Fig. 2. Chart of node cache overload leading to bottleneck

As shown in Fig. 2 on the right, after adding the evaluation function of load balancing, the load attribute is added for each node, which is indirectly measured by the number of path selections passing through the node. As the number of choices increases, the path through the node will be selected at a greater cost in the next calculation. Therefore, although the number of hops of the dashed path is 1 more than that of the solid path via $Sat_{out}L1(4)$, it can still be selected after taking into account the number of hops, delay and node load.

(b) **Selection of Budget Cost h(n)**

Budget cost $h(n)$ is the budget cost from node n to target node. In order to guarantee the optimization and completeness of the algorithm, $h(n)$ is expressed as follows:

$$h(n) = disLayer(n) * \alpha \tag{4.3}$$

In the formula, $disLayer(n)$ is represented as the layer difference from node n to the target node, which means that the smaller the layer difference from the target node n is, the smaller the budget cost of node n corresponding to the smaller node n difference from the target node. α is the adjustment coefficient, eliminating the dimension effect of $h(n)$ and $g(n)$, and balancing the contribution value of both. In the budget cost function, the layer difference effect (approximately equal to the cost of hops) is only considered, other factors are ignored, so $\alpha < 0.5$ is set.

3.2 Routing Planning Technology Based on A* Searching

A* algorithm path planning mainly USES two lists, OPEN table and CLOSE table, to realize the expansion and selection of the optimal node. OPEN table is used to save the subsequent nodes encountered in the search process, and CLOSE table is used to save the points with the minimum value of f in the OPEN table. The initialization OPEN table contains the start node s, and the CLOSE table is empty. The routing planning process based on A* search is as follows (Fig. 3):

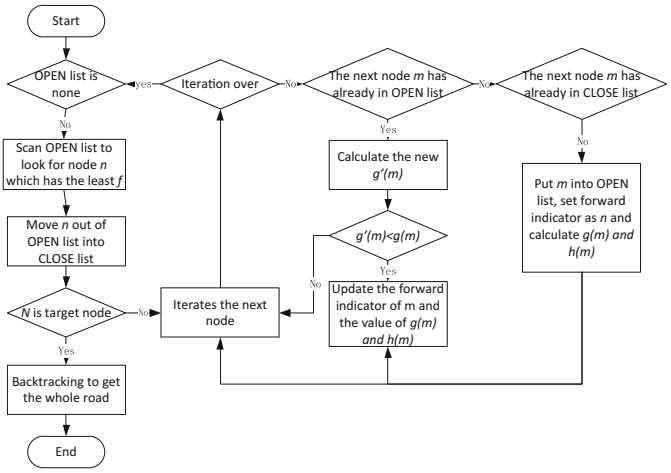

Fig. 3. A* routing planning flow chart

Step 1: select the node n with the minimum f value in the OPEN table and set it as the current node.
Step 2: move the current node n out of the OPEN table and into the CLOSE table;
Step 3: determine whether n is the target point. If n is the target point, the optimal path will be generated according to its forward pointer, and the target node will begin to trace back step by step until it reaches the start node. If n is not the target point, then extend node n and process each subsequent point of n:

Step 3.1: if the subsequent point m exists in the OPEN table, the $g(m)$ value is determined. If the path $g(m)$ value is smaller than the previous path, the forward pointer of m point is changed and the $g(m)$ and $h(m)$ values of m point are updated simultaneously. On the contrary, the original forward pointer and $g(m)$ and $h(m)$ values are maintained.

Step 3.2: if the successor point m is empty, or exists in CLOSE table, it is not processed.

Step 3.3: if the successor point m is not in the CLOSE table or the OPEN table, it is added to the OPEN table. Its forward pointer points to the current node n, and its $g(m)$ and $h(m)$ values are calculated.

Return to Step 1 after the subsequent nodes have been processed.

4 Simulation Verification

The simulation scenarios in this paper include 1 × Ka band ground station, 1 × S band ground station and 8 MEO satellites.

4.1 Visual Analysis

In the visible analysis, it is necessary to analyze the visibility of inter satellite and satellite-earth. There are three types of visible relationships between nodes, persistent visible, persistent invisible and non-persistent visible. The visual relation is analyzed to lay a foundation for the next-step inter-satellite topology.

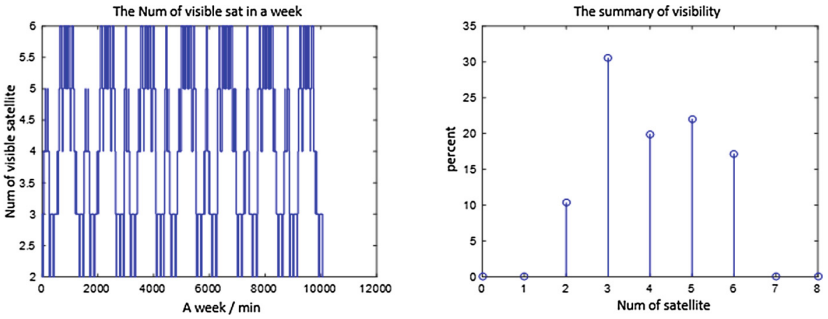

Fig. 4. Ka station and S station are visible to MEO satellite for one week

As shown in Fig. 4, in the one-week simulation results, if the Ka station is associated with the S station, at least two satellites can be seen. In order to meet the need of communication, the more visible satellites, the higher the degree of mission completion. In the visual period of two stars, there are three kinds of topological relationships: one MEO visible to Ka station, one MEO visible to S station (probability is 2.5%), two MEO visible to Ka station (probability is 4.1%), two MEO visible to S stations (probability is 3.6%). The system planning should as far as possible to ensure the performance of the three cases.

4.2 Performance Testing

The test includes link hops and the retransmission delay of a task, and the load of each satellite load during the simulation process. The simulation results are as follows:

(1) **Link Hops and Transmission Delay**

Link hops and retransmission delay are evaluated from the uplink and downlink paths (Fig. 5).

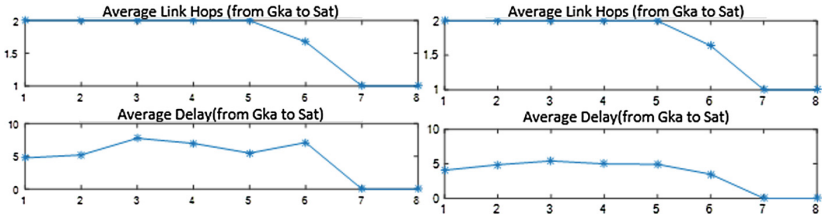

Fig. 5. Simulation results of link hops and delay (Uplink) using the shortest path algorithm and the algorithm in this paper (1–4: MEO25–MEO28, 5–8: MEO33–MEO36)

(a) **Path Performance of Ka Station on the Ground to Satellites (uplink)**

For link hops, there is no difference between the proposed heuristic routing algorithm based on hierarchical satellite networks and the shortest path routing algorithm in uplink hop alignment. Because Sat.6, Sat.7 and Sat.8 can be visible directly with the station on the ground in a certain period of time, so the average number of hops is less. The average number of hops in the uplink paths of other satellites is 2 hops.

For the transmission delay, it can be seen from the diagram that the routing algorithm adopted in this scheme can effectively avoid the bottleneck problem, shorten the transmission delay obviously, and control the transmission delay of Ka station on the ground to all satellites less than five time slots.

(b) **Path Performance of Satellite to Ka Station on the Ground (Downlink)**

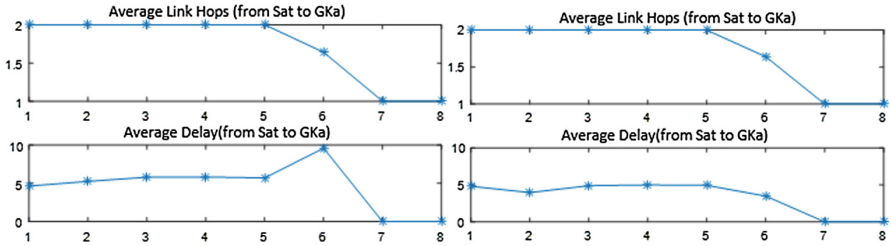

Fig. 6. Simulation results of link hops and delay (Downlink) using the shortest path algorithm and the algorithm in this paper (1–4: MEO25–MEO28, 5–8: MEO33–MEO36)

The simulation result of downlink task is similar to that of uplink task. It is not to be restated here (Fig. 6).

(2) **Load Condition**

Combined with the results of slot and routing planning, the performance of telemetry information recovery service is tested. Under the same rate, the shortest path algorithm and the load balancing routing algorithm proposed in this paper are compared. During the simulation period, the cache results are shown in Fig. 7 and Fig. 8.

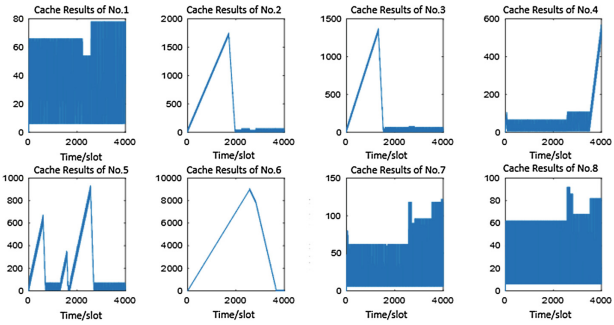

Fig. 7. Cached results of shortest path algorithm (1–4: MEO25–MEO28, 5–8: MEO33–MEO36)

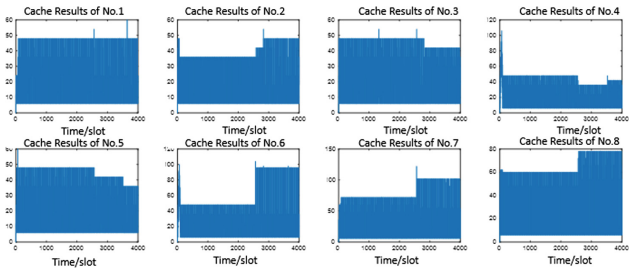

Fig. 8. Planned cache results of considering load balancing routing (1–4: MEO25–MEO28, 5–8: MEO33–MEO36)

As shown in Fig. 7, except for the continuous convergence of the Sat.1, Sat.7 and Sat.8 buffers, the other satellites caches diverge over a period of time, regardless of the load. On the one hand, the divergent cache will cause greater data transmission delay, on the other hand, it will also cause the on-board buffer pressure so the performance of the algorithm is not satisfactory.

As shown in Fig. 8, the telemetry cache of all satellites converges under the combined action of digital priority slot planning and an A * search routing algorithm that takes into account load balancing. The results show that the telemetry data can be transmitted back to the ground Ka station in a short time, and the data congestion can be effectively alleviated. The necessity of load-balanced routing algorithm is further verified.

5 Conclusion

To meet the demand of data transmission service the nodes in the system are stratified according to the visual relations of inter-satellite and earth-satellite, an improved A* algorithm for multilayer satellite network is proposed, which takes the load into account. The simulation results showed that the proposed algorithm can effectively balance the load of satellite nodes to alleviate the link congestion, reduce the number of link hops and delay, and provide better QoS guarantee for services.

References

1. Yang Y (2010) Progress, contributions and challenges of Beidou satellite navigation system. J Geodesy Geoinf Sci 39(1):1–6(6)
2. Hu JH, Yeung KL (2000) Routing and re-routing in a LEO/MEO two-tier mobile satellite communications system with inter-satellite links. In: ICC 2000, vol 1, pp 134–138
3. Stepanek J, Coe E, Sims R, Raghavendra CS (2004) Fault-tolerant routing for satellite command and control. In: IEEE aerospace conference proceeding, pp 1671–1676
4. Long R, Xiong NX, Athanasios VV et al (2010) A sustainable heuristic QoS routing algorithm for pervasive multi-layer satellite wireless networks. Wirel Netw 16(6):1657–1673
5. Wei W Research on strategies of heuristic search in AI planning

Primary Exploration on Approaches to Establish BeiDou Terrestrial Reference Frame

Liqian Zhao[1,2(✉)], Xiaogong Hu[1], Shanshi Zhou[1], Chengpan Tang[1], and Yufei Yang[3]

[1] Shanghai Astronomical Observatory, Chinese Academy of Sciences, Shanghai, China
zhaoliqian@shao.ac.cn
[2] University of Chinese Academy of Sciences, Beijing, China
[3] Information Engineering University, Zhengzhou, China

Abstract. Beidou-2 satellite navigation system adopts China Geodetic Coordinate System 2000 (CGCS2000), which can't meet the requirements of Beidou-3 global service and timely update. This paper discusses two approaches to build BeiDou Terrestrial Reference Frame (BTRF), one is precise point position (PPP) and the other is net-solution with MGEXs. We only relied on BDS observations to determine precise coordinates of each BDS monitoring station under ITRF and verify the two approaches. Especially, we analyzed the improvement for the accuracy of Beidou satellites orbit determination (OD) with regional tracking network after refining and updating the coordinates of tracking stations by means of net-solution. Initial results show that repeatability of PPP for the horizontal and vertical components of a BDS monitoring receiver is better than 2.3 cm and 3.4 cm, respectively, which may be reduced to 0.8 cm and 2.2 cm for net-solution. After the refinement, the OD accuracy of IGSOs 3D overlap increase by 15.4%, while MEOs increase by 25.9%. We also evaluate BDS satellite orbit with SLR measurements, results reveal that SLR residuals of BD-2 satellites reduce from 0.39 m to 0.24 m, the accuracy increases by 38%, the residuals of BD-3 satellites reduce from 0.25 m to 0.18 m, the accuracy increases by 28%.

Keywords: BeiDou Terrestrial Reference Frame · Precise point position · Net-solution · Repeatability

1 Introduction

The definition of the GNSS coordinate system includes the origin, scale, orientation and evolution [1]. As a realization of GNSS coordinate system, the GNSS coordinate reference framework provides the spatial reference for satellite ephemeris of GNSS, it is the basis to realize navigation and location service. International Terrestrial Reference Frame (ITRF) is currently the most widely used global reference framework with

J. Sun et al. (Eds.): CSNC 2019, LNEE 563, pp. 71–80, 2019.
https://doi.org/10.1007/978-981-13-7759-4_7

highest accuracy and best stability, which is realized by the coordinates and velocity of a set of points on the surface of the earth [2]. ITRF can provide a reliable reference for the establishment and maintenance of the GNSS coordinate reference framework, it also serves as a medium for the coordinate framework of different navigation systems [3]. The Terrestrial Reference Frame for GNSS can build a connection with each other by aligning with ITRF, laying the foundation for multi-GNSS compatibility and interoperability [4, 5].

China's Beidou satellite navigation system adopts the 2000 China Geodetic Coordinate System (CGCS2000) whose foundation is based on GPS static observations, and therefore is a national security risk [6]. Due to its long-term invariance, CGCS2000 cannot meet the requirements of the GNSS reference frame for timely update [7, 8]. With the launch of the Beidou-3 satellites, Beidou navigation system is moving from Asia-Pacific regional service to global service, it is of great significance to build a global terrestrial reference framework of Beidou which can maintain high precision on a global scale and be interoperable with other navigation systems [9].

This paper focuses on how to build BeiDou Terrestrial Reference Frame (BTRF). We propose two approaches to obtain accurate coordinates of the domestic Beidou monitoring stations and depend on BDS observations only to verify the feasibility of the approaches. The results can provide theoretical basis and method support for the establishment of the BTRF. In addition, we refine the coordinates of the ground tracking stations and analyze the improvement of BDS orbit determination accuracy with regional tracking network by the root-mean-squares (RMS) of the post-fit residuals, the overlap comparison and the SLR validation after the coordinate update.

2 Experiments on Establishment of BTRF

Considering the interoperability with other satellite navigation systems, the Beidou Terrestrial Reference Frame should be aligned with ITRF, the basis of its realization are frame points whose coordinates are accurately known. Therefore, the primary task of establishing the BTRF is to obtain high-precision coordinates information of these frame points. Precise Point Positioning and net-solution are attempted to get the precise coordinates under ITRF.

2.1 Precise Point Positioning

Since it was first proposed as a major positioning technique, Precise Point Positioning (PPP) has seen numerous important applications [10, 11]. The Multi-GNSS Experiment (MGEX) of the International GNSS Service provides the precise orbits and clock of the BDS satellites using L-band code and carrier phase measurements regularly from a globally distributed network [12, 13]. The radial accuracy of the MGEX precise orbits for the IGSO and MEO satellites is within 10.0 cm in terms of overlap comparisons and satellite laser ranging (SLR) validation [14, 15]. The precise satellite orbit and clock difference which the MGEX provides should be fixed so that it can serve as a medium of

ITRF delivery. PPP experiments are carried out using observations of only Beidou-2 satellites because MGEX has no precise orbit and clock difference products of Beidou-3 satellites. By means of PPP, the coordinates of the monitoring station in ITRF can be directly obtained. Then the repeatability of the coordinate sequence should be analyzed.

2.1.1 Experiment Data and Processing Strategy

Four Beidou monitoring stations in China are selected, located in Qingdao, Xiangyang, Ruili and Jinghong. The observations from 2018/05/16 to 2018/05/29 are processed with PPP. The PPP program adopts one-day solution. We use 5 min-orbit and 30 s-clock-error precise products provided by GFZ MGEX. The pseudorange and phase observation data of the two frequencies of B1I and B2I are selected for the dual-frequency ionosphere-free combination. The observation sampling interval is 30 s, and the threshold of cutoff elevation is 10°. The coordinates of receivers, receivers clock error and atmospheric and ambiguity parameters are estimated while atmospheric parameters are estimated every 2 h. We adopt EOP parameters which are estimated by ESA. In order to be self-consistent with satellite orbit products, the satellite antenna phase center deviation (PCO) is corrected according to the value given by GFZ. Table 1 shows B1I-B2I dual-frequency satellite antenna phase center compensation value provided by GFZ.

Table 1. GFZ MGEX B1I-B2I Dual Frequency Combination Phase Center Correction (unit: mm)

Satellite	X	Y	Z	Satellite	X	Y	Z
C01	600.0	0.0	1100.0	C08	549.0	0.0	3842.6
C02	600.0	0.0	1100.0	C09	549.0	0.0	3973.6
C03	600.0	0.0	1100.0	C10	549.0	0.0	3882.1
C04	600.0	0.0	1100.0	C11	549.0	0.0	2069.5
C05	600.0	0.0	1100.0	C12	549.0	0.0	2313.5
C06	549.0	0.0	3049.0	C13	549.0	0.0	3882.1
C07	549.0	0.0	3236.7	C14	549.0	0.0	2311.7

2.1.2 Results and Analysis

Daily coordinate time series are obtained for each receiver. Repeatability is defined as:

$$\sigma = \sqrt{\frac{(v - \bar{v}) \cdot (v - \bar{v})^T}{n - 1}}$$

in which v is the difference vector between PPP results and the initial coordinates in CGCS2000 for east, north or height components. $\bar{v}$ is the mean value of the time series, n is the dimension of v. Figure 1 below is the summary of the repeatability for the 4 receivers.

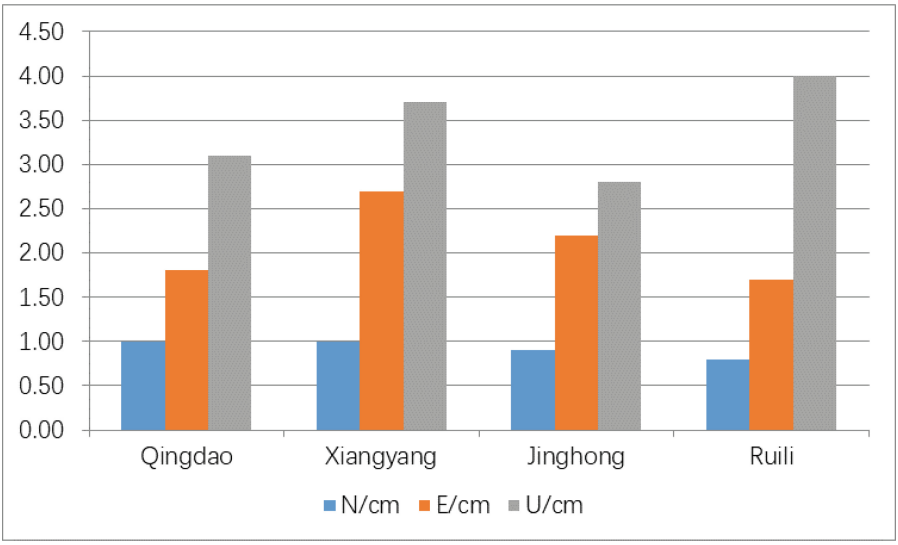

Fig. 1. PPP results repeatability for north, east and height components of 4 receivers in Qingdao, Xiangyang, Jinghong and Ruili

To illustrate the PPP results, Fig. 1 displays positioning time series for 4 receivers. It can be seen from the statistical results in the figure that the coordinate repeatability of each receiver in the horizontal direction is significantly better than the height direction. The solution repeatability of each receiver for north component is within 1 cm, with an average of 0.93 cm. The repeatability for east component is between 1.5 and 2.7 cm, with an average of 2.1 cm, and the average in the horizontal direction is 2.3 cm. Jinghong station has the best repeatability for up component which is 2.8 cm, while Ruili station has the worst, which is 4 cm. The average of each receiver for up component is 3.4 cm.

2.2 BDS Net-Solution

We select MGEX stations for the transmission of ITRF reference. Only BDS observations are used.

2.2.1 Experiment Data and Processing Strategy

The same observations period and domestic Beidou monitoring stations as the PPP method are selected. We choose 45 MGEX stations distributed all over the world which could receive BDS B1I and B2I data. Among the 45 stations, 25 stations whose coordinates are fixed. The precise coordinates of other MGEX stations and 4 domestic Beidou monitoring stations are calculated. The pseudorange and phase observations of the two frequencies of B1I and B2I are selected for the dual-frequency ionosphere-free combination. The observation data sampling interval is 30 s, and the threshold of cutoff elevation is 10°. In addition to the receiver coordinates, it was also necessary to solve the BDS satellite orbit and clock error, receiver clock error, atmospheric and ambiguity

parameters. The atmospheric parameters are estimated every 2 h, and the satellite antenna phase center offset is the same as that published by GFZ (Table 1).

2.2.2 Results and Analysis

To illustrate the net-solution results, Fig. 2 below displays coordinates time series for 4 receivers. From the statistical results in the figure, it is found that the coordinate repeatability of each station in the horizontal direction is better than the height direction, which is consistent with the conclusion obtained by the PPP method. The average repeatability of each station was 0.8 cm for horizontal component and 2.2 cm for height component. It can be seen that the coordinate repeatability of the net-solution is much better than the PPP method.

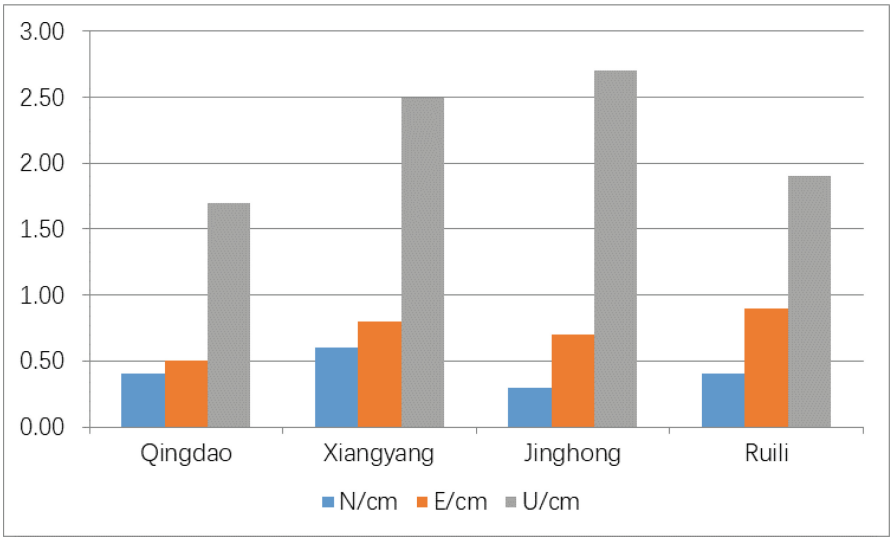

Fig. 2. Net-solution results repeatability for north, east and height components of 4 receivers in Qingdao, Xiangyang, Jinghong and Ruili

3 Improvement of BDS Orbit Determination Accuracy with Regional Tracking Network After Coordinates Refinement

The experiment results in the previous section have preliminarily proved that both PPP and net-solution can obtain the monitoring station coordinate with accuracy of centimeter-level. Since the coordinates results repeatability obtained by the net-solution is better than that of PPP, we refine and update the coordinates of 10 Beidou regional tracking stations in China. The coordinates obtained by means of net-solution are used to update the initial coordinates in CGCS2000, and the tracking stations before and after the coordinates update are respectively used to determine the BDS satellites orbits, then orbit determination accuracy will be compared.

3.1 Orbit Determination Strategy with Regional Tracking Network

Data sets from 2018/08/04 to 2018/08/26 are selected for the experiments. There are 21 3-day orbit determination (OD) arcs involving 10 stations and 19 BDS satellites. B1I and B3I are used to form a dual-frequency ionosphere-free combination, observations sampling interval is 60 s, and the threshold of cutoff elevation is 10°. The dry tropospheric delay can be precisely corrected by models such as Saastamonien model, the one used for experiment, but the wet part is difficult to model [16], so they are treated as measurement parameters and are estimated every 8 h. The 10 ground tracking stations before and after the coordinates update respectively participate in orbit determination experiment.

3.2 Orbit Determination Residual

Figure 3 below shows the root-mean-squares (RMS) of the post-fit code and phase residuals of 21 OD arcs. In the figure, blue part represents the residual with initial coordinates before update, the yellow part represents the residual with coordinates after update. It illustrates that after the update and refinement of coordinate of tracking station, the code and phase residual of each orbital arc reduce significantly. The mean value of the code residual reduces from 87.2 cm to 84.6 cm, and the phase residual reduces from 1.34 cm to 1.05 cm. We can think that the precision of internal alignment of orbit determination with regional tracking network improved after the update of coordinates.

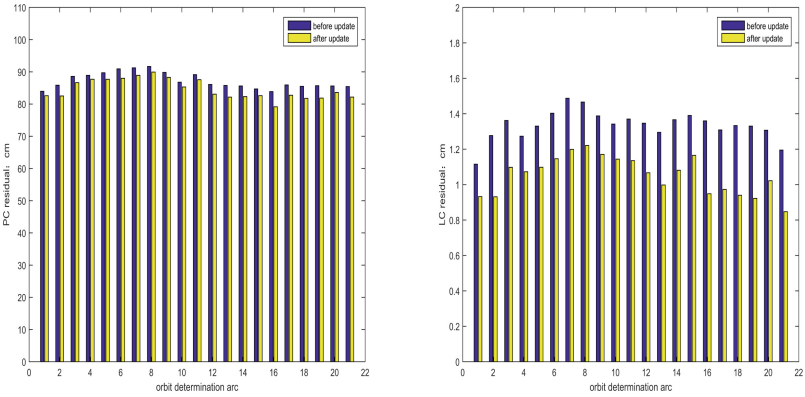

Fig. 3. Code (left) and phase (right) residuals of each arc before and after coordinate refinement

3.3 Orbit Overlap Comparison

The direct comparison of the consecutive orbit solutions is commonly used for the internal validation of the orbit accuracy. The 48-h overlap orbits are obtained by the orbit comparisons of any two groups from the 3-day arc orbit solutions, with a time-lag of one day, to conduct the internal validation. The orbit comparison results are counted and listed in Table 2 and Fig. 4.

Table 2. The satellite orbit overlap comparisons in radial, along-track, cross-track and 3D directions (unit: m)

Satellite	R		T		N		3D	
	Before update	After update	Before update	After update	Before update	After update	Before update	After update
C01	0.217	0.192	1.288	1.442	0.955	0.859	1.618	1.689
C03	0.205	0.171	0.958	0.993	0.807	0.708	1.269	1.231
C06	0.215	0.139	0.839	0.658	0.652	0.597	1.084	0.899
C07	0.180	0.157	1.012	0.780	0.665	0.527	1.224	0.954
C08	0.247	0.193	1.011	0.768	0.812	0.588	1.320	0.986
C09	0.264	0.226	1.040	0.928	0.695	0.618	1.278	1.138
C10	0.216	0.232	0.979	0.945	0.744	0.754	1.248	1.231
C27	0.367	0.263	1.887	1.195	0.584	0.542	2.009	1.338
C28	0.386	0.283	1.735	1.493	0.691	0.538	1.907	1.612
C29	0.326	0.216	1.778	1.273	0.584	0.385	1.900	1.347
C30	0.340	0.266	1.458	1.214	0.555	0.492	1.597	1.337
C31	0.212	0.202	0.977	0.963	0.632	0.647	1.183	1.178
C32	0.199	0.186	1.148	0.845	0.646	0.582	1.332	1.043
C33	0.367	0.194	1.795	0.978	0.847	0.643	2.018	1.186
C34	0.317	0.205	1.513	0.940	0.495	0.392	1.623	1.039
C36	0.349	0.230	1.192	0.803	0.641	0.451	1.398	0.949
C37	0.228	0.184	0.832	0.726	0.535	0.450	1.015	0.874
C38	0.344	0.212	1.221	0.710	0.579	0.415	1.394	0.849
C39	0.257	0.204	1.067	0.872	0.501	0.466	1.206	1.010

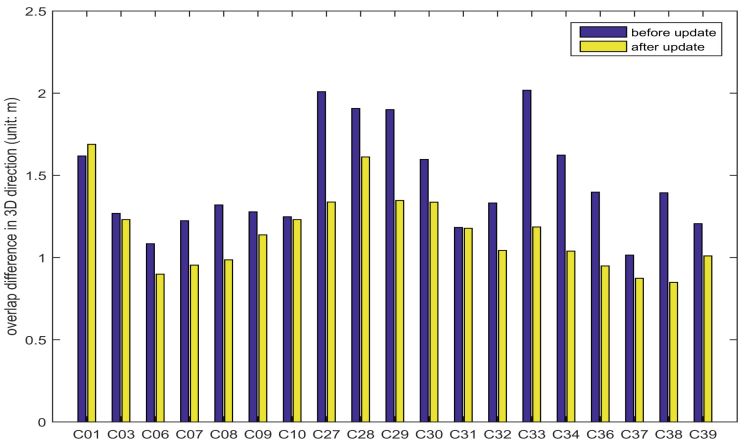

Fig. 4. Satellite overlap comparisons in the 3D direction. The blue part represents the overlap difference before coordinates update, while the yellow part represents the overlap difference after update

According to the statistical results, except for the GEO satellite C01, the accuracy of the overlap comparisons in the 3D direction of all satellites has been improved after tracking station coordinates update. The mean overlap difference of IGSO satellites (C06, C07, C08, C09, C10) decreases from 1.23 m to 1.04 m, and the accuracy increases by 15.5%. The mean overlap difference of MEO satellites (C27–C34, C36–C39) decrease from 1.55 m to 1.15 m, and the accuracy increases by 25.8%.

3.4 SLR Evaluation

SLR provides independent data that can be used to evaluate orbit error in the along-the-sight direction. The range residual of SLR is the difference between observed range and computed range based on the estimated orbits [17]. There were 7 BDS satellites (C01, C08, C10, C29, C30, C37, C38) tracked by the International Laser Ranging Service during the experiments. Figure 5 below shows the distribution of the SLR stations participating in our experiments, including 5 in the Asia-Pacific region, 5 in Europe, and 1 in the United States. The laser data cutoff height angle was 20°, and the SLR residuals greater than 1 m do not participate in statistics. The availability of SLR data for each satellite and the RMS of SLR residuals of estimated orbits is shown in Table 3.

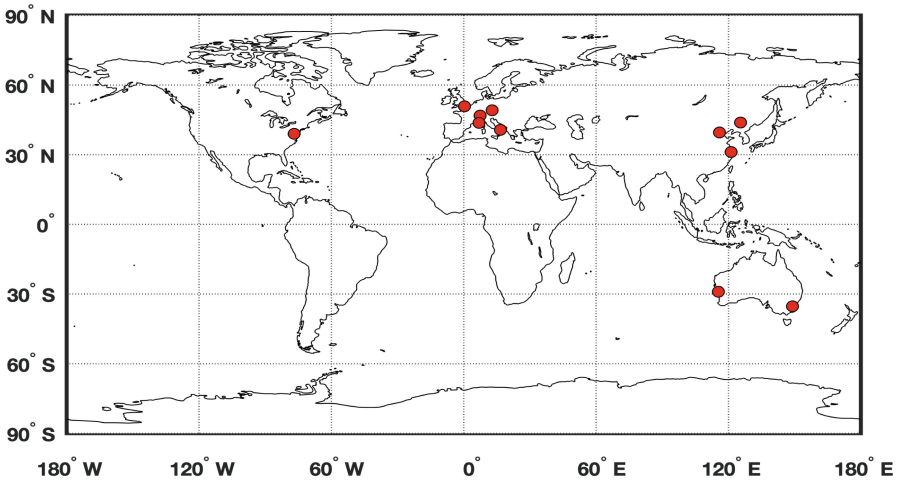

Fig. 5. Distribution map of SLR stations in our experiments

It can be seen from Table 3 that after tracking stations coordinates refinement and update, the accuracy of SLR evaluation improves significantly. For BD-2 satellites (C01, C08, C10), the mean residuals decrease from 0.39 m to 0.24 m, and the accuracy improves by 38%. For BD-3 satellites (C29, C30, C37, C38), the mean residuals decrease from 0.25 m to 0.18 m, and the accuracy improves by 28%. The mean residuals of all satellites decrease from 0.31 m to 0.21 m.

Table 3. The SLR data availability and the RMS of SLR residuals (unit: m)

Satellite	Total data volume	Valid data volume	Elimination rate	Residuals before update	Residuals after update
C01	57	52	8.77%	0.37	0.24
C08	82	75	8.54%	0.39	0.23
C10	161	158	1.86%	0.42	0.25
C29	67	66	1.49%	0.29	0.13
C30	80	75	6.25%	0.18	0.13
C37	125	123	1.60%	0.29	0.26
C38	59	55	6.78%	0.25	0.21
Total	631	604	4.28%	Mean 0.31	Mean 0.21

4 Summary and Conclusions

In this study, we make a preliminary discussion on the establishment of BTRF. Under the premise of using only Beidou observations, PPP and net-solution are attempted to obtain high-precision coordinates of frame points in China. Initial results show that PPP repeatability for the horizontal and vertical components is better than 2.3 cm and 3.4 cm respectively, net-solution repeatability for the horizontal and vertical components is better than 0.8 cm and 2.2 cm respectively. Both PPP and net-solution can realize the centimeter-level accuracy. As a further verification, we refine and update the coordinates of ground tracking stations by means of net-solution and carry out experiments of orbit determination with regional tracking network. Experiments results reveal that after coordinates update, the mean value of the code residuals reduce from 87.2 cm to 84.6 cm, and the phase residuals reduce from 1.34 cm to 1.05 cm, the mean overlap difference of IGSO satellites decreases from 1.23 m to 1.04 m, the mean overlap difference of MEO satellites decreases from 1.55 m to 1.15 m, the SLR residuals of BD-2 satellites reduce from 0.39 m to 0.24 m and the residuals of BD-3 satellites reduce from 0.25 m to 0.18 m.

In this paper, only 14 satellites of Beidou-2 were used in the PPP and net-solution experiments. With the launch of Beidou-3 satellites, the number of available satellites will greatly increase, and the accuracy of PPP and net-solution will also improve. It is feasible to build a global Beidou Terrestrial Reference Frame with high-precision. Meanwhile, since what we do at the current stage is a preliminary study and the accumulation of observation data is not enough, it is not possible to solve the velocity field information. As a global high-precision reference frame, the BTRF must have velocity field information, so obtaining high-precision velocity field information will be the key and focus of subsequent research.

References

1. Yang YX, Li JL, Xu JY et al (2011) Contribution of the Compass satellite navigation system to global PNT users. Chin Sci Bull 56(26):2813–2819
2. Altamimi Z, Collilieux X, Métivier L (2011) ITRF2008: an improved solution of the international terrestrial reference frame. J Geodesy 85(8):457–473
3. Rebischung P, Altamimi Z, Ray J et al (2016) The IGS contribution to ITRF2014. J Geodesy 90(7):611–630
4. Gendt G, Altamimi Z, Dach R et al (2011) GGSP: realization and maintenance of the Galileo terrestrial reference frame. Adv Space Res 47(2):174–185
5. Wei Z (2008) China geodetic coordinate system 2000 and its comparison With WGS84. J Geodesy Geodyn 28(5):1–5
6. Shi C, Wei N, Li M, Song W, Lou Y, Niu Y (2017) Approaches to realize and maintain national terrestrial reference frame based on BDS data. Geomat Inf Sci Wuhan Univ 42 (11):1635–1643
7. Yang YX (2009) Chinese geodetic coordinate system 2000. Chin Sci Bull 54(15):2714–2721
8. Ning J, Wang H, Cheng P, Cheng Y, Wen H, Bei J (2015) System construction and its progress of China geodetic coordinate system 2000. Geomat Inf Sci Wuhan Univ 40(5):569–573
9. Yuanxi Y (2010) Progress, contribution and challenges of Compass/Beidou satellite navigation system. Acta Geodaet Cartogr Sin 39(1):1–6
10. Weber R, Fragner E, Broederbauer V (2002) The international GPS service: resources for precise positioning and geophysical research. In: EGS general assembly conference
11. Kouba J, Héroux P (2001) Precise point positioning using IGS orbit and clock products. GPS Solutions 5(2):12–28
12. Steigenberger P, Montenbruck O, Weber R et al (2013) Status and Perspective of the IGS multi-GNSS experiment (MGEX). In: EGU general assembly conference
13. Montenbruck O, Steigenberger P, Prange L et al (2017) The multi-GNSS experiment (MGEX) of the international GNSS Service (IGS) – achievements, prospects and challenges. Adv Space Res 59(7):1671–1697
14. Fei G, Li X, Zhang X et al (2017) Assessment of precise orbit and clock products for Galileo, BeiDou, and QZSS from IGS multi-GNSS experiment (MGEX). GPS Solutions 21 (1):279–290
15. Fei G, Li X, Zhang X et al (2016) The contribution of multi-GNSS experiment (MGEX) to precise point positioning. Adv Space Res 59:S0273117716302046
16. Yin H, Huang D, Xiong Y (2008) Regional tropospheric delay modeling based on GPS reference station network. Int Assoc Geodesy Symp 132:185–188
17. Sheng C, Gan W, Zhao C et al (2013) Precise orbit determination of JASON-2 satellite: analysis of GPS, SLR and DORIS. Sci Sinica 43(2):219

The Accuracy Evaluation of Galileo Broadcast Clocks

Yangyang Liu[1,2,4], Baoqi Sun[1,2,3(✉)], Xuhai Yang[1,2,3], Meifang Wu[1,2], Yuanxin Wang[1,2], Ke Su[5], Guoqiang Jiao[5], and Shengli Wang[6]

[1] National Time Service Center, Chinese Academy of Sciences, Xi'an, China
sunbaoqi@ntsc.ac.cn
[2] Key Laboratory of Precise Positioning and Timing Technology, Chinese Academy of Sciences, Xi'an 710600, China
[3] School of Astronomy and Space Science, University of Chinese Academy of Sciences, Beijing 100049, China
[4] University of Chinese Academy of Sciences, Beijing 100049, China
[5] Shanghai Astronomical Observatory, Chinese Academy of Sciences, Shanghai 200030, China
[6] Institute of Ocean Engineering, Shandong University of Science and Technology, Qingdao 266590, China

Abstract. Broadcast ephemeris accuracy is an important index of GNSS navigation system performance evaluation. As a component of broadcast ephemeris, the accuracy of predicted clock offset will directly affect the accuracy of navigation, positioning and timing. In order to access the accuracy of Galileo broadcast clocks, the content and characteristics of Galileo broadcast ephemeris are introduced in this paper first. Then, the principle and method of accuracy evaluation of broadcast ephemeris are explained. On this basis, the broadcast ephemeris data in the last two years since Galileo provided the initial service were used to analyze the accuracy of broadcast clock offset. As a comparison, the GBM precision clock offset products provided German Research Centre for Geosciences (GFZ) analysis center was taken as the truth value. The results show that: (1) The STD of broadcast clock offset of 15 Galileo satellites providing normal services is about 1 ns. The RMS of the broadcast clock offset is about 1 ns, except that of E24 which is 5.7 ns. (2) After the Galileo satellites provided service, the STD and the RMS of broadcast clock offset changes are within 1 ns and 1–1.4 ns, respectively, which partly reflects the stability of Galileo space-borne clock. The results would provide some reference for timing applications of Galileo satellite navigation system.

Keywords: Galileo · Broadcast ephemeris · Predicted clock offset · Precision evaluation

1 Introduction

Galileo navigation satellite system is the Europe independent global satellite navigation system, which can provide high-precision and highly reliable positioning, navigation, timing (PNT) services [1]. Since Galileo system was built, it has launched three series

J. Sun et al. (Eds.): CSNC 2019, LNEE 563, pp. 81–91, 2019.
https://doi.org/10.1007/978-981-13-7759-4_8

of 24 navigation satellites [2]. So far, a total of 17 full-operational-capability (FOC) satellites can provide normal service [3]. Galileo satellite carries high-precision hydrogen clock, which attracts more and more scholars' attention [4]. Considering its characteristics of real-time performance and easy acquisition, broadcast ephemeris has been continuously expanded in the application field. And the reliability and stability of its predicted clock offset will directly affect the accuracy of PNT [5]. Hydrogen clock has better short-term stability. As the first navigation satellite carrying hydrogen clock, it is of great significance to evaluate Galileo broadcast clocks.

Many scholars at home and abroad have analyzed and evaluated the broadcast ephemeris accuracy of GPS, GLONASS and BDS [6–9], but there are very few studies on Galileo system broadcast ephemeris, especially on Galileo FOC series satellites. In 2013, Lucas first evaluated the accuracy of Galileo broadcast ephemeris [10]. Subsequently, Montenegro et al. also analyzed Galileo broadcast ephemeris in 2014, whereas the accuracy of Galileo broadcast ephemeris cannot be reflected due to the small amount of data and the length of data [11]. Similarly, due to the limited data, Fan et al. only evaluated the accuracy of Galileo E11, E12 and E19 satellites' one week broadcast clocks accuracy, which could not reflect the long-term change [6]. Yin et al. used the Galileo broadcast ephemeris for two years to evaluate the accuracy, and drew the conclusion that the accuracy of Galileo broadcast clock offset is better than 5 ns. But Yin only studied the IOV series satellites and did not analyze the FOC satellites [12, 13]. In 2018, Oliver studied the signal-in-space range errors (SISRE) which contains the influence of clock of Galileo for January to December 2017. He came to a conclusion, the RMS SISRE values of Galileo are at the 0.2 m level [14]. Therefore, this paper selected the broadcast ephemeris data of Galileo from December 15, 2016 to October 31, 2018, and took the GBM precision clock products provided by GFZ as the truth value to analyze and compare the accuracy of Galileo broadcast clocks.

2 Brief Introduction to Galileo Broadcast Ephemeris

Depending on the carrying signals, Galileo broadcast ephemeris broadcast three types of message, namely I/Nav, F/Nav and C/Nav. The message allocation and general data content are shown in Table 1.

Table 1. Message allocation and general data content [15]

Message type	Services	Component
F/Nav	Open	E5a-I
I/Nav	Commercial/open	E5b-I/E1-B
C/Nav	Commercial	E6-B

Similarly, the above navigation message with different frequency signals contains different satellite clock correction data. The C/Nav message is not the subject because it's just for the commercial service. Table 2 shows the clock correction data of I/Nav and F/Nav.

Table 2. Galileo clock correction data [15]

Message type	Frequency point	Clock correction parameters	Services
F/Nav	(E1, E5a)	a_{f0} (E1, E5a) a_{f1} (E1, E5a) a_{f2} (E1, E5a) t_{0C} (E1, E5a)	Dual-frequency (E1, E5a) Single-frequency E5a
I/Nav	(E1, E5b)	a_{f0} (E1, E5b) a_{f1} (E1, E5b) a_{f2} (E1, E5b) t_{0C} (E1, E5b)	Dual-frequency (E1, E5b) Single-frequency E5b Single-frequency E1

where a_{f0} is the satellite clock bias correction coefficient, a_{f1} is the satellite clock drift correction coefficient, a_{f2} is the satellite clock drift rate correction coefficient, t_{0C} is the clock correction data reference time.

3 The Accuracy Evaluation Method of Broadcast Clock Offset

3.1 Clock Offset Fitting Model

The fitting model of Galileo broadcast ephemeris predicted clock offset is shown in formula 3.1, and the unit is seconds [16–18].

$$\Delta t_{SV}(\mathrm{X}) = a_{f0}(X) + a_{f1}(X)[t - t_{0C}(X)] + a_{f2}(X)[t - t_{0C}(X)]^2 + \Delta t_r \tag{3.1}$$

where $\Delta t_{SV}(\mathrm{X})$ is the satellite clock offset, $a_{f0}(X)$, $a_{f1}(X)$ and $a_{f2}(X)$ are defined in 2.2, t is the observation time and $t_{0C}(X)$ is the reference time for the clock correction, Δt_r is the relativistic delay term.

The relativistic correction term can be expressed as formula 3.2.

$$\begin{aligned} \Delta t_r &= \mathrm{F} e A^{1/2} \sin(E) \\ F &= -2\mu^{1/2}/c^2 \end{aligned} \tag{3.2}$$

where μ is Geocentric gravitational constant, c is the Speed of light, e is the Eccentricity, $A^{1/2}$ is Square root of the semi-major axis, E is the eccentric anomaly.

From the formula 3.2, we can see that the relativistic delay term is mainly related to the eccentricity of satellite orbit. The value of Galileo satellite clock offset can reach 1 ns and that of GPS satellite clock offset can up to dozens of nanoseconds by experiments. So the influence of this item cannot be ignored in clock offset fitting.

3.2 Accuracy Evaluation Method

The time reference of broadcast ephemeris and precise ephemeris are not consistent, so the difference between broadcast clock offset and precise clock offset cannot be simply compared. Therefore, in order to eliminate the influence caused by the inconsistency of time reference, this paper adopted the quadratic difference method. In other words, the satellite clock offset calculated separately makes a primary difference to the same reference satellite (E1 satellite was selected for this paper), and then makes a secondary difference between the broadcast clock offset and the precision clock offset, and takes the secondary difference as the sequence of clock offset for accuracy evaluation [12]. The formula is shown in 3.3.

$$\begin{aligned} d\mathrm{T}^i &= T^i - T^0 \\ d\mathrm{t}^i &= t^i - t^0 \\ \Delta t^i &= d\mathrm{T}^i - d\mathrm{t}^i \end{aligned} \tag{3.3}$$

where the superscript i represents the satellite, T^i and t^i are broadcast clock offset and precise clock offset respectively, T^0 and t^0 are the broadcast clock offset and precise clock offset of the reference satellite respectively, Δt^i is the secondary difference of clock offset.

4 Experimental Analysis

4.1 Data Description and Strategy Analysis

In this experiment, the broadcast ephemeris data of GNSS provided by multi-GNSS experiment (MGEX) were selected to evaluate the accuracy of Galileo predicted clock offset. The GBM precision clock products of the same period provided by GFZ analysis center were used as the truth value. Since the calculation of precision clock products adopts E1/E5a dual-frequency ionosphere-free combination, this paper selects F/Nav message containing E1/E5a information for the accuracy evaluation. The processing time starts from December 15, 2016, on which Galileo started to provide initial service, to October 31, 2018. And the solution strategy is shown in Table 3.

Table 3. Summary of the solution strategy

Broadcast clock offset	Source	The broadcast ephemeris data of GNSS provided by MGEX
	Update rate	10 min
	Navigation message	F/Nav
	Fitting model	Quadratic polynomial + Relativity correction term
Precision clock offset	Source	The GBM precision clock products provided by GFZ
	Sampling	30 s
Reference satellite		E01
Accuracy evaluation method		The quadratic difference method

As Galileo satellite system is still in the initial run stage, only 17 of the 24 satellites in orbit currently provide normal services, and the time for each satellite to provide normal services varies. Figure 1 shows the service period of the 15 satellites in the selected period of this experiment, where E22 satellite ceased service on December 12, 2017. In addition, E21, E25 and E27 satellites began to provide normal services in October 2018, August 2018 and August 2018 respectively. Considering the service time was relatively short, the broadcast ephemeris of these three satellites were not analyzed in this paper.

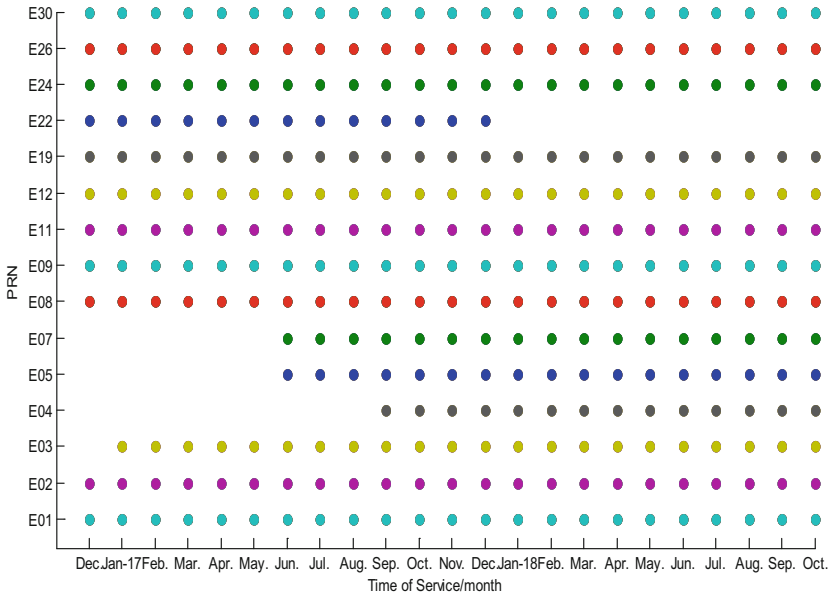

Fig. 1. The service time of Galileo satellites which can provide normal service

4.2 Analysis of Results

The GBM precision clock product provided by GFZ was taken as the truth value, and the accuracy of the broadcast clock offset was evaluated by using the broadcast ephemeris data for the last two years. Figures 2 and 3 respectively calculated STD and RMS of the secondary differences between Galileo satellites broadcast clock offset and GBM precision clock offset, with the unit of nanoseconds and the statistical duration of 686 days. For the statistical time is too long, the points are too dense and unclear. Therefore, the graph shows the secondary difference clock offset sequence of a sampling point in 10 days. Since E01 is the reference satellite, it is not discussed here. The results shows that: (1) Except for some days, the STD of all the satellite broadcast clock offset and GBM precision clock difference is within 2 ns in the sequence of secondary clock offset. The RMS of the secondary difference sequence of all satellites is about 2 ns, except E24 is about 6 ns. (2) It can also be seen from the Figs. 2 and 3 that in the service stage of E22 satellite, the STD and RMS of the sequence of secondary clock

offset show an increasing trend, indicating that the accuracy is getting worse. Meanwhile, the accuracy of other satellites changes randomly with little fluctuation and small accuracy change.

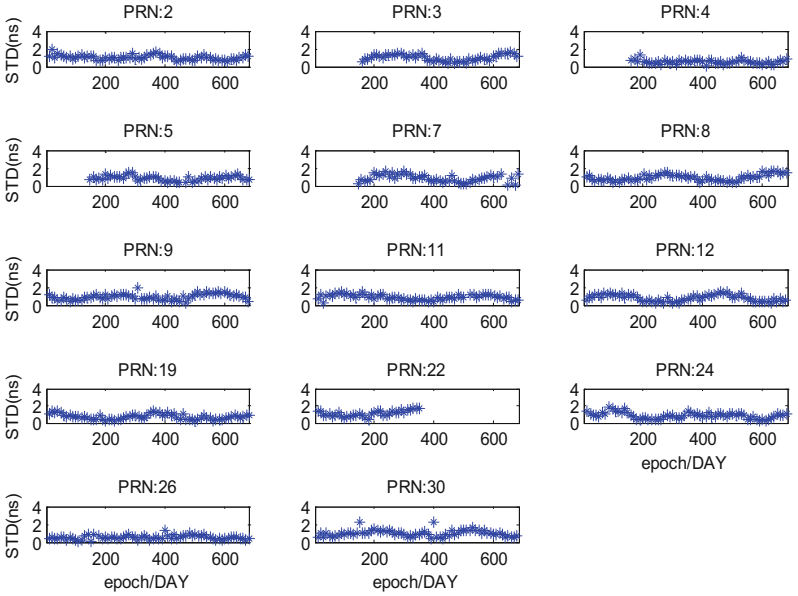

Fig. 2. The STD of the sequence of secondary difference clock offset

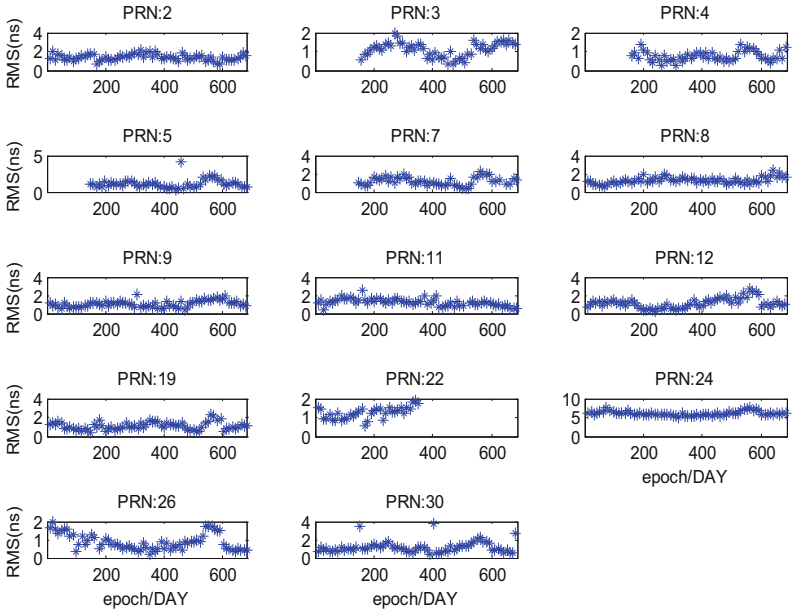

Fig. 3. The RMS of the sequence of secondary difference clock offset

In order to show the variation of Galileo satellite broadcast clock offset in the statistical period, this experiment selected E02, E08, E09, E11, E12, E19, E26 and E30 satellites with complete data, and calculated the average STD and RMS of the secondary difference sequence by month. The results are shown in Figs. 4 and 5. Figure 6 shows the mean STD and RMS peak-to-peak value difference of the secondary difference sequence between the broadcast clock offset and the GBM precision clock products by month. The results show that: (1) During the statistical period from December 2016 to October 2018, the mean STD change value of the secondary difference sequence is about 0.8 ns in monthly statistics, while the average RMS change value was about 1–1.5 ns in monthly statistics, and the maximum change value of E12 satellite was up to 1.8 ns. (2) The average STD and RMS values of the secondary difference sequence by month of each satellite change in a small range. And the accuracy of broadcast clock offset does not increase or decrease obviously with the increase of time, which suggest that Galileo satellite broadcast clock offset accuracy is relatively stable after providing services, and there is no obvious change trend.

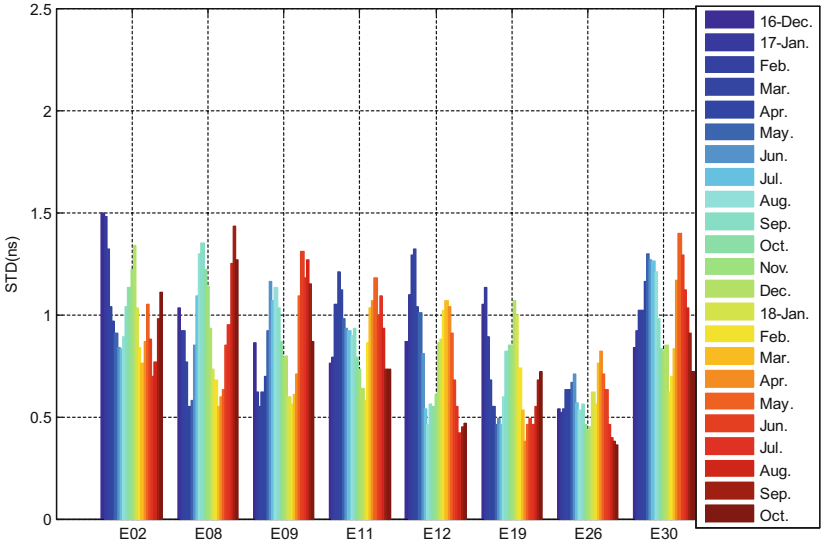

Fig. 4. The average STD of the sequence of secondary difference clock offset by month from December 2016 to October 2018

Finally, the STD and RMS of the secondary difference sequence in 686 days were averaged, and the calculated results are shown in Table 4. The average STD of satellites E2, E3, E22 and E30 ranged from 1 to 1.1 ns, while the average STD of other satellites ranged from 0.58 to 1 ns. The average RMS of satellite E24 is 5.97 ns, the average RMS of satellites E4 and E26 is within 1 ns, and the average RMS of other satellites is between 1 and 1.4 ns. At the same time, the average STD and average RMS are shown in Fig. 7. We can clearly see that the accuracy distribution of Galileo satellite broadcast clock offset. The average STD is about 1 ns, while the average RMS is basically greater than 1 ns, especially the satellite E24 reaches 6 ns.

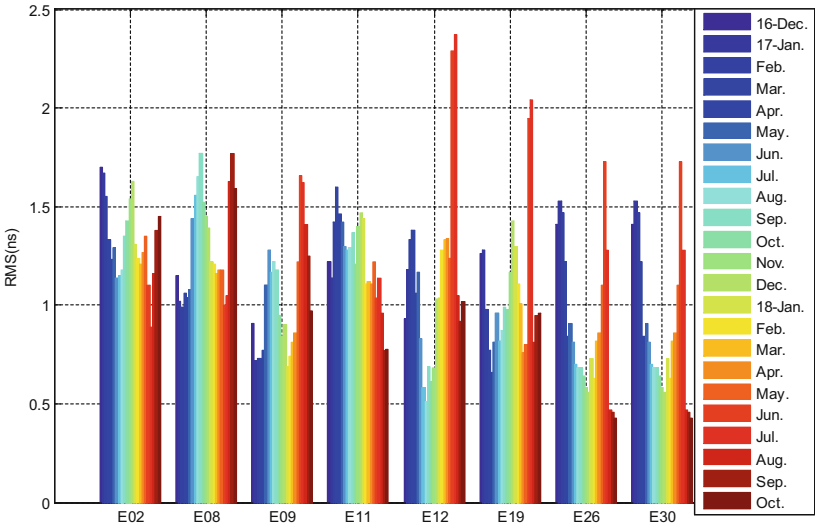

Fig. 5. The average RMS of the sequence of secondary difference clock offset by month from December 2016 to October 2018

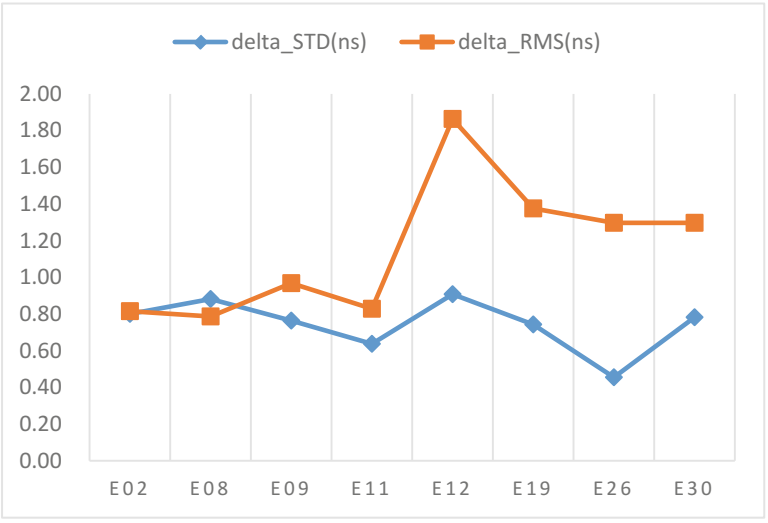

Fig. 6. The mean STD and RMS peak-to-peak value difference of the secondary difference sequence by month

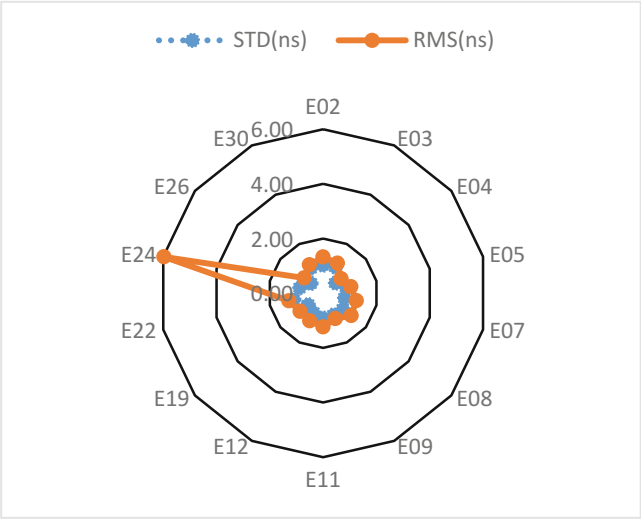

Fig. 7. Summary of Galileo satellite broadcast clock offset accuracy index

Table 4. Summary of Galileo satellite broadcast clock offset accuracy index

PRN	Mean_STD (ns)	Mean_RMS (ns)
E02	1.02	1.32
E03	1.05	1.21
E04	0.58	0.84
E05	0.87	1.04
E07	0.81	1.25
E08	0.94	1.31
E09	0.89	1.03
E11	0.91	1.24
E12	0.80	1.13
E19	0.69	1.07
E22	1.10	1.28
E24	0.87	5.97
E26	0.57	0.89
E30	1.01	1.15

5 Conclusion

Based on the precision clock products provided by GFZ, this paper evaluated the accuracy of the broadcast clock offset of Galileo satellites by using the GNSS broadcast ephemeris data up to two years. The STD and RMS of the secondary difference sequence value in 686 days, the mean STD and mean RMS, and the change of secondary difference sequence value of monthly statistics were calculated respectively since Galileo provided initial service. The results show that:

(1) The mean STD of differences between GBM precision clock product and Galileo broadcast clock offset is approximately 1 ns. In addition to the mean RMS of Galileo E24 satellite broadcast clock offset is 5.7 ns, the RMS of the other 14 satellites broadcast clock offset is less than 1.4 ns. Therefore, if only considering the effect of satellite clock offset, the broadcast clock offset cannot satisfy the requirement of sub-nanosecond precision timing service;
(2) During the period of providing services, the STD and RMS of Galileo satellite broadcast clock offset based on monthly statistics are changing, with the STD changing value around 0.8 ns and the RMS changing value around 1–1.5 ns. And the two are changing randomly with no obvious trend of getting better or worse over time. It suggests that Galileo satellite broadcast clocks accuracy is relatively stable after providing services, which reflects the stability of Galileo satellite clock to a certain extent.

The above evaluation results would be of certain reference significance to the performance evaluation of Galileo space-borne clock and the timing application of Galileo satellite navigation system.

Acknowledgements. This work is supported by National Natural Science Foundation of China (No. 41104021, 11173026, 11703033, 41474029, 41574015). We would like to thank the National R&D Infrastructure and Facility Development Program of China, "Fundamental Science Data Sharing Platform" (DKA2017-12-02-24) who funded the project. The authors gratefully acknowledge thanks to the GFZ for providing the precision clock products and the IGS for providing broadcast products. Many thanks to NTSC iGMAS Analyses Center for providing relevant experimental platform.

References

1. Huang G et al (2018) Characteristics and performance evaluation of Galileo on-orbit satellites atomic clocks during 2014–2017. Adv Space Res. https://doi.org/10.1016/j.asr.2018.01.034
2. Orbit data and resources on active gnss satellites. https://www.gpsworld.com. Accessed 10 Sept 2018
3. Galileo satellite status. http://www.igmas.org/Gnss/Xzztpg/wxzt/cate_id/15.html. Accessed 1 Oct 2018
4. Steigenberger P, Hugentobler U, Loyer S et al (2015) Galileo orbit and clock quality of the IGS multi-GNSS experiment. Adv Space Res 55(1):269–281
5. Fan Y, Lu H, Jia X et al (2016) Study on GNSS Broadcast Ephemeris Precision Evaluation. In: China satellite navigation conference
6. Kim M, Kim J (2015) A long-term analysis of the GPS broadcast orbit and clock error variations. Proc Eng 99:654–658
7. Guo J, Meng X, Li Z (2011) Accuracy analysis of GLONASS satellites broadcast ephemeris. J Geodesy Geodyn 31(1):68–71
8. Wang B, Lou Y, Liu J, Zhao Q, Su X (2016) Analysis of BDS satellite clocks in orbit. GPS Solutions 20(4):783–794
9. Mao Y, Wang Q, Hu C et al (2018) Accuracy analysis of BDS experiment satellite broadcast ephemeris. In: China satellite navigation conference. Springer, Singapore

10. Rodriguez L (2013) Galileo IOV status and results. In: Proceedings of ION GNSS 2013, Nashville, TN, pp 3065–3093
11. Montenbruck O, Steigenberger P, Hauschild A (2015) Broadcast versus precise ephemerides: a multi-GNSS perspective. GPS Solutions 19(2):321–333
12. Yin H, Wu D, Zeng Q et al (2017) Accuracy evaluation of Galileo IOV satellite broadcast ephemeris. Eng Surv Mapp. 26(4):1–5
13. Yong-Jiu C (2015) The precision of GNSS broadcast ephemeris. Geomat Spat Inf Technol 38(6):186–191
14. Montenbruck O, Steigenberger P, Hauschild A (2018) Multi-gnss signal-in-space range error assessment – methodology and results. Adv Space Res 61:3020–3038 S0273117718302813
15. Nan C, Li Y, Qun D (2008) Some features of Galileo OS SIS ICD navigation message. J Geomat Sci Technol 25(5):329–335
16. Zuo-Hu LI, Jin-Ming H, Jian-Wen LI et al (2011) Navigation message designing in Galileo OS SIS ICD. J Geomat Sci Technol 28(1):14–18
17. Xu G, Xu J (2013) Numerical Orbit Determination Orbits. Springer, Heidelberg
18. Li Z, Huang J (2015) GPS survey and data processing. Wuhan University Press, Wuhan, pp 84–113

BDS Long-Term Almanac Fitting Arc Length Design for Autonomous Navigation

Zhiqiao Chang[1(✉)], Xiaogong Hu[2], Rui Guo[1], Hui Ren[1], Li Ma[3], Chengpan Tang[2], and Junyu Pu[1]

[1] 32021 Armies, Beijing 100094, China
zhiqiaochang@163.com
[2] Shanghai Astronomical Observatory, Chinese Academy of Sciences, Shanghai 200030, China
[3] 93658 Armies, Beijing 100061, China

Abstract. In order to meet accuracy requirements of long-term almanac parameters for assisting inter-satellite link signal acquisition in autonomous navigation mode, in this paper, without changing the almanac model, we propose the scheme of different fitting arc length for different types of satellites. Considering position fitting maximum error, fitting stability and satellite storage resources on-board, the optimal fitting arc length for long-term almanac suitable for autonomous navigation is designed for Beidou geostationary earth orbit (GEO), inclined geosynchronous orbit (IGSO) and medium earth MEO navigation satellites. Based on the actual orbit data of 13 Beidou satellites in-orbit in 2013, a variety of fitting arc lengths were used to fit the almanac. The comparative analysis shows that MEO satellites still adopt 7-day fitting arc length while IGSO and GEO satellites utilize 3-day fitting arc length. The verification results show that the optimal fitting arc length scheme proposed in this paper satisfies accuracy requirements of inter-satellite link construction. Furthermore, it has good stability and engineering feasibility.

Keywords: BDS · Almanac fitting · Signal acquisition · Inter-satellite link · Fitting arc length

1 Introduction

High-quality almanac parameters can provide high-precision satellite motion state information, reducing receivers' search range for initial code phase prediction and carrier doppler shift [1]. Almanac parameters are typically used for auxiliary signal capture [2, 3]. There are eight almanac parameters to describe Beidou satellite orbit, including the reference time t_{oa}, six Kepler elements of reference time $(\sqrt{a}, e, \delta_i, \Omega_0, \omega, M)$, and a long-term correction $\dot{\Omega}$ [4, 5]. For normal users, the equipment is kept in status of continuous tracking after tracking and capturing satellite signals. Therefore, the accuracy of almanac only affects the first positioning time, and the error of the user's distance error direction is the main factor interfering signal acquisition. Autonomous navigation based on inter-satellite observation and communication is the development trend of a new generation of global satellite navigation systems. In order to ensure inter-satellite measurement and data transmission performance, inter-satellite

J. Sun et al. (Eds.): CSNC 2019, LNEE 563, pp. 92–101, 2019.
https://doi.org/10.1007/978-981-13-7759-4_9

links usually adopt the time-division mode, which is required to finish acquisition, tracking and demodulation in each short time slot. The limited resources on satellites cause a great challenge to signal acquisition and reliability [6]. For the inter-satellite link of time division mode, each time slot may need to switch to track different satellites. The error affecting the inter-satellite link signal acquisition is the projection in the line of sight direction, and the maximum error can be the sum of two satellite position errors. Therefore, high-precision almanac model is essential for rapid capture of inter-satellite link signals. Literature [7] indicates that if the almanac model is not changed, only one set of almanac parameters cannot meet the auxiliary tracking requirements of inter-satellite link. At present, the effective arc length of the almanac parameters is 7 days. In order to meet the continuous operation requirements of autonomous navigation, multiple sets of almanac parameters are uploaded for once by the ground control system. The RMS or average of fitting residuals over the entire fitting arc is normally used to assess fitting accuracy in conventional ephemeris or almanac fitting process [8–10]. Some relevant calculation analyses show that in condition of 7-day arc length, the fitting statistics RMS of the almanac model are on the order of km. For the inter-satellite link signal acquisition, because more accurate satellite position calculated by the almanac parameters is needed, more attention should be paid to the maximum error of almanac fitting.

Beidou satellite navigation system adopts a mixed constellation including the geostationary earth orbit (GEO), the inclined geosynchronous orbit (IGSO), and the medium earth orbit (MEO) satellites [11]. The orbit heights of GEO and IGSO satellites are higher than MEO's, resulting in different dynamic characteristics, and the almanac fitting accuracy is also different. On the other hand, GEO and IGSO satellites have different periods from MEO satellites, hence, in the same fitting arc, different satellite running tracks result in difference in fitting accuracy and stability. Based on the orbit of Beidou mixed constellation, this paper analyzes the maximum error of the almanac fitting on the annual time scale. By the comparison of maximum fitting error of different fitting arc length, the optimal fit arc length which meets the accuracy requirements and largely saves the storage resources on satellites is finally designed.

2 BDS Satellite Almanac Parameter Fitting

2.1 Almanac User Algorithm

The method of calculating satellite position using the almanac is roughly the same as the one using the broadcast ephemeris. The main difference is that six short-period perturbation parameters are reduced. Related algorithms are as follows:

1. Calculate the mean anomaly

$$\begin{cases} a = a_{ref} + \Delta a \\ n = \sqrt{\frac{\mu}{a^3}} \\ t_k = t - t_{oa} \\ M_k = M_0 + nt_k \end{cases} \tag{1}$$

Where μ is the gravitational constant of the earth.

2. Iteratively calculate the eccentric anomaly E_k

$$E_k = M_k + e \sin E_k \tag{2}$$

3. Calculate satellite radius r_k

$$r_k = a(1 - e \cos E_k) \tag{3}$$

4. Calculate the true anomaly f_k and the argument of latitude u_k

$$\begin{cases} f_k = 2arctg\left(\sqrt{\dfrac{1+e}{1-e}} \cdot tg\dfrac{E_k}{2}\right) \\ u_k = f_k + \omega \end{cases} \tag{4}$$

5. Calculate the coordinates in orbital plane coordinate system

The coordinates in orbital plane coordinate system (X-axis points to the ascending node) are:

$$\begin{cases} x_k = r_k \cos u_k \\ y_k = r_k \sin u_k \end{cases} \tag{5}$$

6. Calculate longitude of ascending node at the observation time

$$\Omega_k = \Omega_0 + (\dot{\Omega} - \omega_e)t_k - \omega_e t_{oa} \tag{6}$$

Where Ω_0 is longitude of ascending node of orbit plane at weekly epoch.

7. Calculate the coordinates in cgcs2000

$$\begin{bmatrix} x \\ y \\ z \end{bmatrix} = \begin{bmatrix} x_k \cos \Omega_k - y_k \cos i_k \sin \Omega_k \\ x_k \sin \Omega_k + y_k \cos i_k \cos \Omega_k \\ y_k \sin i_k \end{bmatrix} \tag{7}$$

2.2 Almanac Fitting Algorithm

The BDS GEO satellites are qualified with small inclination and small eccentricity characteristics. The right ascension of the ascending node and the argument of perigee cannot be strictly distinguished. Thus, the mean anomaly and the argument of perigee cannot be strictly distinguished [8]. In ephemeris fitting, the arc length is short; therefore the equation of ephemeris fitting can be ill-posed. Literature [12] solves the problem of stability and accuracy of ephemeris fitting by combining no singularity orbital elements with coordinate rotation. For almanac fitting model, as the number of parameters decreases, the fitting arc length increases, and the correlation between the almanac parameters is further weakened. During the process of implementation, the parameters are fitted utilizing Kepler orbital parameters, and as for GEO satellites, the coordinate system is no longer rotated.

For Eq. (7), after computing the first-order partial derivative of seven almanac parameters, the linearized observation equation can be obtained.

$$\boldsymbol{R} = \boldsymbol{R}_0 + \frac{\partial \boldsymbol{R}}{\partial \Delta a}\delta\Delta a + \frac{\partial \boldsymbol{R}}{\partial e}\delta e + \frac{\partial \boldsymbol{R}}{\partial i_0}\delta i_0 + \cdots + \frac{\partial \boldsymbol{R}}{\partial \dot{\Omega}}\delta\dot{\Omega} \tag{8}$$

Where $\boldsymbol{R}$ is satellite position vector in the terrestrial fixed coordinate system for observing epoch; $\boldsymbol{R}_0$ is satellite approximation position vector calculated using Eq. (7); $\delta\Delta a$, δe, …, are the correction values of the corresponding almanac parameters respectively. For discrete orbits of k epochs, the following error equation can be obtained:

$$\boldsymbol{V} = \boldsymbol{H} \cdot \boldsymbol{X} + \boldsymbol{L} \tag{9}$$

Where $\boldsymbol{V}$ is $3k$ dimensional residual vector, $\boldsymbol{H}$ is $3k \times 8$ dimensional coefficient matrix, $\boldsymbol{L}$ is $3k$ dimensional observation vector. Once $3k \geq 8$ is satisfied, the corrections values of the almanac parameters can be calculated by the least squares estimation principle.

The parameter convergence condition is set as:

$$\frac{|\sigma_{i+1} - \sigma_i|}{\sigma_i} < 1e-3 \tag{10}$$

Where σ_i is the error in unit weight of the ith iteration.

To fit almanac parameters correctly, the key is to find the partial derivatives of almanac parameters for the terrestrial fixed coordinate system position vector expressed by Eq. (7). To solve these partial derivatives, we divide the fitting parameters into two groups: the parameters of the orbital surface $(\Delta a, e, M_0)$, and the parameters about the orbital plane orientation $(\omega_0, i_0, \Omega_0, \dot{\Omega})$. According to the almanac user algorithm in Sect. 2.1, the first set of parameters and the second one are independent of each other. When the partial derivatives of the first set of parameters are deduced, all the second set of parameters is regarded as constant. Considering paper length limitations, only the

second set of parameters is demonstrated here in detail. The partial derivative calculation method of the first set of parameters is described in literature [13].

Bringing Eq. (5) into Eq. (7), we can get:

$$\begin{bmatrix} x \\ y \\ z \end{bmatrix} = r_k \begin{bmatrix} \cos u_k \cos \Omega_k - \sin u_k \cos i_0 \sin \Omega_k \\ \cos u_k \sin \Omega_k + \sin u_k \cos i_0 \cos \Omega_k \\ \sin u_k \sin i_0 \end{bmatrix} \tag{11}$$

r_k is only related to the orbital plane parameters and not related to the orbital orientation parameters, therefore, r_k is considered to be a constant. The partial derivatives of satellite position vector to the orbital orientation parameters can be deduced from Eqs. (11), (6), and (4).

$$\frac{\partial \boldsymbol{R}}{\partial i_0} = r_k \sin u_k \begin{pmatrix} \sin i_0 \sin \Omega_k \\ -\sin i_0 \cos \Omega_k \\ \cos i_0 \end{pmatrix} \tag{12}$$

$$\frac{\partial \boldsymbol{R}}{\partial \Omega_0} = r_k \begin{pmatrix} -\cos u_k \sin \Omega_k - \sin u_k \cos i_0 \cos \Omega_k \\ \cos u_k \cos \Omega_k - \sin u_k \cos i_0 \sin \Omega_k \\ 0 \end{pmatrix} \tag{13}$$

$$\frac{\partial \boldsymbol{R}}{\partial \omega_0} = r_k \begin{pmatrix} -\sin u_k \cos \Omega_k - \cos u_k \cos i_0 \sin \Omega_k \\ -\sin u_k \sin \Omega_k + \cos u_k \cos i_0 \cos \Omega_k \\ \cos u \sin i \end{pmatrix} \tag{14}$$

$$\frac{\partial \mathbf{R}}{\partial \dot{\Omega}} = -\frac{\partial \mathbf{R}}{\partial \Omega_0} t_k \tag{15}$$

3 Analysis and Discussion of Almanac Fitting Results

In autonomous operating conditions without the ground control support, the almanac parameters are fitted by long-term predicting orbit, so the position error expressed by almanac includes the long-term predicting orbit error and the almanac fitting expression error. The long-term orbit predicting process is as follows: First of all, post accurate orbits are connected with a 10-day numerical orbit. Then, a dynamic method is used to smooth the discrete orbits, and high-precision dynamic parameters can be obtained. Finally, by orbital integration, a continuous orbit of a 90-day can be obtained. By evaluating the predicting accuracy of Beidou 3 types of orbits for 90 days, it is found that URE caused by the orbital predicting is less than 600 m and the error caused by almanac fitting in the 90-day predicting arc is the main factor. It needs to be noted that no matter broadcast ephemeris or almanac parameters, the parameters are only valid in the fitting arc. If the fitting arc is exceeded, the satellite orbit position accuracy will decrease [6]. Therefore, this paper mainly analyzes the error caused by almanac fitting, and does not pay attention to the orbit prediction error or the almanac predicting error.

Using data from the domestic regional monitoring network of the whole year of 2013, a sliding window method was adopted to carry out multi-satellite and multi-station combined precision orbit determination to get a numerical track covering the full year of 2013. Almanac parameter fitting was performed on 13 satellites in orbit with a 7-day arc length throughout 2013. Table 1 lists the fitting position errors for all satellites in orbit, where SAT01-05 are GEO satellites, SAT06-10 are IGSO satellites, and SAT11-14 are MEO satellites. Table 1 indicates that IGSO satellites have the largest fitting errors, GEO fitting errors are the second largest, and MEO fitting errors are the smallest. Also, we can find that the fitting error RMS average value of five GEO satellites is 3.25 km, and that the maximum fitting position error is 10.52 km. The fitting error RMS average of five IGSO satellites is 4.04 km, and the maximum fitting position error is 17.97 km. The fitting error RMS average of three MEO satellites is 1.62 km, and the maximum fitting position error is 5.92 km. When the fitting arc is 7 days, the maximum fitting position errors of IGSO and GEO satellites have exceeded 10 km. Figure 1 depicts details of fitting position errors of all types of satellites in 2013.

High-precision almanac is required due to the existing hardware and software resources of the satellites. We can set the almanac expression error limit to 5 km. The longer the fitting arc length is, the less the number of almanac groups required for the autonomous operation. In order to save the on-board storage resources, the arc length should be as long as possible in accuracy condition. The percentage of almanac express error over 5 km is designed to 2% considering inter-satellite link observation success rate requirements. Table 1 lists the percentage of the almanac position error over 5 km. In the 7-day arc fitting condition, the GEO maximum percentage of position error over 5 km is 15.13%, the IGSO maximum percentage is 30.79%, and MEO maximum is 0.62%. GEO and IGSO satellites have large position errors and the probability of errors over 5 km is also large, which leads to a greater probability that the inter-satellite link cannot be normally captured. However, the probability that MEO satellites cannot be captured normally is small. Therefore, the MEO satellites can still maintain 7-day fitting arc and the interface between the ground control system and satellites is unchanged. As for GEO and MEO satellites, their fitting arc needs to be changed due to large position fitting errors.

Table 1. Position error statistic of almanac fitting with 7-day arc (m)

PRN	RMS	MAX	%[a]	PRN	RMS	MAX	%	PRN	RMS	MAX	%
01	3.18	9.37	8.39	06	4.89	16.35	30.79	11	1.59	5.58	0.62
02	3.14	9.18	11.27	07	3.30	8.98	10.08	12	1.58	5.52	0.33
03	3.71	10.52	15.13	08	4.40	17.97	21.53	14	1.68	5.92	0.13
04	2.99	9.86	8.17	09	4.57	16.99	25.79			–	
05	3.25	10.09	10.82	10	3.03	10.52	7.44			–	
Average	3.25	9.80	10.76	Average	4.04	14.16	19.13	Average	1.62	5.67	0.36

[a]The percentage in the table refers to the percentage exceeding the 5 km limit of the algebra's fitted position error.

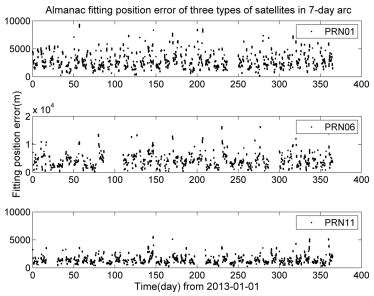

Fig. 1. The almanac fitting position error of three types of satellites (7-day-arc)

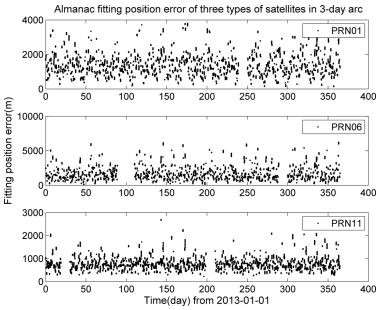

Fig. 2. The almanac fitting position error of three types of satellites (3-dayarc)

Table 2. Position error statistic comparison of almanac fitting with 3-day arc and 1-day arc (m)

PRN	RMS		MAX		百分比		PRN	RMS		MAX		百分比	
	3 day	1 day	3 day	1 day	3 day	1 day		3 day	1 day	3 day	1 day	3 day	1 day
01	1.52	0.97	3.80	2.93	0.00	0.00	06	1.98	0.96	6.23	2.45	1.85	0.00
02	1.63	0.98	5.42	2.51	0.17	0.00	07	1.54	0.97	5.47	2.94	0.05	0.00
03	1.58	1.00	4.47	2.67	0.00	0.00	08	1.85	0.93	7.44	2.46	0.98	0.00
04	1.59	0.97	4.44	2.71	0.00	0.00	09	1.96	0.94	6.27	2.40	1.52	0.00
05	1.57	0.96	4.82	3.01	0.00	0.00	10	1.54	0.98	5.58	2.35	0.04	0.00
Average	1.58	0.98	4.59	2.77	0.03	0.00	Average	1.77	0.96	6.20	2.52	0.89	0.00

We adjusted the fitting arc length to 3 days, and the almanac parameters of the 13 satellites in orbit were fitted again. Figure 2 depicts details of fitting position errors of all types of satellites in 2013 for 3-day fitting arc. Comparing Figs. 1 and 2, shortened arc length reduces position errors and improves the accuracy of almanac fitting. In order to satisfy the fitting accuracy and avoid too short arc length, the comparison of arc lengths of 3 days and 1 day for GEO and IGSO satellites was performed. The almanac fitting position errors are listed in Table 2.

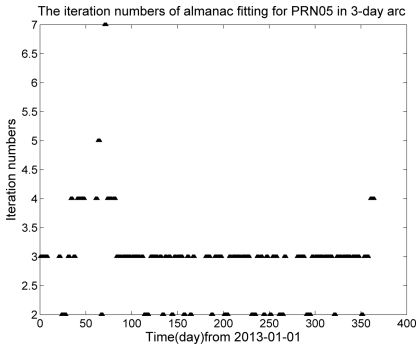

Fig. 3. The iteration numbers of almanac fitting (3 day-arc)

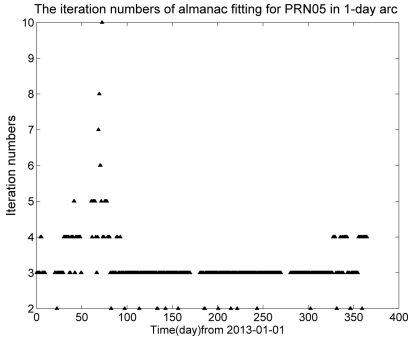

Fig. 4. The iteration numbers of almanac fitting (1 day-arc)

When compared with 3-day arc fitting, the accuracy of 1-day is improved. Figures 3 and 4 respectively describe almanac iteration times of PRN5 satellite in three-day arc and one-day arc. By comparing and analyzing the iteration times, the number of iterations of 1-day fitting arc is more than that of the 3-day arc, and its stability is reduced, especially in the spring and autumnal season (The time of occurrence of the earth shadow is about from February 27 to April 12 and August 31 to October 16, totally about 92 days in the whole year [13]), the number of iterations of 1-day fitting arc is increased to 10 times. On the other hand, every satellite needs to store the long-term almanac parameters of all satellites. The shorter the arc length is, the more the almanac group is and the larger on-board resources are occupied. Taking all the factors described above, the fitting arc is set to 3 days finally. In this way, fitting accuracy and stability can be ensured.

4 Conclusions

It is known that the long-term almanac parameters are used to assist autonomous navigation of inter-satellite link signal acquisition, which is more accurate than the demands of conventional navigation. At present, the effective duration of almanac parameters is 7 days. In order to meet the requirements of continuous operation of autonomous navigation, the ground control system is required to upload multiple sets of almanac parameters for once. Even when utilizing the 7-day arc length, some satellites still have large fitting errors, which affect signal acquisition between satellites. In order to solve the problem, this paper proposes a scheme using different arc for different types of satellites. The longer the arc is, the less the number of almanac groups is required for autonomous operation cycle. For saving the on-board storage resources, the arc length should be as long as possible when the accuracy requirement is met. The percentage of almanac expression error over 5 km is taken as 2%. Not changing the almanac model, we performed the almanac fitting using a variety of fitting arcs based on the actual orbit data of 13 Beidou satellites in-orbit in 2013. The optimal fitting arc was obtained by comparative analysis of position fitting maximum errors, fitting stability and satellite occupancy resources. MEO satellites still use a 7-day fitting arc and IGSO and MEO satellites use 3-day fitting arc.

Acknowledgements. This paper is supported by the National Natural Science Foundation of China (NSFC) (Grant No. 41874043, 41574029, 41804030, 61603397 and 41704037), and the National Key Research Program of China "Collaborative Precision Positioning Project" (Grant No. 2016YFB0501900), and the Opening Project of Shanghai Key Laboratory of Space Navigation and Position Techniques (Grant No. ZZXT_201701).

References

1. Wang L, Huang Z, Zhao Y (2013) Two sets of GPS almanac on time to first fix influence. Geomatics Inf Sci Wuhan Univ 38(2):140–143
2. Van Dierendonk AJ (1994) Navigation message of Global Positioning System. Navigation Satellites Global Positioning System. Surveying and Mapping Press, Beijing, pp 64–87
3. Elliott DK (1996) Understanding GPS Principles and Applications. Artech House, New York
4. China Satellite Navigation Office (2013) BeiDou navigation satellite system signal in space Interface Control Document open service signal (version 2.0). China Satellite Navigation Office, Beijing
5. Liu L, Shi X, Li J et al (2015) The definition and using method of the COMPASS basic navigation message. Sci Sin-Phys Mech Astron 45(7):079509
6. Li X, Wang Y, Chen J (2014) Research on the acquisition search strategy of navigation constellation inter-satellite link. J Astronaut 35(8):946–952
7. Chang Z, Hu X, Chen L et al (2018) High-accuracy long arc almanac model design for BDS. Acta Geod et Cartographica Sin 47(3):298–307
8. Huang H (2012) Research on the broadcast ephemeris parameters model and its fitting algorithm. Nanjing University, Nanjing

9. Zhang Z, Du L, Liu L et al (2014) Parameter design of GEO broadcast ephemeris based on the nonsingular orbital elements. Acta Geod et Cartographica Sin 43(5):452–457
10. Du L, Zhang Z, Zhang J et al (2015) An 18-element GEO broadcast ephemeris based on non-singular elements. GPS Solutions 19(1):49–59
11. He F, Wang G, Liu L et al (2011) Ephemeris fitting and experiments analysis of GEO satellite. Acta Geod et Cartographica Sin 40(Supplement):52–58
12. Chang Z, Hu X, Huang H et al (2017) The broadcast ephemeris fitting algorithm combining no singularity orbital elements with coordinate rotation and its performance evaluation. J Geodesy Geodyn 40(2):54–58
13. Mao Y, Song X, Jia X et al (2014) Earth eclipse status analysis of Beidou navigation satellite. Acta Geod et Cartographica Sin 43(4):353–359

Strategy Analysis of Anchorage Station in Distributed Autonomous Orbit Determination for Beidou MEO Constellation

Xufeng Wen[1(✉)], Jing Wang[2], Jinming Hao[3], and Xiaogong Hu[4]

[1] Beijing Aerospace Control Center, Beijing, China
wenxufeng201@126.com
[2] The 96633 Troops of PLA, Beijing, China
[3] Information Engineering University, Zhengzhou, China
[4] Shanghai Astronomical Observatory,
Chinese Academy of Science, Shanghai, China

Abstract. Beidou-3 Global System Satellite carries the Ka inter-satellite link load. Facing the reality of the on-board environment, the distributed autonomous orbit determination strategy of all constellations is studied. The distributed autonomous orbit determination algorithm under the constraints of long-term forecast ephemeris is deduced, and the relationship between anchorage station setting strategy and orbit determination accuracy is analyzed. The simulation results of full constellation show that under the constraints of long-term forecast ephemeris, the average URE of 60-day orbits is limited to less than 4 m, but URE is still accumulating. 3 Anchorage stations are the optimal scheme in quantity, which can make the average URE converge to 0.5 m in 0.54 days. In the selection of anchorage station location, high latitude anchorage station has no contribution to improve the accuracy of autonomous orbit determination, and low latitude single anchorage station can control URE at about 1 m.

Keywords: Beidou satellite navigation system · Intersatellite link · Distributed autonomous orbit determination · Anchorage station

1 Introduction

Ranging and communication based on Inter-Satellite Link (ISL) can realize autonomous orbit determination and time synchronization of satellite navigation system, and improve the survivability of satellite navigation system when ground operation control is blocked or weakened [1–6]. In addition, ground operation and control can be assisted by joint observation between satellites and earth, which can make up for the shortcomings of the small station arrangement layout of the Beidou system in China [7]. The preliminary results of centralized autonomous orbit determination based on measured data show that the accuracy of Ka ISL two-way observation is better than 10 cm [8], and the accuracy of R-direction supported by a ground station is less than 0.5 m [9].

The problem of constellation rotation exists in autonomous orbit determination under fully autonomous navigation mode, which is caused by the rank deficit problem in the observational equation of inter-satellite link and the invisibility of right ascension

J. Sun et al. (Eds.): CSNC 2019, LNEE 563, pp. 102–114, 2019.
https://doi.org/10.1007/978-981-13-7759-4_10

of ascending node (RAAN) changes. With the prolongation of autonomous orbit determination time, the problem is mainly reflected in the accumulation of ascending node meridian errors [10]. External datum must be introduced to solve this problem. In general, adding ground anchorage station is the main means to solve this problem. The autonomy of satellite orbit determination is weakened to some extent by increasing earth observation. However, anchorage station only participates in the inter-satellite link as a virtual satellite. The method of setting anchorage station is simple and flexible, which alleviates this contradiction to a certain extent. This paper mainly studies the contribution of anchorage station in distributed autonomous orbit determination. The observability of the satellite-ground link to the whole rotation is analyzed, and the relationship between the anchorage station setting and the control ability of the whole rotation of the constellation is deduced. The distributed autonomous orbit determination software of the whole constellation is built, and the simulation data are used to test the effect of the different number and location of the anchorage station on the whole rotation of the constellation.

2 The Function and Application Strategy of Anchorage Station in Autonomous Orbit Determination

2.1 Observability of Astro-Earth Observation on Rising Node Meridian

In this paper, the rank deficiency problem of the normal square matrix of the observation equation under the condition of simple inter-satellite ranging and the invisibility of the RNNA are not discussed. On the other hand, we analyze the observability of the RAAN by satellite-earth observations. The relationship between the geostationary rectangular coordinates and spherical coordinates of satellites and anchorage stations is as follows:

$$\begin{cases} x = \left|\vec{r}\right| \cos\varphi \cos\lambda \\ y = \left|\vec{r}\right| \cos\varphi \sin\lambda \\ z = \left|\vec{r}\right| \sin\varphi \end{cases} \tag{1.1}$$

Where $\vec{r} = [x \quad y \quad z]^T$ is rectangular coordinate of satellite or anchorage station, λ is longitude, φ is latitude, $\left|\vec{r}\right|$ is geocentric distance of satellite or anchorage station. For epoch t, the λ_A and the RAAN Ω_A of satellite A can be transformed into each other:

$$\lambda_A = \Omega_A + f_A(t) \tag{1.2}$$

The equation of satellite-earth observation is expressed as follows:

$$\begin{aligned} P_{AS,CF} &= h(\mathbf{X}_A, t) + v_{AS} \\ &= \left|\vec{r}_S - \vec{r}_A(t)\right| + \varepsilon_{AS} \end{aligned} \tag{1.3}$$

Where ε_{AS} is residual error and S is anchorage station. Thus $\vec{r}_S(t)$ is known. Thus $\vec{r}_S(t)$ is derivative. The derivation of w:

$$\begin{aligned}\frac{\partial P_{AS,CF}}{\partial \Omega_A} &= \frac{\partial h_{AS}}{\partial x_A}\frac{\partial x_A}{\partial \lambda_A}\frac{\partial \lambda_A}{\partial \Omega_A} + \frac{\partial h_{AS}}{\partial y_A}\frac{\partial y_A}{\partial \lambda_A}\frac{\partial \lambda_A}{\partial \Omega_A} \\ &= \frac{1}{\left|\vec{r}_{AS}\right|}(x_S - x_A)\cdot\left|\vec{r}_A\right|\cdot\cos\varphi_A\sin\lambda_A \\ &\quad - \frac{1}{\left|\vec{r}_{AS}\right|}(y_S - y_A)\cdot\left|\vec{r}_A\right|\cdot\cos\varphi_A\cos\lambda_A \\ &= \frac{\left|\vec{r}_A\right|}{\left|\vec{r}_{AS}\right|}\cdot\cos\varphi_A\cos\varphi_S\sin[\Omega_A + f(t) - \lambda_S]\end{aligned} \tag{1.4}$$

It can be seen that under the condition of $\cos\varphi_S \neq 0$ (for anchorage station, that is, latitude is not equal to 90°), the partial derivative $\left|\frac{\partial P_{AS,CF}}{\partial \Omega_A}\right|$ is time-varying and is not constant equal to 0.

The above proves that the satellite-earth observations are observable for the RAAN. In fact, compared with the simple inter-satellite observation, the location of anchor stations in the satellite-to-ground link is known, which increases the observation dimension but does not increase the parameters to be estimated, thus enabling the normal matrix in the observational matrix to be full rank. In a word, anchorage station provides spatial reference for constellation orbit determination.

2.2 Effect of Location and Number of Anchorage Station on Orbit Determination Accuracy

Formula (1.4) shows that the observability to RAAN Ω_A of satellite-to-ground links of satellite A can be expressed as the partial derivative of satellite-to-Earth observations to Ω_A:

$$\frac{\partial P_{AS,CF}}{\partial \Omega_A} = \frac{\left|\vec{r}_A\right|}{\left|\vec{r}_{AS}\right|}\cdot\cos\varphi_A\cos\varphi_S\sin[\Omega_A + f(t) - \lambda_S] \tag{1.5}$$

It can be found that the factor of observability function related to the stability of ground station position is $\cos\varphi_S$. According to the definition of latitude, $-\frac{\pi}{2} \leq \varphi_S \leq \frac{\pi}{2}$, the corresponding cosine value reaches the minimum at two extremes and the maximum at the equator. From this point of view, the control effect of anchorage station in low latitude area is the best, and the closer to the poles, the smaller the effect of anchorage station on track convergence.

In principle, the greater the number of anchorage stations, the stronger the constraints on the track, and the higher the orbit determination accuracy. However, too many anchorage stations violate the principle of autonomy in orbit determination relying on inter-satellite links, and the cost will increase rapidly. It is necessary to study the best strategy of anchorage station setting. In principle, the greater the number of

anchorage stations, the stronger the constraints on the track, and the higher the orbit determination accuracy. However, too many anchorage stations violate the principle of autonomy in orbit determination relying on inter-satellite links, and the cost will increase rapidly. It is necessary to study the best strategy of anchorage station setting.

3 Simulation and Verification

In order to verify the analysis of distributed autonomous orbit determination strategy, the simulation experiment of autonomous orbit determination for all constellations was carried out. Because the Beidou global system has not been built completely, there is no available inter-satellite measured data of the whole constellation, and the existing inter-satellite link data is not enough to carry out the experiment of distributed solution of the whole constellation, so the example in this section is a simulation analysis. In order to be more general, the inter-satellite links of Walker constellation consisting of 24 MEO satellites are studied.

3.1 Setting of Simulation Conditions

(1) Constellation parameters

The MEO satellite orbit of Walker constellation for 60 days is simulated by STK software. The configuration of MEO satellite is 24/3/1 and the satellite SCID is 7–30. The orbital perturbations considered include the third-body gravity, the 30-order non-spherical gravity of the earth, the Bernese ECOM5 parameter solar pressure model, the solid tide model and the ocean tide model (Fig. 1).

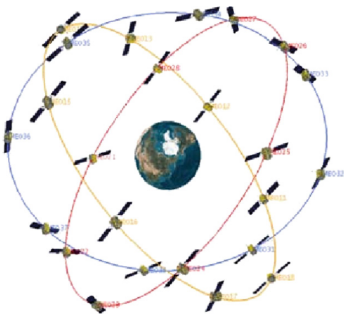

Fig. 1. Schematic diagram of Walker constellation

(2) Ground station installation

Six anchorage stations were selected in Beijing, Sanya, Kashgar, Djibouti, Zhongshan Station in Antarctica and Kamchatka Peninsula. The specific information is shown in Table 1.

Table 1. Anchor station setting information

SCID & Position	01 Beijing	02 Sanya	03 Kashgar	04 Djibouti	05 Zhongshan Station	06 Kamchatka
Geodetic longitude λ_S (°)	−116.28	109.31	75.98	43.14	76.37	158.65
Geodetic latitude φ_S (°)	39.54	18.14	35.47	11.58	−69.37	53.02
Geodetic height h_S (m)	50	10	1300	5	10	33

(3) Inter-satellite and geodetic ranging information

In every 300 s cycle, according to the pre-set time slot table, each satellite completes up to 16 chain-building times in 60 s, and the latter 240 s is used as calculation and redundancy time. The true values of inter-satellite and geodetic ranging are:

$$\rho_{\mathrm{AB}} = \sqrt{(x_B(t+\delta t) - x_A(t))^2 + (y_B(t+\delta t) - y_A(t))^2 + (z_B(t+\delta t) - z_A(t))^2} + \tau_A^{send} + \tau_B^{rcv} + rand(0.1) \tag{1.6}$$

Where δt is the signal line, τ_A^{send} is the transmitting delay of inter-satellite equipment, τ_B^{rcv} is the receiving delay of inter-satellite equipment, and $rand(0.1)$ is the ranging random error of $\sigma = 0.1$ m. When simulating the inter-satellite observation data, the scanning range of Ka device on the satellite is set to be ±60°, and the cut-off angle of the observation height is 15°.

(4) Long-term forecast ephemeris and software parameters

In practical engineering, long-term forecast ephemeris must be injected as an external benchmark before satellite constellation enters the autonomous orbit determination mode, which provides a reference state for on-board filtering calculation. In fitting the orbital dynamics model of long-term forecast ephemeris, the accuracy of optical pressure parameters is reduced. Finally, all long-term forecast orbital UREs are shown in Fig. 2. It can be seen that within 60 days, the average URE of the long-term forecast ephemeris exceeds 300 m, which means that if the satellite is not updated by filtering observation and only extrapolated by orbit, the orbit determination error of the constellation will reach the kilometer level:

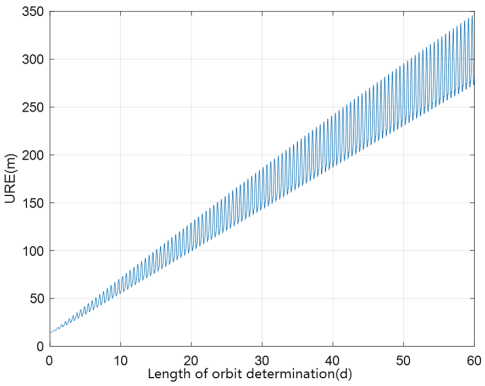

Fig. 2. Average URE of long-term forecast ephemeris

In satellite software programming, all correlation functions and parameters of distributed orbit determination of a single satellite are encapsulated into a class, and navigation messages, ranging values and covariance parameters transmitted between satellites are regarded as public member variables. Create 24 objects, all satellites set the same starting parameters:

$$\begin{cases} x_0 = [5.0 \quad 5.0 \quad 5.0 \quad 0.002 \quad 0.002 \quad 0.002] \\ U_0 = E_{6\times6} \\ D_0 = diag[0.1 \quad 0.1 \quad 0.1 \quad 1e-18 \quad 1e-18 \quad 1e-18] \\ Q_o = diag[1e-7 \quad 1e-7 \quad 1e-7 \quad 1e-13 \quad 1e-13 \quad 1e-13] \\ R_0 = diag(0.1E_{6\times6}) \end{cases} \tag{1.7}$$

All parameters are derived from the basic equation of Extended Kalman Filter (EKF) based on UD decomposition (not to be discussed here). Among them, x_0 is the initial state (i.e. the correction of the initial position and velocity); U_0 and D_0 satisfy $P_0 = U_0 D_0 U_0^T$ (P_0 is the initial one-step filtering variance matrix); Q_o is the initial error covariance matrix of the equation of motion, representing the error of one-step prediction; R_0 is the initial observation error covariance matrix. For all ground anchorage stations, fixed parameters of mutual transmission are set: the covariance matrix is set to zero. When each satellite performs data pre-processing, the epoch is reduced to 0 time of each ranging period.

3.2 Experimental Content

In order to verify the role of anchorage station and to explore the influence of different anchorage station working strategies on the accuracy of orbit determination, the following experiments are conducted under the condition of long-term forecast ephemeris injection on the ground.

(1) Orbit determination without anchorage station

Without anchoring station, UD decomposition Kalman filter is used to determine orbit by relying only on long-term forecast ephemeris, inter-satellite ranging data and covariance parameters. The validity of the filtering algorithm and the rotation characteristics of the constellation are investigated and used as the control group of the subsequent experiments.

(2) Setting up anchorage station for orbit determination

On the basis of the previous experiment, six anchorage stations were added to the whole process to participate in orbit determination, and the effect of the anchorage station on controlling the overall rotation in distributed long-term orbit determination was verified.

(3) Orbit determination with different numbers of anchorage stations

Among the six anchorage stations, 1 to 5 anchorage stations are selected to carry out multi-group orbit determination tests. In each group of experiments, anchorage stations were introduced uniformly on the 46th day to investigate the control ability of different anchorage stations on orbit determination deviation. The optimum number of additional anchorage stations is analyzed.

(4) Single station location analysis

The six anchorage stations set up by simulation have different latitudes. The representative anchorage stations of different latitudes are selected to carry out the orbit determination test of single anchorage station to verify the analysis of the control ability of the latitude of anchorage station to the overall rotation.

3.3 The Influence of the Existing of Anchorage Station

According to the experimental scheme, the orbit determination experiment is carried out. The results of the orbit determination without anchorage station are shown in Figs. 3 and 4. It can be seen that under the constraints of long-term ephemeris, the average orbit determination URE of all constellations relying solely on inter-satellite ranging within 60 days can be limited to less than 4 m. This result is obviously different from that of centralized orbit determination without satellite observation, because the long-term predicted ephemeris is used as a prior constraint in this example.

However, with the increase of the orbit determination time, the URE of the orbit increases gradually, which is mainly reflected in the T direction according to Fig. 3. With the increase of orbit determination arc length, the filtering results of T-direction error accumulate gradually, reaching about 14 m at last; R-direction error always approaches zero; N-direction error keeps near zero, and the dispersion increases gradually. The results validate that the orbital drift occurs at the ascending point of the red longitude in the distributed orbit determination, and verify that the accumulation of the total rotation in the autonomous orbit determination can not be completely eliminated by the long-term forecast ephemeris constraint in advance.

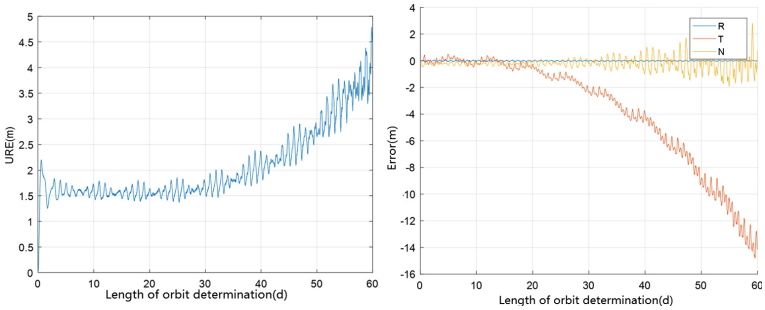

Fig. 3. Average URE (left) and Error (right) of all constellations in orbit determination without anchorage station

After adding 6 anchorage stations, the 60-day orbit determination test is carried out again. The results are shown in Fig. 4. It can be seen that the accuracy of autonomous orbit determination is greatly improved by adding anchorage stations, and the average URE is stable below 0.1 m. The cumulative error in T direction is weakened obviously, and the drift converges within 0.3 m.

With the prolongation of orbit determination arc, the dispersion of orbit URE increases. The analysis shows that this is because the one-step extrapolation accuracy of orbit decreases with the decline of long-term ephemeris accuracy.

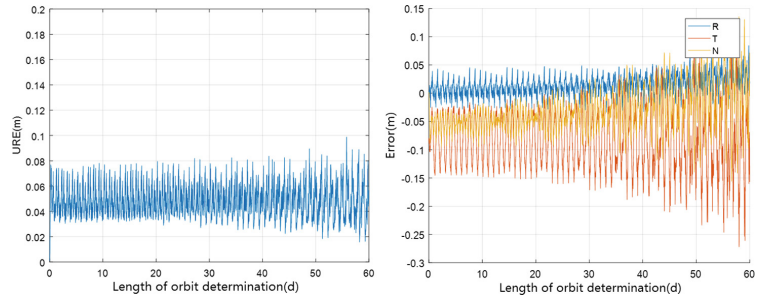

Fig. 4. Average URE (left) and Error (right) of 6 anchorage stations participating in orbit determination

This part of the experimental results verify the effectiveness of the distributed orbit determination algorithm, and verify the role of anchorage station in controlling the overall rotation.

3.4 The Influence of the Number of Anchorage Station

The excessive number of anchorage stations conflicts with the autonomy requirement of satellite operation. The contradiction between the requirement of orbit determination accuracy and the economic requirement of anchorage stations should be solved. In

order to explore the best anchorage station strategy, six 60-day orbit determination test conditions are set as follows:

(1) Introduce all six anchorage stations on the 46th day;
(2) The Zhongshan Station in Antarctica was reduced from the introduced anchorage stations, with a total of 5 anchorage stations.
(3) Four anchorage stations have been reduced.
(4) The Djibouti station will be reduced to three anchorage stations.
(5) The Kashgar Station has been reduced to 2 anchorage stations.
(6) Reduce Sanya Station, only Beijing Station

The average RMS of the three directions error of the convergent satellite orbit is recorded as sum. Due to space limitation, only the first and sixth groups of experimental orbital determination results are taken as examples to show the orbital determination accuracy before and after the introduction of anchorage stations (Figs. 5 and 6). All the results are listed in the table (Table 2).

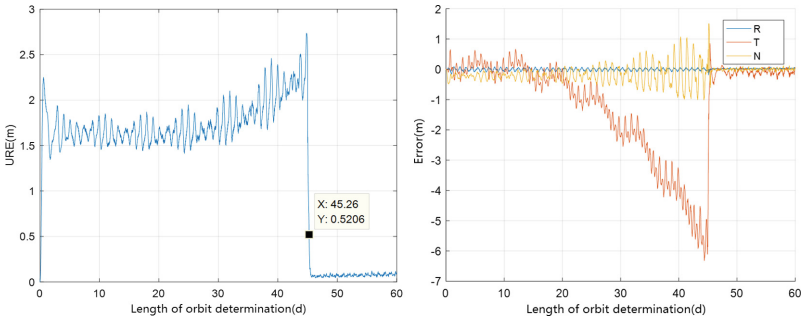

Fig. 5. Average URE (left) and Error (right) when 6 anchor station participating in orbit determination

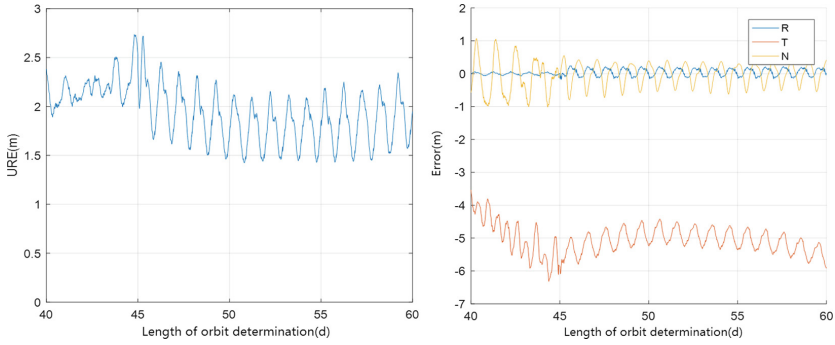

Fig. 6. Average URE (left) and Error (right) when 1 anchor station participating in orbit determination

Table 2. A orbit determination results of anchorage stations with different numbers

Anchorage station number	Convergence time to 0.5 m (d)	Convergent average URE (m)	RMS_R (m)	RMS_T (m)	RMS_N (m)
6	0.26	0.0612	0.0953	0.3989	0.1992
5	0.28	0.0861	0.1399	0.4680	0.2525
4	0.34	0.1445	0.2002	0.4555	0.2760
3	0.54	0.2225	0.2434	0.4913	0.2930
2	2.11	0.4235	0.3587	0.7451	0.9141
1	N/A	1.7665	1.3405	2.2145	2.5658

In the first group of experiments, after introducing six anchorage stations on the 46th day, the average URE decreased to less than 0.1 m in 0.5 d and the average error of T direction decreased to less than 0.2 m. As the number of anchorage stations decreases, the convergence rate decreases with the introduction of anchorage stations. When the time of convergence is less than 0.5 m, the number of anchorage stations can be reduced to 3, and the convergence can still be guaranteed within 1 day. But when the number of anchorage stations is 2, the convergence time increases to 2.11 days, which is more obvious than the former. This shows that the control of the whole rotation of anchorage station 2 is obviously reduced. When the number of anchorage stations is reduced to 1 (single anchorage station is Beijing station), the introduction of anchorage stations can no longer converge the results of orbit determination, but Beijing station still controls the drift trend of the results of orbit determination and keeps the accuracy of orbit determination stable. This shows that single anchorage station can maintain the stability of the overall rotation of the constellation.

It can be seen that the accuracy of orbit determination is positively correlated with the number of anchorage stations, but the three anchorage stations can achieve high accuracy, and the number of anchorage stations more than three improves the accuracy of orbit determination very slightly. When the number of anchorage stations decreases to 2, the convergence time increases obviously, the average RMS of T and N direction errors increases obviously after convergence, and the control of overall rotation of anchorage stations is unstable. When only one anchorage station is installed, the contribution to the accuracy of autonomous orbit determination is very low, but it still limits the growth of overall rotation. The above analysis shows that single anchorage station has the ability to control the overall rotation, but in general, three anchorage stations are the most advantageous.

3.5 The Influence of the Location of Single Anchorage Station

According to the previous analysis, the latitude of anchorage station will affect the control ability of the overall rotation of the constellation. The examples in this group of experiments are taken from Djibouti station (11.58° N), Kamchatka station (53.02° N) and Zhongshan station in Antarctica (69.37° S), which are representative of latitude, respectively, to carry out orbit determination experiments of single anchorage station, and to analyze the results of Beijing single station in the previous group of experiments. The experimental results are as follows (Figs. 7, 8 and 9):

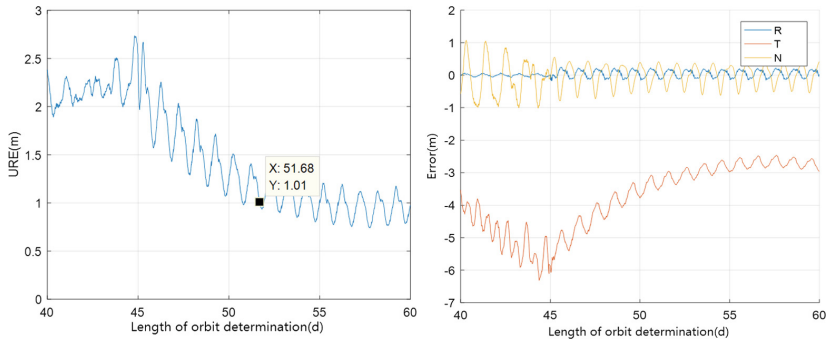

Fig. 7. Average URE (left) and Error (right) when Djibouti station participating in orbit determination

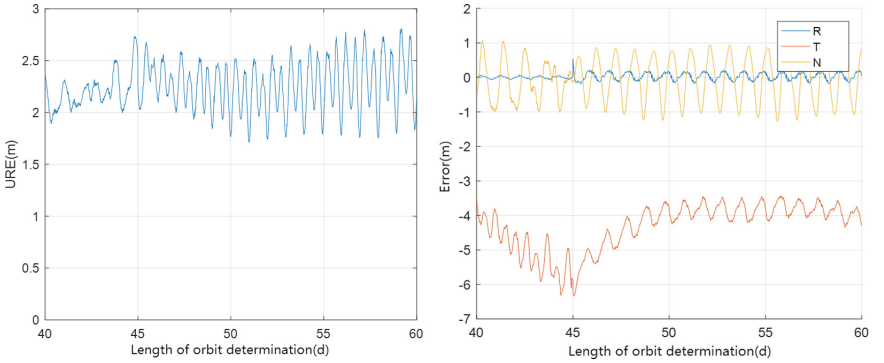

Fig. 8. Average URE (left) and Error (right) when Kamchatka station participating in orbit determination

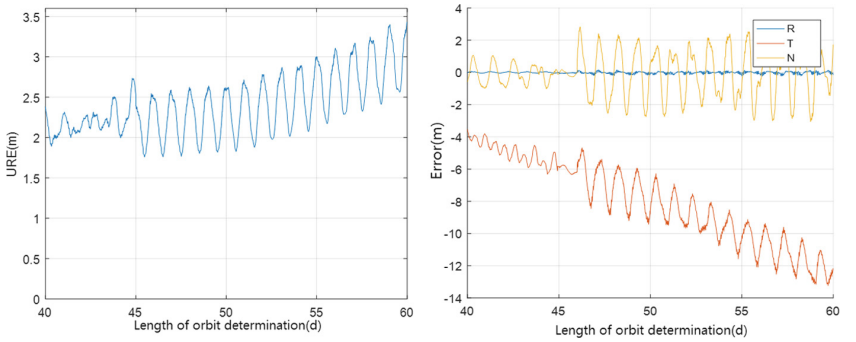

Fig. 9. Average URE (left) and Error (right) when Zhongshan station participating in orbit determination

It can be seen that with the increase of the dimension of single anchorage station, the ability of overall rotation control is gradually weakened. The Djibouti station at the lowest latitude can control the orbit determination URE slowly to about 1 m within 7 days, while the Zhongshan station in Antarctica can not control the orbit drift at all. After the introduction of anchorage station, not only the orbit determination error continues to accumulate, but also the dispersion of the orbit determination results is increased. This verifies that the visibility of anchorage stations at different latitudes to the ascending intersection is different.

4 Summary and Discussion

In this paper, the role of anchorage station in autonomous orbit determination of all constellations is studied. The influence of anchorage station location on the ability of the ascending node to correct the right ascending meridian is analyzed. The 60-day orbit simulation, long-term forecast ephemeris simulation and observation data simulation of 24/3/1 Walker constellation are carried out. A simulation platform for distributed orbit determination of the whole constellation is built, and a number of independent orbit determination experiments with different strategies are carried out. The experimental results show that:

(1) Distributed autonomous orbit determination filtering based on inter-satellite link observations can limit URE to less than 4 m within 60 days of orbit under the constraints of long-term forecast ephemeris. However, with the passage of time, the overall drift of the orbit will accumulate gradually.
(2) Increasing the anchorage station can significantly improve the accuracy of autonomous orbit determination, and has a significant effect on the overall rotation control of the constellation. In terms of the number of anchorage stations, the best strategy is to introduce three anchorage stations, which can converge the track URE to less than 0.5 m within 0.54 days. Increasing the number of anchorage stations can not significantly improve the accuracy of orbit determination.
(3) Single anchorage station can control track divergence, but it can not improve the accuracy of orbit determination. The control ability of single anchorage station is related to latitude. The control ability of single anchorage station is better in low latitude area (Djibouti station controls URE around 1 m), while the anchorage station in high latitude area can not control track drift.

The results of this chapter provide a reference for the establishment and use of anchorage stations during the autonomous operation of Beidou constellation.

References

1. Hofmann-Wellenhof B, Lichtenegger H, Wasle E (2008) GNSS—Global navigation satellite systems. Springer
2. Ananda MP, Bernstein, H, Cunningham KE, Feess WA (1990) Global positioning system (GPS) autonomous navigation. In: Position location and navigation symposium, Record, The 1990s - a decade of excellence in the navigation sciences, IEEE PLANS 1990, vol 27. IEEE, pp 497–508
3. Menn MD, Bemstein H (1994) Ephemeris observability issues in the global positioning system (GPS) autonomous navigation (AUTONAV). In: Position Location and Navigation Symposium, vol 94. IEEE, pp 677–680
4. Rajan JA, Brodie P, Rawicz H (2003) Modernizing GPS autonomous navigation with anchor capability. In: Proceedings of international technical meeting of the satellite division of the institute of navigation, pp 1534–1542
5. Rajan JA (2002) Highlights of GPS II-R autonomous navigation. In: Proceedings of annual meeting of the institute of navigation and CIGTF guidance test symposium, pp 354–363
6. Rajan J, Orr M, Wang P (2003) On-orbit validation of GPS IIR autonomous navigation. In: Proceedings of the institute of navigation 59th annual meeting, 23–25, pp 411–419
7. Shuai P, Qu G, Chen Z (2006) Studies on autonomous navigation techniques for navigation constellations. Eng Sci 8(3):22–30
8. Tang CP, Hu XG, Zhou SS (2017) Centralized autonomous orbit determination of Beidou navigation satellites with inter-satellite link measurements: preliminary results. Sci Sin Phys Mech Astron 47(02):95–105
9. Song X, Mao Y, Feng L, Jia X, Jianfeng JI (2017) The preliminary result and analysis for BD orbit determination with inter-satellite link data. Acta Geodaet Et Cartographica Sin 46 (5):547–553
10. Guo FX (2013) Research on navigation satellite autonomous orbit determination based on ground anchor stations. Doctoral dissertation, PLA Information Engineering University

Spatial Frames and Precise Positioning

The Research on Optimal Tropospheric Combined Model Based on Multi-GNSS PPP

Guoqiang Jiao[1,2], Shuli Song[1(✉)], Ke Su[1,2], and Weili Zhou[1,2]

[1] Shanghai Astronomical Observatory,
Chinese Academy of Sciences, Shanghai 200030, China
slsong@shao.ac.cn
[2] University of Chinese Academy of Sciences, Beijing 100049, China

Abstract. This paper combines ten tropospheric combined empirical models based on the atmospheric element prediction model of GPT/GPT2, the Saastamoinen and the Modified Hopfield model and the mapping function of VMF1/GMF/NMF, and combines two tropospheric combined numerical weather prediction models based on the pressure-level data of ECMWF. This paper focuses on the impact of different tropospheric models on the positioning and zenith tropospheric delay (ZTD) accuracy of multi-GNSS precise point positioning (PPP) based on International GNSS Monitoring and Assessment System (iGMAS) products. The results show that the accuracy of GPT2 +Saastamoinen is 12.69% higher than UNB3M and the accuracy of Numerical Weather Model (NWM) is 63.80% higher than UNB3M based on the data of IGS ZTD. In terms of PPP positioning accuracy, the accuracy of GPT2+VMF1 +Modified Hopfield is 5.30% higher than UNB3M and the accuracy of NWM (GMF) is 8.77% higher than UNB3M. This paper gives a reference for the best empirical models of GPT2+VMF1+Modified Hopfield and the best numerical weather prediction model of NWM (GMF) and provides a more accurate tropospheric model for standard point positioning (SPP), PPP, and medium and long baseline positioning.

Keywords: iGMAS · GPT2 · ECMWF · NWM · Precise point positioning · Positioning accuracy · ZTD

1 Introduction

Tropospheric delay is one of the main error sources in GNSS positioning, which restricts the convergence time and positioning accuracy of GNSS precise point positioning (PPP) and medium or long baseline differential positioning [1]. Since the tropospheric delay is a non-dispersive delay and has nothing to do with the signal frequency, it cannot be eliminated by the linear combination of signals of different frequencies. Tropospheric delay can be divided into dry and wet components. The dry delay accounts for 90% of the total delay and the main physical properties of dry delay are related to the pressure, which can be accurately solved by the models. The wet delay accounts for only 10% of the total delay and it is difficult to model using surface meteorological data, because the distribution of water vapor in the atmosphere is

J. Sun et al. (Eds.): CSNC 2019, LNEE 563, pp. 117–130, 2019.
https://doi.org/10.1007/978-981-13-7759-4_11

uneven and complex over time [2]. At this stage, the value of zenith troposphere delay (ZTD) calculated by empirical models is used as the initial value and the prior variance is set, and the bias is solved as an unknown parameter in PPP and long baseline differential positioning. However, the inaccurate prior variance will directly lead to divergence of the tropospheric and ambiguity parameters of the user station during the filtering process [3–5]. Hence, choosing an accurate tropospheric model as a priori information can improve the positioning accuracy of PPP and improve the convergence rate of PPP and the accuracy of ZTD. In the research of the tropospheric combined models, Xu et al. compared GPT2+GMF+Saastamoinen model with the meteorological data. It is concluded that the combined model can meet the requirements of high-precision positioning when meteorological data cannot be obtained [4]. Wang and Chen combined the GPT+NMF, GPT+GMF, GPT2+VMF1 models and test these combined models based on PPP. The result shows that the GPT+GMF and GPT2 +VMF1 is 22.0% higher than GPT+NMF [6]. Liu et al. combined GPT2/GPT2w +Saastamoinen model and compared it with IGS ZTD to conclude that the accuracy of GPT2w+Saastamoinen model is better than GPT2+Saastamoinen [7]. At this stage, the analysis of tropospheric combined models focused on the analysis of the precision of the troposphere model in the ZTD, and less consideration is given to the influence of different troposphere models on the accuracy of PPP positioning. Among the existing model combinations, most of them are based on the Saastamoinen model for calculation, and there are fewer combinations of other solution models. Among the existing model combinations, there are more combinations based on the GPT2 model, and less exploration of other metrological data, especially the Numerical Weather Model (NWM). In the research of real-time processing and post-processing of standard point positioning (SPP) and PPP, there are few papers that give a clear model of the optimal tropospheric combined model. Based on the model of GPT/GPT2/NWM combined the Saastamoinen model, the Modified Hopfield model and the mapping function of VMF1/GMF/NMF, this paper combines 12 tropospheric models. Based on iGMAS products, this paper explores the influence of tropospheric combined model on PPP positioning accuracy, and ZTD final estimation accuracy, in order to obtain the optimal combined model to provide a more accurate tropospheric model for users to perform SPP, PPP or medium and long baseline positioning.

2 Tropospheric Combined Models and Multi-GNSS PPP Model

2.1 Tropospheric Combined Models

2.1.1 Meteorological Data Models

In this paper, the meteorological data required for tropospheric solution is provided by GPT, GPT2 and NWMs. The GPT model is an empirical model based on the 3 years (September 1999 to August 2002) of $15° \times 15°$ global grids of monthly mean profiles for pressure and temperature from the European Centre for Medium-Range Weather Forecasts (ECMWF) 40 years reanalysis data (ERA40) [8].

$$P = P_r(1 - 0.0000226(h - h_r))^{5.225} \tag{1}$$

$$dT/dh = -0.0065^{\circ}\ \mathrm{C/m} \tag{2}$$

Then, the pressure values P on the Earth surface at height h are reduced to pressure values P_r at mean sea level (MSL) h_r and dT/dh is a linear decrease of temperature T with height [8]. The pressure and temperature at MSL are available from Eq. 3:

$$a = a_0 + A\cos\left(\frac{doy - 28}{365.25} \times 2\pi\right) \tag{3}$$

$$a_0 = \sum_{n=0}^{9}\sum_{m=0}^{n} P_{nm}(\sin\varphi)[A_{nm}\cos(m\lambda) + B_{nm}\sin(m\lambda)] \tag{4}$$

where P_{nm} denotes the Legendre polynomials, φ and λ are latitude and longitude, A_{nm} and B_{nm} are spherical harmonic coefficients.

The GPT2 model is an empirical model based on the 10 years (2001–2010) of global monthly mean profiles for pressure P, temperature T, specific humidity Q, and geopotential from ERA-Interim, discretized at 37 pressure levels and 1° of latitude and longitude. The GPT2 model can provide the meteorological parameters P, T, Q, the temperature lapse rate and the coefficients ah and aw of the hydrostatic and wet mapping functions of VMF1. At each grid point, each meteorological parameter $r(t)$ contains an annual term and a semi-annual term [9].

$$\begin{aligned} r(t) = A_0 + A_1\cos\left(\frac{doy}{365.25} \times 2\pi\right) + B_1\sin\left(\frac{doy}{365.25} \times 2\pi\right) \\ + A_2\cos\left(\frac{doy}{365.25} \times 4\pi\right) + B_2\sin\left(\frac{doy}{365.25} \times 4\pi\right) \end{aligned} \tag{5}$$

A_0, A_1, A_2, B_1, B_2 have been calculated in advance and stored in a text file in grid form. In the vertical direction, Lagler et al. assumed that the temperature near the earth follows a linear change with height, while the vertical change in pressure is expressed by an exponential function, and the following formula is used to correct the height of the meteorological parameters [9]:

$$\begin{cases} T = T_0 + dT/dh, P = P_0 \times e^{\frac{-c\times dh}{100}}, c = g_m \times \frac{dMtr}{R_g \times T_v}, \\ g_m = 9.784 \times (1.0 - 2.66 \times 10^{-3}\cos(2 \times lat) - 2.8 \times 10^{-7}h_s), \\ T_v = T_0 \times (1 + 0.6077Q), e = Q \times \frac{P}{0.622 + 0.378Q} \end{cases} \tag{6}$$

where T_0 and P_0 are temperature (K) and pressure (hPa) on grid, T and P are the temperature and pressure when the grid points increase the height of dh. dT is the temperature lapse rate, Q is specific humidity, e is water vapor pressure (hPa), g_m is gravitational acceleration, and its value is 9.80665 m/s^2, and $dMtr$ and R_g are

atmospheric molar masses and gas constants, respectively, with values of 0.028965 kg/mol and 8.3143 J/K/mol.

2.1.2 Tropospheric Models

The Saastamoinen model is a ZTD solution model based on the meteorological data of the station, which can be expressed as:

$$ZTD_{Saastamoinen} = 0.002277 \times \frac{P_{sta} + \left(0.05 + \frac{1255}{T_{sta}}\right)e}{f(\varphi, H)} \tag{7}$$

where P_{sta} is the surface pressure, T_{sta} is the surface temperature, e is the vaper pressure and $f(\varphi, H)$ is the mapping function. Saas is used to represent the Saastamoinen model unless otherwise specified below.

The Modified Hopfield model is a ZTD solution model based on the meteorological data of the station, which can be expressed as:

$$ZTD_{Modified\ Hopfield} = ZTD_{dry} + ZTD_{wet} \tag{8}$$

$$ZTD_i = 10^{-6} N_i \sum_{k=1}^{9} \frac{f_{k,i}}{k} r_i^k, i = dry, wet \tag{9}$$

$$\begin{aligned}
&r_i = \sqrt{(R_E + h_i)^2 - R_E^2 \sin^2 z} - R_E \cos z \\
&f_{1,i} = 1, f_{2,i} = 4a_i, f_{3,i} = 6a_i^2 + 4b_i, f_{4,i} = 4a_i\left(a_i^2 + 3b_i\right) \\
&f_{5,i} = a_i^4 + 12a_i^2 b_i + 6b_i^2, f_{6,i} = 4a_i b_i\left(a_i^2 + 3b_i\right) \\
&f_{7,i} = b_i^2\left(6a_i^2 + 4b_i\right), f_{8,i} = 4a_i b_i^3, f_{9,i} = b_i^4 \\
&a_i = -\frac{\cos z}{h_i}, b_i = -\frac{\sin^2 z}{2h_i R_E} \\
&h_d = 40136 + 148.72(T_{sta} - 273.16), h_w = 11000 \\
&N_d = 77.64\frac{P_{sta}}{T_{sta}}, N_w = -12.96\frac{e}{T_{sta}} + 371800\frac{e}{T_{sta}^2}
\end{aligned} \tag{10}$$

where z is the zenith angle of satellite and R_E is the Earth radius. Hope is used to represent the Modified Hopfield model unless otherwise specified below.

The integration method is mainly used for the pressure-level data, which can be expressed as:

$$ZTD_{grid} = 10^{-6} \int_{H_{Station}}^{H_{top}} NdH = 10^{-6} \sum_i N_i \Delta H_i \tag{11}$$

where ZTD_{grid} is the ZTD value of the grid dot at the height of the IGS station, $H_{Station}$ is the elevation of the IGS station, H_{top} is the top-level height of the ECMWF meteorological data and N is the total refraction. The model of the total refraction can be expressed as:

$$N = k_1 \frac{P-e}{T} + k_2 \frac{e}{T} + k_3 \frac{e}{T^2} = N_{dry} + N_{wet} \tag{12}$$

$$e = Sh \frac{P}{0.622 + 0.378Sh} \tag{13}$$

where k_1 = 77.690 K/mbar, k_2 = 71.2952.79 K/mbar and k_3 = 375463.0 K^2/mbar [10], P is the atmospheric pressure, T is the temperature and Sh is the relative humidity. Integration is used to represent the integration model unless otherwise specified below. Based on the model of GPT/GPT2/NWM combined the Saastamoinen model, the Modified Hopfield model and the mapping function of VMF1/GMF/NMF, this paper combines 12 tropospheric models. The combined models will be shown in Fig. 1.

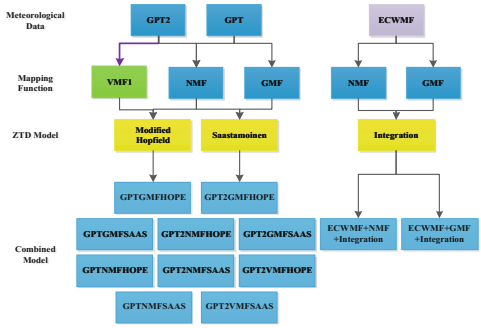

Fig. 1. Flow chart of calculation of tropospheric combined model

2.2 Multi-GNSS PPP Model

The PPP model used in this paper is ionosphere-free (IF) model. IF model uses dual-frequency pseudorange and carrier-phase observations of IF positioning model, which is expressed as follows [11]:

$$P_{IF} = \frac{f_1^2 \cdot P_1 - f_2^2 \cdot P_2}{f_1^2 - f_2^2} = \rho_r^s + c \cdot \delta t_r - c \cdot \delta t^s + T_r^s + \varepsilon_P \tag{14}$$

$$\Phi_{IF} = \frac{f_1^2 \cdot \varphi_1 - f_2^2 \cdot \varphi_2}{f_1^2 - f_2^2} = \rho_r^s + c \cdot \delta t_r - c \cdot \delta t^s + T_r^s + \lambda_{r,IF} N_{r,IF}^s + \varepsilon_\Phi \tag{15}$$

where P_{IF} is IF code observation, Φ_{IF} is the IF carrier-phase observation, ρ_r^s denotes the computed geometrical range, T_r^s is the tropospheric delay, N_r^s is the float ambiguity; ε_P and ε_Φ are the pseudorange and carrier phase observation noises including multipath, respectively. Based on the traditional single GNSS positioning model and taking into account the influence of inter-time bias and inter-frequency bias, the multi-GNSS PPP equation can be obtained by introducing an inter-system bias (ISB) for each additional system.

$$\begin{cases} P_r^G = \rho_r^s + c \cdot \delta t_r - c \cdot \delta t^s + T_r^s + \varepsilon_{P_r^G} \\ \Phi_r^G = \rho_r^s + c \cdot \delta t_r - c \cdot \delta t^s + T_r^s + \lambda_{r,IF} N_{r,IF}^s + \varepsilon_{\Phi_r^G} \\ P_r^C = \rho_r^s + c \cdot \delta t_r - c \cdot \delta t^s + c \cdot ISB_r^C + T_r^s + \varepsilon_{P_r^C} \\ \Phi_r^C = \rho_r^s + c \cdot \delta t_r - c \cdot \delta t^s + c \cdot ISB_r^C + T_r^s + \lambda_{r,IF} N_{r,IF}^s + \varepsilon_{\Phi_r^C} \\ P_r^{R_k} = \rho_r^s + c \cdot \delta t_r - c \cdot \delta t^s + c \cdot ISB_r^{R_k} + T_r^s + \varepsilon_{P_r^{R_k}} \\ \Phi_r^{R_k} = \rho_r^s + c \cdot \delta t_r - c \cdot \delta t^s + c \cdot ISB_r^{R_k} + T_r^s + \lambda_{r,IF} N_{r,IF}^s + \varepsilon_{\Phi_r^{R_k}} \\ P_r^E = \rho_r^s + c \cdot \delta t_r - c \cdot \delta t^s + c \cdot ISB_r^E + T_r^s + \varepsilon_{P_r^E} \\ \Phi_r^E = \rho_r^s + c \cdot \delta t_r - c \cdot \delta t^s + c \cdot ISB_r^E + T_r^s + \lambda_{r,IF} N_{r,IF}^s + \varepsilon_{\Phi_r^E} \end{cases} \tag{16}$$

where the indices G, C, R and E refer to GPS, BDS, GLONASS and Galileo, respectively, ISB_r^C is the ISB between the BDS and GPS, ISB_r^E are the ISB between the Galileo and GPS, $ISB_r^{R_k}$ is the ISB between the GLONASS and GPS. Since the GLONASS uses signal deconstruction of frequency division multiple access (FDMA), the ISB of GLONASS is related to station R and satellite S.

3 Data Sets and Processing Strategy

The datasets utilized in this study are collected at 16 stations on 30 days, from January 1, 2018 to January 30, 2018. The experiment tests 30 days of observation data. All selected stations can receive the observations from GPS, BDS, GLONASS, and Galileo constellations. The observation data has a sampling interval of 30 s. Figure 2 shows the distribution of the selected station in multi-GNSS Experiment (MGEX). The orbit and clock offset of iGMAS integrated products have a sampling of 15 min and 5 min, respectively, and the time system of products is Beidou Time (BDT). In this paper, the pressure-level data of the ERA-Interim (Jan 1979-present) product from ECMWF are used. The horizontal resolution of the data is 0.125° × 0.125°, the vertical resolution is 37 pressure levels, and the time resolution is 6 h (0, 6, 12, 18 UTC).

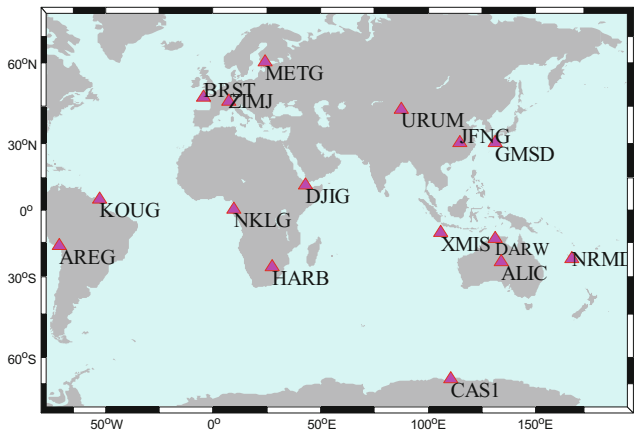

Fig. 2. Geographical distribution of the selective MGEX stations

The PPP model used in this paper is IF model. In IF model, the estimated parameters include the receiver position, the zenith wet tropospheric delay (ZWD), the receiver clock offset, the ISB, and the ambiguity. The 3-D position parameters (x, y, z) of the receiver are processed in static mode. The receiver clock error is treated as white noise. The Kalman filtering algorithm is applied in the multi-GNSS PPP processing. Phase Center Offset (PCO) and Phase Center Variations (PCV) of satellite and receiver antennas are corrected using the ANTEX file provided by IGS. Table 1 summarizes the detailed processing strategy for multi-GNSS PPP. In order to study the influence of different tropospheric models on the accuracy of PPP positioning, two methods of estimating ZWD and not estimating ZWD are used in this paper. Table 2 shows that the comparison of multi-GNSS PPP models with ZWD parameters. Table 3 shows that the comparison of multi-GNSS PPP models without ZWD parameters. Where m, n, p, q are the number of satellites for GPS, BDS, GLONASS, and Galileo, respectively. The model with ZWD parameters is one parameter less than the model without ZWD parameters and one more redundant observation.

Table 1. Multi-GNSS PPP processing strategy

Items	Model
Observations	Pseudorange and carrier-phase observations
Signal selection	G:L1/L2; C:B1/B2; R:G1/G2; E:E1/E5a
Sampling rate	30 s
Elevation cutoff	10°
Observation weighting	A priori precision 0.6 m and 0.004 m for code and phase observations, respectively [11]
Tropospheric delay	Tropospheric combined models
Ionospheric delay	Ionosphere-free linear combination
Satellite antenna	IGS ANTEX PCO+PCV
Receiver antenna	IGS ANTEX PCO+PCV
Phase windup effect	IERS2010 [14]
Earth rotation	IERS2010 [14]
Relativistic effect	IERS2010 [14]
Station displacement	Solid earth, pole and ocean tide (IERS2010) [14]
Receiver coordinate	Estimation
Receiver clock offset	Estimation
Troposphere	Estimation/no operation
ISB	Estimation
Ambiguity	Estimation

Table 2. The comparison of multi-GNSS PPP models with ZWD parameters

	G	G/C	G/R	G/E	G/C/R	G/R/E	G/C/R/E
Observed quantity	2m	2m + 2n	2m + 2p	2m + 2q	2m + 2n + 2p	2m + 2n + 2q	2m + 2n + 2p + 2q
Number of the parameter	m + 5	m + n + 6	m + p + 6	m + q + 6	m + n + p + 7	m + n + q + 7	m + n + p + q + 8
Redundancy	m − 5	m + n − 6	m + p − 6	m + q − 6	m + n + p − 7	m + p + q − 7	m + n + p + q − 8

Table 3. The comparison of multi-GNSS PPP models without ZWD parameters

	G	G/C	G/R	G/E	G/C/R	G/R/E	G/C/R/E
Observed quantity	2m	2m + 2n	2m + 2p	2m + 2q	2m + 2n + 2p	2m + 2n + 2q	2m + 2n + 2p + 2q
Number of the parameter	m + 4	m + n + 5	m + p + 5	m + q + 5	m + n + p + 6	m + n + q + 6	m + n + p + q + 7
Redundancy	m − 4	m + n − 5	m + p − 5	m + q − 5	m + n + p − 6	m + p + q − 6	m + n + p + q − 7

4 Data Tests and Results Analysis

4.1 The Analysis of the Accuracy of Tropospheric Models

This subsection studies the accuracy of the tropospheric combined models based on GPT, GPT2, and ECMWF meteorological data with Saastamoinen, Modified Hopfield, and integral models. The tropospheric combined models are compared with the UNB3M model commonly used in PPP to study the improvement rate of the tropospheric combination model compared to UNB3M model. Figure 3(a) shows the root mean square error (RMS) of the ZTD of the tropospheric combination model and the UNB3M model. It can be seen from Fig. 3 that the accuracy of the UNB3M model is lower than the tropospheric combination model and the NWM. The accuracy of the NWM is optimal and the accuracy of the NWM is 34.20 mm better than the UNB3M model. The accuracy of the tropospheric prior combination model is 3–7 mm better than the UNB3M model. Figure 3(b) shows the increasing rate of the accuracy of the tropospheric combined models compared to UNB3M model, and the specific rates are detailed in Table 4. From Fig. 3 and Table 4, it can be seen that the accuracy of the NWM model is higher than that of the UNB3M model, and its improvement rate is 63.81%. GPT+Modified Hopfield has a low rate of improvement, only 5.78%. From the perspective on the accuracy of the meteorological data, the pressure-level meteorological data provided by ECMWF is the best, the second is the GPT2 model, and the GPT and UNB3M models have less accurate meteorological data [12]. From the perspective on the accuracy of the ZTD calculated by the troposphere model, the accuracy of the Saastamoinen model is better than Modified Hopfield model.

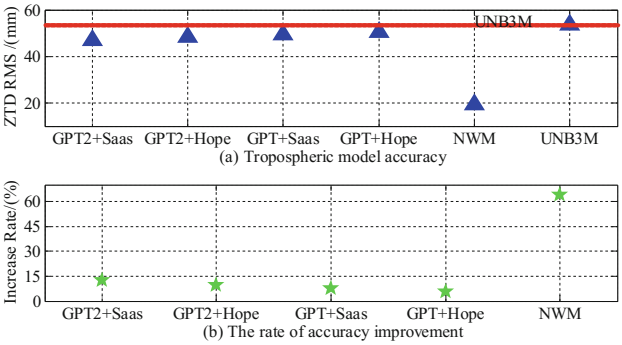

Fig. 3. The comparison of ZTD accuracy of tropospheric combined models

Table 4. The increase rate of ZTD accuracy of tropospheric combined models based on UNB3M

	GPT2+Saas	GPT2+Hope	GPT+Saas	GPT+Hope	NWM
Increase rate	12.69%	9.70%	7.65%	5.78%	63.81%

4.2 The Analysis of PPP Result Based on Tropospheric Models

In order to study the performance of the different tropospheric models in the positioning process, 12 tropospheric combined models for multi-GNSS PPP in this subsection were tested according to the processing strategies described in Sect. 3. Because the correlation relationship between the positioning accuracy in the Up direction and ZTD is strong and the correlation relationship between the positioning accuracy in the East and North direction and ZTD is weak [13], this section only gives the positioning accuracy in the Up direction to discuss the accuracy of the troposphere model.

Figure 4(a, b, c) shows the positioning accuracy in the Up direction based on the NMF, VMF1, and GMF mapping functions. Figure 4(d) shows the increasing rate of the positioning accuracy of the tropospheric combined models compared to UNB3M model in the Up direction. From the perspective on the accuracy of the mapping function, it can be seen that the mapping function of VMF1 has superior precision, the accuracy of the mapping function of GMF is weak, and the mapping function of NMF has poor accuracy. From the perspective on the accuracy of the calculation of multi-GNSS PPP, both the positioning accuracy in the Up direction and ZTD has improved. Because of the increase in the number of satellites, the optimization of the geometry of the satellites, the optimization of the observation conditions, and the increase in the number of redundant observations, the accuracy of PPP in the Up direction and the accuracy of ZTD have been have been improved. From the perspective on the accuracy of the meteorological data, Fig. 4(a, b) shows the positioning accuracy in the Up

direction using the NWM model is optimal and Fig. 5(a, c) shows the accuracy of ZTD estimated by Multi-GNSS PPP using the NWM model is optimal. From the PPP positioning accuracy and ZTD accuracy of the NMW model, it can be seen that the NWM meteorological data are more accurate, the second is the GPT2 model, the GPT and UNB3M models have less accurate meteorological data. From the perspective on the accuracy of the tropospheric model, Fig. 4(d) and Table 5 show the improvement rate of the positioning accuracy of the combination of NWM+GMF+integral is 8.77% compared to UNB3M model; The improvement rate of the positioning accuracy of the combination of GPT2+VMF1+Modified Hopfield is 5.30% compared to the UNB3M model in several prior tropospheric combined models. Under the condition of similar meteorological data model and similar mapping function, comparing the precision of the Modified Hopfield model and the Saastamoinen model, we can see that Table 5 shows the Modified Hopfield model is better than the Saastamoinen model in PPP solution process, and Table 4 shows the Saastamoinen model is better than the Modified Hopfield model in the process of solving the ZTD. To find out the reasons, ZWD is a more accurate value estimated by setting parameters, it is the zenith hydrostatic delay (ZHD) that really plays a role in the tropospheric model in PPP calculation. From this we can conclude that the Saastamoinen model is superior to the Modified Hopfield model in solving the ZTD, but the Modified Hopfield model is superior to the Saastamoinen model in solving the ZHD. The experiment shows that in the PPP post-processing process, the combination of NWM+GMF+Integral is optimal, and it's the positioning accuracy in the Up direction can be increased by 8.77%, and the accuracy of ZTD can be increased by 4.44%; In the real-time PPP processing process, the combination of GPT2+VMF1+Modified Hopfield is optimal, and the positioning accuracy in the Up direction can be increased by 5.30%, and the accuracy of ZTD can be increased by 0.25%.

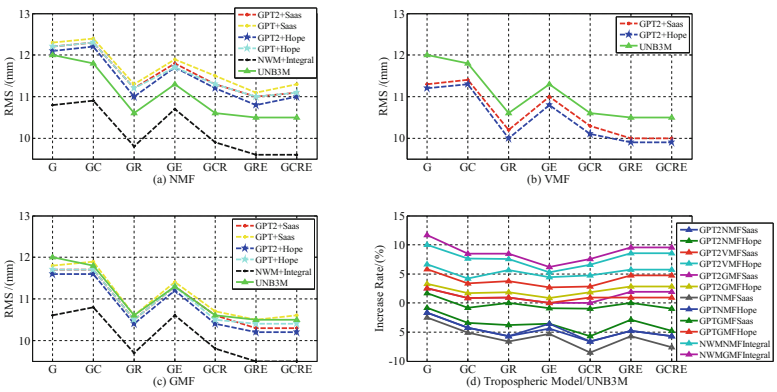

Fig. 4. The comparison of PPP up directional positioning accuracy of different tropospheric models with ZWD parameters

Table 5. The increasing rate of PPP up directional positioning accuracy of different tropospheric models based on UNB3M with ZWD parameters

Mete	Mapping	Model	G	GC	GR	GE	GCR	GRE	GCRE	Mean
GPT2	NMF	Saas	−1.67%	−4.24%	−5.66%	−4.42%	−6.60%	−4.76%	−5.71%	−4.72%
		Hope	−0.83%	−3.39%	−3.77%	−3.54%	−5.66%	−2.86%	−4.76%	−3.55%
	VMF1	Saas	5.83%	3.39%	3.77%	2.65%	2.83%	4.76%	4.76%	4.00%
		Hope	6.67%	4.24%	5.66%	4.42%	4.72%	5.71%	5.71%	5.30%
	GMF	Saas	2.50%	0.85%	0.94%	0%	0%	1.90%	1.90%	1.16%
		Hope	3.33%	1.69%	1.89%	0.88%	1.89%	2.86%	2.86%	2.20%
GPT	NMF	Saas	−2.50%	−5.08%	−6.60%	−5.31%	−8.49%	−5.71%	−7.62%	−5.90%
		Hope	−1.67%	−4.24%	−5.66%	−3.54%	−6.60%	−4.76%	−5.71%	−4.60%
	GMF	Saas	1.67%	−0.85%	0%	−0.88%	−0.94%	0%	−0.95%	−0.28%
		Hope	2.50%	0.85%	0.94%	0%	0.94%	0.95%	0.95%	1.02%
NWM	NMF	Integral	10.00%	7.63%	7.55%	5.31%	6.60%	8.57%	8.57%	7.75%
	GMF	Integral	11.67%	8.47%	8.49%	6.19%	7.55%	9.52%	9.52%	8.77%

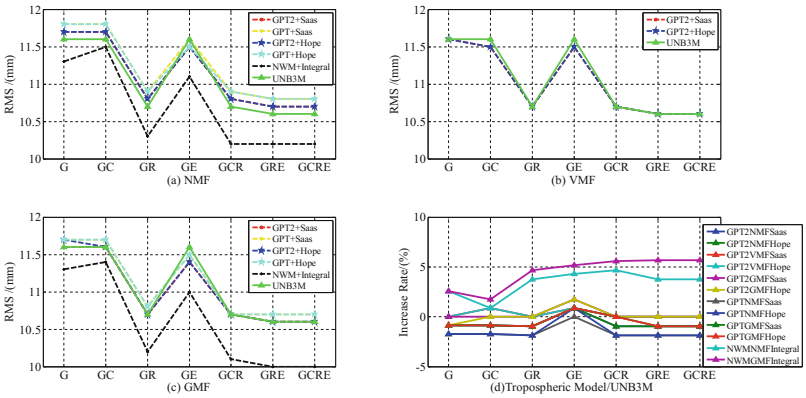

Fig. 5. The comparison of PPP ZTD accuracy with ZWD parameters

Table 6. The increasing rate of PPP ZTD accuracy of different tropospheric models based on UNB3M with ZWD parameters

Mete	Mapping	Model	G	GC	GR	GE	GCR	GRE	GCRE	Mean
GPT2	NMF	Saas	−0.86%	−0.86%	−0.93%	0.86%	−0.93%	−0.94%	−0.94%	−0.66%
		Hope	−0.86%	−0.86%	−0.93%	0.86%	−0.93%	−0.94%	−0.94%	−0.66%
	VMF1	Saas	0%	0.86%	0%	0.86%	0%	0%	0%	0.25%
		Hope	0%	0.86%	0%	0.86%	0%	0%	0%	0.25%
	GMF	Saas	0%	0%	0%	1.72%	0%	0%	0%	0.25%
		Hope	−0.86%	0%	0%	1.72%	0%	0%	0%	0.12%
GPT	NMF	Saas	−1.72%	−1.72%	−1.87%	0%	−1.87%	−1.89%	−1.89%	−1.57%
		Hope	−1.72%	−1.72%	−1.87%	0.86%	−1.87%	−1.89%	−1.89%	−1.44%
	GMF	Saas	−0.86%	−0.86%	−0.93%	0.86%	0%	−0.94%	−0.94%	−0.53%
		Hope	−0.86%	−0.86%	−0.93%	0.86%	0%	−0.94%	−0.94%	−0.53%
NWM	NMF	Integral	2.59%	0.86%	3.74%	4.31%	4.67%	3.77%	3.77%	3.39%
	GMF	Integral	2.59%	1.72%	4.67%	5.17%	5.61%	5.66%	5.66%	4.44%

In the case of setting parameters to estimate ZWD, ZWD is a more accurate value estimated by setting parameters. In the PPP process, it is the ZHD that really plays a role in the troposphere models. In order to more intuitively explain the accuracy of the tropospheric model (ZWD + ZHD) in the actual solution, this section uses PPP solutions without ZWD parameters. Figure 6 shows the positioning accuracy in the Up direction without ZWD parameters. From the perspective on the accuracy of the mapping function, since the ZWD parameter is not set, the mapping function does not work in the process of PPP calculation. From Fig. 6, it can be seen that the different mapping functions exhibit the same computational accuracy based on the same meteorological parameter model and the same computational model. From the perspective on the accuracy of the calculation in Multi-GNSS PPP, the solutions of different systems are relatively stable. From the perspective on the accuracy of the troposphere model, it can be seen that the NWM accuracy is optimal and the positioning accuracy in the Up direction is about 72.8% higher than that of the UNB3M model by comparing Fig. 6(a), (b) and (c). The GPT2+Saastamoinen model is the best in the prior tropospheric combination model, which is 22.66% higher than UNB3M. Combined with the analysis of the troposphere model accuracy in the Sect. 4.1, we can conclude that the NWM model has the highest accuracy; The GPT2+Saastamoinen model has the highest accuracy in the prior tropospheric combination model (Table 7).

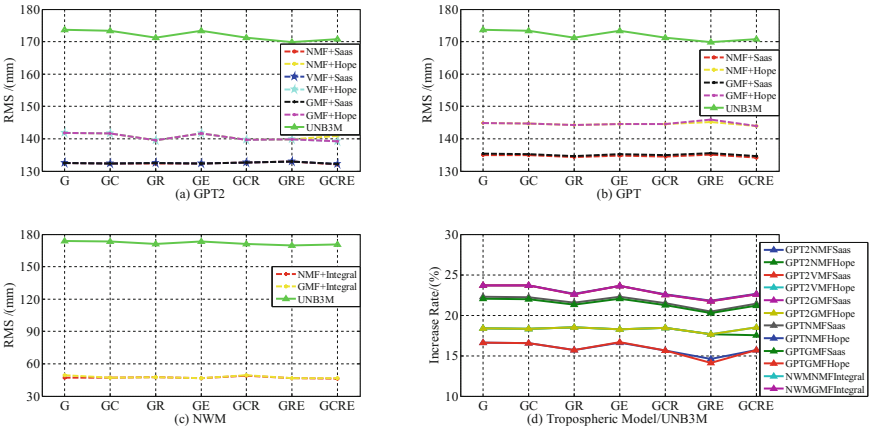

Fig. 6. The comparison of PPP up directional positioning accuracy of different tropospheric models without ZWD parameters

Table 7. The increasing rate of PPP up directional positioning accuracy of different tropospheric models based on UNB3M without ZWD parameters

Mete	Mapping	Model	G	GC	GR	GE	GCR	GRE	GCRE	Mean
GPT2	NMF	Saas	23.72%	23.70%	22.66%	23.64%	22.59%	21.78%	22.66%	22.97%
		Hope	18.36%	18.34%	18.52%	18.28%	18.45%	17.66%	17.51%	18.16%
	VMF1	Saas	23.72%	23.70%	22.61%	23.64%	22.53%	21.72%	22.60%	22.93%
		Hope	18.36%	18.34%	18.52%	18.28%	18.45%	17.66%	18.50%	18.30%
	GMF	Saas	23.72%	23.70%	22.61%	23.64%	22.53%	21.72%	22.60%	22.93%
		Hope	18.36%	18.34%	18.52%	18.28%	18.45%	17.66%	18.50%	18.30%
GPT	NMF	Saas	22.28%	22.20%	21.55%	22.26%	21.48%	20.48%	21.43%	21.67%
		Hope	16.64%	16.55%	15.71%	16.61%	15.65%	14.60%	15.69%	15.92%
	GMF	Saas	22.05%	21.97%	21.32%	22.03%	21.25%	20.25%	21.19%	21.44%
		Hope	16.64%	16.55%	15.71%	16.67%	15.65%	14.13%	15.69%	15.86%
NWM	NMF	Integral	72.94%	72.90%	72.25%	73.07%	71.28%	72.63%	72.89%	72.57%
	GMF	Integral	71.50%	72.78%	72.14%	72.95%	71.10%	72.51%	72.72%	72.24%

5 Conclusion

Based on the observation data of the MGEX station, this paper analyzes and compares the tropospheric model and mapping function in the aspects of both post process and real time. This paper compares the accuracy difference of different troposphere models from three aspects: the accuracy of the tropospheric combination models, the positioning accuracy on PPP Up direction and the accuracy of ZTD solution. We can come to the following conclusions.

1. From the perspective on the accuracy of the meteorological data, the accuracy of the pressure-level meteorological data provided by the ECMWF is the best, the second is the GPT2 model in the empirical model and the GPT and UNB3M models have less accurate meteorological data.
2. From the perspective on the accuracy of the calculation of multi-GNSS PPP, in the PPP post-processing process, the combination of NWM+GMF+Integral is optimal, and it's the positioning accuracy in the Up direction can be increased by 8.77%, and the accuracy of ZTD can be increased by 4.44%. In the real-time PPP processing process, the combination of GPT2+VMF1+Modified Hopfield is optimal, and it's the positioning accuracy in the Up direction can be increased by 5.30%, and the accuracy of ZTD can be increased by 0.25%.
3. From the perspective on the accuracy of the tropospheric model, the accuracy of the NWM model is the most obvious than that of the UNB3M model in the tropospheric combination model, and its improving rate is 63.81%; the accuracy of GPT2 +Saastamoinen is the most obvious than that of the UNB3M model in tropospheric empirical model, and its improvement rate is 63.81%; The Saastamoinen model is superior to the Modified Hopfield model in solving the ZTD, but the Modified Hopfield model is superior to the Saastamoinen model in solving the ZHD.

In summary, in the case of the PPP post-processing process, the tropospheric combination model of NWM+GMF+Integral can be used to improve the positioning and

ZTD accuracy. In the case of real-time PPP process, the GPT2+VMF1+Saastamoinen model can be used to improve the positioning and ZTD accuracy. The GPT2+VMF1 +Saastamoinen model can be used to improve the positioning accuracy without ZWD parameters such as SPP et al.

Acknowledgements. This work is supported by National Key R&D Program of China (2016YFB0501503-3). The authors gratefully acknowledge iGMAS for providing multi-GNSS precise orbit and clock products. Many thanks to the IGS MGEX for providing the observation data. Many thanks to the ECMWF for providing the meteorological pressure-level data.

References

1. Song SL, Zhu WY, Chen QM et al (2011) Establishment of a new tropospheric delay correction model over China area. Sci China Phys Mech Astron 54:2271
2. Song SL, Zhu WY, Ding JC et al (2006) 3D water-vapor tomography with Shanghai GPS network to improve forecasted moisture field. Chin Sci Bull 51:607–614
3. de Oliveira PS, Morel L, Fund F et al (2017) Modeling tropospheric wet delays with dense and sparse network configurations for PPP-RTK. GPS Solut 21:237
4. Xu Y, Jiang N, Xu G, Yang Y, Schuh H (2015) Influence of meteorological data and horizontal gradient of tropospheric model on precise point positioning. Adv Space Res 56 (11):2374–2383
5. Yao YB, Zhang B, Yan F et al (2015) Two new sophisticated models for tropospheric delay corrections. Chin J Geophys 58(05):1492–1501 (in Chinese)
6. Wang J, Chen J, Wang J (2014) Analysis of tropospheric propagation delay mapping function models in GNSS. Prog Astron 32(03):383–394
7. Liu J, Chen X, Sun J, Liu Q (2016) An analysis of GPT2/GPT2w+Saastamoinen models for estimating zenith tropospheric delay over Asian area. Adv Space Res 59(3):824–832
8. Boehm J, Heinkelmann R, Schuh H (2007) Short note: a global model of pressure and temperature for geodetic applications. J Geodesy 81(10):679–683
9. Lagler K, Schindelegger M, Nilsson T et al (2013) GPT2: empirical slant delay model for radio space geodetic techniques. Geophys Res Lett 40(6):1069
10. Chen Q, Song S, Heise S et al (2011) Assessment of ZTD derived from ECMWF/NCEP data with GPS ZTD over China. GPS Solut 15:415
11. Cai C, Gao Y, Pan L, Zhu J (2015) Precise point positioning with quad-constellations: GPS, BeiDou, GLONASS and Galileo. Adv Space Res 56 https://doi.org/10.1016/j.asr.2015.04.001
12. Su K, Jin S (2018) Improvement of multi-GNSS precise point positioning performances with real meteorological data. J Navig 71(6):1363–1380
13. Li B, Feng Y, Shen Y, Wang C (2010) Geometry-specified troposphere decorrelation for subcentimeter real-time kinematic solutions over long baselines. J Geophys Res 115: B11404. https://doi.org/10.1029/2010JB007549
14. Petit G, Luzum B (2010) IERS conventions (No. IERS-TN-36). Bureau International Des Poids Et Mesures Sevres (France)

Preliminary Evaluation on the Precision of the BDS-3 Global Ionospheric Model

Shun Yu[1(✉)], Fujian Ma[2], Wei Wang[1], Renpan Wu[1], and Qi Zeng[1]

[1] Beijing UniStrong Science & Technology Co., Ltd., Beijing, China
shun.yu@unistrong.com
[2] School of Geodesy and Geomatics, Wuhan University, Wuhan, China

Abstract. The BDS-3 basic system has already been established, starting to provide global service. As a new generation navigation system, the BDS-3 adopts a global ionospheric model, called BDGIM. Single-frequency users can use the BDGIM along with nine ionospheric parameters broadcasted in the navigation message to perform ionospheric correction. This paper analyzes the deficiency of the current BDS and GPS Klobuchar models, and then by using the high precision CODE's global ionospheric map (GIM) as a reference, the precision of BDGIM model is evaluated. Finally, the performance of applying this model to the positioning is verified by experimental data. The results show that the global accuracy of the BDGIM model is about 3.6 TECU, which is better than that of the Klobuchar model and more uniform on a global scale. In terms of the BDS standard point positioning, ionospheric correction with the BDGIM model obtains higher accuracy compared to that with the Klobuchar model, especially in the vertical direction.

Keywords: BDS-3 · Ionospheric model · BDGIM · Precision evaluation · Standard point positioning

1 Introduction

Ionospheric delay is one of the main error sources in global navigation satellite system (GNSS) positioning. Dual-frequency users can use the ionosphere-free combination to correct the ionospheric delay. While for single-frequency users, the appropriate ionospheric model must be selected for ionospheric error correction [1]. At present, GPS, BDS and Galileo all broadcast ionospheric parameters in the navigation message [2–4]. The BDS-2 regional navigation system adopts an improved Klobuchar model. With the implementation of the BDS-3, the basic system was established at the end of 2018, and the existing broadcast ionospheric delay correction model and method are difficult to meet the global demand, so the new generation of navigation systems will use the new ionospheric model BDGIM (BeiDou Global Ionospheric delay correction Model). The accuracy of the BDGIM global ionospheric model and its application to positioning are undoubtedly the focus of the user's concern. This paper introduces the basic principles of the BDGIM model in detail, the deficiency of the GPS and BDS Klobuchar model is

J. Sun et al. (Eds.): CSNC 2019, LNEE 563, pp. 131–139, 2019.
https://doi.org/10.1007/978-981-13-7759-4_12

analyzed as well. Then by using the global ionospheric map (GIM) provided by Center for Orbit Determination in Europe (CODE) as reference ionospheric values, the precision of BDGIM is evaluated. Finally, the applicability of BDGIM in single-frequency positioning is verified.

2 BDS-3 Global Ionospheric Model

The BDGIM is based on the periodicity of the ionosphere and adopts modified spherical harmonics method. Single frequency user can use it to correct the effect of ionospheric delay [5, 6]. The BDGIM model coefficients are divided into low-order and high-order spherical harmonic function coefficients, respectively. The low-order terms have 9 parameters (α_1–α_9), which have a great influence on the ionospheric total electron content (TEC) and are broadcasted in the B-CNAV1 subframe 3 and B-CNAV2 type 30 of navigation messages. The higher order coefficients describe the small-scale variation of the ionospheric TEC. Because higher spherical harmonic order generate much more coefficients, they only exist in a non-broadcast way in the interface control document and can be calculated by users according to the given method.

The specific method for the user to compute the ionospheric delay correction with BDGIM is as follows:

$$d_{ion} = M_F \cdot \frac{40.28 \cdot 10^{16}}{f^2} \cdot VTEC \tag{1}$$

$$VTEC = A_0 + \sum_{i=1}^{9} \alpha_i A_i \tag{2}$$

where d_{ion} is the line-of-sight ionospheric delay from the satellite to receiver; M_F is the ionospheric mapping function; f is the carrier frequency of the current signal; $VTEC$ is the total electron content in the vertical direction at the ionospheric pierce point (IPP); α_i is the BDGIM parameter broadcasted in the navigation message; A_0 is high-order term of spherical harmonic function, representing the predictive part in VTEC; A_i denotes the low-order term of spherical harmonic function, the expanded form is as follows:

$$A_i = \begin{cases} N_{n_i,m_i} \cdot P_{n_i,m_i}(\sin\varphi') \cdot \cos(m_i \cdot \lambda') & m_i > 0 \\ N_{n_i,m_i} \cdot P_{n_i,m_i}(\sin\varphi') \cdot \sin(-m_i \cdot \lambda') & m_i < 0 \end{cases} \tag{3}$$

where N_{n_i,m_i} is the normalization function; P_{n_i,m_i} is the classic, un-normalized Legendre function; n_i and m_i take the absolute values when calculating; φ' and λ' are the geomagnetic latitude and longitude of IPP.

The ionospheric prediction value is calculated as:

$$\begin{cases} A_0 = \sum_{j=1}^{17} \beta_j B_j \\ B_j = \begin{cases} N_{n_j,m_j} \cdot P_{n_j,m_j}(\sin\varphi') \cdot \cos(m_j \cdot \lambda') & m_j > 0 \\ N_{n_j,m_j} \cdot P_{n_j,m_j}(\sin\varphi') \cdot \sin(-m_j \cdot \lambda') & m_j < 0 \end{cases} \end{cases} \tag{4}$$

with

$$\begin{cases} \beta_j = \sum_{k=0}^{12} \left(a_{k,j} \cdot \cos(\omega_k t_p) + b_{k,j} \cdot \sin(\omega_k t_p)\right) \\ \omega_k = \frac{2\pi}{\mathrm{T}_k} \end{cases} \tag{5}$$

where $a_{k,j}$ and $b_{k,j}$ are the non-broadcast coefficients of the BDGIM model; T_k is the period for prediction; t_p is an odd hour of the corresponding day in modified Julian date, while the user should choose the nearest t_p from the current calculation time. After calculating A_0 and A_i, the VTEC can be calculated according to Eq. (2). By using the mapping function and combined with Eq. (1), the ionospheric delay along the signal propagation path can be obtained. The mapping function M_F is as follows:

$$M_F = \frac{1}{\sqrt{1 - \left(\frac{Re}{Re + H_{ion}}\cos(E)\right)^2}} \tag{6}$$

where Re represents the mean radius of the Earth; E is the satellite elevation angle; $H_{ion} = 400$ km represents the altitude of the ionosphere single layer shell, which is different from the value of 375 km in the BDS-2 Klobuchar model.

3 Insufficient of Klobuchar Model

The Klobuchar model sets the nighttime ionospheric delay to a constant of 5 ns, and the diurnal ionospheric delay as a cosine function. The amplitude and period can be calculated from the 8-parameter broadcasted in the navigation message. The user calculates the ionospheric vertical delay as:

$$I_z(t) = \begin{cases} 5 \cdot 10^{-9} + A_2 \cos[\frac{2\pi(t-50400)}{A_4}], & |t - 50400| < A_4/4 \\ 5 \cdot 10^{-9} & |t - 50400| \geq A_4/4 \end{cases}, \tag{7}$$

For GPS Klobuchar model, when calculating the ionospheric delay, the amplitude A_2 and period A_4 are calculated by using the geomagnetic latitude:

$$A_2 = \begin{cases} \sum_{n=0}^{3} \alpha_n \phi_m^n, & A_2 \geq 0 \\ 0, & A_2 < 0 \end{cases}$$
$$A_4 = \begin{cases} \sum_{n=0}^{3} \beta_n \phi_m^n, & A_4 \geq 72000 \\ 72000, & A_4 < 72000 \end{cases} \tag{8}$$

In Eq. (8), α_n and β_n are the ionospheric parameters; ϕ_m is the geomagnetic latitude.

$$\phi_m = \phi_i + 0.064 \cos(\lambda_i - 1.617) \tag{9}$$

$$\phi_i = \begin{cases} \phi_u + \psi \cos A, & |\phi_i| \leq 0.416 \\ +0.416, & \phi_i > 0.416 \\ -0.416, & \phi_i < -0.416 \end{cases} \tag{10}$$

where, ϕ_i and λ_i are the geographic latitude and longitude of IPP; ϕ_u is the geographic latitude of the user; ψ is the Earth's central angle between the user position and IPP; A is the satellite elevation angle. It is noted that if the geographic latitude of IPP is higher than $\pm 74.88°$ (0.416π), then the geographic latitude is limited to $\pm 74.88°$. Therefore, when IPP is at high latitude, the ionospheric delay amplitude and period obtained by different latitudes of the same geographic longitude are the same, this characteristic is different from that of actual ionosphere.

For BDS Klobuchar model, when calculating the ionospheric delay, the amplitude A_2 and period A_4 are calculated by using the geographic latitude, and the calculated values of the southern hemisphere model are symmetric with the northern hemisphere with respect to the equator (ϕ_{M} adopts the absolute value). The equation is as follows:

$$A_2 = \begin{cases} \sum_{n=0}^{3} \alpha_n |\phi_{\mathrm{M}}|^n, & A_2 \geq 0 \\ 0, & A_2 < 0 \end{cases}$$
$$A_4 = \begin{cases} 172800, & A_4 \geq 172800 \\ \sum_{n=0}^{3} \beta_n |\phi_M|^n, & 172800 > A_4 \geq 72000 \\ 72000, & A_4 < 72000 \end{cases} \tag{11}$$

where ϕ_{M} is the geographic latitude of IPP, which is calculated according to

$$\phi_{\mathrm{M}} = \arcsin(\sin \phi_u \cdot \cos \psi + \cos \phi_u \cdot \sin \psi \cdot \cos A) \tag{12}$$

Different from GPS Klobuchar model, the BDS Klobuchar model is a regional-type ionospheric model. When calculating the geographic latitude of IPP according to

Eq. (12), the range is not limited, that is, there is no limitation like that in Eq. (10), furthermore the 8 parameters are calculated from the observation data of the China regional monitoring station, so if the BDS Klobuchar model is applied to high latitudes, the amplitude will increase sharply, and the calculated ionospheric delay will be very large. As shown in Fig. 1, for GPS, the amplitude of the north and south hemispheres is asymmetrical, and at 120° E longitude, the amplitude is constant when IPP has geographic latitude higher than 75° N and 65° S. These characteristics are different from the characteristics of the real ionosphere.

The GIM of CODE, one of the international GNSS service (IGS) analysis centers, has high precision, generally 2–8 TECU [7, 8], and its calculated VTEC can be used as a reference value. As shown in Fig. 1, The VTEC calculated by BDS Klobuchar model is north-south symmetric and it differs greatly from CODE's GIM model in low latitude and high latitude areas which are basically not applicable. The difference between GIM and BDS Klobuchar is smaller in the mid-latitudes of northern hemisphere than that of the southern hemisphere. In addition, the VTEC of GPS Klobuchar model is constant in high latitudes which is different from that of CODE's GIM.

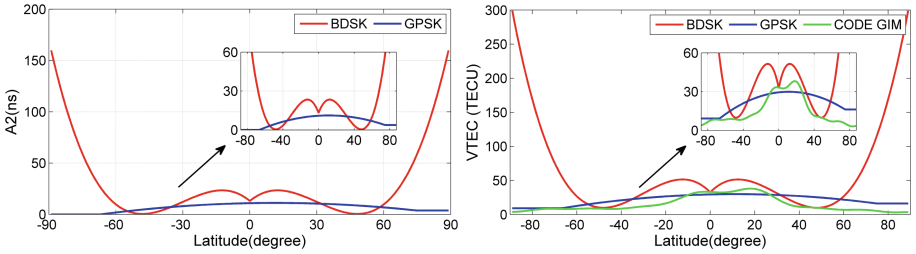

Fig. 1. The amplitude (left) and VTEC (right) of Klobuchar model varies with latitude (GPST 06:00 October 11, 2018, 120° E)

4 BDGIM Model Precision

The VTEC calculated by CODE's GIM can be taken as reference to evaluate the precision of BDGIM. By calculating the ionospheric VTEC values of CODE's GIM and BDGIM at the grids from latitude −87.5° to 87.5° and longitude −180° to 180° with a resolution of 2.5° × 5° in latitude and longitude, the RMS can be calculated according to [9, 10]. The equation is as follow:

$$RMS = \sqrt{\frac{\sum_{i=1}^{71}\sum_{j=1}^{73}\left(VTEC_{MOD_{ij}} - VTEC_{GIM_{ij}}\right)^2}{71 \times 73}} \tag{13}$$

where $VTEC_{MOD_{ij}}$ and $VTEC_{GIM_{ij}}$ represent the VTEC at the grids provided by the model and CODE's GIM, respectively.

This paper selects the BDS-3/GPS ionospheric parameters received by high-precision GNSS receiver which is independently developed by Unistrong from October 5 to November 4, 2018, and then the precision of BDGIM and GPS Klobuchar is evaluated and compared.

Figure 2 shows the difference between the BDGIM and the CODE's GIM (left), as well as the difference between the GPS Klobuchar model and the CODE's GIM (right) on October 11, 2018 (DOY 284). As can be seen from the figure, the difference

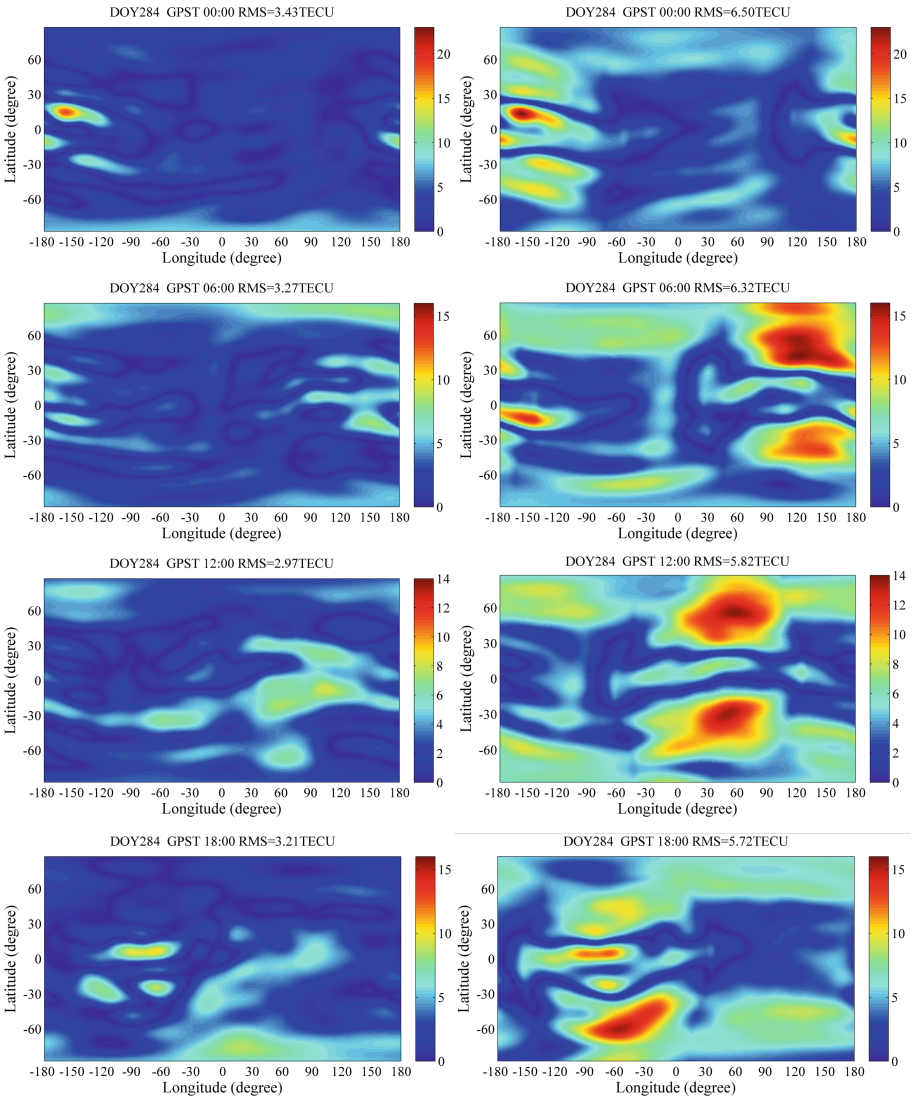

Fig. 2. Difference between the BDGIM and CODE's GIM (left), as well as the GPS Klobuchar and CODE's GIM (right)

between the BDGIM or GPS Klobuchar and the CODE's GIM is different at different time. As a whole, the difference between BDGIM and CODE's GIM is basically within 10 TECU, and the overall statistical accuracy is 3.6 TECU. The performance of the BDGIM model is more consistent with the CODE's GIM than that of the GPS Klobuchar, even in high latitude regions the accuracy is still good.

In most areas of the world, the difference between GPS Klobuchar and CODE's GIM is within 15 TECU, and reaches the maximum at local time of 14:00–16:00 because of the most active ionosphere and the largest model error at this moments. In addition, the error is also high in the high latitude area. The overall statistical accuracy is 6.5 TECU, which is slightly worse than that of the BDGIM model.

Table 1 summarizes the accuracy of the BDGIM and GPS Klobuchar models at different latitudes around the world. It can be seen that the accuracy of the BDGIM model in the southern hemispheres is slightly worse than that in the northern hemisphere, reaching 5.23 TECU at 50° S. In addition, the BDGIM model accuracy is better than the GPS Klobuchar model at different latitudes.

Table 1. Statistical accuracy of the BDGIM and GPS Klobuchar

Longitude range	Ionospheric model	VTEC RMS (TECU)								Mean/TECU
		70°	50°	30°	10°	−10°	−30°	−50°	−70°	
(−180° W–180° E)	BDGIM	3.02	3.42	2.66	3.31	3.32	2.96	5.23	5.20	3.64
	GPSK	6.67	6.11	4.80	8.99	7.29	4.85	6.49	6.80	6.50

5 Positioning Performance of BDGIM

In order to verify the effect of BDGIM model applied in positioning, the BDS observation data of 12 IGS stations in different latitude regions for one month (October 5–November 4, 2018) are selected for BDS standard point positioning (SPP). The distribution map of the stations is shown in Fig. 3, in which 4 IGS stations (urum, jfng, lhaz and hkws) are located in China, and 8 IGS stations (sod3, metg, mizu, sin1, ftna, cut0, dund and maw1) are located outside China. The SPP strategies are as follows: the B1I data is used for single-frequency SPP and the satellite elevation mask angle is set to 10°. The ionospheric model adopts BDGIM, BDS Klobuchar, GPS Klobuchar and CODE GIM respectively for full comparison and analysis. The Saastamoinen model is applied to correct the tropospheric error. The stochastic model uses a sinusoidal elevation model **[**11**]**, which is shown as follows

$$\sigma_i^2 = \mathrm{a}^2 + \frac{b^2}{\sin^2 \theta_i} \tag{14}$$

where σ_i^2 is the observation variance of the i satellite; a and b are the empirical coefficients and both set to 0.3 in this paper; θ_i is the elevation angel of the i satellite.

The external accuracy as shown in Table 2 is obtained by substracting the positioning results with the reference values. It can be seen that in the four ionospheric

models, the CODE's GIM has the highest positioning accuracy, followed by the BDGIM model. In the three broadcast ionospheric models of BDGIM, BDS Klobuchar and GPS Klobuchar, the horizontal accuracy is not much different except for the sod3, metg and maw1 stations located in high latitudes where the accuracy of BDS Klobuchar is poor, but the difference in the elevation direction is relatively obvious. The vertical accuracy of positioning with the BDGIM for ionospheric correction is 0.3–2.3 m better than that with the BDS Klobuchar, and 0.4–1.3 m better compared with the GPS Klobuchar. Whichever ionospheric models are used, stations sod3, metg, dund and maw1 show larger positioning errors than the others. This is due to fewer BDS satellites tracked by the stations with bad geometry and the ionospheric models themselves have worse accuracy at high latitudes and in the south hemisphere.

Overall, the BDGIM model applied to positioning has a better applicability on a global scale, which is closer to CODE's GIM.

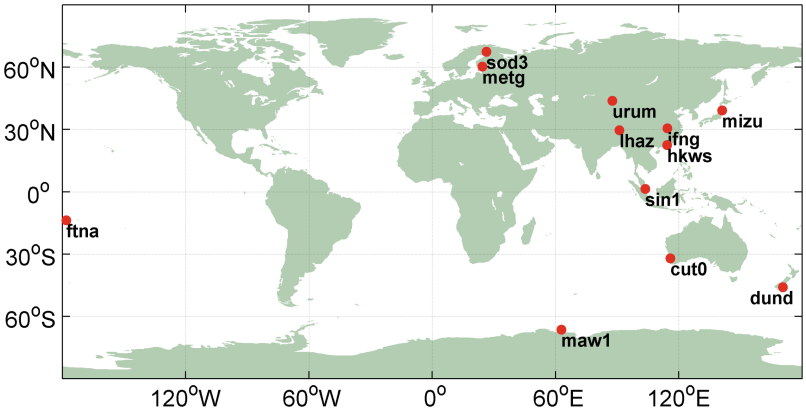

Fig. 3. Location of selected IGS stations

Table 2. RMS values of BDS standard point positioning at B1I frequency

Marker name	Outline coordinates	Horizontal RMS (m)				Vertical RMS (m)				3D RMS (m)			
	(Lat., Lon.)	BDGIM	BDSK	GPSK	CODE	BDGIM	BDSK	GPSK	CODE	BDGIM	BDSK	GPSK	CODE
sod3	(67.421, 26.289)	6.46	7.35	6.55	6.35	5.29	6.52	5.79	5.10	8.35	9.82	8.74	8.14
metg	(60.242, 24.384)	5.86	6.53	5.82	5.46	5.25	5.88	5.67	5.16	7.86	8.79	8.12	7.51
urum	(43.808, 87.601)	1.65	1.66	1.71	1.60	2.40	2.82	3.56	2.11	2.91	3.27	3.95	2.64
mizu	(39.135, 141.133)	1.92	2.04	1.89	1.86	3.68	3.99	4.28	3.55	4.15	4.48	4.68	4.01
jfng	(30.516, 114.491)	1.24	1.34	1.22	1.23	2.64	3.82	3.27	2.11	2.91	4.04	3.49	2.44
lhaz	(29.657, 91.104)	1.39	1.54	1.38	1.40	2.74	3.88	3.40	2.53	3.07	4.17	3.67	2.89
hkws	(22.434, 114.335)	1.30	1.19	1.50	1.12	2.21	2.62	2.88	2.08	2.56	2.87	3.24	2.36
sin1	(1.343, 103.679)	1.20	1.40	1.15	1.05	1.75	3.02	2.46	1.59	2.12	3.33	2.72	1.91
ftna	(−13.692, −178.12)	5.29	5.40	5.69	5.06	6.17	8.26	6.82	6.03	8.13	9.87	8.88	7.87
cut0	(−31.996, 115.895)	1.55	1.78	1.66	1.54	2.60	4.96	3.56	2.29	3.02	5.27	3.80	2.75
dund	(−45.884, 170.597)	3.91	4.10	4.10	3.88	5.65	6.55	6.91	5.31	6.87	7.72	8.03	6.57
maw1	(−66.395, 62.870)	4.02	6.04	4.06	4.00	4.24	5.98	5.52	4.06	5.84	8.50	6.85	5.70
Mean	–	2.98	3.36	3.06	2.88	3.72	4.86	4.51	3.49	4.82	6.01	5.51	4.57

6 Conclusions

This paper introduces the BDS-3 global ionospheric model BDGIM in detail and analyzes the deficiency of the current BDS and GPS Klobuchar model, then by using the high precision CODE's GIM as a reference, the precision of BDGIM model is evaluated. Finally, the effect of the model on positioning is verified by experimental data. The results show that:

(1) The accuracy of the BDGIM model is approximately 3.6 TECU worldwide, which is superior to the Klobuchar model.
(2) The BDGIM global ionospheric model compensates for the deficiency of the GPS and BDS Klobuchar models, and still performs well in high latitudes, with more uniform accuracy on a global scale.
(3) In the aspect of SPP, ionospheric correction with the BDGIM model obtains higher accuracy compared to that with the Klobuchar model, especially in the vertical direction.

With the constructions of the BDS global monitoring stations, more observation data will be obtained for the refinement of the BDS-3 global ionospheric model, and the accuracy of the model will be further improved.

References

1. Li Z, Huang J (2010) GPS Surveying and Data Processing. Wuhan University Press, Wuhan
2. China Satellite Navigation Office (2011) BeiDou navigation satellite system signal in space interface control document open service signal (version 2.1)
3. ICD-GPS-200 (2012) Navistar GPS space segment-navigation user segment interfaces (revision G). Glob Position Syst Direct
4. European Union (2015) European GNSS (Galileo) open service signal in space interface control document
5. China Satellite Navigation Office (2017) BeiDou navigation satellite system signal in space interface control document open service signal B1C and B2a (test version)
6. Li Z (2012) Study on the mitigation of ionospheric delay and the monitoring of global ionospheric TEC based on GNSS/compass. Ph.D. thesis, Institute of Geodesy and Geophysics, University of Chinese Academy of Sciences, Wuhan, China (in Chinese)
7. Schaer S (1997) How to use CODE's global ionosphere maps. Astronomical Institute, University of Berne
8. Schaer S, Gurtner W, Feltens J (1998) IONEX: the ionosphere map exchange format version 1. IGS AC workshop, Darmstadt, 9–11 February 1998
9. Wu X, Hu X, Wang G, Zhong H, Tang C (2013) Evaluation of COMPASS ionospheric model in GNSS positioning. Adv Space Res 51(6):959–968
10. Zhang Q, Zhao Q, Zhang H, Hu Z, Wu Y (2013) Evaluation on the precision of Klobuchar model for BeiDou navigation satellite system. Geomat Inf Sci Wuhan Univ 39(2):142–146
11. King RW, Bock Y (1999) Documentation for the GAMIT GPS analysis software (version 9.8), Unpublished, Massachusetts Institute of Technology

Research on Multi-GNSS Wide-Lane FCB Estimation Method Based on MGEX

Lin Han(✉), Yansong Meng, and Lang Bian

China Academy of Space Technology (Xi'an), Xi'an 710100, China
hanlin_504@163.com

Abstract. With the rapid development of Global Navigation Satellite System (GNSS) Precise Point Positioning (PPP) ambiguity resolution, high-quality Multi-GNSS fractional cycle biases products are urgently needed. In this contribution, the ambiguity resolution in Multi-GNSS is deduced in detail based on the observation and precise products provided by multi-GNSS Experiment (MGEX). Meanwhile, a Multi-GNSS wide-lane FCB product estimation method is proposed. Then the wide-lane FCB products of GPS, Galileo and BDS are generated by observations in 2017, DOY24 to 2017, DOY30. It is found that, the wide-lane FCB products of GPS, Galileo and BDS have a good stability after on-board multipath correction. Finally, the validity of FCB products is verified by the wide-lane residual distribution of GPS, Galileo and BDS, in which the correctness of the proposed method is also proved.

Keywords: Multi-GNSS · Wide-lane · MGEX · Fractional cycle biases

1 Introduction

With the rapid development of Global Navigation Satellite System (GNSS), the Positioning, Navigation, Timing (PNT) services also have rapid development in depth and width, among them Precise Point Positioning (PPP) [1, 2] has been widely used in scientific research and engineering applications, such as GNSS seismology, GNSS meteorology, precision agricultural services, etc. [3, 4]. However, the traditional PPP is also constrained by long convergence time and may be easily disturbed. With the construction of more GNSS constellations and the progress of PPP ambiguity resolution method, these constraints are gradually solved. For the fixed solution of multi-GNSS, the integer carrier phase ambiguity is destroyed by the Fractional Cycle Biases (FCB) of receiver and satellites [5], the high quality FCB product is crucial for multi-GNSS fixed solution.

With the increasing demand of high-precision service in real-time, many scholars have conducted extensive research on solving FCB products. In Ref. [6], the influence of ambiguity's fractional part is deduced in detail, and the FCB products of GPS with the ambiguity of wide-lane and narrow-lane are calculated by using the single-difference averaging method between satellites, and the validity of these products is verified by PPP integer solution. On the basis of Ref. [6], the Ref. [7] proposed an improved FCB product estimation method, which improved the calculation by combining the observation information of all stations in a matrix and the FCB products are

J. Sun et al. (Eds.): CSNC 2019, LNEE 563, pp. 140–150, 2019.
https://doi.org/10.1007/978-981-13-7759-4_13

obtained by least squares, the calculation accuracy and speed are improved. In Ref. [8], the FCB product was generated by the "integer" phase clock method, and the wide-lane FCB and clock product containing narrow-lane FCB were regularly published on the website of the Groupe de Recherche de Géodésie Spatiale of the Centre National d'Etudes Spatiales (CNES-GRG). On the basis of Ref. [7], based on International GNSS Service (IGS) stations, Ref. [9] calculates GPS wide-lane and narrow-lane FCB products corresponding to different analysis center's clock products and regularly publish on the website of School of Geodesy and Geomatics at Wuhan University (WHU-SGG). In Ref. [10], GPS wide-lane and narrow-lane FCB products are generated by Kalman filter method, and compared with those products by CNES-GRG and WHU-SGG to verify the validity of this method. In Ref. [11], the methods of solving multi-GNSS FCB product and fixed solution are deduced in detail, and the effectiveness of multi-GNSS fixed solution for shortening the convergence time is verified. The above methods have studied the solution of FCB products in detail, but most of them are based on IGS stations. With the completion of BDS and Galileo global networking and the modern transformation of GPS and GLONASS, multi-GNSS fusion processing has gradually became the mainstream. Therefore, it is very necessary to study multi-GNSS FCB product estimation method.

In order to adapt to the development trend of multi-GNSS, IGS launched multi-GNSS Experiment (MGEX). MGEX stations provide multi-GNSS observations, while the analysis centers provide multi-GNSS orbits and clocks products and other high-precision products. This contribution will study multi-GNSS wide-lane FCB product estimation method based on the observation and high-precision products provided by MGEX, and verify its validity by analysing.

2 FCB Product Estimation Method for Multi-GNSS

In this section, we will mainly investigate the estimation method of multi-GNSS FCB product. Firstly, the basic observation equations of GNSS are introduced, then the observation equations of multi-GNSS are analyzed. Finally, the FCB product estimation method of multi-GNSS is proposed.

2.1 Basic Observation Equation

GNSS observations generally include pseudo-range, carrier phase and Doppler observations. In PPP, pseudo-range and carrier phase observations are commonly used. These two observations can be expressed as [12]:

$$P_{r,f}^{s} = \rho_r^s + c(dt_r - dt^s) + T_r^s + I_{r,f}^s + d_{r,f} - d_f^s + e_{r,P,f}^s \tag{1}$$

$$L_{r,f}^{s} = \rho_r^s + c(dt_r - dt^s) + T_r^s - I_{r,f}^s + \lambda_f\left(N_{r,f}^s + b_{r,f} - b_f^s\right) + e_{r,L,f}^s \tag{2}$$

In the above equations, $P_{r,f}^s$, $L_{r,f}^s$ are pseudo-range and carrier phase measurements expressed by distance, where s means satellites, subscript r represents the receiver, f

represents the corresponding frequency. ρ_r^s represents the real geometric distance between satellite s and receiver r. c represents the speed of light, dt_r and dt^s are clock error of satellites and receive. The tropospheric delay represented by T_r^s is a non-dispersive term, which does not distinguish between frequency and observation type. The ionospheric delay represented by $I_{r,f}^s$ on frequency f is different from that of carrier and pseudo-range due to the inconsistent influence of ionosphere on group velocity and phase velocity. $d_{r,f}$ and d_f^s represent the receiver and satellite hardware delay of pseudo-range on frequency f. λ_f is the wavelength of frequency f, $N_{r,f}^s$ is the integer ambiguity, $b_{r,f}$ and b_f^s are the uncorrected carrier phase delays (UPD) of the receiver and the satellite that contain integer cycles and FCB, in which FCB destroys the integer characteristics of ambiguity. $e_{r,P,f}^s$ and $e_{r,L,f}^s$ are measurement errors of pseudo-range and carrier phase on frequency f. In the above observation equations, the Phase Center Offsets (PCO) and Phase Center Variations (PCV) of the antenna on receiver and satellite have been corrected already, while the relativistic effect and phase wrapping have been corrected through error models [2, 13].

In order to eliminate the first-order ionosphere delay in pseudo-range and carrier phase measurements, the ionosphere-free (IF) combination is usually used in parameter estimation of PPP. The IF combination of pseudo-range and carrier phase can be expressed as:

$$P_{r,\mathrm{IF}}^s = \frac{f_i^2}{f_i^2 - f_j^2} P_{r,i}^s - \frac{f_j^2}{f_i^2 - f_j^2} P_{r,j}^s \tag{3}$$

$$L_{r,\mathrm{IF}}^s = \frac{f_i^2}{f_i^2 - f_j^2} L_{r,i}^s - \frac{f_j^2}{f_i^2 - f_j^2} L_{r,j}^s \tag{4}$$

In the above equation, P and L represent pseudo-range and carrier phase on different frequency. f_i and f_j represent different frequencies respectively. The above combination is a widely used combination of observations, and the algorithm is also mature.

2.2 Observation Equation of Multi-GNSS

At present, most MGEX observation stations can observe four systems. In this contribution, we mainly analyse the satellite system using Code Division Multiple Access (CDMA) modulation mode, and the estimation of GPS, Galileo and BDS FCB products. Although the rapid construction of BDS-3, there are few MGEX stations that can provide BDS-3 observation data at present, so the FCB products of BDS-2 are mainly generated when the MGEX stations observation are used. The following table shows the current status of CDMA systems:

Table 1. Current status of CDMA modulation systems

System	Blocks	Signal	Number
GPS	IIR	L1 C/A, L1/L2 P(Y)	12
	IIR-M	L1 C/A, L1/L2 P(Y), L2C, L1/L2 M	7
	II-F	L1 C/A, L1/L2 P(Y), L2C, L1/L2 M, L5	12
Galileo	IOC	E1, E6, E5(ab)	
	FOC	E1, E6, E5(ab)	
BDS-2	GEO	B1I, B2I, B3	6
	IGSO	B1I, B2I, B3	6
	MEO	B1I, B2I, B3	3
BDS-3	GEO	/	1
	IGSO	B1I, B1C, B2a, B3	2
	MEO	B1I, B1C, B2a, B3	21

As can be seen from Table 1, BDS, Galileo and part of GPS satellites broadcast three-frequency signals, so there are many frequency signals can be selected when using the IF combinations in the previous section. But in general, IF combinations should be same with multi-GNSS products of the Analysis Center. Usually the IF combination is of GPS L1 and L2 frequencies, while for Galileo are E1 and E5a. For BDS-2, the combination of B1I and B2I is adopted. At present, BDS-3, which is still in the construction, generally uses B1C and B2a, thus forming interoperability with GPS and Galileo. The equations of pseudo-range and carrier phase of GPS, Galileo and BDS IF combinations are as follows:

$$\begin{aligned} P_{r,IF}^{G} &= \rho_r^G + c\left(dt_r - dt^G\right) + T_r^G + d_{r,IF}^G - d_{IF}^{s,G} + e_{r,P,IF}^G \\ P_{r,IF}^{E} &= \rho_r^E + c\left(dt_r - dt^E\right) + T_r^E + d_{r,IF}^E - d_{IF}^{s,E} + e_{r,P,IF}^E \\ P_{r,IF}^{C} &= \rho_r^C + c\left(dt_r - dt^C\right) + T_r^C + d_{r,IF}^C - d_{IF}^{s,C} + e_{r,P,IF}^C \end{aligned} \tag{5}$$

$$\begin{aligned} L_{r,IF}^{G} &= \rho_r^G + c\left(dt_r - dt^G\right) + T_r^G + \lambda_{IF,G}\left(N_{r,IF}^G + b_{r,IF}^G - b_{IF}^{s,G}\right) + e_{r,L,IF}^G \\ L_{r,IF}^{E} &= \rho_r^E + c\left(dt_r - dt^E\right) + T_r^E + \lambda_{IF,E}\left(N_{r,IF}^E + b_{r,IF}^E - b_{IF}^{s,E}\right) + e_{r,L,IF}^E \\ L_{r,IF}^{C} &= \rho_r^C + c\left(dt_r - dt^C\right) + T_r^C + \lambda_{IF,C}\left(N_{r,IF}^C + b_{r,IF}^C - b_{IF}^{s,C}\right) + e_{r,L,IF}^C \end{aligned} \tag{6}$$

In the above equations, G, E and C represent GPS, Galileo and BDS respectively, $d_{r,IF}$ and d_{IF}^s are the hardware delay of pseudo-range of the IF combination at receiver and satellite, $N_{r,IF}^s$ is the integer ambiguity of carrier phase measurement in IF combination, $b_{r,IF}$ and b_{IF}^s are the uncalibrated phase delay (UPD) of IF combination at receiver and satellites, λ_{IF} is the wavelength of the IF combination, $e_{r,P,IF}^s$ and $e_{r,L,IF}^s$ are measurement errors of pseudo-range and carrier phase.

Generally, PPP need to use precise products provided by various analysis centers. At present, the orbit and clock products of MGEX's main analysis centers are as follows [14]:

Table 2. Product provided by MGEX analysis center

Organization	Abbreviation	Satellites	Orbit (min)	Clock error (min)
CNES/CLS	GRM	GRE	15	0.5
CODE	COM	GRECJ	15	5
GFZ	GBM	GRECJ	15/5	5/0.5
TUM	TUM	EJ	5	5
WU	WUM	GRECJ	15	5

The J in the table stands for QZSS of Japan, which is a regional augmentation system and will not be discussed in this contribution (Table 2). Here we use the precise orbit and clock products provided by GFZ, because the sample interval of clock product is shorter, which can reduce the error caused by interpolation. Meanwhile, the products of GFZ include the constellation transmitting CDMA signal.

When calculating precise clock products, MGEX analysis center adopts the IF combination, and the hardware delay of pseudo-range at satellite will be absorbed into clock products. For receivers capable of processing multi-system signals, the delay $d^G_{r,IF}$, $d^E_{r,IF}$ and $d^C_{r,IF}$ of pseudo-range are different due to the different frequency and modulation mode of each system. The UPD $b^G_{r,IF}$, $b^E_{r,IF}$ and $b^C_{r,IF}$ of carrier phase are also different. Such deviation is defined as Inter-System Biases (ISB). In multi-GNSS PPP, because all systems use one clock error of a receiver, GPS is usually selected as the reference, and then the deviation between systems is introduced to each system. The observation equation after using precision products is as follows:

$$\begin{aligned} P^G_{r,IF} &= \rho^G_r + cdt_r + d^G_{r,IF} + e^G_{r,P,IF} \\ P^E_{r,IF} &= \rho^E_r + cdt_r + d^E_{r,IF} + e^E_{r,P,IF} \\ P^C_{r,IF} &= \rho^C_r + cdt_r + d^C_{r,IF} + e^C_{r,P,IF} \end{aligned} \tag{7}$$

$$\begin{aligned} L^G_{r,IF} &= \rho^G_r + cdt_r + d^G_{r,IF} + \lambda_{IF,G}\bar{N}^G_{r,IF} + e^G_{r,L,IF} \\ L^E_{r,IF} &= \rho^E_r + cdt_r + d^E_{r,IF} + \lambda_{IF,E}\bar{N}^E_{r,IF} + e^E_{r,L,IF} \\ L^C_{r,IF} &= \rho^C_r + cdt_r + d^C_{r,IF} + \lambda_{IF,C}\bar{N}^C_{r,IF} + e^C_{r,L,IF} \end{aligned} \tag{8}$$

In the above equation, non-dispersive tropospheric delays are added. Because of the precise products with satellite hardware delays, pseudo-range observations provide absolute reference for receiver clock errors. The ambiguity of carrier phase observations is as follows:

$$\begin{aligned} \bar{N}^G_{r,IF} &= N^G_{r,IF} + b^G_{r,IF} - d^G_{r,IF} \Big/ \lambda^G_{IF} - b^{s,G}_{IF} + d^{s,G}_{IF} \Big/ \lambda_{IF} \\ \bar{N}^E_{r,IF} &= N^E_{r,IF} + b^E_{r,IF} - d^E_{r,IF} \Big/ \lambda^E_{IF} - b^{s,E}_{IF} + d^{s,E}_{IF} \Big/ \lambda_{IF} \\ \bar{N}^C_{r,IF} &= N^C_{r,IF} + b^C_{r,IF} - d^C_{r,IF} \Big/ \lambda^C_{IF} - b^{s,C}_{IF} + d^{s,C}_{IF} \Big/ \lambda_{IF} \end{aligned} \tag{9}$$

2.3 Multi-GNSS Wide-Lane FCB Estimation Method

Generally, after the ambiguity of the IF combination deduced in the previous section is obtained, it is decomposed into wide-lane and narrow-lane ambiguity fixed respectively because of the short wavelength. In this contribution, we mainly study the estimation method of wide-lane FCB products. Usually, the ambiguity of wide-lane is solved by HMW (Hatch-Melbourne-Wübbena) combination [15–17], and the combined observation of wide-lane can be obtained as follows:

$$\begin{aligned}\lambda_{r,WL}^{G}\bar{N}_{r,WL}^{G} &= \frac{f_1 L_{r,f_1}^{G} - f_2 L_{r,f_2}^{G}}{f_1 - f_2} - \frac{f_1 P_{r,f_1}^{G} + f_2 P_{r,f_2}^{G}}{f_1 + f_2} \\ &= \lambda_{r,WL}^{G}\left(N_{r,WL}^{G} + B_{r,WL}^{G} - B_{WL}^{s,G}\right)\end{aligned} \tag{10}$$

$$\begin{aligned}\lambda_{r,WL}^{E}\bar{N}_{r,WL}^{E} &= \frac{f_1 L_{r,f_1}^{E} - f_2 L_{r,f_2}^{E}}{f_1 - f_2} - \frac{f_1 P_{r,f_1}^{E} + f_2 P_{r,f_2}^{E}}{f_1 + f_2} \\ &= \lambda_{r,WL}^{E}\left(N_{r,WL}^{E} + B_{r,WL}^{E} - B_{WL}^{s,E}\right)\end{aligned} \tag{11}$$

$$\begin{aligned}\lambda_{r,WL}^{C}\bar{N}_{r,WL}^{C} &= \frac{f_1 L_{r,f_1}^{C} - f_2 L_{r,f_2}^{C}}{f_1 - f_2} - \frac{f_1 P_{r,f_1}^{C} + f_2 P_{r,f_2}^{C}}{f_1 + f_2} \\ &= \lambda_{r,WL}^{C}\left(N_{r,WL}^{C} + B_{r,WL}^{C} - B_{WL}^{s,C}\right)\end{aligned} \tag{12}$$

The FCBs destroy the ambiguity integer characteristic in the equations above are:

$$\begin{aligned}B_{r,WL}^{G} &= b_{r,f_1}^{G} - b_{r,f_2}^{G} - \frac{f_1 d_{r,f_1}^{G} + f_2 d_{r,f_2}^{G}}{\lambda_{r,WL}^{G}(f_1 + f_2)} \\ B_{r,WL}^{E} &= b_{r,f_1}^{E} - b_{r,f_2}^{E} - \frac{f_1 d_{r,f_1}^{E} + f_2 d_{r,f_2}^{E}}{\lambda_{r,WL}^{E}(f_1 + f_2)} \\ B_{r,WL}^{C} &= b_{r,f_1}^{C} - b_{r,f_2}^{C} - \frac{f_1 d_{r,f_1}^{C} + f_2 d_{r,f_2}^{C}}{\lambda_{r,WL}^{C}(f_1 + f_2)}\end{aligned} \tag{13}$$

$$\begin{aligned}B_{WL}^{s,G} &= b_{f_1}^{s,G} - b_{f_2}^{s,G} - \frac{f_1 d_{f_1}^{s,G} + f_2 d_{f_2}^{s,G}}{\lambda_{r,WL}^{G}(f_1 + f_2)} \\ B_{WL}^{s,E} &= b_{f_1}^{s,E} - b_{f_2}^{s,E} - \frac{f_1 d_{f_1}^{s,E} + f_2 d_{f_2}^{s,E}}{\lambda_{r,WL}^{E}(f_1 + f_2)} \\ B_{WL}^{s,C} &= b_{f_1}^{s,C} - b_{f_2}^{s,C} - \frac{f_1 d_{f_1}^{s,C} + f_2 d_{f_2}^{s,C}}{\lambda_{r,WL}^{C}(f_1 + f_2)}\end{aligned} \tag{14}$$

In order to eliminate the influence of FCB at the receiver, single-difference between satellites is adopted. For multi-system, because of the existence of ISB, each system

should select a reference satellite instead of only one reference satellite. The ambiguity and standard deviation after single-difference between satellites are obtained as follows:

$$\begin{aligned}
\bar{N}_{WL}^{G,m,n} &= \bar{N}_{r,WL}^{G,m} - \bar{N}_{r,WL}^{G,n} = N_{WL}^{G,i,j} - B_{WL}^{G,i,j} \\
\bar{N}_{WL}^{E,p,q} &= \bar{N}_{r,WL}^{E,p} - \bar{N}_{r,WL}^{E,q} = N_{WL}^{E,p,q} - B_{WL}^{E,p,q} \\
\bar{N}_{WL}^{C,x,y} &= \bar{N}_{r,WL}^{C,x,y} - \bar{N}_{r,WL}^{C,x,y} = N_{WL}^{C,x,y} - B_{WL}^{C,x,y}
\end{aligned} \tag{15}$$

$$\begin{aligned}
\sigma_{\bar{N}_{WL}^{G,m,n}} &= \sqrt{\sigma^2_{\bar{N}_{r,WL}^{G,m}} + \sigma^2_{\bar{N}_{r,WL}^{G,n}}} \\
\sigma_{\bar{N}_{WL}^{E,p,q}} &= \sqrt{\sigma^2_{\bar{N}_{r,WL}^{E,p}} + \sigma^2_{\bar{N}_{r,WL}^{E,q}}} \\
\sigma_{\bar{N}_{WL}^{C,x,y}} &= \sqrt{\sigma^2_{\bar{N}_{r,WL}^{C,x}} + \sigma^2_{\bar{N}_{r,WL}^{C,y}}}
\end{aligned} \tag{16}$$

After the above equations are simultaneous solved, the matrix of multi-system wide-lane ambiguity combination can be obtained. It is assumed that the first satellite of each system is the reference satellite of each system.

$$\begin{bmatrix}
-\mathbf{1}_1 & \mathbf{I}_1 & \mathbf{0} & \mathbf{0} & \mathbf{0} & \mathbf{0} \\
\vdots & \vdots & \vdots & \vdots & \vdots & \vdots \\
-\mathbf{1}_n & \mathbf{I}_n & \mathbf{0} & \mathbf{0} & \mathbf{0} & \mathbf{0} \\
\mathbf{0} & \mathbf{0} & -\mathbf{1}_q & \mathbf{I}_q & \mathbf{0} & \mathbf{0} \\
\vdots & \vdots & \vdots & \vdots & \vdots & \vdots \\
\mathbf{0} & \mathbf{0} & -\mathbf{1}_q & \mathbf{I}_q & \mathbf{0} & \mathbf{0} \\
\mathbf{0} & \mathbf{0} & \mathbf{0} & \mathbf{0} & -\mathbf{1}_y & \mathbf{I}_y \\
\vdots & \vdots & \vdots & \vdots & \vdots & \vdots \\
\mathbf{0} & \mathbf{0} & \mathbf{0} & \mathbf{0} & -\mathbf{1}_y & \mathbf{I}_y
\end{bmatrix}
\begin{bmatrix}
f_G^1 \\ \vdots \\ f_G^m \\ f_E^1 \\ \vdots \\ f_E^p \\ f_C^1 \\ \vdots \\ f_C^x
\end{bmatrix}
=
\begin{bmatrix}
B_{1,G}^{m,1} \\ \vdots \\ B_{n,G}^{m,1} \\ B_{1,E}^{p,1} \\ \vdots \\ B_{q,E}^{p,1} \\ B_{1,G}^{x,1} \\ \vdots \\ B_{y,G}^{x,1}
\end{bmatrix} \tag{17}$$

The number of GPS, Galileo and BDS stations is n, q and y respectively. Because FCB usually has one cycle incontinuity, that −0.4 and +0.6 are equivalent. In order to eliminate this incontinuity, we can use iteration method to add or subtract one cycle in Eq. (17) to make wide-lane FCB continuous. In the process of solving, attention should be paid to eliminating large errors to reduce the impact on FCB estimation.

3 Experimental Results

Multi-GNSS wide-lane FCB products are generated by using MGEX's station data. The station distribution is shown in Fig. 1. When generating observations, some stations with none or very few observation data are excluded.

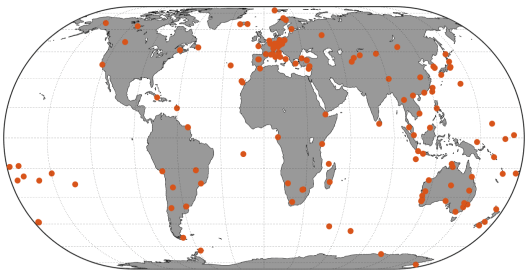

Fig. 1. MGEX stations distribution

Use the method in the previous section to generate GPS, Galileo, BDS wide-lane products, the selected data is 2107, DOY (Day of Year) 24 ~ 2017, DOY30 one week data, BDS only generates IGSO and MEO's wide-lane FCB products Data, using the method of reference [18] to eliminate the on-board multipath. Figure 2 is a schematic diagram of the GPS wide-lane FCB product. The reference satellite is G01. The average standard deviation of the GPS wide-lane FCB product is 0.026 cycle. The maximum standard deviation is 0.041 cycle for G13 satellite and the minimum is 0.012 cycle for G08 satellite. As can be seen from the figure, the stability of the wide-lane FCB of GPS is very high. It can be controlled within −0.5–0.5 cycle by adding or subtracting one cycle.

Figure 3 is a schematic diagram of Galileo's wide-lane FCB product. E01 is the reference satellite, and Galileo's stability during the week is also very high. The average standard deviation was 0.015 cycle, the largest standard deviation was 0.026 cycle for E02 satellite, and the smallest was 0.008 cycle for E8 satellite.

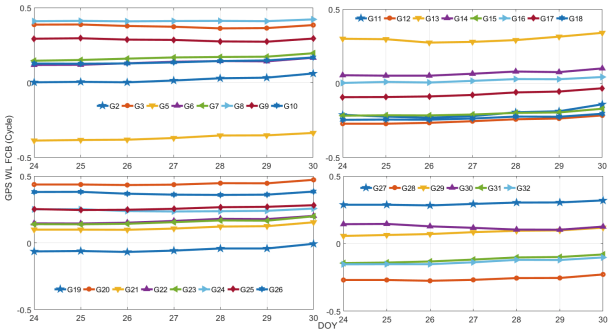

Fig. 2. GPS wide-lane FCB products

Figure 4 is a schematic diagram of the BDS wide-lane FCB product. C06 is the reference satellite. The above two subgraphs do not use the model to eliminate the on-board multipath. It can be seen that the stability of the wide-lane product is very poor, and the values of the adjacent days changed more than 0.1 cycle. The following two

subgraphs are a map of the wide-lane FCB products after correcting the on-board multipath, and the stability of the wide-lane products is significantly improved. Table 3 shows the average standard deviation of BDS IGSO and MEO wide-lane FCB before and after on-board multipath correction.

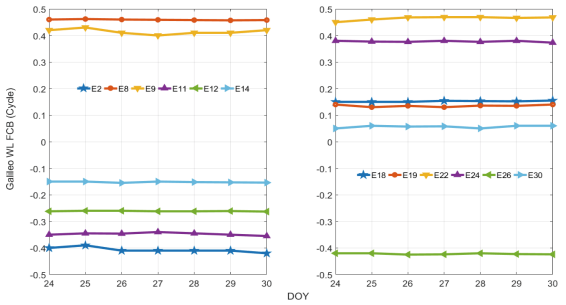

Fig. 3. Galileo wide-lane FCB products

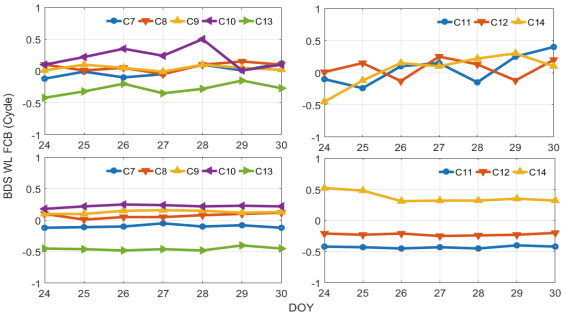

Fig. 4. BeiDou wide-lane FCB products

Table 3. The average standard deviation of wide-lane FCB before and after multipath correction

	IGSO (cycle)	MEO (cycle)
Before correction	0.151	0.245
After correction	0.028	0.033

In order to verify the validity of the product, the residual after using the wide-lane product is calculated, and the effective property of the product can be analyzed by using the distribution of the residual. Figure 5(a), (b), and (c) are the residual distribution maps of GPS, Galileo, and BDS respectively. The proportions of GPS, Galileo, and BDS's residuals within ±0.25 cycle are 95.0%, 93.2%, 91.8% respectively. Thus, proved the effectiveness of the multi-GNSS wide-lane product and the estimation method.

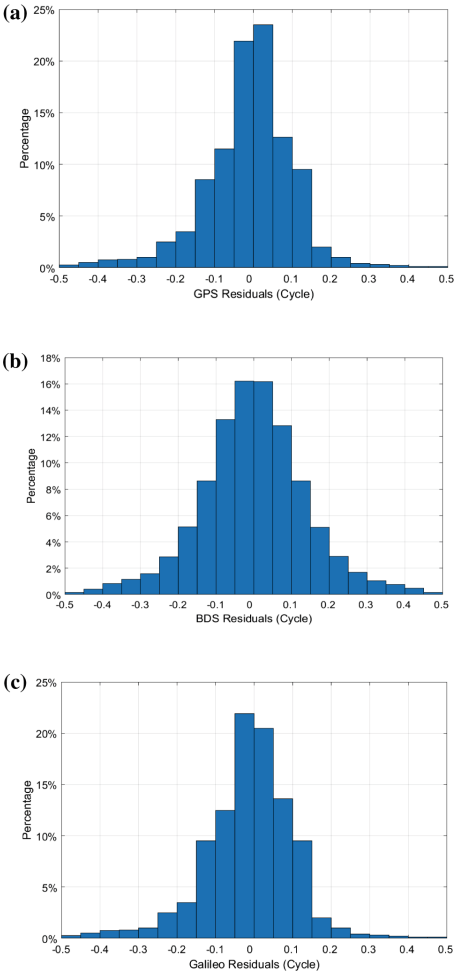

Fig. 5. (a) GPS residual distribution (b) Galileo residual distribution (c) Corrected BDS residual distribution

4 Conclusion

Based on the observations and precise products provided by MGEX, the ambiguity resolution of multi-GNSS carrier phase is deduced in detail, and a multi-GNSS wide-lane FCB products estimation method is proposed. By using the observation data in 2017, DOY24 ~ 2017, DOY30, the wide-lane FCB products of GPS, Galileo and BDS were generated. The GPS and Galileo products have good stability during this period, and after on-board multipath correction the FCB products of BDS wide-lane are equivalent to the stability of GPS and Galileo. At the same time, the validity of FCB products is verified by analyzing the wide-lane residuals of GPS, Galileo and BDS, and the correctness and feasibility of the proposed method are proved.

References

1. Zumberge JF, Heflin MB, Jefferson DC et al (1997) Precise point positioning for the efficient and robust analysis of GPS data from large networks. J Geophys Res Solid Earth 102 (B3):5005–5017
2. Kouba J, Héroux P (2001) Precise point positioning using IGS orbit and clock products. GPS Solutions 5(2):12–28
3. Li X, Ge M, Lu C et al (2014) High-rate GPS seismology using real-time precise point positioning with ambiguity resolution. IEEE Trans Geosci Remote Sens 52(10):6165–6180
4. Li X, Dick G, Ge M et al (2014) Real-time GPS sensing of atmospheric water vapor: Precise point positioning with orbit, clock, and phase delay corrections. Geophys Res Lett 41 (10):3615–3621
5. Geng J, Teferle FN, Shi C et al (2009) Ambiguity resolution in precise point positioning with hourly data. GPS Solutions 13(4):263–270
6. Ge M, Gendt G, Rothacher M et al (2008) Resolution of GPS carrier-phase ambiguities in precise point positioning (PPP) with daily observations. J Geodesy 82(7):389–399
7. Li X, Ge M, Zhang H et al (2013) A method for improving uncalibrated phase delay estimation and ambiguity-fixing in real-time precise point positioning. J Geodesy 87(5):405–416
8. Loyer S, Perosanz F, Mercier F et al (2012) Zero-difference GPS ambiguity resolution at CNES–CLS IGS analysis center. J Geodesy 86(11):991–1003
9. Li P, Zhang X, Ren X et al (2015) Generating GPS satellite fractional cycle bias for ambiguity-fixed precise point positioning. GPS Solutions 20(4):771–782
10. Xiao G, Sui L, Heck B et al (2018) Estimating satellite phase fractional cycle biases based on Kalman filter. GPS Solutions 22(3):82
11. Li X, Li X, Yuan Y et al (2017) Multi-GNSS phase delay estimation and PPP ambiguity resolution: GPS, BDS, GLONASS, Galileo. J Geodesy 92(6):579–608
12. Li X, Ge M, Dai X et al (2015) Accuracy and reliability of multi-GNSS real-time precise positioning: GPS, GLONASS, BeiDou, and Galileo. J Geodesy 89(6):607–635
13. Kouba J (2009) A guide to using international GNSS service (IGS) products
14. Guo F, Li X, Zhang X (2017) The contribution of Multi-GNSS Experiment (MGEX) to precise point positioning. Adv Space Res 59(11):2714–2725
15. Hatch R (1982) The synergism of GPS code and carrier measurements. In: International Geodetic Symposium on Satellite Doppler Positioning at Physical Sciences Laboratory of New Mexico State University, pp 1213–1231
16. Melbourne WG (1985) The case for ranging in GPS-based geodetic systems. In: Proceedings of First International Symposium on Precise Positioning with the Global Positioning System, pp 373–386
17. Wübbena G (1985) Software developments for geodetic positioning with GPS using TI-4100 code and carrier measurements. In: Proceedings of First International Symposium on Precise Positioning with the Global Positioning System, pp 403–412
18. Wanninger L, Beer S (2015) BeiDou satellite-induced code pseudo-range variations: diagnosis and therapy. Springer, New York, pp 639–648

Ambiguity Single Epoch Fixing Method Based on Prior Coordinate Constraints

Jianjian Jin(✉), Chengfa Gao, Ruicheng Zhang, and Bo Chen

School of Transportation, Southeast University, Nanjing 211189, China
jinjj_seu@foxmail.com

Abstract. In this paper, based on the condition that the coordinates of the base station are precisely known, when the coordinate error of the rover is centimeter, a method of fixing the ambiguity single epoch under the short baseline based on GPS dual-frequency observation is proposed. Firstly, the GPS dual-frequency linear combination is searched to select a combination of (−3, 4) and (1, −1) wide lanes with longer wavelength and less noise, then, the two sets of wide lane ambiguity are directly solved by using the higher precision station distance and double difference combined observations, and the ambiguity is directly fixed by rounding method; The two fixed wide lane ambiguities are linearly combined to obtain the basic ambiguity of the GPS system, and the ambiguity is returned to the observation equation to realize the single epoch solution baseline vector. The experimental results show that the proposed method can achieve single-epoch fixation of ambiguity when the error of each direction of the rover coordinates is centimeter, and for satellites with large observation noise can be eliminated by gross error detection, thus ensuring the reliability of the single epoch positioning solution.

Keywords: Coordinate constraint · Integer ambiguity · Short baseline · Single epoch · GPS

1 Introduction

With the development of the past forty years, GPS technology has made great progress. In static positioning, thousands of kilometers of baseline can be solved through long-term observation. If GAMIT is used, the positioning accuracy can reach centimeter level [1]. For short baselines of static measurements, typically within 10 km, it takes only a few minutes to fix the ambiguity and achieves millimeter accuracy. For medium and long baselines, the base ambiguity between reference stations can be quickly determined in a short time by additional ionospheric constraints, and the baseline solution can be achieved [2]. GPS positioning generally uses carrier and pseudorange observations. Only when the full-circumference ambiguity is correctly fixed, the carrier observations can be used to achieve high-precision positioning. Therefore, the fast and accurate fixation of the integer ambiguity is crucial.

The fixation of ambiguity mainly includes two aspects, one is to solve the ambiguity floating point value, and the other is the ambiguity searching. The solution of the ambiguity floating point value uses the least squares estimation, but due to the strong

J. Sun et al. (Eds.): CSNC 2019, LNEE 563, pp. 151–161, 2019.
https://doi.org/10.1007/978-981-13-7759-4_14

collinearity of the coordinate three-dimensional parameters and the ambiguity parameter, the accuracy of the calculated ambiguity floating point value is very poor [3]; In addition, the search for ambiguity mainly includes least squares searching method, LAMBDA algorithm, fast ambiguity approximation method (FARA) and ARCE algorithm [4, 5].

The search algorithm mentioned above generally require the use of multiple observation epoch data, and the ambiguity cannot be correctly fixed in a single epoch. In the practical application of GPS, there are many constraints on the coordinates and ambiguity parameters. For example, in the slope deformation measurement, the coordinates of the base station are accurately known. The coordinates of the monitoring station are within a certain error range [6], and the prior coordinates can be used as constraints. Based on the dual-frequency observation of GPS system, this paper searches for its linear combination, constructs a linear combination with long wavelength, small noise and weak ionosphere, and uses the constraints of prior coordinates to realize the fixation of the ambiguity single epoch under the short baseline.

2 Dual Frequency Observations and Their Linear Combinations

Considering the influence of the ionosphere and troposphere on the refraction of satellite signals, the difference between the receivers k, l and the satellites s and r, the carrier double-difference observation equation can be obtained as:

$$\Delta\nabla\phi^{sr}_{(i,j)kl} = \Delta\nabla\rho^{sr}_{kl} + \Delta\nabla T^{sr}_{kl} - \eta_{(i,j)} \cdot \Delta\nabla I^{sr}_{kl} + \lambda_{(i,j)} \cdot \Delta\nabla N^{sr}_{(i,j)kl} + \Delta\nabla\varepsilon_{\phi^{sr}_{(i,j)kl}} \tag{1}$$

In the formula, $\Delta\nabla$ is a double-difference operator. $\Delta\nabla\phi^{sr}_{(i,j)kl}$ is the combined carrier observation in meters, $\Delta\nabla\rho^{sr}_{kl}$, $\Delta\nabla T^{sr}_{kl}$ are the double-difference station star distance and double-difference tropospheric delay values, $\Delta\nabla I^{sr}_{kl}$ is the double-difference ionospheric delay at the L1 frequency of the GPS system, $\Delta\nabla N^{sr}_{(i,j)kl}$ is the integer ambiguity of the combined observations, $\eta_{(i,j)}$ is the ionospheric delay factor for combined observations, $\Delta\nabla\varepsilon_{\phi^{sr}_{(i,j)kl}}$ is the residual error of the carrier, i, j are the two frequencies of the GPS system.

The dual-frequency linear combination observations as follows:

$$\Delta\nabla\phi_{(i,j)} = \frac{(i \cdot f_1 \cdot \Delta\nabla\phi_1 + j \cdot f_2 \cdot \Delta\nabla\phi_2)}{f(i,j)} \tag{2}$$

i, j are the coefficient of the linear combination of observations, $f(i,j)$ is the frequency of combined observations, f_1, f_2 represent the frequency of the L1 and L2 bands of the GPS system, $\Delta\nabla\phi_1$, $\Delta\nabla\phi_2$ indicate the carrier observations of the L1 and L2 bands of the GPS system.

The ambiguity of dual-frequency linear combined observations as follows:

$$\Delta\nabla N_{(i,j)} = i \cdot \Delta\nabla N_1 + j \cdot \Delta\nabla N_2 \tag{3}$$

The frequency and wavelength of the dual-frequency linear combination observations are expressed as:

$$\begin{cases} f_{(i,j)} = i \cdot f_1 + j \cdot f_2 \\ \lambda_{(i,j)} = \frac{c}{f_{(i,j)}} \end{cases} \tag{4}$$

The accuracy of the observation values in each frequency band of the GPS system is generally considered identical, and assume it $\sigma\Delta\nabla\phi$, the accuracy of the observation value is calculated as:

$$\begin{aligned} \sigma\Delta\nabla_{(i,j)} &= \pm \frac{\sqrt{(i \cdot f_1)^2 + (j \cdot f_2)^2}}{f_{(i,j)}} \sigma\Delta\nabla\phi \\ &= \mu_{(i,j)} \sigma\Delta\nabla\phi \end{aligned} \tag{5}$$

In the formula, $\mu_{(i,j)}$ is the noise amplification factor of the combined observation.

$$\eta_{(\mathrm{i},j)} = \frac{f_1^2 (i/f_1 + j/f_2)}{f_{(i,j)}} \tag{6}$$

In the formula, $\eta_{(\mathrm{i},j)}$ is the ionospheric delay factor for combined observation.

The observation values on the two frequency bands of the GPS system L1 and L2 are linearly combined. In order to maintain the combined ambiguity $\Delta\nabla N_{(i,j)}$ as an integer characteristic, the combination coefficient (i, j) should take an integer. $\mu_{(i,j)}$ is the noise amplification factor of the combined observations, the larger the noise, the more difficult it is to fix the ambiguity. Therefore, the combination coefficient is limited here, the value is in the interval [−10, 10], and is not zero at the same time, the frequency $f_{(i,j)}$ of the combined observation should be greater than zero. By linearly combining the dual-frequency observations of the GPS system, the following common combinations can be obtained. The combined results are shown in Table 1.

Table 1. GPS dual-frequency linear combination

Combination number	Combination factor (i, j)	Wavelength $\lambda_{(i,j)}/m$	Ionospheric factors $\eta_{(i,j)}$	Noise factor $\mu_{(i,j)}$
1	(−7, 9)	14.6526	350.3500	762.9685
2	(4, −5)	1.8316	−23.2604	53.7448
3	(−3, 4)	1.6281	18.2519	37.0120
4	(1, −1)	0.8619	−1.2833	5.7422
5	(−6, 8)	0.8140	18.2519	37.0120
6	(5, −6)	0.5861	−8.3160	21.0836
7	(−2, 3)	0.5636	5.4788	9.1111

3 Wide Lane Ambiguity Fixed

In the case of a short baseline, after the double-difference between the base station and the rover, the satellite clock difference and the receiver clock difference can be eliminated, and the satellite orbit error and the ionospheric residual error are negligible. The tropospheric delay error is related to the meteorological conditions of the station, and the model correction can be used. The multipath effect has no correlation and is related to the observation environment around the station. The ambiguity $\Delta\nabla N_{(i,j)}$ can be directly solved according to the formula (1). The formula is:

$$\Delta\nabla N_{(i,j)} = \frac{(\Delta\nabla\phi_{(i,j)} - \Delta\nabla\rho - \Delta\nabla T + \eta_{(i,j)} \cdot \Delta\nabla I)}{\lambda_{(i,j)}} \tag{7}$$

The error in ambiguity $\Delta\nabla N_{(i,j)}$ can be expressed as:

$$\sigma_{N_{(i,j)}} = \frac{1}{\lambda_{(i,j)}} \sqrt{\sigma^2_{\Delta\nabla\phi_{(i,j)}} + \sigma^2_{\Delta\nabla\rho} + \sigma^2_{\Delta\nabla T} + \eta^2_{(i,j)} \cdot \Delta\nabla I^2} \tag{8}$$

$\sigma_{\Delta\nabla\phi_{(i,j)}}$ is the intermediate error of the combined phase observations, $\sigma_{\Delta\nabla\rho}$ is the medium error of the double-difference geometric distance, $\sigma_{\Delta\nabla T}$ is the error in the residual error of the double-difference troposphere, $\sigma_{\Delta\nabla I}$ is the error in the double-difference ionospheric error. Assume that the medium errors in the three directions of the rover coordinates are equal, $\sigma_x = \sigma_y = \sigma_z$, Then there are:

$$\sigma_{\Delta\nabla\rho} = \sqrt{2}\sigma_x \tag{9}$$

Make some transformations to Eq. (8):

$$\sigma_{N_{(i,j)}} = \sqrt{\frac{1}{\lambda^2_{(i,j)}}(2\sigma^2_x + \sigma^2_{\Delta\nabla T} + \eta^2_{(i,j)} \cdot \Delta\nabla I^2) + \sigma^2_\varphi} \tag{10}$$

In the case of a short baseline, the medium error of the tropospheric error is assumed to be $\sigma_{\Delta\nabla T} = 0.01$ m, Error in ionospheric error is $\sigma_{\Delta\nabla I} = 0.01$ m, The double-difference carrier observation noise σ_φ is approximately 0.02 weeks. It can be seen from Table 1 that although the combined observation value $\Delta\nabla\phi_{(-7,9)}$ has a maximum wavelength of 14.6662 m, the combined observation noise amplification factor and the ionospheric factor are both large, so the combined observation is discarded. Selecting (4, −5), (−3, 4), (1, −1), (1, 0), (0, 1), a total of five sets of linear combination observations, the relationship between the error $3\sigma_{N_{(i,j)}}$ and σ_x in the three times of ambiguity is plotted. The results are shown in Figs. 1 and 2, respectively.

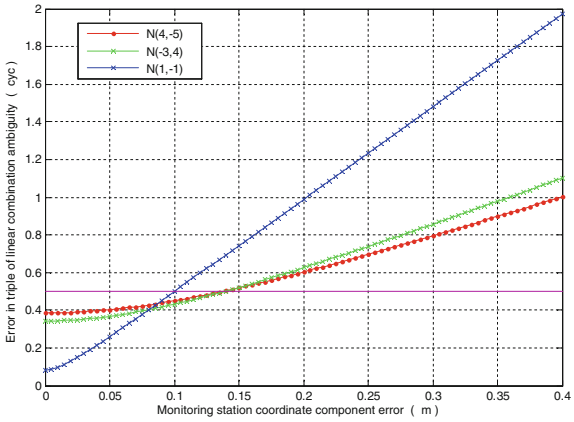

Fig. 1. The relationship between the coordinate error of the monitoring station and the error of triple the combined ambiguity

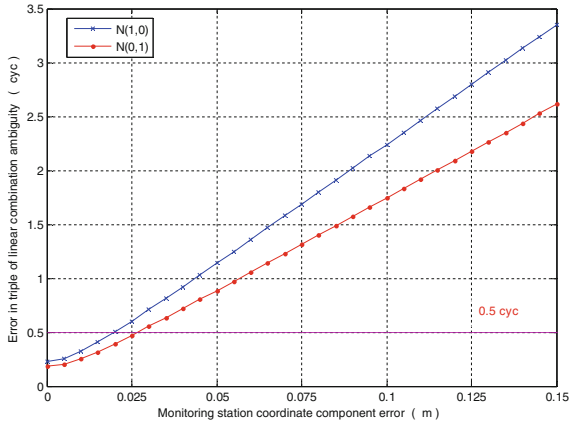

Fig. 2. The relationship between the coordinate error of the monitoring station and the error of triple the combined ambiguity

As seen from Fig. 1, when the initial coordinate error of the monitoring station is 10 cm, The error of three times of the combined observations $\Delta\nabla\phi_{(4,-5)}$, $\Delta\nabla\phi_{(-3,4)}$, $\Delta\nabla\phi_{(1,-1)}$ is less than 0.5 weeks, and the ambiguity floating point value that is calculated according to the formula (7) can be directly fixed, when the initial coordinate error of the monitoring station is greater than 10 cm and less than 14 cm, the error between the three times of the combined observations $\Delta\nabla\phi_{(4,-5)}$ and $\Delta\nabla\phi_{(-3,4)}$ is still less than 0.5 weeks. At this time, the error in the triple of the wide lane combination $\Delta\nabla\phi_{(1,-1)}$ is greater than 0.5 weeks, and the ambiguity floating point value cannot be directly rounded to obtain a fixed solution, ambiguity search space $\left[\Delta\nabla N_{(i,j)} - 3\sigma_{N_{(i,j)}}, \Delta\nabla N_{(i,j)} + 3\sigma_{N_{(i,j)}}\right]$ should be established, searching for ambiguity to get a fixed

solution. In Fig. 2, when the initial coordinate error of the monitoring point exceeds 2 cm, the error of three times the basic ambiguity is greater than 0.5 weeks, and the fixed ambiguity cannot be rounded off for the ambiguity floating point value.

In the small deformation monitoring, such as slopes and dams, the initial coordinates of the monitoring points are known, and the point coordinates change little or periodically with time. In this case, whether it is post-processing data processing or real-time deformation monitoring, the observations can be linearly combined, the ambiguity floating point solution is calculated using formula (7), and then the fixed combination ambiguity is rounded. It can be seen from Fig. 1 that when the coordinate error is less than 10 cm, that is, when the point deformation is less than 17 cm, the ambiguity floating point value of the combined observation value can be directly rounded to obtain a fixed ambiguity solution. Since the medium error and the noise amplification factor ratio of the combined observations $\Delta\nabla\phi_{(-3,4)}$ and $\Delta\nabla\phi_{(1,-1)}$ are smaller than $\Delta\nabla\phi_{(4,-5)}$, the linear combination of (−3, 4) and (1, −1) is preferable in the ambiguity fixation.

If the ambiguity of any two linear combinations of the GPS system can be obtained, the fundamental ambiguity may be solved according to formula (11).

$$\begin{bmatrix} N_1 \\ N_2 \end{bmatrix} = \begin{bmatrix} i & j \\ m & n \end{bmatrix}^{-1} \begin{bmatrix} N_{(i,j)} \\ N_{(m,n)} \end{bmatrix} \tag{11}$$

When the combined observations select $\Delta\nabla\phi_{(-3,4)}$ and $\Delta\nabla\phi_{(1,-1)}$, the base ambiguity can be solved according to Eq. (12), where round() means rounding the ambiguity.

$$\begin{bmatrix} N_1 \\ N_2 \end{bmatrix} = \begin{bmatrix} round(\Delta\nabla N_{(-3,4)}) + 4 \cdot round(\Delta\nabla N_{(1,-1)}) \\ round(\Delta\nabla N_{(-3,4)}) + 3 \cdot round(\Delta\nabla N_{(1,-1)}) \end{bmatrix} \tag{12}$$

In the experiment, the already fixed GPS base ambiguity is used, and the equation is constructed back to the equation. In the data processing process, the system internal stochastic model adopts the elevation angle weighting model [7], as shown in formula (14). At the same time, in order to improve the accuracy of the model solution, the pseudorange and the carrier observation equation are connected. According to the accuracy of the carrier phase and pseudorange measurement, the empirical weighting method is adopted, and the ratio is 100:1. The equation is:

$$\begin{bmatrix} l_r^i & m_r^i & n_r^i \\ l_r^i & m_r^i & n_r^i \end{bmatrix} \cdot \begin{bmatrix} \delta x \\ \delta y \\ \delta z \end{bmatrix} = \begin{bmatrix} \Delta\nabla P^i \\ \Delta\nabla L_{(1,0)}^i - \lambda_{(1,0)} \cdot \Delta\nabla N_{(1,0)}^i \end{bmatrix} \tag{13}$$

In formula 13, $\Delta\nabla L = \Delta\nabla\phi - \Delta\nabla\rho - \Delta\nabla T + \eta_{(i,j,k)} \cdot \Delta\nabla I$, the superscript number i represents the satellite number. $\delta x, \delta y, \delta z$ are the baseline vector for the base and rover station.

$$\sigma_i^2(E) = \begin{cases} \frac{\sigma}{\sin^2(E)}, E < 30^\circ \\ \frac{\sigma}{\sin(E)}, E \geq 30^\circ \end{cases} \tag{14}$$

In formula 14, σ_i is the error in the observation, E is the elevation angle of the satellite.

When the original data is collected, the observation data is inevitably caused by the external observation environment. If the monitoring data is directly used for the positioning solution, unexpected results or errors will occur, and the real point coordinates cannot be obtained. In the process of adjustment, due to the influence of least squares, an observation with a coarse error will cause the residual of multiple observations to exceed the limit. Therefore, it is difficult to judge which observation value has a gross error (including a fixed ambiguity error) by observing the residual value of the observation value. Therefore, in the single epoch baseline data processing process, after obtaining the satellite's full-circumference ambiguity, the residuals of the satellite observations should be normalized, and the satellites whose standardized residuals exceed the threshold value should be eliminated, and the least squares estimation can be performed again.

In the baseline solution of a short baseline single epoch, the least squares solution of the baseline vector $\hat{X}$ is:

$$\hat{X} = \left(B^T PB\right)^{-1} \cdot (B^T PL) \tag{15}$$

The residual of the observation and its cofactor matrix can be expressed as:

$$\begin{cases} v = B \cdot \hat{X} - L \\ Q_v = P^{-1} - B(B^T PB)^{-1} B^T \end{cases} \tag{16}$$

The diagonal element $q_{v_1}, q_{v_2} \cdots q_{v_n}$ of Q_v is the reciprocal of the weight of the satellite observation residual. When the observations are independent of each other, there are:

$$q_{v_1} = \frac{1}{P_i} - B_i (B^T PB)^{-1} B_i^T \tag{17}$$

Standardizing the residuals yields:

$$\tilde{v}_i = \frac{v_i}{\sigma_0 \sqrt{q_{v_i}}} \tag{18}$$

σ_0 is the error in unit weight, v_i is the $i-th$ satellite observation residual. When there is no gross difference in the observed value, $\tilde{v}_i$ is a random variable that conforms to the standard positive distribution. When $|\tilde{v}_i|$ is greater than 2, there is a 95% confidence interval that the satellite has gross error or ambiguity fixed error, reject this satellite, and then re-evaluate the parameter.

4 Experiment Analysis

The experimental data used the two-hour static data of the JLH0 station measured on the campus on November 20, 2018, and formed a short baseline of 3.8 km with the JNNF of the Nanjing Metrology Institute CORS station. The data sampling rate was 5 s.

In the data processing process, the cut-off height angle is set to 15°, the stochastic model adopts the elevation angle model as shown in formula (14), the tropospheric delay is corrected using the UNB3M model [8], and the satellite coordinate calculation uses the broadcast ephemeris. In order to see the fixed effect of the wide lane ambiguity, the deformation was simulated in the experiment, and a coordinate error of 10 cm was added to the initial coordinates of the rover station JLH0.

In the experiment, the GPS system G20 satellite has the highest altitude angle, and will be set as the reference satellite. The non-reference satellite numbers are G10, G12, G15, G21, G24, G32. The dual-frequency observations of the GPS system are linearly combined, and the wide lane ambiguity floating-point value is solved by the formula (7). Since the coordinates of the two stations are known, the wide lane ambiguity can be solved according to the network RTK mode. By subtracting the fixed solution from the ambiguity floating point value, the wide lane ambiguity deviation can be obtained. The results are shown in Figs. 3 and 4, respectively.

In the case where the deviation of the initial coordinates in each direction is 10 cm, the effect of fixing the ambiguity using the LAMBDA algorithm is examined, and the ambiguity deviation on the L1 frequency band of each satellite is separately counted, and the result is shown in Fig. 5.

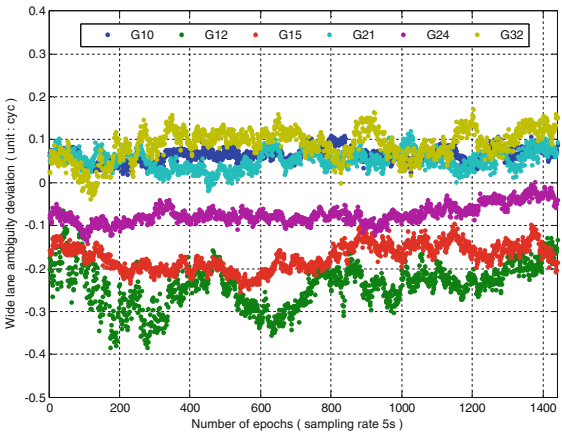

Fig. 3. GPS wide lane ambiguity $\Delta\nabla N_{(1,-1)}$ deviation

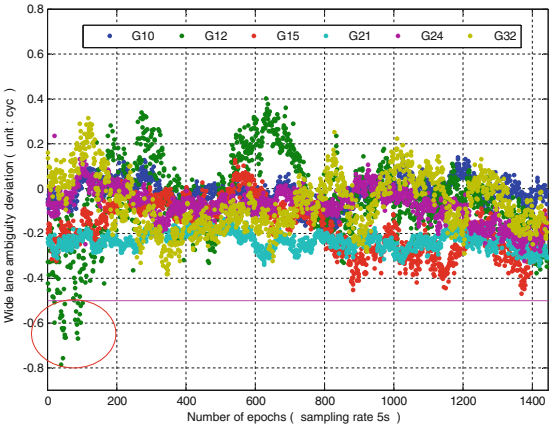

Fig. 4. GPS wide lane ambiguity $\Delta\nabla N_{(-3,4)}$ deviation

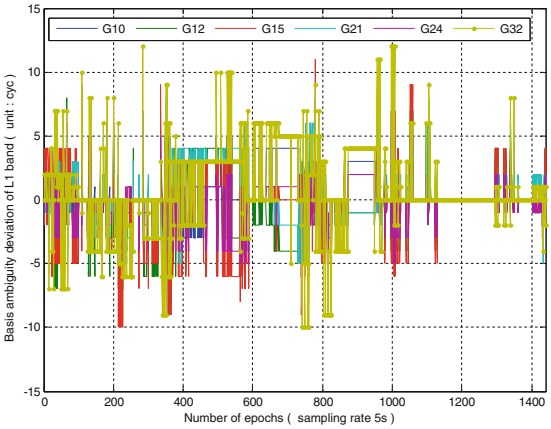

Fig. 5. GPS L1 ambiguity deviation

From Fig. 3, it can be seen that the GPS wide lane ambiguity $\Delta\nabla N_{(1,-1)}$ deviation is within ± 0.4 week, and the deviation results are evenly distributed without a large amplitude jump. Therefore, a single epoch is rounded to the ambiguity floating point value, and $\Delta\nabla N_{(1,-1)}$ can be fixed. In Fig. 4, the ambiguity floating point value deviation of the G10, G15, G21, G24, G32 satellites is within ± 0.4 week, the single epoch has a fixed success rate of ambiguity floating point value rounding up to 100%. In the beginning of the G12 satellite, the wide lane ambiguity deviation exceeds 0.5 week, as shown in the circle in Fig. 4, the number of wide-lane ambiguity deviations over 0.5 weeks in the whole period is counted, divided by the total epoch number, and the fixed success rate of the G12 satellite wide lane ambiguity is 97.9%. In Fig. 5, the single epoch uses the least squares to solve the ambiguity floating point value, and then uses the LAMBDA algorithm to search for the fixed base ambiguity based on the ambiguity floating point value and its covariance matrix. During the observation

period, the deviation of the fixed solution of most satellite ambiguities from the true value is 5 weeks, indicating that the initial point error has a large fixed influence on the fundamental ambiguity.

In the experiment, due to the low elevation angle of the G12 satellite, the observation value is relatively noisy, and the deviation of the wide lane ambiguity floating point value solved by the Eq. (7) is too large. If the $\Delta\nabla N_{(-3,4)}$ ambiguity floating point value is rounded, the result has a one-week deviation from the true value. According to Eq. (12), this will result in a one-week deviation between the underlying ambiguity and the correct fixed solution. At this time, gross error rejection should be performed. Firstly, the residual value of the observation value of each satellite is solved and normalized. When the standardized residual is greater than 2, the satellite is considered unhealthy, it will be eliminated, the parameter estimation is repeated to solve the baseline vector.

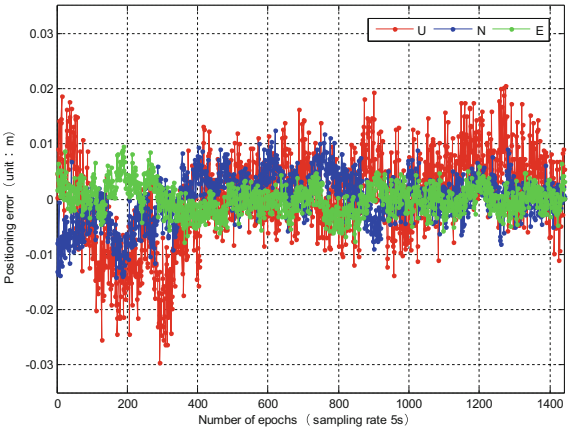

Fig. 6. NEU positioning error in all directions

When the standardized residuals satisfy the threshold, the deviations of the respective epochs N, E, and U are counted as shown in Fig. 6. In Fig. 6, the errors in the plane N and E directions are 4.3 mm and 2.6 mm, respectively. The elevation direction is slightly weaker than the plane, and the medium error is 8.2 mm. There is no large deviation in the whole, which indicates that the positioning result is reliable when the initial coordinates of the monitoring station are 10 cm in each direction.

5 Conclusion

In this paper, GPS dual-frequency is the focal point. Firstly, the dual-frequency linear combination is searched, which is preferred to combine the long-wavelength, low-noise (−3, 4) and (1, −1) wide lanes. Under the condition that the coordinates of base and rover station are known as a priori, the ambiguity is directly fixed by rounding the

ambiguity floating value, and then the two sets of wide lane ambiguities are linearly combined to solve the basic ambiguity on the L1 and L2 bands of GPS; The base ambiguity of the solution is solved, and the solution of the baseline vector is realized by a single epoch using least squares estimation. At the same time, the residuals of the observations are screened to eliminate the satellites with large observation noise or the satellites whose ambiguity is fixed due to noise, thus ensuring the reliability of the solution results. The proposed method in this paper solves the baseline solution more than the traditional multi-epoch, which greatly reduces the number of epochs required for correct fixed ambiguity, effectively improves the timeliness of GPS ambiguity resolution, and can be applied to small-scale deformation. During monitoring, such as dam and slope monitoring, the coordinates of the monitoring station are known as a priori, and the deformation is in the centimeter level, the ambiguity can be fixed by using the single epoch method proposed in the paper.

References

1. Blewitt G (1989) Carrier phase ambiguity resolution for the global positioning system applied to geodetic baselines up to 2000 Km. J Geophys Res 94(B8):10187–10203
2. Wielgosz P (2011) Quality assessment of GPS rapid static positioning with weighted ionospheric parameters in generalized least squares. GPS Solution 15(2):89–99
3. Li B, Shen Y (2009) Fast GPS ambiguity resolution constraint to available conditions. Geomatics Inf Sci Wuhan Univ 34(1):117–121
4. Teunissen PJG (1994) A new method for fast carrier phase ambiguity estimation. In: IEEE PLANS 1994, Las Vegas (1994)
5. Park C, Kim I, Lee JG et al (1996) Efficient ambiguity resolution using constraint equation. In: IEEE PLANS, position location and navigation symposium, pp 277–284
6. Xiong Y, Huang D, Zhang X (2001) A reliable GPS single epoch processing algorithm with known deformation interval constraints. Geomatics Inf Sci Wuhan Univ 26(1):51–57
7. Li D (2016) Influence of stochastic model on GPS/BDS joint positioning accuracy. Shandong University of Technology
8. Leandro RF, Langley RB, Santos MC (2008) UNB3m_pack: a neutral atmosphere delay package for radiometric space techniques. GPS Solutions 12(1):65–70

The Algorithm for Cycle Slip Detection and Repair Based on Pseudo-phase and Ultra-wide Lane Carrier

Lilu Cui[1,3], Jiangyu Qian[1], Zhengbo Zou[2(✉)], Xiaolong Wang[3], and Shi Du[1]

[1] School of Architecture and Civil Engineering, Chengdu University, Chengdu 610106, China
lilucui@l26.com
[2] Key Laboratory of Earthquake Geodesy, Institute of Seismology, China Earthquake Administration, Wuhan 430071, China
zouzb@l26.com
[3] School of Geodesy and Geomatics, Wuhan University, Wuhan 430079, China

Abstract. Aiming at the problem of cycle-slip detection and repair, the ultra-wide lane combination is used to assist the pseudo-distance phase combination in order to detect and repair cycle-slip because of its characteristics of weak noise and weak ionosphere in this paper. In order to remove the influence of insensitivity cycle-slip, the optimal combination coefficient is obtained according the numerical analysis results and the ill-posed equation has been avoided by using the minimum 2-norm as condition. The BeiDou triple-frequency measured data has been processed by this algorithm. These results show that this algorithm can effectively detect and repair all cycle-slip including different sizes and insensitive ones.

Keywords: Pseudo-phase · Cycle-slip test · Insensitive cycle-slip · Ultra-wide lane

1 Introduction

Accurate and effective algorithm for cycle-slip detection and repair is the necessary condition for high-precision navigation and positioning [1]. According to the characteristics of triple-frequency carrier phase observation, domestic and foreign scholars have successively researched on the detection and repair triple-frequency cycle-slip algorithm. The pseudo-range combination method is a commonly used processing algorithm at present, which is simple and easy to implement and has high accuracy, but it is easily affected by ionospheric delay and observation noise [2–4]. Ionospheric residuals method is susceptible to ionospheric activity and there is multiple solutions problem [5–7]. Geometric-free phase combination has high detection accuracy, but there is insensitive cycle-slip problem and cycle-slip repair is complex, which is bad for programming [8, 9]. Therefore, combining the two algorithms to detect cycle-slip is the research hotspot in this field.

J. Sun et al. (Eds.): CSNC 2019, LNEE 563, pp. 162–173, 2019.
https://doi.org/10.1007/978-981-13-7759-4_15

In this paper, due to the features of pseudo-range combination which is high precision detection and easy realization of program and ones of ultra-wide lane combination which is long wavelength, weak ionospheric delay and weak noise, a new algorithm is proposed by using ultra-wide lane combination to improve pseudo-range combination. Finally, the validity and reliability of cycle-slip detection are analyzed in detail by calculating the BeiDou measured data, including insensitive cycle-slip. And the results show that the detection and repair of this method is accurately and effectively.

2 Cycle-Slip Detection

2.1 Pseudo-phase Model

The observation equation of triple-frequency pseudo-phase combination [10] is

$$P_{abc} = \rho + \kappa_{abc} I_1 + d_{abc} + m_{abc} + \varepsilon_{abc} \tag{1}$$

$$\lambda_{\alpha\beta\gamma}\Phi_{\alpha\beta\gamma} = \rho + \kappa_{\alpha\beta\gamma} I_1 + d_{\alpha\beta\gamma} + m_{\alpha\beta\gamma} + \lambda_{\alpha\beta\gamma} N_{\alpha\beta\gamma} + \varepsilon_{\alpha\beta\gamma} \tag{2}$$

Where ρ is the geopotential space with tropospheric influence, $P_{\alpha\beta\gamma}$ and $\Phi_{\alpha\beta\gamma}$ are respectively the pseudo-range and carrier combined observations, $\lambda_{\alpha\beta\gamma}$ is combination wavelength, α, β, γ is carrier phase combination coefficient, $\alpha, \beta, \gamma \in Z$, a, b, c is pseudo-phase combination coefficient, and $a + b + c = 1$, $a = b = c = 1/3$; κ_{abc} and $\kappa_{\alpha\beta\gamma}$ are respectively combination ionospheric delay amplification factor of pseudo distance and carrier phase, I_1 is ionospheric delay, m_{abc} and $m_{\alpha\beta\gamma}$ are respectively the multi-path effects of pseudo-range and carrier combination observations, $N_{\alpha\beta\gamma}$ is integer ambiguity, d_{abc} and $d_{\alpha\beta\gamma}$ are respectively the hardware delay of two combination observations, ε_{abc} and $\varepsilon_{\alpha\beta\gamma}$ are respectively the observation noise of two combination observations. Since the satellite and receiver are the same, the error related to satellite and receiver is negligible.

Due to the multipath effect and hardware delay little change with time, it can be neglected. Equation (1) subtract Eq. (2), then differentiated between the calendats.

$$\Delta N_{\alpha\beta\gamma} = \Delta\Phi_{\alpha\beta\gamma} - \frac{\Delta P_{abc}}{\lambda_{\alpha\beta\gamma}} + \frac{\kappa_{\alpha\beta\gamma} + \kappa_{abc}}{\lambda_{\alpha\beta\gamma}} \Delta I_1 - \frac{\Delta\varepsilon_{\alpha\beta\gamma} - \Delta\varepsilon_{abc}}{\lambda_{\alpha\beta\gamma}} \tag{3}$$

The last two terms on the right side of the equation are negligible because of the ionospheric changes between epoch and their coefficients are small. So the cycle-slip valuation and standard deviation of pseudo-phase combination are

$$\Delta\widehat{N}_{\alpha\beta\gamma} = \Delta\Phi_{\alpha\beta\gamma} - \frac{\Delta P_{abc}}{\lambda_{\alpha\beta\gamma}} \tag{4}$$

$$\sigma_{\Delta N_{\alpha\beta\gamma}} = \sqrt{2}\sqrt{(a^2 + b^2 + c^2)\sigma_p^2 \Big/ \lambda_{\alpha\beta\gamma}^2 + (\alpha^2 + \beta^2 + \gamma^2)\sigma_\Phi^2} \tag{5}$$

Where σ_p and σ_Φ are respectively observation mean square error of pseudo distance and carrier phase, $\sigma_P = 0.3$ m and $\sigma_\Phi = 0.01$ [11].

2.2 The Selection of Optimal Combination Coefficient

The key to construct the optimal cycle-slip test is to choose the combination coefficient. These coefficients should satisfy the following conditions [11]: (1) the bigger value of $\lambda_{\alpha\beta\gamma}$ is better, because the influence of multipath error can be reduced effectively; (2) the smaller coefficient of ΔI is better, then it can reduce the effect of ionospheric delay change between epoch; (3) the smaller value of $\sigma_{\Delta N_{\alpha\beta\gamma}}$ is better, because it could guarantee the detection and repair ability of cycle-slip test.

According above selection principles, the combination wavelength which is greater than 3 m, $|\alpha+\beta+r| \le 2$ and $\sigma_{\Delta N_{\alpha\beta\gamma}} \le 0.16$ week as search condition, α, β, γ has been searched within [−10, 10]. The search results are shown in Table 1.

Table 1. The parameter statistics of part of the phase combination coefficient

$\alpha+\beta+\gamma$	(α, β, γ)	$\lambda^{\alpha\beta\gamma}/m$	ζ/m^{-1}	$\sigma_{\Delta N_{\alpha\beta\gamma}}$/week	$4\sigma_{\Delta N_{\alpha\beta\gamma}}$/week
1	(−4, 0, 5)	3.055	12.186	0.121	0.484
1	**(−4, 1, 4)**	**8.146**	**12.225**	**0.087**	**0.347**
1	(−3, 5, −1)	3.576	12.551	0.108	0.433
1	**(−3, 6, −2)**	**13.330**	**12.590**	**0.101**	**0.403**
0	(−1, −6, 7)	3.963	−0.404	0.145	0.580
0	(−1, −5, 6)	20.947	−0.365	0.112	0.448
0	**(0, −1, 1)**	**4.888**	**−0.039**	**0.054**	**0.216**
0	**(1, 4 ,−5)**	**6.375**	**0.326**	**0.099**	**0.398**
0	(2, 8, −10)	3.188	0.652	0.199	0.795
−1	(3, −7, 3)	7.717	−12.629	0.12	0.48
−1	(4, −3, −2)	3.491	−12.303	0.104	0.414
−1	**(4, −2, −3)**	**12.219**	**−12.264**	**0.079**	**0.315**

According to Table 1, the three condition of optimal combination coefficient can't be met simultaneously. So $\sigma_{\Delta N_{\alpha\beta\gamma}}$ and ζ should be a priority in order to minimize the impact of ionospheric delay and observed noise. The bold part in Table 1 is the selected optimal pseudo-phase combination coefficient.

If the value of (i,j,k) cycle-slip combination are multiplied by the combination coefficients (α,β,γ) is zero, (i,j,k) is the insensitivity cycle slip of combinaton coefficients (α,β,γ). In order to test the detection ability of insensitivity cycle-slip of pseudo-phase combination, the number of insensitivity cycle-slip of these optimal combination coefficients within 10 weeks have been counted, and the results are shown in Table 2.

Table 2. The insensitive cycle-slip of pseudo-phase combination

(α,β,γ)	The number of insensitivity cycle-slip
(−4, 1, 4)	29
(−3, 6, −2)	**23**
(0, −1, 1)	120
(1, 4, −5)	**24**
(4, −2, −3)	**29**

According to the results of Table 2, Every pseudo-phase combination has insensitivity cycle-slip. In order to reduce the number of insensitive cycle-slip, two different pseudo-phase combination can commonly be used to detect cycle-slip. The number of insensitivity cycle-slip of these two combination coefficients within 10 week and 100 week have been counted, and the results are shown in Table 3. From this table, the number of insensitive cycle-slip of the first four combinations all are zeros, so these combinations are selected as the optimal combination coefficient.

Table 3. The of two pseudo-phase combination

(α,β,γ)	$(\lambda)_{\min}/m$	$(\zeta)_{\max}/m^{-1}$	$(\sigma_{\Delta N_{\alpha\beta\gamma}})_{\max}/\text{week}$	The number of insensitivity cycle-slip	
				≤ 10	≤ 100
(−4, 1, 4) (−3, 6, −2)	8.146	12.590	0.101	0	0
(−4, 1, 4) (0, −1, 1)	4.888	12.225	0.087	0	0
(−4, 1, 4) (1, 4, −5)	6.375	12.225	0.099	0	0
(−4, 1, 4) (4,−2, −3)	8.146	12.264	0.087	0	0
(−3, 6, −2) (0, −1, 1)	4.888	13.330	0.101	2	25
(−3, 6, −2) (1, 4, −5)	6.375	13.330	0.101	0	4
(−3, 6, −2) (4, −2, −3)	12.219	13.330	0.101	0	4
(0, −1, 1) (1, 4, −5)	4.888	6.375	0.099	10	100
(0, −1, 1) (4, −2, −3)	4.888	12.219	0.079	2	20
(1, 4, −5) (4, −2, −3)	**6.375**	**12.219**	**0.099**	**0**	**4**

2.3 Ultra-wide Lane Combination

The expression of triple-frequency M-W combination is [7]:

$$N_{i,j} = \frac{f_i - f_j}{f_i + f_j}\left(\frac{P_i}{\lambda_i} + \frac{P_j}{\lambda_j}\right) - (\varphi_i - \varphi_j) \tag{6}$$

Where $N_{i,j}$ is the combination cycle-slip, P_i, P_j is pseudo distance observation data. If combination coefficient is $(0, -1, 1)$, the ultra-wide lane combination can be acquired, which can make detection ability of cycle-slip to raise greatly and the effect of ionospheric delay and observation noise are weakened.

3 Cycle-Slip Repair

Combined pseudo-phase and ultra-wide lane combination, the equations are as follows [12, 13]:

$$\begin{bmatrix} \alpha_1 & \beta_1 & \gamma_1 \\ \alpha_2 & \beta_2 & \gamma_2 \\ 0 & -1 & 1 \end{bmatrix} \begin{bmatrix} \Delta N_1 \\ \Delta N_2 \\ \Delta N_3 \end{bmatrix} = \begin{bmatrix} \Delta \widehat{N}_{\alpha_1\beta_1\gamma_1} \\ \Delta \widehat{N}_{\alpha_2\beta_2\gamma_2} \\ N_{2,3} \end{bmatrix} \tag{7}$$

Where $(\Delta N_1, \Delta N_2, \Delta N_3)$ are respectively three cycle-slip value of carrier phase observation data. In order to prevent the problem of ill-posed equations, the smaller conditions number of coefficient matrix is better. So the 2-norm condition number of the coefficient matrix is calculated, which are shown in Table 4.

Table 4. Condition number of 2-norm of different combination coefficient matrix

Combination style	Condition number
(−4, 1, 4) (−3, 6, −2)	7.3818
(−4, 1, 4) (1, 4, −5)	7.7063
(−4, 1, 4) (4, −2, −3)	7.8234

Since the coefficient of ultra-wide lane combination coefficient is (0, −1, 1), pseudo-phase combination can't use the same coefficient. Based on the results in Tables 3 and 4, two coefficients of (−3, 6, −2) and (−4, 1, 4) have been adopted in this paper, which combinated ultra-wide lane combination to detect and repair cycle-slip.

4 Numerical Calculation and Analysis

The cycle-slip detection and repair ability of this algorithm has been verify under different condition including insensitive cycle-slip in this paper. The BeiDou no cycle-slip and no gross error measured data is from the GNSS center of Wuhan university, which is a sampling rate of 30 s and at Shanghai station on January 12, 2018. The data is from BeiDou-2 system, and the three frequency is 1561.098 MHz, 1207.14 MHz and 1268.52 MHz.

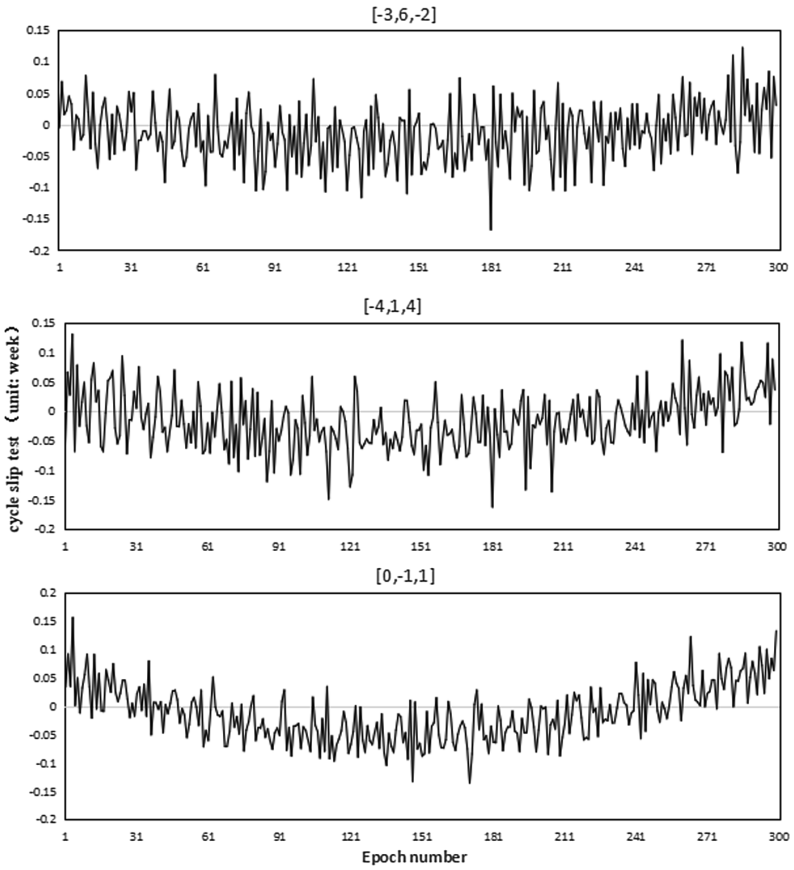

Fig. 1. The combination observation without cycle slip

Table 1 show that the value of three combination test quantities without cycle-slip. From this figure, the test quantities of two pseudo-phase combination and M-W combination were all in the range of [−.015, .0, 15]. So it is considered that the cycle-slip occurred when the test exceeds the above range (Fig. 1).

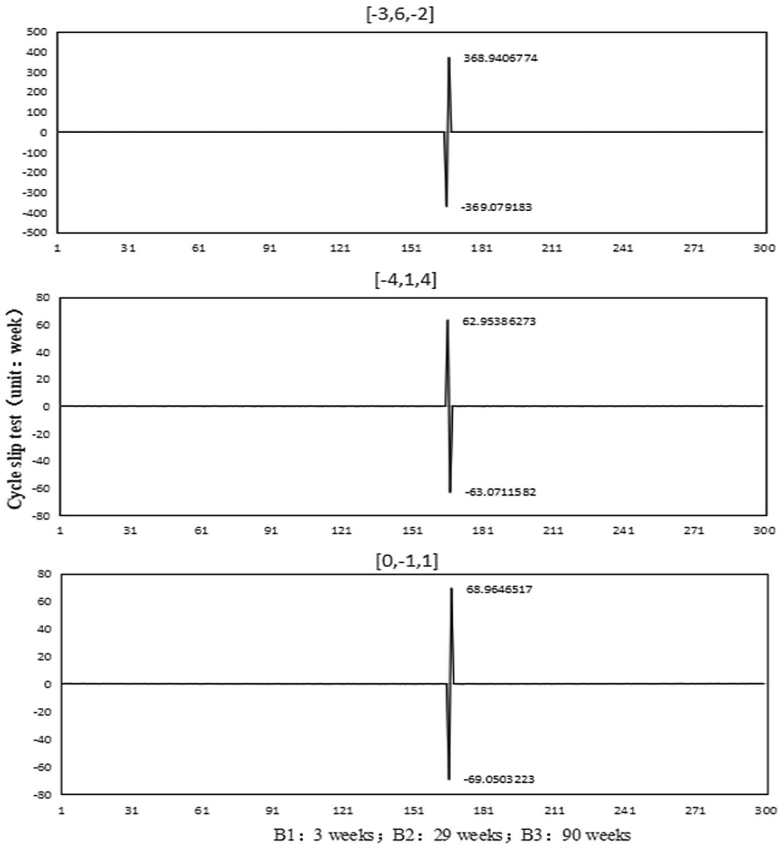

Fig. 2. The combination observation with different size of cycle slip

4.1 Different Size of Cycle-Slip Detection

The three different size cycle-slip of 3 week, 21 week and 90 week are respectively added on 168th epoch of B1, B2 and B3 frequency of original observation data without cycle-slip, and the detection result is showed in Fig. 2. The theoretical values of the three combination tests is [−63, 369, 69]. From this figure, the calculated value are basically consistent with the theoretical ones. The cycle-slip value is [3, 21, 90] by the calculated value substituted into Eq. (7).

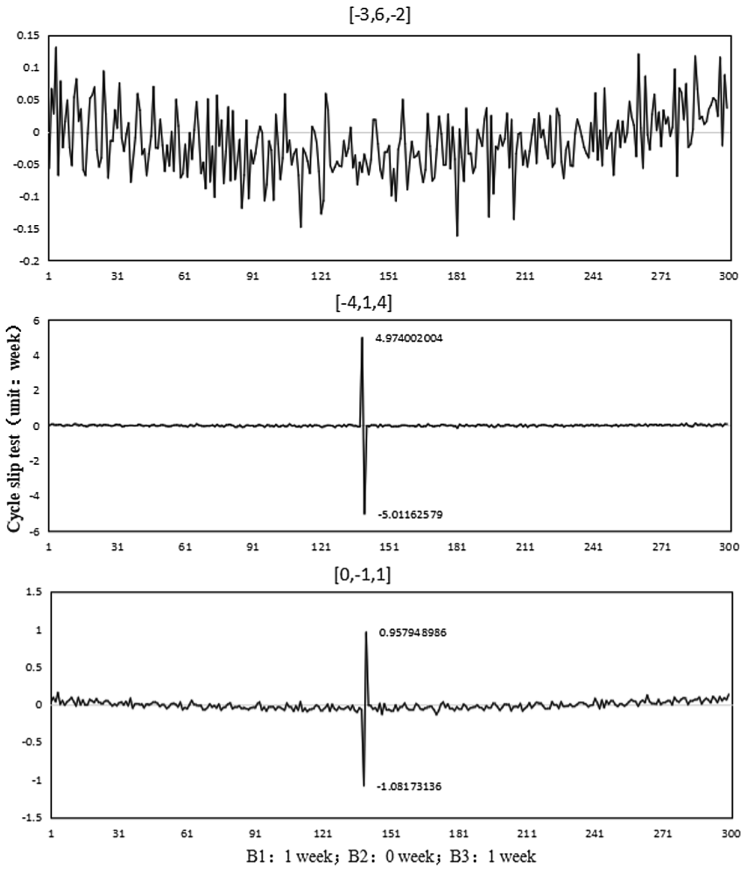

Fig. 3. Insensitive cycle-slip detection (1, 0, 1)

4.2 Insensitive Cycle-Slip Detection

In order to verify insensitive cycle-slip detection ability of this algorithm, (1, 0, 1), (2,1,0) and (2, 1, 1) are respectively added on 141st, 151st, 161st epoch of non cycle-slip original observation data, which are respectively insensitive cycle-slip of (−3, 6, −2), (−4, 1, 4) and (0, −1, 1) combination. This experiment results are shown in Figs. 3, 4 and 5. Form these figures, when one combination can't detecte its corresponding insensitive cycle-slip, other two combinations can effectively detecte this one.

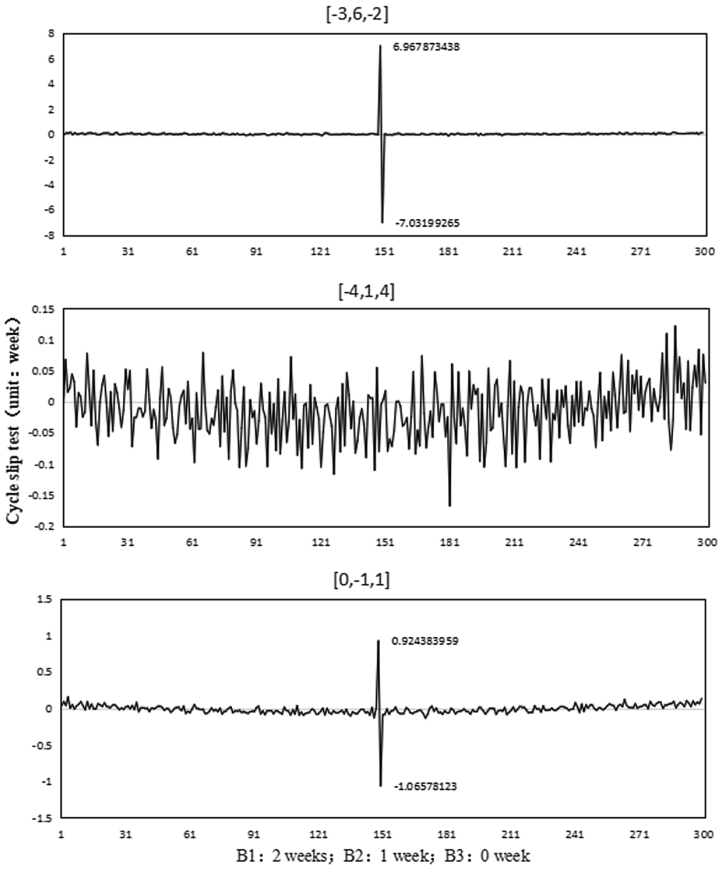

Fig. 4. Insensitive cycle-slip detection (2, 1, 0)

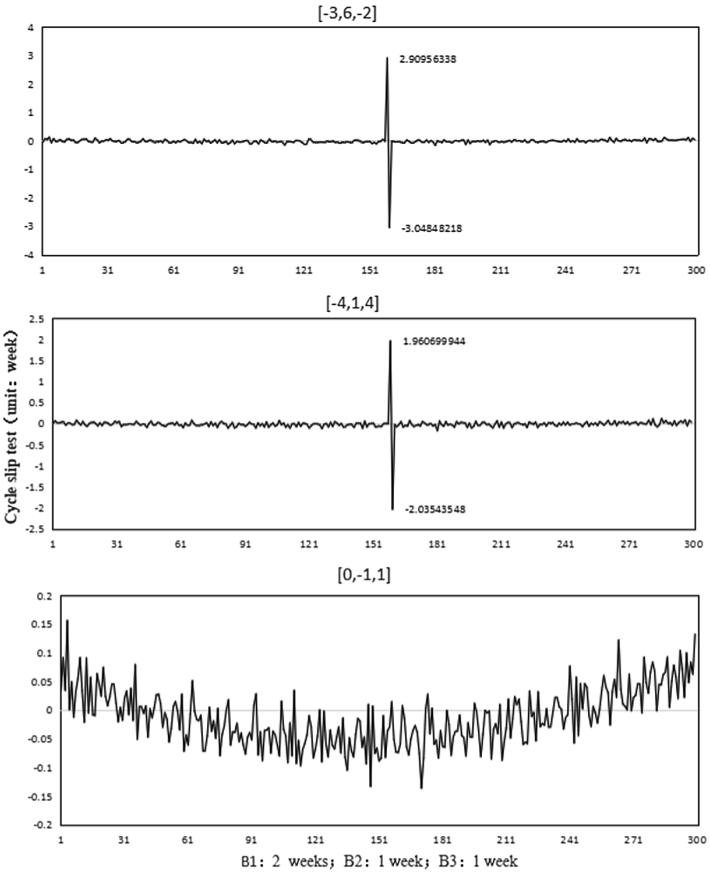

Fig. 5. Insensitive cycle-slip detection (2, 1, 1)

Figure 6 show detection results of two cycle-slip test's common insensitive cycle-slip. (26, 20, 21) is added on 171st epoch of three frequency non cycle-slip original observation data, which are common insensitivite cycle-slip of (−4, 1, 4) 和 (−3, 6, −2) combination. Form Fig. 6, these two pseudo-phase combinations can't detect this insensitive one, but ultra-wide lane combination can effectively detecte it. Combined with Figs. 3, 4 and 5, this algorithm has effective and reliable detection capability for all cycle-slip including insensitive cycle-slip.

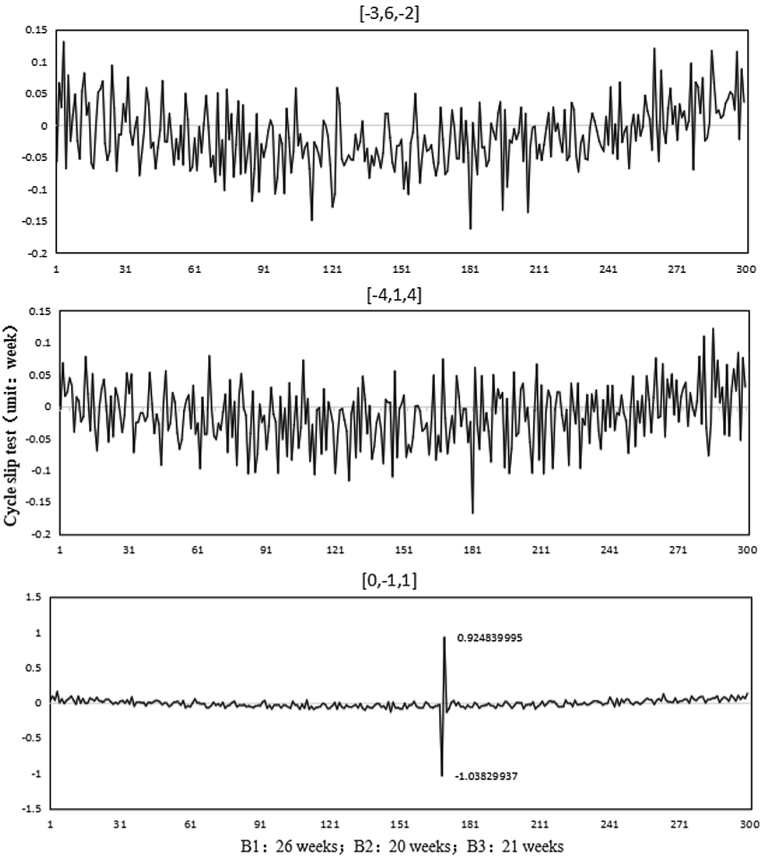

Fig. 6. Insensitive cycle-slip detection (26, 20, 21)

5 Conclusion

Aim at cycle-slip detection and repair problem, the advantages of pseudo-range combination and ultra-wide lane combination are combined to improve the detection accuracy. The relation between combination coefficient and insensitive cycle-slip has been analyzed in order to choose the optimal combination in this paper. At the same time, the ill-posed equation problem has been avoided by the principle of 2-norm minimum. Finally, the accuracy and reliability and the detection ability for insensitive cycle-slip of this algorithm and has been verified by processing the BeiDou triple-frequency measured data. The calculation results show that the algorithm can effectively detect and repair all cycle-slip including insensitive cycle-slip, and can adapt to data processing in static and dynamic environments.

Acknowledgements. The work was supported by the National Natural Science Foundation of China (No. 41431069) and Key Laboratory of Geospace Environment and Geodesy, Ministry of Education, Wuhan University (16-01-14). The authors are very grateful to the reviewers for their

insightful and professional suggestions to this paper, and we also would like to thank Chinese Antarctic Center of Surveying and Mapping in Wuhan University for providing to BDS data.

References

1. Cui L, Wen X, Han Y et al (2017) Research on detection and restoration of BeiDou cycle slip based on ionosphere residual method. J Chengdu Univ (Nat Sci Ed) 36(1):62–65
2. Blewitt G (1990) An automatic editing algorithm for GPS data. Geophys Res Lett 17 (3):199–202
3. Li J, Yang Y, Xu J et al (2011) Real-time cycle-slip detection and repair based on code-phase combination for GNSS triple-frequency un-differenced observation. Acta Geod Cartogr Sin 4(6):717–722
4. Cui L, Chen D, Wang X et al (2018) BDS three-frequency pseudo-range/carrier linear combination cycle-slip detection and correction. Eng Surveying Mapp 27(12):1–3, 7
5. Bisnath SB, Kim D, Langley RB (2001) Innovation: carrier-phase cycle slip. GPS World 12 (5):46–51
6. Cui L, Zhang Y, An J (2018) Detection and repair of BDS based on ionosphere residual method combined with ultra-wide lane carrier. Sci Technol Eng 18(1):1–5
7. Cui L, Zhang Y, Du S et al (2018) Detection and repair of BeiDou triple-frequency using ultra-wide lane carrier and ionosphere residual method. J Chengdu Univ (Nat Sci Ed) 37 (2):163–167
8. Huang L, Song L, Wang Y et al (2012) BeiDou triple-frequency geometry-free phase combination for cycle-slip detection and correction. Acta Geodaetica et Cartographica Sin 41 (5):763–768
9. Cui L, Du S (2018) The real-time detection and repair of BeiDou triple-frequency cycle slip based on geometry-free phase combination. Sci Technol Eng 18(29):7–12
10. Huang L, Lu Z, Zhai G et al (2015) A new triple-frequency cycle-slip detecting algorithm validated with BDS date. GPS Solutions 1–9
11. Yang YX, Li JL, Wang AB et al (2014) Preliminary assessment of the navigation and positioning performance of BeiDou regional navigation satellite system. Sci China: Earth Sci 44(1):72–81
12. Wang Z, Wang X, Ji S et al (2016) Optimal cycle slip detection and correction with reliability. Surv Rev 48(349):233–239
13. Wang X (2015) Research on the algorithms of cycle slip detection and correction for BeiDou observations. Qingdao: China University of Petroleum (East China)

Assessment of BeiDou-2 Orbit and Clock Quality Based on Analysis of Wide-Lane Ambiguities Derived from PPP Models

Sijing Liu[1,2(✉)], Gang Chen[2], and Qile Zhao[3]

[1] College of Marine Science and Technology, China University of Geosciences, Wuhan 430074, China
sijingliu@cug.edu.cn
[2] Institute of Geosciences and Geomatics, China University of Geosciences, Wuhan 430074, China
[3] GNSS Research Center, Wuhan University, Wuhan 430079, China

Abstract. Precise point positioning (PPP) technique has been widely employed for precise positioning as it does not explicitly need any reference stations. The BeiDou satellite navigation system (BDS) helps the technique to achieve more accurate and more robust positioning, particularly when combined with other global satellite navigation systems. The quality of precise orbit and clock is crucial for PPP users. Our earlier study has proved that orbit and clock errors of global positioning system (GPS) can be detected through comparing geometry-free (GF) and geometry-based (GB) wide-lane (WL) ambiguities in PPP model. In this contribution, we will focus on the evaluation of BDS orbit and clock quality. This paper compares and analyzes WL ambiguities derived from the GF and GB model using raw BDS B1 and B2 observations. The methodology is firstly described in order to explain why the differences of these two types of ambiguities can be used as a quality index of orbit and clock. After that, three types of BDS precise orbit and clock products, namely final determined products and real-time predicted and filtering products, are collected and produced. A number of stations in Asia-Pacific regions are selected to derive GF and GB WL ambiguities of each individual BDS satellite for a comparison using these types of orbit and clock products. The results are demonstrated and analyzed in detail. This contribution reveals that our methodology can be used to evaluate the BDS orbit and clock quality at the line-of-sight direction externally and independently in real-time. This is particularly important for real-time users.

Keywords: BDS · Orbit and clock quality · Wide-lane ambiguity · Geometry-free · Geometry-based

1 Introduction

The Precise Point Positioning (PPP) technique utilizes one single receiver to determine its position without using differential operator with any reference stations (Zumberge 1997, Kouba and Heroux 2001). In this case, orbit and clock errors cannot be eliminated. Precise orbit and clock products are therefore crucial for obtaining high-precision

J. Sun et al. (Eds.): CSNC 2019, LNEE 563, pp. 174–183, 2019.
https://doi.org/10.1007/978-981-13-7759-4_16

positioning results. However, the PPP users, in many cases, just employ the orbit and clock products without knowing their quality. The traditional quality assessment is usually done separately for orbit and clock (Guo et al. 2016). For orbit part, the orbit overlap is used to validate the consistency of consecutive orbits produced from the same Analysis Centers (ACs). Direct comparison of orbit positions from different ACs is also often employed to assess the orbit qualities of different ACs (Kazmierski et al. 2018). In this case, the orbit cannot be evaluated independently. In order to do it independently, the satellite laser ranging (SLR) residuals are used to validate the satellite orbits. However, it is not realistic to assess orbits in real-time and not every satellites have SLR reflectors. For clock part, since it is determined in relative sense, the double-difference approach is often used to compare with a reference clock product, for instance, the IGS final clock. In this case, the clock products cannot be evaluated independently and in real-time. It is possible to evaluate the quality of orbit and clock as a whole through analysis of PPP positions. The method is difficult to distinguish the contribution of each constellation and each satellite to the final PPP solutions. In our earlier research, we proposed a new approach to assess the qualities of orbit and clock products by analysing the wide-lane (WL) ambiguity difference between geometry-free (GF) and geometry-based (GB) models from user's perspective (Chen et al. 2018). The principal of the approach is that the GF WL ambiguities do not contain the orbit and clock error as they are eliminated, while the GB WL ambiguities contain the orbit and clock error mapping into Line-Of-Sight (LOS) direction. The advantage of this approach is that the orbit and clock error can be assessed independently and separately for each satellite in real-time. The approach has been successfully applied to evaluate GPS orbit and clock for both determined and real-time products (Chen et al. 2018). It was confirmed that the discrepancies of GF and GB WL GPS ambiguities are coincide with time-variant errors in the used orbit and clock at the LOS direction. In this paper, we apply the method to assess the orbit and clock product quality for the BeiDou Navigation Satellite System (BDS-2).

The BDS-2 was constructed first in 2007, and came into operation in 2012. The space segment of BDS-2 contains 14 satellites. At the experiment period of this study, there are five satellites in geostationary earth orbit (GEO), six satellites in inclined geosynchronous orbit (IGSO) and three satellites in medium earth orbit (MEO) respectively. These five operational GEO satellites are C01, C02, C03, C04 and C05. These six IGSO satellites are C06, C07, C08, C09, C10 and C13 (formally changed from C15). Three operational MEO satellites are C11, C12 and C14. For the Asia-Pacific region, it is sufficient to guarantee the regional navigation service only relying on the combination of GEO and IGSO satellites without MEO satellites. These MEO satellites mainly serve the global satellite navigation system. The BDS-2 signals are based on code division multiple access (CDMA), which is consistent with GPS and Galileo, and different from the frequency division multiple access (FDMA) of GLONASS. The BDS-2 transmits signals in three different frequency bands: B1, B2 and B3, and its service range cover from 55° to 55° in latitude and 70° to 150° in longitude (Yang and Tang 2017).

This paper aims at assessment of the quality of various orbit and clock products of BDS-2 satellites. The GF and GB models are respectively presented briefly at first, then the methodology is described. After that, the WL ambiguity differences between GF

and GB model are respectively produced with three orbit and clock products. Furthermore, we compare numerical results and analyse the qualities of these three products from user's perspective. Finally, some conclusions are summarized.

2 WL Ambiguities Derived from the GF and GB Models

The measurements of code p and phase φ tracked by a receiver at location r from BeiDou satellites $s(s = 1, 2, \cdots, m)$, at frequency $i(i = 1, 2)$ at epoch k, can be expressed in meters as follows:

$$\begin{aligned} E\left\{p_{i,r}^{s}(k)\right\} &= R_r^s(k) + \mu_i \widetilde{I}_r^s(k) \\ E\left\{\varphi_{i,r}^{s}(k)\right\} &= R_r^s(k) - \mu_i \widetilde{I}_r^s(k) + \lambda_i \widetilde{N}_{i,r}^s \end{aligned} \tag{1}$$

where $E\{\cdot\}$ denotes the expectation operator; the geometry part $R_r^s(k)$ combines all non-dispersive terms, including the geometric range, satellite and receiver clock and tropospheric delay. The so-called GF observation model dispenses with geometric a priori information. $\mu_i = \lambda_i^2/\lambda_1^2$, λ_i the carrier wavelength of frequency i; $\widetilde{I}_r^s(k)$ the ionospheric delay; $\widetilde{N}_{i,r}^s$ the carrier phase ambiguity terms. All terms with (k) are supposed to be significantly changed in time. The receiver and satellite hardware delays are ignored here for brevity. We only make use of dual-frequency observations in this paper.

The model is for a single satellite. The epoch-wise solution of the GF ambiguity term is simply computed as follows:

$$\mathbf{x}_k^s = \mathbf{H}\,\mathbf{z}_k^s \tag{2}$$

where the phase and code measurements can be written in a vector form as $\mathbf{z}_k^s := \left[p_{1,r}^s(k) \quad p_{2,r}^s(k) \quad \varphi_{1,r}^s(k) \quad \varphi_{2,r}^s(k)\right]^T$ and the parameters that we are interested is ambiguity term $\mathbf{x}_k^s := \left[\widetilde{N}_{wl,r}^s \quad \widetilde{N}_{2,r}^s\right]^T$, where $\widetilde{N}_{wl,r}^s = \widetilde{N}_{1,r}^s - \widetilde{N}_{2,r}^s$ is WL ambiguities. H is the coefficient matrix derived from Eq. (1) only for ambiguity parameters:

$$\mathbf{H} := \begin{bmatrix} -\frac{1}{\lambda_1}\frac{\mu_2+\mu_1}{\mu_2-\mu_1} + \frac{1}{\lambda_2}\frac{2\mu_2}{\mu_2-\mu_1} & \frac{1}{\lambda_1}\frac{2\mu_1}{\mu_2-\mu_1} - \frac{1}{\lambda_2}\frac{\mu_2+\mu_1}{\mu_2-\mu_1} & \frac{1}{\lambda_1} & -\frac{1}{\lambda_2} \\ -\frac{1}{\lambda_2}\frac{2\mu_2}{\mu_2-\mu_1} & \frac{1}{\lambda_2}\frac{\mu_2+\mu_1}{\mu_2-\mu_1} & 0 & \frac{1}{\lambda_2} \end{bmatrix} \tag{3}$$

The WL ambiguities can be directly derived from above linear equation with considering the stochastic model. Since the ambiguities are considered as a constant, therefore, the filtering solution can be derived using the current and all the past epochs in real-time, for detail, see Chen et al. (2018).

According to Chen et al. (2018), the geometry-based PPP model can be expressed as follows:

$$\begin{aligned} E\left\{\delta p_{i,r}^{s}(k)\right\} &= m_r^s T_r + t_r(k) + \mu_i \widetilde{I}_r^s(k) \\ E\left\{\delta \phi_{i,r}^{s}(k)\right\} &= m_r^s T_r + t_r(k) - \mu_i \widetilde{I}_r^s(k) + \lambda_i \widetilde{N}_{i,r}^s \end{aligned} \tag{4}$$

where $\delta p_{i,r}^{s}(k)$ and $\delta \varphi_{i,r}^{s}(k)$ are Observed minus Computed values, which are derived from raw observations and station coordinates as well as precise satellite orbit and clock at epoch k; $t_r(k)$ is the receiver clock term; T_r the zenith tropospheric delay with mapping function m_r^s.

The functional model of deriving GB WL ambiguity for a single satellite can be written as:

$$\begin{bmatrix} \delta p_{1,r}^{s}(k) \\ \delta p_{2,r}^{s}(k) \\ \delta \varphi_{1,r}^{s}(k) \\ \delta \varphi_{2,r}^{s}(k) \end{bmatrix} = \begin{bmatrix} m_r^s & 1 & \mu_1 & 0 & 0 \\ m_r^s & 1 & \mu_2 & 0 & 0 \\ m_r^s & 1 & -\mu_1 & \lambda_1 & \lambda_1 \\ m_r^s & 1 & -\mu_2 & 0 & \lambda_2 \end{bmatrix} \cdot \begin{bmatrix} t_r(k) \\ T_r \\ \widetilde{I}_r^s(k) \\ \widetilde{N}_{wl,r}^s \\ \widetilde{N}_{2,r}^s \end{bmatrix} \tag{5}$$

However, the equation of a single satellite is rank defect, all observed satellites should therefore be involved in one functional model. In this case, there are redundancy for parameter estimation. Regarding to the stochastic model and the process of filtering in real-time can be seen in Chen et al. (2018). The main difference of the paper is that we produce WL ambiguities directly instead of two steps in Chen et al. (2018) (i.e. first L1 and L2 ambiguities and then compute WL ones).

3 Experiment and Results Analysis

In order to evaluate orbit and clock impacts on WL ambiguities, we selected six sites from the Multi-GNSS Experiment and Pilot Project (MGEX) of IGS database which has 1 s interval GNSS measurements (Montenbruck et al. 2017), see Fig. 1. The date of these data is September 27, 2017. These sites are equipped with receivers enabled the tracking of BeiDou satellites. Three kinds of orbit and clock products are used in this study, two types of which are determined orbit and clock products provided to the IGS by Wuhan University (Guo et al. 2016) and German Research Centre for Geosciences (Uhlemann et al. 2015) respectively. The product names are respectively WUM and GBM. Another type is the real-time orbit and clock for this study, which is described in Chen and Zhao (2014). The satellite orbit interval is 15 min and the sampling rate is 30 s in all these various products. The standard GB PPP solutions, in parallel with the GF process, are computed using raw B1 and B2 observations with the parameters being tropospheric zenith delay, ionosphere, receiver clock bias, and WL, B2 ambiguity terms for the GB process, while the GF process just produces the WL and B2 ambiguity terms. All observations from four GNSS constellations are used with their

corresponding precise orbit and clock. The elevation-dependent data weighting is used for both GF and GB processes identically for all constellation satellites. The entire process is implemented through a strictly forward computation. Although WL ambiguities of all satellites of four constellations are produced, we will only focus on the analysis of BDS satellites in this study. The first half hour of ambiguities of any time series are in the convergence and will not be included in the analysis.

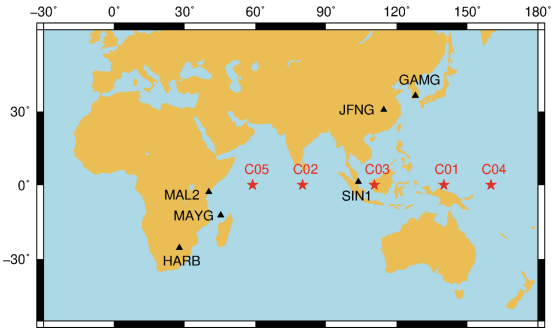

Fig. 1. Distribution of sites that are used for this study with 5 GEO satellites.

Figure 2 displays GF and GB WL ambiguities of IGSO C09 and their standard deviations computed from observations tracked by the receiver at GAMG. A same offset is removed from the GF epoch-wise, GF filtering and GB WL ambiguities in order to display them more intuitively. In the top panel, it is obvious that the values of GF epoch-wise (GF 1) WL ambiguities fluctuate mostly in a range of 1.5 cycles while the GF filtering (GF 2) counterparts remain stable in 0.25 cycles. The reason is that the epoch-wise ambiguities are computed only using observations at current epoch, while the filtering solutions are equivalent to the averaged ambiguities from the observations of the current and all the past epochs, resulting in better accuracy. Compared with the GF WL filtering solutions, the GB counterparts have a similar resemble trend. Ideally the differences should close to zero because they are physically the same thing in terms of parameterization. However, the GB ambiguities deviate slightly with GF WL one. This is largely due to the fact that GB WL ambiguities are affected by residual errors in orbit and clock. The difference values of GF filtering and GB WL ambiguities (GF 2 - GB) stay steady between ± 0.2 cycles in general. The orbit and clock of IGSO C09 satellite is relatively of high quality in this experiment. In the bottom panel, it is noticed that the formal standard deviations of GF epoch-wise WL ambiguities are two orders of magnitude larger than GF filtering ones, which means that the epoch-wise ambiguities are not accurate. The standard deviations of GF filtering and GB WL ambiguities are all convergent after several tens of minutes, and stabilize at better than 0.01 cycles. In

addition, they are almost identical. This means that these WL ambiguities derived from GF and GB models are statistically equivalent following the fact that the measurement noises and the process noises of parameters are formally set the same (which is the case of this study) (Teunissen and Khodabandeh 2015). However, if these estimates themselves are not identical as their formal precisions are, there must be something else which make the differences (ignoring the computation errors which are significantly small). In our case, orbit and clock errors play this role.

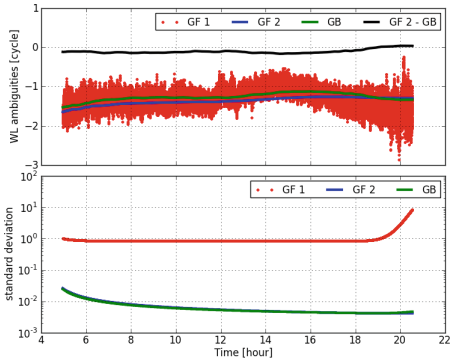

Fig. 2. Various WL ambiguities (top) of IGSO C09 and their formal standard deviations (bottom) computed with observations from the receiver GAMG using WUM final orbit and clock products: (1) GF epoch-wise (red), GF filtering (blue), and GB WL ambiguities (green) as well as differences of GF filtering and GB WL ambiguities (black) are indicated in top panel; (2) standard deviations of GF epoch-wise (red), GF filtering (blue), and GB WL ambiguities (green) are indicated in bottom panel.

Figure 3 compares the GF-GB WL ambiguities of GEO, IGSO and MEO satellites using WUM orbit and clock product for site GAMG and SIN1, respectively. It can be seen that the values of GEO WL differences undulate mostly between ± 0.2 cycles (stands for about 16 cm errors), which are larger than that of IGSO and MEO. This indicates that the orbit and clock quality of GEO at LOS is worse than that of IGSO and MEO. This coincide with earlier study using traditional evaluation strategies in Guo et al. (2016). The reason for GEO having less orbit and clock quality is that the GEO satellites are geostationary with altitude of up to 36,000 km. Their observable angles from the Earth surface are not wide enough, resulting in poor geometry strengths, compared with other two types of satellites. The IGSO satellites have longer visibility than the MEO satellites. Their GF-GB WL ambiguities both behave relatively good and comparable stableness.

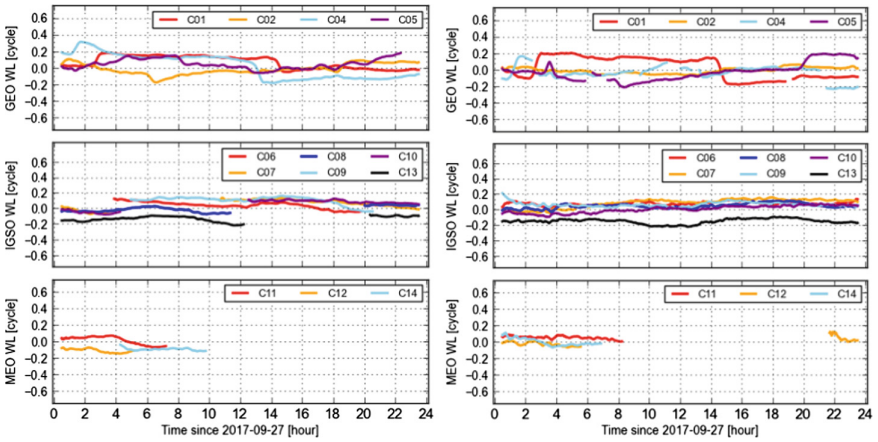

Fig. 3. WL ambiguity differences between GF and GB model of GEO (top), IGSO (middle) and MEO (bottom) computed from observations of receiver GAMG (left) and SIN1 (right) using WUM final orbit and clock product.

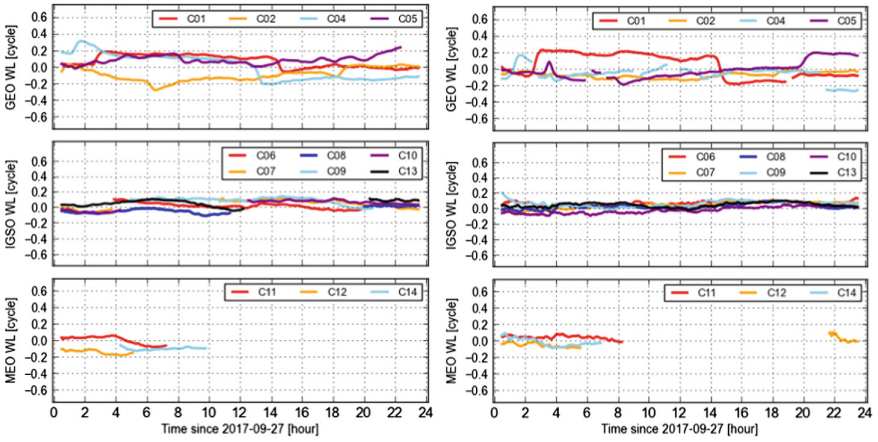

Fig. 4. WL ambiguities differences between GF and GB model of GEO (top), IGSO (middle) and MEO (bottom) computed from observations of receiver GAMG (left) and SIN1 (right) using GBM final orbit and clock product.

Figure 4 displays the same time series at sites GAMG and SIN1 as Fig. 3, while they are produced using the GBM final orbit and clock product. These WL differences have remarkably the similar behavior as that of WUM counterparts except for C13, for which WUM products show larger bias. Again, stabilities of IGSO and MEO are better than GEO satellites, though it is not very significant for MEOs as they have shorter visibilities.

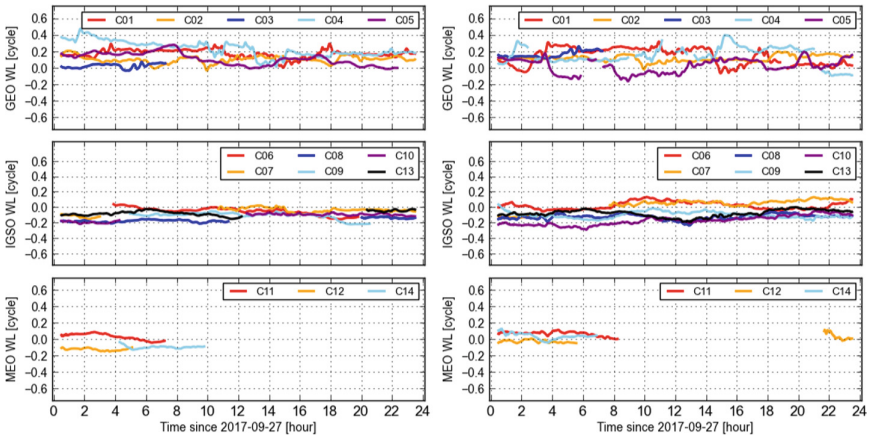

Fig. 5. WL ambiguities differences between GF and GB model of GEO (top), IGSO (middle) and MEO (bottom) computed from observations of receiver GAMG (left) and SIN1 (right) using real time orbit and clock product.

Figure 5 displays the time series of WL ambiguities at sites GAMG and SIN1, which are produced using the real time orbit and clock product. It is obvious that these time series show the resemble behaviour to the determined products, but with higher high-frequency noise. This indicates that the real-time orbit is not as smooth as determined one. For GEO satellites, it looks that real-time products display less low-frequency variation, particularly for C01. The scattering ambiguities derived from real time product are generally larger than that produced from the determined orbit and clock.

In order to further evaluate the qualities of orbit and clock for both determined (i.e. WUM and GBM) and real time products, six independent sites are selected to derive their root mean squares (RMS) of GF-GB WL ambiguities, see Fig. 6. The RMS values of GEO satellites (C01-C05) are, in average, larger than that of IGSO satellites. We could also see that some GEO observations are not available for MAL2, MAYG and HARB sites as their locations exceed the service range of GEO, which reflects the regional limitations of GEO satellites. The RMS values are closer between two final products than the real-time, reflecting that the qualities of two final products are comparable except for C12 and C13 (WUM produced larger biases). Most of these RMS values of determined products are better than 0.1 cycles with WUM having only 20% and GBM having only 17% values larger than 0.1 cycles. Obviously the real-time products produce larger RMS values, of which 53% are above 0.1 cycles. 8% of them are even larger than 0.2 cycles. We realize that these larger RMS values originate from inconsistence of used code observations with different tracking modes in clock filtering and WL derivation, consequently resulting in biases in time series of WL ambiguities. One has to be careful when dealing with such biases for integer ambiguity resolution. If the discrepancies of GF and GB WL ambiguities is larger than a certain value, e.g. 0.1 cycle, the GF and GB phase biases are not interchangeable.

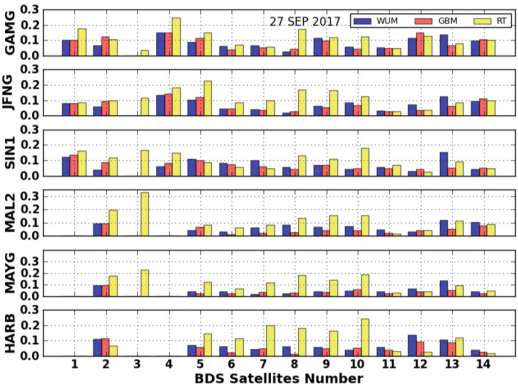

Fig. 6. Root mean square values (unit: cycle) of 14 satellites derived from observations of six different sites and three different orbit and clock products respectively.

4 Conclusions and Outlooks

This paper derives WL ambiguities directly from the GF and GB PPP model. Raw BDS-2 observations of GEO, IGSO and MEO satellites are used to compute WL ambiguity differences with three types of orbit and clock products provided by different institutions. The main results and conclusions are summarized in the following.

The GF filtering solutions are more stable and accurate than that of epoch-wise ones. Formal standard deviations of latter ones are two orders of magnitude larger than filtering ambiguities (i.e. 0.01 cycle). The GF filtering and GB WL ambiguities are equivalent in statistics sense. The differences in estimates are primarily come from orbit and clock errors projected on LOS. Therefore, they can be used to evaluate the quality of orbit and clock from the user's perspective.

The time series of GEO, IGSO and MEO WL ambiguity are analyzed. The GEO satellites have obviously larger variation than IGSOs. MEOs are also better than GEO satellites, but it is not very significant as MEOs have shorter visibilities.

The qualities of three orbit and clock products are evaluated. WUM and GBM products show remarkable similar quality. Most of their RMS values are better than 0.1 cycles. Only 20% of WUM and 17% of GBM RMS values are larger than 0.1 cycles. The real-time products have 53% RMS values above 0.1 cycles, of which their larger biases are required a further investigation.

It should be noticed that the approach in this study is used to evaluate the qualities of orbit and clock product in LOS direction from the user's perspective in order for real-time application. The errors in the tangential and normal direction of orbit need a network data processing, which is beyond the scope of this study, however, it could be a further development of this research.

In this paper, the qualities of selected orbit and clock products are relatively good and the estimation values of WL ambiguity differences are relatively stable. It is more interesting to investigate the behavior of BDS satellites when they are in the eclipse and yaw-fixed mode and evaluate different attitude strategies of orbit determination. In

addition, the lack of publicly available BDS-2 high-frequency data do not allow intensive analysis in this study. Hopefully, this situation will be changed in future. Furthermore, the BDS-3 orbit and clocks are worthy of evaluation using the proposed approach in near future as it is announced to provide global service.

References

Chen G, Liu S, Zhao Q (2018) Analysis of wide-lane ambiguities derived from geometry-free and geometry-based precise point positioning models and their implication for orbit and clock quality. Sensors 18(6):1760. https://doi.org/10.3390/s18061760

Chen G, Zhao Q (2014) Near-field surface displacement and permanent deformation induced by the Alaska Mw 7.5 earthquake determined by high-rate real-time ambiguity-fixed PPP solutions. Chin Sci Bull 59:4781–4789. https://doi.org/10.1007/s11434-014-0609-7

Guo J, Xu X, Zhao Q et al (2016) Precise orbit determination for quad-constellation satellites at Wuhan University: strategy, result validation and comparison. J Geodesy 90:143. https://doi.org/10.1007/s00190-015-0862-9

Kazmierski K, Sosnics K, Hadas T (2018) Quality assessment of multi-GNSS orbits and clocks for real-time precise point positioning. GPS Solut 22(1):11. https://doi.org/10.1007/s10291-017-0678-6

Kouba J, Heroux P (2001) Precise point positioning using IGS orbit products. GPS Solution 5:12–28. https://doi.org/10.1007/PL00012883

Montenbruck O, Steigenberger P, Prange L et al (2017) The multi-GNSS experiment (MGEX) of the international GNSS service (IGS) – achievements, prospects and challenges. Adv Space Res 59(7):1671–1697. https://doi.org/10.1016/j.asr.2017.01.011

Teunissen P, Khodabandeh A (2015) Review and principals of PPP-RTK methods. J Geod 89:217–240. https://doi.org/10.1007/s00190-014-0771-3

Uhlemann M, Gendt G, Ramatschi M et al (2015) GFZ Global multi-GNSS network and data processing results. In: Rizos C, Willis P (eds) IAG 150 Years. International Association of Geodesy Symposia, vol 143. Springer, Cham. https://doi.org/10.1007/1345_2015_1

Yang Y, Tang J (2017) Chinese navigation satellite system. In: Montenbruck O (ed) Springer handbook of global navigation satellite system. Springer Nature, Switzerland

Zumberge F, Heflin B, Jefferson C et al (1997) Precise point positioning for the efficient and robust analysis of GPS data from large networks. J Geophys Res 102:5005–5017. https://doi.org/10.1029/96JB03860

Satellite Navigation Augmentation Technology

LEO Navigation Augmentation: Satellite Antenna PCV Requirement for Precise Positioning

Wenying Lei(✉), Wenshan Liu, Hong Han, Fei Ling, and Yansong Meng

China Academy of Space Technology (Xi'an), Xi'an 710100, China
lordleid@163.com

Abstract. Global navigation satellite system (GNSS) augmentation based on low earth orbit (LEO) satellite constellation can significantly shorten the convergence time of precision point positioning due to the large geometric diversities added by rapid moving LEO satellites. In LEO satellite navigation augmentation systems that enable rapidly convergent precise point positioning (PPP), LEO satellite antenna phase center variation (PCV) corrections are usually indispensable for precise ranging signal transmissions over the period of LEO-augmented PPP convergence. However, the rapid geometric changes of LEO satellites lead to fast changes in satellite antenna PCVs. Their satellite PCV correction frequency needs to be increased compared to its counterpart in a GNSS satellite, which makes the corresponding satellite antenna PCV correction difficult to a receiver. In this paper, the overall satellite antenna PCV requirements for three-dimensional decimeter level positioning precisions in the LEO-augmented fast PPP application are analyzed, when no LEO satellite antenna PCV correction models are needed. With the proposed scheme, the LEO-augmented fast PPP user can avoid storing tens or hundreds of high dimensional satellite antenna PCV correction matrices in the LEO satellite navigation constellation. The experimental results show that the LEO satellite antenna PCV fluctuations should lie in the range [−12.6, 8.1] mm for the L1 band, and in the range [−19.5, 19.2] mm for the L2 band, in the LEO-augmented decimeter-level precision PPP application where the receiver does not need to correct the LEO satellite antenna PCV.

Keywords: Low earth orbit · Navigation augmentation · Satellite antenna · Phase center variation · Precise point positioning

1 Introduction

The LEO constellation represented by the new generation Iridium satellite system is characterized by its low signal attenuation, short satellite ground signal delay, fast satellite geometrical variation, etc. [1–4]. In global LEO constellation GNSS navigation augmentation, satellite communication, and network, there are strong advantages in network interconnection, aircraft and ship traffic control. The advantage of the LEO satellite constellation in navigation augmentation is mainly that it can significantly

J. Sun et al. (Eds.): CSNC 2019, LNEE 563, pp. 187–195, 2019.
https://doi.org/10.1007/978-981-13-7759-4_17

reduce the convergence time of precise point positioning (PPP). When a single LEO satellite is participated in the fast PPP solution of the GNSS system, the point positioning convergence time could be reduced from 30 min to about 10 min [5, 6]. If the uncalibrated phase delays of the satellites and the receiver in addition with other ionospheric delay products and tropospheric delay products, the convergence time can be further reduced. The value of LEO satellite constellation is acknowledged and used by GNSS researchers in technologically advanced countries around the world. The discovery was accompanied by corresponding research and development of GNSS navigation augmentation system with a LEO satellite constellation in various countries [2–6].

The LEO satellite navigation augmentation signal is broadcasted by the satellite antenna of a LEO satellite to the user. The user measures LEO observation values such as satellite-to-user pseudoranges, Dopplers and carrier phases, and then combines satellite positioning, satellite speed and satellite time in the satellite ephemeris to obtain its position, velocity and timing information. However, the result of the orbit determination given by the navigation augmentation satellite ephemeris is located at the satellite mass center [2, 7–9]. The user measured range observations are starting from the positions of the LEO navigation augmentation satellite antenna phase centers to the receiver antenna phase center. Satellite antenna phase center and satellite center of mass often do not coincide, this deviation is an important error source in the LEO satellite navigation augmentation systems. This deviation will introduce centimeter-to-decimeter level errors for navigation positioning results. Therefore, in the LEO navigation augmented precision positioning service, it is necessary to analyze, model, and correct the error term.

The deviation between the phase center of the satellite antenna and the mass center of the satellite is divided into fixed deviation part that does not depend on the user observation angle, and is often referred to as the phase center offset (PCO) of the satellite antenna; and the angle-dependent variation part that changed with the user observation angle, it is also often referred to as phase center variation (PCV) [10–13]. The error introduced by the PCO of the satellite antenna does not change as the user observation direction changes in the azimuth and elevation angle, and its correction is relatively easy. The error introduced by the PCV of the satellite antenna changes as the user observation angle changes in the azimuth and elevation, and the correction is relatively complex.

This paper is devoted to solving the problem of precision loss caused by phase deviation between LEO satellite antenna phase center and satellite mass center in LEO satellite navigation augmentation system. Combined with the characteristics of LEO satellite antenna PCV, the analysis points out the difficulty of satellite antenna PCV correction in the satellite navigation augmentation application. The technical index of satellite antenna PCV, which should be satisfied in the decimeter-level precision fast PPP without LEO satellite antenna PCV corrections in the user segment, are provided eventually.

2 Satellite Antenna Phase Deviation Mathematical Model

The users that use a LEO satellite navigation augmentation service also have an antenna phase center variation problem of the user antenna similar to that of the satellite. The discussion in this paper is limited to the effect of satellite center antenna phase center variation on measurements.

When the LEO navigation augmentation satellites adopt signals compatible with GNSS, the satellite pseudoranges and carrier phase measurements obtained by the user receiver observed measurements can be expressed as [12, 13]

$$P_{r,i}^{s} = \left\|\mathbf{r}^{s}(t^{s}) + \mathbf{PCO}_{i}^{s} - \mathbf{r}_{r}(t_{r})\right\| - PCV_{i}^{s}(\theta,\varphi) + ISB + c(dt_{r}(t_{r}) - dT^{s}(t^{s})) + I_{r,i}^{s} + T_{r}^{s} + \varepsilon_{P} \tag{1}$$

$$\lambda_{i}\phi_{r,i}^{s} = \left\|\mathbf{r}^{s}(t^{s}) + \mathbf{PCO}_{i}^{s} - \mathbf{r}_{r}(t_{r})\right\| - PCV_{i}^{s}(\theta,\varphi) + ISB + c(dt_{r}(t_{r}) - dT^{s}(t^{s})) - I_{r,i}^{s} + T_{r}^{s} + \lambda_{i}B_{r,i}^{s} + \varepsilon_{\Phi} \tag{2}$$

where $P_{r,i}^{s}$ is the satellite pseudorange measurement of the ith frequency band, λ_i is the wavelength of the ith frequency signal. $\lambda_i\phi_{r,i}^{s}$ is the carrier phase measurement in meters. $\mathbf{r}^{s}(t^{s})$ is the 3D position of the satellite s in the t^{s} time moment. $\mathbf{PCO}_{i}^{s}$ is the antenna phase center offset of the ith frequency band of the satellite s, $PCV_{i}^{s}(\theta,\varphi)$ is the antenna phase center variation of the ith frequency band for the satellite s with respect to azimuth angle θ and zenith angle φ. c is light speed, $dt_{r}(t_{r})$ is the receiver clock bias at t_r clock moment, $dT^{s}(t^{s})$ is the satellite clock bias of satellite s at the t^{s} clock moment, $I_{r,i}^{s}$ is the ionospheric delay of the i th frequency band. T_{r}^{s} is the tropospheric delay. $B_{r,i}^{s}$ is the carrier phase bias of the i th frequency band, including carrier phase hardware delay and integer cycle ambiguity. ISB is the inter-system bias of the LEO system relative to the augmented reference GNSS. When the system of the augmented reference GNSS system is a GPS system, the inter-system bias between the systems is zero. ε_P and ε_Φ are random noises in the pseudorange and carrier phase measurements.

From Eqs. (1) and (2), the effect of the phase deviation of the LEO-augmented satellite antenna on the pseudorange and carrier phase can be seen. It should be noted that since the satellite's position $\mathbf{r}^{s}(t^{s})$ in the satellite's precision ephemeris is the value in the geocentric geodetic coordinate system, the measured value of the satellite antenna's PCO is relative to the satellite's body coordinate system and needs to be converted to a geocentric geodetic coordinate system. The satellite antenna PCV appears as a scalar parameter related to the observation angle. The reason for this is that the amplitude, phase, and group delay between the antenna elements vary in different directions when the satellite antenna is beamformed. Taking the L-band downlink antenna of GPS IIR satellite as an example [14], Fig. 1 shows the radiation characteristics of the satellite downlink signal antenna ideally without PCV and the radiation characteristics of the satellite antenna with PCV.

The radiation characteristics of the ideal satellite downlink antenna in Fig. 1(b) are obtained under the premise that there is no amplitude phase error between each omnidirectional antenna element and no mutual coupling between the elements. The

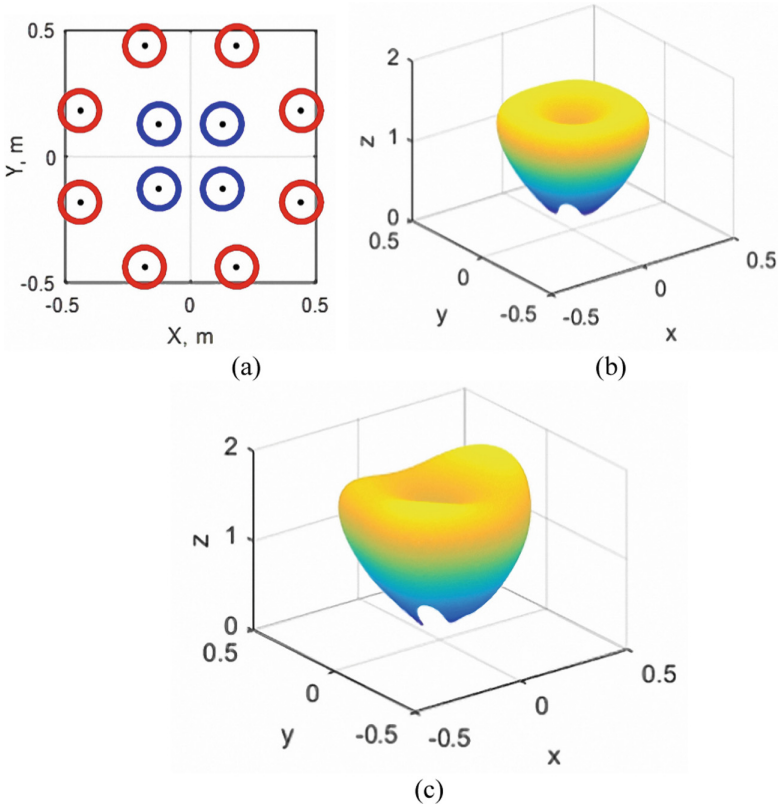

Fig. 1. GPS IIR downlink antenna and its PCV characteristic illustration. (a) antenna element locations; (b) ideal radiation characteristic; (c) actual radiation characteristic with PCV

wave fronts observed from different azimuths and different elevation angles are identical. Figure 1(c) is the antenna radiation characteristics obtained by adding the antenna PCV caused by mutual coupling of the array elements to Fig. 1(b). It can be seen from the figure that the wave front of the antenna exhibits a significant azimuth and elevation angle dependent feature. The satellite antenna PCV correction generally needs to be implemented by bilinear interpolation.

Even though the design of LEO satellite navigation augmented satellite antenna is different, it still produces the phenomenon that the phase center of radiated signal varies with the direction of signal propagation as shown in Fig. 1, similar to the PCV characteristics of GPS IIR antennas. The difference is that LEO-navigation augmentation satellites move faster than the medium earth orbit (MEO) GPS satellites. The PCV of LEO satellite antenna changes more rapidly with azimuth and elevation angles and requires a higher sampling rate to model than the GNSS system. The PCV correction requires a PCV measurement data table with smaller azimuth and elevation angle intervals to ensure that PCV bilinear interpolation achieves sufficient accuracy within the observation interval. However, there are two disadvantages to this: First, the user needs to store the PCV value of all LEO navigation enhanced constellation satellites, which requires a large amount of storage resources; second, the PCV of the satellite

antenna changes with time, and the PCV tables on the user side also need to be updated regularly, which increases the application complexity and reduces the user experience.

3 The PCV Requirement Analysis of Fast PPP Service for LEO Navigation Augmentation Satellite Antenna

Assuming that the satellite antenna PCO has been corrected, the PCO and PCV of the receiving antenna have been corrected, using dual-frequency observations. The non-difference ionospheric linear combination model including the observation model of the satellite antenna PCV can be expressed as

$$\Phi^s_{r,LC} = \rho^s_r + c(dt_r(t_r) - dT^s(t^s)) + T^s_r + B^s_{r,LC} - PCV^s_{IF}(\theta,\varphi) + \varepsilon_\Phi \tag{3}$$

$$P^s_{r,LC} = \rho^s_r + c(dt_r(t_r) - dT^s(t^s)) + T^s_r - PCV^s_{IF}(\theta,\varphi) + \varepsilon_P \tag{4}$$

The PCV in the non-differential ionospheric linear combination model can be expressed as

$$PCV^s_{IF}(\theta,\varphi) = C_i PCV^s_i(\theta,\varphi) + C_j PCV^s_j(\theta,\varphi) \tag{5}$$

$$C_i = \frac{f_i^2}{f_i^2 - f_j^2} \tag{6}$$

$$C_j = \frac{-f_j^2}{f_i^2 - f_j^2} \tag{7}$$

where f_i and f_j are carrier frequencies on the i, j frequency point.

$PCV^s_i(\theta,\varphi)$ and $PCV^s_j(\theta,\varphi)$ can be measured using a vector network analyzer in an anechoic chamber. The PCV values off the sampling grid can be interpolated with bilinear interpolation of the PCV values of four nearest points.

The four surround points around (θ,φ) can be expressed as $Q_{11} = (\theta_1,\varphi_1)$, $Q_{12} = (\theta_1,\varphi_2)$, $Q_{21} = (\theta_2,\varphi_1)$, $Q_{22} = (\theta_2,\varphi_2)$, whose measured PCV values are denoted as $PCV^s_i(Q_{11})$, $PCV^s_i(Q_{12})$, $PCV^s_i(Q_{21})$ and $PCV^s_i(Q_{22})$. $PCV^s_i(\theta,\varphi)$ can be calculated with the following equation

$$PCV^s_i(\theta,\varphi) = \mu \frac{\begin{bmatrix}\theta_2-\theta \\ \theta-\theta_1\end{bmatrix}^T \begin{bmatrix}PCV^s_i(Q_{11}) & PCV^s_i(Q_{12}) \\ PCV^s_i(Q_{21}) & PCV^s_i(Q_{22})\end{bmatrix} \begin{bmatrix}\varphi_2-\varphi \\ \varphi-\varphi_1\end{bmatrix}}{(\theta_2-\theta_1)(\varphi_2-\varphi_1)} \tag{8}$$

where $\mu \geq 1$ is a scalar multiplier used to quantitatively analyze the impact of PCV variation on PPP positioning results. According to Eqs. (5) and (8), when using the non-difference ionospheric linear combination model for precise single-point positioning, the effect of the PCV of the LEO satellite on the precise positioning is determined by two factors: the PCV model precision on the two frequencies and the interpolation accuracy.

Because the LEO satellites move faster, the two-dimensional grid of the antenna PCV needs to be denser than the GNSS system. When the sampling grid point of the PCV antenna is dense, the above calculation process is complicated and requires a large storage space. This contribution proposes a LEO satellite antenna PCV processing mode, which forces the satellite antenna to satisfy certain requirements when the LEO satellite antenna PCV correction is not required.

4 Simulation Results

The PCV values of the navigation downlink antennas of E1 and E5 bands given by the E11 satellite in the Galileo system are used to simulate the PCV values of the LEO navigation augmentation satellite antenna on the GPS L1 and L2 frequency bands, as shown in Fig. 2 [15].

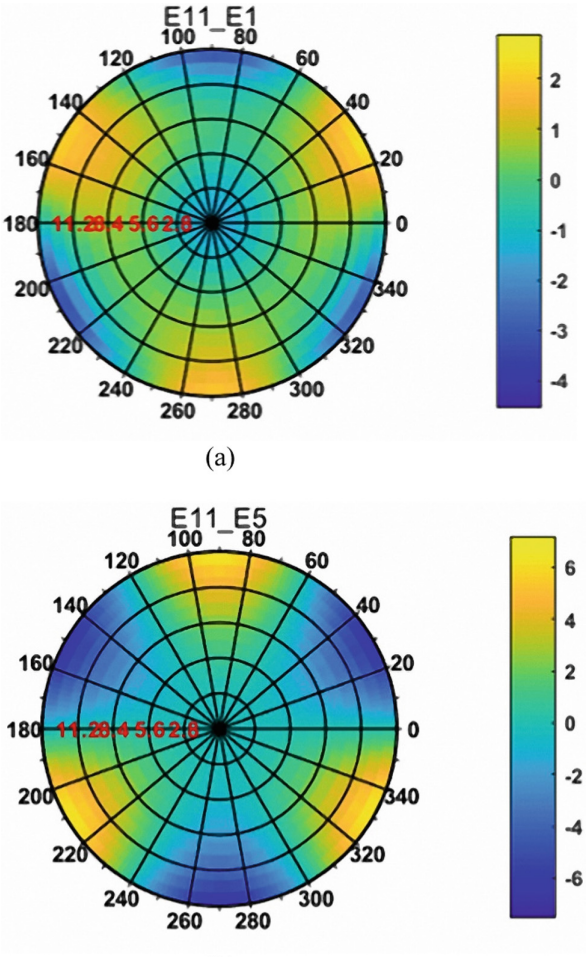

Fig. 2. Dual frequency satellite antenna PCV characteristics of a LEO navigation augmentation satellite. (a) L1 frequency band; (b) L2 frequency band

The unit of the antenna PCV in Fig. 2 is millimeter. It can be seen that the PCV fluctuations of the antenna are different on different frequency bands, and the PCV inconsistently varies against the azimuth and nadir angle.

Because the orbit of LEO satellite is lower than that of GNSS satellite orbit, its range of nadir angles exceeds 0–14°, so it is scaled up to the range of 0–90°. Adopting the data of the GPS time of September 21, 2013 of the Australian CUT2 station, the IGS SP3 precision ephemeris and the 30-s precision clock bias data of the corresponding date, plus a LEO satellite with an orbital altitude of 900 km, the LEO satellite navigation scenario is composed.

The dual-frequency pseudorange and carrier phase observations are added PCV biases of $\mu C_i PCV_i^s(\theta, \varphi)$ and $\mu C_j PCV_j^s(\theta, \varphi)$ respectively for the LEO satellites. Then, the LEO augmented fast PPP simulation is performed. Figure 3 shows the convergence of precision point positioning with a LEO satellite and the GPS satellites under three different PCV multipliers. The truth value is selected as the position after GPS PPP convergence.

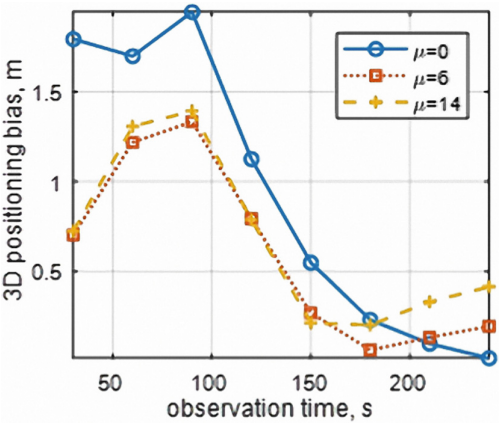

Fig. 3. PPP convergence curves under different PCV multiplier (GPS + 1 LEO satellite)

In Fig. 3, $\mu = 0$ corresponds to the PPP convergence curve without LEO satellite antenna PCV, and the positioning error at the final time point is about 1.6 cm. As can be seen from Fig. 3, under different LEO satellite antenna PCV, PPP convergence results have a greater impact. When the LEO satellite antenna PCV is increased, the PPP convergence curve will upturn and the convergence results will not converge to the true value.

When the LEO satellite PCV has a great change $(\mu = 14)$, the PPP converged result could deviate from the true value more than 20 cm. Let μ changes from 0 to 20, the effects of LEO satellite PCV changes under different amplitudes on the LEO-augmented fast PPP results are analyzed, as shown in Fig. 4.

It can be seen from Fig. 4 that the positioning error less than 0.1 m corresponds to $\mu = 3$. The corresponding LEO satellite PCV requirement is that the LEO satellite

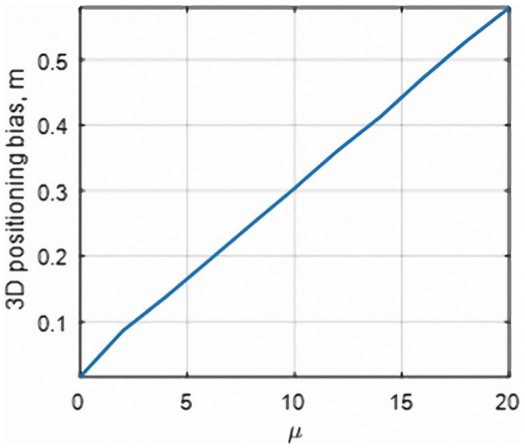

Fig. 4. PPP biases against different PCV multiplier (GPS + 1 LEO satellite)

antenna PCV fluctuations should lie in the range [−12.6, 8.1] mm for the L1 band, and in the range [−19.5, 19.2] mm for the L2 band.

5 Conclusions

This paper studies the technical indicators that the PCV of the LEO satellite antenna should satisfy in the decimeter-level precision LEO-augmented PPP application without LEO satellite antenna PCV corrections. Combining the dual-frequency PCV model of the Galileo satellite antenna, the design requirements of a LEO satellite antenna are numerically verified for decimeter-level precise point positioning application, in the LEO-augmented fast PPP application scenario where the receiver does not need to correct the LEO satellite antenna PCV. The experimental results show that the LEO satellite antenna PCV fluctuations should lie in the range [−12.6, 8.1] mm for the L1 band, and in the range [−19.5, 19.2] mm for the L2 band. With the proposed scheme, the LEO-augmented fast PPP user can avoid storing tens or hundreds of high dimensional satellite antenna PCV correction matrices in the LEO satellite navigation constellation. The analysis results can provide support and reference for satellite antenna design of a LEO navigation augmentation system.

Acknowledgment. This work is supported by National Natural Science Foundation of China (61627817, 11803023).

References

1. Haddock PC et al (2012) Integrated communications and navigation module. In: 2012 IEEE international Carnahan conference on security technology (ICCST)
2. Joerger M et al (2010) Analysis of Iridium-augmented GPS for floating carrier phase positioning. Navigation 57(2):137–160

3. Pratt J et al (2013) Satellite clock bias estimation for iGPS. GPS Solutions 17(3):381–389
4. Shiyue F et al (2012) Performance analysis and simulation of Iridium navigation satellite based on STK. In: 2012 second international workshop on earth observation and remote sensing applications
5. Meng Y et al (2018) A global navigation augmentation system based on LEO communication constellation. In: 2018 European navigation conference (ENC)
6. Li X et al (2018) LEO constellation-augmented multi-GNSS for rapid PPP convergence. J Geodesy
7. Araszkiewicz A, Völksen C (2017) The impact of the antenna phase center models on the coordinates in the EUREF Permanent Network. GPS Solutions 21(2):747–757
8. Montenbruck O et al (2008) Antenna phase center calibration for precise positioning of LEO satellites. GPS Solutions 13(1):23
9. Schmid R et al (2016) Absolute IGS antenna phase center model igs08.atx: status and potential improvements. J Geodesy 90(4):343–364
10. Schmid R et al (2007) Generation of a consistent absolute phase-center correction model for GPS receiver and satellite antennas. J Geodesy 81(12):781–798
11. Steigenberger P et al (2016) Estimation of satellite antenna phase center offsets for Galileo. J Geodesy 90(8):773–785
12. Yao Y et al (2017) Phase center variation modification on BDS high-precision baseline solution. In: 2017 4th international conference on information science and control engineering (ICISCE)
13. Zheng KK, Chu QX (2017) A novel annular slotted center-fed BeiDou antenna with stable phase center. IEEE Antennas Wirel Propag Lett PP(99):1
14. Yang W et al (2016) Analysis and correction of BDS code multipath bias. In: 2016 proceedings of the China satellite navigation conference (CSNC), vol III. Springer, Singapore
15. European GNSS Service Centre Galileo Satellite Metadata. https://www.gsc-europa.eu/support-to-developers/galileo-satellite-metadata. Accessed 08 Oct 2017

Analysis and Modeling on Interference of Solar Radio Burst on GNSS Signal

Dun Liu(✉), Chao Han, Ruimin Jin, and Weimin Zhen

No. 22nd Research Institute, CETC, Qingdao 266107, Shandong, China
Dun.L@163.com

Abstract. When the GNSS signal is overshadowed by the wide-range radio noise incited by a solar burst event, a potential interference would happen. Theoretical analysis shows the solar radio burst could impact GNSS signal in the way of a directional interference. A new parameter, Solar Radio Burst Index (SRBI), is put forward to indicate the severity of impact on signals. The SRBI is defined on the variation of carrier-to-noise ratio (C/N_0) of GNSS signal under solar burst impacts with respect to the quiet period of solar activity. Based on SRBI, a model on signal fading caused by the interference is developed further. The model is tested with GNSS observation from significant solar burst events from 2001 to 2017. The result shows an accuracy of 80% has been achieved. The SRBI and signal fading model could be used to monitor the solar burst with GNSS signal itself.

Keywords: Solar radio burst · Radio noise · RF interference · GNSS · SRBI

1 Introduction

Although GNSS could provide more accurate service for navigation applications, there are mounting concerns on its vulnerability as the weak GNSS signal is susceptible to interference. Solar Radio Burst (SRB) will radiate strong electromagnetic noise. If this electromagnetic radiation covers the working band of GNSS signal, it can produce a Radio-Frequency (RF) like interference to GNSS receivers. When the burst is strong enough, disruption in GNSS signal tracking would happen [1, 2]. ICAO has listed SRB as one of the interfering factors for GNSS vulnerability in aviation applications [3]. The Interference Mitigation and Elimination (IDM) Working Group under the International Committee on GNSS (ICG) also categorized SRB as one of the interfering sources to GNSS [4].

Early in 1999, Klobuchar etc. had pointed out the potential SRB interference to GPS signal [1]. In September 2005, Cerruti, of Cornell University observed the anomalous GPS signal 'scintillation', a phenomenon generally occurs after sunset, during the daytime in South America. Kintner, of Cornell University analyzed the event and concluded that it was caused by the radio noise radiated during the solar radio burst on September 7, 2005 which covered a broad range of radio frequency band including that of GPS works in [5]. The finding gained attention immediately and in-depth analysis was carried out consequently [6–8].

J. Sun et al. (Eds.): CSNC 2019, LNEE 563, pp. 196–206, 2019.
https://doi.org/10.1007/978-981-13-7759-4_18

Study has also been carried out in our previous work, including the analysis of the sudden ionospheric disturbances (SID) triggered by the solar burst, and monitoring of the GPS signal 'scintillation' phenomena caused by the solar radio burst event occurred on Dec. 13 2006 [9].

In scientific research, the wide-band radiation noise is generally monitored with special instruments, such as OVSA (Owens Valley Solar Array) or RSTN (Radio Solar Telescope Network), to determine whether a solar radio burst would has an interference effect on GNSS [10]. The electromagnetic radiation caused by the solar radio burst propagates at the speed of light, reaching the earth after about 8.3 min, and the impact can last for tens of minutes or even two hours. Therefore, it is difficult to provide timely interference monitoring and identification information for GNSS applications with these scientific observations.

The interference from solar radio bursts impacts GNSS receivers in the similar way to the ionospheric scintillation [5]. Therefore, methods in ionospheric scintillation study can be transferred to work in monitoring and modeling of solar radio bursts effects. In this paper, we develop the method to monitor and identify a solar radio burst event by using GNSS signal widely available.

To this end, this paper first analyzes the effect of solar radio burst on GNSS signal, and then put forward the solar radio burst index (*SRBI*), an index defined to indicate fluctuation of GNSS signal under SRB impact. Based on this, a model is established to predict the signal fading caused by SRB. The accuracy of the model is test with IGS GPS data collected in typical SRB events. Conclusion is given at last.

2 SRB Interference to GNSS Receiver

The effect of solar radio burst on GNSS receivers is essentially an electromagnetic interference. The solar radio burst interference is directional to GNSS receiver, injecting interfering energy at the solar zenith angle at the receiver position. Since the receiver antenna pattern varies with zenith angle (or elevation angle), the GNSS receivers at various locations are subject to different solar radio burst impacts depending on its received interference intensities [2, 8].

For a GNSS receiver with antenna pattern $g(\gamma)$, where γ is the zenith angle, carrier-to-noise ratio of the received signal during the period of calm solar activity is [8]:

$$(C/N_0)^0(e) = \frac{S}{P_N}\left[\frac{g(90-e)}{g(0)}\right] \tag{1.1}$$

where S is the signal strength received by the antenna and P_N is the background noise strength, e is the elevation angle.

When a solar radio burst happens, the carrier-to-noise ratio of the received signal then is [8]:

$$(C/N_0)(e,\theta) = S\left[\frac{g(90-e)}{g(0)}\right]\left[P_N + P_{SRB}\frac{g(\theta)}{g(0)}\right]^{-1} \tag{1.2}$$

where, P_{SRB} is the equivalent solar radio burst power, θ is the solar zenith angle at the site. It can be seen that the solar radio burst impacts GNSS receivers in the same way as RF interference, and its intensity is depended on the energy of the SRB-generated radiation noise locating in the GNSS working band. The interference effect is also depended on the solar zenith angle and gain of the antenna used by receivers [8, 11].

3 Solar Radio Burst Index - *SRBI*

3.1 Definition of SRBI

The interference of solar radio burst to GNSS receiver decreases the carrier-to-noise ratio of the received signal. This reduction can be treated as a fading variation of received signal strength. Therefore, as the ionospheric amplitude scintillation index S_4, the Solar Radio Burst Index (*SRBI*) can be introduced to depict the SRB effects. The definition of *SRBI* is as follows:

$$SRBI = \sqrt{\frac{\sum_{i=1}^{N}\left(\frac{C}{N_0}\right)_i^2 - \left(\sum_{i=1}^{N}\left(\frac{C}{N_0}\right)_i\right)^2}{\left(\sum_{i=1}^{N}\left(\frac{C}{N_0}\right)_i\right)^2}} \tag{1.3}$$

where, C/N_0 is the de-trended carrier-to-noise ratio of the GNSS signal, and N is the number of data in a period of time.

In practice, the *SRBI* could be calculated with the differential carrier-to-noise ratio $\Delta C/N_0$ with the data of the burst day and that of the previous quiet day. Since the orbital period of GNSS is generally 12 h (for instance GPS is actually 11 h and 58 min), signal strength received by GNSS receivers at the same site is almost the same at the same time in two successive days. In this way, one can easily identify and eliminate the potential multipath effects that could confused with SRB interference.

Figure 1 shows the time series of carrier-to-noise ratio for GPS PRN 11 satellite obtained from observation data of IGS PERT station during the SRB event on Dec. 13 2006. The length of $\Delta C/N_0$ time series is 2 h started at UT 02:00. The data sampling rate is 1 s, so there are total 7200 epochs of data in the time series. In the figure, the green curve is the carrier-to-noise ratio for the quiet day before the solar radio burst, the red curve is for the solar radio burst day, and the blue curve is the differential carrier-to-noise ratio after removed the trend.

With RSTN data, it has be shown that the SRB event started at UT 02:23, and reached the peak value of 130,000 SFU (Solar Flux Unit, 1 SFU = 10^{-22} Wm^{-2} Hz^{-1}) at UT 03:36 [5, 8]. With the figure, it can be seen that at the 1400 epoch (approximately corresponding to UT 02:23) deep fading emerges, leading to the decrease of carrier-to-noise ratio of received signal. The time series interrupted at the 5700 epoch (corresponding to UT 03:36), indicating the interference caused by SRB had the greatest impact on GPS signal tracking. At that time, the flux density reached the maximum and caused the receiver to lose of lock on signal of PRN 11 satellite.

Figure 2 shows the Solar Radio Burst Index *SRBI* sequence calculated with the $\Delta C/N_0$ time series. The calculation was made with a sliding window with the length of 3 min, and moving step of 1 min. It can be seen that the *SRBI* index reached a value of 0.6 in the case of deep fading caused by solar radio bursts. Since the GPS carrier-to-noise ratio data output by the IGS receiver is in discrete values, the obtained $\Delta C/N_0$ time series shows a discrete variation, a characteristics especially apparent in the quiet period (see Fig. 1). Consequently, the value of *SRBI* is about 0.1 instead of zeros during the quiet period.

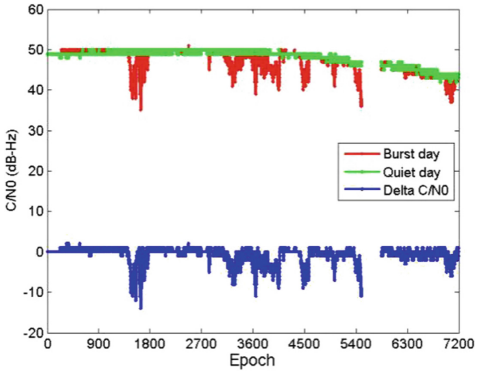

Fig. 1. C/N_0 series for GPS PRN11 signal under SRB. IGS PERT, Dec. 13 2006.

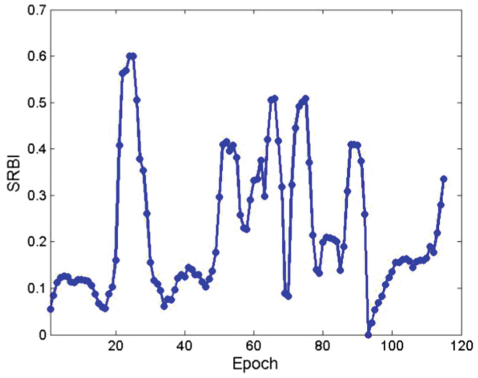

Fig. 2. *SRBI* series for GPS PRN11 signal under SRB. IGS PERT, Dec. 13 2006.

3.2 Identification of SRB Event Based on SRBI

To identify solar radio burst events with the *SRBI* index, the following factors should be taken into account.

Since the $\Delta C/N_0$ time series obtained with GNSS receiver output varied discretely, the *SRBI* value in period of calm solar activity is not 0 (about 0.1). Therefore, the value

of 0.1 is chosen as the detection threshold for the effects of solar radio burst events. A solar radio burst event generally lasts for about ten minutes to dozens of minutes or even longer. Consequently, a segment of *SRBI* sequence with values larger than 0.1 and lasting for more than 10 min would be selected as the indicator for a potential solar radio burst event.

Ionospheric scintillation can also cause GNSS signal fades, making the calculated *SRBI* value greater than 0.1. It is necessary to discriminate the effect of SRB event from that of ionospheric scintillation. Since ionospheric scintillation typically occurs after sunset at local time, while the solar radio burst impacts the dayside regions on earth, it will be convenient to distinguish SRB event from ionospheric scintillation by judging the location of GNSS receiver [12].

In addition, the multipath effect on GNSS receiver can also cause larger values of C/N_0 measurement. Due to the periodicity of GNSS satellite orbit, the multipath effect also appears periodically. With the comparison of *SRBI* sequence in the corresponding time period for two consecutive days, one can effectively identify the SRB event and separate it from the multipath effects. This is also why the *SRBI* is calculated using the differential carrier-to-noise ratio from two successive days instead of the absolute carrier-to-noise ratio values in the burst day.

It should be noted that the solar radio burst will impact all the GNSS receivers located in daytime areas to varying extents. As a consequence, all the signals tracked by receivers in a larger areas will be interfered simultaneously. On the contrary, ionospheric scintillation or multipath effect only affects part of the satellites observed by a receiver, and RF interference can only impact receivers in a limited area. This is one of the significant characteristics to distinguish solar radio burst events from other effects.

4 Modeling of Signal Fading Under SRB Effects

For ionospheric scintillation, the range of signal fading variation over time has the exponential relationship with S_4, the ionospheric amplitude scintillation index [12]. Similarly, a model can also be established to predict the fading depth of SRB impacted GNSS signal based on the *SRBI* index.

The differential carrier-to-noise ratio $\Delta C/N_0$ is obtained from the difference of carrier-to-noise ratios between the solar calm day and the next solar active day. When expressed in dB, the differential carrier-to-noise ratio $\Delta C/N_0$ can be expressed as:

$$\begin{aligned}\Delta(C/N_0) &= (C/N_0)^0 - (C/N_0) \\ &= P_N - \left[P_N + P_{SRB}\frac{g(\theta)}{g(0)}\right]\end{aligned} \tag{1.4}$$

It can be seen that, in the ideal case, the differential carrier-to-noise ratio $\Delta C/N_0$ is only depended on the equivalent solar radio burst power P_{SRB} and the antenna pattern. In practice, *SRBI* index is generally calculated once using a segment of data with the length of a few minutes. The satellite elevation angle changes little during this short

period of time. This makes the change of antenna gain from varying elevation angle contributing little to the signal intensity variation. Therefore, the signal fading depth and *SRBI* index is only depended on P_{SRB} (as the effect from antenna gain changing has been removed by de-trending $\Delta C/N_0$). As a result, a model of signal fading depth could be constructed based on the *SRBI* index.

Figure 3 shows the signal fading depth with respect to the *SRBI* index with data from IGS PERT station for the solar radio burst event on Dec. 13, 2006. The signal fading depth is calculated as follows:

$$P_{fade} = Max(\Delta C/N_0) - Min(\Delta C/N_0) \tag{1.5}$$

where, $\Delta C/N_0$ is the carrier-to-noise ratio time series of each satellite signal in *SRBI* index calculation. The length of data is taken as 3 min.

It can be seen that there is a power law relationship between the *SRBI* index (blue asterisk) and the GNSS signal fading depth P_{fade} (red circle). Also can be seen that the fading depth P_{fade} is saturated at a certain *SRBI* threshold. This is similar to the signal fading depth caused by ionospheric scintillation [12]. Therefore, the following fading model is proposed:

$$P_{fade} = \begin{cases} a * SRBI^b & SRBI < 0.6 \\ C & SRBI \geq 0.6 \end{cases} \tag{1.6}$$

$$C = a * 0.6^b$$

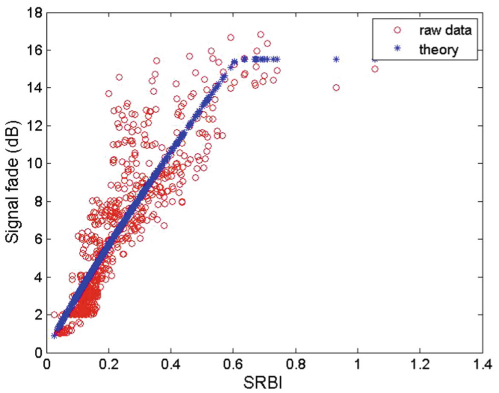

Fig. 3. Fading model for GNSS signal under SRB. IGS PERT, Dec. 13 2006.

Table 1 shows the model fitting results with GPS observation from IGS site of PERT (115.8852°E, −31.8019°N), PIMO (121.0777°E, 14.63357°N) and GUAM (144.8683°E, 13.5893°N) for the solar radio burst event on Dec. 13, 2006.

Table 1. Coefficients of GNSS signal fading model for SRB

IGS site	Coeff. a	Coeff. b
PERT	24.2171	0.9003
PIMO	20.4177	0.8080
GUAM	20.2469	0.8078

It can be seen that there is much in common between the constructed fading models. Taking the result of PIMO station and GUAM station as examples, both stations are located in the northern hemisphere with almost the same latitudes, and the solar zenith angles are similar for both sites during the SBR event, so the estimated coefficients of signal fading models are almost the same. For PERT station, the established signal fading model is also similar to those of PIMO and GUAM, although the site locates in the southern hemisphere. Therefore, it is reasonable to construct models to predict the GNSS signal fading for all receivers interfered by the same SRB event.

5 Accuracy of GNSS Signal Fading Model

The GNSS signal fading model has been established and tested with IGS data for solar radio burst events since 2001.

5.1 Cross-Validation of the Models

The following process was adopted to cross-validate the signal fading models.

(1) Select the solar radio burst events

The electromagnetic radiation generated by the solar radio bursts should be strong enough to impact GNSS observation. Spectral range of radiated noise should cover the L-band of GPS working. And the most important, high sampling rate of GPS observation (1 s) during the SRB events should be available from IGS.

(2) Select sites for cross-validation

Determine the dayside areas for a solar radio burst event and the available IGS sites, and select two IGS stations for modeling and testing purpose respectively.

(3) Estimate signal fading model

Calculate the *SRBI* index and signal fading depth using the observation of modeling station, and estimate coefficients of the fading model.

(4) Predict signal fading depth

Calculate the *SRBI* index with the data of testing station, and then with the estimated model from modeling station, the signal fading depth $P_{fade-model}$ for testing station is predicted.

(5) Calculate true signal fading depth

Extract the fading depth of GPS signal $P_{fade-real}$ at the corresponding time from the observation at testing station.

(6) Estimate accuracy of fading model

The accuracy of the GNSS signal fading model from the modeling station is estimated as the following:

$$Relative\,Err = 1 - \frac{\left|P_{fade-model} - P_{fade-real}\right|}{P_{fade-real}} \times 100\% \tag{1.7}$$

(7) Analyze the fading model accuracy statistically

Model accuracy are test statistically with data from multiple IGS stations for each solar radio burst event, and then for all selected solar radio burst events.

5.2 Results of GNSS Signal Fading Models

The solar radio burst events during years of 2001–2017 were selected with the principles in the above method (step 1). The events that has GNSS interfering effects are shown in Table 2. For each solar radio burst event, five IGS stations located in daytime regions were picked up for model cross-validation.

Table 2. SRB events for model verification

Time Y-M-D	Start time UT	Max. time UT	Duration min	Max. flux intensity 10^{-22} W/m^{2}Hz
2003-10-28	1131.0	1201.0	221.0	25000.0
2005-09-07	1724.0	1738.0	98.0	12000.0
2006-12-06	1842.0	1917.0	318.0	150000.0
2006-12-13	0223.0	0225.0	63.0	150000.0
2011-09-24	–	–	120.0	114144

Table 3 shows the test results for the solar radio burst event on Dec. 13, 2006. The cross-validation of the GNSS signal fading model was made with data from IGS stations of PERT, PIMO, and GUAM.

Table 3. Testing result of fading model for GPS signal

	PERT model	PIMO model	GUAM model
PERT data	26.15%	26.62%	26.29%
PIMO data	20.55%	18.36%	18.13%
GUAM data	19.44%	17.17%	16.9%

Further analysis was made to all the five solar radio burst events given in Table 2. The main results are:

(1) For the five solar radio bursts events, the accuracy of the model is 75.4% (Oct. 28, 2004), 85.3% (Sep. 7, 2005), 78.4% (Dec. 6, 2006), 79.4% (Dec. 13, 2006) and 84.2% (Sep. 24, 2011) respectively. The average accuracy of the model is about 80%.
(2) Certain stations show a poor performance in the model cross-validation test. The accuracy degradation is mainly due to the large solar zenith angle (receiver was less affected by solar radio burst), large multipath effect, and the poor receiver measurement.

6 Further Discussion

From the analysis results for typical solar radio burst events, it can be seen that:

(1) For a special solar radio burst event, a common signal fading model can be constructed to predict the variation of GNSS signal fading.

From the analysis, it can be seen that there is close similarity between the GNSS signal fading models established with observations from various stations. Specially, for stations located in the same hemisphere with similar latitudes, the estimated model coefficients are almost the same. So for a special SRB event, the signal fading model could be constructed with the high quality measurement from GNSS receivers located in low latitude areas (with a higher solar zenith angle). The model can then be used for signal fading prediction for other stations located in the radio burst affected areas. Consistency check among stations can also be performed to make a rapid identification of a possible solar radio burst event.

(2) The signal fading model shows saturation at large *SRBI* value, making the model less accurate.

It has been found that when the *SRBI* index exceeds 0.6, the fading depth of the GNSS signal reaches a saturation. The GNSS signal fading model works well in the range of 0.1–0.6 for *SRBI* index. However, in the saturation region, the model performance decreases. In saturation region, the fading depth of the GNSS signal varies generally between 14–18 dB. The specific value is depended on factors such as the solar zenith angle and the antenna gain etc.

(3) Quality of the GNSS signal measurement plays an important role on the model accuracy.

When affected by multipath environment, the received signal strength fluctuates and creates larger *SRBI* estimation. Also, limited by realization, receivers might output carrier-to-noise ratio at discrete integer values, impacting the accuracy of constructed models. This is especially true for early IGS observations before the year of 2003. The analysis has shown that the limiting model performance occurred more frequently with the data during this period. In addition, shallow fading in GNSS signal will also make

the model less accuracy. This will be the case for a weak solar radio burst or a low solar zenith angle interference.

(4) Only strong solar radio bursts pose severe interference to GNSS.

It also can be seen that the solar radio burst would has a significant impact on GNSS receivers only when the radio burst is strong enough, and at the same time, the electromagnetic radiation noise should cover the GNSS working band. Dozens of solar radio bursts have happened from 2001 to 2017, however, only a few of these events have had a significant impact on GNSS. Among them, the two solar radio burst events in December 2006 had the most severe impacts on a global scale. The GPS receivers experienced signal fading of more than 10 dB and even 20 dB under the most serious condition. On the contrary, the solar radio burst event in October 2003 and September 2005 are the weak ones, reducing the receiver's carrier-to-noise ratio only by 3–5 dB, posing no serious affect to GPS receivers.

7 Conclusion

Strong electromagnetic radiation generated by solar radio burst could cause interruption of GNSS signal tracking, making it one of the main interference source.

This paper proposes an index, solar radio burst index (*SRBI*), to describe the interference effects of radio bursts. GNSS signal fading varies with *SRBI* following a power law rule. According this, a model has been constructed to predict the signal fading depth. IGS GPS data are used to test the established model for typical solar radio burst events from the year 2001 to 2017. The results show the model has an average accuracy of 80%.

The model can be used for fading depth prediction for GNSS signals affected by solar radio bursts. The *SRBI* and the fading model can also be used to identify a possible solar radio burst event rapidly.

Acknowledgments. This study is funded by the National Key R&D Program of China (No. 2018YFB0505100) - "GNSS interference detection and localization technology and application demonstration for urban area and critical infrastructure".

References

1. Doherty PH, Klobuchar JA, Kunches JM (2000) Eye on the ionosphere: the correlation between solar 10.7 cm radio flux and ionospheric range delay. GPS Solution 3(4):75–79
2. Bala B, Lanzerotti LJ, Gary DE, Thomson DJ (2002) Noise in wireless systems produced by solar radio bursts. Radio Sci. 37(2):1018. https://doi.org/10.1029/2001RS002481
3. International Civil Aviation Originations (2017) DOC 9849 - Global Navigation Satellite System (GNSS) Manual, Montreal, Quebec, Canada
4. Zhen WM (2013) Suggestion on standardized reporting form of GNSS interference. In: The 8th meeting of ICG, 11–13 November Dubai, UAE
5. Cerruti AP (2008) Solar radio burst effects on global positioning system receivers, Ph.D. thesis, Cornell University, Ithaca, NY

6. Chen Z, Gao Y, Liu Z (2005) Evaluation of solar radio bursts' effect on GPS receiver signal tracking within International GPS Service network. Radio Sci 40. https://doi.org/10.1029/2004RS003066. RS3012
7. Kintner PM Jr, O'Hanlon B, Kintner PMS (2009) Global positioning system and solar radio burst forensics. Radio Sci 44. https://doi.org/10.1029/2008RS004039. RS0A08
8. Carrano CS, Bridgwood CT, Groves KM (2009) Impacts of the December 2006 solar radio bursts on the performance of GPS. Radio Sci https://doi.org/10.1029/2008RS004071
9. Liu D, Zhen WM, Quan L (2018) Development of space weather support system for BDS applications. In: The 29th conference of spacecraft TT&C technology in China, Shanghai, China
10. National Geophysical Data Center (2004) Solar radio data. http://www.ngdc.noaa.gov/stp/SOLAR/ftpsolarradio.html. Boulder, Colo
11. Ward P (1999) Effects of RF interference of GPS satellite signal receiver tracking. In: Kaplan ED (ed) Understanding GPS principles and applications, Artech House, Norwood, Mass, pp 209–236
12. ITU (2012) Ionospheric propagation data and prediction methods required for the design of satellite services and systems (ITU-R P.531-11), Geneva

Research on Receiver Autonomous Integrity Monitoring Technology Based on GNSS Baseband Signal

Ershen Wang[1,2] and Di Yang[1(✉)]

[1] Shenyang Aerospace University, Shenyang 110136, China
wanges_2016@126.com, jcy_1408@163.com
[2] Liaoning General Aviation Key Laboratory, Shenyang Aerospace University, Shenyang 11013, China

Abstract. With the increasing requirements for satellite navigation and positioning technology, the detection and identification of faulty satellites has become the focus of attention. Therefore, this paper proposes a receiver autonomous integrity monitoring algorithm based on the original navigation signal to realize the detection and elimination of faulty satellites. This method firstly expresses the signal to noise ratio of the channel by using the original navigation signal; secondly, construct a new covariance matrix by using signal to noise ratio and channel bandwidth; then use the covariance matrix to derive the PVT covariance matrix; finally, the detection and identification of the faulty satellite is carried out. Tests show that the method can detect the influence of slight noise more sensitively; Therefore, the method not only applies the original navigation signal to the integrity monitoring, but also improves the sensitivity of the integrity monitoring, thereby greatly improving its performance.

Keywords: Satellite navigation signal · Integrity · Positioning · Sensitivity · Fault detection

1 Introduction

With the rapid advancement of the BeiDou/GNSS networking process, more satellites and navigation signals can be provided. The comprehensive use of rich satellite navigation information has become the development trend of the new generation of aviation navigation high integrity monitoring technology. The essence of integrity monitoring technology is the application of redundant observation methods to improve integrity and availability. The existing traditional integrity monitoring algorithms use the pseudo-range redundancy information to realize the positioning function and at the same time realize the function of integrity monitoring. For example, the parity vector algorithm rejects multiple gross errors and is a receiver autonomous integrity monitoring (RAIM) algorithm that obtains multiple satellites simultaneously failing [1, 2]. An improved RAIM algorithm based on least squares residuals can handle multiple satellite failures [3]. The BeiDou/GPS data is processed and fault detected by weighted least squares method [4, 5].

J. Sun et al. (Eds.): CSNC 2019, LNEE 563, pp. 207–218, 2019.
https://doi.org/10.1007/978-981-13-7759-4_19

The receiver's autonomous integrity monitoring is mainly for detecting and eliminating fault satellite signal. The idea of fault detection and elimination is to construct statistics on navigation positioning errors and compare them with alarm thresholds [14]. In the algorithm, the test statistic and the detection threshold are designed. When the test statistic is less than the detection threshold, it indicates that there is no fault, otherwise, there is a fault. However, there are certain requirements for the number of visible satellites. At least 5 visible satellites are required for fault detection, and more than 6 visible satellites are needed for fault identification. At present, these methods use the satellite redundancy information to check the consistency of the navigation and positioning solution [6]. However, these traditional methods only use the solution results in the current epoch [13]. If the navigation signal has been affected during the propagation process, it cannot be used for normal navigation and positioning. The traditional algorithm obtains the navigation message and related observations after demodulating the navigation signal, and then calculates the pseudo-range, and then performs the integrity detection. However, the impact of the satellite navigation signal itself on integrity monitoring is not considered. Therefore, it is possible to consider the information obtained during the capture tracking process and detect that the navigation signal has been affected.

Therefore, this paper designs a receiver integrity monitoring algorithm based on navigation baseband signal, uses the navigation baseband signal to capture the information that is not used for integrity monitoring during the tracking process, introduces it into the new algorithm, constructs the test statistic, and realizes integrity monitoring function. It enables it to detect the presence of faults earlier, thereby improving the sensitivity of integrity monitoring.

2 Original Signal-Assisted Integrity Monitoring Algorithm

RAIM technology was originally developed for aerospace engineering, performing consistency checks on satellite measurements, providing users with reliable positioning, and RAIM technology provides high performance. However, the existing RAIM algorithm does not consider the error that may have existed before the pseudo-range is calculated, but the original satellite navigation signal received by the receiver actually contains a wealth of unprocessed a priori information, that is, the signal-to-noise ratio obtained during the capture tracking and the parameters such as the timely correlation peak. Therefore, this paper introduces these parameter information into the integrity monitoring algorithm, so that the faults that may already exist are detected before the pseudo-range is obtained. Compared with the traditional method, the earlier detection of the fault signal is realized, thereby better avoiding the positioning error caused by the error information.

2.1 Fundamental

Considering that the visible satellite is K, the baseband signal model can be expressed as:

$$x = \sum_{i=1}^{K} \alpha_i a_i(\theta) + n \tag{1.1}$$

Where x represents the received signal, which is an N × 1 dimensional vector; α_i represents the complex amplitude of the signal; $a_i(\theta)$ represents the vector of the transmitted unified signal; n is Gaussian white noise;

$$a_i(\theta) = \begin{bmatrix} c_i(t_1 - \tau_i(\theta))e^{-i2\pi f_i(\theta)t_1} \\ \cdots \\ c_i(t_N - \tau_i(\theta))e^{-i2\pi f_i(\theta)t_N} \end{bmatrix}.$$

Its vector mode can be expressed as:

$$x = \alpha A(\theta) + n \tag{1.2}$$

First, the original channel signal-to-noise ratio is represented by the original navigation signal:

$$SNR_i = \frac{x^H P_i(\hat{\theta})x}{x^H Q_i(\hat{\theta})x} \tag{1.3}$$

among them:

$$Q_i(\hat{\theta}) = I - P_i(\hat{\theta}) = Q_i \tag{1.4}$$

$$P_i(\hat{\theta}) = a_i(\hat{\theta})\left(a_i(\hat{\theta})^H a_i(\hat{\theta})\right)^{-1} a_i(\hat{\theta})^H \tag{1.5}$$

x represents the original digital baseband signal, $a_i(\hat{\theta})$ representing the vector of the transmitted unified signal.

Secondly, the estimated delay $\hat{\tau}_i$ of the established signal on each channel is a Gaussian distribution centered on the true delay τ_i. The variance corresponds to CRB and is:

$$\hat{\tau}_i \sim N(\tau_i, CRB_i) \tag{1.6}$$

$$CRB_i = \frac{1}{4B^2 SNR_i} \tag{1.7}$$

B represents the filter bandwidth. Therefore, by introducing the signal-to-noise ratio, the progressive covariance matrix of the delay can be represented by the original navigation signal, and the expression is as follows:

$$C_r = \frac{X^H X}{4B^2} \begin{bmatrix} \frac{1}{X^H P_1(\hat{\theta}) X} & \cdots & 0 \\ \vdots & \ddots & \vdots \\ 0 & \cdots & \frac{1}{X^H P_K(\hat{\theta}) X} \end{bmatrix} \tag{1.8}$$

When a delayed asymptotic covariance matrix is obtained, the prior method PVT covariance matrix can be derived:

$$Cov(\hat{\theta}) = (H^T C_p^{-1} H)^{-1} = \begin{bmatrix} \sigma_x^2 & \sigma_{yx} & \sigma_{zx} & \sigma_{bx} \\ \sigma_{xy} & \sigma_y^2 & \sigma_{zy} & \sigma_{by} \\ \sigma_{xz} & \sigma_{yz} & \sigma_z^2 & \sigma_{bz} \\ \sigma_{xb} & \sigma_{yb} & \sigma_{zb} & \sigma_b^2 \end{bmatrix} \tag{1.9}$$

among them, $C_P = cC_r$, c represents the speed of light, which in turn gives three independent parameters $(\sigma_x^2, \sigma_y^2, \sigma_z^2)$.

The PVT standard deviation obtained by this method is:

$$T_{DRAIM} = \sqrt{\sigma_x^2 + \sigma_y^2 + \sigma_z^2} \tag{1.10}$$

And thus construct the test statistic. Finally, the distribution of the PVT standard deviation is empirically evaluated from the expected false alarm probability, combined with the new test statistic to determine the threshold. When the test statistic is greater than the threshold, it indicates that there is a fault; when the test statistic is less than the threshold, it indicates that there is no fault.

3 Detection Threshold Calculation

In the receiver autonomous integrity monitoring algorithm, different test statistics are obtained according to different modeling methods. When the test statistic is constructed, the corresponding detection threshold is calculated, and the test statistic is compared with the detection threshold to realize the detection of the fault signal. It can be seen that the construction of the detection threshold is important. The currently constructed test statistic is based on the different configurations of the tracking process and is derived from the empirical distribution, which is different compared to the traditional algorithm. In this chapter, the traditional method, the calculation method of the detection threshold of the least squares method, is also listed.

In the least squares receiver-based autonomous integrity monitoring algorithm, the GNSS pseudo-range observation linearization equation is:

$$y = HX + \varepsilon \tag{1.11}$$

Where y represents the observed pseudo-range amount minus the n × 1 dimensional vector consisting of the distance calculated using the coordinates of the satellite and the coordinates of the user receiver; H is an n × 4 dimensional observation matrix, representing a linearization matrix composed of a direction vector of each satellite to the user receiver and a fourth column of all 1; X is a 4 × 1 dimensional unknown vector, including a three-dimensional position vector and receiver clock difference [7]; ε is an observation noise vector of n × 1 dimension, obeying a Gaussian distribution with mean zero and variance (when SA is used, σ is 33.3 m; when there is no SA, the σ of C/A code is 12.5 m, the σ value of the P code is 2 m) [12].

From the principle of least squares estimation, a state estimation value [8] that minimizes the sum of the squares of the noise errors ε is required to be solved as:

$$\hat{X} = (H^T H)^{-1} H^T y \tag{1.12}$$

Therefore, the sum of the squares of the pseudo-range residuals can be expressed as:

$$SSE = V^T V = (y - H\hat{X})^T (y - H\hat{X}) \tag{1.13}$$

Where, SSE obeys a chi-square distribution with a degree of freedom of n − 4. The test statistic at this time is:

$$T = \sqrt{SSE/(n-4)} \tag{1.14}$$

It can be seen that the test statistic follows the chi-square distribution with a degree of freedom of n − 4 [9].

Make a binary hypothesis for SSE. In the case where the false alarm rate Pfa and the probability density function are known, t_{LS} can be obtained by the following formula:

$$P(SSE > t_{LS}) = \int_{t_{LS}}^{\infty} f(x)dx = P_{FA} \tag{1.15}$$

The detection threshold is:

$$T_{th} = \sqrt{t_{LS}/(n-4)} \tag{1.16}$$

In this paper, in the receiver integrity monitoring algorithm based on the original navigation signal, the test statistic cannot be described by the existing distribution. The empirical distribution function should be used to obtain the detection thresholds for different configurations. When based on the configuration shown in the following table, the threshold value is taken to be 100 m [10] (Table 1).

Table 1. Signal tracking related configurations

Number of visible satellites	5
Sampling frequency	30 MHz
Carrier tracking	10 Hz
Code tracking	1 Hz

4 Simulation Test

The probability of a failure is the risk of integrity. Often, the two concepts of faults and errors are considered to be completely equivalent. All possible fault sources of GNSS are summarized into three types according to time-varying characteristics: random noise, strong stability constant deviation and slowly changing Mar Kov Process [11]. Among them, GNSS noise, such as Gaussian noise; GNSS deviation, such as satellite clock difference. The original navigation signal is introduced into the receiver integrity monitoring algorithm, in order to use the data obtained during the capture tracking for integrity monitoring, and the data acquired during the capture tracking is introduced into the algorithm to obtain a new test statistic, and the test statistic is compared with the detection threshold. If the value of the test statistic is greater than the detection threshold, it indicates that the satellite signal has become an unavailable signal, that is, the existence of the fault is determined.

Therefore, this paper uses the navigation signal simulator to simulate and acquire the IF sampling data, and at the same time obtain the visible satellite state information during the analog signal. The relevant configuration is as follows (Table 2):

Table 2. Signal acquisition related configuration

Acquisition time	2017.7.20.4:00
Time length of signal acquisition	10 s
Acquisition signal type	BDS signal
Number of visible satellites	5

The performance of RAIM technology may be reduced by several factors: the small number of satellites in the field of view, receiving unwanted or stray signals such as multipath (MP) or interference (RFI). RAIM's integrity monitoring is based on pseudo-range redundancy, the correlator output, which is a posteriori method; RAIM does not consider the received raw data before the relevant step. However, GNSS signals may be affected by multipath or interference signals, resulting in inconsistencies. It must be discovered early to avoid potential hazards in the navigation process. Based on the correlator output, RAIM may not detect some special conditions, such as MP reception, interference, and so on. The multipath signal is added to attenuate the original signal energy, and the signal-to-noise ratio is reduced. The algorithm introduces the signal-to-noise ratio into the integrity monitoring, so any event that may affect the integrity performance can be detected. The following experiment is carried out to show the test

result graph, and the signal-to-noise ratio of the signal after the fault-free signal is compared with the signal-to-noise ratio of the signal after the multipath signal is added.

Firstly, the analog IF sampling data is simulated and received, and then the IF sampling data is captured and tracked. The tracking signal duration is 1.2 s, and the tracking signal data is output every 1 ms. Therefore, the correlation peak value of 1200 points and the value of the timely signal to noise ratio can be obtained. That is, even if the signal-to-noise ratio and the correlation peak are obtained through the tracking process, and the observation matrix H is obtained by using the navigation message, and the obtained correlation parameters are brought into the algorithm, the corresponding test statistic per 1 ms can be obtained, and then determine the existence of the fault. As shown in Fig. 1:

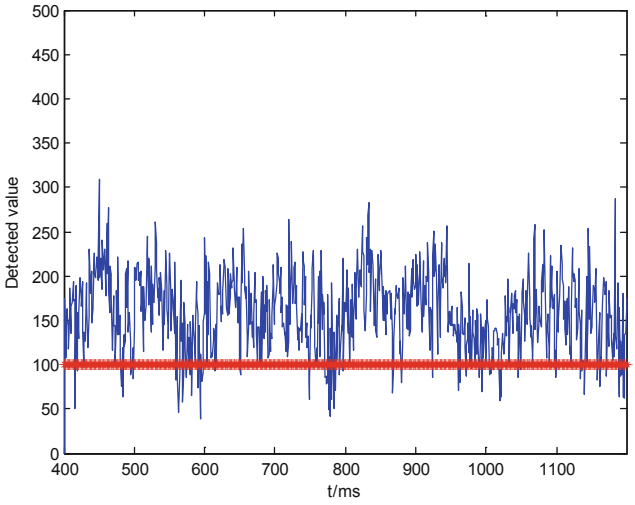

Fig. 1. BDS signal failure detection result graph

The current analog signal is normal at 4:00 on July 20, 2017, because it has been disturbed, so the associated noise or environmental impact can also be verified. As can be seen from Fig. 1, at this time, the test statistic of 718 points is larger than the detection threshold.

For the collected 10 s IF sampling data, a multipath delay of 10 m is added to the BDS signal during the period, and the multipath signal is added to the first star, and the other configurations are unchanged. Using the timely correlation peak and the timely signal-to-noise ratio obtained at this time, the signal-to-noise ratio is compared, and the test statistic of the 1200 points is calculated, as shown in Figs. 2 and 3. The BDS signal with a 10 m multipath delay is detected by the least squares method, as shown in Fig. 4:

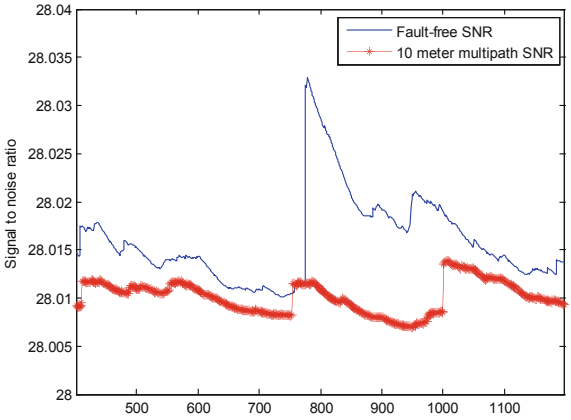

Fig. 2. Signal-to-noise ratio of signal without fault and signal-to-noise ratio of signal after adding 10 m multipath signal

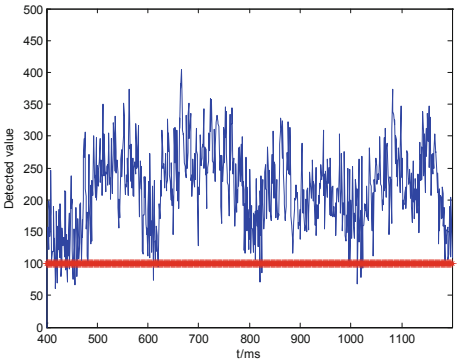

Fig. 3. BDS signal fault detection result with 10 m multipath delay

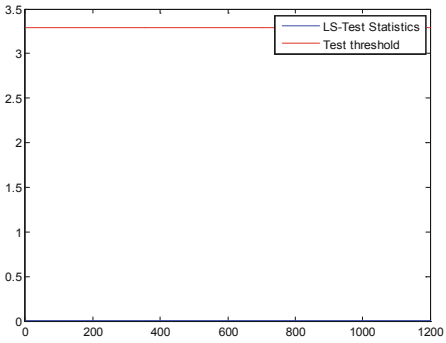

Fig. 4. Least squares fault detection result

It can be seen from Fig. 3 that when a multipath delay of 10 m is added, the value of the test statistic of 1200 points is increased. At this time, the failure detection rate is 97.25%. The least squares method cannot be detected.

For the collected 10 s data, the configuration still uses the initial parameters, but at this time, the multipath delay of 5 m is added, the multipath signal is added to the first star, and the IF sampling data obtained by adding the 5 m multipath delay is processed and obtained in time. The correlation peak and the timely signal-to-noise ratio compare the signal-to-noise ratio of the signal without fault with the signal-to-noise ratio of the signal after adding 5 m multipath, and at the same time, the test statistic of 1200 points at this time is obtained. As shown in Figs. 5 and 6; The BDS signal with 5 m multipath delay is detected by least squares method, as shown in Fig. 7:

It can be seen from Fig. 6 that when a multipath delay of 5 m is added to the signal, the value of the test statistic is increased compared with the multipath delay result of adding 10 m. At this time, the failure detection rate is 96.75%. It shows that the

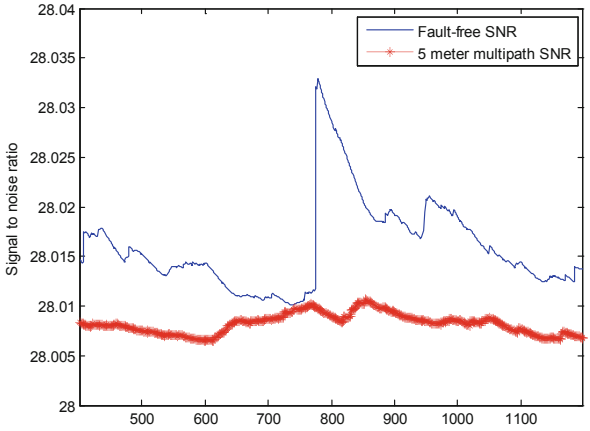

Fig. 5. Signal-to-noise ratio of signal without fault and signal-to-noise ratio of signal after adding 5 m multipath signal

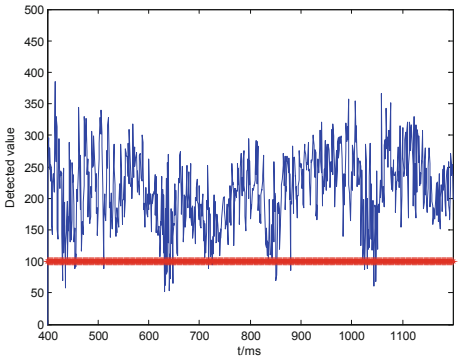

Fig. 6. BDS signal fault detection result with 5 m multipath delay

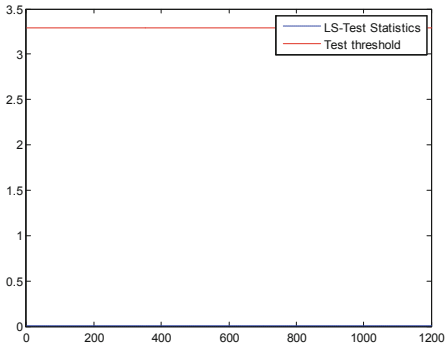

Fig. 7. Least squares fault detection result

algorithm can still detect when there is 5 m multipath delay. However, the least squares method does not detect the existence of 5 m multipath.

When simulating and collecting the 10 s BDS signal, if a multipath delay of 2 m is added to the relevant configuration, the multipath signal is added to the first star, and the other configurations remain unchanged. The IF sampling data of the signal with 2 m multipath delay at this time is collected, and the tracking and tracking processing is performed to obtain the timely correlation peak and the timely signal to noise ratio, and the value of the observation matrix is obtained by using the navigation message at this time. Comparing the signal-to-noise ratio of the signal without fault with the signal-to-noise ratio of the signal after adding 5 m multipath, the test statistic of 1200 points with 2 m multipath delay added at this time can be obtained. As shown in Figs. 8 and 9. The BDS signal with 2 m multipath delay is detected by least squares method, as shown in Fig. 10 (Table 3):

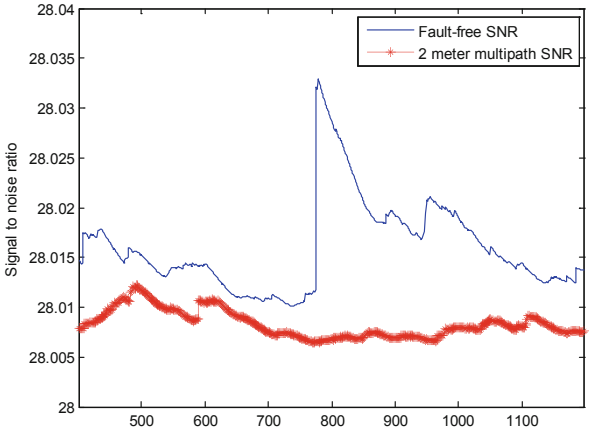

Fig. 8. Signal-to-noise ratio of signal without fault and signal-to-noise ratio of signal after adding 2 m multipath signal

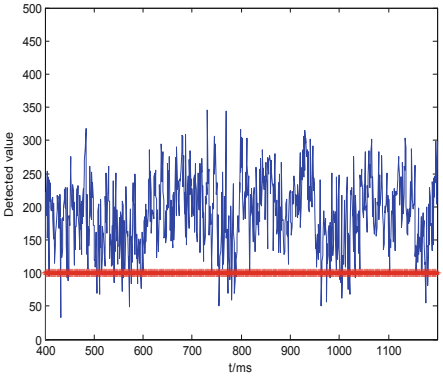

Fig. 9. BDS signal fault detection result with 2 m multipath delay

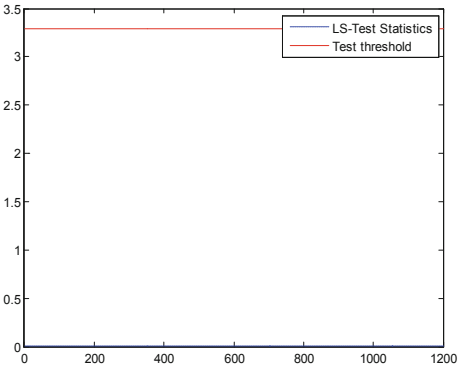

Fig. 10. Least squares fault detection result

Table 3. Test statistic and detection threshold table

Test statistics	Detection threshold
0.280514873493427	3.29052673149190
0.000976998425709399	3.29052673149190
1.64257700468638e-07	3.29052673149190
7.73685428617538e-08	3.29052673149190
5.95297125774980e-08	3.29052673149190
9.76039521790220e-08	3.29052673149190
6.52123281603924e-08	3.29052673149190

As can be seen from Fig. 9, compared with Fig. 1, even if a multipath delay of 2 m is added, 759 points exceed the detection threshold, thereby detecting the presence of a fault. At this time, the failure detection rate is 94.88%. However, the least squares method does not detect the existence of 2 m multipath. Therefore, this algorithm can detect that a smaller fault is identified, and its sensitivity is higher.

5 Conclusion

This paper proposes to introduce the original navigation signal into the integrity monitoring algorithm, and capture the missing information in the process of capturing and tracking the IF sampling data, and use it for integrity monitoring. And through experiments, we can see that the multi-path delay of 10 m, 5 m, and 2 m is added to the IF data of the acquisition time of 10 s, the value of the test statistic will increase to different degrees, thereby detecting the existence of the fault. The simulation experiment shows that the algorithm is related to signal energy, and has high sensitivity. It can detect any event that may have a weak influence on PVT, so that the potential risk of navigation can be predicted.

Acknowledgment. This study is funded by the National Natural Science Foundation of China (61571309, 6111161); the Open Program of Key Laboratory of Intelligent Waterway Transport of Ministry of Transport and the Fundamental Research Funds for the Central Universities (No. 3132016317); Liaoning BaiQianWan Talents Program; Scientific Study Project for Liaoning Province Ministry of Education (L2014059, L201716, UPRP2018198); Program for Liaoning Excellent Talents in University (LR2016069).

References

1. Zhang Q, Zhang X, Chang X (2007) Research on RAIM algorithm under the assumption of simultaneous multiple satellites failure. In: Proceedings of the eighth ACIS international conference on software engineering, artificial intelligence, networking, and parallel/distributed computing, Qingdao, China, pp 719–725
2. Zhang Q, Zhang X, Chang X (2008) RAIM algorithm for identifying two faulty satellites. J Beijing Aerosp Univ 7:773–777
3. Li J, Lu M, Cui X, Feng Z (2007) Theoretical analysis of RAIM in the occurrence of simultaneous two-satellite faults. IET Radar Sonar Navig 1(2):92–97
4. Jiang H, Chang Q, Xiu C (2009) Design and implementation of GPS/BD-2 compatible receiver information processing system. J Beijing Aerosp Univ 7(6):506–510
5. Sun Y, Wei P (2011) Research on independent integrity monitoring algorithm of GPS+BD dual mode receiver. Comput Technol Dev 23(7):238–241
6. Zhou F (2017) Research on multimode GNSS receiver with user autonomous integrity monitoring. University of Electronic Science and Technology, Chengdu
7. Lou S (2011) Receiver autonomous integrity monitoring and system simulation study. Harbin Engineering University, Harbin
8. Lin X, Fan S, Song J, Wang H (2016) Autonomous navigation monitoring algorithm and performance analysis of Beidou navigation system receiver. J Naval Aeronaut Eng Inst 32 (6):619–624

9. Li C, Zhun L, Yang Q, Yang Y (2016) Navigation receiver self-integrity monitoring method based on least squares residual. Glob Position Syst 41(1):69–72
10. Charbonnieras C, Vincent F (2017) Integrity monitoring improvement by exploiting the raw GNSS signals. In: 30th international technical meeting of the satellite division of the institute of navigation (ION GNSS+ 2017)
11. Liu X (2018) Research and implementation of satellite positioning integrity monitoring method based on software receiver. Beijing Jiaotong University, Beijing
12. Yang F (2018) Research on Beidou/GPS combination RAIM algorithm. Shenyang Aerospace University, Shenyang
13. Wang L, Sui L, Xiang Z, Wu L, Liu C (2015) Autonomous integrity monitoring algorithm for GPS dynamic navigation receiver. Surv Sci 40(12):140–143
14. Jia C (2015) GPS_GLONASS_BDS multi-constellation navigation receiver autonomous integrity monitoring. Civil Aviation University of China, Tianjin

Rapid PPP Integer Ambiguity Resolution Assisted with RTK Technology Based on VRS

Jun Xu(✉), Zhi Jiang, and Liang Chen

QianXun Spatial Intelligence Inc., Shanghai, China
jun.xu@wz-inc.com

Abstract. The data processing center of ground-based augmentation system utilizes Precise Point Positioning (PPP) ambiguity resolution (AR) technology to determine the carrier phase integer ambiguities of virtual reference station (VRS). Afterwards, the carrier phase ranges without phase ambiguities at VRS-end are broadcasted to user-end. Based on the aforementioned technique, rapid PPP integer ambiguity resolution assisted with RTK technology based on VRS is realized in this study. By using single-differenced RTK solutions between the rover station and VRS, single-differenced ambiguities between them can be obtained. Since the broadcasted carrier phase observations of VRS is not affected by the phase ambiguities, the single-differenced ambiguities are then equivalent to the undifferenced phase ambiguities at the rover station. The single-differenced ambiguities can be fixed like RTK, which indirectly realizes the PPP AR at the rover station. Compared with the positioning results derived from the traditional PPP method, the PPP AR assisted with RTK based on VRS can effectively reduce the positioning convergence time and improve the positioning accuracy.

Keywords: Precise Point Positioning (PPP) · Virtual Reference Station (VRS) RTK · Integer ambiguity · Ground-based augmentation system

1 Introduction

Precise Point Positioning (PPP) can achieve high-precision positioning with only one receiver. It works flexibly and does not depend on the network, which can achieve centimeter and millimeter-level positioning with a certain convergence time. But length of convergence time is a hard problem needs to be solved. Virtual Reference Station (VRS) RTK technology can achieve centimeter and millimeter-level positioning accuracy in a short period of time, but relies on the network to transmit differential information.

With the gradual improvement of the ground-based augmentation system construction, ground-based augmentation differential information can be received through network communication in major urban areas, and users can also receive SSR (State Space Representation) information through satellite broadcast or network. If continuous high-precision positioning results are required, the user can only perform PPP through satellite-supplied SSR correction information without network, but the real-time PPP positioning initialization time is long. To achieve the positioning accuracy of centimeters or even millimeters, it usually takes 30 min or even longer to initialize, which is unacceptable to most users [1]. Combining the advantages and disadvantages of real-time

J. Sun et al. (Eds.): CSNC 2019, LNEE 563, pp. 219–227, 2019.
https://doi.org/10.1007/978-981-13-7759-4_20

PPP and network RTK, users hope to use both technologies simultaneously to achieve high precision and seamless positioning in many current applications. In order to shorten the convergence time of PPP solution, the position coordinates and ambiguity information obtained by RTK fixed solution are used to assist PPP solution to accelerate the convergence speed of PPP ambiguity and improve the accuracy of solution.

2 Algorithm Principle

The method proposed in the paper mainly includes the following steps: the VRS observation is processed by the PPP-AR technology, and the user is broadcasted to the user through the network. After receiving the observation information, the user performs the RTK single-differenced solution to obtain the carrier undifferenced ambiguity. The user obtains the RTK fixed solution and the undifferenced ambiguity and calculates the tropospheric parameters. After obtaining the above parameters, the PPP solution is used to obtain high-precision positioning results (Fig. 1).

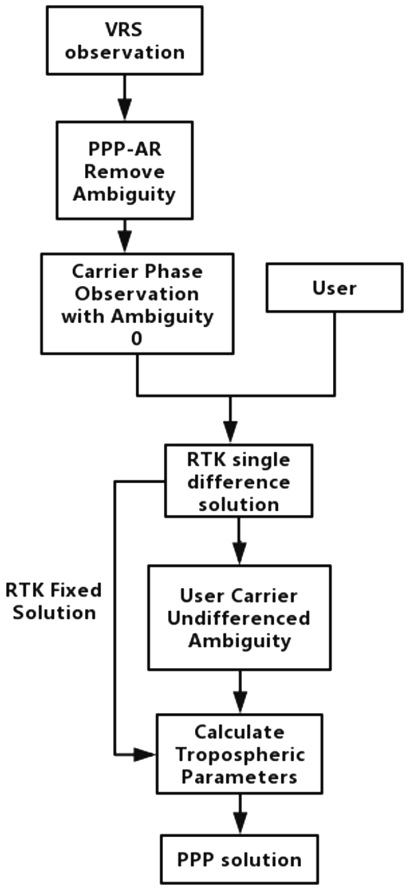

Fig. 1. Rapid PPP integer ambiguity resolution assisted with RTK technology based on VRS flow chart

2.1 VRS Undifferenced Ambiguity Fixed

Usually, the VRS carrier phase observation received by user has integer ambiguity parameter, even if the single-differenced integer ambiguity obtained by the RTK solution still includes the integer ambiguity of the VRS carrier phase and the user carrier phase, the undifferenced integer ambiguity of the user carrier phase can not be separated.

Ground-based augmentation data center solves VRS observations undifferenced ambiguity through PPP-AR technology [2], After the carrier phase undifferenced ambiguity is fixed, the fixed ambiguity is added to the carrier phase observation value, and the integer ambiguity of the carrier phase observation value is 0, and the data center broadcasts the processed observation value to the user through the network. The general process is as follows (Fig. 2):

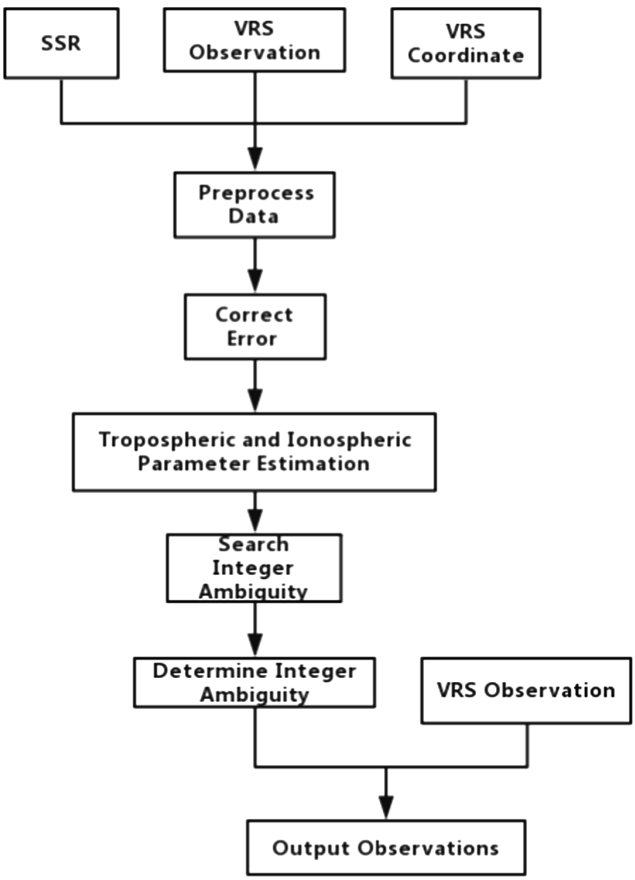

Fig. 2. VRS observation measurement integer ambiguity processing flow chart

The VRS service is all-weather. After a period of PPP-AR solution to determine the integer ambiguity, the carrier phase observation value with the ambiguity of 0 can be continuously broadcast to the user.

2.2 Single-Differenced Ambiguity Determination

From Sect. 2.1, the data center broadcasts to the user a carrier phase observation with zero ambiguity. Without considering multipath and noise, the VSR virtual reference station A carrier phase observation equation is [3]:

$$\varphi_A^p = \frac{f}{c}\rho_A^p - fV_A + fV_p - N_A^p - \frac{f}{c}ion_A^p - \frac{f}{c}trop_A^p \tag{2.1}$$

φ_A^p is the carrier phase observation of satellite p to VRS, ρ_A^p is the distance from satellite p to VRS, V_A is the receiver clock error of user, V_p is the clock error of satellite p, N_A^p is p satellite to VRS carrier phase integer ambiguity, ion_A^p is the satellite p to user ionospheric error, $trop_A^p$ is the satellite p to the user tropospheric error, **f** is the carrier frequency, **c** is the speed of light. Since $N_A^p = 0$, the formula can be simplified to:

$$\varphi_A^p = \frac{f}{c}\rho_A^p - fV_A + fV_p - \frac{f}{c}ion_A^p - \frac{f}{c}trop_A^p \tag{2.2}$$

The carrier phase observation equation of rover B is:

$$\varphi_B^p = \frac{f}{c}\rho_B^p - fV_B + fV_p - N_B^p - \frac{f}{c}ion_B^p - \frac{f}{c}trop_B^p \tag{2.3}$$

φ_B^p is the carrier phase observation of the satellite p to the user, ρ_B^p is the satellite distance from the satellite p to the user, V_B is the receiver clock error of the user, V_p is the clock error of the satellite p, and N_B^p is carrier phase integer ambiguity of the satellite p to the user, ion_B^p is the ionospheric error of the satellite p to the user, $trop_B^p$ is the tropospheric error of the satellite p to the user.

$$\varphi_{AB}^p = \frac{f}{c}\rho_{AB}^p - fV_{AB} - N_B^p - \frac{f}{c}ion_{AB}^p - \frac{f}{c}trop_{AB}^p \tag{2.4}$$

φ_{AB}^p is the single-differenced carrier phase observation of satellite p, ρ_{AB}^p is the single-differenced distance of satellite p, V_{AB} is the single-differenced receiver clock error, ion_{AB}^p is single-differenced ionospheric error of the satellite p, $trop_{AB}^p$ is single-differenced tropospheric error of the satellite p. Because the baseline formed by VRS and users is a short baseline, the effects of the ionosphere and troposphere can be ignored by model correction:

$$ion_{AB}^p = 0, \quad trop_{AB}^p = 0 \tag{2.5}$$

Equation (2.4) can be simplified to:

$$\varphi_{AB}^{p} = \frac{f}{c}\rho_{AB}^{p} - fV_{AB} - N_{B}^{p} \tag{2.6}$$

Since the single-differenced receiver clock error V_{AB} has the same effect on the carrier phase observation of each satellite, and the ambiguity of each satellite is different, so by observing more than four satellites at the same time, the single differenced integer ambiguities and he single-differenced receiver clock error are fixed by the LAMBDA method. When the observation environment is good, the undifferenced ambiguities of the rover can be fixed by combining the single epoch of the pseudorange observation equation [4]. After the RTK ambiguities are fixed, high-precision user position can be obtained.

2.3 User PPP Solution

After the user obtains the high-precision coordinates and the undifferenced ambiguities of the carrier phase through the RTK fixed solution, The dual-frequency ionosphere-free model is used as the basic model of PPP solution. The observation model is as follows:

$$L_{IF} = \frac{f_1^2}{f_1^2 - f_2^2}L_1 - \frac{f_2^2}{f_1^2 - f_2^2}L_2 = \boldsymbol{\rho} + \mathbf{c}(\mathbf{dt} - \mathbf{dT}) - \lambda_{IF}N_{IF} - \boldsymbol{trop} + b_R - b^S + \sum V \tag{2.7}$$

L_{IF} is the combined ionosphere-free observation, f_1 is the L_1 carrier frequency, f_2 is the L_2 carrier frequency, $\boldsymbol{\rho}$ is the satellite-ground distance, **dt** is the receiver clock error, **dT** is the satellite clock error, λ_{IF} is the wavelength of combined observation value, N_{IF} is the combined observation ambiguity, and **trop** is the tropospheric delay.

$$\mathbf{trop} = d_{dry}MF_{dry} + d_{wet}MF_{wet} \tag{2.8}$$

$d_{dry/\mathbf{wet}}$ is the zenith tropospheric dry/wet component delay, and $MF_{dry/wet}$ is the dry/wet component delay projection function. b^S is the delay term of the signal inside the satellite, b_R is the delay term of the signal inside the receiver. $\sum V$ includes solid tide correction, ocean load tidal correction, earth rotation correction, antenna phase center deviation correction, antenna phase entanglement, and satellite clock relativistic effect correction. According to the SSR parameters broadcast by the satellite, b^S can be obtained. The error of $\sum V$ and the dry component of the tropospheric delay can be accurately repaired according to the error model [5]. N_1 and N_2 can be obtained according to the ambiguity calculated by the RTK fixed solution in Sect. 2.2.

$$N_{IF} = \frac{f_1^2}{f_1^2 - f_2^2}N_1 - \frac{f_2^2}{f_1^2 - f_2^2}N_2 \tag{2.9}$$

N_{IF} can be solved by bringing N_1 and N_2 into the Eq. 2.9. The accurate user position and the satellite position obtained by the precise ephemeris calculated by the RTK can obtain an accurate satellite-ground distance **ρ**, and the precise satellite clock error **dT** can also be obtained by the precision satellite clock product.

$$\mathbf{V} = \mathbf{Ax} - \mathbf{L} \tag{2.10}$$

V is the observed residual vector; **A** is the design matrix; **L** is the constant vector; **x** is the unknown increment vector, including **dt**, b_R, d_{wet}. By observing multiple satellites, d_{wet} can be obtained more accurately by using the observation of one epoch by least squares calculation by Eq. (2.10). Usually, the zenith wet delay d_{wet} is constant in one continuous arc. By returning these parameters to the observation Eq. (2.7), higher-precision position coordinates can be obtained continuously.

3 Experimental Results and Analysis

The top of the building in Shanghai Qianxun Building is selected as the rover, the data center generates the VRS virtual reference station as the reference station in the vicinity. The VRS grid point is 1.5 km away from the user, after the data center measures the VRS, the carrier phase ambiguity of the broadcast is 0 and is broadcast to the user. The data collection date is 2018-07-01 and the time period is 14:00–16:00. The precision ephemeris and satellite clock error and the satellite carrier phase time delay are provided by Qianxun SI. The receiver sampling interval is 1 s, the elevation angle cutoff angle is 15°, and the receiver type is Trimble Net R9. Under this experimental condition, the traditional PPP method and the RTK-assisted PPP fast-fixing method are compared. The user does not use the VRS information after the RTK-assisted PPP convergence. The number of satellites available for GPS, GLONASS, and Beidou systems is as follows (Fig. 3):

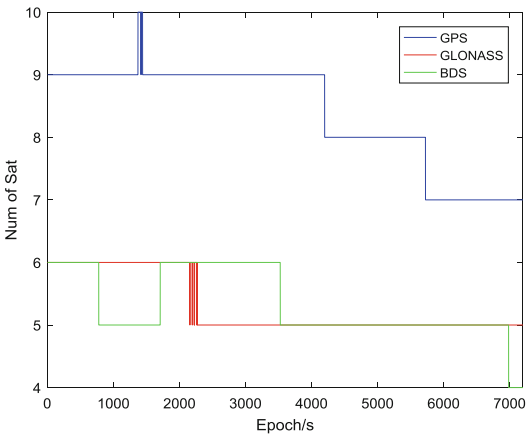

Fig. 3. Statistics: available satellites

Two methods solve the same set of data, and the error analysis of the solution coordinates and the true value points is as follows:

It is shown in Fig. 4 that the traditional PPP solution can converge to within 2 dm in three directions after 40 min, and the accuracy of the solution can be maintained at a decimeter level after a period of time.

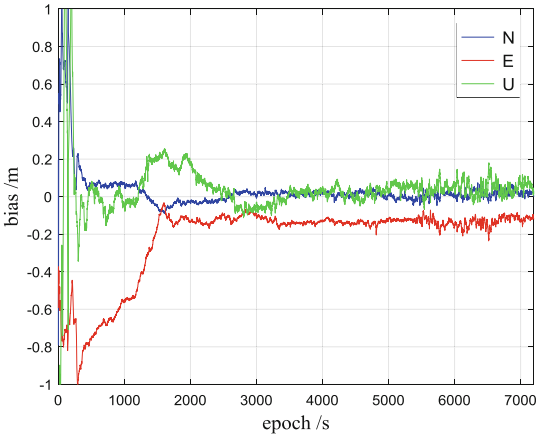

Fig. 4. NEU bias for traditional PPP

It is shown in Fig. 5 that the RTK-assisted PPP solution can reach within 2 dm in three directions within 100 s, and the accuracy after convergence can be stabilized within 7 cm. The NEU RMS (Root Mean Square) statistics are as follows after half an hour after power on:

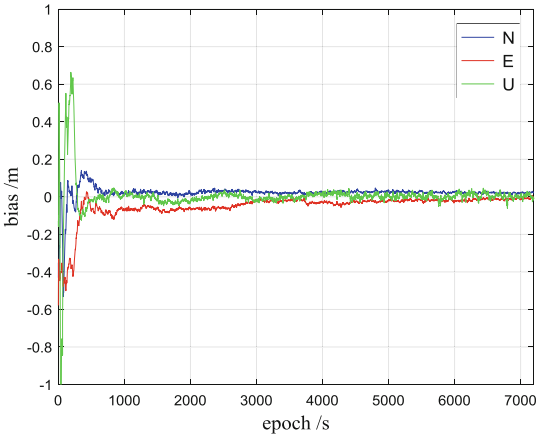

Fig. 5. NEU bias for PPP assisted with RTK

It can be concluded from Table 1 that the convergence accuracy of the RTK-assisted PPP solution in the E and U directions after half an hour is higher than that of the PPP solution RMS.

Table 1. Statistics: NEU RMS

	N	E	U
PPP solution RMS (m)	0.02	0.13	0.06
RTK assisted PPP solution RMS (m)	0.02	0.03	0.01

It can be seen from Table 2 that the RTK-assisted PPP solution has improved convergence speed and accuracy compared with the traditional PPP solution method. The RTK-assisted PPP solution can achieve centimeter accuracy within 1000 s, while the traditional method has an accuracy of only 0.552 m in 1000 s, and the accuracy is still not up to the centimeter level after 7000 s.

Table 2. NEU three-way comprehensive error

Epoch (s)	PPP solution error (m)	RTK assisted PPP solution error (m)
1000	0.552	0.074
2000	0.219	0.067
3000	0.114	0.039
4000	0.132	0.035
5000	0.125	0.038
6000	0.177	0.032
7000	0.143	0.023

4 Conclusion

Experiments show that the VRS observations are eliminated and the integer ambiguity is broadcast to the user. The RTK single-differenced ambiguity determination can effectively decompose the integer ambiguity into the user's undifferences ambiguity, and the coordinates can be fixed quickly according to the RTK. The solution determines the tropospheric zenith wet delay parameters. The user can obtain convergence in integer ambiguity and tropospheric zenith wet delay parameters combined with satellite SSR information PPP.

Compared with the traditional PPP solution mode, the RTK-assisted PPP ambiguity fixed method can converge in a short time. Experiments show that the RTK-assisted PPP ambiguity fixed method can converge within 2 min under the same conditions, while the traditional PPP method takes 40 min. Only within can convergence, RTK-assisted PPP ambiguity fixed method can converge to centimeter accuracy. The RTK-assisted PPP ambiguity fixing method not only speeds up the convergence of PPP, but

also improves the convergence accuracy. When the network coverage is not good, the user can quickly switch the PPP mode by the RTK, and the PPP can quickly converge in the case of RTK information assistance.

References

1. Li XX (2013) Rapid ambiguity resolution in GNSS precise point positioning. Wuhan University, Wuhan
2. Li P (2016) Research on methodology of rapid ambiguity resolution for GNSS precise point postioning. Wuhan University, Wuhan
3. Li ZH, Huang JS (2014) GPS Surveying and Data Processing. Wuhan University Press, Wuhan
4. Gao XW, Liu JN, Ge MR (2002) An ambiguity searching method for network RTK baselines between base stations at single epoch. Acta Geodaet Cartogr Sin 31(4):305–309
5. Liu ZQ, Wang JX (2014) Realization and analysis of real-time precise point position based on SSR boardcast ephemeris corrections. Sci Surv Mapp 39(1):15–19

Study on the Prediction Method of Single and Dual Frequency Service Area for BDSBAS

Shanshan Chen(✉), Biao Jin, Dongjun Li, and Pengcheng Qu

Space Star Technology, Beijing, China
chenss@spacestar.com.cn

Abstract. Satellite-Based Augmentation Systems (SBAS) argument the Global Navigation Satellite System (GNSS) by providing correction and integrity informations through GEO to meet the navigation requirement for all phases of civil flight, such as WAAS, EGNOS and so on. Now, BDS has entered global construction stage, so the availability assessment for BDSBAS is important for its planed application in civil aviation. The paper provides the key algorithms for service area prediction, establish the error transfer model from monitoring receiver, data processing center to user's receiver. The simulation software is developed and verified by comparing with WAAS report. The service area of single frequency and dual frequency SBAS for different service level is simulated and analyzed, which can be a reference for BDSBAS in China.

Keywords: SBAS · BDSBAS · Service area prediction · Service availability

1 Introduction

The Satellite-based augmentation system (SBAS) was first proposed and built by the USA FAA to improve the availability, accuracy and integrity of basic global navigation satellite system to meet the navigation requirements of life safety services such as civil aviation. At present, many countries has built SBAS system and started to provide service for civil users, such as USA's Wide Area Augmentation System (WAAS), Europe's European Geostationary Navigation Overlay System (EGNOS), and Japan's MTSAT Satellite-based Augmentation System (MSAS). At present, the SBAS system provides SBAS services based on L1 signals and cannot meet the requirements of CAT-I operation. Therefore, the current SBAS systems are gradually upgrading to the DFMC SBAS system.

As an important part of BeiDou Navigation Satellite System (BDS), the BeiDou Satellite-Based Augmentation System (BDSBAS) is scheduled to be deployed in a timely fashion and gradually incorporated into the international standard system. In the 2016 version of SBAS L5 DFMC Interface Control Document, BDS was recognized as the fourth augmented constellation [1, 2]. In October 2017, BDSBAS obtained three PRN code on the GPS L1 and L5 signal.

In this paper, we studied the SBAS integrity parameters. The error model is built including reference station, processing center and the users end, and the error transfer process is given. The service area prediction method based on error transfer model can

J. Sun et al. (Eds.): CSNC 2019, LNEE 563, pp. 228–237, 2019.
https://doi.org/10.1007/978-981-13-7759-4_21

effectively predict and analyze the service area of the SBAS system in order to optimize the system design.

2 Overview

According to the ICAO SARPs Annex 10 [3], the SBAS system uses GEO satellites to provide services for users, and shall perform one or more of the following functions: (1) Ranging function: provide an additional pseudo-range signal to improve the availability of the basic GNSS; (2) Corrections function: Improve the accuracy of the basic GNSS by providing the fast and long-term corrections and the ionospheric corrections; (3) Integrity function: Improve the integrity of the basic navigation system by providing UDRE, GIVE and other integrity parameters.

The SBAS system consists of three parts: ground segment, space segment and user segment. Firstly, reference stations to get the observations and augment information and sends it to the data processing center; the data processing center completes the data preprocessing and do the quality check, and finally generates the corrections and integrity information. The uplink station receives the argument information from the data processing center, do the modulation and up-conversion after comparison and verification and then sent it to the GEO satellite; the GEO satellite retransmit the uplink signal through L-band and broadcasts the augment information to SBAS users; and at last SBAS users use the correction information for positioning solution, and use the integrity information to calculate the Protection Level (PL) [4], and achieve the integrity protection function by comparing with the Alert Limit (AL).

The SBAS service area prediction is to compute the user's PL through the target service area given the basic navigation constellation and the reference station geometry, evaluate the availability by comparing it to AL, and statistic the percentage of serviceable areas in the whole target service area. So we need to establish the error transfer model.

3 Modeling of Service Area Prediction

This part we will establish the error transfer model from the reference station observation error, data processing center, and then to the users' end, and in data processing model there are two parts: UDRE model and GIVE model.

3.1 Reference Station Error Model

The reference station of SBAS system is used to get the observations and augment information which will be sent to the data processing center to generate the corrections and integrity parameters. The accuracy and reliability of reference stations' observations are the basis for the system to provide high-precision and high-integrity services.

The GNSS observation error is affected by the measurement performance of the reference station receiver and the observation environment, including receiver noise $\sigma_{noise,i}$, multipath error $\sigma_{multipath,i}$, tropospheric correction error $\sigma_{trop,i}$ [5], as follows:

$$\sigma_i = \sqrt{\sigma_{noise,i}^2 + \sigma_{multipath,i}^2 + \sigma_{trop,i}^2} = \sqrt{\sigma_{CNMP,i}^2 + \sigma_{trop,i}^2} \tag{1}$$

In the process of data processing, the correction is generated using smoothed pseudo-range observations by dual-frequency phase observations. The residual error $\sigma_{CNMP,i}$ after removing the multipath correction from the pseudo-range can be obtained by the CNMP model [6]. Then Eq. (1) can be written as follows.

$$\sigma_i = \sqrt{\sigma_{CNMP,i}^2 + \sigma_{trop,i}^2} \tag{2}$$

3.2 Data Processing Center Error Model

The SBAS system processing center calculates UDRE and GIVE parameters by using the GNSS observations from each reference station. The UDRE parameter reflects the accuracy of the fast and slow corrections. The smaller the UDRE and GIVE, the higher the users' position accuracy and the higher the availability of the system. However, the system must be guaranteed with a certain degree of confidence to ensure the security of each user in the service area, so the UDRE and GIVE must be bigger enough to bound the satellite ranging error and ionospheric error. The two-parameter simulation is modeled as follows.

3.2.1 UDRE Model

Similar to the principle of calculating the users' position using multi-satellite observations, the data processing center can determine the orbit and clock error of the satellite by using the observations of multi-stations whose coordinates are known precisely. The geometry and data quality of the station determines the accuracy of the GNSS's position and clock error [7]. Defining user direction-cosine satellite geometry matrix is G_i, the relationship between the residual of the pseudo-range observation and the position and clock error of satellite broadcast ephemeris is as follows:

$$\Delta \mathrm{y} = G_i \Delta x_{sv} + \varepsilon \tag{3}$$

Where Δx_{sv} is the difference between the real position and clock of satellite and the broadcast orbit and clock, Δy is residual of the pseudo-range observation, ε is the observation error.

The solution methods of Eq. (3) include least squares (LS) method, weighted least squares (WLS) method, and minimum-variance (MV) estimation. The LS and WLS method are sensitivity to the reference station geometry and observations noise. The MV method can use the prior accuracy of satellite ephemeris error to reduce this

sensitivity. So in this paper we use the MV method. The orbital and clock estimation error $\hat{P}_{MV}$ can be written as follows:

$$\hat{P}_{MV} = (P_0^{-1} + G^T W G)^{-1} \tag{4}$$

Among them, P_0 is the prior accuracy of the satellite ephemeris, and W is the weight of the observation data of each reference station whose calculation method is referred to Sect. 3.1. In order to reflect the error's change with space, the SBAS system broadcast UDRE parameter and the covariance parameter [7, 8] MT28 together. In this paper the user protection level is calculated directly using $\hat{P}_{MV}$ without considering the encoding process.

3.2.2 GIVE Model

Due to ionospheric irregularity, the calculation of GIVE parameters is more complicated than UDRE parameters. The GIVE generation algorithms include planar fit method [9], Kriging method [10] and so on. At present, the WAAS/MSAS system uses the planar fit algorithm to generate ionospheric correction information [9, 11], and GIVE is calculated as follows.

$$\begin{aligned} \sigma^2_{GIVE} &= R^2_{irreg}\sigma^2_{IGP_k} + \sigma^2_{rate-of-change} + \max(R^2_{irreg}\sigma^2_{decorr}, \sigma^2_{un\,\mathrm{de}\,rsampled}) \\ GIVE &= 3.29\sigma_{\mathrm{GIVE}} \end{aligned} \tag{5}$$

Where, $R^2_{irreg}\sigma^2_{IGP_k}$ is general error term, $R^2_{irreg}\sigma^2_{decorr}$ is spatial error term, $\sigma^2_{un\,\mathrm{de}\,rsampled}$ is the threat term by the undersampled ionospheric pierce points (IPPs), $\sigma^2_{rate-of-change}$ is time-varying error term. The value 3.29 indicates that the GIVE bound ionospheric estimation error with a probability of 99.9%. R^2_{irreg} is called the inflating coefficient and is calculated by false alarm rate P_{FA}, and missed alarm rate P_{MD}, as follows [12]:

$$R^2_{irreg} = \sqrt{\chi^2_{1-P_{FA}}(n-3)/\chi^2_{P_{\mathrm{MD}}}(n-3)} \tag{6}$$

Where n-3 is the freedom of the planar fit estimation. $\sigma^2_{IGP_v}$ is the maximum value of four farth points' estimation error around the calculation grid, which is calculated as follows:

$$\begin{aligned} \sigma^2_{\hat{I}_{v,IGP}} &= [(G_{\mathrm{I}}^T W G_{\mathrm{I}})^{-1}]_{1,1} \\ \sigma^2_{\hat{I}_v}(\Delta\lambda, \Delta\phi) &= [1 \quad \Delta\lambda \quad \Delta\phi][(G_{\mathrm{I}}^T W G_{\mathrm{I}})^{-1}][1 \quad \Delta\lambda \quad \Delta\phi]^{\mathrm{T}} \\ \sigma^2_{IGP_v} &= \max\left(\sigma^2_{\hat{I}_v}(2.5, 2.5), \sigma^2_{\hat{I}_v}(-2.5, 2.5), \sigma^2_{\hat{I}_v}(2.5, -2.5), \sigma^2_{\hat{I}_v}(-2.5, -2.5)\right) \end{aligned} \tag{7}$$

Where: W represent for the weighted matrix which can be calculated referring to [10]; G_{I} represent for the design matrix which describe the geometry of the IPPs.

3.2.3 User's Error Model

According to the RTCA standard, the SBAS single-frequency user terminal uses the corrections to perform the least-squares position [4] and uses the UDRE and GIVE to calculate the protection level, as follows:

$$\begin{aligned} HPL_{SBAS} &= \begin{cases} K_{H,NPA} \cdot d_{major}, \text{form enroute to } LNAV \\ K_{H,PA} \cdot d_{major}, LNAV/VNAV, LP, LPV \end{cases} \\ VPL_{SBAS} &= K_V d_U \\ d_{major} &\equiv \sqrt{(d_{east}^2 + d_{north}^2)/2 + \sqrt{\left((d_{east}^2 - d_{north}^2)/2\right)^2 + d_{EN}^2}} \\ [d_{east}^2 \quad d_{north}^2 \quad d_{EN}^2 \quad d_U^2] &= [\sum_{i=1}^{N} s_{east,i}^2 \sigma_i^2 \quad \sum_{i=1}^{N} s_{north,i}^2 \sigma_i^2 \quad \sum_{i=1}^{N} s_{east,i} s_{north,i} \sigma_i^2 \quad \sum_{i=1}^{N} s_{U,i}^2 \sigma_i^2] \end{aligned} \tag{8}$$

Where: $s_{east,i}, s_{north,i}, s_{U,i}$ represent for the direction of north east and up. The observation error σ_i^2 of each satellite includes the satellite' orbital and clock error term $\sigma_{flt,i}^2$, the ionospheric error term $\sigma_{UIRE,i}^2$, the noise and multipath error terms $\sigma_{air,i}^2$, and the tropospheric model error term $\sigma_{trop,i}^2$, as follows.

$$\sigma_i^2 = \sigma_{flt,i}^2 + \sigma_{UIRE,i}^2 + \sigma_{air,i}^2 + \sigma_{trop,i}^2 \tag{9}$$

Among them, the tropospheric error and the user receiver noise error term are calculated according to the RTCA standard. The simulation in this paper does not consider the quantization loss and degradation parameters such as MT10. The users' calculation of $\sigma_{flt,i}^2$ and $\sigma_{UIRE,i}^2$ can be simplified as:

$$\sigma_{UIRE,i}^2 = \sum_{\mathrm{n}=1}^{n_{IGP}} W_n(x_{pp}, y_{pp}) \cdot \sigma_{n,GIVE}^2 \tag{10}$$

$$\sigma_{flt,i}^2 = \left(\sigma_{UDRE,i} \cdot \delta UDRE\right)^2 \tag{11}$$

In the formula, the weight value W_n of the Ionospheric Grid Point (IGP) is calculated referring to [4]. In the paper, $\sigma_{flt,i}^2$ is directly calculated using orbital and clock covariance, that is:

$$\sigma_{flt,i}^2 = G \cdot P_{MW} \cdot G^T \tag{12}$$

In order to meet the integrity requirements, the GIVE parameters' calculation must consider the effects of anomalies such as ionospheric storms, so GIVE is always large and leads to the larger XPL which limits the application level of SBAS. So the second civilian frequency L5 is proposed for the DFMC SBAS system. In DFMC SBAS

system, the user uses the ionospheric-free combination to eliminate the ionospheric delay error. The observation error is as follows:

$$\sigma_i^2 = \sigma_{flt,i}^2 + (2.6 \times \sigma_{air,i})^2 + \sigma_{trop,i}^2 \tag{13}$$

As above, the ionospheric-free combination increased the noise error to 2.6 times that of L1-only., but the problem caused by the ionospheric anomaly is avoided, and the protection level of the user end is only affected by UDRE.

3.3 Service Area Prediction Method

According to the above analysis, given the broadcast ephemeris, reference station location and the target service area, the calculation process from the reference station error to the user terminal's protection level is as follows:

(1) Calculate the measurement error of reference station by using Eq. (1);
(2) Calculate the position of each navigation satellite, and use Eq. (4) to calculate the orbital and clock correction error of each visible satellite;
(3) Calculate the IPPs, search for the pierce point that meets the conditions for each IGP, and use Eq. (5) to complete the calculation of the vertical delay error of the ionosphere grid point to generate the GIVE parameter;
(4) Calculate the user' visible satellite, and use Eq. (8) to calculate the PL.

During the simulation period, the user position is simulated using a certain position resolution, and the number of points whose PL < AL is counted, and then the service area prediction can be completed.

4 Simulation Analysis

4.1 WAAS Service Area Simulation

WAAS system can provide service for civil aviation users' RNP to LPV200 operations. The LPV200 service requirement is between the APVI and APVII service requirement in the ICAO standard whose Horizontal Alert Limit (HAL) is 40 m and the Vertical Alert Limit (VAL) is 35 m. To verify the validity of the method in this paper, we do the service area prediction for WAAS LPV200 Service using WAAS stations' coordinate and GPS ephemeris data and compare the simulation result to the WAAS assessment report.

The simulation uses GPS broadcast ephemeris on January 1, 2017. The distribution of WAAS reference station, IGPs and WAAS GEO satellite CRE and CRW are shown in Fig. 1 and the model parameters is referring to [5, 6, 10]. The prediction LPV200 service area is the area whose XPL is smaller than XAL for more than 99.9% of the time periods in a day. The result is shown in Fig. 2.

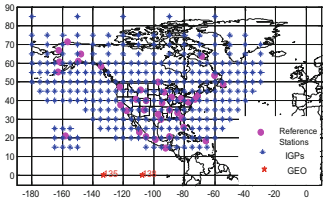

Fig. 1. Distribution of WAAS station and IGPs

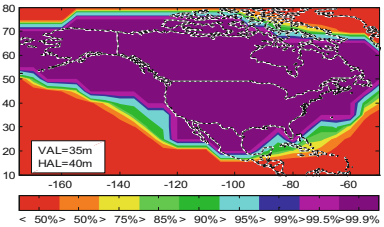

Fig. 2. LPV200 service of WAAS

By comparison, the result in the above figure is in good agreement with the WAAS' report [13] and the validity of the method is verified.

4.2 Simulation of BDSBAS Service Area

As an important part of BDS, BDSBAS will be built in accordance with international standards to provide services to users in China and the surrounding countries [14]. BDSBAS consists of three parts: space segment, ground segment and user segment. The space segment includes three GEO satellites (located at 80° E, 110.5° E, and 140° E). The ground segment consists of Operation Control Center, Data Processing Centers, Uplink Stations and Monitoring Stations (MS). The user segment refers to BDSBAS terminals used in all modes of transport. BDSBAS will provide APV-I services in the first place and then provide CAT-I services through DFMC SBAS [15].

In order to predict the service area, the distribution of MS should be determined according to the construction planning and service requirement. Considering GIVE parameters requires more stations than UDRE parameters, we will analyze the station distribution from the GIVE solution demand. In Table 1, the number of grid points that can be provided under different station distributions is compared.

Table 1. Compare of IGP points under different station number

Time/h	10Sta	20	25	27	32
0	3	40	52	60	70
2	3	24	38	46	51
4	7	35	44	50	59
6	13	41	54	58	65
8	3	42	54	59	69
10	3	27	39	46	51
12	7	35	45	50	59
14	12	43	54	57	65
16	5	41	51	57	67
18	4	27	35	41	46
20	8	34	46	50	59
22	11	40	51	58	66
Mean	6.6	35.8	46.9	52.7	60.6

As above, the system can provide most IGPs' information above China using 32 stations, which is shown in Fig. 3 below. Considering the service level and implementation feasibility, the subsequent simulations are simulated using 30 stations, as shown in Fig. 4.

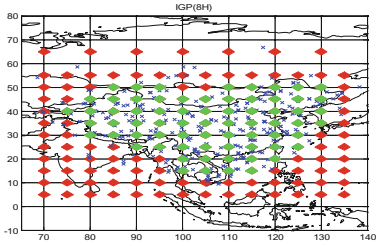

Fig. 3. Available IGPs of 32 stations

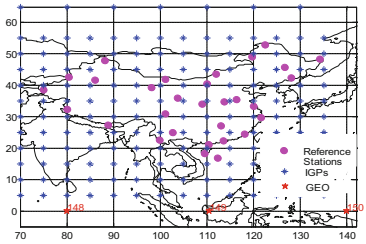

Fig. 4. Distribution of station and IGPs

Considering the requirements of the APVI service, LPV200 service and CAT-I service, the single-frequency (SF) and dual-frequency (DF) user service areas in the case of 30 stations in China is simulated as follows (Figs. 5, 6, 7 and 8).

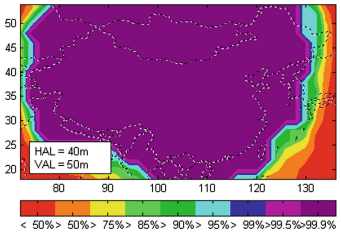

Fig. 5. APVI service area of SF SBAS

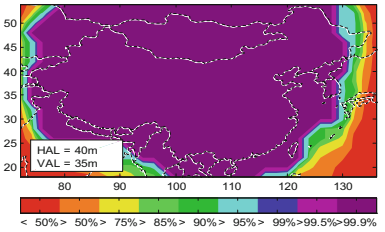

Fig. 6. LPV200 service area of SF SBAS

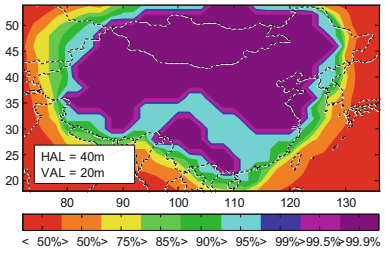

Fig. 7. CAT-I service of SF SBAS

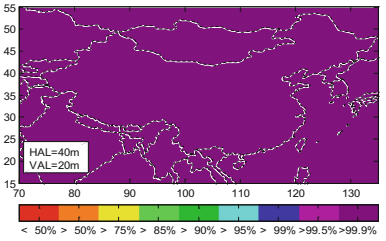

Fig. 8. LPV200 service area of DF SBAS

According to the simulation, the SF SBAS system can provide LPV200 services for 99.52% and CAT-I services for 88% of single-frequency users in China using the selected 30 stations. The DFMC SBAS systems can provide CAT-I services for 100% of dual-frequency users in China using the selected 30 stations.

5 Conclusion

The article built the error transfer model from the stations to the user end, and gives a method to predict the SBAS service area. The validity of the method is verified by comparing with WAAS report firstly and then we do the analysis for BDSBAS using this method. Considering the calculation requirement of IGPs, we chose 30 stations for BDSBAS simulation finally. The simulation result shows that using the selected 30 stations: the SF SBAS system can provide LPV200 service for more than 99% of single-frequency users in China, and DFMC SBAS can provide CAT-I service for 100% of dual-band users in China. At present, China has begun the construction of BDSBAS. The simulation tools in this paper can provide reference for system planning. And in order to improve the model accuracy, we will study the error model of BDS' observation and the ionospheric threat model in China in future.

References

1. Shao B, Geng Y, Ding Q et al (2017) Summarize of international satellite based augmentation system. Mod Navig 3:157–161
2. SBAS L5 DFMC Interface Control Document, IWG (2016)
3. ICAO Annex 10, vol. I Radionavigation Aids, Chap 3 (2006)
4. RTCA, Minimum Operational Performance Standards for Global Positioning System/Wide Area Augmentation System Airborne Equipment. RTCA DO 229 (2006)
5. Samuel PP, Enge PK, Parkinson BW (1995) A new method for coverage prediction for the wide area augmentation system (WAAS). IONAM 1995:1–13
6. Shallberg K, Sheng F (2008) WAAS measurement processing: current design and potential improvements. In: Position location & navigation symposium, IEEE/ION, vol 2008, pp 253–262. (CNMP)
7. Walter T, Hansen A, Enge P (2001) Message type 28. ION ITM 2001(4):595–599
8. Blanch J, Walter T, Enge P (2014) Evaluation of a covariance-based clock and ephemeris error bounding algorithm for SBAS. ION ITM 2014:3270–3276
9. SBAS safety assessment guidance related to anomalous ionospheric conditions. International civil aviation organization Asia and pacific office (2016)
10. Sparks L, Blanch J, Pandya N (2011) Estimating ionospheric delay using kriging: 1. Methodology. Radio Sci 46(RS0D21):1–13
11. Cormier D, Altshuler E, Shloss P (2003) Providing precision approach SBAS service and integrity in equatorial regions. In: Proceedings of the 2003 National Technical Meeting of the Institute of Navigation, Portland, OR, pp 1728–1735
12. Walter T, Hansen A, Blanch J et al (2001) Robust detection of ionospheric irregularities. Navigation 48(2):89–100

13. WAAS Performance analysis report #60[EB/OL] (2017). http://www.nstb.tc.faa.gov
14. China (2017) The Development Plan of the BeiDou Satellite-Based Augmentation System (BDSBAS), CNS SG 21, Thailand Bangkok, pp 1–4
15. Walter T, Blanch J, Enge P (2010) Coverage improvement for dual frequency SBAS. ION ITM 3(4):344–353

Improvement for BeiDou-3 Receiver Autonomous Integrity Monitoring with Missed Detection Probability Equal Allocation

Jie Zhang, Liang Li(✉), Fuxin Yang, and Lin Zhao

College of Automation, Harbin Engineering University, Harbin 150001, China
liliang@hrbeu.edu.cn

Abstract. Compared with BeiDou-2, BeiDou-3 has obvious advantages in geometric configuration and frequency richness, which can improve satellite geometric distribution, greatly reduce observation noise, and provide users with higher integrity positioning service. The simulation method is used to analyze the influence of the increase of BeiDou satellite number and the improvement of observation quality on RAIM performance. It is found that the RAIM algorithm after the global coverage of BeiDou-3 is too conservative in terms of false alarm and missed detection performance, and its availability level is too strict. Then the paper proposes a method based on the equal risk allocation of missed detection probability. By averaging the missed detection probability to the visible satellite, a more reasonable risk allocation can be achieved. The simulation test results show that compared with the classical method, the RAIM algorithm with equal risk allocation method can obtain less integrity risk and improve the availability level.

Keywords: BeiDou-3 · RAIM · False alert probability · Missed detection probability · Equal allocation

1 Introduction

BeiDou Navigation Satellite System (BDS) is a global satellite navigation system independently developed by China. The currently operating BeiDou-2 system consists of five geostationary orbit satellites (GEO), five incided geosynchronous orbits (IGSO) and four medium earth orbits (MEO) [1]. BeiDou-2 system has achieved full coverage in the Asia-Pacific region. It's positioning accuracy, orbital or clock difference performance, signal modulation method and observation noise have been fully studied [2]. At present, the design life of some BeiDou-2 satellites is close to the limit, and it is difficult to maintain service performance. On November 5, 2017, the first and second BeiDou-3 satellites were launched, which opened the construction project of the BeiDou global system network. BeiDou-3 system constellation will consist of three GEO satellites, three IGSO satellites and twenty-four MEO satellites. In addition, five BeiDou-3 test satellites have been launched before 2017 to verify the performance of BeiDou-3 system. BeiDou-3 system predicts a 2-h user range accuracy of about 0.5 m, and the single-double frequency horizontal positioning accuracy is 3.5–4.3 m, which is

J. Sun et al. (Eds.): CSNC 2019, LNEE 563, pp. 238–253, 2019.
https://doi.org/10.1007/978-981-13-7759-4_22

better than result of the BeiDou-2 system. In terms of satellite payload, BeiDou-3 satellite has added new hydrogen atom species; and in signal design, BeiDou-3 system has added S-band Bs signal as an important frequency resource in the future [3].

The BeiDou-3 system will provide users with higher integrity positioning services in the optimization of geometric constellation configuration, improvement of signal modulation mode, and satellite atomic clock. Integrity is mainly to ensure the quality of positioning services provided by the system to reduce integrity risk (IR) [4]. It is defined as the probability that user positioning error exceeds the error limit but does not cause alarm [5]. There are two types of methods for integrity monitoring: one is the external augment method, which monitors the status of the satellite and the system itself by setting up monitoring stations, such as the current wide area augmentation system and local area augmentation system [6]. The second is receiver autonomous integrity monitoring algorithm (RAIM), which uses the internal observation information of the receiver or auxiliary information such as inertial navigation to detect and identify satellite faults [7]. These integrity monitoring methods can be combined for users. The RAIM method responds quickly to satellite faults and abnormalities, and has lower application cost. Currently, it is the most widely used.

With the wide application of GNSS navigation equipment in civil aviation field, when it comes to safety of life applications, people not only hope to obtain high-precision positioning information, but also hope that the obtained positioning information has high reliability, so the navigation system Integrity has become a problem that civil aviation users must consider. RAIM is an integrity algorithm for fault detection and fault identification using redundant observations in receivers or other auxiliary information. It does not require the support of ground facilities. It has the advantages of low cost, high speed and wide coverage. the emergence of this technology has a milestone significance in the civil aviation field [8, 9]. Currently RAIM algorithms mainly include: pseudorange comparison method, least squares residual method and parity vector method, and these three popular RAIM algorithms are mathematically equivalent in nature [10, 11]. Therefore, this paper will mainly introduce the RAIM algorithm based on least squares residual.

Compared with the BeiDou-2 system, the BeiDou-3 system has better geometric configuration, better code rate, richer frequency and lower observation noise. In fact, these favorable changes will also affect the performance of the BeiDou RAIM algorithm, and the design of the RAIM algorithm according to the BeiDou-2 system may no longer be applicable. In fact, these favorable changes will also affect the performance of the BeiDou RAIM algorithm, and the RAIM algorithm according to the BeiDou-2 system may be not applicable. This article firstly analyzes the performance of the RAIM algorithm after the BeiDou globalization, then compares it with the performance of the BeiDou RAIM algorithm under the current BeiDou-2 system. Finally as RAIM algorithm is quite conservative in terms of false alarm and missed detection performance after BeiDou system becomes globalized, the paper proposes an equal risk allocation scheme on missed detection probability.

2 A Brief Overview of RAIM

The principle of least squares can be used for both positioning and error detection. The least squares residual method is a chi-square test based on the sum of squared residuals for satellite fault detection.

Assuming that n satellites are visible, the linearized observation equation is:

$$y = Gx + \varepsilon \tag{1}$$

Where y is the pseudorange observation vector; x is the state variable, including three user position parameters and the receiver clock error parameter; G is the observation geometric matrix; ε is the observed noise, and obeys the Gaussian distribution with zero mean and σ^2 variance.

The pseudorange residual v contains pseudorange error information, which can provide a basis for judging whether the satellite has a fault. The error in the post-test unit weight of the pseudorange residual vector is:

$$\hat{\sigma} = \sqrt{v^T v/(n-4)} = \sqrt{SSE/(n-4)} \tag{2}$$

In the application, $d = \sqrt{SSE/(n-4)}$ is usually used as the detection statistic. SSE is the sum of squares of each element in the pseudorange residual vector, and obeys the chi-square distribution.

Making a binary hypothesis for detection statistic d, the system is either assumed to be fault free, the H_0 hypothesis, and d^2 will have a chi-square distribution with n-4 degrees of freedom. Or there is assumed to be a large bias error on one satellite measurement. The faulted case is referred to as the H_1 hypothesis.

For fault detection, the detection statistic d will be compared to the threshold T_d. Under the condition of satisfying fault detection, if it exists $d > T_d$, that indicates the current system has a fault. There are many references to calculate RAIM fault detection threshold. This part will analyze the relationship between detection threshold and missed detection probability (Pmd) and false alarm probability (Pfa).

Figure 1 shows the RAIM fault detection algorithm using classical hypothesis testing. If the H_0 hypothesis is true, the probability density function (pdf) of the detection statistic obeying the distribution is indicated by the pink line, and the pfa is the yellow area beyond the detection threshold. The H_1 hypothesis is true, the pdf of the detection statistic obeying the distribution is shown by the blue line, and the pmd is the red area below the detection threshold.

Therefore, the fault detection threshold can be calculated according to the specific false alarm probability in the case of no fault condition as follows:

$$\int_{TD}^{\infty} f_{\chi v}(x, v)dx = P_{fa} \tag{3}$$

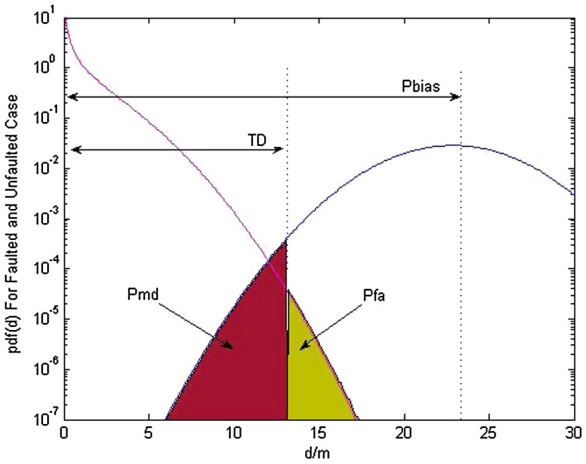

Fig. 1. Threshold set to meet Pmd and Pfa requirement

The value of the detection threshold T_d can be calculated by the above formula, and the relationship between the threshold and the missed detection probability P_{md} can be obtained in a similar manner:

$$\int_0^{TD} f_{n\chi v}(x, v, \lambda)dx = P_{md} \tag{4}$$

In this state, both the threshold T_d and the missed detection P_{md} probability are available, then the centrality parameter λ can be calculated.

When the RAIM algorithm based on least squares residual is used for fault detection, the number of visible satellites needs to be 5 or more. However, due to obstacle occlusion and multipath, the satellite geometry in many regions is not ideal. There is a negligible impact on integrity monitoring [12, 13]. Therefore, it is necessary to determine whether the satellite geometry meets the requirements before fault detection.

Assuming there is a large bias in pseudorange, then the bias is projected into the detection space with a size of B meters. The distribution of d^2 is non-central chi-square with a centrality parameter of $\lambda = B^2$. If the projected bias is represented by *Pbias*, *Pbias* can be calculated by the centralization parameter:

$$Pbias = \sqrt{\lambda} \tag{5}$$

Pbias is the largest projection into the detection domain of a pseudorange error in certain P_{md}. The formula for projecting the pseudorange error into the detection domain is:

$$S = (I - GA) = (I - G(G^T G)^{-1} G^T) \tag{6}$$

Before doing a hypothesis test, it is necessary to determine whether the current satellite geometry is satisfied [14]. Fault detection needs to be returned to the location domain. For given geometric distribution, the pseudorange can be entered into the location domain [15, 16] by

$$A = (G^T G)^{-1} G^T \tag{7}$$

For each satellite, the ratio of the projection of the errors into the position domain to the projection of that error into the detection domain is defined as:

$$H_{slope}(i) = \sqrt{\frac{(A_{1,i}^2 + A_{2,i}^2)}{S_{i,i}}} \tag{8}$$

Pbias indicates the maximum error when meet the missed detection probability. Therefore the maximum positioning error for each satellite is:

$$HPL = \max(H_{slope}(i)) \times Pbias(n) \tag{9}$$

The above formula is the most basic calculation method of the Horizontal Protection Level (HPL). Usually HPL will be compared with the Horizontal Alarm Level (HAL). If it exists $HPL < HAL$, the current geometric distribution meets the requirements and RAIM fault detection can be performed [17].

3 Performance of False Alarm Probability

The false alarm probability refers to the probability that the system applying the integrity algorithm does not exceed the threshold, but alerts the user [4]. System alarms are related to the continuity risk requirements and correlation time for the navigation system.

In classical RAIM algorithm, the number of satellites is known to determine the freedom in the test statistics, and the normalized threshold of fault detection can be determined:

$$\int_{T_n^2}^{\infty} f_{\chi v}(x, n-4)dx = P_{fa} \tag{10}$$

The normalized threshold T_n can be obtained by the above formula. The fault detection threshold needs to consider the measurement noise of the navigation system. The measurement noise level of the current stable BeiDou-2 system is about 2.4 m [18]. As the BeiDou-3 system has been greatly improved in measurement accuracy, the measurement noise of the system is reduced. That means when the RAIM algorithm

designed by BeiDou-2 system is applied to the BeiDou-3 system, the actual detection threshold and false alarm probability will be affected. Under the reference of the BeiDou-3 experimental satellites, it is currently assumed that the 1-sigma value of the measurement noise in BeiDou-3 system is 0.9 m. This assumption is relatively conservative. However, the use of 0.9 m conservative value is sufficient to illustrate the impact of this change on RAIM algorithm in BeiDou-3 system.

The detection statistic of RAIM algorithm under BeiDou-3 system still obeys the chi-square distribution, and the actual false alarm rate can be calculated as:

$$\int_{T_{n,real}^2}^{\infty} f_{\chi^2}(x, n-4)dx = eP_{fa} \tag{11}$$

Where:

$$T_{n,real} = T_n \times \frac{\sigma_{BDS-II}}{\sigma_{BDS-III}} \tag{12}$$

It can be seen from the above equation that the real normalized threshold and false alarm probability are affected by the measurement noise of BeiDou system. On the other hand, the BeiDou-3 system has increased the possibility of observing more satellites in the same area than the previous system. Figure 2 shows the real normalization threshold and the assumed normalization threshold for the number of satellites between 5 and 14.

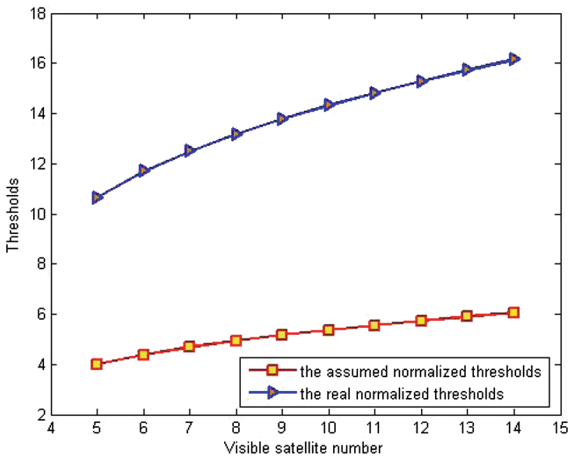

Fig. 2. Real or assumed normalized thresholds under different visible satellites

Figure 2 shows the reason why the RAIM algorithm is too conservative when applied to the Beidou-3 system. The real normalization threshold is much higher than the assumed threshold under the Beidou-3 system with a smaller measurement noise

level. In addition, since the Beidou-3 system can provide more observable satellites in the same area, the threshold difference is further enlarged.

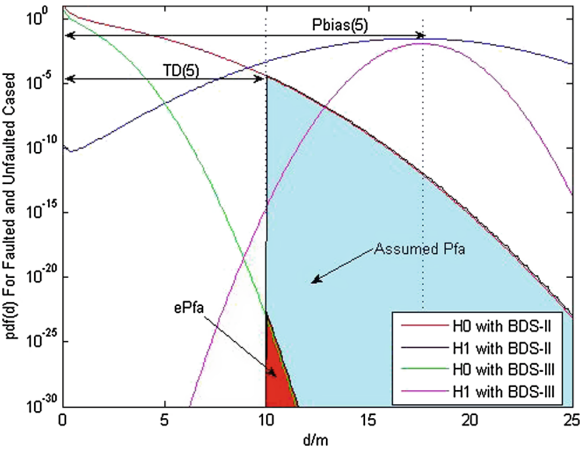

Fig. 3. Distribution of test statistic under fault free hypothesis and faulted hypothesis

Figure 3 shows the detection statistic distribution of RAIM algorithm at the corresponding noise level (H_0 hypothesis and H_1 hypothesis). The blue marked area indicates the false alarm probability parameter assumed under the five BeiDou-3 satellites. The red marked area indicates the real false alarm probability, and it can be seen that the real false alarm probability is much lower than the assumed false alarm probability. On the surface, we should accept that the real false alarm probability is lower than the target requirement, but too conservative false alarm probability increases the requirement for high performance of hardware facilities, and adds unnecessary costs. On the other hand, the actual normalized threshold is much higher than the design value, resulting in waste of availability.

4 Performance of Missed Detection Probability

The missed detection probability refers to the probability that the integrity algorithm detects that the system has not exceeded the detection threshold but has actually failed [4]. The Pmd derives from the integrity risk probability and is also related to the satellite failure probability. In classical RAIM applications, integrity risk usually does not exceed $10^{-7}/\mathrm{h}$. If the probability of satellite failure is $10^{-4}/\mathrm{h}$, the missed detection probability is 0.001 [19].

Figure 4 shows the distribution of the detection statistics of the RAIM algorithm under the H_0 hypothesis and H_1 hypothesis. Considering that the actual pseudorange error of BeiDou-3 system has smaller noise, the real distribution of the fault-free H_0 hypotheses and fault H_1 hypotheses is very narrow. Since the real normalization

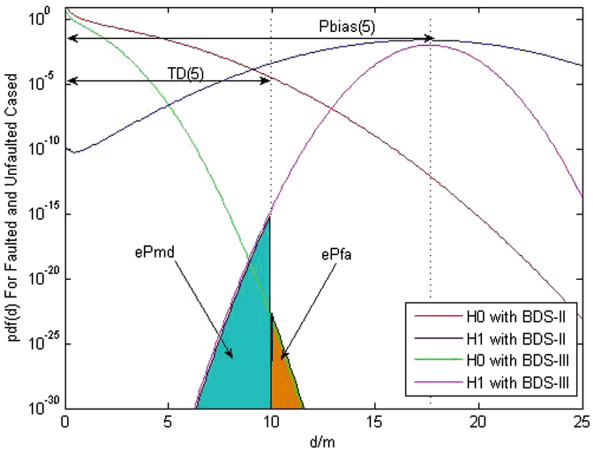

Fig. 4. Distribution of test statistic under fault free hypothesis and faulted hypothesis

threshold is much higher than the design value, the real Pmd represented by the blue area is much smaller than the original Pmd index, the performance is very conservative.

From the equation of missed detection probability, it can be seen that the detection threshold, freedom and decentralized parameter are three parameters closely related to Pmd. As the BeiDou system reduces the measurement noise of the system and increases the number of satellites during the globalization process, these improvements lead to changes in the aforementioned parameters, which in turn affect the Pmd performance. Next, the impact on Pmd is considered from the perspective of decentralized parameters and freedom.

The relationship between the pseudorange domain and the detection domain As mentioned earlier, the influence of the decentralized parameter on the missed detection probability can be considered as a function of the pseudorange in the detection domain under the bias value B, as follows:

$$P_{md}(B) = \int_0^{T_n^2} f_{nc\chi}\left(x, n-4, \left(\frac{B}{\sigma}\right)^2\right) dx \tag{13}$$

Since the BeiDou-3 system has a smaller measurement noise, the distribution of the fault hypothesis becomes very narrow, and the missed detection probability as a function of the deviation B will also be affected. Equation (13) can be adjusted to:

$$P_{md}(B) = \int_0^{T_{n,real}^2} f_{nc\chi}\left(x, n-4, \left(K\frac{B}{\sigma}\right)^2\right) dx \tag{14}$$

Where:

$$K = \frac{\sigma_{BDS-II}}{\sigma_{BDS-III}} \tag{15}$$

Figure 5 shows the Pmd as a function of the detection domain deviation when assuming five satellites. The red curve is the Pmd under the BeiDou-2 system, and the yellow curve represents the Pmd under the BeiDou-3 system with less noise. It can be seen that the real Pmd curve decreases faster. When the Pmd reaches the design index of 0.001, the deviation value B corresponding to the actual missed detection curve is much smaller than the detection domain deviation under the BeiDou-2 system.

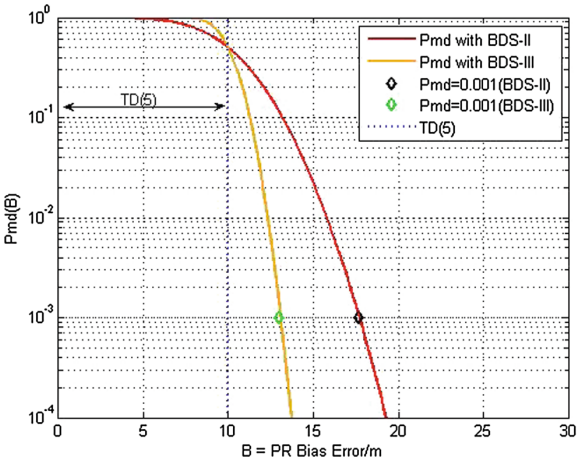

Fig. 5. Pmd as a function of bias error under different BeiDou system

In classical RAIM algorithm, the maximum deviation *Pbias* of the satellite pseudorange error projected into the detection domain is fixed. Since Pbias has been determined under the BeiDou-2 system, when it is applied to the BeiDou-3 system with less noise measurement, it can be obtained from Fig. 6, the actual miss detection probability corresponding to the fixed deviation Pbias is much smaller than the design requirement. It is worth noting that HPL is considered to be the upper bound of the positioning error range. In classical RAIM applications, the HPL requirement is usually no more than 10^{-7}. The actual miss detection probability reaches 10^{-14}, so the actual HPL is 10^{-18} or less. The magnitude is much lower than the original positioning error limit. Such stringent requirements have caused excessive waste of availability and are no longer applicable.

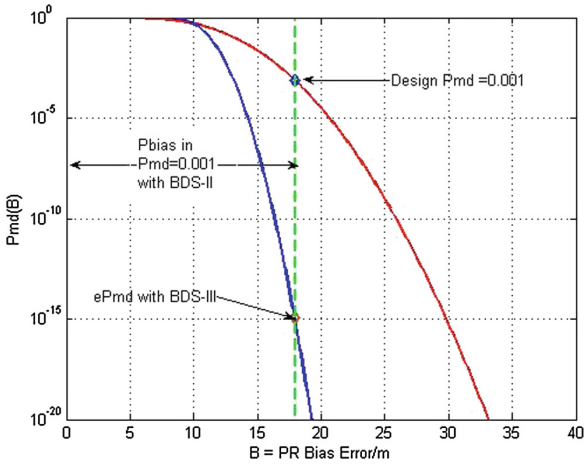

Fig. 6. Assumed Pmd and real Pmd under fixed Pbias error

The globalization process of the BeiDou system provides users with the possibility of observing more satellites. The increase in the number of satellites means a change in the degree of freedom, which also affects the performance of the Pmd.

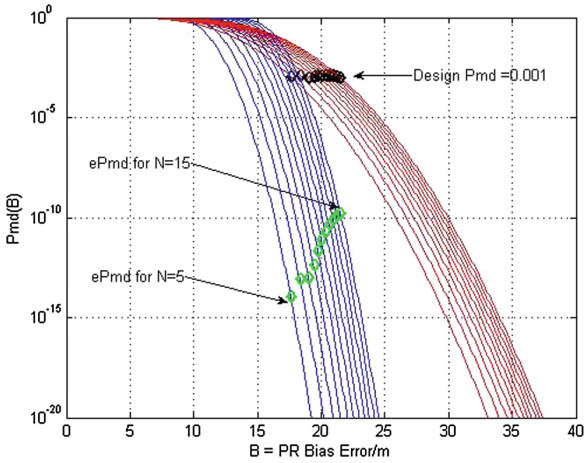

Fig. 7. Effective probability of missed detection as a function of the used satellites

Figure 7 shows the real Pmd curve in the range of 5 to 15 satellites. It can be seen that the order of real Pmd is in the range of $10^{-10} - 10^{-14}$, which is much smaller than the design value. And it also exceeds the constraint of the positioning error limit and the integrity risk. The real Pmd performance is too conservative. It increases the burden on the receiver and has no practical significance.

Through the above analysis, when the RAIM algorithm based on the Beidou-2 system is applied to the Beidou-3 system, the RAIM algorithm performs very conservatively in terms of false alarm and missed detection. It exceeds the constraints of integrity risk and continuity risk and caused excessive waste of availability. Current receivers are no longer able to meet such demanding performance requirements. Therefore, the new RAIM algorithm should fully consider the improvement of the observation noise and geometric satellite distribution of the Beidou-3 system. In addition, in order to obtain higher availability, providing users with better integrity services, the next part will seek a more realistic risk allocation method.

5 RAIM Risk Allocation

In the classical RAIM algorithm, the risk allocation method is that the assumed a priori failure probability is all allocated to the "hardest to protect" satellite, that is, the satellite with the largest Hslope at the current time [19]. This section will explore a more realistic approach to risk allocation.

Through analysis, Pmd is calculated by Eq. (13) as a function of pseudo-range deviation projected into the detection domain. Further, the function in the detection domain can be projected into the location domain by Eq. (8).

In the classical risk allocation method, the Pmd is regarded as a function of minimum detectable error. The relationship can be expressed as follows:

$$P_{md}(MDE) = \int_0^{T_n^2} f_{nc\chi}\left(x, n-4, \left(\frac{MDE}{Hslope(\max)}\right)^2\right)dx \tag{16}$$

Furthermore, the relationship between the minimum detectable error and Pmd under fault condition can be determined. In other words, that is the relationship between the minimum detectable error and integrity risk:

$$IR_{CA}(MDE) = P_{md}(MDE) \times P_{ap} \tag{17}$$

IR_{CA} is the integrity risk under the classical allocation method; MDE is the minimum detectable error; P_{ap} is the current global a priori failure probability of the satellite.

In order to explore a more realistic risk allocation, this paper proposes an equal allocation method for Pmd. The probability of failure is equally distributed to all satellites in the current time, not just the maximum Hslope satellite.

Therefore, in equal allocation method, the missed detection probability as a function of the minimum detectable error can be expressed as:

$$P_{md}(MDE) = \sum_{i=1}^{N} \int_0^{T_n^2} f_{nc\chi}\left(x, n-4, \left(\frac{MDE}{Hslope(i)}\right)^2\right)dx = \sum_{i=1}^{N} P_{md}(MDE, i) \tag{18}$$

Furthermore, the relationship between the minimum detectable error and integrity risk is:

$$IR_{EA}(MDE) = \sum_{i=1}^{N} \left(P_{md}(MDE, i) \times P_{ap}(i) \right) \tag{19}$$

IR_{EA} is the integrity risk under equal allocation method; $P_{ap}(i)$ is the prior probability of each satellite; N is the number of visible satellites.

The equal risk allocation method distributes the assumed a priori failure probability equally to all satellites in the current time. This method fully considers the impact of each satellite which may fail at present on the missed detection probability, which makes the risk allocation of RAIM algorithm more realistic. The next section will further analyze the performance of the equal risk allocation method.

5.1 Experimental Results and Analysis

In classical RAIM applications, when GNSS is used as an auxiliary navigation method, the integrity parameters such as integrity risk and continuity risk are usually certain. In this section, the performance of RAIM algorithm under different risk allocation methods is analyzed by simulation method. The specific parameter settings in the simulation process are shown in Table 1.

Table 1. Simulation parameter settings

Simulation parameter	Value
Integrity risk	10^{-7}
Continuity risk	6.667×10^{-5}
Satellite overall prior probability of failure	1.1×10^{-4}
Satellite average prior probability of failure	1.4×10^{-5}
σ_{BDS-II}	2.4/m
$\sigma_{BDS-III}$	0.9/m

Suppose there are five visible satellites at the current time, and the corresponding Hslope = [1.00, 0.66, 0.43, 0.18, 0.2]. The paper first analyzes the relationship between minimum detectable error and integrity risk under different risk allocation methods.

The purple line in Fig. 8 indicates the relationship between the classical risk allocation and the positioning error and integrity risk under the BeiDou-2 system. The classical RAIM algorithm distributes the satellite prior probability of failure to the satellite with the maximum Hslope, while other satellites are ignored. Since the integrity risk requirement of the classical RAIM application does not exceed 10^{-7}/h and the relationship between detection domain and location domain is linear mapping, the point of the curve at 10^{-7} can be understood as the HPL set by the RAIM algorithm. The blue line in the figure indicates the classical risk allocation method, but based on the BeiDou-3 system with less observed noise. It can be noted that the blue solid line at 10^{-7} corresponding abscissa points is far smaller than HPL.

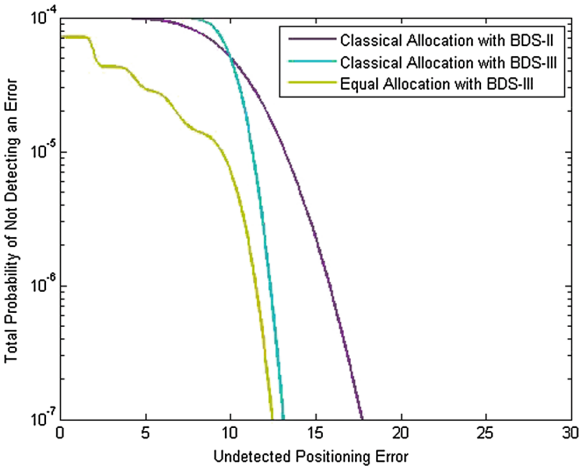

Fig. 8. Integrity risk under classical allocation or equal allocation

The yellow line in Fig. 8 indicates the equal risk allocation method based on the BeiDou-3 system. The system equally distributes the probability of satellite prior failure to each satellite at the current time. Since the risk of missed detection probability is evenly distributed, the Pmd of each satellite in the detection domain can be projected into the position domain by the corresponding Hslope. Then the total probability is obtained by summing in the position domain. It can be seen from Fig. 8 that the equal allocation method of Pmd under any positioning error has less integrity risk than the other two curves in the set range. This means that the RAIM algorithm using the equal risk allocation method can better protect satellites with smaller *Hslope* when considering each potentially faulty satellite.

The relationship between minimum detectable error and integrity risk under different risk allocation methods has been obtained. This section will further analyze the availability of the RAIM algorithm.

It can be determined that when the integrity risk is 10^{-7}/h, the pseudorange error is projected into the maximum deviation in the detection domain. That is Pbias mentioned in the previous section. If the number and geometric distribution of visible satellites are determined, the Hslope factors in the currently visible satellite can be determined. The Hslope are not affected by the noise level under the BeiDou system, so the HPL can be reflected by Pbias.

Considering that BeiDou-3 system provides the possibility of observing more satellites in the same area, Fig. 9 reflects the corresponding Pbias when the number of visible satellites ranges from 5 to 14. It can be seen that the *Pbias* calculated by the classical risk allocation method based on the BeiDou-3 system is much smaller than the design value based on the BeiDou-2 system. In addition, the RAIM algorithm using the missed detection probability equal risk allocation method has the smallest Pbias, which means that the RAIM algorithm using the equal risk allocation method can provide a better protection level.

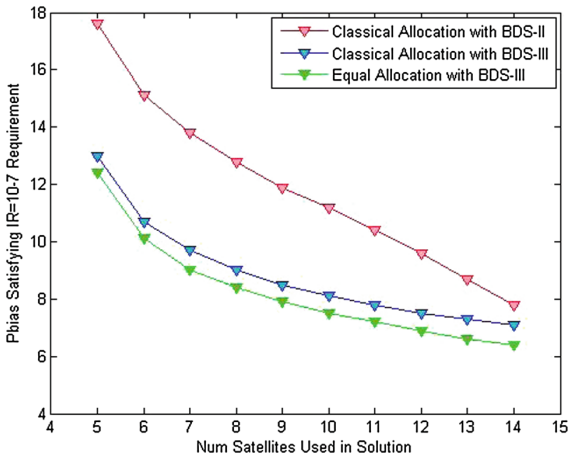

Fig. 9. Pbias meet integrity risk requirement under different risk allocation modes

The red line in Fig. 10 shows the ratio between the HPL obtained by the equal risk allocation method under BeiDou-3 system and the HPL designed by the classical risk allocation method under BeiDou-2 system. It can be noted that the HPL obtained by the equal allocation method was reduced by 20% to 35%. The blue line is the ratio between the HPL obtained by the equal risk allocation method under BeiDou-3 system and the HPL obtained by the classical risk allocation method under BeiDou-3 system. In this case, the HPL obtained by the average distribution method is reduced by 5%–10%. In summary, compared with the other two states the RAIM algorithm with equal risk allocation of missed detection probability can provide smaller protection level. Therefore, the RAIM improved algorithm with equal risk allocation method can provide higher availability and better integrity services for users.

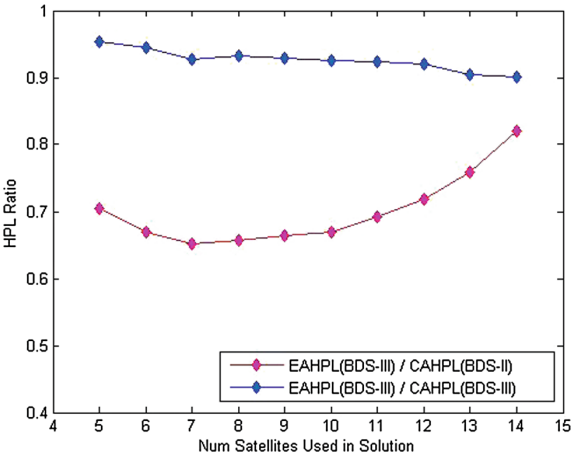

Fig. 10. HPL ratio under different risk allocation

6 Conclusion

The Beidou-3 system has greatly improved its geometric configuration, signal modulation method and frequency richness in the process of globalization. This paper analyzes that the performance of RAIM algorithm based on Beidou-2 system is too conservative in terms of false alarm and missed detection when applied to the Beidou-3 system. And it break through the constraints of continuous risk and integrity risk, resulting in excessive waste of usability. After fully considering the improvement of geometry and observation in Beidou-3 system, this paper proposes a method based on the equal risk allocation of missed detection probability. Through simulation test, Compared with classical method under BeiDou-2 system, the HPL obtained by the equal allocation method was reduced by 20% to 35%. And when compared with classical method under BeiDou-3 system, the HPL was reduced by 5% to 10%. The RAIM improved algorithm has a smaller integrity risk and satisfies the integrity and continuity requirement. It also provides a better protection level and improved system availability.

References

1. Yuanxi Y (2010) Progress, contribution and challenges of compass/BeiDou satellite navigation system. Acta Geodaetica Cartogr Sin 39:1–6
2. Zhang X, Ding L (2013) Quality analysis of the second generation compass observables and stochastic model refining. Geomatics Inf Sci Wuhan Univ 7:832–836
3. Yang Y, Xu Y, Li J, Yang C (2018) Progress and performance evaluation of BeiDou global navigation satellite system: data analysis based on BDS-3 demonstration system. Sci China Earth Sci 61:614–624
4. Li L, Wang H, Jia C, Zhao L, Zhao Y (2017) Integrity and continuity allocation for the RAIM with multiple constellations. GPS Solutions 21:1503–1513
5. Brown RG, Chin GY (1998) GPS RAIM: calculation of threshold and protection radius using chi-square methods—a geometric approach. Navigation
6. Sturza MA (1988) Navigation system integrity monitoring using redundant measurements. Navig: J ION 35:69–87
7. Blanch J, Walter T (2010) RAIM with optimal integrity and continuity allocations under multiple failures. IEEE Trans Aerosp Electron Syst 46(3):1235–1247
8. Parkinson B, Axelrad P (1988) Autonomous GPS integrity monitoring using the pseudorange residual. Navig: J ION 35:255–274
9. Van Dyke KL (2000) GPS availability for aviation applications: how good does it need to be? In: Institute of Navigation GPS 2000 Conferrence
10. Ene A, Blanch J, Walter T et al (2008) Failure detection and exclusion via range consensus. In: European navigation conference GNSS/Toulouse space show
11. Brown RG (1992) A baseline GPS RAIM scheme and a note on the equivalence of three RAIM methods. Navigation 39(3):301–306
12. Lee YC (2005) GPS and Galileo with RAIM or WAAS for vertically guided approaches. In: Proceedings of the ION GNSS 2005, London Beach, CA
13. Rife JH (2013) The effect of uncertain covariance on a Chi square integrity monitor. Navigation 60(4):291–303

14. Hwang P, Brown R (2006) RAIM FDE revisited: a new breakthrough in availability performance with NIORAIM (Novel Integrity Optimized RAIM). Navigation 53(1):41–51
15. Lee YC (2008) Optimization of position domain relative RAIM. In: Proceedings of ION GNSS 2008, Institute of Navigation, 16–19 September, pp 1299–1314
16. Feng S, Ochieng W, Walsh D, Ioannides R (2006) A measurement domain receiver autonomous integrity monitoring algorithm. GPS Solutions 10(2):85–96
17. Walter T, Enge P (1995). Weighted RAIM for precision approach. In: Proceedings of ION GPS-95, Institute of Navigation, September 12–15, pp 1995–2004
18. Wu Y, Liu X, Liu W, Ren J, Lou Y (2017) Long-term behavior and statistical characterization of BeiDou signal-in-space errors. GPS Solutions 21:1907–1922
19. Tim M, Matt H (2008) RAIM performance in the post SA era. Navig: J ION 55:139–150

Propagation Characteristics of Pseudolite Array Signals Indoors

Xinyi Wang, Shuguo Pan(✉), Yue Zhao, and Yan Xia

School of Instrument Science and Engineering, Southeast University,
2 Sipailou, Nanjing 210096, China
psg@seu.edu.cn

Abstract. Multipath effect is considered to be one of the main factors affecting the positioning accuracy of pseudolite. Using antenna array to generate strong directional signal as an advanced multipath suppression method can be applied to pseudolite indoor positioning, but the indoor pseudolite array signal propagation effect is an important but not well solved problem. This paper mainly studies the propagation direction and received power of indoor pseudolite array signals. In this paper, a pseudolite array antenna structure suitable for indoor positioning and pseudolite array indoor positioning algorithm are proposed for the special signal system of pseudolite. Combined with the indoor practical application environment of pseudolite, the propagation direction and received power of the isotropic antenna and two special uniform linear arrays in the room are verified by the image method. The results show that the lobes of the two array-type pseudolite antennas are more concentrated than the isotropic antenna, and the energy can be concentrated more from the side lobes to the main lobe, and the radiation range is relatively large. At the same time, the two array antennas can generate high gain in the direction of arrival of the useful signal, and the received power can reach the maximum value of −40 dB, and the interference signal is attenuated, which provides the possibility for the establishment of the remote pseudolite transmission link.

Keywords: Pseudolite · Uniform linear array · Propagation direction · Received power

1 Introduction

Pseudolites are faced with many difficulties due to their complicated building structure and changeable environment during indoor positioning. Multipath effect is one of the main factors affecting the accuracy of pseudolite positioning [1]. Using antenna arrays to generate strong directional signals as an advanced multipath suppression method can be applied to pseudolite indoor positioning, which generates high gain in the direction of arrival of the direct signal, attenuates interference signals in other directions to suppress multipath [2]. At present, the knowledge of the propagation characteristics of pseudolite array signals is a key problem to be solved for indoor positioning of array pseudolites. The research on the propagation characteristics of pseudolite array also provides a theoretical basis for the improvement of multipath suppression algorithm for indoor positioning.

J. Sun et al. (Eds.): CSNC 2019, LNEE 563, pp. 254–265, 2019.
https://doi.org/10.1007/978-981-13-7759-4_23

Experts at home and abroad have achieved plenteous results in the research of multipath suppression using array antennas. Iwamatsu et al. proposed three AAA systems with multipath equalizer to solve the problem of the degradation of multipath suppression performance when adaptive array antenna is used in the same direction of the desired signal and interference signal. The system has good performance in suppressing interference signals from arbitrary angles of arrival [3]. Bjorklund et al. used digital array antennas and rough surface reflectors to perform multipath measurements, and analyzed multipath and direct signals by eigenvalues of power arrival direction spectra and spatial correlation matrices [4]. In the paper, Fujii proposed a joint processing method of adaptive array and maximum likelihood sequence estimator (MLSE), which can provide better bit error rate performance than traditional adaptive array antenna or traditional multipath channel MLSE [5]. Ray proposed an algorithm for estimating carrier phase multipath in a static environment using measurements from multiple closed antennas, mainly to eliminate the effects of longer period carrier phase multipath [6]. Selva et al. proposed an effective method for calculating maximum likelihood estimation based on modified variable projection (MVP) algorithm in estimating the angle of arrival of uniform linear arrays [7]. The experimental results in the above literature indicate that the array antenna has a significant effect on the analysis and suppression of multipath signals, but the objects of the above methods are all orbiting satellite signals. So far, the research on the signal propagation effects of indoor pseudolite arrays is rarer.

This paper aims to study the signal propagation effects of array pseudolites indoors. In this paper, the radiation principle of uniform linear array and the influencing factors of array directivity are analyzed in detail. For the unique signal system of pseudolite, two special uniform linear arrays are selected as the pseudolite array antenna structure suitable for indoor positioning, and for the problems of time synchronization and multipath effect faced by indoor positioning, the pseudolite array indoor positioning algorithm is proposed based on the characteristics of pseudolite array signal homology, same path transmission and the same degree of ambiguity. The propagation direction and received power of the isotropic antenna and two special uniform linear arrays are verified by the mirror method. The results show that the pseudolite array signal has strong directivity.

2 Theoretical Study on Directional Pseudolite

Depending on the spatial position of the array elements in the array, the array antennas can be divided into linear arrays, area arrays and volume arrays. Linear arrays can provide good directivity, and its radiation characteristics depend on the number, distribution, cell spacing, excitation amplitude and phase of the element antenna [8]. By controlling the above five factors, the signal can be superimposed at a specified place or direction and destructive interference can occur at other locations, thereby achieving the purpose of changing the signal propagation direction. In this paper, a special linear array (uniform linear array) is selected for array pseudolite directivity research.

2.1 Uniform Linear Array Radiation Principle

A uniform linear array refers to a linear array in which all unit antennas have the same structure, and are equally spaced, equally amplified, and the phases are sequentially increasing or decreasing in the same order along the axis of the array (Fig. 1).

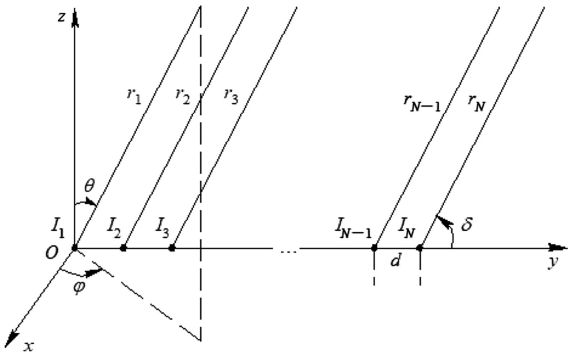

Fig. 1. Uniform linear array

Let N array elements line up along the x-axis, the spacing of each array element is equal, the phase difference between adjacent array elements is ξ, ϕ is the maximum radiation direction of the antenna array, and the far-field function generated by the N-elements uniform line array at the remote observation point (r, θ, φ) is:

$$\begin{aligned} E(\theta, \varphi) &= E_m \frac{F_{element}(\theta, \varphi)}{r} e^{-jkr} \sum_{i=0}^{N-1} e^{ji(kd\cos\phi + \xi)} \\ &= E_m N \frac{e^{-jkr}}{r} F_{element}(\theta, \varphi) f(\theta, \varphi) \end{aligned} \tag{1}$$

In the above formula, E_m is the excitation amplitude, $f(\theta, \varphi) = \frac{1}{N} \sum_{i=0}^{N-1} e^{ji(kd\cos\phi + \xi)}$, $\cos\phi = \sin\theta\cos\varphi$,

The pattern function of the N-ary uniform linear array is expressed as:

$$F(\theta, \varphi) = F_{element}(\theta, \varphi) f(\theta, \varphi) \tag{2}$$

where $F_{element}(\theta, \varphi)$ is Element Factor, which is related to the structure and erection orientation of the array element; $f(\theta, \varphi)$ is Array Factor, which depends on the current ratio and relative position between the array elements, and is independent of the unit antenna [9]. Since the array elements constituting the antenna generally have a wide pattern, when the excitation of the array element is given, the directivity of the array is mainly controlled by the Array Factor. Apply the sum of the equal series, the Array Factor can be simplified to:

$$f(\theta,\varphi)=\frac{1}{N}\sum_{i=0}^{N-1}e^{ji\psi}=\frac{1}{N}\frac{1-e^{-jN\psi}}{1-e^{-j\psi}}=\frac{\sin\frac{N\psi}{2}}{N\sin\frac{\psi}{2}} \tag{3}$$

among them, $\psi = \text{kd}\cos\phi+\zeta$

2.2 Main Factors Affecting Array Directivity

According to reference [9], the main lobe direction, main beam width and side lobe level are the basic parameters for evaluating the directivity of a uniform linear array. Therefore, this section evaluates the main factors affecting array directivity by analyzing these three parameters.

2.2.1 Main Lobe Direction

The direction of the main lobe refers to the direction of the largest radiation beam on the antenna pattern. The maximum value of the uniform linear array occurs when ψ=0, that is, $\text{kd}\cos\phi+\zeta=0$ which leads to:

$$\cos\phi_m=-\frac{\zeta}{kd} \tag{4}$$

The maximum radiation direction of a uniform linear array has two more specific positions. The maximum radiation direction of the edge array is perpendicular to the direction of the array axis, that is, $\phi_m=\pm\pi/2$, $\xi=0$, and there is no phase difference between the currents of the array elements. Conversely, when the maximum radiation direction is in the direction of the axis, the line array is called an end fire array. That is, $\phi_m=0$ or π, $\xi=kd(\phi_m=0)$ or $\xi=-kd(\phi_m=\pi)$, the current of each array element advances or lags kd in the direction of the array axis. Therefore, the change of the maximum radiation direction of the pattern can be caused by adjusting the current phase difference ξ between adjacent elements of the linear array [10].

2.2.2 Main Beam Width

The beam width is a parameter that describes the sharpness of the main beam direction. The beam width is expressed in reference [11] as:

$$\theta_{null}=2\sin^{-1}\left(\frac{\lambda}{Nd}\right) \tag{5}$$

$$\theta_{-3dB}=2\sin^{-1}\left(0.4\frac{\lambda}{Nd}\right) \tag{6}$$

By formula (5) and formula (6), to obtain sharp beams, one is to increase the number of array elements or the distance between them, and the other is to increase the frequency of incident waves.

2.2.3 Sidelobe Level

The sidelobe level is a parameter that describes the peak value of the sidelobe relative to the peak value of the main lobe. It can be known from reference [11] that if a lower sidelobe level is to be obtained, first, the distance between the elements is constant, and the number of array elements used is increased. Second, the number of array elements remains unchanged, increasing the distance between array elements. The third is to increase the signal frequency, but the high frequency is prone to spatial aliasing, that is, the grating lobes. According to the spatial sampling theorem, in order to avoid the appearance of grating lobes, $d \leq \frac{\lambda_{\min}}{2}$ must be satisfied.

2.3 Directional Pseudolite Array Design

(1) Frequency: in order to achieve maximum compatibility with existing hardware equipment and improve the ability of signal location and calculation, the pseudolite signal carrier adopts L-band, the frequency is 1575.42 MHz, and the wavelength is about 0.2 m UHF signal.
(2) Number of Array Elements: The purpose of indoor positioning is to obtain four unknown parameters including determining the three-dimensional coordinates of a point and achieving synchronization, so it must be determined by measuring the distance of at least 4 pseudolites. At the same time, the width of the main lobe is inversely proportional to the number of pseudolites. Considering the hardware cost, the number of array elements is set to 10.
(3) Distance Between Array Elements: The wavelength of pseudolite signal is about 0. 2 m. In order to avoid the occurrence of grating lobes, the distance between array elements should be less than or equal to 1/2 wavelength. At the same time, to obtain the smallest main lobe width, the maximum distance between array elements is 0. 1 m.
(4) Phase Difference Between Array Elements: As can be seen from Sect. 1.2.1, the directionality of the array can be changed by adjusting the phase difference between the array elements. This paper mainly studies the edge array and the end array. The pseudolite array is equally in-phase excitation, that is, the phase difference between adjacent array elements is 0°, and the maximum radiation direction is perpendicular to the antenna array axis; conversely, when the phase difference between adjacent array elements is 180°, the maximum radiation direction is the direction of the array axis.

3 Pseudolite Array Indoor Positioning Algorithm

3.1 Pseudolite Array Positioning Principle

When the pseudolite array is used for indoor positioning, a single point array type indoor pseudolite network can be used. According to the characteristics of pseudolite array signal homology, same path transmission, and the same degree of ambiguity, it is

possible to establish a carrier phase difference measurement equation independent of the whole week ambiguity, clock error and multipath error, so as to obtain accurate indoor positioning result.

3.2 Carrier Phase Observation Equation

The observation error of indoor positioning system based on pseudolite carrier phase measurement mainly comes from whole-cycle hopping, multipath effect, pseudolite clock difference and receiver clock error [12]. Considering the above error factors, the following carrier phase observation equation is obtained (wherein the superscript i represents the pseudolite array element number and the subscript is the number of the reception point to be sought):

$$\lambda\varphi_1^i = \mathrm{R}_1^i + N + t1 - t^i + M_1^i + e_1 \tag{7}$$

In the above formula, R_1^i and M_1^i are the geometric distance and multipath error of array element i to receiving point 1, respectively, N is the weekly ambiguity, $t1$ is the receiver clock error, t^i is the pseudolite clock error, and e_1 is the remaining error such as receiver noise [13].

The single-point array type pseudolite system has multiple array elements, and the original carrier phase observation equations of each array element to the receiving point 1 are connected to a system of equations, which can be expressed as:

$$\begin{cases} \lambda\varphi_1^i = \mathrm{R}_1^i + N + t1 - t^i + M_1^i + e_1 \\ \lambda\varphi_1^j = \mathrm{R}_1^j + N + t1 - t^j + M_1^j + e_1 \\ \qquad\qquad \vdots \\ \lambda\varphi_1^k = \mathrm{R}_1^k + N + t1 - t^k + M_1^k + e_1 \end{cases} \tag{8}$$

The same path transmission can eliminate the multipath error, and the 1/2 wavelength makes the whole cycle number the same. Therefore, the equations in formula (8) are all different from the first equation, and the differential carrier phase observation equations are obtained.

$$\begin{cases} \lambda\left(\varphi_1^j - \varphi_1^i\right) = \mathrm{R}_1^j - \mathrm{R}_1^i + e_1 \\ \qquad\qquad \vdots \\ \lambda\left(\varphi_1^k - \varphi_1^i\right) = \mathrm{R}_1^k - \mathrm{R}_1^k + e_1 \end{cases} \tag{9}$$

In the above formula, the geometric distance is expressed as:

$$\begin{cases} R_1^i = \sqrt{(X^i - X_1)^2 + (Y^i - Y_1)^2 + (Z^i - Z_1)^2} \\ R_1^j = \sqrt{(X^j - X_1)^2 + (Y^j - Y_1)^2 + (Z^j - Z_1)^2} \\ \vdots \\ R_1^k = \sqrt{(X^k - X_1)^2 + (Y^k - Y_1)^2 + (Z^k - Z_1)^2} \end{cases} \tag{10}$$

Substituting the formula (10) into the formula (9), by solving the nonlinear measurement equations, accurate indoor positioning results can be obtained.

4 Simulation Verification of Pseudolite Array Propagation Characteristics

In this paper, the image method with high practical value in ray tracing method is used to track and capture pseudolite signals. The image method can calculate the field strength distribution of pseudolite signals according to the obstacle shape and the material-related reflection coefficient and transmission coefficient in the modeled scene, while using the electric field combined with a specific antenna to calculate the electrical parameters of a specific scene [14]. It can accurately describe the propagation characteristics of pseudolite array signals indoors.

4.1 Modeling Indoor Scenes

In this paper, Wireless Insite software is used for indoor scene modeling. Indoors are prone to multipath. Walls, floors, and furniture all change the trajectory of pseudolite signals. Therefore, in order to compare the directionality of the pseudolite antenna array, no obstacles are placed in the indoor model, and the simplified indoor model is equally divided into three regions, and three different types of antennas are selected as pseudolite transmission points. An isotropic antenna is arranged in the area 1, a single point edge array is arranged in the area 2, and a single point end array is arranged in the area 3. The pseudolite transmitting device is located at the midpoint of the area, and the transmitting antenna is 2 m high. The pseudolite parameters are shown in Table 1.

Table 1. Pseudolite antenna parameters

	Isotropic antenna	Single point edge array	Single point end array
Frequency (MHZ)	1575.42	1575.42	1575.42
Number of array elements	—	10	10
Array spacing (m)	—	0.1	0.1
Phase difference between array elements	—	0°	180°

The pattern of three different types of pseudolite antennas is shown in Fig. 2:

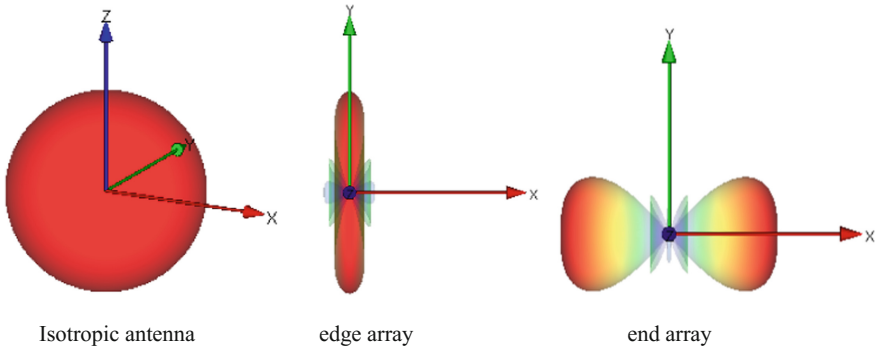

Fig. 2. Pseudolite antenna pattern

In order to avoid the directionality of the pseudolite signal being interfered by the receiving antenna, the receiving device uses the isotropic antenna with the lowest directivity. At the same time, in order to explore the correlation between received power and distribution position, we divide each region into 620 equidistant grids evenly, each grid covering about 0.5 m^2, and there is only one data collection point in

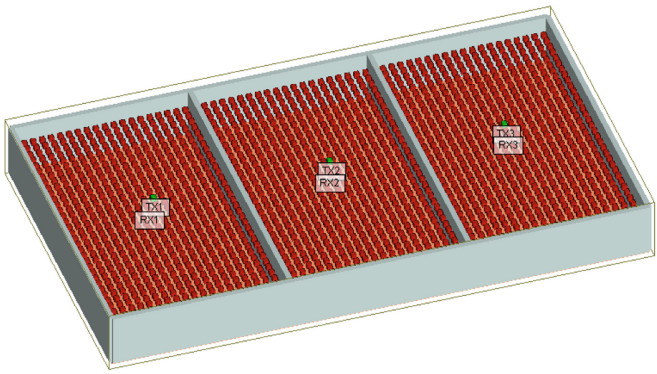

Fig. 3. Top view of the indoor model

each grid. The distribution of these receiving points is shown in Fig. 3.

4.2 Simulation Results

In this section, the far-field propagation of the above three pseudolite antennas is accurately calculated by the image method, and analyzes the propagation characteristics of the array signals based on the extracted pseudolite signals. The propagation

direction and received power of the pseudolite array signals are the main research parameters of this paper.

4.2.1 Direction of Propagation

It can be seen from Sect. 1.1 that the antenna array can generate high gain in the direction of arrival of the direct signal, while the signal in the other directions is attenuated. The strong directivity of the array antenna characterizes its multipath suppression capability. The pseudolite signal components are extracted from 620 data acquisition points in each region of Fig. 2 to obtain a radiation power distribution map

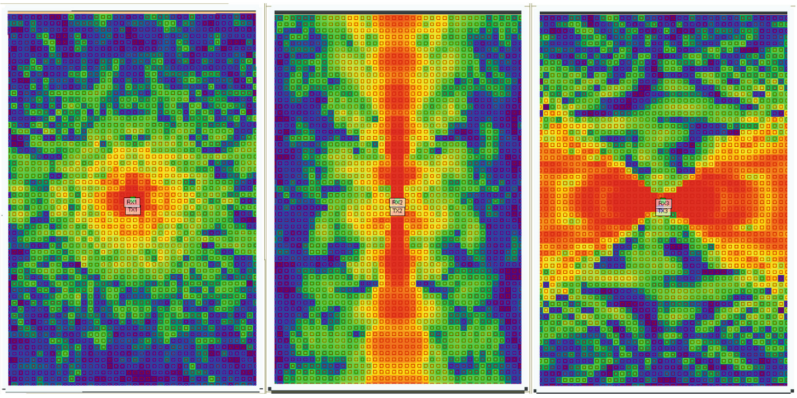

Fig. 4. Radiation power distribution map of pseudolite antenna

as shown in Fig. 4. The graph can be used as a predictor of the propagation direction of the pseudolite signal and characterizes the radiated power and radiation range of the pseudolite array signal along the spatial dimension.

Figure 4 shows the radiation power distribution of isotropic antenna, edge array and end array in an indoor scene from left to right. The three antennas have the same transmission power, warm color represents strong radiation capability, and cool color represents weak radiation capability. It can be seen from the above figure that the isotropic antenna radiates pseudolite signals uniformly around, and the signal power gradually decreases with the increase of the transmission distance, and because the transmission direction is more dispersed, the radiation range is smaller than the latter two antennas. Array pseudolites have obvious directionality due to the superposition of signals between array elements. The maximum radiation direction of the edge array is perpendicular to the antenna array (Y axis), and the maximum radiation direction of the end array is concentrated in the direction of the array axis (X axis). Compared with the isotropic antenna, the lobes of the array antenna are more concentrated, the energy is concentrated from the side lobes to the main lobe, and the radiation range is relatively large, which makes possible to establish a long-distance pseudolite transmission link.

The experimental results are consistent with the pattern of the pseudolite antenna in Fig. 2.

4.2.2 Received Power

The received power distribution curve characterizes the variation of the average received power of the pseudolite array signal with the transmission distance. Limited by the size of the indoor scene in Fig. 3, the transmission distance of the pseudolite signal is 0 m (minimum) to 60 m (maximum), and the transmission distance is divided

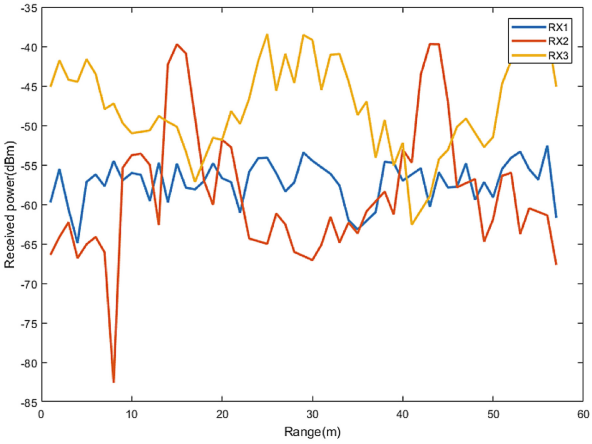

Fig. 5. Pseudolite signal receiving power distribution curve

into 6 groups, and the distance between each group is 10 m, and then the average value of the received power of the pseudolite signal components falling in each interval is calculated to obtain a pseudolite receiving power distribution curve as shown in Fig. 5.

It can be seen from Fig. 5 that the edge array has a maximum receiving power of −40 dB (the signal transmission power is 0 dB) at a transmission distance of 15 m and 45 m, corresponding to the vertical direction of the axis. When the received power of the edge array reaches the minimum value, the received power of the end array reaches a maximum value of −40 dB, and the corresponding transmission distance is about 0, 30, and 60 m, indicating that the maximum radiation directions of the two pseudolite array antennas are perpendicular to each other. The blue curve corresponds to the isotropic antenna, and the average received power is uniformly distributed with the increase of the transmission distance, and the value is greater than the minimum received power of the array antenna and smaller than the maximum received power of the array antenna. Therefore, the pseudolite receiving device can be disposed in the maximum radiation direction of the array antenna to achieve high gain in the direction of arrival of the useful signal and attenuate the interference signal. The concentrated main beam energy can radiate the pseudolite signal to the receiving end further away.

5 Conclusions

In this paper, the pseudolite array antenna structure suitable for indoor positioning and the indoor positioning algorithm of pseudolite array are proposed by studying the radiation characteristics of uniform linear array and the influence factors of array directivity. Combined with the indoor practical application environment of pseudolite, the propagation direction and received power of the isotropic antenna and two special uniform linear arrays in the room are verified by the mirror method. It is concluded that the lobes of the two array pseudolite antennas are more concentrated than the isotropic antennas, and the energy can be concentrated more from the side lobes to the main lobes, and the radiation range is relatively large, which make it possible to establish a long-distance pseudolite transmission link. At the same time, the two array antennas can generate high gain in the direction of arrival of the useful signal, and the received power reaches a maximum of −40 dB, and the interference signal is attenuated. The above conclusions have deepened our understanding of the propagation characteristics of pseudolite array antennas in indoor environments and will contribute to the design and application of pseudolite array antennas.

Acknowledgments. We appreciate anonymous reviewers for their valuable comments and improvements to this manuscript. Thanks also go to the National Key Technologies R&D Program (Grant Number 2016YFB0502101) and National Natural Science Foundation of China (No: 41574026, 41774027).

References

1. Veeranath P, Rao DN, Vathsal S et al (2013) Reducing multipath effects in indoor channel for analysis of GPS/pseudolite signal acquisition. Int J Sci Res Publ 3(2):1–6
2. Marathe T, Daneshmand S, Lachapelle G (2015) Pseudolite interference mitigation and signal enhancements using an antenna array. In: 2015 International conference on indoor positioning and indoor navigation (IPIN). IEEE, pp 1–9
3. Iwamatsu T, Umeda M, Wakasugi K (2011) Configurations and performance evaluations for a long-delay multipath interference based on the combinational use of an adaptive array antenna and multipath equalizers. In: The 2011 international conference on advanced technologies for communications (ATC 2011). IEEE, pp 239–243
4. Bjorklund S, Grahn P, Nelander A (1999) Measurement and analysis of multipath by a rough surface reflector using a digital array antenna. In: International symposium on signal processing and its applications, vol 2. IEEE, pp 859–862
5. Fujii M (1996) Joint processing of an adaptive array and an MLSE for multipath channels. In: Global telecommunications conference, vol 1. IEEE, pp 560–564
6. Ray JK (1999) Use of multiple antennas to mitigate carrier phase multipath in reference stations. In: Proceedings of the ION-GPS, pp 269–279
7. Selva J (2005) An efficient Newton-type method for the computation of ML estimators in a uniform linear array. IEEE Trans Signal Process 53(6):2036–2045
8. Van Lil E, De Bleser J, Van de Capelle A (2012) Analytical formulas for the directivity of general antenna arrays. In: European conference on antennas and propagation. IEEE, pp 1–4
9. Clemente A, Delaveaud C, Rudant L (2015) Analysis of electrical dipole linear array maximum directivity. In: European Conference on Antennas and Propagation. IEEE, pp 1–5

10. Konovalenko AA, Tokarsky PL, Erin SN (2010) The directivity characteristics of an antenna array receiving the UWB signal. In: 2010 5th International conference on ultrawideband and ultrashort impulse signals (UWBUSIS). IEEE, pp 249–251
11. Sarac U, Harmanci FK, Akgul T (2008) Detection and localization of emitters in the presence of multipath using a uniform linear antenna array. In: 5th IEEE sensor array and multichannel signal processing workshop, SAM 2008. IEEE, pp 419–422
12. Selmi I, Samama N, Vervisch-Picois A (2013) A new approach for decimeter accurate GNSS indoor positioning using carrier phase measurements. In: 2013 international conference on indoor positioning and indoor navigation (IPIN). IEEE, pp 1–6
13. Samama N, Vervisch-Picois A, Taillandier-Loize T (2016) A GNSS-based inverted radar for carrier phase absolute indoor positioning purposes first experimental results with GPS signals. In: 2016 international conference on indoor positioning and indoor navigation (IPIN). IEEE, pp 1–8
14. Zhang LZL, Liu WLW, Langley RJ (2009) A minimum variance beamformer with linear and quadratic constraints based on uniform linear antenna arrays. In: Antennas and propagation conference. IEEE, pp 585–588

Error Prediction Model of Klobuchar Ionospheric Delay Based on TS Fuzzy Neural Network

Yaqi Peng[1(✉)], Chengdong Xu[1], Fei Niu[2], and Yiwen Wang[1]

[1] School of Aerospace Engineering, Beijing Institute of Technology, Beijing, China
pengyaqi666@163.com, xucd@bit.edu.cn, l3269437055@163.com

[2] Beijing Satellite Navigation Center, Beijing, China
niufei009@sina.com

Abstract. The ionospheric delay has a very important influence on the positioning accuracy of satellite navigation. It can be effectively reduced by establishing an accurate and reasonable ionospheric correction model. At present, Klobuchar parameter model is widely used in single-frequency receiver, but the correction rate of this model can only reach about 60%, which can not meet the need of high precision navigation and positioning. Through the research and analysis of the ionospheric error data of the Klobuchar parameter model, it is found that there are some periodic phenomena objectively. Aiming at the error information which cannot be represented by definite mathematical model, a TS (Takagi-Sugeno) fuzzy neural network prediction model applied to Klobuchar ionospheric delay error is established by combining TS fuzzy theory with neural network. The simulation results show that the model has good fitting ability and prediction effect on the Klobuchar ionospheric delay error. Using this model to provide error compensation for the ionospheric delay can reduce the error by about 20%. It is of great significance to improve the accuracy of navigation and positioning.

Keywords: Ionospheric delay · Fuzzy neural network · Klobuchar model · Error prediction

1 Introduction

The influence of the space ionosphere on the navigation signal is mainly due to the deflection of the signal when it passes through the ionosphere. Thus, the propagation velocity and direction are changed, resulting in the ionospheric delay error, which is one of the important error sources in GNSS measurement [1–3]. At present, there are three kinds of models for correcting ionospheric delay: dual frequency correction model, measured data model and empirical model [4]. Among them, the empirical model is less complicated and more convenient to use. So it is widely used by users of single frequency receiver. Klobuchar ionospheric model is one of the most commonly used empirical models for GPS and BDS [5]. This model fully considers the ionospheric variation of amplitude and period on the parameters setting, which intuitively and

J. Sun et al. (Eds.): CSNC 2019, LNEE 563, pp. 266–274, 2019.
https://doi.org/10.1007/978-981-13-7759-4_24

succinctly reflects the variation characteristics of the ionosphere, and can correct the ionospheric delay in real-time fast positioning of single-frequency receivers [6, 7].

However, the correction accuracy of the Klobuchar ionospheric model is limited, which can only reach about 60%. Moreover, the ionospheric changes in the polar region and near the equator are so intense that the model can not effectively reflect the true state of the ionosphere, so the model can no longer meet the increasing demand for accuracy [8]. Many researchers have improved the model from different aspects. In reference [9], a 14-parameter Klobuchar model was proposed, and six additional parameters were added to describe the change of the initial phase and the night flat field. The model is more suitable for the actual variation of the ionosphere in China. In reference [10], the initial phase and amplitude were corrected by least square fitting, and the ionospheric delay correction model suitable for small region was established. In reference [11], by improving the amplitude of night term and cosine term, the modified Klobuchar model of single frequency GNSS users in polar region is established without increasing the parameters.

Although most of the research findings at home and abroad have improved the model from various aspects and achieved good correction results, the overall correction rate of the ionospheric delay is not high enough to reflect the changes of the ionosphere at night and so on. In the data processing practice of Klobuchar ionospheric error, through the comparison with the ionospheric products of the international GNSS Monitoring & Assessment System (iGMAS), it is found that there are some periodic regularities in the Klobuchar model error. Therefore, a new method is proposed in this paper, which combines the advantages of TS fuzzy theory and neural network, and establishes the error prediction model based on TS Fuzzy Neural Network (TS-FNN). By training and learning the error data, the nonlinear mapping relationship between input and output can be grasped, and then the model error can be compensated to improve the accuracy of the Klobuchar ionospheric model.

2 Error Analysis of Klobuchar Ionospheric Model

2.1 Klobuchar Ionospheric Model

In the Klobuchar model used by GPS, the maximum influence of the daily ionosphere is fixed at 14:00 local time, and the cosine function is used to fit the daytime delay variation. The nighttime ionospheric zenith delay is regarded as a constant of 5 ns. Converted to the total electron content (TEC) of the ionosphere is 9.23 TECU (1TECU = 10^{16} electrons per square meter). The Klobuchar model is calculated by using eight model parameters and the geomagnetic latitude at the ionospheric puncture point, and converted to ionospheric delay on the propagation path by mapping function. The model details can be found in the reference [12], which will not be repeated here.

The Klobuchar model parameters of this paper are extracted from the broadcast ephemeris header file downloaded from Wuhan University IGS Data Center. In order to simplify the problem and facilitate data extraction, this paper mainly analyzes the ionospheric error in the vertical direction of the puncture point, and the ionospheric delay on the propagation path can be converted by the mapping function.

2.2 iGMAS Ionospheric Products

iGMAS is a platform that can monitor and evaluate GNSS system service performance such as positioning accuracy, continuity and reliability, etc. It can generate high-precision ephemeris, satellite clock and global ionospheric TEC grid products. Among the main products, the global ionospheric TEC grid product has become an important basic data for studying ionospheric delay correction.

The iGMAS navigation data analysis center integrated GPS global network and selected 250 stations suitable for solving the ionosphere. The daily TEC changes are divided into 12 intervals every 2 h, that is, a global ionospheric TEC map product is generated every 2 h. Its resolution in the latitude and longitude directions reaches 2.5° × 5°, and finally released in IONEX (Ionospheric Map Exchange) format [13]. According to the iGMAS official document, the accuracy of the final ionospheric TEC grid data is 2-8TECU, and the accuracy is above 90%. Therefore, this paper regards it as the true value of the ionospheric TEC, and then analyzes the error data.

For the solution of the TEC at any time, the piecewise linear method can be used. After the user interpolates the time, longitude and latitude, the TEC data of a certain place can be obtained, then the corresponding vertical ionospheric path delay can be obtained by Eq. (1.1).

$$\Delta S = -\frac{40.28TEC}{f^2} \tag{1.1}$$

Where f is the system frequency.

2.3 Error Analysis

Taking the L1 signal as an example, its system frequency f_{L1} = 1575.42 MHz, calculate the Klobuchar ionospheric path delay error at 12 o'clock on October 8, 2017, as shown in Fig. 1. It can be seen that the Klobuchar model is relatively rough, and can only roughly fit the distribution of the ionosphere compared to the real delay, and there is still a large error near the peak of the ionospheric delay.

In the error analysis based on time series, three points at different latitudes are selected to calculate the ionospheric delay within a week, as shown in Fig. 2. It is obvious that there are great differences in the true ionospheric delay at different latitudes and the Klobuchar model can not fit this change well, but it can be seen that the Klobuchar model bias has some periodic characteristics.

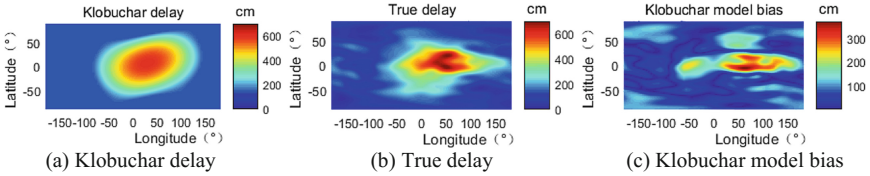

(a) Klobuchar delay (b) True delay (c) Klobuchar model bias

Fig. 1. Klobuchar ionospheric path delay error

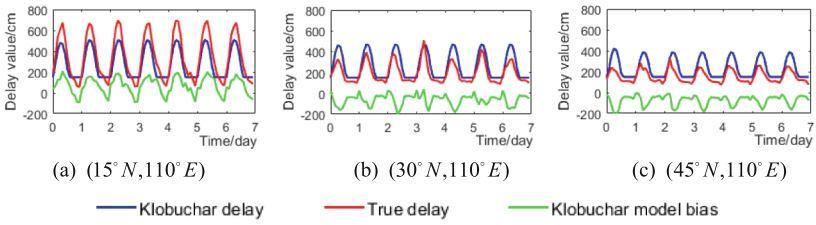

Fig. 2. Ionospheric delay at different points

3 TS Fuzzy Neural Network Prediction Model

3.1 TS Fuzzy Neural Network

The TS fuzzy system is a fuzzy inference model proposed by Japanese scholars Takagi and Sugeno for systematic output as an exact value. In fuzzy theory, there are basic concepts of membership degree and membership functions. The membership degree refers to the degree to which the elements μ belong to the fuzzy subset f. It is usually represented by a number $\mu_f(\mu)$ in $[0, 1]$, the closer $\mu_f(\mu)$ is to 1, the greater the extent to which μ belongs to f, and vice versa. The membership function is used to calculate the propensity of an element in the subset for both sides of the difference [14].

TS fuzzy neural network (TS-FNN) combines fuzzy theory with neural network, integrates logical inference and nonlinear dynamics, and establishes new inference by modifying the membership function of fuzzy subsets [15]. The TS-FNN structure is shown in Fig. 3.

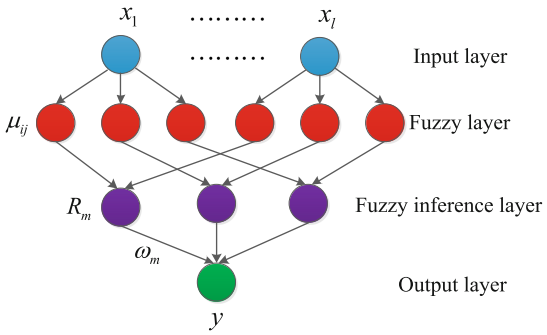

Fig. 3. TS-FNN structure diagram

TS-FNN has a 4-layer structure as follows:

(1) Input layer: Vector $x_1, x_2, \cdots, x_l$ is the input layer variable, l is the number of nodes. In this paper, longitude, latitude, weekly seconds and hours of the puncture point are taken as input parameters, so the number of input layer nodes is 4. In addition, in order to eliminate the dimensional effects between the parameters, the data needs to be normalized before the data analysis.

(2) Fuzzy layer: Each membership function corresponds to a node. μ_{ij} is the i th membership function of the j th input variable. This article uses a Gaussian function as a membership function, then the membership of the input variable x_i is

$$\mu_{ij}(x_i) = \exp\left[-\frac{(x_i - c_{ij})^2}{\sigma_{ij}}\right] \tag{1.2}$$

Where, μ_{ij} is the j th membership function of x_i; c_{ij} and σ_{ij} is the center and width of the membership function, respectively, these two parameters can change the position and shape of the membership function, and its value will move towards the optimal trend with the training process of the network.

(3) Fuzzy inference layer: The number of nodes in this layer corresponds to the number of fuzzy rules, R_m represents the m th fuzzy inference, the inference of the rule R_i can be defined in the form of "*if – then*":

$$\begin{aligned} R^i : &\, if\ x_1\ is f_1^i, x_2\ is f_2^i, \cdots, x_k\ is f_k^i \\ &\, then\ y_i = p_0^i + p_1^i x_1 + p_2^i x_2 + \cdots + p_k^i x_k. \end{aligned} \tag{1.3}$$

Where: f_j^i and $p_j^i (j = 1, 2, \cdots, k)$ are the fuzzy subset and fuzzy system parameters, respectively; y_i is the network output. The inference can be regarded as an output obtained by linearly combining the fuzzy input parts.

The membership degree of this paper uses the multiplicative operator, then the connection weight of the j th fuzzy inference layer neuron to the i th output layer neuron is

$$\omega_{ij} = \mu_{j1}(x_1) \cdot \mu_{j2}(x_2) \cdots \mu_{jk}(x_k), i = 1, 2, \cdots, m. \tag{1.4}$$

(4) Output layer: Clearly calculate the output through defuzzification and denormalization. The output layer corresponds to the Klobuchar ionospheric model bias. The calculation method is

$$y = \frac{\sum_{i=1}^{n} \omega_{ij}(p_0^i + p_1^i x_1 + \cdots + p_k^i x_k)}{\sum_{i=1}^{n} \omega^i} \tag{1.5}$$

3.2 Learning Algorithm of TS Fuzzy Neural Network

The parameters that need to be learned in the TS-FNN are mainly the fuzzy system parameters related to the network connection weight, as well as the central value and width of the membership functions of each node in the fuzzy layer. The main steps are as follows:

(1) Calculate the bias e between the expected output and the predicted model output:

$$e = |y_e - y_r| \tag{1.6}$$

Where: y_e and y_r is the expected output and the predicted output, respectively.

(2) Determine whether the bias meets the error requirements, if it is, then the training process is terminated. With the increase of training times, the bias will gradually decrease, and when it is reduced to a certain value, the bias will be basically unchanged. In order to avoid over-fitting of the network and save computing resources, an upper limit is usually set on the training times.

(3) The fuzzy system parameter p_j^i of corrected TS-FNN is

$$p_j^i(k) = p_j^i(k-1) - \alpha \frac{\partial e}{\partial p_j^i} \tag{1.7}$$

$$\frac{\partial e}{\partial p_j^i} = \frac{(y_e - y_r)\omega_{ij}}{\sum_{i=1}^{m} \omega_{ij} x_j} \tag{1.8}$$

Where, α is the network learning rate. When α is selected to be larger or smaller, the learning process will oscillate and the convergence speed will be slower. It needs to be selected according to the specific experiment.

(4) The center parameter c_{ij} and width parameter σ_{ij} of the corrected membership function are

$$c_{ij}(k) = c_{ij}(k-1) - \beta \frac{\partial e}{\partial c_{ij}} \tag{1.9}$$

$$\sigma_{ij}(k) = \sigma_{ij}(k-1) - \beta \frac{\partial e}{\partial \sigma_{ij}} \tag{1.10}$$

Where β is the parameter learning rate.

4 Error Prediction Experiment Based on TS Fuzzy Neural Network

The error data is sampled according to the content and data source described in Sect. 2. The sampling interval is 2 h. The test data is selected from the data of 30 days from October 1, 2017. The first 25 days of data were used to train the TS-FNN model, while the last 5 days of data were used to verify the accuracy of the model. The number of input layer nodes is 4; each input parameter defines 3 fuzzy sets; according to the network structure shown in Fig. 3, the number of fuzzy layer nodes is $4 \times 3 = 12$; and output layer node is 1, so the network structure is 4-12-3-1. The maximum training times are set to 500, and the model training bias target is 5 cm, and the learning rates α and β are 0.5 and 0.3, respectively. In this experiment, 9 ionospheric puncture points of

different longitude and latitude were selected as test points: $P_1(15°N, 80°E)$, $P_2(15°N, 100°E)$, $P_3(15°N, 120°E)$, $P_4(30°N, 80°E)$, $P_5(30°N, 100°E)$, $P_6(30°N, 120°E)$, $P_7(45°N, 80°E)$, $P_8(45°N, 100°E)$, $P_9(45°N, 120°E)$. As shown in Fig. 4.

Fig. 4. Distribution map of test points selection

The experiment results are shown in Fig. 5. It can be seen from the diagram that the periodic variation of the Klobuchar ionospheric delay error can be well fitted by the TS-FNN model, and the prediction effect is satisfactory. Although the model prediction deviation is slightly divergent over time, the divergence is also very small and still acceptable.

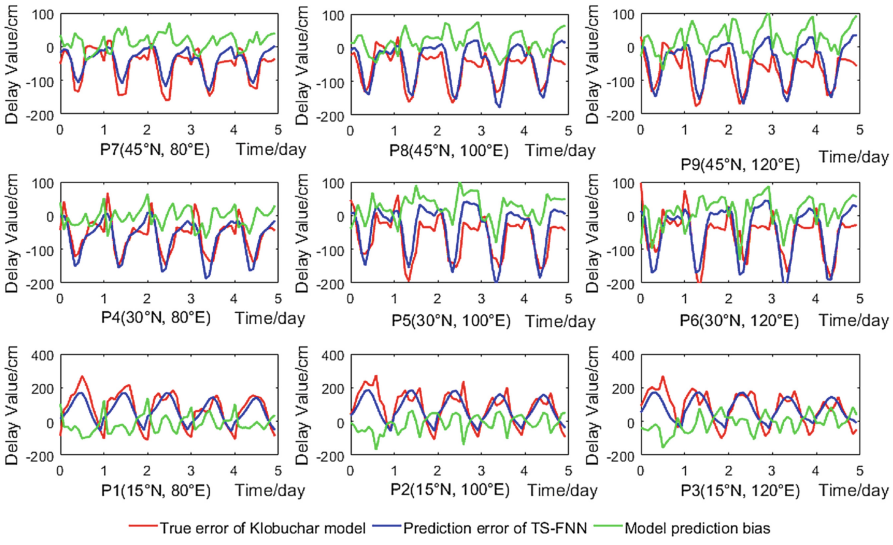

Fig. 5. Prediction bias of 9 test points

To further illustrate the prediction effect of the TS-FNN model, the mean values within 5 days of its prediction bias at different test points are calculated and compared with the mean values of the Klobuchar model error, as shown in Table 1. It can be seen that using Klobuchar model to calculate ionospheric delay can only correct the error to 60%–75% of the original, and there are still large errors. After using the TS-FNN model compensation, the ionospheric delay error can be corrected to 85%–92% of the original, so the average accuracy can be increased by about 20%.

Table 1. Improvement of prediction accuracy of TS-FNN model

Test points		P1	P2	P3	P4	P5	P6	P7	P8	P9
True delay/cm		274.5	275.4	276.4	254.6	257.3	256.9	218.5	222.6	221.0
Klobuchar model delay	Error/cm	109.5	106.4	105.2	65.4	65.6	65.5	57.4	61.26	68.8
	Accuracy	60%	61%	62%	74%	75%	75%	74%	72%	69%
TS-FNN model delay	Error/cm	40.5	35.9	41.8	28.1	30.5	31.2	22.9	18.7	20.5
	Accuracy	85%	87%	85%	89%	88%	88%	89%	92%	91%

In fact, the ionospheric delay is affected by many factors. In addition to positional and time factors, other factors such as geomagnetic changes, sunspot flares, and earth motion and so on, all have an impact on it. With the research of these physical phenomena, the related parameters can also be added to the input parameters of the training model to further improve the accuracy, which will be the next research direction.

5 Conclusion

In the practice of using the Klobuchar ionospheric delay model to calculate the delay error, it is found that the model bias exists a periodic feature, which can not be expressed and eliminated by a definite mathematical model at present. Aiming at this problem, by using fuzzy theory and neural network, a prediction model of Klobuchar ionospheric delay error based on TS fuzzy neural network is established.

The accuracy of the prediction model is verified by using the iGMAS final ionospheric product data as a reference. The results show that the TS-FNN model has good fitting ability and prediction effect on the Klobuchar ionospheric delay error. Using this model to compensate the result of Klobuchar ionospheric delay calculation, the accuracy can be improved by about 20%. It is of great significance for improving navigation system accuracy and reducing signal propagation error.

Acknowledgment. This article is grateful to the IGS data center of Wuhan University and the observation data provided by the international GNSS Monitoring & Assessment System (iGMAS).

References

1. Li M, Yuan Y, Wang N et al (2018) Statistical comparison of various interpolation algorithms for reconstructing regional grid ionospheric maps over China. J Atmos Solar Terr Phys 172:129–137
2. Wang N, Li Z, Li M et al (2018) GPS, BDS and Galileo ionospheric correction models: an evaluation in range delay and position domain. J Atmos Solar Terr Phys 170:83–91
3. Sivavaraprasad G, Ratnam DV (2017) Performance evaluation of ionospheric time delay forecasting models using GPS observations at a low-latitude station. Adv Space Res 60:475–490
4. Liu L, Chen J, Huang L et al (2018) A sophisticated Klobuchar model based on the Holt exponential smoothing model. Geomat Inf Sci Wuhan Univ 43(4):599–604
5. Wang F, Wu X, Zhou T et al (2014) Performance comparison between different Klobuchar model parameters. Acta Geodaet Cartogr Sin 43(11):1151–1157
6. Wu Y, Chen X, Wu C et al (2008) Review of the ionospheric delay correction methods. GNSS World China 2:1–5
7. Zhang Q, Zhao Q, Zhang H et al (2014) Evaluation on the precision of Klobuchar model for BeiDou navigation satellite system. Geomat Inf Sci Wuhan Univ 39(2):142–146
8. Luo W, Liu Z, Li M (2014) A preliminary evaluation of the performance of multiple ionospheric models in low- and mid-latitude regions of China in 2010–2011. GPS Solutions 18(2):297–308
9. Zhang H (2006) Study on GPS based China regional ionosphere monitoring and ionospheric delay correction. Shanghai Astronomical Observatory, Chinese Academy of Sciences
10. Cai C, Liu L, Li J et al (2015) Establishment of region ionospheric delay model in Nanning based on improved Klobuchar model. J Geodesy Geodyn 35(5):797–806
11. Bi T, An J, Yang J et al (2016) A modified Klobuchar model for single-frequency GNSS users over the polar region. Adv Space Res 59:833–842
12. Lin Q, Guo J, Yan J et al (2016) Precision and influential factors analysis of Klobuchar ionospheric model based on GIM on global scale. GNSS World China 41(5):93–98
13. Yang H (2016) Improvement of iGMAS observation quality and research of high-precision ionospheric monitoring. National time service center, Chinese Academy of Sciences
14. Zhang W, Wang L (2015) Analysis of characteristics of Ying River water quality change of time and space based on T-S Fuzzy neural network. Environ Sci Technol 38(12):254–261
15. Cervantes J, Yu W, Salazar S et al (2017) Takagi-Sugeno dynamic neuro-fuzzy controller of uncertain nonlinear systems. IEEE Trans Fuzzy Syst 25(6):1601–1615

Research on Fault Detection Algorithm Based on Cumulative Improvement of Parity Vector Sliding Window

Chuanyi Li, Rong Wang(✉), Jianye Liu, and Zhi Xiong

Navigation Research Centre, College of Automation Engineering,
Nanjing University of Aeronautics and Astronautics, Nanjing 211106, China
rongwang@nuaa.edu.cn

Abstract. Various forms of faults have a significant impact on the performance of navigation systems, especially satellite navigation system faults occur most frequently, so accurate fault detection of navigation systems is particularly important. At present, the commonly used satellite navigation system fault detection algorithms include parity vector method, least squares method and other detection methods. Such methods have good detection effects on large faults with large deviations in measurement information, but the system is slowly reduced. The detection effect of the fault is not obvious. However, the detection and correction of small gradual deviations is an important issue that navigation systems must address in high-precision applications.

Aiming at the fact that most fault detection methods are insensitive to slow fault detection, and have large delay, and cannot judge various fault categories, a fault detection algorithm based on parity vector sliding window accumulation improvement is proposed. The method comprehensively utilizes the observations of the current and previous epochs, firstly detecting the current epoch measurement information by using the traditional parity vector method to determine whether the system has a hard fault. On this basis, the sliding window is used to calculate the square of the parity of the first N epochs at the current time, construct a new detection statistic, and solve the detection state in real time by constructing a sliding window. The simulation results show that the proposed method can detect and isolate faults in time when the integrated navigation system has hard faults and slow faults, thus improving the fault tolerance of the system.

Keywords: Fault-tolerant navigation · Fault detection · Parity vector · Sliding window accumulation

1 Introduction

With the increasing application of GNSS to military and civilian applications, its positioning accuracy, continuity and reliability have become the focus of attention. Since a single beidou satellite navigation is susceptible to external interference, there are often cases of abnormal positioning or inability to locate. Therefore, combined with other navigation systems, the integrated navigation formed has extremely important

J. Sun et al. (Eds.): CSNC 2019, LNEE 563, pp. 275–285, 2019.
https://doi.org/10.1007/978-981-13-7759-4_25

theoretical significance and practical application value. However, in the case of multiple system combinations, the failure of the satellite navigation system will greatly affect the positioning accuracy of the entire navigation system, and even the situation that cannot be located. Therefore, it is very important to study the detection and elimination of multiple faults in satellite navigation systems.

In satellite navigation systems, RAIM has to perform two functions: fault detection and elimination. When the number of satellite observations is more than 5, the fault detection is performed using the calculated pseudo-range residual of each satellite. When the number of satellite observations is more than 6, the pseudo-satellite residual characteristics of each satellite are used to identify the faulty satellite number, and the faulty satellite is eliminated, and the positioning is re-positioned. The traditional fault detection algorithms include pseudo-distance comparison method, least squares residual method [1] and parity vector method [2]. These three algorithms have a good effect on detecting and eliminating large pseudo-range errors, but cannot detect small slow-changing faults. The occurrence of minor faults will cause large missed detection and detection delays in the detection algorithm. In [3], a new RAIM algorithm for multi-epoch accumulation detection is proposed. By directly accumulating the squared sum of the parity vectors at multiple moments, the fault detection value is constructed to detect and correct the small pseudo-range deviation. However, when the pseudo-range deviation occurring at a certain moment in the system is between a large deviation and a small deviation, the squared sum of the parity vectors is accumulated at a plurality of times to construct a fault detection value, and after the normalization processing, the pseudo-range deviation of the fault is equally divided, resulting in the reductions of detection efficiency and the failure of fault detection. Therefore, in view of the shortcomings of the traditional fault detection method and the new detection algorithm of multi-epoch parity vector accumulation, this paper proposes a fault detection method based on the parity vector sliding window accumulation improvement. The method sets the length of the sliding window, and performs the cumulative sum of squares of the parity vector in the sliding window from a single moment to a plurality of moments through loop iteration, normalizes the processing to construct a new statistical detection quantity, and detects the small slow fault and the sudden fault. And through the simulation analysis algorithm detection performance.

2 Fault Detection Scheme Based on Sliding Window Cumulative Improvement

Aiming at the shortcomings of traditional fault detection algorithm and multi-epoch parity vector accumulating RAIM algorithm, this paper proposes a fault detection method based on parity vector sliding window accumulation improvement. This method realizes loop nesting of single epoch detection to multi-epoch parity vector accumulation detection by sliding window. The overall scheme of the algorithm is shown in Fig. 1.

Firstly, according to the linearization measurement equation of the system, the algorithm solves the odd-even vector at each moment before the current time k and k, sets the length of the sliding window, and then performs a cumulative squaring sum of a single epoch to a plurality of epochs by a loop iteration on the parity vector in the sliding window, normalizes the processing to construct a new statistical detection amount. Finally, the fault detection threshold is set and compared with the new statistical detection amount to judge the fault condition and identify and eliminate the faulty satellite.

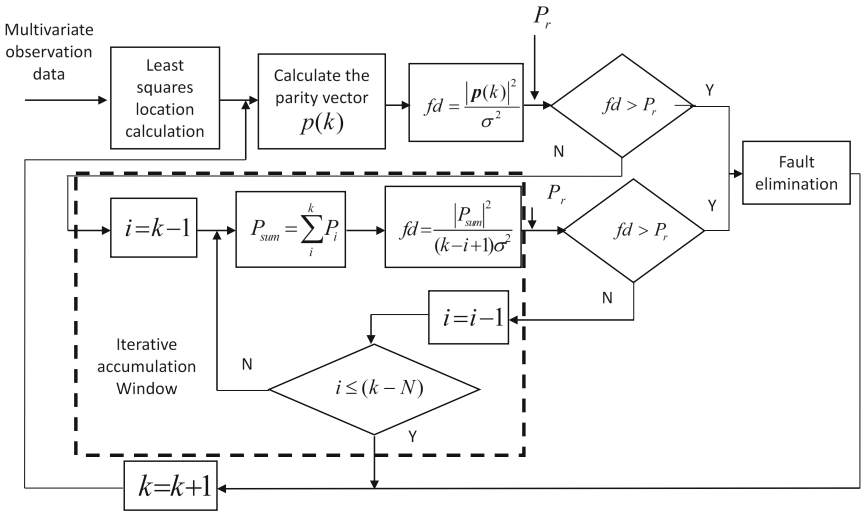

Fig. 1. Scheme of improved parity vector sliding-window accumulation algorithm

3 System Measurement Equation Construction

According to the working characteristics of multi-navigation sensors and the currently available measurement information, the linearization measurement equation of the system is established.

$$\boldsymbol{y}(k) = \boldsymbol{G}(k)\boldsymbol{x}(k) + \boldsymbol{\varepsilon}(k) \tag{1}$$

where $\boldsymbol{y}(k) = [y_{o1}, y_{o2}, \cdots\cdots, y_{on}]^T$ is the system observation measured by the available measurement information at the current time, $\boldsymbol{G}(k)$ is the observation coefficient matrix, $\boldsymbol{x}(k) = [\Delta x, \Delta y, \Delta z, \Delta e_1, \Delta e_2, \cdots, \Delta e_m]^T$ is the system state quantity, $\Delta x, \Delta y, \Delta z$ is the carrier three-dimensional position error state quantity respectively, and $\Delta e_1, \Delta e_2, \cdots, \Delta e_m$ is the amount of error state of each sensor subsystem modeled, $\boldsymbol{\varepsilon}(k)$ is measurement noise, variance is σ^2.

4 Research on Cumulative Improvement Algorithm for Parity Vector Sliding Window

4.1 Traditional Parity Vector Algorithm

After the least squares positioning solution is solved, the traditional parity vector algorithm performs QR factorization [4] on the observation coefficient matrix $\boldsymbol{G}(k)$, and obtains the orthogonal matrix $\boldsymbol{M}$ and the upper triangular matrix $\boldsymbol{R}$:

$$\boldsymbol{G}(k) = \boldsymbol{M}\boldsymbol{R} \tag{2}$$

Transpose the $\boldsymbol{M}$ matrix and take the next $n - m - 3$ rows to form the parity transformation matrix $\boldsymbol{Q}$:

$$\boldsymbol{M}^T = \begin{bmatrix} \boldsymbol{S} \\ \boldsymbol{Q} \end{bmatrix} \tag{3}$$

Where $\boldsymbol{S}$ is a $(m+3) * n$ dimensional matrix and $\boldsymbol{Q}$ is a $(n - m - 3) * n$ dimensional matrix; $\boldsymbol{Q}$ changes the n dimensional observation vector into a $n - m - 3$ dimensional parity vector $\boldsymbol{p}(k)$:

$$\boldsymbol{p}(k) = \boldsymbol{Q}\boldsymbol{y}(k) = \begin{cases} \boldsymbol{Q}\boldsymbol{\varepsilon} & H_0 \\ \boldsymbol{Q}_{:,s} f_s + \boldsymbol{Q}\boldsymbol{\varepsilon} & H_1 \end{cases} \tag{4}$$

Where $\boldsymbol{Q}_{:,s}$ is the column vector of the s column of the matrix $\boldsymbol{Q}$, f_s is the fault information in the s observation, $0 < s \leq n$, H_0 is the case of no fault, and H_1 is the faulty condition. The traditional parity vector method constructs the detection statistic by constructing the parity vector $|\boldsymbol{p}(k)|^2$ at each moment.

$$fd = \frac{|\boldsymbol{p}(k)|^2}{\sigma^2} \tag{5}$$

Equation (5) is the detection statistic normalized according to the measurement noise, where in fd obeys the degree of freedom $n - m - 3$ center and the non-center x^2 distribution, and compares the fault detection statistic with the detection threshold to determine whether there is a fault currently. When a fault is detected, the traditional parity vector algorithm will identify the faulty subsystem according to the parity vector, and then eliminate the fault subsystem to avoid information pollution.

The detection threshold P_r of fd is determined by the false alarm probability P_{fa}

$$P_r = (fd < a) = \int_0^a f_{x^2(on-m-3)}(x)dx = 1 - P_{fa} \tag{6}$$

where fd is the fault detection statistic, a is the set probability, P_r is the fault detection threshold, x is the system state quantity, on is the available observation dimension of the system, and P_{fa} is the false alarm probability.

From Eqs. (4) and (6), the decentralized parameter λ can be derived as:

$$\lambda = \frac{f_s^2 \left| Q_{:,\,s} \right|^2}{\sigma^2} \tag{7}$$

Generally, the probability of fault detection is related to the decentralized parameter. When the false alarm probability P_{fa} is fixed, the probability of fault detection is only related to the decentralized parameter, and is positively correlated [5]; the larger the pseudo-range deviation, the decentralized parameter The larger the fault, the easier it is to detect; the smaller the pseudo-range deviation and the slowly changing pseudo-range deviation, the non-centralized parameters are generally consistent with the non-fault, making the fault difficult to detect.

4.2 Multi-epoch Parity Vector Accumulation Algorithm

Based on the traditional parity vector algorithm, the multi-epoch parity vector accumulation algorithm accumulates consecutive N epoch parity vectors, increases the normalized pseudo-range deviation and decentralized parameters, and improves the detection probability of the small slow-changing pseudo-range deviation. The detection statistic P_{sum} obtained by accumulating N epoch parity vectors is:

$$P_{sum} = \sum_{i=1}^{N} P_i \tag{8}$$

Where P_i is the parity vector when observing epoch i, N is the cumulative epoch number, and it is assumed that the visible satellite constellation of the receiver does not change during the N epochs. If the satellite constellation changes, the end of the parity vector time accumulation is given, the result of this test is given, and the next fault detection is started.

After the detection statistic P_{sum} is normalized according to the measured noise variance, the fault judgment detection amount fd is obtained:

$$fd = \frac{|P_{sum}|^2}{N\sigma^2} \tag{9}$$

fd also obeys the $n - m - 3$ center and non-central x^2 distributions of degrees of freedom. Regardless of the size of the window, if there is no fault, the new detection statistic obeys the central symmetric x^2 distribution, so the detection threshold under the constant false alarm rate remains unchanged. That is, the false alarm detection threshold is also the formula (6); the fault determination detection amount fd is compared with the detection threshold to determine whether the current fault has occurred.

The multi-epoch parity vector accumulation algorithm essentially increases the noise variance by accumulating the parity vectors of N epochs, and the equivalent pseudo-range deviation also increases, the normalized pseudo-range deviation increases, and the accumulated detection amount. The decentralized parameters are also increased, so this method can detect small gradual failures. However, when the pseudo-range deviation occurring in the system is between the large pseudo-range deviation and the small pseudo-range deviation, the multi-epoch parity vector accumulation will equally divide the pseudo-range deviation, which may cause the fault-missed, thus affecting the positioning accuracy of the system.

4.3 Parity Vector Sliding Window Accumulation Improvement Algorithm

The parity vector sliding window accumulation improvement algorithm combines the advantages of the traditional parity vector method and the multi-epoch parity vector accumulation algorithm. This method performs the loop nesting of the single epoch detection to the multi-epoch parity vector accumulation detection through the sliding window, which not only solves the problem that the traditional parity vector method cannot detect the small gradual change fault but also makes up for the defect that the multi-epoch parity vector accumulation algorithm cannot detect the fault between large faults and small faults.

Firstly, the algorithm uses the traditional parity vector method to calculate the parity vector $\boldsymbol{p}(k)$, constructs the test statistic fd, solves the detection threshold P_r by the formula (6), compares the test statistic fd and the detection threshold P_r, if $fd > P_r$, identifies and eliminates the fault, Conversely, cumulative multi-epoch parity vector construction test statistic P_{sum}

$$P_{sum} = \sum_{i}^{k} P_i \quad (k - N + 1 \le i \le k - 1) \tag{10}$$

Where P_i is the parity vector when observing epoch i;

After the detection statistic P_{sum} is normalized according to the measured noise variance, the fault judgment detection amount fd is obtained:

$$fd = \frac{|P_{sum}|^2}{(k - i + 1)\sigma^2} \tag{11}$$

when $i = k - 1$, the accumulation of two epoch parity vectors is performed, a new test statistic fd is constructed, the test statistic fd and the detection threshold P_r are compared, and if $fd > P_r$, the fault is identified and eliminated, and perform fault detection at the next moment; otherwise, $i = i + 1$, the accumulation of 3 epoch parity vectors, if the fault has not been detected, continue to accumulate the epochs until the parity vectors of N epochs are accumulated.

The essence of the parity-sliding window accumulation improvement algorithm is that it performs cyclic detection of single epoch parity vector and multi-epoch parity

vector accumulation at each moment, which takes into account the advantages of the parity vector algorithm and the multi-epoch parity vector accumulation algorithm, and makes up for the shortcomings of the two algorithms.

5 Simulation Results and Analysis

A fault detection method based on the cumulative improvement of the parity vector sliding window is verified by simulation. The simulated GPS satellite navigation system simulates the constellation of the satellite by setting the satellite navigation parameters. The lowest elevation angle of the visible star is 15°, the sampling frequency is 1 Hz, the standard deviation of the pseudo-range observation noise is 4 m, and the sliding serial port cumulative epoch is 10, and the carrier flight path is dynamic. The track has a simulated flight time of 3000 s, including maneuvers such as accelerated climb, cruise flight, and motorized turn.

The visible satellite received during the simulation flight is shown in Fig. 2. In order to test the effectiveness of the algorithm, different satellites are injected with different faults at different times during the flight process of the carrier. The injection faults are shown in Table 1 below. The error rate is 1/1000000 [6], which is verified by the parity vector method, the multi-epoch parity vector accumulation algorithm and the parity vector sliding window accumulation improvement algorithm.

According to the set simulation conditions and fault injection information, the traditional parity vector method, the multi-epoch parity vector accumulation algorithm and the parity vector sliding window accumulation improvement algorithm are respectively tested. The fault detection cures are shown in Fig. 3.

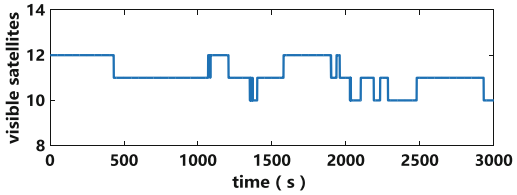

Fig. 2. Number of visible satellites observed during simulated flight

Table 1. Injection of fault information

Fault type	Satellite number	Fault injection time (s)	Fault size (m)
Hard fault	18	1000–1100	15
Soft fault 1	3	1300–1400	5 + 0.5 * t
Soft fault 2	16	2000–2100	2.5 + 0.75 * t

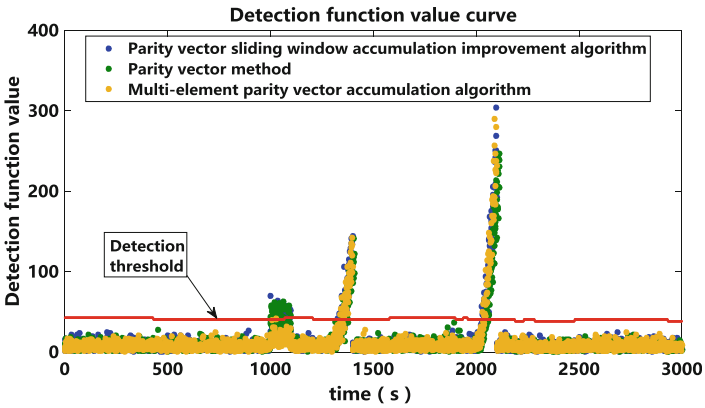

Fig. 3. Improved before and after detection function value curve in the whole simulation process

In Fig. 3 the red dot represents the parity vector algorithm fault detection function value, the green dot represents the multi-epoch parity vector accumulation algorithm fault detection function value, and the yellow dot represents the parity vector sliding window accumulation improvement algorithm fault detection function value. In Fig. 3, the change in the detection threshold is due to the change in the number of visible stars received during the entire flight of the simulated flight. It can be seen from Fig. 3 that in the hard fault period, the detection effect of the multi-epoch parity vector accumulation algorithm is quite different from the parity vector algorithm and the parity vector sliding window accumulation improvement algorithm, so the detection function value curve of the 1000 s–1100 s time period is selected for comparative analysis, the curve is shown in Fig. 4.

In Fig. 4, the detection function value curve of the multi-epoch parity vector accumulation algorithm does not exceed the detection threshold within 1000 s–1100 s and the fault cannot be detected, and the parity vector sliding window accumulation improvement algorithm and the traditional parity vector method detection function value curve. The detection threshold was exceeded within 1000 s–1100 s and a fault was detected. The reason why the multi-epoch parity vector accumulation algorithm does not detect the fault is that when a large pseudo-range deviation occurs at a time of the satellite, the accumulation of the plurality of epoch parity vectors is performed and normalized, and the pseudo-range deviation is equally divided to each. The epochs reduce the value of the detection function and do not exceed the detection threshold, so that the failure cannot be detected. The parity vector sliding window accumulation improvement algorithm and the parity vector algorithm can detect the pseudo-range deviation of the satellite and timely eliminate it to ensure the reliability of the system.

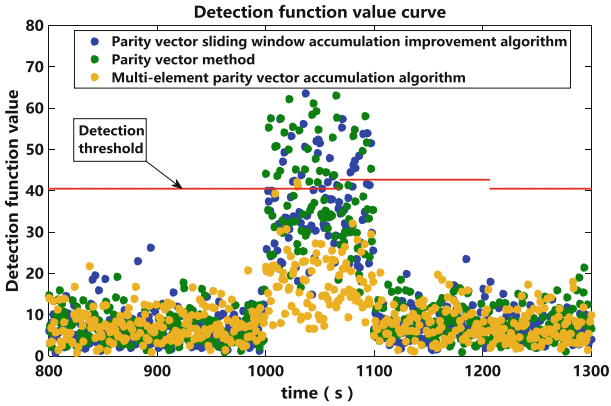

Fig. 4. 1000 s–1100 s detection function value graph

In Fig. 3, we know that in the period of soft failure, the time when the parity vector method detects the fault is quite different from the multi-epoch parity vector accumulation algorithm and the parity vector sliding window accumulation improvement algorithm, so 1300 s–1400 s and 2000 s–2100 s will be used. The time-out detection function value curve is cut out and analyzed separately. The curve is shown in Fig. 5.

In Fig. 5(a), we know that for soft fault 1, the multi-epoch parity vector accumulation algorithm detects a soft fault in 1337 s, the parity vector sliding window accumulation improvement algorithm detects a soft fault in 1333 s, and the parity vector method is delayed to 1347 s. Only when a soft fault is detected, as shown in Fig. 5(b), for soft fault 2, the multi-epoch parity vector accumulation algorithm detects a soft fault in 2035 s, and the parity vector sliding window accumulation improvement algorithm detects a soft fault at 2029 s. However, the traditional parity vector method delays to 2045 s to detect a soft fault. Therefore, the parity vector sliding window accumulation improvement algorithm and the multi-epoch parity vector accumulation algorithm detect the failure about 15 s earlier than the parity vector algorithm That is, the parity vector sliding window accumulation improvement algorithm and the multi-epoch parity vector accumulation algorithm are more sensitive to the soft fault of the slow change, and can detect and eliminate the fault earlier, thereby ensuring the integrity of the system.

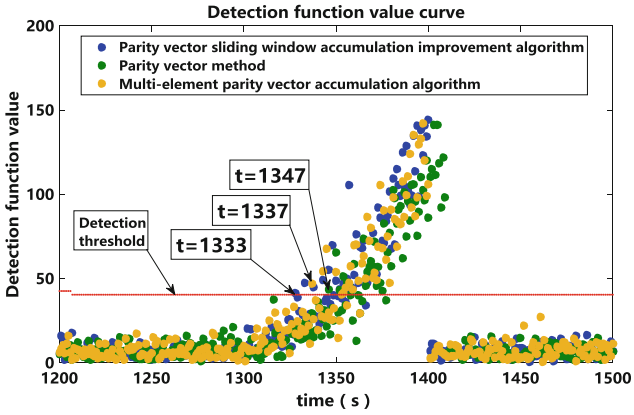

(a) 1300s-1400s detection function value graph

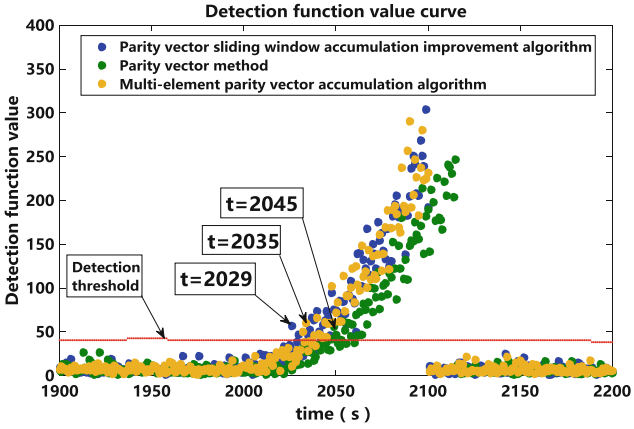

(b) 2000s-2100s detection function value graph

Fig. 5. 1300 s–2100 s detection function value graph

6 Conclusion

In this paper, a fault detection algorithm based on parity vector sliding window accumulation improvement is proposed. As the traditional parity vector method is not ideal for slow-changing slope fault detection and the multi-epoch parity vector accumulation algorithm cannot detect the small faults, this algorithm performs a cumulative iteration of a single epoch to multiple epochs on a parity vector in a sliding window by loop iteration. After normalization, a new statistical detection quantity is constructed to realize the identification of the faulty satellite. The simulation results show that the parity vector sliding window accumulation improvement algorithm and the multi-epoch parity vector accumulation algorithm have better detection effect when the satellite has a slowly changing slope fault, and the fault can be detected earlier. When the satellite has a small fault, the parity vector sliding window accumulation

improvement algorithm and the traditional parity vector method have better detection effect, and timely identify and eliminate the faulty satellite, thus ensuring the navigation and positioning accuracy of the satellite system.

Acknowledge. This work was partially supported by the National Natural Science Foundation of China (Grant No. 61703208, 61673208, 61873125, 61533008, 61533009), Foundation Research Project of Jiangsu Province (The Natural Science Foundation of Jiangsu Province, Grant No. BK20170815, BK20170767, BK20181291), the Aeronautic Science Foundation of China (Grant No. 20165552043, 20165852052), the Science and Technology Innovation Project for the Selected Returned Overseas Chinese Scholars in Nanjing, the Fundamental Research Funds for the Central Universities (Grant No. NS2017016, NP2018108, NZ2018002, NJ20170005, NP2017209, NZ2016104), the "333 project" in Jiangsu Province (Grant No. BRA2016405), the Scientific Research Foundation for the Selected Returned Overseas Chinese Scholars (Grant No. 2016), the peak of six personnel in Jiangsu Province (Grant No. 2013-JY-013), Foundation of Jiangsu Key Laboratory "Internet of Things and Control Technologies" & the Priority Academic Program Development of Jiangsu Higher Education Institutions.

References

1. Li C, Zhu L, Yang Q, Yang Y (2016) Research on receiver by least squares residuals. Glob Position Syst 41(1):69–72
2. Wang W, Zhang P, Xu C (2016) The research on parity vector RAIM algorithm based on BDS/GPS multi-constellation. In: China satellite navigation academic conference
3. Hu Y, Lu J, Cao K, Li B RAIM algorithm based on correlation distance with several epoch. J Detect Control 42–45
4. Chen T, Si R, Shi Y (2013) Research on autonomous integrity monitoring algorithms of GNSS receiver. Electron Design Eng 21(2):97–99
5. Liu W, Li Z, Wang F (2010) A new RAIM method for detecting and correcting weak pseudo-range bias under gradual change. Aerosp J 31(4):1024–1029
6. Sha H, Huang X, Liu W, Xu B, Ou G (2014) Research on the RAIM method based on non-coherent accumulation for tiny pseudo-range bias. Aerosp J 35(6):708–712

Research on Regional Instantaneous Availability Evaluation Method of Satellite Navigation System

Xi Gao(✉), Chao Sun, Hongbo Zhao, Wenquan Feng, and Zebin Sun

School of Electronics and Information Engineering,
Beihang University, Beijing, China
buaa_gaoxi@163.com

Abstract. With the development of global navigation satellite system (GNSS), research on evaluation theory of GNSS availability has drawn increasing attention. The current studies about GNSS availability mainly focus on long-term fault monitoring and global navigation constellation, however, the availability evaluation theory with respect to regional instantaneous situations is still unestablished. This article extends the global availability of GNSS to the availability in a regional area. The GNSS availability model under the influence of navigation signal fault is reviewed. Based on that, the number of visible satellites and PDOP (Position Dilution of Precision) values in the service area are considered and analysed. The method of regional instantaneous availability evaluation is then proposed. The regional availability is simulated and verified, which shows the feasibility of the proposed evaluation method.

Keywords: Global satellite navigation system (GNSS) · Regional instantaneous · Availability evaluation · Visible satellites

1 Introduction

Global navigation satellite system (GNSS) is an important space infrastructure that provides high-precision positioning, speed measurement and timing services. The availability of GNSS is one of the four basic performance indicators developed by the International Civil Aviation Organization (ICAO) [1], which refers to the percentage of time that the navigation system can provide users with available services within its service area. It reflects the navigation service capability that a navigation system can provide [2].

Research on the availability analysis method is of great importance to improve the performance of GNSS, thus many studies focused on this area. Li [3] studied the performance monitoring and evaluation methods of navigation systems, and presented the parallel progressive model structure of the four major performance indicators of GNSS. Hu [4] proposed the performance evaluation theory of Beidou navigation system, pointing out that the SIS single-satellite availability is related to the daily maintenance strategy and the processing time of various faults. And the constellation availability is mainly affected by the availability of single satellite and related backup

J. Sun et al. (Eds.): CSNC 2019, LNEE 563, pp. 286–297, 2019.
https://doi.org/10.1007/978-981-13-7759-4_26

replacement strategies. With the development of technology and the continuous enhancement of the application of navigation systems, the research on availability is becoming more and more complete. However, the existing availability studies are aimed at global availability, focusing on long-term fault monitoring and the entire navigation constellation. The research on the availability evaluation method in regional instantaneous situations is relatively limited.

In terms of the availability of satellite navigation under regional instantaneous conditions, it can be seen that the number and geometry of the navigation satellite change with time, and the Position Dilution of Precision (PDOP) of the navigation constellation also changes with the position of the user receiver. For applications requiring high GNSS availability, it is important to evaluate the instantaneous availability in the regional area. Li [5] established a mathematical model for the availability of navigation constellations under the interruption of navigation satellite services, and provided an effective method for evaluating the performance of regional navigation constellations. Cai [6] combined PDOP availability with single-satellite availability to model service availability and analyse constellation weaknesses.

In this paper, the global navigation signal availability is extended to the regional area. The Markov model is used to characterize the navigation signal availability under the influence of power anomalies, correlation peak distortion and other failure modes. The overall risk of navigation signal fault detection is analysed. On this basis, the number of visible satellites and PDOP values in the service area are studied. The regional instantaneous service availability model is established, and the availability of the regional navigation system is simulated and analysed. An effective method of evaluating the availability of a regional navigation system is provided.

2 Global Navigation Availability

According to [3], GNSS availability can be classified into two categories: global navigation availability and regional instantaneous availability. The global navigation availability is evaluated in terms of individual satellites, which is then employed to evaluate the availability of constellations. The analysis of the regional instantaneous availability considers the current visible satellites in the regional area. The relationship of the mentioned concepts is illustrated in the Fig. 1.

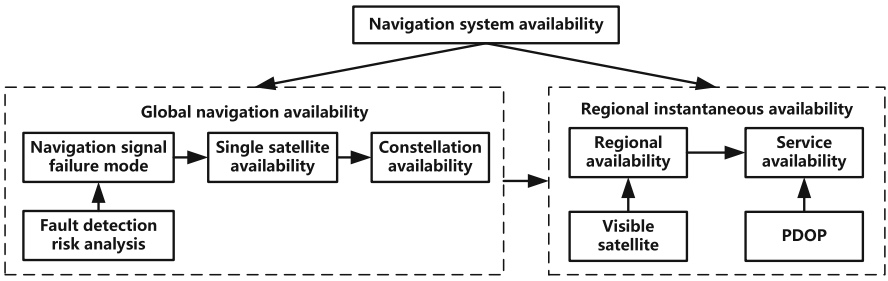

Fig. 1. Navigation system availability research diagram

2.1 Navigation Signal Fault Detection Risk Analysis

The study of global availability is the basis of regional instantaneous service availability research. Due to the long-term orbital operation of the satellite and the hostile external electromagnetic environment, the navigation load is vulnerable to various failures, which will result in the service interruption and affect the availability of the navigation system [7]. The navigation signal failure modes considered in this paper mainly include code and carrier consistency, power anomalies, carrier leakage [8], correlation peak distortion [9, 10], etc.

Real-time monitoring of navigation signal faults may result in false detections, so the risk of false detection needs to be analyzed. The navigation signal fault detection method mainly adopts signal coherent integration detection method, multi-correlator detection method [10], pseudo code phase and carrier phase difference detection method [11]. To determine whether the navigation system has failed, it is necessary to make a decision based on the random observation information of the system. This article assumes that there is a fault that the system is unavailable, then there are two assumptions of available and unavailable, which is a binary hypothesis test problem. H_0 represents the fault-free case, which means the system is available. H_1 means a fault is present and the system is unavailable. Only considering the case of a single failure, Fig. 2 shows the relationship of the four possibilities [12], where P_F and P_M represent the false alarm probability and missed alarm probability, respectively.

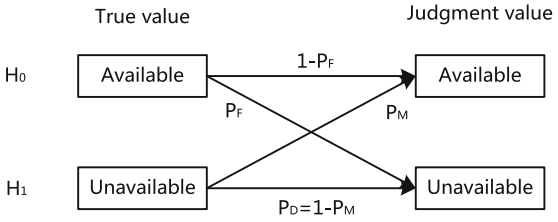

Fig. 2. Navigation fault detection risk

For the navigation system, the false alarm rate and the missed alarm rate are both false detection probabilities, then the overall risk probability is given by

$$P_{risk} = P_M + P_F \tag{1}$$

The fault detection of the fault will affect the judgment of the navigation signal availability, so the judgment criterion in the availability evaluation should be able to produce the larger correct detection probability and the smaller error detection probability. In practical applications, the false alarm rate is generally much smaller than the missed alarm rate, so only needs to meet the missed alarm rate is small enough to judge the availability.

This section discusses the false alarm rates and missed alarm rates for the different navigation signal failure modes and total system failures. Assume that the faults are independent, only one fault occurs at a time, and different fault modes are set as F^i,

$i = 1, 2, \ldots, N$. In the case of the missed alarm rate, the missed alarm rate of various faults is P_m^i, and the total missed alarm rate of the system is P_M. We made $P_m^1 = P_m^2 = \ldots = P_m^N = P_m$, then $n = 2$,

$$P_M = 1 - \left(1 - P_m^1\right)\left(1 - P_m^2\right) = 1 - (1 - P_m)^2 \tag{2}$$

In the navigation signal availability analysis, the false alarm rate and the missed alarm rate of signal fault detection must meet certain conditions. It is generally considered that the false alarm rate and the missed alarm rate are very small. Most of the time fault detection is correct detection or no false detection, which can be satisfied the performance requirements of the availability of satellite navigation systems. Therefore, simplifying the above formula,

$$P_M = 1 - (1 - P_m)^2 \approx 2P_m \tag{3}$$

Similarly, it can be inferred that the missed alarm rate of fault detection when $n = N$

$$P_M = 1 - \prod_{i=1}^{N}\left(1 - P_m^i\right) = 1 - (1 - P_m)^N \tag{4}$$

Simplified by the binomial theorem, Eq. (4) can be rewritten as

$$P_M = \sum_{i=1}^{N} P_m^i = NP_m \tag{5}$$

2.2 Single Satellite Availability

Single-satellite availability is the percentage of time that a satellite occupying a orbital position emits a healthy, trackable spatial signal [13]. Here, we discuss single-satellite availability under the influence of code and carrier inconsistency, power anomalies, carrier leakage, and correlation peak distortion.

Assume that the satellite failure rate follows an exponential distribution, the average failure interval time (MTBF) is the average time between failures, and the average fault duration (MTTR) is the average time required to repair the failure. 0 means the system status is normal, 1 means the system status is faulty. λ is the failure rate of the satellite, which is the reciprocal of the average failure interval; μ is the satellite repair rate, which is the reciprocal of the average fault duration; Δt is the state transition time interval. According to the reliability theory, the steady-state availability A of a single satellite is:

$$A = \frac{\mu}{\lambda + \mu} = \frac{MTBF}{MTBF + MTTR} \tag{6}$$

It is assumed that there are F different navigation signal failure modes with failure rates $\lambda_1, \lambda_2 \cdots \lambda_F$ respectively, and the corresponding repair rates are $\mu_1, \mu_2 \cdots \mu_F$, respectively. Also assume that at most one fault occurs at a moment and the mutual transformation between faults is not considered. The state transition relationship is as shown in Fig. 3. The equivalent fault interval and equivalent fault duration after fault synthesis can be obtained according to the reliability principle:

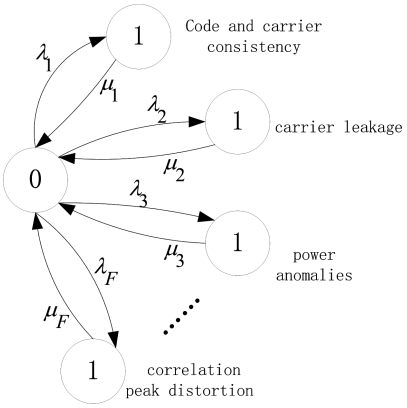

Fig. 3. Transition relationship of navigation signal failure mode

$$MTBF' = 1 \Big/ \left(\sum_{i=1}^{F} \frac{1}{MTBF_i} \right) \tag{7}$$

$$MTTR' = MTBF' \cdot \left(\sum_{i=1}^{F} \frac{MTTR_i}{MTBF_i} \right) \tag{8}$$

2.3 Constellation Availability

This section analyses the constellation availability using the Markov constellation availability model [14], which considers the constellation backup strategy. The navigation constellation system has a total of α orbital satellites and β non-orbital satellites, and we assume that one satellite can be repaired at a time. According to the number of constellation satellites which failed, the constellation system has different fault states, and its state space is $E = \{0, 1, 2, \ldots, \alpha + \beta\}$. The corresponding Markov state transition is shown in the Fig. 4.

Let $P_i(t)$ $i = (0, 1, \ldots, \alpha + \beta)$ denote the probability that the constellation state space is i at time t. At the beginning $t = t_0$, when $t = t_0 + \Delta t$, the probability of each state in the state space can be derived:

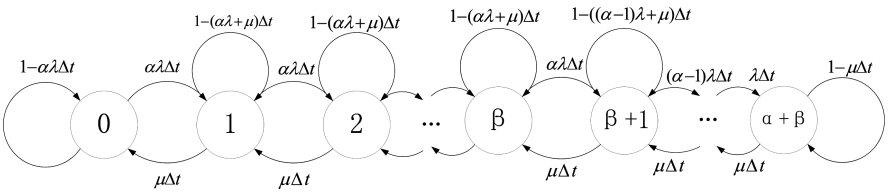

Fig. 4. Markov fault state transition of satellite constellation

$$\vec{P}(t_0 + k\Delta t) = \vec{P}(t_0 + (k-1)\Delta t) \bullet \vec{P}(\Delta t) \tag{9}$$

$$\vec{P}(t_0 + k\Delta t) = [\, P_0(t_0 + k\Delta t) \quad P_1(t_0 + k\Delta t) \quad \ldots \quad P_{\alpha+\beta}(t_0 + k\Delta t) \,] \tag{10}$$

$$\vec{P}(t_0 + (k-1)\Delta t) = [\, P_0(t_0 + (k-1)\Delta t) \quad P_1(t_0 + (k-1)\Delta t) \quad \ldots \quad P_{\alpha+\beta}(t_0 + (k-1)\Delta t) \,] \tag{11}$$

$$\vec{P}(\Delta t) = \begin{bmatrix} 1-\alpha\lambda\Delta t & \alpha\lambda\Delta t & 0 & \ldots & 0 & 0 & \ldots & 0 \\ \mu\Delta t & 1-(\alpha\lambda+\mu)\Delta t & \alpha\lambda\Delta t & \ldots & 0 & 0 & \ldots & 0 \\ \vdots & \mu\Delta t & 1-(\alpha\lambda+\mu)\Delta t & \ldots & 0 & 0 & \ldots & 0 \\ \vdots & \vdots & \vdots & \ddots & \vdots & \vdots & \ldots & \vdots \\ 0 & 0 & 0 & \ldots & 1-(\alpha\lambda+\mu)\Delta t & \alpha\lambda\Delta t & \ldots & 0 \\ 0 & 0 & 0 & \ldots & \mu\Delta t & 1-(\alpha\lambda+\mu)\Delta t & \ldots & 0 \\ \vdots & \vdots & \vdots & \vdots & \vdots & \vdots & \ldots & \vdots \\ 0 & 0 & 0 & \ldots & 0 & 0 & \ldots & 0 \\ 0 & 0 & 0 & \ldots & 0 & 0 & \ldots & 0 \\ \vdots & \vdots & \vdots & \vdots & \vdots & \vdots & \ddots & \vdots \\ 0 & 0 & 0 & \ldots & 0 & 0 & \ldots & 1-\mu\Delta t \end{bmatrix} \tag{12}$$

Assuming that the constellation system has no satellite failure at the beginning, the initial condition is: $t_0 = 0$, $P_0(t_0) = 1$. According to the completeness principle, we can obtain $P_i(t_0) = 0$, $i = (1, 2, \ldots, \alpha + \beta)$. Thus, the availability probability of constellation system at different states after time $T = k\Delta t$ can be calculated.

3 Regional Instantaneous Availability

The previous section discussed the global availability of the navigation system, which reflects more about the macroscopic and long-term availability of the entire constellation system. However, the real-time availability of a regional area cannot accurately obtained. For user receiver with various positions at different moments, the number and geometry of the visible satellites are different, thus the performance of GNSS availability is changing. The service availability of the navigation system is generally reflected in two aspects: one is the number of visible satellites in the service area, and the other is the PDOP availability of the navigation constellation [5].

3.1 Regional Availability

This section examines the availability of regional instantaneous conditions. It's essential to introduce the concept of visible satellites. In the navigation system, the visible satellite is the satellite whose broadcast signal can be reliably received by the ground point under the condition that the minimum elevation angle is satisfied. [15]. Generally speaking, the more the visible satellites are in the service area with a coverage angle greater than 5° and the better the satellites are distributed, the higher the constellation availability is.

In the global navigation availability, it is assumed that the constellation system has a total of N satellites, and the number of available satellites is calculated based on the Markov model as x. Then, in a regional area, if the number of visible satellites at a certain moment is M, the proportional relationship can be used to compute the number of available and visible navigation satellites y, which is given by

$$y = \frac{M}{N} \cdot x \tag{13}$$

$$P(x|N,T) = P(y|M,t) \tag{14}$$

where $P(x|N,T)$ denotes the probability that, in the constellation system of N navigation satellites, the number of available satellites is x after time T. $P(y|M,t)$ denotes the probability that, in the regional area where the number of visible satellites is M, the number of available satellites is y at a certain instant t.

This section provides an effective way to evaluate the availability of regional navigation systems. Based on the long-term fault detection situation and the number and distribution of instantaneous visible satellites, the number of regional instantaneous available satellites can be obtained by the Markov model and the proportional relationship. This method avoids the monitoring of the status of each satellite by multiple large antenna receivers, which can save a lot of resources and costs.

3.2 Service Availability

Based on the study of visible satellites, this section studies the availability of PDOP to derive the instantaneous availability of service areas. The PDOP availability of the regional navigation constellation can be defined that, during the constellation operation period the satellite obscuration angle >5°, the percentage of time that the PDOP is less than or equal to the specified threshold in a particular service area [13]. Assume that the impact of any failure mode on availability is independent. the service availability can be obtained by:

$$A(t) = \sum_{y=4}^{M} \sum_{k=1}^{C_M^y} \left(\prod_{j=1}^{y} p_{k_j} \right) \left(\prod_{i=y+1}^{M} (1 - p_{k_i}) \right) \varphi_{M,k} \tag{15}$$

Assuming that the available probability of each constellation satellite is equal and let the probability be p, then the above equation can be simplified as

$$A(t) = \sum_{y=4}^{M} \sum_{k=1}^{C_M^y} p^y (1-p)^{M-y} \varphi_{M,k} \tag{16}$$

where y represents the number of satellites visible and available in the service area, and $y = 4, 5, \ldots, M$ to meet the positioning requirements. The y available satellites selected from the satellites are visible in the current area, and the remaining $M - y$ satellites are interrupted. There are C_M^y types in this combination, and $\varphi_{M,k}$ is the PDOP availability of the regional navigation constellation in the service area under the *k-th* combination. The calculation formula is

$$\varphi_{M,k} = \frac{\sum_{t=t_0}^{t_0+T} \sum_{p,q} bool\left(PDOP_{t,p,q} < \eta\right)}{T \times p \times q} \times 100\% \tag{17}$$

where *bool(x)* is a Boolean function. The total number of $1^\circ \times 1^\circ$ grid points in the service area is $p \times q$, and $PDOP_{t,p,q}$ is the PDOP value of the grid point (p, q) at time t. t_0 is the initial time of sampling, and η is the PDOP threshold.

4 Simulation Results

In this paper, the navigation system availability is simulated. Taking the GPS as an example, it is assumed that the navigation constellation has 24 satellites in orbit and 3 backup satellites. The simulation time is 200 days. According to the classification of faults [13], different fault modes are classified into short-term faults and long-term faults. The fault interval time and fault duration of the *F*-type navigation signal fault modes are equal. Using data in different fault modes [3], the equivalent fault parameters can be obtained as MTBF = 492 days and MTTR = 7.25 days, then the state probability of the navigation constellation is calculated (Table 1).

Table 1. State probability of GPS navigation constellation

P0	P1	P2	P3	P4
0.955409	0.043541	0.001033	1.65E−05	1.97E−07

In order to further study the influence of different fault parameters on the constellation state probability, firstly set the MTBF as a constant and change the parameter MTTR, to study the function relationship between the constellation state probability and MTTR. The availability of different navigation constellations is discussed. According to the total number of navigation constellation satellites, 24 GPS satellites, 30 Galileo satellites, and 35 Beidou satellites, the influence of the total number of constellation satellites on the state probability of the constellation is studied. The results are shown in the Fig. 5.

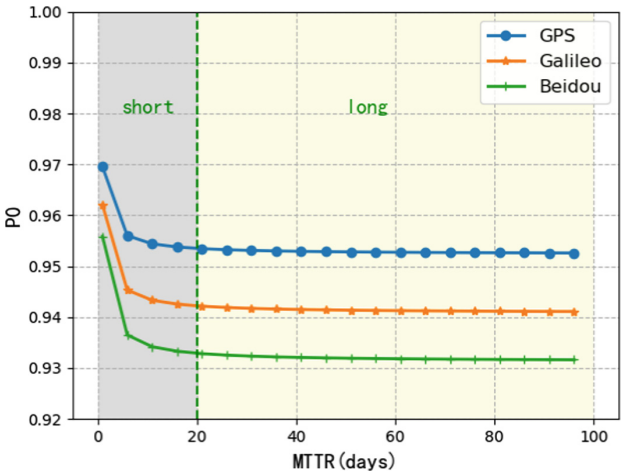

Fig. 5. The relationship between MTTR and constellation state probability of different navigation constellations

Analysis of the results shows that in the case of a certain MTBF, the availability probability of the constellation in the same state decreases as the MTTR increases. Assuming that the fault interval time is constant, the fault mode is divided into short-term faults and long-term faults with a fault duration of 20 days. It can be seen that the availability of short-term faults is significantly higher than that of long-term faults. For the availability of different navigation constellations, as the total number of satellites in the navigation constellation increases, the probability of the constellation state decreases, in other words, the probability of no satellite failure decreases. Therefore the P_0 of Beidou navigation constellation is the smallest and the P_0 of GPS navigation constellation is the largest.

Then set the MTTR as a constant and change the parameter MTBF to study the function relationship between the constellation state probability and MTBF. At the same time, the availability of different navigation constellations is also discussed. The influence of the total number of constellation satellites on the state probability of the constellation is studied. The results are shown in the Fig. 6. It shows that the availability probability of the constellation goes up with the increase of MTBF. For different navigation constellations, with the total number of satellites in the navigation constellation increases, the probability of no satellite failure decreases.

When the navigation satellite is working normally, the number of the visible satellites of the GPS navigation constellation in the service area is within the range from 4 to 16 [5]. The study shows the impact of the number of satellites on service availability. In general, at least four visible satellites are required for positioning. Let P_A denote the availability probability. When the number of visible satellites in the area is less than 4, the positioning requirement cannot be satisfied and $P_A = 0$. When the number of visible satellites in the area is 4, $P_A = P_0$. When the number of visible satellites is 5, $P_A = P_0 + P_1$ and so on. So, in the case of R visible satellites, we have

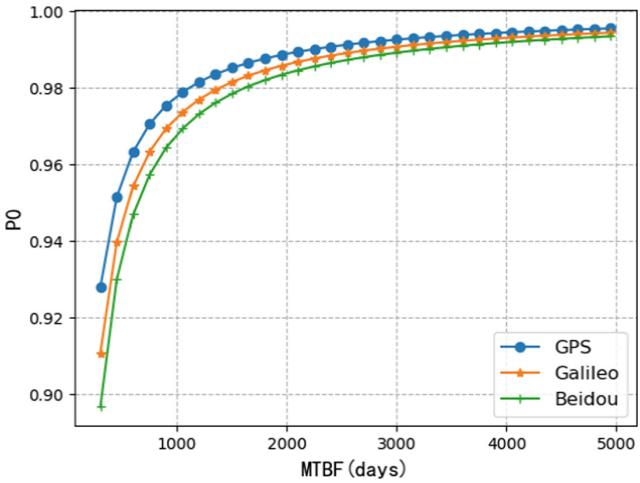

Fig. 6. The relationship between MTBF and constellation state probability of different navigation constellations

$$P_A = \sum_{i=0}^{R-4} P_i, R = 4, 5, \ldots, 16 \tag{18}$$

This gives a functional relationship between the availability of the service area and the number of visible satellites.

Figure 7 shows that when the number of visible satellites in the area is 1, 2, and 3, $P_A = 0$. When the number of visible satellites is 5, the regional availability is 0.99997, which is close to 1. When the number of visible satellites is more than 5, the regional availability is closer to 1. The results show that as the number of visible satellites increases, the availability of regional services increases. According to the proportional relationship discussed in the previous section, when the total number of satellites in the navigation constellation increases, the number of satellites visible in the region increases, then the regional service availability increases.

The STK (Satellite Tool Kits) software was then used to simulate the PDOP value of the satellite constellation to study the PDOP availability. Assume that the availability probability of each GPS satellite is equal and let $P = 0.957$, the maximum number of visible satellites in the service area is $M = 16$. According to the GPS service performance standard [13], the PDOP threshold is analyzed by taking values as 5 and 6, and the simulation result is that the availability of PDOP < 5 was 99.98%, and the availability of PDOP < 6 was 100%. The result satisfies the GPS service performance standard requirements (the availability of PDOP $\leq$ 6 is no less than 98%).

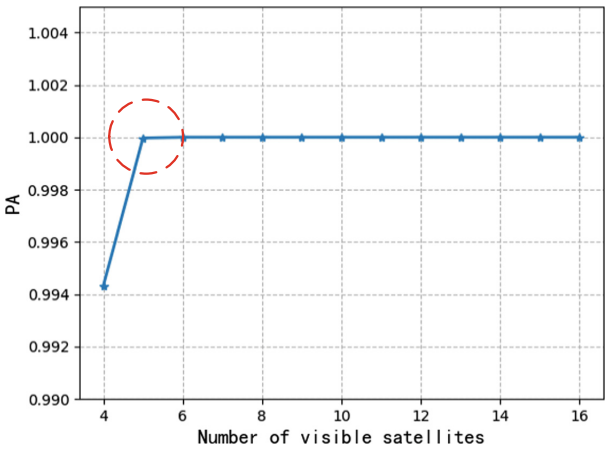

Fig. 7. The relationship between the number of visible satellites and regional availability

5 Conclusions

In this paper, the global navigation signal availability is extended to the regional area. The fault detection risk of navigation signal is studied. The global navigation availability analysis model is established based on Markov model. And the number of visible satellites and PDOP values in the service area are analyzed to establish the theory of regional instantaneous availability analysis. The simulation results show that when the fault interval time is constant, the availability of short-term faults is higher than that of long-term faults. When the total number of satellites in the navigation constellation increases, the number of visible satellites in the region increases, thus the regional service availability increases. When the PDOP threshold is analyzed by taking values as 5 and 6, the PDOP availability simulation result satisfies the GPS service performance standard requirements.

References

1. ICAO (2000) Validated ICAO GNSS Standards and Recommended Practices. International Civil Aviation Organization
2. Hou H, Xie F, Zhang W et al (2014) Constellation availability analysis of navigation system based on Markov process. Syst Eng Electron 36(4):685–690
3. Li Z (2012) Research on performance monitoring and evaluation methods of satellite navigation systems. University of Information Engineering
4. Hu Z (2013) Performance evaluation and experimental verification of Beidou satellite navigation system. Wuhan University
5. Li G, Li J, Li J et al (2010) Availability analysis of regional navigation constellations under service interruption. In: China satellite navigation academic annual conference
6. Cai H, Li X (2014) Analysis of weak links in navigation constellation based on service availability. In: China satellite navigation academic annual conference

7. Luo X, Jie J (2013) Research on real-time satellite navigation signal quality monitoring method. In: China satellite navigation academic annual conference
8. Sun C, Zhao H, Feng W, Zhuang C (2016) A novel digital threat model and effect analysis on modernized BeiDou signals. In: Proceedings of the ION ITM 2016, Monterey, California, USA, 25–28 January, pp 401–413
9. Sun C, Zhao H, Zhuang C, Feng W (2017) The IFFT-based SQM method against digital distortion in GNSS signals. GPS Solut. 21(4):1457–1468
10. Sun C, Du S, Zhao H, Feng W (2017) Autonomous carrier leakage monitoring technique for GNSS signal. In: Proceedings of the CSNC 2017, Shang Hai, China
11. Wang H, Liu C (2009) Satellite navigation signal quality monitoring system and its application. Glob Positioning Syst 34(6):60–63
12. Qin Y, Zhang H, Wang S (2012) Kalman Filtering and Integrated Navigation Principles, 2nd edn. Northwestern Polytechnical University Press
13. Department of Defense of United States of America. Global Positioning System Standard Positioning Service Performance Standard, 4th edn, September 2008 [S/OL]
14. Zhang Q (2017) Research on performance evaluation method of satellite navigation system. Shenyang Aerospace University
15. Liu H, Zhang N (2000) Constellation visibility of global navigation satellite system. Syst Eng Electron 22(5):23–25

The Challenges of LEO Based Navigation Augmentation System – Lessons Learned from Luojia-1A Satellite

Lei Wang[1,2], Ruizhi Chen[1,2(✉)], Beizhen Xu[1], Xinxin Zhang[1], Tao Li[1], and Cailun Wu[3]

[1] State Key Laboratory of Information Engineering in Surveying, Mapping and Remote Sensing, Wuhan University, Wuhan 430079, China
Ruizhi.chen@whu.edu.cn
[2] Collaborative Innovation Center for Geospatial Technology, Wuhan 430079, China
[3] State Key Laboratory of Satellite Navigation System and Equipment Technology, Shijiazhuang, China

Abstract. The Low earth orbiter (LEO) based navigation signal transmitters have advantages in fast-changing geometry and low free space signal loss, which can be served as a complementary or extension of current MEO/GEO based GNSS. Broadcasting navigation signals from LEO can significantly reduce the convergence time for the long baseline RTK\precise point positioning (PPP) and improve the signal strength. Hence LEO based navigation is considered as one of the key technology of next-generation positioning, navigation and timing (PNT) systems. This study assessed the pseudorange and carrier phase measurements observed from Luojia-1A satellite with the geometry-free combination method and the zero-baseline method. The assessment results indicate that the pseudorange precision variation subject to elevation angle is caused by both signal strength variation and multipath effect. The pseudorange measurement precision reaches 0.7 m and 0.8 m respectively for the dual frequency pseudorange measurements and the carrier phase precision is 2.8 mm and 2.6 mm respectively. Based on the data collected from Luojia-1A satellite, the challenges of LEO navigation augmentation data processing were addressed. The most distinguishing features of LEO navigation signals are their large signal strength variation, large Doppler variation and large acceleration variation. All these features have adversary effect on LEO signal processing and data processing, which has not been revealed. These challenges still need to be seriously investigated to further improve the performance of the LEO based navigation augmentation system.

Keywords: Navigation augmentation · Signal augmentation · Low earth orbiters · Luojia-1A

J. Sun et al. (Eds.): CSNC 2019, LNEE 563, pp. 298–310, 2019.
https://doi.org/10.1007/978-981-13-7759-4_27

1 Introduction

The global navigation satellite systems (GNSS) have been widely used in many applications and play an increasingly important role in our daily life. Currently, there are four global navigation satellite systems, known as GPS, GLONASS, Beidou and Galileo. Particularly, the Chinese Beidou satellite system is currently in the rapid deployment phase. It will provide navigation service to the 'silk and road' region by the end of 2018 and hopefully provides global navigation service by 2020. Beidou satellite system is one of the key infrastructures in the positioning, navigation and timing (PNT) systems. People become increasingly relying on the GNSS technique, but it also increases the risk that when current GNSS systems work improperly. Therefore, the remaining challenge is how to build a more robust, reliable positioning, navigation and timing (PNT) system. The key of next-generation PNT system includes pulsar navigation, LEO based navigation augmentation, ground communication fusion and underwater navigation techniques (Yang 2018). Particularly, the LEO based navigation augmentation system can increase the robustness of navigation signals, improve the convergence time and also improve the availability and integrity of current GNSS system. Hence it is considered as a very promising technique to augment and extend the navigation capacity of the current GNSS systems. The LEO based navigation augmentation system is also capable of providing global service without limited by the ground infrastructure. In addition, the LEO satellite can also be served as a moving monitoring station to improve Beidou GEO satellite orbit determination (Wang et al. 2017; Zeng et al. 2017; Zhao et al. 2017).

Comparing to current navigation satellite, the shortcomings of the LEO satellite is its small signal coverage. Hence it requires more LEO satellites than the medium earth orbiters (MEO) to establish a global coverage satellite network. Fortunately, the LEO broadband communication constellation develops rapidly recent years and the navigation augmentation service can serve as value-adding services of these communication constellations. There are many ambitious commercial constellation plans from different companies, such as the OneWeb constellation, the SpaceX constellation, the Boeing constellation etc. (Reid et al. 2016), which contains hundreds or even thousands of LEO satellites. China is also developing their own LEO communication constellations and many of them also consider the navigation augmentation demanding. The 'Hongyan' LEO broadband communication constellation proposed by China Aerospace Science and Technology (CAST) Corporation plans to launch over 300 satellites (Meng et al. 2018). In addition, the 'Hongyun' constellation proposed by the China Aerospace Science &industry corporation (CASIC) also planned to launch 156 satellites to build next-generation LEO based broadband communication system. Both constellations took the LEO navigation augmentation concept in their plan.

Although the big constellation is still on the plan, the LEO navigation augmentation technique has attracted many researchers. Generally, the navigation augmentation techniques include two types: the information augmentation and signal augmentation. The information augmentation means the transmit the correction information from the ground tracking network. Users can improve the positioning accuracy by applying the correction information. The corrections can be delivered to users by either satellite

communications or the ground communication techniques, which correspond to the satellite-based augmentation system (SBAS) and ground-based augmentation system (GBAS) concepts. The information augmentation is relatively mature and there are many commercial SBAS and GBAS systems in operation, such as the RTX system operated by Trimble (Chen et al. 2011; Leandro et al. 2011), Atlas by Unistrong (Guo and Zhang 2016) the StarFire operated by NavCom (Dixon 2006) etc. Currently, the SBAS relies on the geo-synchronized satellite since it provides stable data links and wider data communication bandwidth. The signal augmentation means the LEO can broadcast ranging signals. The LEO platform is close to the ground so the satellite geometry changes faster and signal loss is mitigated and the convergence time can be reduced (Ge et al. 2018; Li et al. 2018a; Li et al. 2018b). Correspondingly, the benefit of LEO navigation is more obvious than the information augmentation. In practice, the LEO navigation augmentation system may assemble both information augmentation and signal augmentation capability.

Wuhan University has been dedicated to research and development of LEO based navigation system for years. They launched a scientific experimental satellite call Luojia-1A satellite, which successfully carried out the LEO based navigation signal augmentation experiment. They collected the first hand ranging data from LEO satellite and published their first results recently (Wang et al. 2018b). This study reported the latest progress of Luojia-1A satellites and the challenges of LEO based navigation system is also discussed.

2 LEO Navigation Augmentation System of Luojia-1A Satellite

Luojia-1A satellite is developed by Wuhan University, which has two major functions: nighttime light remote sensing and LEO navigation signal augmentation experiment. The satellite has been successfully launched in Jiuquan satellite center on 2nd June 2018. Luojia-1A satellite operates in 645 km sun-synchronized orbit. The period of the satellite is about 94.6 min. The total weight of the satellite is less than 23 kg and the satellite is tri-axis stabilized. The configuration of the satellite is shown in Fig. 1. The outlook configuration of the satellite is regular and the size of the satellite is 870 mm $\times$ 520 mm $\times$ 390 mm with the solar panel unfolded. The major payloads of the satellite are the camera and the navigation augmentation system. The satellite body frame (SBF) is established as shown in Fig. 1. The +x axis points toward the flight direction and +z faces to the earth in the mission period. The +y axis is perpendicular to the XZ plane. The navigation augmentation system on Luojia-1A satellite includes three antennas and one payload. The three antennas are installed on +z and $-$z side respectively. Two of them are used to tracking GPS/Beidou dual frequency data and one for dual-band ranging signal transmission. The receiving antennas were installed on +z and $-$z respectively for continuously tracking the GPS/Beidou signals without affected by the satellite attitude. The transmitting antenna was installed on the +z side since the satellite +z side faces to the earth when it transmitting augmentation signals.

Fig. 1. The configuration of the satellite and the GNSS antennas installed on +z (left) and −z (right) side

The Luojia-1A satellite navigation augmentation system includes the payload and the ground receivers. Due to the constraint of the satellite platform, the navigation payload employs a compact design (left panel of Fig. 2). The size of the payload is 100 mm × 100 mm × 50 mm and its weight is less than 500 grams. Hence it is can be easily integrated on most satellite platforms, even the cube-satellites. The long-term power consumption of the payload is less than 2 W, which is also acceptable for most communication satellites. The payload can track GPS/Beidou dual frequency observations, autonomous orbit determination, output 1PPS pulse for time synchronization and generating the dual frequency ranging signals.

We also developed the ground receivers for the LEO navigation augmentation experiments. The ground receivers are capable of tracking dual frequency observations from GPS/Beidou and Luojia-1A satellites. It is capable of tracking up to 12 visible LEO satellites simultaneously (right panel of Fig. 2).

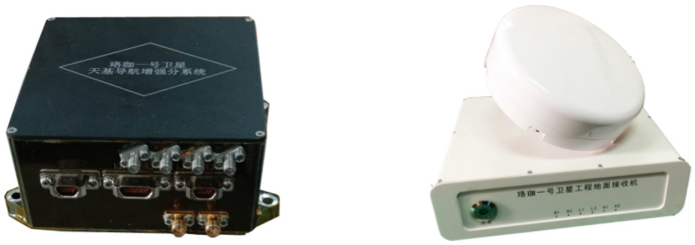

Fig. 2. The LEO navigation augmentation payload (left) and ground receivers (right) for Luoija-1A satellite

3 Luojia-1A Satellite Augmentation Signal Analysis

The navigation signals from Luojia-1A satellite was firstly received in 9th, June 2018 and a number of experiments has been carried out so far. Since the characteristics of the navigation signal from Luojia-1A satellite is unknown, it is difficult to design a high-performance receiver for both GPS/Beidou and LEO satellites.

One of the major tasks of Luoija-1A satellite is to investigate the characteristics of the navigation signal from the LEO satellite. However, there is only one satellite in space, so it is impossible to form double differenced measurements for the noise assessment. In this study, the measurements are assessed with both the Geometry-free combination method and zero-baseline method.

3.1 Measurement Noise Assessed with the Geometry-Free Combination

The geometry-free (GF) combination can eliminate most geometry-specified terms in the observation and thus is a useful tool for measurement noise assessment with a single receiver approach (Wang et al. 2013). The geometry-free combination is given as:

$$\begin{aligned} \mathrm{P}_{GF} &= P_1 - P_2 = I_1 - I_2 + 2\varepsilon_{Pi} \\ L_{GF} &= L_1 - L_2 = I_1 - I_2 + (\lambda_1 N_1 - \lambda_2 N_2) + 2\varepsilon_{\phi i} \end{aligned} \tag{1}$$

where P_{GF} and L_{GF} are the geometry-free combinations of the pseudorange and carrier phase measurements. I_i is the ionospheric delay. λ_i and N_i are the wavelength and unknown integer ambiguity on ith frequency respectively. The GF combination eliminated most errors except the ionosphere and the ambiguities. Since each LEO pass takes only a few minutes, the ionosphere delay can be roughly taken as a constant bias for the code measurements (Wang et al. 2018a). A time-difference GF combination is used to assess to measurement noise of carrier phase measurements.

This approach has been used in the initial assessment of navigation augmentation signals of Luojia-1A (Wang et al. 2018b). In this study, we present the measurement noise assessed by more extensive measurement data. The C/N0 of the Luojia-1A navigation augmentation signals and the sky plot of the satellite over multiple experiments are presented in Fig. 3. The navigation augmentation system on Luojia-1A satellite works well so far, so more experimental data is collected. Luojia-1A satellite transmits dual-band ranging signals known as The figure indicates that the relationship between C/N0 and the elevation angle is slightly different. which has been captured in Wang et al. (2018a) previously. The reason has been confirmed that caused by the receiver antenna gain since this phenomenon can be mitigation or eliminated by changing the antenna orientation. We still investigating the optimal signal tracking strategy for optimally tracks LEO navigation signal, so the signals are tracked with different tracking strategies. Some of the strategies have been proven as not suitable for LEO signal tracking, which may cause loss of lock or C/N0 fluctuation etc.

The relationship between the measurement noise and the elevation angle is presented in Fig. 4. This evaluation employs the same approach as presented in Wang et al. (2018a), but we use a more extensive data set. The high dynamics of the LEO signals property has been addressed from our experiments and we optimized the code tracking loop to optimally balance the measurement noise and the dynamics. After the optimization of the ground receivers, the precision of pseudorange measurement has been significantly improved. The standard deviation of the GF pseudorange noise has been reduced from 15 m to 10 m at 10° elevation. The carrier phase measurement precision is similar as reported in Wang et al. (2018a) since it is not sensitive to the dynamics status.

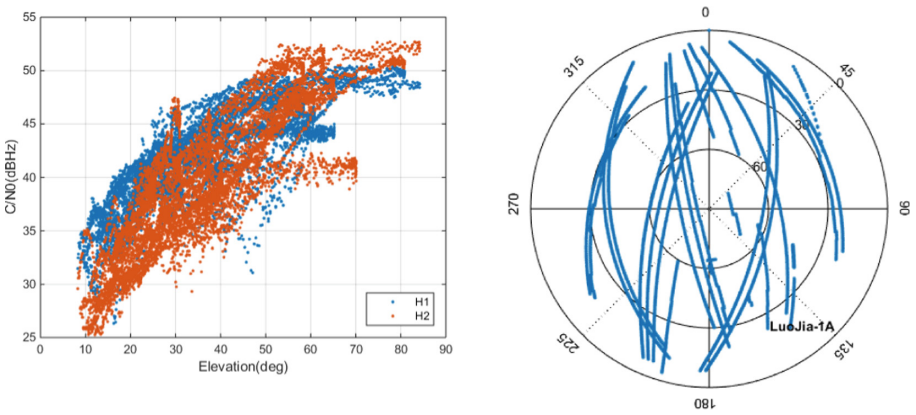

Fig. 3. The C/N0 (left) and skyplot (right) of Luojia-1A satellite observed by Wuhan station

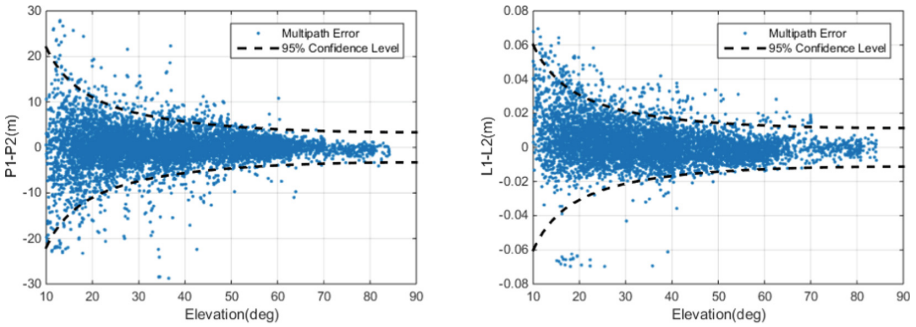

Fig. 4. The pseudorange (left) and carrier phase (right) measurement precision assessed by the geometry-free combination method

3.2 Measurement Noise Assessed with the Zero-Baseline

The geometry-free combination method only gives an approximate measurement noise, since the ionosphere effect still remains. Another limitation of the method is that it does not allow to assess H1 and H2 measurement noise respectively. In this study, we employ a zero-baseline method to solve this problem. The zero-baseline method is widely used to evaluate the receiver noise in GNSS data processing, but it is normally based on the double-differenced measurements. In this study, we use a single-differenced measurement to evaluate the measurement noise. The experimental set up is presented in Fig. 5. Since the double-differenced measurement can eliminate receiver-specified errors, so it does not require clock synchronization. In our case, the inter-station differenced measurements cannot eliminate the biases caused by the receiver clock. Therefore, we use a chip scale atomic clock (CSAC) to synchronize both receivers, so that we can acquire the expected results.

The zero-baseline approach allows assessing the measurement noise of H1 and H2 respectively. The initial results are presented in Figs. 6 and 7. The results present the

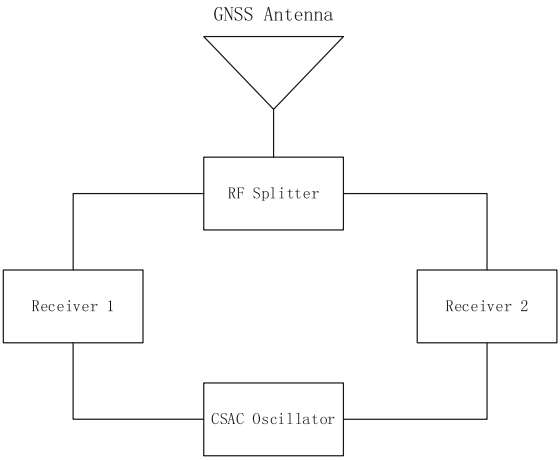

Fig. 5. Experiment setup of zero-baseline observation noise assessment.

difference between H1 and H2 signals. Both P1 and P2 present severe elevation angle dependent noise variation, which is caused by the rapid signal strength variation. The multipath effect can be completely eliminated by the zero-baseline approach, so the noise variation is not caused by the multipath effect. The pseudorange noise is also affected by the signal-noise ratio (SNR) or carrier-noise ratio (C/N0). The signal with poorer signal strength has larger tracking noise. The free space loss of GPS L1 signals (1575.42 MHz) on LEO satellite and GPS satellite is compared in Fig. 8. The figure indicates that in each satellite pass, the signal loss of the LEO satellite changes more than 10 dB, while GPS satellite only changes 1.6 dB. Assuming the transmit power does not change, it means the receiver signal strength from LEO satellite changes more dramatically. The signal strength changes 2 dB will have little effect on the signal quality, but signal strength changes more than 10 dB will cause substantial measurement noise change. This simulation only reveals the elevation angle lower than 50° case. The signal strength change will be more dramatically for the higher elevation angle case. Large signal variation extent may require modification of the radio frequency (RF) frontend to achieve the best performance. The LEO satellite pass only takes about 10 min while the GPS satellite pass takes more than 5 hours. The simulation indicates that the challenge of LEO navigation is large signal strength variation extent and inhomogeneous measurement noise. The signal strength variation can be partially compensated by the specially designed the signal transmitting antenna radiation figure. GPS satellites also adjust its transmitting antenna gain to balance its free space signal loss variation. For the LEO satellite, the radiation pattern gain should be a U-shape to compensate the free space loss at low elevation angle.

The signal strength variation of LEO satellite is more dramatically, that is why the code noise variation is also significant for zero-baseline measurements. Comparing to the GF pseudorange noise, the H1 and H2 pseudorange noise is significantly smaller with the zero baseline measurements. The overall precision of the single-differenced P1 and P2 measurement noise is 1.15 m and 1.00 m. Assuming the receiver noise between

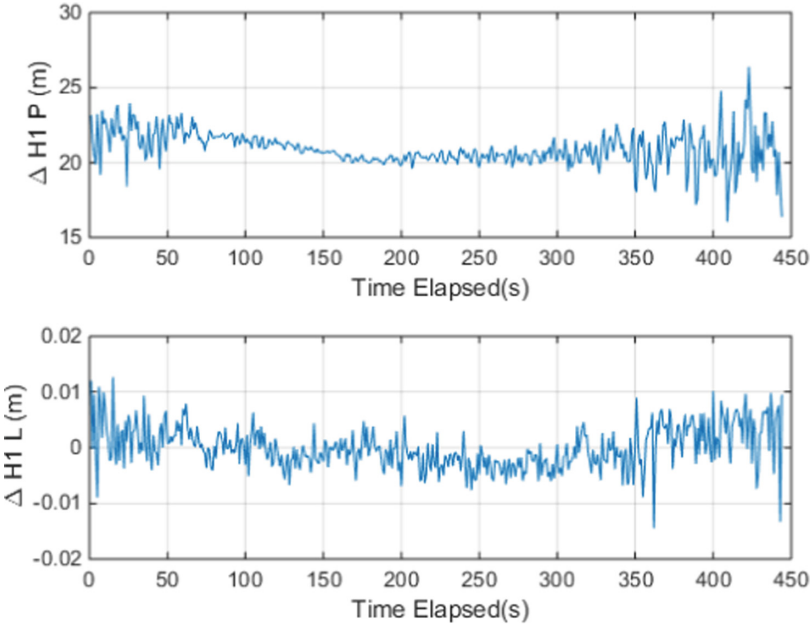

Fig. 6. The pseudorange and carrier phase precision of H1 signals assessed by the zero-baseline approach.

two receivers are independent, then the P1 and P2 measurement noise is 0.707 m and 0.816 m respectively. Meanwhile, the estimated pseudorange measurement noise from the geometry-free combination is 1.5 m in high elevation angle scenario (Wang et al. 2018a). Therefore, the multipath still plays an important role in LEO navigation augmentation signal noise assessment. The figure also shows that there is a systematical bias in the single differenced measurement. This bias is different between P1 and P2, which corresponds to the differential hardware delay. Fortunately, the bias does not affect the measurement noise assessment.

Figures 6 and 7 also show that the precision of the carrier phase measurements suffers less elevation dependent noise. Therefore, the elevation angle dependent noise in GF combination assessment is mainly contributed by the multipath and remaining ionosphere residuals. The precision of the carrier phase measurement estimated from the zero baseline method is similar to the geometry-free method. The overall precision of the single differenced L1 and L2 measurements are 3.9 mm and 3.6 mm respectively. Assuming the carrier phase noise between different receivers are independent, then the precision of the L1 and L2 measurements are 2.8 mm and 2.6 mm respectively. The carrier phase noise estimated from the geometry-free combination is 1.5 mm in high elevation angle scenarios (Wang et al. 2018a). There is no systematically bias presence in carrier phase measurements since they are calibrated alone the ambiguity parameters.

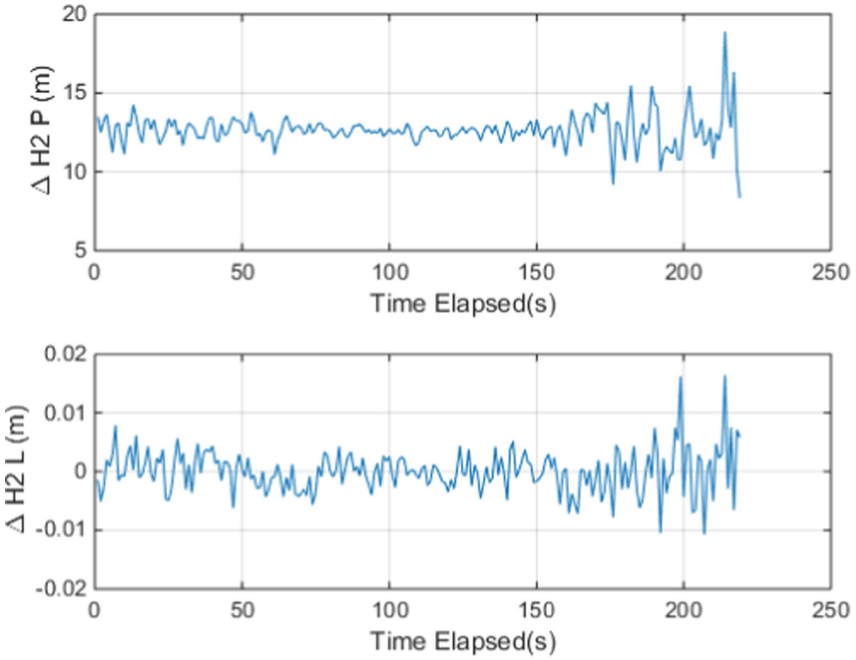

Fig. 7. The pseudorange and carrier phase precision of H2 signals assessed by the zero-baseline approach.

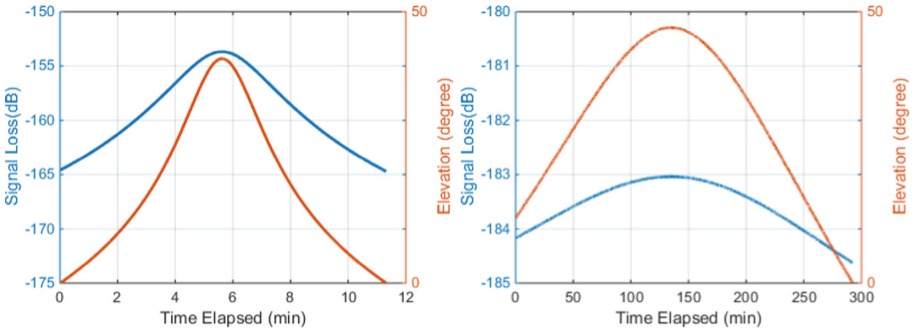

Fig. 8. Free space signal loss of LEO satellite (left) and GPS satellite (right)

4 Characteristic Analysis of Navigation Signals from LEO Satellite

The benefit of LEO based navigation augmentation has been understood, but the challenges are difficult to foresee. The contribution of Luojia-1A satellite is that we capture the real navigation signals from LEO platform, which helps us understand the characteristic of LEO ranging signal well.

The LEO navigation augmentation signal has three distinguishing characteristics: large signal strength variation, large Doppler variation and large acceleration variation. All these characteristics have a significant impact on the receiver design or signal characteristics.

The large signal strength variation issue has been presented in Fig. 8. The large signal variation is because the satellite is close to the earth and the distance variation. The geometrical change of the satellite subject to different elevation angle is presented in Fig. 9. The figure shows that for a satellite with 650 km altitude. The satellite-receiver distance at 0° elevation reaches 2940 km, which is over 4 times long as the 90° case. The signal strength changes as the distance change. Large signal strength dynamic makes the receiver noise inhomogeneous and also change the RF frontend since the GPS signal does not have such property. Improper RF frontend may affect the tracking performance of the receiver. Signal strength variation also leads to inhomogeneous pseudorange precision.

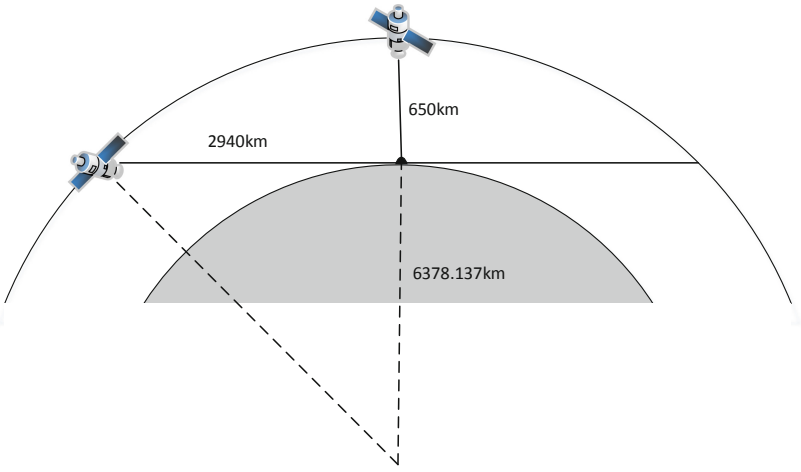

Fig. 9. LEO satellite geometry variation subject to different elevation angle.

Large Doppler variation is associated with the fast geometry change, which affects the signal acquisition efficiency. A comparison of the Doppler variation and acceleration variation between Luojia-1A satellite and GPS satellite is illustrated in Fig. 10. The figure shows the Doppler variation of single satellite pass of Luojia-1A satellite reaches about 40 kHz, while the Doppler variation of GPS satellite is only about 4 kHz. During the signal acquisition stage, the receiver needs searching the signal in both frequency domain and time domain to find the peak (Borre et al. 2007), which is the most time-consuming procedure. The Doppler variation becomes larger means the searching time increases dramatically.

Large acceleration variation affects the code tracking loop parameters. Figure 10 indicates that the Line-of-sight acceleration of LEO satellite reaches 70 m/s^2 for a static user, while the line-of-sight acceleration of GPS satellite is only 2 m/s^2. Large

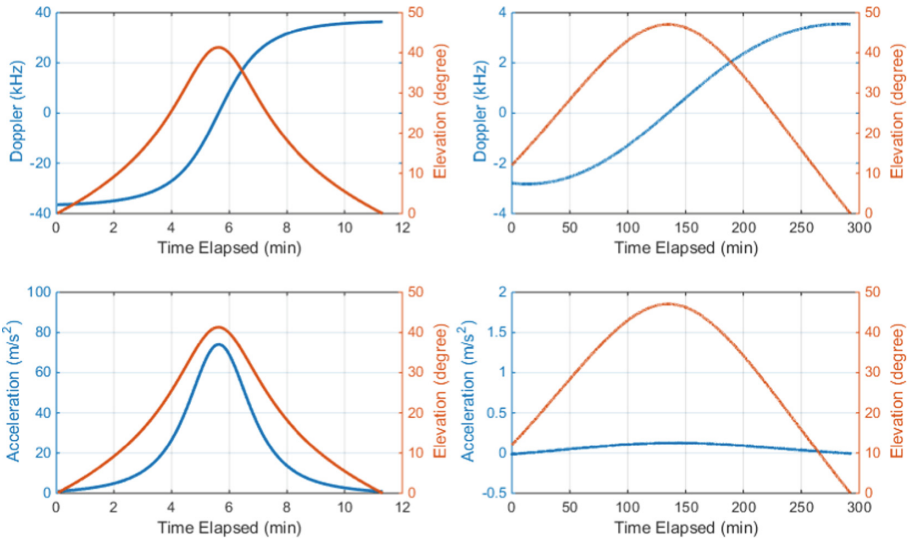

Fig. 10. Comparison of the line-of-sight Doppler (upper) and acceleration (lower) characteristics between Luojia-1A satellite (left) and GPS satellite (right).

acceleration variation means high dynamics scenario in GNSS receiver design. Large acceleration means large Doppler prediction uncertainty, hence it requires shorter coherent integration time and consequently larger code noise and lower sensitivity. The dynamics and the code precision is a contradiction in GNSS signal processing, which only happens in special applications, but commonly happened in LEO navigation. How to improve the pseudorange precision in the high dynamic scenario is the most challenging issue for LEO navigation signal processing.

5 Conclusion

LEO navigation augmentation is a promising technique that extending the performance of the current GNSS systems. Luojia-1A satellite is a pioneer experimental satellite developed by Wuhan University that successfully performed the LEO navigation augmentation experiment. This study introduced the background of the satellite and the navigation augmentation payload. The characteristics of the LEO navigation augmentation is analyzed accordingly. The measurement noise of pseudorange and carrier phase from Luojia-1A satellite is analyzed with two different methods. The geometry-free method allows roughly estimating the measurement noise and the zero-baseline method can estimate the receiver internal noise of each frequency. The evaluation results from zero-baseline method indicate that the pseudorange noise variation is also caused by the signal strength variation. The precision of pseudorange measurement on H1 and H2 frequencies achieves 0.7 m and 0.8 m. The carrier phase measurement precision of Luojia-1A signals is 2.8 mm and 2.6 mm for H1 and H2 respectively. The benefit of LEO navigation augmentation has been well understood, but the challenges

of LEO navigation augmentation has not been revealed. In this study, the challenges of the LEO navigation signals processing are identified based on Luojia-1A data processing experience. Generally, there are three distinguishing features: large signal strength variation, large Doppler variation and large acceleration variation. Large signal strength variation requires specially designed radio frequency frontend and create inhomogeneous pseudorange measurement precision. Large Doppler variation increases the signal acquisition time and the large acceleration decreases the pseudorange accuracy. These challenges are still worth to investigate so that the performance of LEO based navigation augmentation system can be further improved.

Acknowledgments. This research is support by the National Natural Science Foundation of China (NSFC 41704002, 91638203), China Postdoc Science Foundation (2017M620337) and the Fundamental Research Funds for the Central Universities.

References

Borre K, Akos DM, Bertelsen N, Rinder P, Jensen SH (2007) A Software-Defined GPS and Galileo Receiver A Single-Frequency Approach. Birkhauser, Boston

Chen X, Allison T, Cao W, Ferguson K, Grunigh S, Gomez V, Kipka A, Kohler J, Laundau H, Leandro R, Lu G, Stolz R, Talbot N (2011) Trimble RTX, an Innovative New Approach for Network RTK. ION GNSS+2011, Portland, OR, pp 2214–2219

Dixon K (2006) StarFire™: A Global SBAS for Sub-Decimeter Precise Point Positioning. ION GNSS 2006, Fort Worth, Texas, pp 2286–2296

Ge H, Li B, Ge M, Zang N, Nie L, Shen Y, Schuh H (2018) Initial assessment of precise point positioning with LEO enhanced global navigation satellite systems (LeGNSS). Remote Sens 10:984

Guo S, Zhang D (2016) Analysis and comparison of satellite based augmentation system 'Atlas' and CORS network. Geospatial Inf 14:1–4

Leandro R, Landau H, Nitschke M, Glocker M, Seeger S, Chen X, Deking A, Bentahar M, Zhang F, Ferguson K (2011) RTX positioning: the next generation of cm-accurate real-time GNSS positioning. ION GNSS+2011, Portland, OR, p 1002-7

Li B, Ge H, Ge M, Nie L, Shen Y, Schuh H (2018a) LEO enhanced global navigation satellite system (LeGNSS) for real-time precise positioning services. Adv Space Res 63:73–93

Li X, Ma F, Li X, Lv H, Bian L, Jiang Z, Zhang X (2018b) LEO constellation-augmented multi-GNSS for rapid PPP convergence. J Geodesy

Meng Y, Bian L, Wang Y, Yan T, Lei W, He M, Li X (2018) Global navigation augmentation system based on Hongyan satellite constellation. Space Int 10

Reid TGR, Neish AM, Walter TF, Enge PK (2016) Leveraging commercial broadband LEO constellations for navigation. ION GNSS+2016, Portland, Oregon, pp 2300–2314

Wang L, Chen R, Li D, Yu B, Wu C (2018a) Quality Assessment of the LEO Navigation Augmentation Signals from Luojia-1A Satellite. Geomatics and Information science of Wuhan University

Wang L, Chen R, Li D, Zhang G, Shen X, Yu B, Wu C, Xie S, Zhang P, Li M, Pan Y (2018b) Initial assessment of the LEO based navigation signal augmentation system from Luojia-1A satellite. Sensors 18:3919

Wang L, Feng Y, Wang C (2013) Real-time assessment of GNSS observation noise with single receivers. J Glob Positioning Syst 12:73–82

Wang L, Yan X, Zhang Q, Huang G, Qin Z (2017) Discussion on technology of BDS Satellite orbit determination enhanced by LEO satellite. J Navig Positioning 5:51–57

Yang C (2018) Development plan for comprehensive positioning, navigation, timing system of Chinese Beidou navigation system. China Sci Technol Ind 2018:32–35

Zeng T, Sui L, Jia X, Ji G, Zhang Q (2017) Results and analysis of BDS precise orbit determination with the enhancement of Fengyun-3C. Acta Geodaetica Et Cartographic Sinica 46:824–833

Zhao Q, Wang C, Guo J, Yang G, Liao M, Ma H, Liu J (2017) Enhanced orbit determination for BeiDou satellites with FengYun-3C onboard GNSS data. GPS Solut 21:1–12

Test and Assessment Technology

Research on Test Method of Complex Electromagnetic Environment Adaptability of GNSS Receivers

Gaobo Liang[1(✉)], Lin Li[2], Xiangyu Yuan[1], Xiaohang Zhang[1], and Peiwei Xu[1]

[1] Luoyang Electronic Equipment Test Center, Luoyang, China
lianggb2005@sohu.com
[2] Beijing Satellite Navigation Center, Beijing, China

Abstract. With the rapid development of satellite navigation technology, the application fields of GNSS receivers are also extending. In various military and civil application scenarios, the complex electromagnetic environment will affect the performance of the GNSS receivers, and even make receivers work improperly. Therefore, it is important to test the performance of the GNSS receivers in the complex electromagnetic environment by adaptability test. Based on the analysis of the concept of complex electromagnetic environment, this paper discusses key issues in complex electromagnetic environment adaptability test of GNSS receivers, such as the construction and evaluation of complex electromagnetic environment, adaptability test procedures, test evaluation method, and so on. The research achievements may provide technique reference for the further research on the adaptability test of GNSS receiver in complex electromagnetic environment.

Keywords: GNSS · Receiver · Complex electromagnetic environment · Adaptability · Test

1 Introduction

As a satellite-based radio navigation system which using artificial satellites as navigation stations, GNSS (Global Navigation Satellite System) provides high-precision position, speed and time information in all-weather for various kinds of carriers globally on land, on the sea, in the air, or in space [1, 2]. Nowadays satellite navigation has penetrated into more and more fields of military and civilian area, and has been playing an increasingly important role.

Complex electromagnetic environment is a prominent feature of electronic information warfare. On the future battlefield, GNSS will be up against more complex and changeable confrontation and non-confrontation environment. The navigation and positioning performance of GNSS is more and more closely related to complex electromagnetic environment [3–5]. Therefore, complex electromagnetic environment adaptability test of GNSS receivers is the key measure to test whether the receivers can adapt to complex electromagnetic environment and give full play to its effectiveness. At

J. Sun et al. (Eds.): CSNC 2019, LNEE 563, pp. 313–324, 2019.
https://doi.org/10.1007/978-981-13-7759-4_28

present, there are few relevant reports on research of evaluation of complex electromagnetic environment adaptability test of GNSS receivers. Starting with the concepts and connotations, Paper [6] puts forward the basic idea and approach for construction and evaluation of complex electromagnetic environment, along with evaluation method of complex electromagnetic environment adaptability test. But it doesn't relate to GNSS receivers. Paper [7] only does some research on GNSS complex electromagnetic environment monitoring analysis, but not adaptability test of GNSS receivers. Paper [8] focuses on the design, construction and maintenance of simulation and test system for complex electromagnetic environment of GNSS receivers, but not method of adaptability test of GNSS receivers in complex electromagnetic environment.

Based on the analysis of technical characteristics and application modes of GNSS receivers, this paper focuses on key problems of Complex Electromagnetic Environment Adaptability Test of GNSS Receivers, including What Complex Electromagnetic Environment Is, How to Build Complex Electromagnetic Environment, How to Evaluate the Adaptability Test, and so on. These works can provide a reference for further research on related issues of the Complex Electromagnetic Environment Adaptability Test of GNSS Receiver.

2 Technical Characteristics and Application Modes of GNSS Receivers

2.1 Basic Composition and Principle

GNSS receivers are used to receive satellite navigation signals to achieve the navigation, location, timing and other functions. Usually, GNSS receivers are composed of functional modules such as RF front-end processing module, baseband digital signal processing module, and positioning and navigation calculation module, etc., as shown in Fig. 1. By receiving satellite signals from more than 4 satellites to obtain the corresponding distance measurement and navigation message, GNSS receivers calculate the position of each satellite according the navigation message, and finally obtain the present position and time of the receiver by solving equations.

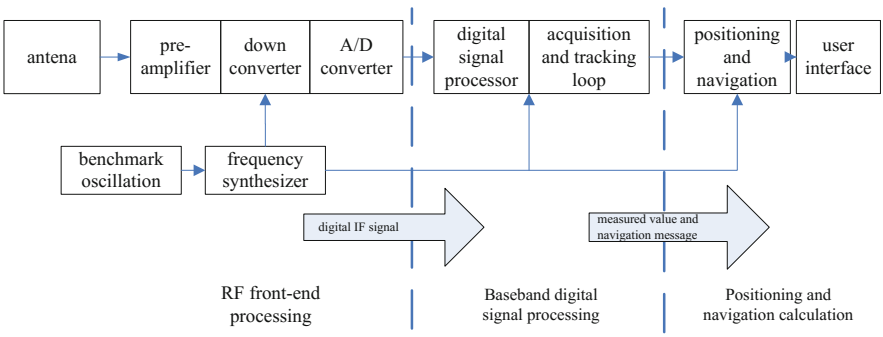

Fig. 1. The general composition of GNSS receivers

2.2 Technical Characteristics

At present, the receiving frequency and signal information of GPS, BDS, GLONASS and Galileo receivers are as shown in Table 1 [1, 9]. Besides that, in the ITU conference of 2012, 2483.5 MHz–2500 MHz had been legal global navigation frequency.

For the reception frequency and signal situation of the BD III receiver are not disclosed, Table 1 does not cover the BD III receiver.

Table 1. The receiving frequency and signal information of GNSS receiver

GNSS receivers	GPS	BDS	GLONASS	Galileo
Carrier frequency (MHz)	L1: 1575.42 L2: 1227.60 L5: 1176.45	B1: 1561.098 B2: 1207.14 B3: 1268.52 S: 2491.75	G1: 1598.0625–1605.375 G2: 1242.9375–1248.625	E1: 1575.42 E5a: 1176.45 E5b: 1207.14 E6: 1278.75
Receiving frequency (MHz)	1166–1590	1191–1571	1242–1606	1164–1591
Signal type	L1: C/A, P (Y), M L2: C, P(Y), M L5: C	B1: C, P B2: C, P B3: C, P	G1: C/A, P G2: C/A, P	E1: PRS, OS, SOL, CS E5a: OS E5b: OS, SOL, CS E6: PRS, CS
Multiple access mode	CDMA	CDMA	FDMA	CDMA

The main technical characteristics of GNSS receivers as follows:

(a) Matched reception technology is used in receiving navigation signals. Because the received navigation signals are already known parameters signals (including frequency, bandwidth, rate, modulation mode, information format, etc.), matched filtering, matched demodulation, matched despreading and other matched reception technology are used in the signal receiving and processing process. For the receiving bandwidth is limited to the navigation signals bandwidth, it is difficult for other signals outside the band to enter the receiver.

(b) It has a certain anti-jamming ability by using correlation receiving mode. The satellite navigation signals have good autocorrelation and cross-correlation performance by adopting direct sequence spread spectrum (DSSS) and the pseudo-random (PRN) code technology. As a result, when carrying out correlation processing such as navigation signal acquisition and tracking, a certain anti-interference ability is obtained [10, 11].

(c) The received navigation signals are weak and susceptible to be jammed. Since the intensity of navigation signals received are mostly lower than −120 dBm, GNSS receivers would not work normally within the radius of 9 km of 1 W interference source (equivalent radiation power), even if the anti-jamming ability of GNSS receivers are as high as 35 dB.

Focusing on the vulnerability of the GNSS receivers, researchers have proposed various anti-jamming technologies in the antenna, signal processing, external assistance, and so on. In which, frequency filtering technology, adaptive nulling antenna technology, inertial/GNSS integrated navigation technology and other technologies have been widely used [12–14].

2.3 Application Mode

GNSS receivers have been widely used globally, penetrating into almost all fields of civilian and military fields [15–18]. In civilian fields, GNSS receivers have an increasing application in transportation, marine fisheries, hydrological surveillance, emergency rescue, mobile communication, and so on. In military fields, GNSS receivers can provide high-precision position, speed and time information for individuals, vehicles, aerial platforms and precision striking weapons. In addition, the BD receivers can also provide short message communication, location reporting and other services.

In practical use, the application modes of GNSS receivers include different modes such as handheld, airborne, missile borne, and so on. Among them, the handheld mode and vehicle mode are mostly low dynamic applications, and the airborne mode and the missile borne mode are mostly high dynamic applications. In order to improve the high dynamic adaptability of the GNSS receivers, integrated navigation mode (such as inertial/satellite integrated navigation) is commonly used, and other navigation system information (such as inertial navigation information) are used to assist GNSS receivers in fast acquisition and tracking of satellite navigation signals.

3 Analysis of Complex Electromagnetic Environment of GNSS Receiver

3.1 About Complex Electromagnetic Environment

For GNSS receivers, the electromagnetic environment refers to the electromagnetic environment consisting of all electromagnetic radiation or conductive electromagnetic emission that arrives at the receivers. The electromagnetic environment not only include the lightning, electrostatic discharge environment and the electromagnetic environment radiated by civil equipments, but also the electromagnetic environment radiated by warring parties when utilizing and controlling electromagnetic spectrum, high power microwave and strong electromagnetic pulse, etc.

3.2 The Composition of Complex Electromagnetic Environment

For the parameters (including frequency, style, spread spectrum code, code rate, etc.) of the received signals are known, GNSS receivers would acquire the navigation and positioning information in signals through capturing, tracking, demodulation, navigation message calculation and other processing. In receiving signals, GNSS receivers would face the electromagnetic environment composed of all the electromagnetic signals received by the antenna. For GNSS receivers far away from the war zone, the electromagnetic environment mainly includes the electromagnetic signals radiated by the peripheral civilian equipment, as well as the multipath GNSS signals generated by the scattering of complex terrain or buildings. For GNSS receivers in the war zone, the electromagnetic environment mainly includes all kinds of electromagnetic signals generated by the radiation of electronic equipment of warring parties, by backup radiation, by radiation or scattering of other electronic equipment. Similarly, Multipath signals generated by scattering of complex terrain or buildings should also be considered.

According the source and influence of the electromagnetic signals, the electromagnetic environment which GNSS receivers are facing can be divided into threatening electromagnetic environment and background electromagnetic environment. Threatening electromagnetic environment mainly refers to the electromagnetic environment generated by the radiation of enemy electronic equipment, which can directly interfere GNSS receivers. The background electromagnetic environment is composed of all electromagnetic signals besides threatening the electromagnetic environment, such as radar signals, communication signals, photoelectric signals and electromagnetic signals radiated by civil equipment.

3.3 Complex Electromagnetic Environment Effects on GNSS Receivers

GNSS receivers are used to provide users with navigation, positioning, timing and other information. Complex electromagnetic environment will have a certain degree of interference to the signal processing in GNSS receivers. When there are strong interference signals in the receiving frequency band, the received signal-to-noise ratio (or equivalent signal-to-noise ratio) of GNSS receivers will be reduced, which will make it impossible for receivers to capture, track or demodulate signals normally. As a result, the positioning accuracy and timing accuracy of GNSS receivers would deteriorate, or make it difficult to obtain navigation, positioning and timing information.

Complex electromagnetic environment effects on GNSS receiver is mainly the interference effect in signal capturing and tracking.

(1) Interference effect on the capturing of navigation signal

The capturing of navigation signal is the alignment process between the local pseudo random code generated by GNSS receiver and the pseudo random code in satellite signals received, which judged by the correlation value of the two codes exceed the detection threshold. For there is a certain Doppler shift (generally $\pm$ 5 kHz) in satellite signals received, and the signal transmission time is unknown, GNSS receivers need

two-dimensional search in time domain (code phase) and frequency domain (Doppler frequency range).

When there are interference signals or other background signals, the local pseudo random code generated by GNSS receiver would be correlated with interference signals and other background signals. If the interference signals or other background signals are strong enough, the correlation value may exceed the detection threshold, GNSS receivers would not be able to capture the real satellite navigation signals.

(2) Interference effect on the tracking of navigation signal

After GNSS receivers capture the satellite signals, carrier and pseudo-code loops can be used to track signals, and accurate synchronization between the local reference signal and the received signals would be achieved. The tracking loop usually consists of carrier tracking loop and non-coherent delay locked code tracking loop. The carrier tracking loop is divided into phase-locked loop (PLL) and frequency-locked loop (FLL). The PLL can provide higher tracking precision and SNR, and the FLL can tolerate larger Doppler shift (high dynamic application). The non-coherent delay locked code tracking loop adopts three kinds of pseudo random codes: advance, instant and lag. The precise alignment of the code phase can be achieved by using the correlation values between the three kind of codes and pseudo random code of satellite signals correspondingly.

Theoretical analysis shows that both the PLL tracking error and the loop tracking error are closely related to equivalent SNR, noise band and pre-detection integral time. When there are interference signals or other background signals, the equivalent SNR will be reduced, and the tracking error of carrier tracking loop and code tracking loop

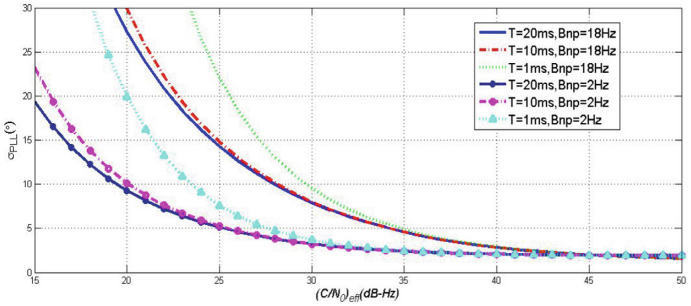

Fig. 2. The relation between the equivalent SNR and the PLL tracking error

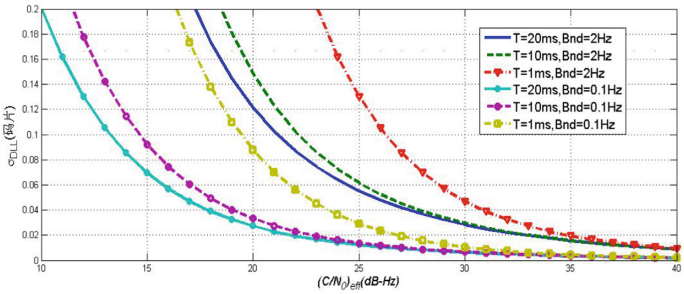

Fig. 3. The relation between the equivalent SNR and the PN code loop tracking error

would increase correspondingly. When the tracking errors exceed the threshold, carrier tracking loop and code tracking loop would lose lock. The relation between the equivalent SNR and the PLL tracking error, the loop tracking error are shown in Figs. 2 and 3. The empirical threshold of carrier tracking loop is 15°, and The empirical threshold of code tracking loop is 1/6 chip [18].

4 Evaluation Method of Complex Electromagnetic Environment Adaptability Test of GNSS Receivers

Complex electromagnetic environment adaptability test of GNSS receivers are to test whether GNSS receivers can achieve desired performance and complete scheduled tasks in specified complex electromagnetic environment. Specified complex electromagnetic environment refers to the complex electromagnetic environment in the test according to the mission and typical tasks of GNSS receivers.

4.1 General Procedure of Test

The general procedure of complex electromagnetic environment adaptability test of GNSS receivers is as follows:

(1) Determinating test contents and requirement

The test contents and requirement of complex electromagnetic environment adaptability test should be determined according to the mission of GNSS receivers.

(2) Correlation construction and evaluation of electromagnetic environment.

Firstly, the confrontation conditions (such as the alignment, deployment and performance of the electronic equipment of warring parties in war zone, the tactical tactics maybe used, electromagnetic signals propagation environment, etc.) and the technical conditions (such as the response characteristics of receivers to electromagnetic signals) should be analyzed and determined according to mission and application of GNSS receiver.

Secondly, according to the confrontation conditions determined, the electromagnetic environment of GNSS receiver should be predicted by synthetically using the measured data, theoretical calculation results and mathematical simulation data.

Then, according to the requirement of correlation construction, the electromagnetic environment predicted should be trimmed, the construction requirements of equivalent electromagnetic environment should be put forward, the equipment used to construct the electromagnetic environment should be chosen, and the prescribed complex electromagnetic environment should be constructed.

Finally, it is necessary to evaluate the similarity between the electromagnetic environment in test and the prediction electromagnetic environment.

(3) Evaluation of adaptability test

The complex electromagnetic environment adaptability test of GNSS receivers should be carried out to test the main tactical indicators of GNSS receivers in complex electromagnetic environment, and evaluate adaptability of GNSS receivers comprehensively.

4.2 Construction and Evaluation Method of Electromagnetic Environment of GNSS Receivers

4.2.1 Correlation-Based Construction Method of Electromagnetic Environment

Construction of complex electromagnetic environment is the key in complex electromagnetic environment adaptability test. When constructing the complex electromagnetic environment, not all the predicted electromagnetic signals need to be constructed. According to the response characteristics of GNSS receivers to electromagnetic signals, only electromagnetic signals that have high relativity with GNSS receivers should be selected to construct.

Relativity between the electromagnetic signals and GNSS receivers can be measured by Correlation Degree, which mainly reflected the correlation between electromagnetic signals and GNSS receivers in frequency domain, time domain, power domain, and polarization domain. For GNSS receiver, Correlation Degree of electromagnetic signals can be calculated by reference formula (1):

$$c_i = c_{\mathrm{f}i} \cdot c_{\mathrm{t}i} \cdot c_{\mathrm{p}i} \tag{1}$$

Where, $c_{\mathrm{f}i}$ is the frequency domain correlation factor between number i electromagnetic signal and GNSS receiver, it is necessary to consider whether the spectrum of the signal falls into the receiver's scheduled receiving bandwidth. c_{ti} is the time domain correlation factor between number i electromagnetic signal and GNSS receiver, it is necessary to consider whether the signal appears in the predetermined receiving time of the GNSS receiver; c_{pi} is the power domain correlation factor between number i electromagnetic signal and GNSS receiver, it is necessary to consider whether the power of the signal exceed the receiver's sensitivity or the background noise power. For polarization domain, it is generally considered in the power domain correlation factor synthetically.

According to the principle of Power Equivalence or Functional Equivalence, the electromagnetic environment should be constructed by using physical equipment, analog equipment, simulation equipment, vector signal source, etc. There are many related research literatures in this field, such as paper [19], which put forward an evaluation method of complex electromagnetic environment based on interference scenario, interference technology, interference tactics, and interference intensity. It also discusses equivalent construction methods of complex electromagnetic environment, such as mathematical simulation, hardware in the loop simulation, ground static test, captive flight test, flight test, etc. Paper [20] proposes a construction method of electronic warfare complex electromagnetic environment simulation system, which includes battlefield electromagnetic environment scenario, battlefield signals playback, intentional electromagnetic radiation, unintentional electromagnetic radiation, natural electromagnetic radiation, and battlefield electromagnetic environment visualization. Paper [21] proposes an implementation method of hardware-in-the-loop simulation platform for complex electromagnetic environment that can be used in microwave anechoic chamber test.

4.2.2 Similarity-Based Evaluation Method of Electromagnetic Environment

Assessment of electromagnetic environment similarity can be measured by Similarity Degree [4]. The general calculation method of Similarity Degree is:

First, the similarity of every single electromagnetic signal in complex electromagnetic environment should be calculated, and similarity factors in frequency domain, time domain, power domain, modulation domain, and polarization domain should be taken into account.

Then, the similarity of single electromagnetic signal should be weighted to calculate the similarity of threatening electromagnetic environment and background electromagnetic environment respectively.

At last, according to the response characteristics of GNSS receiver, the similarity of threatening electromagnetic environment and background electromagnetic environment should be weighted to evaluate the similarity of complex electromagnetic environment.

The specific calculation method of Similarity Degree will be discussed in following papers.

4.3 Contents of Complex Electromagnetic Environment Adaptability Test

4.3.1 Evaluation Indexes of Electromagnetic Environment Adaptability

According to the mission of GNSS receiver, evaluation of complex electromagnetic environment adaptability should focus on the accuracy and timeliness in providing position information, speed information, time information and other services. Considering the short message communication and location report service of BD receivers, and the current trend of integration of GNSS system with satellite communication and satellite search and rescue, it is necessary to verify the coordination of GNSS receivers.

(1) Indexes related to accuracy

Indexes reflecting the accuracy of GNSS receivers in complex electromagnetic environment mainly include Positioning Accuracy, Rate Accuracy, Timing Accuracy, RAIM (receiver autonomous integrity monitoring) capability. Positioning Accuracy, Rate Accuracy and Timing Accuracy are used respectively to test the positioning capability, velocity measurement capability, timing capability of GNSS receivers in complex electromagnetic environment. RAIM capability is used to test the capability of GNSS receiver in complex electromagnetic environment to provide timely alarm when positioning error exceeds the permissible threshold.

(2) Indexes related to timeliness

Indexes reflecting the timeliness of GNSS receivers mainly include Reaction Time and Service Continuity. Reaction Time include First Start-up Time (according to the application requirement of GNSS receiver, including cold start, warm start and hot start) and Recapture Time after loss of lock, which are used to test capability of the GNSS receiver to provide timely service in complex electromagnetic environment. Service Continuity is the time probability of providing continuous satisfying positioning, rate measuring and timing service in specified time. It is used to test the capability of GNSS receiver to provide continuous service (meeting relevant needs) in complex electromagnetic environment.

(3) Indexes related to coordination

Indexes reflecting the coordination of GNSS receivers mainly include Command-and-control Capability, and Communication Capability. Command-and-control Capability refers to the management and monitoring capability. Communication Capability refers to information transfer ability between GNSS receiver and other users.

Evaluation indexes of complex electromagnetic environment adaptability of GNSS receivers are shown in Fig. 4. These indexes are generally tested in different time periods under the constructed complex electromagnetic environment.

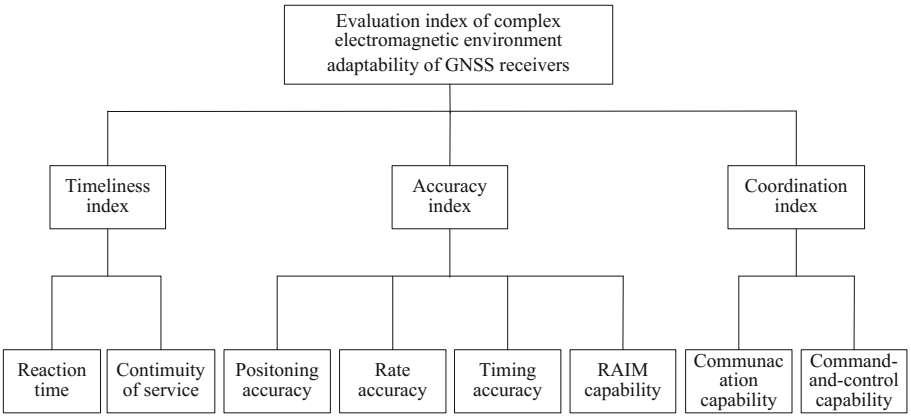

Fig. 4. Evaluation indexes of GNSS receiver complex electromagnetic environment adaptability

4.3.2 Evaluation Method of Electromagnetic Environment Adaptability

Evaluation of complex electromagnetic environment adaptability is final purpose of complex electromagnetic environment adaptability test. For GNSS receivers, indexes selected should be closely related to the ability to fulfill its mission. Evaluation of complex electromagnetic environment adaptability of GNSS receivers should be done through weighted evaluation of single index.

For example. For a certain GNSS receiver, the task requires that the Positioning Accuracy should not be less than 10 m, Recapture Time should not be more than 10 s, and Service Continuity probability should not be less than 95%. In test electromagnetic environment, Positioning Accuracy of the GNSS receiver is 30 m, Recapture Time is 20 s, and Service Continuity probability is 30%. According to the mission requirement, Positioning Accuracy, Recapture Time and Service Continuity are affected in different degree. The effects are severe (value 0.8), moderate (value 0.5) and severe (value 0.8) respectively. The weights are 0.4, 0.3, and 0.3 respectively. Then the complex electromagnetic environment adaptability coefficient of this GNSS receiver is $(1-0.8)\times 0.4+(1-0.5)\times 0.3+(1-0.8)\times 0.3\approx 0.29$, which means Unavailability (when the coefficient is below 0.5, it means Unavailability).

5 Summary

Aiming at the problems that need to be solved urgently in complex electromagnetic environment adaptability test of GNSS receivers, this paper analyses the influence of complex electromagnetic environment on GNSS receivers acquisition and tracking links, puts forward the correlation-based construction method of complex electromagnetic environment, the similarity-based evaluation method of experimental electromagnetic environment, and designs the adaptability evaluation indexes system of GNSS receivers based on Accuracy, Timeliness and Coordination. The above ideas and methods can provide reference for further research on the electromagnetic environment adaptability test of GNSS receivers.

References

1. Xie G (2015) Principles of global navigation satellite system-GPS, Glonass and Galileo systems. Electronics Industry Press
2. Xie G (2012) GPS principle and receiver design. Electronics Industry Press
3. Sun G, Liu S, Chen J (2006) The effect of battlefield electromagnetic environment on information warfare. Mil Oper Res Syst Eng 20(3):43–47
4. Tang C, Liu P (2007) Analysis of complex electromagnetic environment in informationized battlefield. Defense Technol 28(8):25–28
5. Li L, Sun Z, Li L et al (2009) Research on complex electromagnetic environment in equipment shaping test. J Coll Equip Command Technol 20(2):73–76
6. Liang G, Zhang H, Hao G et al (June 2016) Cognize on the test of complex electromagnetic environment adaptability. In: The 2016 national electronic warfare academic conference symposium, pp 1608–1615

7. Chen G, Liu C, Du L et al (2011) Monitoring and analysis method for complex electromagnetic environment of global navigation satellite system. Glob Position Syst 36 (4):1–5
8. Tan S, Yang J, Ming D et al (2018) Theory and application of simulation and test system for complex electromagnetic environment of satellite navigation terminal. Science Press, Beijing
9. Zeng Q, Liu J, Hu Q et al (2011) Research on Beidou system and GNSS multi-constellation integrated navigation performance. Glob Position Syst 36(1):53–57
10. Liang G, Chen J, Wang D (2006) Anti-jamming performance analysis of GPS/SINS combination. Radio Eng 36(10):36–39
11. Zhang C (2013) Analysis and research on anti-jamming performance of Beidou second generation navigation signal. Xi'an University of Electronic Science and Technology
12. Wu C, Peng Y, He Z et al (2014) Overview of satellite navigation jamming and anti-jamming technology. Navig Position Timing 1(2):36–39
13. Xu J, Yao R, Chen Y et al (2015) Research on anti-jamming technology of cascaded navigation in frequency domain and space-time domain. J Missiles Guidance 35(2):137–140
14. Wang J (December 2007) Research on accuracy and perfection technology of GPS/Beidou dual-mode application system. National University of Defense Science and Technology
15. Si D, Wang H, Zhang M (May 2012) Application status and development suggestions of Beidou navigation system. China Satellite Navigation Academic Annual Meeting
16. Liu K, Liu H (2005) Application and trend research of GPSINS integrated guidance technology in modern warfare. China Aerosp 09:35–37
17. Tian L, Yang J, Hu W (2010) Application of GPS in high dynamic precision strike weapon. Winged Missile 01:70–74
18. Kaplan ES (2005) Understanding GPS principles and applications, 2nd edn. Artech House Publishers, Norwood
19. Rong J, Tang M, Wang X et al (2014) Realistic construction method of complex electromagnetic environment in battlefield. Aerosp Electron Countermeas 30(1):24–28
20. You J, Lai L (2014) Simulation technology of complex electromagnetic environment in electronic warfare. J China Acad Electron Sci 9(5):517–520
21. Guo S, Dong Z, Liu M et al (2013) Research on simulation technology of complex electromagnetic environment. Electron Meas Technol Abroad 32(7):21–25

Impact of the Ionosphere and GPS Surveying Caused by Coronal Mass Ejection on May 23 2017

Teng Peng[1(✉)], Dangwei Wang[1,2,3], Xiaolin Jia[2(✉)], and Yuanzheng Ma[3(✉)]

[1] Xi'an Unistrong Defense Technology Co., Ltd., Xi'an 710077, Shaanxi, China
2298452014@qq.com
[2] Xi'an Research Institute of Surveying and Mapping, Xi'an 710054, Shaanxi, China
13891907401@139.com
[3] The Second Topographic Surveying Brigade of Ministry of Natural Resources, Xi'an 710054, Shaanxi, China
mayzhl992@126.com

Abstract. We analyzed the disturbance anomaly in the global ionosphere TEC caused by Coronal mass Ejection on May 23, 2017, based on the GPS ionosphere detection technology. Affected by the Coronal mass Ejection toward Earth, The ionosphere TEC first has a disturbance anomaly on May 23 2017. 20 o'clock. Because of the earth rotation, the ionosphere TEC anomaly area would move to the west along with the sun point-blank point. The ionosphere TEC disturbance maximum is 21TECU. In addition, we analyzed the influence of the Coronal mass Ejection on the correction effect and positioning accuracy of the ionosphere model of the IGS GPS monitoring station. The result shows that the Coronal mass Ejection has the greatest impact on the correction of the GPSK8 model, and the impact on the positioning accuracy of monitoring stations are 2–5 m.

Keywords: CME · Ionosphere TEC · BDSGIM · KLOBUCHAR

1 Introduction

Since the first discovery of the Coronal Mass Ejection (CME) in 1971, it has been gradually recognized that CME is a frequent and intense phenomenon in the solar atmosphere. The CME event is not only a transient phenomenon of the sun's Sundial, but also related to the long-term evolution of the sundial [1, 2]. The Geomagnetic storm caused by the coronal mass ejection will cause the magnetic layer to compress and deform and cause abnormal ionospheric disturbance. The occurrence of ionospheric storms will have a serious impact on the accuracy of communication systems, space vehicles and GNSS navigation and timing. Therefore, studying the anomalies of the ionosphere during the special space environment has an important role.

Due to the emergence of technologies such as the Global Positioning System (GPS), the spatiotemporal distribution of the global ionosphere TEC during magnetic

J. Sun et al. (Eds.): CSNC 2019, LNEE 563, pp. 325–336, 2019.
https://doi.org/10.1007/978-981-13-7759-4_29

storms can be accurately detected. It has been studied to use the TEC data obtained by GPS to analysis the changes of the ionosphere during a magnetic storm. Xia et al. [3] used the TEC data obtained by GPS during the two large magnetic storms in July 2000 and October 2003 to explore the response characteristics of the low-latitude ionosphere TEC in East Asia. Xu et al. [4] studied the response characteristics of ionospheric TEC in Wuhan and its adjacent areas during the strong magnetic storm in November 2004. Xu et al. [5] analyzed the impact of solar storm on the ionosphere and GPS measurements on August 1, 2010. The results shows that the impact of the M3.2 flare event on the high-order terms of the ionosphere reaches the centimeter level.

Affected by the Coronal Mass Ejection on May 23, 2017, a large number of low-energy particles arrived at the Earth on May 27, 2017. The southward component of the interplanetary magnetic field is at least −20 nt. after 2 h, a medium magnetic storm appeared, and then developed into a large magnetic storm. During the period of 27–28 days, the geomagnetic field reached the level of large magnetic storm for 3 h, the medium magnetic storm level reached 9 h, the small magnetic storm level reached 3 h, and the active level reached 3 h. This paper uses ionosphere detection technology to analyze the abnormal effects of this magnetic storm on the global ionosphere TEC. Analysis of the correction effect of the model during the magnetic storm days of five IGSGPS monitoring stations in China, and analysis the pseudo-single point positioning accuracy of the BDS B1I frequency.

2 GNSS Global Broadcast Ionosphere Model

2.1 GPS Global Broadcast Ionosphere Model

The GPS system uses the Klobuchar8 parameter model (hereinafter referred to as GPSK8). This model was proposed by KLOBUCHAR in 1987 [6]. This model sets the night time ionospheric delay to a constant of 5 ns. Cosine function for the inter-day ionospheric delay. The amplitude and period can be calculated from the 8-parameter calculations broadcast by the navigation message. A detailed user algorithm for the GPSK8 model can be found in the literature [6, 7].

2.2 Galileo Global Broadcasting Ionosphere Model

The Galileo system uses the NeQuick model as a model for ionospheric delay correction, the NeQuick2 model is currently used. It is based on the NeQuick1 model to improve the analytical equations of the bottom and top ionosphere. Making NeQuick2 calculate the electron density value closer to the measured value than NeQuick1 [8]. Specific input and output parameter calculations for the NeQuick2 model are detailed in Ref. [8, 9].

2.3 Beidou Global Broadcast Ionosphere Model

The BeiDou Global Ionospheric Delay Correction Model (BDGIM) combines the periodicity of the ionosphere with the improved spherical harmonic function to solve the global ionospheric model for single-frequency users [10]. The coefficients of the BDGIM model are divided into low-order spherical harmonic function coefficients and high-order

spherical harmonic function coefficients. The low-order terms have a great influence on the ionospheric TEC. This part has 9 parameters in the navigation message B-CNAV1 subframe 3 and B-CNAV2. Type 30 in the broadcast, The higher-order coefficients describe the small-scale variation of the ionospheric TEC, Therefore, it is given in the ICD as a non-casting coefficient [11, 12], which can be calculated and used by the user according to the given method. Calculate the use according to the given method. For the user to calculate the use according to the given method. The basic steps for calculating the ionosphere delay correction for the BDSGIM model can be found in [13, 14].

3 Global Ionospheric TEC Disturbance Anomaly Analysis

Based on the solar activity provided by the Space Environment Forecasting Center of the Chinese Academy of Sciences and the space weather weekly report provided by the China Meteorological Administration, the CME event occurred on May 23, 2017, affected by the high-speed flow of the tunnel, affected by the Earth, on May 27 A magnetic storm occurred around 20 o'clock on the day, and a magnetic storm occurred on the 28th. The geomagnetic activity on 29–30 was calm to perturbation. 2017-05-27-29 Three-day KP index, DST index results information as shown in Figs. 1 and 2:

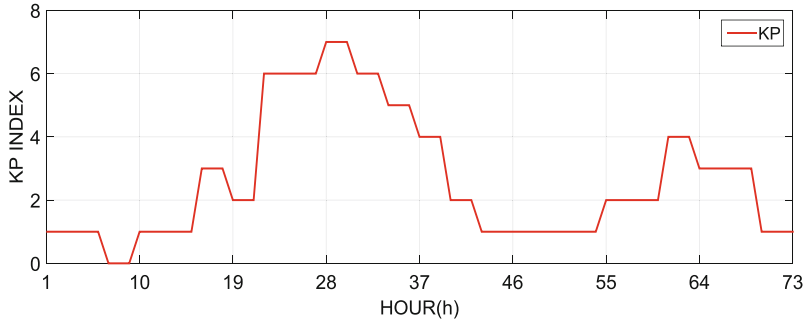

Fig. 1. Geomagnetic KP index from May 27 to 29

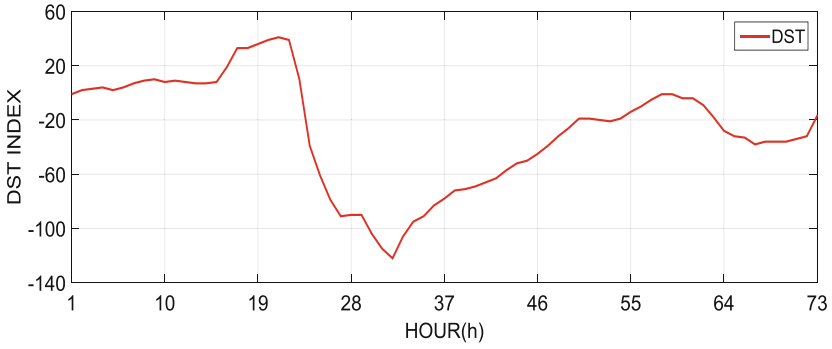

Fig. 2. Geomagnetic DST index from May 27 to 29

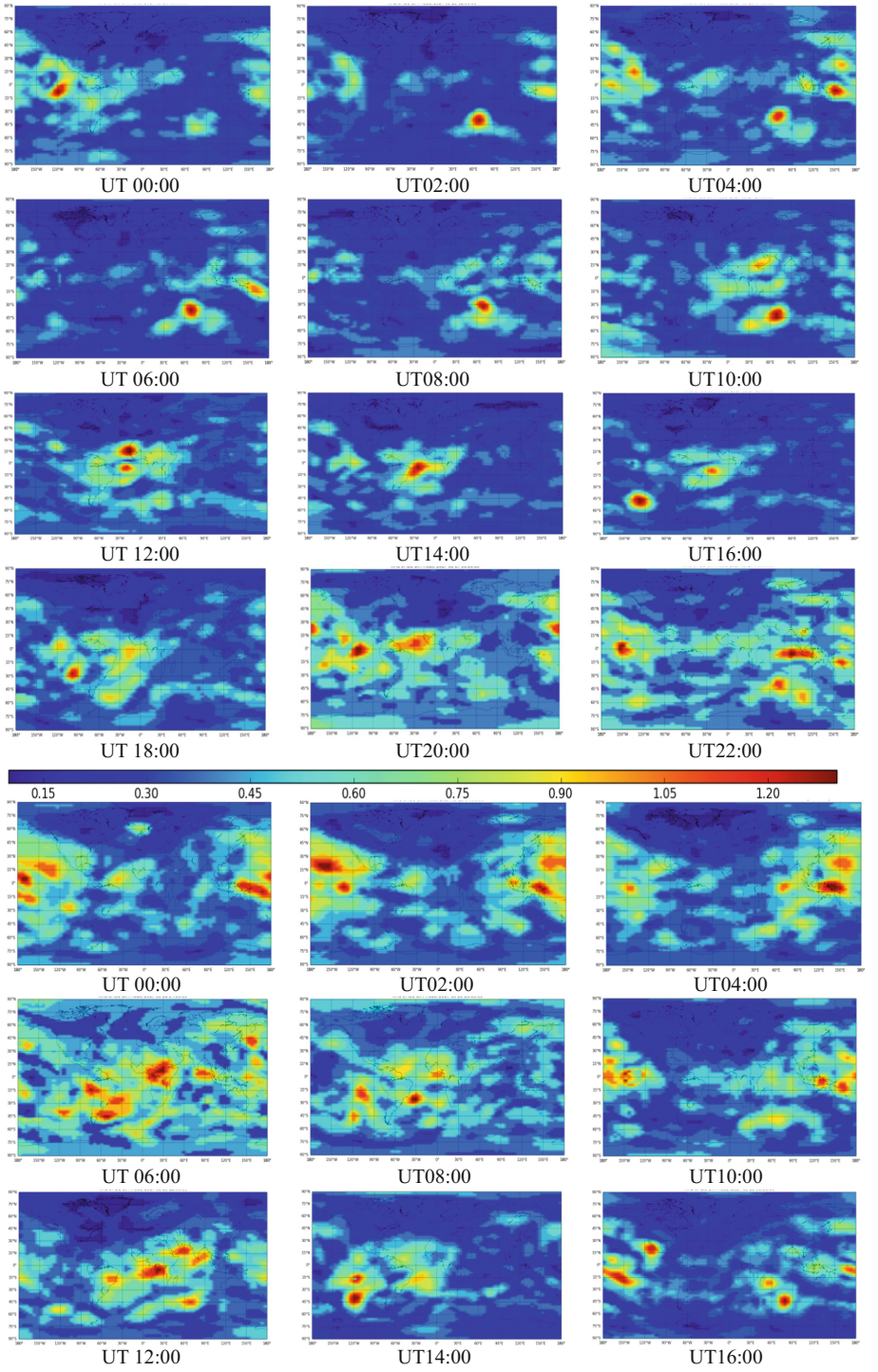
UT 00:00
UT02:00
UT04:00
UT 06:00
UT08:00
UT10:00
UT 12:00
UT14:00
UT16:00
UT 18:00
UT20:00
UT22:00
0.15
0.30
0.45
0.60
0.75
0.90
1.05
1.20
UT 00:00
UT02:00
UT04:00
UT 06:00
UT08:00
UT10:00
UT 12:00
UT14:00
UT16:00

Fig. 3.

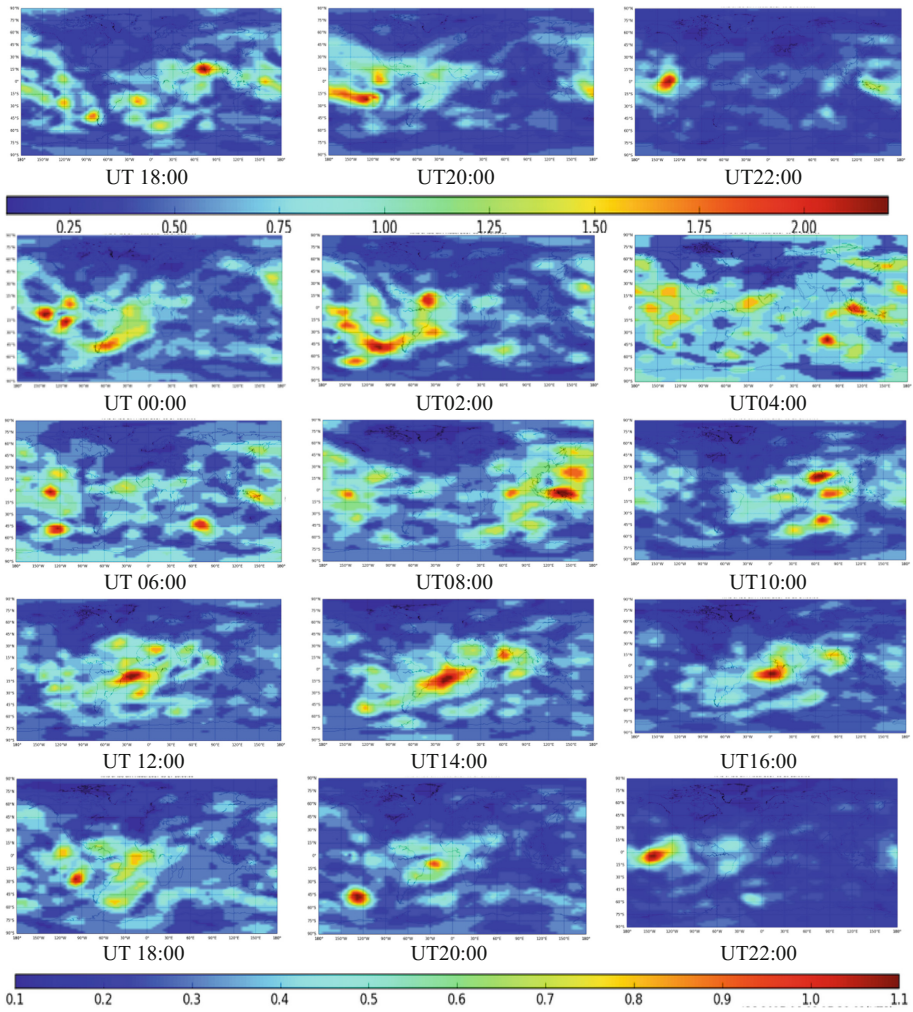

Fig. 3. (*continued*)

Using IGS ionospheric grid products, the TEC data of May 24–26, 30–31, and five days are taken as the reference value, the difference between the TEC observations during the magnetic storm day is obtained, and the ionospheric TEC difference information of each grid point is obtained. Then, fitting is performed to obtain TEC perturbation information at each moment during the magnetic storm day. Figure 3 shows the variation of the ionospheric TEC anomaly disturbance from May 27 to May 29 at intervals of two hours.

The information comparison of the ionospheric TEC disturbance during the magnetic storm day can be seen:

(1) Although there was a flare incident on the day of 05–23, the global ionosphere TEC did not disturb the abnormal situation. Mentioned in reference [5], two flares of grades M5.1 and M4.6 have less impact on global TEC than 1TECU, the X-ray flare event did not occur during the coronal mass ejection, which is difficult to distinguish from the effects of the ionospheric TEC obtained by GPS inversion.
(2) On May 27th, UT 20:00, significant ionospheric TEC disturbance anomalies first appeared in the Americas and mid-low latitudes, and the maximum value exceeded 12TECU. At this time, the sun directly hits North America (about 12:00 local time), and the low-energy particles generated by the coronal mass ejection reach the earth, directly affecting the ionospheric TEC information in the local area of the Americas.
(3) At UT0:00 on May 28, the anomalous disturbance area of the ionospheric TEC further expanded and moved westward with direct sunlight. At 06 o'clock on the 28th, the disturbance area reached the maximum, and the ionospheric disturbance in the central area was the largest 21TECU. It can be seen from the figure (b) that after the UT 10:00 time, the ionospheric TEC disturbance amount begins to weaken, and the abnormal region gradually disperses. This TEC abnormal disturbance amount lasts for 12 h.
(4) At UT12:00 on May 29, In the equatorial region, the ionospheric TEC increases again, and the affected area is concentrated. The geomagnetism reaches the level of small magnetic storm. This is because the new wave of low-energy particles interferes with the ionosphere in the equatorial region after reaching the earth. Outliers and abnormal regions are gradually reduced, after 5–30, the global ionospheric TEC did not exhibit TEC anomalous disturbance, indicating that the abnormal disturbance caused by the geomagnetic storm to the global ionosphere TEC is over.

In summary, the disturbance of the global ionospheric TEC to the CME event reached 21 TECU, mainly due to the upper boundary anomaly. Due to the influence of the Earth's rotation, the concentrated area where the ionospheric TEC anomalies occur will move westward as the sun's point directs. The abnormal concentration area is generally around 12:00 to 16:00.

4 Analysis of the Effect of Magnetic Storm on the Correction Effect of Monitoring Station Model and the Single Point Positioning of Pseudorange

4.1 Analysis of the Influence of Magnetic Storm on Model Correction Effect

On the magnetic storms on May 27th and 28th, the ionospheric forward disturbance was observed in Beijing station, and the critical frequency (f0F2) and electron content (TEC) of the ionospheric F2 layer were higher than the background value. In order to objectively reflect the impact of the magnetic storm on the correction effect of the model, Select 5 monitoring stations (URUM, BJFS, LHAZ, SHAO, TWTF distributed

in China) observation data from 2017-05-15 to 2017-05-31 (year 135–151), using the model correction rate (P) and root mean square errors (RMS) as statistical indicators of model correction effect. The formula is:

$$P = \sum_{i=1}^{n} (1 - \frac{|VTEC_{评估} - VTEC_{基准}|}{VTEC_{基准}}) / n$$
$$RMS = \sqrt{\sum_{i=1}^{n} (VTEC_{评估} - VTEC_{基准})^2 / n} \quad (1) \qquad (1)$$

In the formula, $VTEC_{评估}$ is the VTEC information is calculated using a user algorithm of three broadcast ionospheric models. $VTEC_{基准}$ is the VTEC information at the puncture point of the selected monitoring station.

The correction rate and RMS statistics of the URUM and BJFS stations are shown in Figs. 4 and 5.

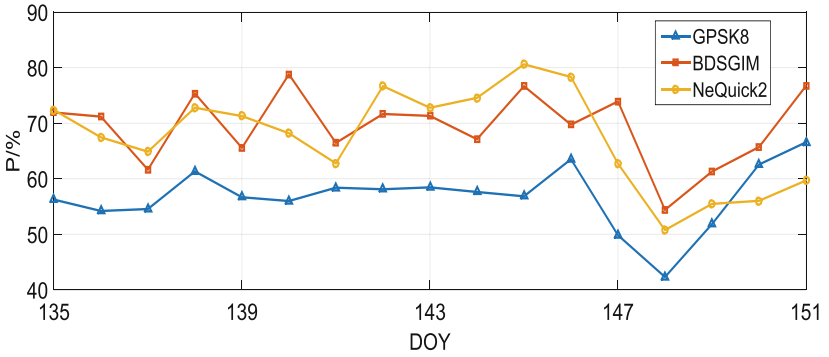

Figure (a) URUM station model correction rate

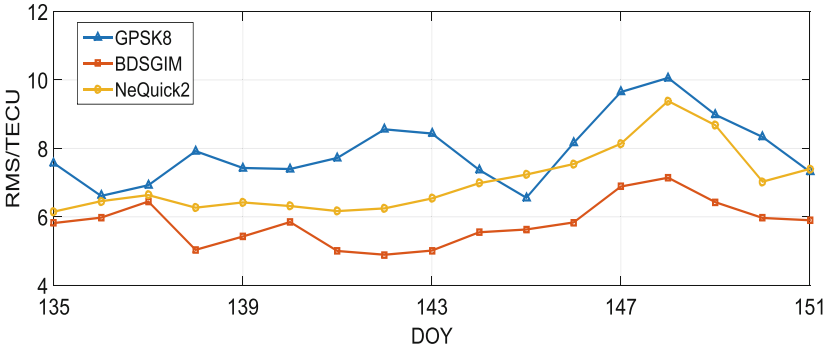

Figure (b) URUM station RMS statistics

Fig. 4. URUM station model correction effect statistics

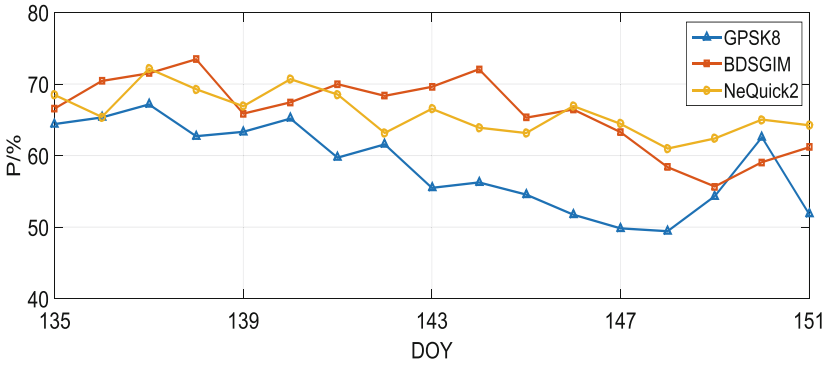

Figure (a) BJFS station model correction rate

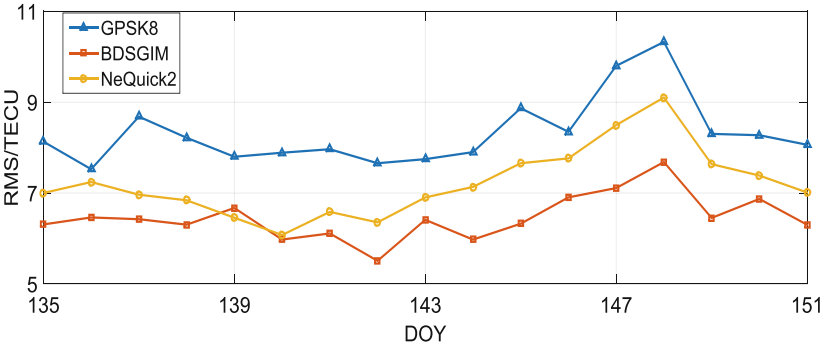

Figure (b) BJFS station RMS statistics

Fig. 5. BJFS station model correction effect statistics

It can be seen from the statistical results:

(1) In terms of correction rate: magnetic storm (annual accumulation date 147–148) has a certain impact on the correction rate of the three models, but the impact is different. In the comparison of the three models, the magnetic storm has the greatest impact on the correction rate of the GPSK8 model, and the correction rate is less than 50%.
(2) In terms of root mean square error: compared with the quiet period, the magnetic storm has a certain influence on the RMS of the three models. In the comparison of the three models, the magnetic storm has the greatest influence on the GPSK8 model and the least impact on the BDGIM model.

It shows that the GPSK8 model is slightly worse than the BDGIM and NeQuick2 models in the adaptability of the magnetic storm.

4.2 Analysis of the Influence of Magnetic Storm on Single Point Positioning Accuracy

The magnetic storm will cause certain interference to the satellite signal, increasing the ranging error between the station stars, resulting in inaccurate position information calculated by the receiver. In order to analyze the influence of magnetic storm on the

positioning accuracy, the observation data and ephemeris data during the magnetic storm days of five monitoring stations were selected, and the accuracy of Beidou B1I single frequency positioning was analyzed by RTKLIB software. The correction of the ionosphere is corrected by the BDGIM model, and the troposphere is corrected by the

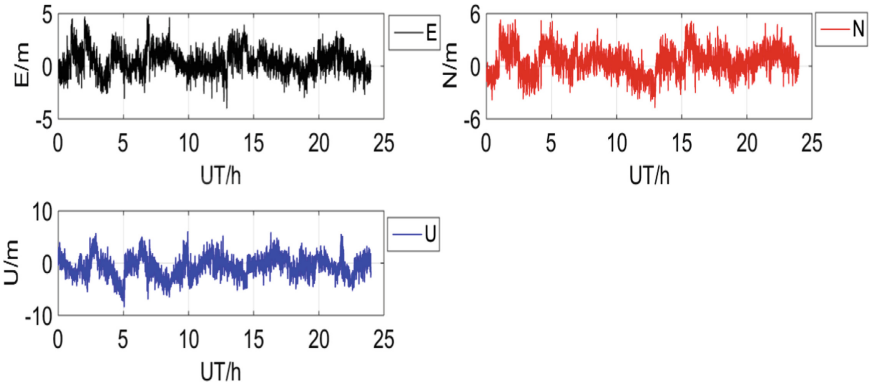

Figure (a) URUM station B1I positioning result information

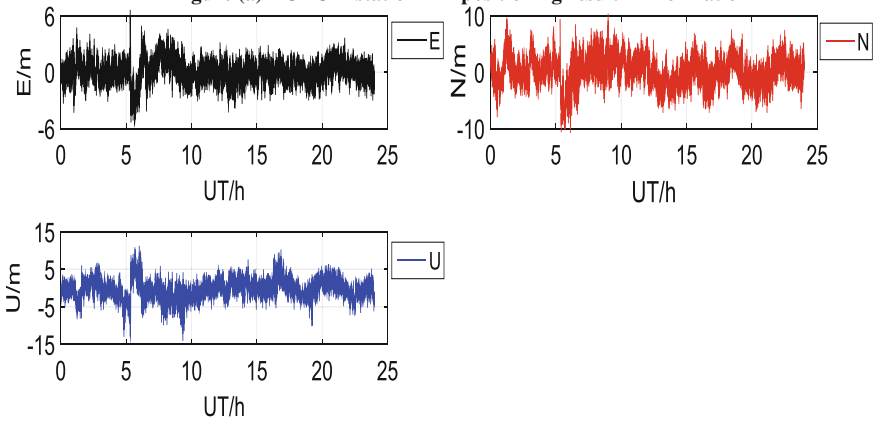

Figure (b) SHAO station B1I positioning result information

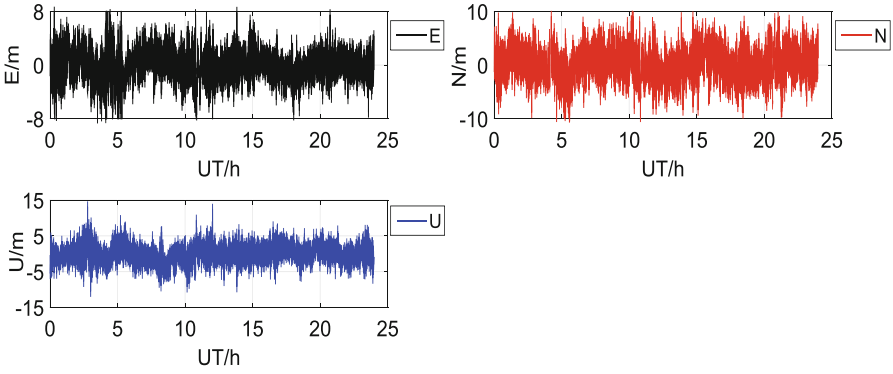

Figure (c) BJFS station B1I positioning result information

Fig. 6. B1I positioning accuracy statistics during the selected station magnetic storm day

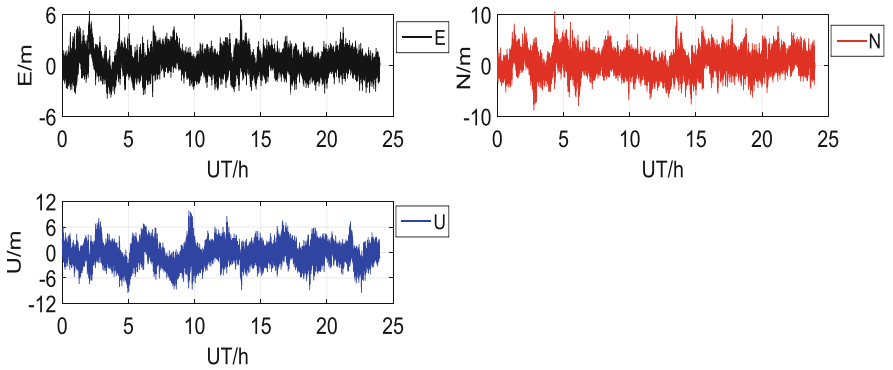

Figure (d) LHAZ station B1I positioning result information

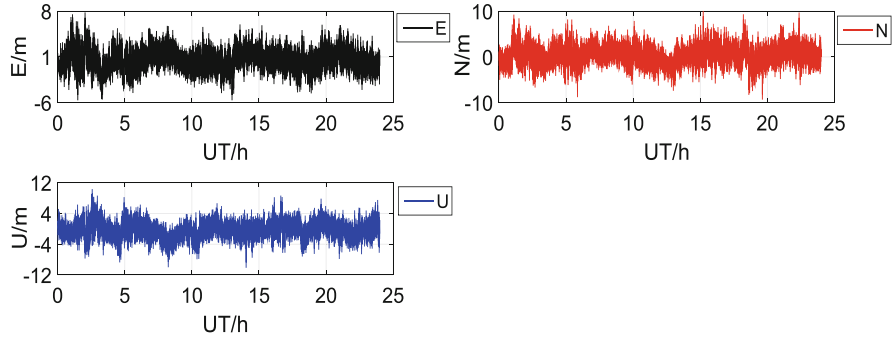

Figure (e) TWTF station B1I positioning result information

Fig. 6. (*continued*)

Saastamoinen model. The station information given in the SNX file is used as the "reference value". In the analysis, the results of the calm period of May 16 (136 days of the year) were also selected as the comparison. The BDS B1I single-frequency single-point positioning result of the selected station during the magnetic storm day is shown in Fig. 6 (Table 1):

Table 1. Analysis of positioning accuracy on May 16

测站	RMS		
	E	N	U
URUM	3.442	3.618	4.019
BJFS	3.626	3.766	4.992
SHAO	3.112	3.821	4.843
LHAZ	3.011	4.087	4.125
TWTF	3.864	3.829	5.971

The accuracy of the BDS B1I single-frequency positioning accuracy in the E and N directions is better than 8 m in the selected station during the magnetic storm day, and the overall accuracy in the U direction is better than 15 m. Compared with the quiet period, the influence of the magnetic storm on the positioning accuracy of the station is 2–5 m.

5 Conclusion

Taking the geomagnetic storm induced by the Coronal Mass Ejection on May 23, 2017, this paper analyzes the abnormal effects of magnetic storm on the global ionosphere TEC, and can get the following conclusions:

(1) The magnetic storm has a certain disturbance to the global ionospheric TEC. From UT 20:00 on May 5–27, the ionospheric TEC disturbance in the middle and low latitudes has a significant increase, and the maximum value exceeds 12 TECU. 05-28 06:00 The affected area reaches its maximum, and the maximum value of its central area is 21TECU.
(2) It can be seen from the comparison of the correction effects of the model before and after the magnetic storm day that the magnetic storm has a certain influence on the correction effect of the broadcast ionospheric model, but the impact is different. In the overall comparison, the correction effect of the GPSK8 model has the greatest influence, and the correction effect of the BDSGIM model is minimal, indicating that the BDGIM model is slightly better than the GPSK8 model and the NeQuick2 model in the adaptability of the magnetic storm.
(3) Compared with the quiet period, the influence of the magnetic storm on the pseudorange positioning accuracy of the BDS B1I frequency point is 2–5 m.

Acknowledgement. Thanks to the documentation provided by the Space Environment Forecast Center of the Chinese Academy of Sciences, and the observation data and grid products provided by the IGS monitoring station.

References

1. Yao Y-B, Shao C-W, Shi S-B, Li W-H, Xu C, Liu Y-Y (2005) Primary analysis of CME associated with the radio emission during October 22 to November 03, 2002. Astron Res Technol 02:105–113
2. Song W-L, Sou Y-M, Zhen W-M, Liu D (2011) Analysis of solar storm effects on GNSS. GPS 36(05):11
3. Xia CL, Wan WX, Yuan H et al (2005) Analysis of the intense magnetic storm of July, 2000 and of October, 2003 using the technique for now casting of GPS TEC data. Chin J Space Sci 25(4):259–266
4. Xu J-S, Zhu J, Cheng G-H (2006) GPS observation of ionosphere effects of the major storm of Nov. 7–10, 2004. Chin J Geophys 49(4):950–956 (in Chinese)
5. Xu CQ, Yao YB, Zhang B, Yan F (June 2013) Geomatics and information science of Wuhan University, vol 38, no 6

6. Klobuchar JA (1987) Ionosphere time delay algorithm for single frequency GPS use. IEEE Trans Eros Pace Electron Syst 3(3):325–331
7. Yuan YB (2002) Study on theories and methods of correcting ionospheric delay and monitoring ionosphere based on GPS. Institute of Geodesy and Geophysics Chinese Academy of Sciences
8. Li S-J (2015) Performance evaluation of NeQuick2 ionosphere model. Eng Surv Mapp 24(1)
9. Wang J, Dang YM, Xue SQ (2007) Application of NeQuick ionospheric model in China. Sci Surv Mapp 32(4):38–40
10. Li ZS (2012) Research on GNSS/Compass ionosphere delay correction and TEC monitor theory and method. Institute of Geodesy and Geophysics Chinese Academy of Sciences, Wuhan
11. (2016) Bei Dou satellite navigation system spatial signal interface control file public service signal (2.1) China Navigation Satellite Management Office, November 2016
12. (2017) Bei Dou satellite navigation system spatial signal interface control file public service signal B1C (1.0) China Navigation Satellite Management Office, November 2017
13. Wu X, Hu X, Wang G et al (2013) Evaluation of COMPASS Ionospheric model in GNSS positioning. Adv Space Res 51(6):959–968
14. Wang NB (2016) GNSS differential code deviation processing method and global broadcast ionospheric model research. Institute of Geodesy and Geophysics Chinese Academy of Sciences, WuHan

Separation and Evaluation Method of GNSS Authorized Service Signals

Tao Yan(✉), Ying Wang, Guoyong Wang, Bo Qu, Wenying Lei, and Yansong Meng

China Academy of Space Technology (Xi'an), Xi'an 710000, China
iamyantao@126.com

Abstract. The modernized global navigation satellite system (GNSS) provides the open service (OS) signal and authorized service (AS) signal for users. Each service signal includes a data component and a pilot component. All the signal components need to be combined into a composite signal for broadcast. To verify whether the transmitted signal generated by satellite payload can meet the design requirements, the signal in space is collected by high gain antenna, and the signal quality is evaluated. However, the spreading spectrum code sequences of AS signal are unknown. In order to evaluate the signal quality of AS signal, the code sequences of AS signal have to be recovered. The current methods are based on the following assumptions: the expression of the constant envelope composite signal or the power/phase relationship of AS signal is known. Nevertheless, the above assumptions may be not satisfied. This paper studies the code sequences estimation method when the expression of the constant envelope composite signal and the power/phase relationship of AS signal are unknown. The proposed method treats the code sequences as the optimized variables. The utility function to obtain the maximum cross-correlation value is exploited. The optimization problem is solved by the binary genetic algorithm. On this basic, the separation method of AS signal component is presented. The correlation function of AS signal is obtained, and the correlation characteristics of AS signal component are evaluated. The performance of the proposed method is verified by the theoretical analysis and numerical simulation. Finally, based on the proposed method, we evaluate the signal quality of Galileo E1 signal collected by a 6 m antenna, which shows the effectiveness of the proposed method.

Keywords: Authorized service signal · Code sequence recovery · Signal quality · GNSS

1 Introduction

In Global Navigation Satellite System (GNSS), the quality of signal-in-space (SIS) has a significant effect on the system performance. To evaluate the signal quality generated by satellite payload, each GNSS develops and builds the signal quality monitoring and assessment system. To ensure the analysis precision, these systems usually exploit the high gain antenna to collect signal, such as the 47 m dish antenna at Stanford [1], the 30 m dish antenna of DLR [2] and the 40 m antenna of National Time Service Center in Chinese Academy of Sciences [3].

J. Sun et al. (Eds.): CSNC 2019, LNEE 563, pp. 337–346, 2019.
https://doi.org/10.1007/978-981-13-7759-4_30

As is known, the modernized GNSS signals provide the open service (OS) and authorized service (AS) simultaneously [4]. Each service signal includes a data component and a pilot component [5]. For signal generation, to maximize the efficiency of power amplifier and reduce the signal distortion, it is necessary to combine multiple signal components into a constant envelope composite signal [6]. The pseudo random noise (PRN) codes of open service signals can be obtained from the interface control document (ICD) [4, 7], while the PRN codes of AS signals are encrypted, such as the M code in GPS [8] and public regulated service (PRS) signal in Galileo [9]. In order to analyze the AS signals, we need to recover the unknown PRN code sequence.

Recently, several works about PRN code recovery have been done. Reference [10] studies the recovery method of AS signals with different constant envelope multiplexing schemes, including the QPSK, CASM/Interplex and POCET. The demodulation thresholds of different bit error rate (BER) are analyzed. However, in order to obtain the AS signals, the constant envelope multiplexing scheme, i.e. the analytical expression should be known. In this case, the recovery method of AS signals is equivalent to the demodulation of data bit. Reference [11] analyzes the CASM signal on L1 frequency points for GPS BIIF-5 satellite, and adopts the matched filtering technology to recover the PRN codes of P(Y) and M code. This method generates locally the four combinations of P(Y) and M code during one chip, and then correlates them with the received signal during one chip. The combination with the maximum correlation value corresponds to the PRN code combination. This method can recover the PRN code chip by chip in the case that the power ratio and phase relationship between signal components are known.

Generally speaking, the modulation types of AS signals are known, but the constant envelope multiplexing scheme is unknown. Moreover, the power ratio between signal components may change with time [12]. This paper studies the separation method of AS signal when the expression of the constant envelope composite signal and the power/phase relationship of AS signal are unknown. The proposed method includes mainly three steps. Firstly, The OS signal component is acquired and tracked, and then the received composite signal is converted into the baseband signal. Secondly, the baseband signal is segmented in time domain according to the chip width of AS signal component. Then each segmentation is correlated with the modulated symbol of AS signal, and the correlation values during one chip are obtained. Finally, the code sequences of AS signal are treated as the optimized variables. The object function is to maximize the cross-correlation value during one integration period. The PRN code sequence is estimated based on the binary genetic algorithm.

This paper first presents the signal model and problem formulation. Then, the separation method of AS signal is proposed. The performance of the proposed method is analyzed by simulation. Finally, based on the proposed method, we evaluate the signal quality of Galileo E1 signal collected by a 6 m antenna. The correlation function and s-curve bias (SCB) of AS signal component are presented.

2 Signal Model and Problem Formulation

2.1 Signal Model

The baseband expression of the constant envelope multiplexing signal can be given by [6]

$$s(t) = \sum_{n=1}^{N} A_n e^{j\theta_n} s_n(t) + IM(t) \tag{1.1}$$

where A_n and θ_n are the amplitude and phase of the nth signal component respectively. $IM(t)$ is the inter-modulation (IM) term. N is the total number of signal component. $s_n(t)$ is the nth signal component, which is expressed as

$$s_n(t) = \sum_{l=0}^{L_n-1} c_{l,n} p_n\left(t - l \cdot T_{c,n}\right) \tag{1.2}$$

where ignoring the navigation message data. $p_n(t)$ is the modulated symbol of the nth signal component, which is generally known. $\{c_{l,n}\}$ is the PRN code sequence of the nth signal component, and the value of the nth signal component is 1 or −1.

In general, the power of IM term is lower than that of useful signal terms. Considering the orthogonality of PRN code sequences, all the signal components are uncorrelated, i.e.

$$\frac{1}{T_p}\int_{T_p} s_n(t) s_m(t) dt = 0, \ m \neq n \tag{1.3}$$

2.2 Problem Formulation

The composite signal $s(t)$ includes OS signal components and AS signal components. These existing two methods to recover the AS signal components from $s(t)$. They are direct demodulation method and matched filtering method.

The direct demodulation method requires that the constant envelope scheme of GNSS signal is known. An example is shown in (1.4).

$$s(t) = A_1 s_1(t) + A_2(t) s_2(t) + j(A_3 s_3(t) + A_{IM} s_1(t) s_2(t) s_3(t)) \tag{1.4}$$

In this case, the AS signals can be obtained by demodulating the data bit. Assume that $s_1(t)$ is a OS signal component, $s_2(t)$ and $s_3(t)$ are AS signal components. In an ideal condition, $s_2(t)$ and $s_3(t)$ can be recovered by

$$\begin{aligned}\tilde{s}_2(t) &= \text{sign}\left(\frac{s_I(t) - A_1 s_1(t)}{A_2}\right) \\ \tilde{s}_3(t) &= \text{sign}\left(\frac{s_Q(t)}{A_3 + A_{IM} s_1(t) s_2(t)}\right) = \text{sign}\left(\frac{A_2 s_Q(t)}{A_{IM} s_1(t) s_I(t) + A_2 A_3 - A_1 A_{IM}}\right)\end{aligned} \tag{1.5}$$

where s_I(t) and $s_Q(t)$ are the real part and imaginary part of $s(t)$ respectively.

The matched filtering method generates locally all the combinations of AS signal components, and correlate these combinations with the received signal during one chip. The combination with the maximum correlation value is the estimated PRN code sequences. For example, there are only two AS signal components at in-phase branch, i.e.

$$s_I(t) = A_1 \sum_{l=0}^{L-1} c_{l,1} p_1\left(t - l \cdot T_{c1,n}\right) + A_2 \sum_{l=0}^{L-1} c_{l,2} p_2\left(t - l \cdot T_{c2,n}\right) \tag{1.6}$$

where $\{c_{l,1}\}$ and $\{c_{l,2}\}$ are the PRN code sequences of two AS signal components. During the nth chip, for different values of $c_{n,1}$ and $c_{n,2}$, the possible combinations are

$$\begin{aligned} s_{I,1}(t) &= A_1 p_1\left(t - l \cdot T_{c1,n}\right) + A_2 p_2\left(t - l \cdot T_{c2,n}\right) \\ s_{I,2}(t) &= A_1 p_1\left(t - l \cdot T_{c1,n}\right) - A_2 p_2\left(t - l \cdot T_{c2,n}\right) \\ s_{I,3}(t) &= -A_1 p_1\left(t - l \cdot T_{c1,n}\right) + A_2 p_2\left(t - l \cdot T_{c2,n}\right) \\ s_{I,4}(t) &= -A_1 p_1\left(t - l \cdot T_{c1,n}\right) - A_2 p_2\left(t - l \cdot T_{c2,n}\right) \end{aligned} \tag{1.7}$$

For clarity, let $T_{c1,n} = T_{c1,n} = T_c$. Generate locally these four combinations, and correlate them with $s_I(t)$ during the nth chip. Four correlation values are

$$A_1^2 c_{l,1} + A_2^2 c_{l,2}, A_1^2 c_{l,1} - A_2^2 c_{l,2}, -A_1^2 c_{l,1} + A_2^2 c_{l,2}, -A_1^2 c_{l,1} - A_2^2 c_{l,2} \tag{1.8}$$

In (1.8), the assumption $\frac{1}{T}\int_T p_1(t) p_2(t) = 0$ is adopted. The combination with the maximum correlation value is the estimated PRN code sequences.

The above two methods require that the constant envelope scheme, or the power ratio and phase relationship between signal components are known. The proposed method could estimate the PRN code sequences of AS signal components when the constant envelope scheme, the power ratio and phase relationship between signal components are unknown.

3 The Proposed Methods

3.1 Basic Principle

The proposed method is based on formula (1.3), i.e. all the signal terms are uncorrelated with each other. The PRN code sequences of AS signal components during one

period are treated as the optimized variables, and then are estimated by optimization algorithm. There are three steps in our method.

Step One. The OS signal component of the received composite signal is acquired and tracked firstly. After the tracking loop is stable, the received composite signal is down converted to baseband, i.e.

$$s(t) = \sum_{n=1}^{N} A_n e^{j\theta_n} s_n(t) + IM(t) = \sum_{n=1}^{N} A_n e^{j\theta_n} \sum_{l=0}^{L_n-1} c_{l,n} p_n\left(t - l \cdot T_{c,n}\right) + IM(t) \tag{1.9}$$

where L_n is the PRN code length of the nth signal component. $T_{c,n}$ is the chip duration of the nth signal component. Obviously, the OS signal components are known, and can be cancelled from the received composite signal. Assume that signal component n is OS signal.

Step Two. Correlate $s(t)$ with the modulated symbol $p_n(t)$ during every one chip duration. We can obtain L_n correlation values, i.e.

$$R_{l,n} = \frac{1}{T_{c,n}} \int_{(l-1)T_{c,n}}^{lT_{c,n}} s(t) p_n\left(t - lT_{c,n}\right) dt \approx A_n e^{j\theta_n} c_{l,n} + \frac{1}{T_{c,n}} \sum_{\substack{m=1, \\ m \neq n}}^{N} A_m e^{j\theta_m} c_{l,m} P_{m,n}^{l} \tag{1.10}$$

where

$$P_{m,n}^{l} = \int_{(l-1)T_{c,n}}^{lT_{c,n}} p_m\left(t - l \cdot T_{c,n}\right) p_n\left(t - lT_{c,n}\right) dt \tag{1.11}$$

Usually the power of IM terms is enough small and can be ignored.

If $\sum_{\substack{m=1, \\ m \neq n}}^{N} A_m e^{j\theta_m} c_{l,m} P_{m,n}^{l} = 0$ for all possible m, we have

$$R_{l,n} \approx A_n e^{j\theta_n} c_{l,n} \tag{1.12}$$

Step Three. Estimate the PRN code sequence and obtain the estimation $\left\{\hat{c}_{l,n}\right\}$. The object function is given by

$$\arg \max_{\left\{\hat{c}_{l,n}\right\}} \left| \sum_{l=0}^{N-1} R_{l,n} \hat{c}_{l,n} \right| \tag{1.13}$$

There are 2^N possible sequences for $\left\{\hat{c}_{l,n}\right\}$. We suggest that the optimization problem is solved by the binary genetic algorithm [13].

3.2 Application Cases

The preceding condition $\sum_{\substack{m=1,\\ m\neq n}}^{N} A_m e^{j\theta_m} c_{l,m} P^{l}_{m,n} = 0$ is only for the sake of convenience, and is a sufficient and unnecessary condition for the proposed method, which is difficult to be met. In fact, the essence of the proposed method is to find a PRN code sequence, which can achieve the maximum correlation value of AS signal. Consider the following four cases.

Case One. The proposed method is applicable for the case that the modulation types of all the AS signal components are different from each other. In this case, for any random code sequence $\{\hat{c}_{l,n}\}$, we have

$$\int_0^{L_n T_{c,n}} \sum_{l=0}^{L_n-1} \hat{c}_{l,n} p_n\left(t - l \cdot T_{c,n}\right) s_m(t) dt = 0,\ m \neq n \tag{1.14}$$

When the optimization result can ensure $\hat{c}_{l,n} \approx c_{l,n}$, $\left|\sum_{l=0}^{N-1} R_{l,n}\hat{c}_{l,n}\right|$ can reach the maximum value.

Case Two. The proposed method is also applicable for the case that the modulation types of two AS signal components are the same, but they are at orthogonal branches.

Case Three. The proposed method is theoretically applicable for the case that the modulation types of two AS signal components are the same, but they are not at orthogonal branches, and not at the in-phase branches.

Case Four. If two AS signal components have the same power, the same modulation types, and at the in-phase branches, as expressed as

$$s_I(t) = s_1(t) + s_2(t) \tag{1.15}$$

There are no methods to recover s_1(t) and $s_2(t)$, even in the ideal and noiseless environment. The reason is that the value of s_I(t) is unchanged when exchanging the values between $s_1(t)$ and $s_2(t)$. When estimating the $\{\hat{c}_{l,n}\}$, $\left|\sum_{l=0}^{N-1} R_{l,n}\hat{c}_{l,n}\right|$ can reach the maximum value. When the nth chip values of $s_1(t)$ and $s_2(t)$ are the same, $\hat{c}_{l,n}$ is the right value. When the nth chip values of $s_1(t)$ and $s_2(t)$ are different from each other, it is impossible to decide the value of $\hat{c}_{l,n}$ is right or not. Thus, there are only 75% chip signs in the optimized code sequences $\{\hat{c}_{l,n}\}$ are the same with the chip signs in $s_1(t)$ and $s_2(t)$.

4 Simulation Analysis

The performance analysis takes the Galileo E1 signal as an example. Galileo E1 provides one OS signal and one AS signal. The OS signal includes a data component E1B and a pilot component E1C, having the modulation types CBOC^{+}(6, 1, 1/11) and CBOC^{-}(6, 1, 1/11) respectively. The AS signal is denoted as E1A, whose modulation type is BOC$_c$(15, 2.5). The constant envelope scheme of Galileo E1 signal is given by [14]

$$s_{E1}(t) = c_{E1B}(t)\left(\sqrt{\tfrac{10}{11}}sc_{1,1}(t) + \sqrt{\tfrac{1}{11}}sc_{6,1}(t)\right) + c_{E1B}(t)\left(\sqrt{\tfrac{10}{11}}sc_{1,1}(t) - \sqrt{\tfrac{1}{11}}sc_{6,1}(t)\right) + j(\alpha s_{PRS}(t) - \beta s_{PRS}(t)c_{E1-D}(t)c_{E1-P}(t)) \tag{1.16}$$

where $c_{E1B}(t)$ and $c_{E1C}(t)$ are the PRN code sequences of E1B and E1C respectively. $sc_{1,1}(t)$ and $sc_{6,1}(t)$ are the square waveform subcarrier of BOC(1, 1) and BOC(6, 1) respectively. α and β are adjustable parameters. To meet the requirement of constant envelope, we have $\alpha \cdot \beta = 11/9$.

When $\alpha = 2$, the power ratio of E1A and E1B is 4:1 [15]. Using the proposed method to estimate the PRN code sequences of E1A signal, the BER performance in different carrier-to noise-density (C/N_0) conditions is shown in Fig. 1. The x axis is the C/N_0 of the composite signal $s_{E1}(t)$. The coherent integration time is 4 ms in simulation. It can be seen that BER is less than 0.001 when the C/N_0 is higher than 76 dB-Hz.

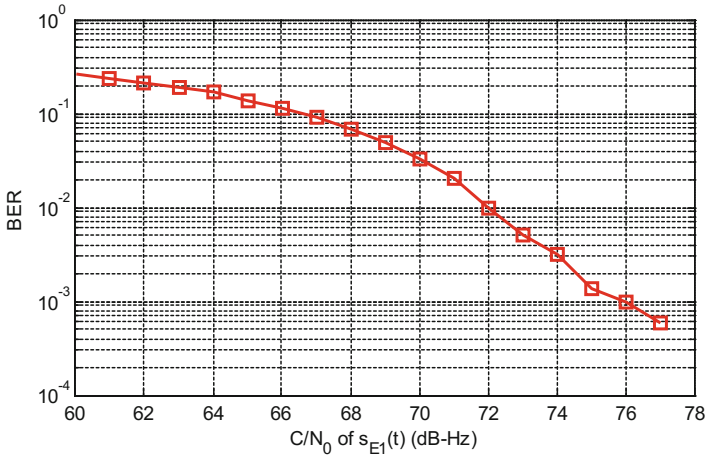

Fig. 1. BER performance

5 Experimental Results

To verify the effectiveness of the proposed method, we collected the Galileo E1 signal using a 6 m dish antenna. The satellite PRN code is CSAT0209. Figure 2(a) shows the 6 m dish antenna. Figure 2(b) is the power spectrum density (PSD) of the collected Galileo E1 signal. The signal is directly RF sampled with 650 MHz sampling rate.

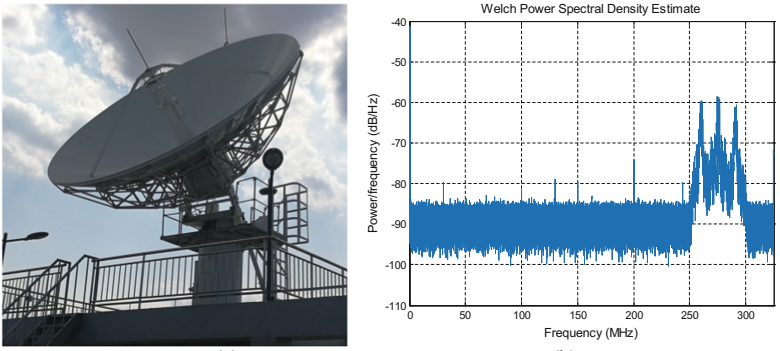

Fig. 2. Data collection. (a) 6 m dish antenna (b) Power spectrum density (PSD)

The E1B signal component is acquired and tracked using a software receiver. After the tracking loop is stable, the E1 signal is converted into baseband. Then the PRN code sequences of E1A signal are estimated. Finally, the signal quality, such as PSD, correlation functions and SCB are analyzed. The PSD is obtained using Welch method [15], the analysis result is shown in Fig. 3. It can be found that the real PSD agrees well with the theory PSD at the main-lobes, but there are some deviations at other frequency. The main reason is that there is strong RF interference around the antenna.

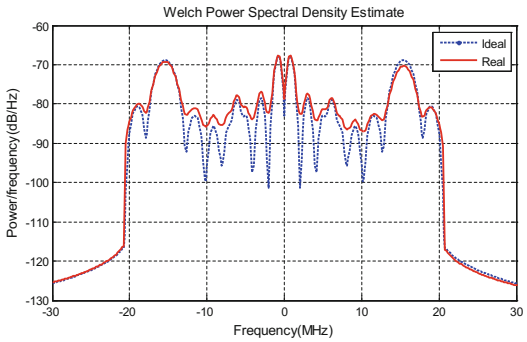

Fig. 3. The power spectrum density of Galileo E1 signal

Figure 4 shows the correlation functions of E1B, E1C and E1A. Each correlation function is an average result of 100 correlation functions. The coherent integration time is 4 ms. Two tracking modes of E1B and E1C are given out. The analysis bandwidth is 40.92 MHz.

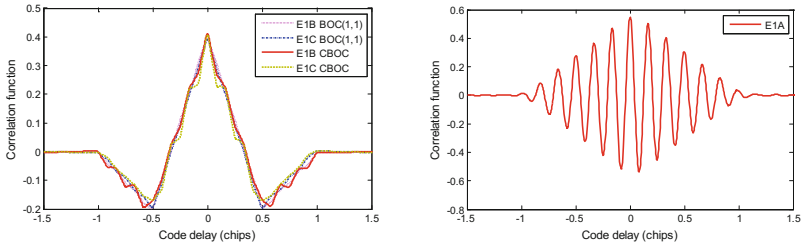

Fig. 4. The correlation functions. (a) E1B and E1C (b) E1A

Figure 5 shows the assessment results of SCB with 40.92 MHz bandwidth. SCB indicates the symmetry of correlation function. For E1B and E1C, only the BOC(1, 1) component is tracked. The correlation spacing is form 0 to 0.5 chip. Their SCBs are 3.0496 ns and 2.4508 ns respectively. For E1A, the correlation spacing is form 0 to 1/12 chip. SCB is 0.0561 ns.

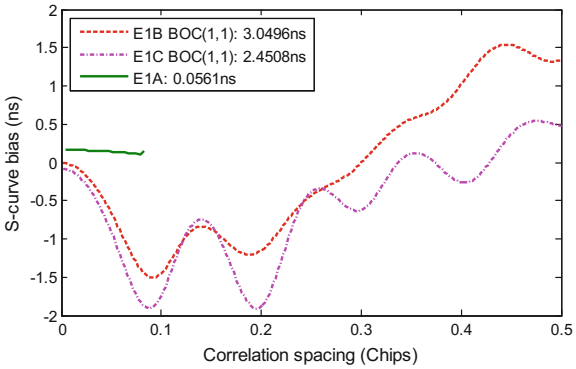

Fig. 5. The assessment results of SCB

6 Conclusions

This paper proposes a separation and evaluation method of GNSS AS signals. The proposed method can estimate the PRN code sequences of AS signals even if the constant envelope scheme, the power ratio and phase relationship between signal components are unknown. On this basic, the correlation domain characteristic of AS

signal can be assessed. Taking Galileo E1 signal as example, the BER performance of the proposed method is analyzed by simulation. Result shows that BER is less than 0.001 when the C/N_0 is higher than 76 dB-Hz. The effectiveness of the proposed method is further verified using the Galileo E1 signal collected by a 6 m dish antenna. The PRN code sequences of E1A are estimated, and the correlation function of E1A is obtained. Results can provide a reference for AS signal quality assessment.

Acknowledgment. This work is supported by National Natural Science Foundation of China (Grant 11803023).

References

1. Christie JRI, Bentley PB, Ciboci JW, Gellrich CA, Gondek JM, Knoth BK, Ressler MB, Oetzel GN (2004) GPS signal quality monitoring system. In: ION GNSS 17th international technical meeting of the satellite division, Long Beach, CA, 21–24 September 2004, pp 2239–2245
2. Graf S, Gunther C (2006) Analysis of GIOVE-A L1-signals. In: ION GNSS 19th international technical meeting of the satellite division, Fort Worth, TX, 26–29 September 2006, pp 1560–1566
3. He C, Guo J, Lu X, Lu J (2015) Generation mechanisms of GNSS navigation signal distortions and influence on ranging performance. Syst Eng Electron 37(7):P1611–P1620
4. European GNSS (2016) (Galileo) Open Service Signal-In-Space Interface Control Document, Issue 1.3, European Union
5. Betz JW (2013) Something old, something new. InsideGNSS July/August, 34–42
6. Yan T, Tang Z, Wei J, Qu B, Zhou Z (2015) A quasi-constant envelope multiplexing technique for GNSS signals. J Navig 68(4):791–808
7. (2018) NAVSTAR GPS Space Segment/USER Segment L1C Interface (IS-GPS-800E)
8. Betz JW (2000) Design and performance of code tracking for the GPS M code signal. In: Proceedings of the 13th international technical meeting of the satellite division of the institute of navigation (ION GPS 2000), Salt Lake City, UT, September 2000, pp 2140–2150
9. Turner M, Richardson A, Haddon J, Batiste M, Aguado E, Wales B, Dumville M, Bowden R, Togneri P (2015) Galileo public regulated services (PRS) with limited key distribution. ION GNSS+ 2015, pp 3397–3404
10. Xiao W, Liu W, Mou W, Yong L, Sun G (2018) Research into a recovery method of GNSS authorized service signal component. IEEE Access 6:27651–27658
11. Kang L, Lu X, Wang X, He C, Rao Y, Yang D (2018) Authorized signals quality assessment on GPS L1. J Electron Inf Technol 40(4):905–910
12. Thoelert S, Hauschild A, Steigenberger P, Langley RB, Antreich F (2018) GPS IIR-M L1 transmit power redistribution: analysis of GNSS receiver and high-gain antenna data. Navig: J Inst Navig 65:423–430
13. Ren Z, San Y (2006) Improved adaptive genetic algorithm and its application research in parameter identification. J Syst Simul 18(1):41–43, 66
14. Hein GW, Avila-Rodriguez JA, Ries L, Lestarquit L, Issler JL, Godet J, Pratt T (2005) A candidate for the Galileo L1 OS optimized signal. In: Proceedings of the 18th international technical meeting of the satellite division (ION GNSS 2005), Long Beach, CA, September 2005, pp 833–845
15. Yang D, Lu X, Wang X (2017) Analysis and evaluation of Galileo E1 signal. J Time Freq 40 (3):178–192

Analysis of BDS Satellites Code Multipath

Haichun Wang[1(✉)], Xialin Jia[2], and Liang Zhang[1]

[1] School of Geology Engineering and Surveying, Chang'an University, Xi'an, China
2272218896@qq.com
[2] Xi'an Research Institute of Surveying and Mapping, Xi'an, China

Abstract. The multipath of BDS-2 medium earth orbit (MEO) satellites and BDS-3 satellites is analyzed. The multipath bias of BDS-2 satellites is corrected by second order polynomial fitting. By calculating Pearson correlation coefficient between multipath and elevation angle, it is found that the correlation coefficient between multipath and elevation angle of BDS-3 satellites is less than 0.1, and the correlation is not strong. Further, the fourth polynomial fitting model is used to verify that there is no code multipath bias for BDS-3 satellites. By comparing the Root Mean Square (RMS) of BDS-3 satellites code multipath, it is found that the multipath of B1C signal is the largest, approaching 0.5 m, while that of other signals is better than 0.3 m.

Keywords: BDS-3 · Code multipath · Polynomial fitting

1 Introduction

BDS-2 consists of MEO, geostationary earth orbit (GEO) and inclined geosynchronous orbit (IGSO) satellites and provides signals of B1, B2 and B3 [10]. On November 5, 2017, China successfully launched two BDS-3 global networking satellites, marking the Beidou Satellite Navigation System entering a new era of global networking [9]. By the end of October 2018, the number of BDS-3 satellites launched reached 16 and all belonged to MEO satellites. China plans to complete the construction of BDS-3 by 2020, when the number of BDS-3 satellites will reach 30, including 24 MEO satellites, 3 GEO satellites and 3 IGSO satellites. The BDS-3 satellites will transmit signals of B1, B1C, B2a and B3 at frequencies of 1561.098 MHz, 1575.420 MHz, 1176.450 MHz and 1268.520 MHz, respectively. Multipath is one of the important factors affecting high precision positioning and timing, and has been widely concerned [1]. Hauschild et al. discovered for the first time the code multipath deviation of BDS-2 satellite [4]. [11] verified that the deviation was independent of the station by using multiple stations. [8] corrected the multipath deviation of MEO and IGSO satellites by piecewise linear fitting. [5] compared the second order polynomial fitting and piecewise linear fitting. It is found that effect of second order polynomial is better than piecewise linear fitting. With the continuous launch of BDS-3 global networking satellite, the multipath of BDS-3 satellites will also be widely concerned.

J. Sun et al. (Eds.): CSNC 2019, LNEE 563, pp. 347–354, 2019.
https://doi.org/10.1007/978-981-13-7759-4_31

2 Theory of Multipath

The multipath (MP) can be obtained by using the linear combination of single-frequency pseudorange and dual-frequency carrier phase measurements. In 1992, Rocken and Mertens first proposed MP combination [3]. The formula is as follows:

$$\mathrm{MP}_1 = \rho_1 - \frac{f_1^2 + f_2^2}{f_1^2 - f_2^2}\lambda_1\varphi_1 + \frac{2f_2^2}{f_1^2 - f_2^2}\lambda_2\varphi_2 + B_1 \quad (1)$$

$$\mathrm{MP}_2 = \rho_2 - \frac{2f_1^2}{f_1^2 - f_2^2}\lambda_1\varphi_1 + \frac{f_1^2 + f_2^2}{f_1^2 - f_2^2}\lambda_2\varphi_2 + B_2 \quad (2)$$

In the formula, MP_1 and MP_2 are multipath combined observations, ρ_1 and ρ_2 are pseudorange observations, φ_1 and φ_2 are carrier phase observations, λ_1 and λ_2 are carrier wavelength, f_1 and f_2 are carrier frequencies, B_1 and B_2 contain constant parts of ambiguity and hardware delay. The combination eliminates tropospheric delay, first-order ionospheric delay, receiver clock difference, satellite clock difference and geometric distance from satellite to receiver. In theory, the multipath of carrier phase observation does not exceed 1/4 cycle of carrier wavelength, and is much smaller than the multipath of pseudorange observation [6]. At the same time, the noise of carrier phase is much less than that of pseudorange, so the influence of carrier phase observation on multipath effect can be neglected. B_1 and B_2 are constants in the absence of cycle slips. The magnitude of B_1 and B_2 can be obtained by taking the mean value in a continuous time, and then subtracted from the original combination, thus the pseudorange multipath [12].

3 Corrections for Code Multipath Bias of BDS-2 Satellites

In order to compare with the multipath of BDS-3 satellites, only the BDS-2 MEO satellites are analyzed here. Figure 1 shows the relationship between code multipath and elevation angle of MEO satellite (C12) of Sha1 station on 272th day in 2018. Because there is no observation of B2 signal, only B1 and B3 frequency signals are analyzed here. MP1 and MP3 in the figure represent code multipath of B1 and B3 respectively. It can be seen from the figure that the code multipath bias of B1 frequency signal is more serious than that of B3 and approaches 1 m at high elevation angle.

In this paper, second order polynomial model is used to correct this deviation. In order to establish a second order polynomial model, 10 iGMAS stations were used for 10 days from 264th to 273th days in 2018. The location distribution of these 10 stations is shown in Fig. 2.

The code multipath of each satellite is modeled by elevation, and the polynomial coefficients of each satellite are obtained. Finally, the polynomial of each signal is obtained by taking the average value of the polynomial coefficients of each satellite. Figure 3 draws the second order polynomial fitting correction curves of B1 and B3.

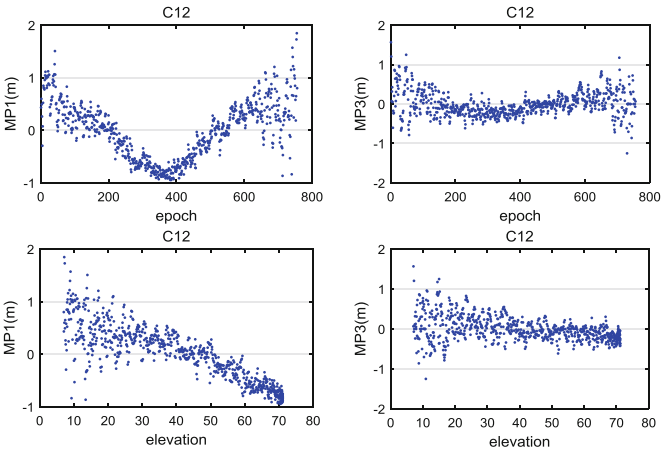

Fig. 1. Relationship between code multipath and elevation angle of BDS-2 MEO satellite

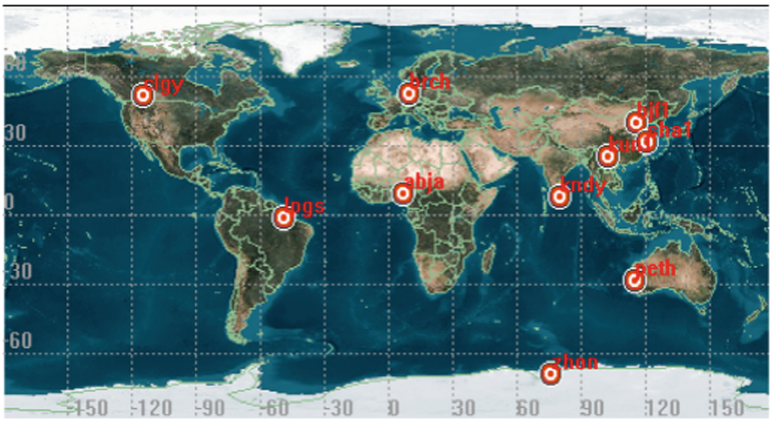

Fig. 2. Station distribution map

It can be seen from the graph that the multipath deviation of B1 has exceeded 1 m at high elevation. Moreover, the multipath deviation of B1 is much larger than that of B3.

Figure 4 shows the change of a single MEO satellite at Sha1 station before and after correction by second order polynomial fitting. From the figure, it can be seen that the deviation of B1 and B3 frequency signals at high elevation has been greatly improved. In order to verify the validity of the model, the standard deviations of all satellite B1 and B3 signal multipath before and after correction are counted, and the average values of all satellites are taken. The statistical results are shown in Table 1. From Table 1, we can see that the improvement rate of B1 frequency signal is 30% and that of B3 is 16%. This shows that the second order polynomial fitting model has played a significant role. Because the code multipath bias of B1 frequency signal is greater than that of B3, the improvement of B1 frequency signal is more obvious.

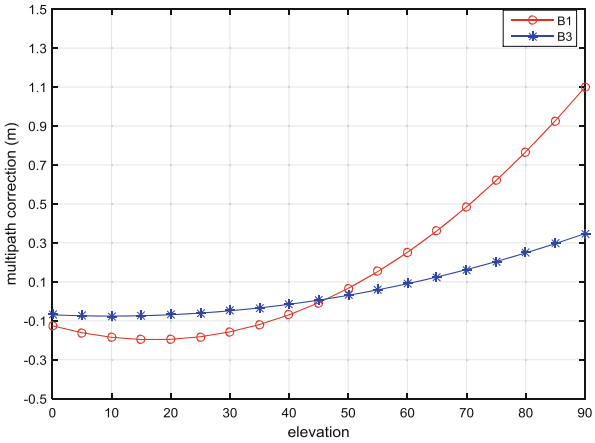

Fig. 3. Correction of code multipath

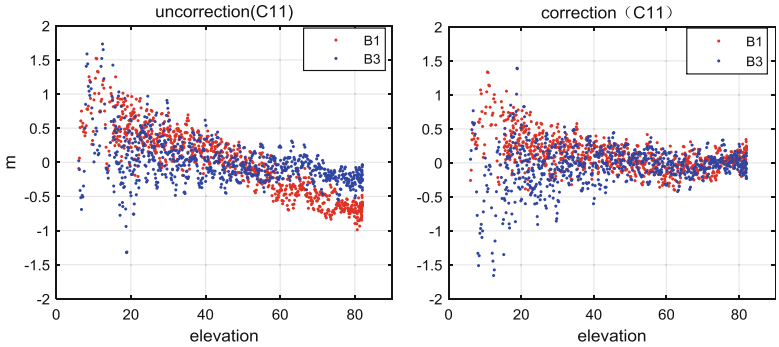

Fig. 4. Comparison between correction and uncorrection of code multipath

Table 1. Statistical results of standard deviation

Signal	Uncorrection	Correction	Improvement
B1	0.511	0.357	30.14%
B3	0.386	0.323	16.32%

4 Analysis of Code Multipath of BDS-3 Satellites

By the end of October 2018, BDS-3 has launched 16 MEO satellites. Considering the number of satellites in the observed data, only 8 satellites in Table 2 are analyzed here. The PRN and launch time of these eight satellites are listed in Table 2. [2] analyzed the multipath of BDS-3 experimental satellites. It was found that there was almost no multipath deviation at each signal of BDS-3 experimental satellites, but only single station data were used. It is explained here that the experimental data in this chapter are

from the other eight stations because the data of BIC and B2a signals were not received at kun1 and sha1 stations.

Table 2. Statistical results of standard deviation

PRN	Orbit	Launch time
C20	MEO	2017.11.05
C21	MEO	2018.02.12
C22	MEO	2018.02.12
C23	MEO	2018.07.29
C24	MEO	2018.07.29
C27	MEO	2018.01.12
C29	MEO	2018.03.30
C30	MEO	2018.03.30

Figure 5 shows the variation of code multipath sequence with elevation of C21 at bjf1 station for 10 days. MP1-MP4 shows the multipath of B1, B1C, B2a and B3 respectively. It can be seen from the figure that the multipath of BDS-3 satellites has almost no correlation with elevation.

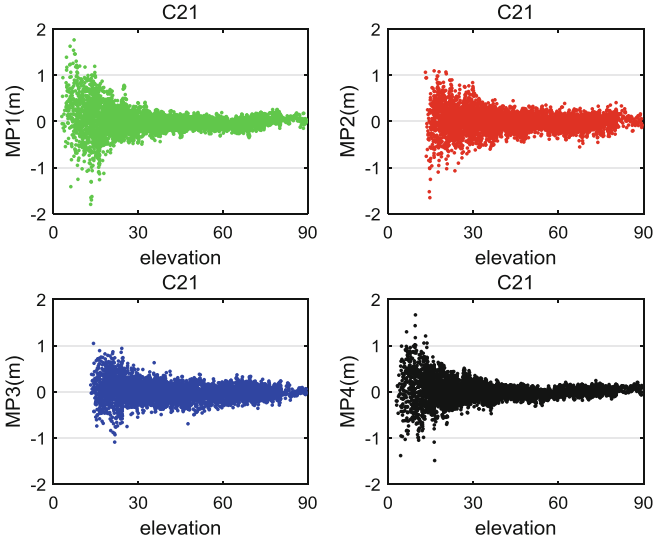

Fig. 5. Relationship between code multipath and elevation angle of BDS-3 satellite

In order to compare the multipath characteristics of BDS-3 and BDS-2 satellites, Pearson correlation coefficient [7] between multipath and elevation of BDS-2 MEO satellites and BDS-3 satellites is obtained by using observed data from 8 stations here. Pearson correlation coefficient is a linear correlation coefficient with a value of −1 to 1, and zero indicates no correlation. In order to facilitate comparison, all coefficients are

taken as absolute values. From Table 3, it can be seen that the correlation coefficient of B1 frequency signal of BDS-2 satellites almost exceeds 0.5, which belongs to moderate correlation, and that of B3 frequency signal belongs to weak correlation around 0.3. The correlation coefficient of each signal of BDS-3 satellites is less than 0.1, so it can be concluded that there is no correlation between multipath and elevation of BDS-3 satellites.

Table 3. Correlation coefficient between multipath and elevation

PRN	B1	B1C	B2a	B3
C11	0.5372	–	–	0.3088
C12	0.5478	–	–	0.2729
C14	0.5790	–	–	0.2993
C20	0.0839	0.0868	0.0324	0.0241
C21	0.0714	0.0521	0.0591	0.0423
C22	0.0800	0.0292	0.0753	0.0550
C23	0.0282	0.0744	0.0617	0.0301
C24	0.0266	0.1369	0.0521	0.0181
C27	0.0514	0.0734	0.0839	0.0600
C29	0.0518	0.0131	0.0787	0.0391
C30	0.0412	0.0827	0.0745	0.0321

In order to further compare with BDS-2, the fourth order polynomial is used to model the code multipath of each BDS-3 satellite, and the polynomial coefficients of each satellite are obtained. Finally, the average of the polynomial coefficients of each satellite is taken to obtain the polynomial of each signal. The processing strategy is the same as that of BDS-2.

Table 4 shows the fourth order polynomial coefficients for each signal of BDS-3. In the table, A0–A4 represent the constant term of the polynomial and the coefficient of the first term to the fourth term. Figure 6 draws the image of the polynomial equation corresponding to all frequency signals. From the picture, we can see that the BDS-3 satellites image is smooth at each signal, and there is no big deviation at high elevation. Although there are small fluctuations in BDS-3 frequency signals, they are all at the centimeter level. It is not considered that there exists a multipath bias phenomenon in BDS-3 frequency signals. The fourth order polynomial fitting can again show that the BDS-3 satellites have no multipath bias.

Table 4. Polynomial fitting parameters for each signal

Signals	A0	A1	A2	A3	A4
B1	0.011878	1.57E−03	−1.09E−04	1.51E−06	−4.79E−09
B1C	−0.002282	3.35E−03	−1.78E−04	2.65E−06	−1.16E−08
B2a	−0.010833	7.32E−03	−3.84E−04	6.10E−06	−3.02E−08
B3	0.003838	1.35E−03	−1.12E−04	2.31E−06	−1.37E−08

In order to compare the multipath of each frequency signal, the average value of each satellite multipath of each station is counted here. It can be seen from Table 5 that the multipath of the B1, B2a and B3 frequency signals are smaller than B1C, generally around 0.3 m. The multipath of B1C is close to 0.5 m.

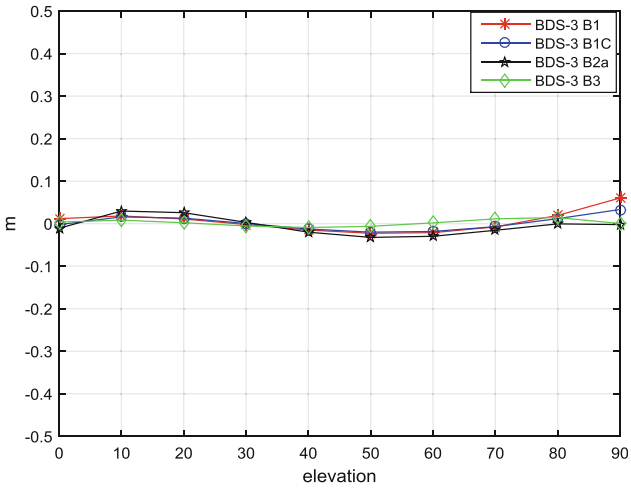

Fig. 6. Image of second order polynomial

Table 5. Code multipath of each station (RMS/m)

Stations	B1	B1C	B2a	B3
abja	0.315	0.624	0.265	0.256
bjf1	0.139	0.208	0.183	0.122
brch	0.449	0.626	0.422	0.418
clgy	0.324	0.469	0.367	0.310
kndy	0.252	0.393	0.313	0.233
lpgs	0.286	0.487	0.228	0.224
peth	0.325	0.435	0.294	0.263
zhon	0.251	0.522	0.313	0.236
Mean	0.293	0.471	0.298	0.258

5 Conclusions

Aiming at the multipath deviation of BDS-2 MEO satellites, second order polynomial is used to fit the code multipath of B1/B3 frequency signal and correct it. Statistical standard deviation of each signal shows that B1 and B3 are increased by 30% and 16%, respectively. The correlation coefficients between multipath and elevation of each satellite are obtained. It is found that the correlation coefficients between multipath and

elevation of BDS-3 satellites belong to the range of non-correlation. The fourth order polynomial is used to fit the signals of BDS-3 satellites. It is found that the fitting equation image of each signal is gentler than that of BDS-2, and only the fluctuation of centimeter level exists, which indicates that there is no multipath bias in BDS-3 satellites. By comparing the multipath RMS of BDS-3 frequency signal, it is found that the B1C has the largest multipath, the average value is close to 0.5 m, and the other signals are below 0.3 m.

References

1. De Bakker PF (2016) On user algorithms for gnss precise point positioning 38:191–194
2. Li X, Zhang XH (2018) Comparison of pseudo range multipath bias characteristics between BDS-2 and BDS-3 satellites. Geodesy Geodyn (2)
3. Rocken C, Meertens C (1994) UNAVCO receiver tests
4. Sleewaegen JM, Huisman L et al (2012) Characterization of compass M-1 signals. GPS Solutions 16(1):117–126. https://doi.org/10.1007/s10291-011-0210-3
5. Yang W, Tong H, Pan L et al (2016) Analysis and correction of BDS Code multipath bias. In: China satellite navigation conference. https://doi.org/10.1007/978-981-10-0940-2_44
6. Wang G, Jong KD, Zhao Q et al (2015) Multipath analysis of code measurements for BeiDou geostationary satellites. GPS Solutions 19(1):129–139. https://doi.org/10.1007/s10291-014-0374-8
7. Wang S, Jia X, Ji G et al (2017) Multipath effect analysis of Beidou satellite pseudorangeand its correction. https://doi.org/10.1007/978-981-10-4588-2_47
8. Wanninger L, Beer S (2015) BeiDou satellite-induced code pseudorange variations: diagnosis and therapy. GPS Solutions 19(4):639–648. https://doi.org/10.1007/s10291-014-0423-3
9. Yang X, Chen B, Xie Q et al (2017) The Beidou satellite navigation system into the new era of global network. Satell Appl 12(11):70
10. Yang Y, Li J, Wang A et al (2014) Preliminary assessment of the navigation and positioning performance of Beidou regional satellite navigation system. China Sci: Geosci 44(1):72
11. Zhao Q, Wang G, Liu Z et al (2015) Analysis of BeiDou satellite measurements with code multipath and geometry-free ionosphere-free combinations. Sensors 16(1):123. https://doi.org/10.3390/s16010123
12. Zhang XH, Ding LL (2013) Quality analysis of the second generation compass observables and stochastic model refining. Geomat Inf Sci Wuhan Univ 38(7):832–836

Accuracy Analysis of GNSS Broadcast Ionospheric Model

Guang Sun[1], Lirong Shen[2(✉)], Xiangyu Zhu[1], Xiaolin Jia[3], Xiaogang Liu[3], Meijun Guo[1], Wei Zhai[1], Yingjie Hong[1], and Jie Zheng[1]

[1] Xi'an Aerors Data Technology Co. Ltd., Xi'an 710054, China
sunguang2l6@l63.com
[2] School of Aerospace Science and Technology, Xidian University, Xi'an 710071, China
slr_xidian@l63.com
[3] Xi'an Research Institute of Surveying and Mapping, Xi'an 710054, China

Abstract. In order to verify and evaluate the correction precision of the model and parameters of Klobuchar 8 parameters (k8) and Klobuchar 9 parameters (k9) of BDS global ionospheric delay correction model (BDGIM), and the GPS-k8 ionospheric correction model as well as the NeQuick correction model of Galileo, this paper uses GNSS radio ionospheric correction parameters provided by iGMAS and global ionospheric grid data of the CODE to analyze the ionosphere model correction accuracy. Data analysis shows that in China and the surrounding areas, the correction accuracy of BDS-k9 model and parameters is basically the same as that of GPS-k8. The correction accuracy of BDS-k9 model and parameters is obviously better than that of BDS-k8 model, and the optimal RMS of BDS-k9 is 0.72 m. At 20° to 45° mid-latitude areas, GPS-K8 correction precision is highest, the optimal RMS of GPS-K8 is 0.705 m. However, the correction accuracy at southern hemisphere is not well. The global ionosphere correction results of Galileo which uses the NeQuick2 model are smooth and the correction accuracy in northern and southern hemispheres is similar.

Keywords: GNSS · Performance evaluation · iGMAS · Ionospheric model

1 Introduction

There are various sources of errors in the propagation path of spatial signals, of which the ionospheric delay error is one of the main sources of error [1]. When electromagnetic waves of different frequencies propagate through the ionosphere, since the ionosphere is the dispersion medium, the propagation speed and direction will changed after passing through the ionosphere. Thus, the ionospheric error is introduced, which should be eliminated. In the GNSS system, navigation messages broadcast the parameters of Klobuchar 8 model, Klobuchar 9 model and NeQuick model to realize the elimination of the ionospheric error.

Broadcast ionospheric delay correction is of great significance to GNSS single frequency users [2, 3]. As the electron density in the ionosphere is subject to seasonal

J. Sun et al. (Eds.): CSNC 2019, LNEE 563, pp. 355–367, 2019.
https://doi.org/10.1007/978-981-13-7759-4_32

temperature variation and the influence of sunspot activity, which lead to the ionospheric delay correction models and parameters of different satellite navigation systems to be different. In order to objectively evaluate the performance of the different satellite navigation systems, it is necessary to evaluate the actual corrections of broadcast ephemeris ionospheric model and parameters.

This paper mainly described the broadcast ionospheric model and parameters used in GPS, BDS and Galileo system and deduced the formula, and introduced the content of CODE global ionospheric map. Then, the ionospheric errors of the corresponding systems are corrected by using ionospheric parameters broadcast by each system. Finally, the correction accuracy of the new K9 model and other ionosphere models has been evaluated.

2 GNSS Broadcast Ionospheric Model

The ionosphere is an atmosphere about 60–1000 km away from the earth's surface. Due to the physical properties of the ionosphere, the original propagation speed and direction of electromagnetic waves passing through the ionosphere will be changed. And the electromagnetic waves will be reflected, refracted, absorbed and so on, which will introduce the ionospheric delay error into GNSS measurement sysytem.

The propagation velocity of electromagnetic wave in the ionosphere varies with the frequency of the electromagnetic wave. The relation between ionospheric delays I and signal frequency f is as shown in formula 1.1.

$$I = 40.28\frac{N_e}{f^2} \tag{1.1}$$

N_e is the total number of electrons contained in the channel space per unit area, namely TEC (Total Electron Content). The ionospheric delay is generally a few meters in size and varies with altitude, time, temperature and latitude and longitude of the earth. When the universe is active strongly, the electron density will increase and the ionosphere time delay will reach ten meters. Therefore, ionospheric delay error must be suppressed in satellite navigation and positioning sysytem. For single frequency users, ionospheric model should be used for time delay correction. For dual frequency users, the ionospheric delay can be eliminated by dual-frequency observations.

2.1 GPS Klobuchar Model

Klobuchar model is an ionospheric delay correction model for single frequency GPS observations [4], which regards the ionospheric delay error at night as a constant of 5 ns and the ionospheric delay error during the day as a positive part of the cosine function as shown in formula 1.2.

$$I_{ION}\begin{cases} = cF \times 5ns + Q\cos x & |x| < 1.57 \\ = cF \times 5ns & |x| \geq 1.57 \end{cases} \tag{1.2}$$

where c is the speed of light and F is the mapping function of the ionosphere error in the zenith direction to the signal transmission path.

$$x = 2\pi(t - 50400)/P$$

$$Q = \begin{cases} \sum_{i=3}^{3} \alpha_i \varphi_m^i & (Q \geq 0) \\ 0 & (Q < 0) \end{cases}, \quad P = \begin{cases} \sum_{i=0}^{3} \beta_i \varphi_m^i & (P \geq 72000) \\ 72000 & (P < 72000) \end{cases} \tag{1.3}$$

where, $\alpha_i, \beta_i (\mathrm{i} = 0, 1, 2, 3,)$ are the local time at the ionospheric puncture point from the broadcast ephemeris, as shown in formula 1.4.

$$t = t_{UT} + \frac{\lambda_{IP}}{15} \tag{1.4}$$

t_{UT} is the universal time. λ_{IP} is the longitude of the puncture point. φ_{IP} is the latitude of the puncture point. φ_m is the geomagnetic latitude which can be obtained by the following formula 1.5 (Fig. 1).

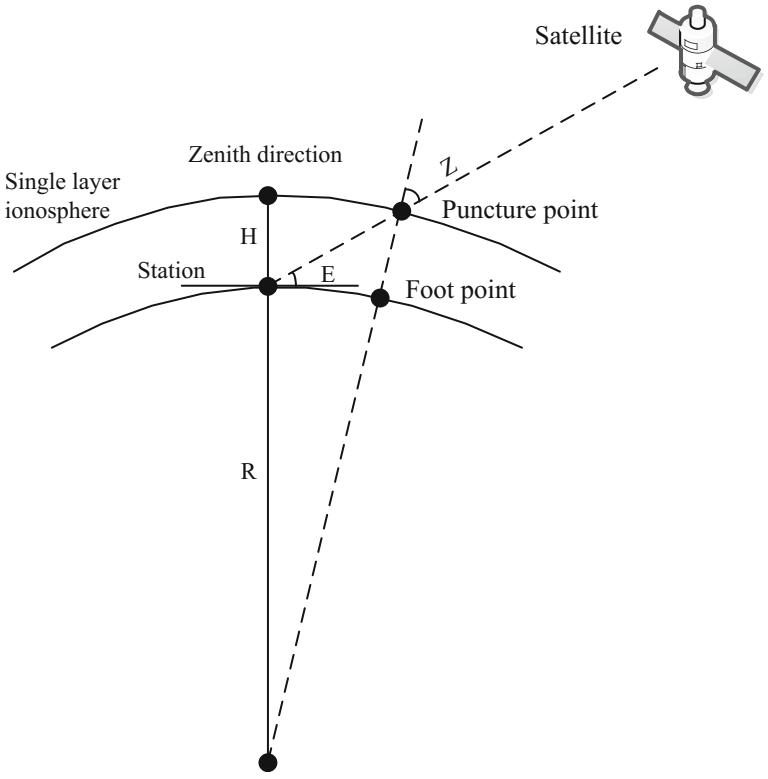

Fig. 1. Schematic diagram of a single layer ionosphere

$$\varphi_m = \varphi_{IP} + 0.064\cos(\lambda_{IP} - 1.167) \tag{1.5}$$

In order to facilitate the calculation, the ionosphere is regarded as a single-layer sphere. And the intersection point of the navigation signal sphere is the puncture point. The calculation formula of relevant parameters is as follows.

$$\varphi_{IP} = \begin{cases} \varphi_0 + \psi_0 \cos A & |\varphi_{IP}| \leq 0.416 \\ 0.416 & \varphi_{IP} > 0.416 \\ -0.416 & \varphi_{IP} < 0.416 \end{cases} \tag{1.6}$$

$$\psi_0 = \frac{0.0137}{E + 0.11} - 0.022,\ \lambda_{IP} = \lambda_0 + \psi_0 \sin A / \cos \varphi_{IP}$$

where, A is the azimuth Angle of the satellite. E is the altitude Angle of the satellite. λ_0 and φ_0 is the longitude and latitude of the receiver. And ψ_0 is the Angle between the centers of the earth.

2.2 BDS Broadcast Ionospheric Model

(1) K8 ionospheric model in BDS region

Parameters 8 and parameters 9 of the BDS Klobuchar ionosphere model is used to correct the ionospheric delay. The Klobuchar model of BDS uses a daily and fixed geographic coordinate system, which can better reflect the diurnal and weekly variations of the ionosphere [5]. The 8 parameters and 9 parameters used are been calculated based on the measured dual-frequency observation data of IGMAS monitoring station, and they are been updated every 2 h [6].

BDS uses the parameters 8 and parameters 9 transmitted by the system and the Klobuchar model to correct the ionospheric vertical delay $I_z(t)$, as shown in formula 1.7. [7].

$$I_z(t) = \begin{cases} 5 \times 10^{-9} + A_2 \cos\left[\frac{2\pi(t-50400)}{A_4}\right] & |t - 50400| < A_4/4 \\ 5 \times 10^{-9} & |t - 50400| \geq A_4/4 \end{cases} \tag{1.7}$$

where, t is the local time at the puncture point of the ionosphere, in seconds. A_2 is the amplitude of the daytime cosine curve, which α_n is calculated by the coefficient.

According to the above formula, the vertical ionospheric delay at the puncture point can be calculated from eight ionospheric delay correction parameters.

(2) BDS K9 ionospheric model

The BDGIM model is based on the improved spherical harmonic function, and the specific formula for calculating the ionospheric delay correction by the user receiver according to BDGIM is as follows.

$$T_{\text{ion}} = M_F \cdot \frac{40.28 \times 10^{16}}{f^2}\left[A_0 + \sum_{i=1}^{9} \alpha_i A_i\right] \tag{1.8}$$

where, T_{ion} is the ionospheric delay correction in the line of sight of the satellite and the receiver, in meters; M_f is a projection function used for conversion between vertical and oblique ionospheric total electron content (TEC); f is the carrier frequency corresponding to the current signal, the unit is Hz; a_1–a_9 are the nine parameters of ionospheric delay correction models, and the unit is TECU; A_0 is the predicted ionospheric delay calculated in TECU.

2.3 Galileo NeQuick Model

NeQuick model is a semi-empirical model describing the spatio-temporal changes of the ionospheric electron density. Its model is characterized by layering the ionosphere and calculating the corresponding electron density at a given time and position through the model, so as to integrate the electron density at a single point and obtain the total electron content on any propagation path [8]. Using the data files such as CCIR and R12, NeQuick model can calculate the electronic density at any point in a specific time and space and the ionospheric TEC information between any two points.

The NeQuick model requires the input of geomagnetic latitude files and coefficient files. When calculating the total electron content in the inclined path, the model needs the geographic coordinates (latitude and longitude), altitude, month, universal time and solar activity parameters of the two endpoints on the transmission path of the input signal. The effective ionization factor was calculated through the parameters in the Galileo transmission message and transmitted to the global single frequency receiver users once a day [9]. The calculation formula of A_z is as follows.

$$A_Z = a_0 + a_1\mu + a_2\mu^2 \tag{1.9}$$

where μ is the geomagnetic dip angle, a_0, a_1 and a_2 are the ionospheric correction coefficient of Galileo broadcast ephemeris [10].

3 Experiment and Evaluation Analysis

3.1 Evaluation Criteria and Methods

The average accuracy deviation of the CODE global ionospheric map provided by the European geodetic center is 1TECU, and the STD is 4 TECU [11]. In this paper, GIM is used as the model evaluation benchmark to evaluate the correction accuracy of GNSS broadcasting ionospheric model.

The accuracy of the model in this paper is evaluated by ionospheric correction R_{cor} and root-mean-square error (RMS), as shown in formula 1.10 to 1.11.

$$R_{cor} = \sum_{i=1}^{n} \left(1 - \frac{|TEC_{\mathrm{mod}} - GIM_i|}{GIM_i}\right)/n \tag{1.10}$$

$$RMS = \sqrt{< (TEC_{\mathrm{mod}} - GIM_i)^2 >} \tag{1.11}$$

Where i is the grid point, TEC_{mod} and GIM_i are the calculated value of the model and the modified value of GIM grid respectively.

3.2 Processing and Analysis

Data on ionospheric parameters for broadcasting of GPS, BDS and Galileo systems provided by the iGMAS monitoring and evaluation center in 2017 are used. The VTEC of corresponding grid points are calculated, and the ionospheric model and parameter accuracy of GPS, BDS and Galileo system are evaluated with the final ionospheric grid product of CODE as the benchmark.

(1) Area processing analysis

According to the regional characteristics of BDS-k8, China, the United States and Europe are selected for area processing analysis. Make a detailed analysis of China and Europe. China area: 70–145° east longitude, latitude 7–55°; European region: west longitude 10–60° east longitude, latitude 30–70°. American regions: west longitude 75–130°, latitude 25 to 55°. Each area includes the grid partition with the longitude and latitude of 5° by 5°.

The GPS-K8, BDS-K8, BDS-K9 and NeQuick2 correction models were processed for the three regions respectively. Figures 2, 3, 4, 5, 6 and 7 shows the ionospheric correction rate and corrected RMS of China, Europe and the United States respectively. Table 1 shows the annual average correction accuracy of the four models in 2017.

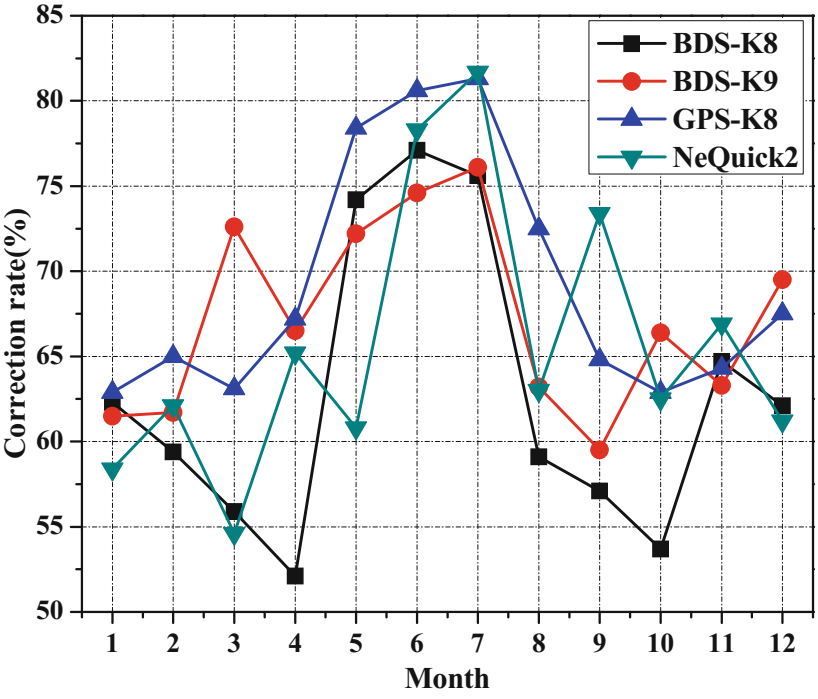

Fig. 2. Ionospheric model correction rate in China regional

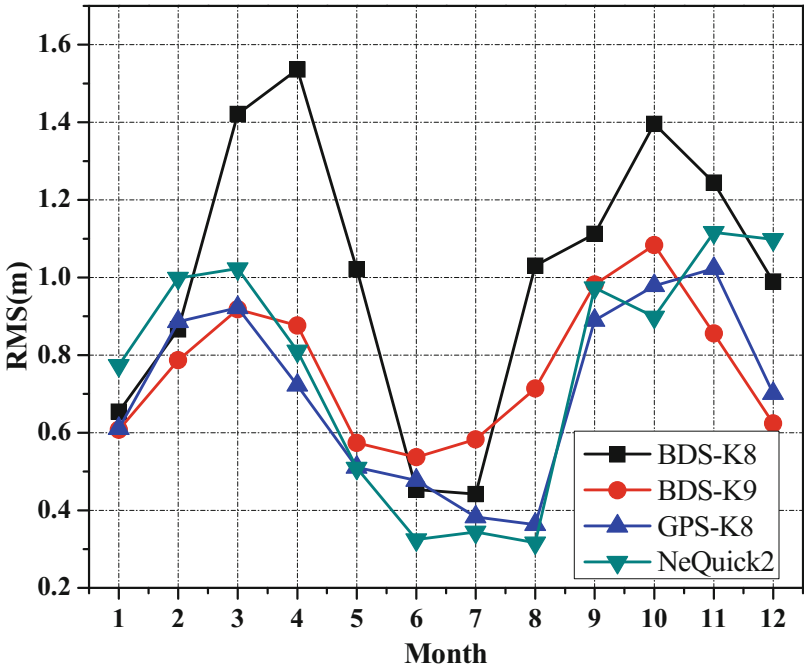

Fig. 3. Ionospheric model correction RMS (m) in China regional

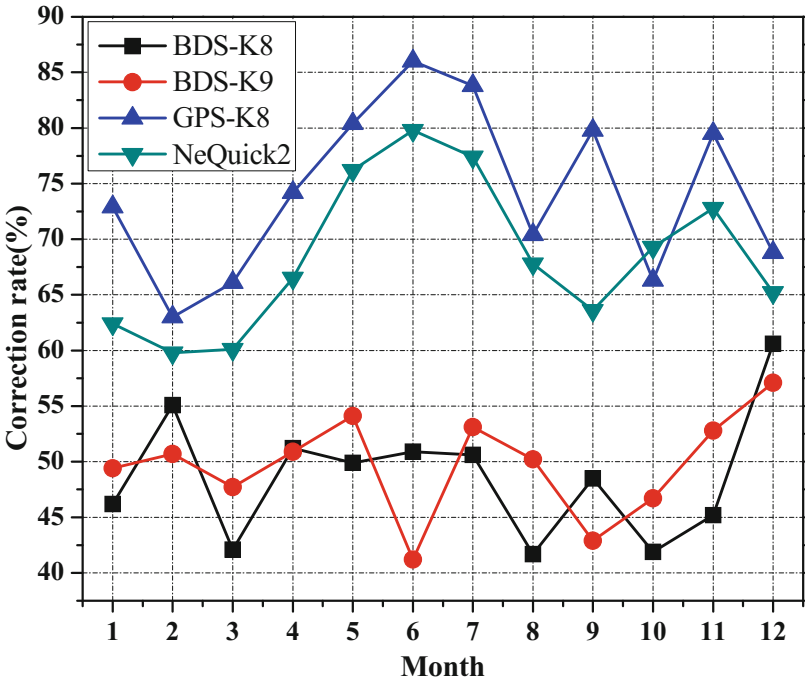

Fig. 4. Ionospheric model correction rate in European regional

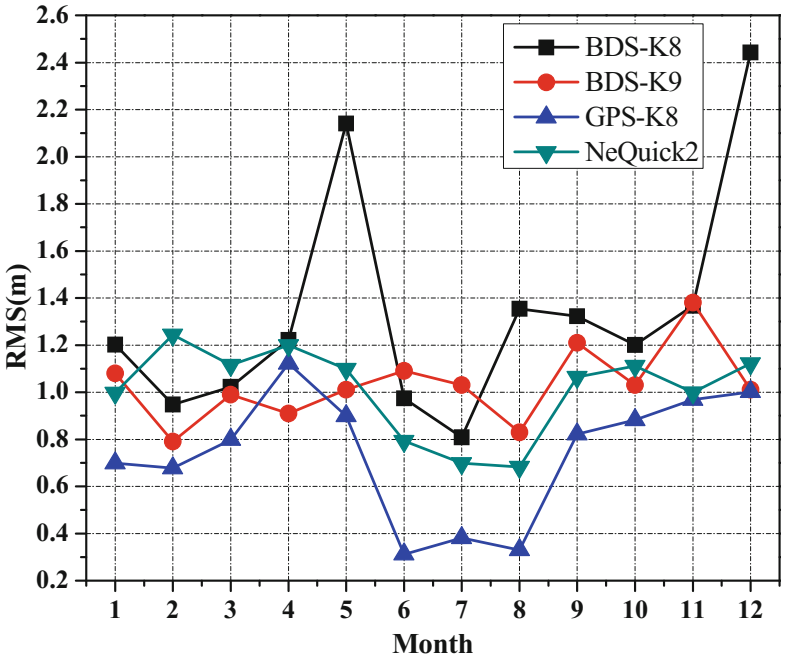

Fig. 5. Ionospheric model correction RMS (m) in European regional

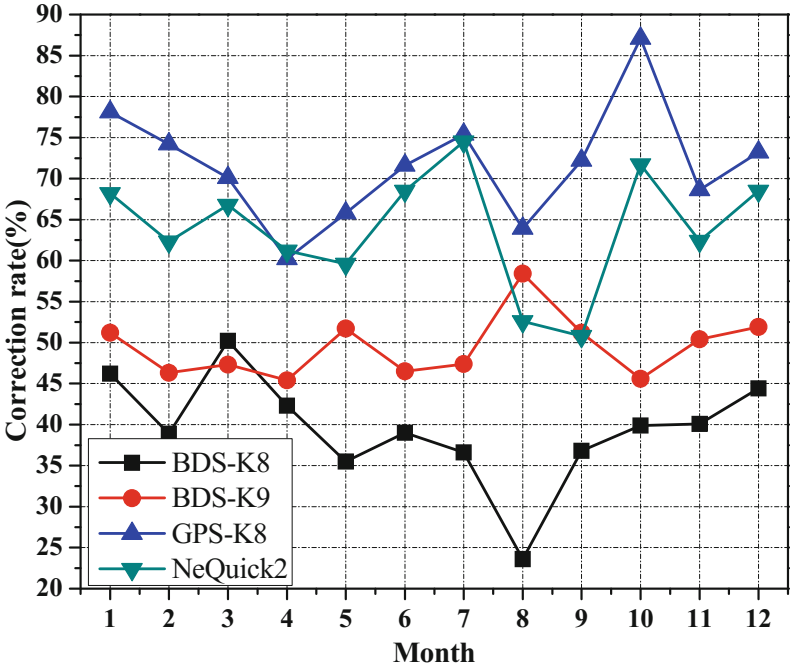

Fig. 6. Ionospheric model correction rate in US regional

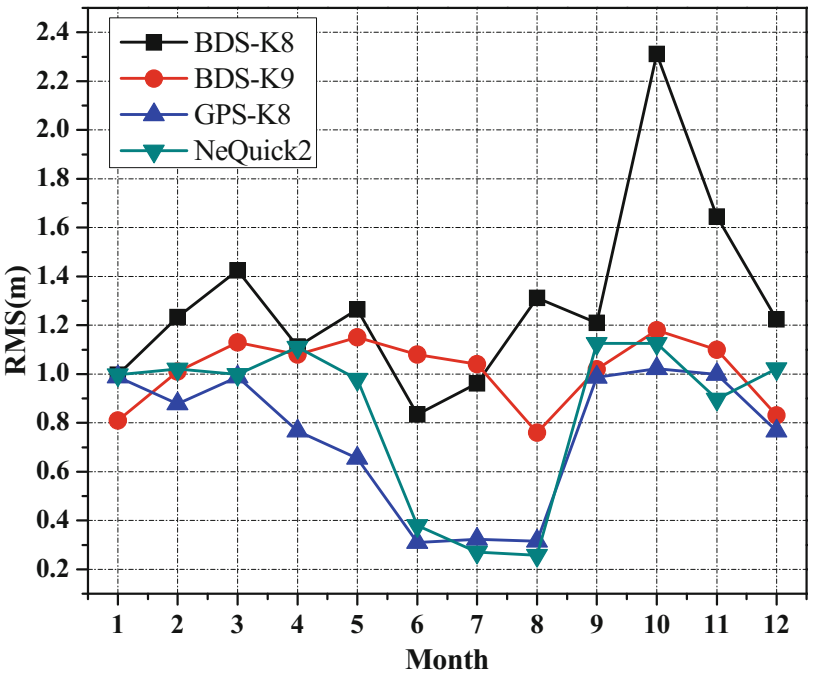

Fig. 7. Ionospheric model correction RMS (m) in US regional

Table 1. Correction accuracy of ionospheric model area (annual average)

Area	Broadcast model	GPS-K8	BDS-K8	BDS-K9	NeQuick2
China regional	Correction rate (%)	69.2%	62.7%	67.2%	65.6%
	RMS (m)	0.705	1.221	0.721	0.765
US regional	Correction rate	71.7%	39.5%	48.5%	63.9%
	RMS (m)	0.749	1.294	1.015	0.848
European regional	Correction rate	74.3%	48.6%	49.8%	68.4%
	RMS (m)	0.741	1.333	1.031	1.011

Table 1 depicted that the correction results using the four ionospheric models in China are basically consistent with the CODE as the benchmark, and the correction rate is around 62–69%. The correction rate of BDS-k9, GPS-k8 and NeQuick2 are basically the same, while the change of RMS is obvious between different months, which are about 0.7 m–1.2 m. Compared with the four models, the correction accuracy of BDS-k9 and GPS-k8 and NeQuick2 models are basically the same throughout the year. However, from the processing results of each month we can see that the BDS-k9 has the best correction results in 4 months. GPS-k8 has the best correction results in 3 months. NeQuick2 model has the best correction results in 5 months. It can be seen

from the curves in the figure that the correction results of ionosphere by different models are also influenced by seasonal temperature and other factors.

In the United States, the correction rate and accuracy of the GPS model are significantly higher than those of the BDS-k8, BDS-k9 and NeQuick2 models. The model correction rate in the United States reaches 71%, and the RMS is less than 0.8 m. Compared with the NeQuick2 model, the correction rate increases by 8% and the RMS decreases by about 0.1 m. In the European region, the correction rate and accuracy of the GPS model are also better than the other three models, and the accuracy of the NeQuick2 model is close to that of the GPS model.

(2) Global processing analysis

Select all ionospheric correction data of the year of 2017 to analysis the ionosphere model correction accuracy with the computational grid density of 5° by 5°. The results are shown as Figs. 8, 9, 10 and 11,which are the global ionospheric model correction precision of the model of GPS-K8, BDS-K8, BDS-K9 and NeQuick2, respectively.

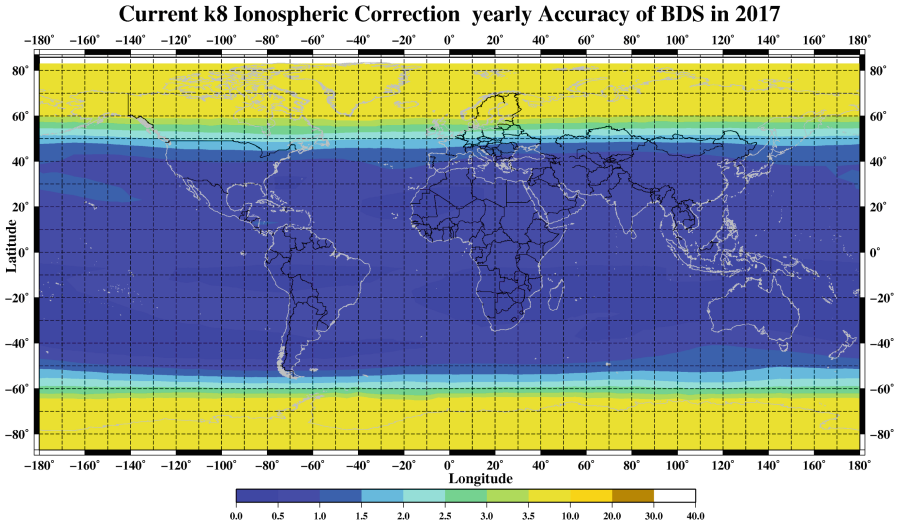

Fig. 8. Global ionospheric model correction accuracy (BDS-K8)

Figure 8 shows that the global correction accuracy of the BDS-k8 model is poor at the poles and in the African region. The reason of that is that BDS-k8 is regional model. Figure 9 shows that the global correction accuracy of BDS-K9 model has soared compared with BDS-K8, where the highest precision is in the region of 40° to 45° mid-latitudes. In other regions, the correction accuracy of GPS-k8 model decreases gradually with the increase of southern latitude. As can be seen from Fig. 10, the GPS global correction accuracy in the northern hemisphere using K8 model is superior to the southern hemisphere, where the highest accuracy is in the region of 20° to 45° mid-latitude areas. The correction accuracy is best especially in the United States and the

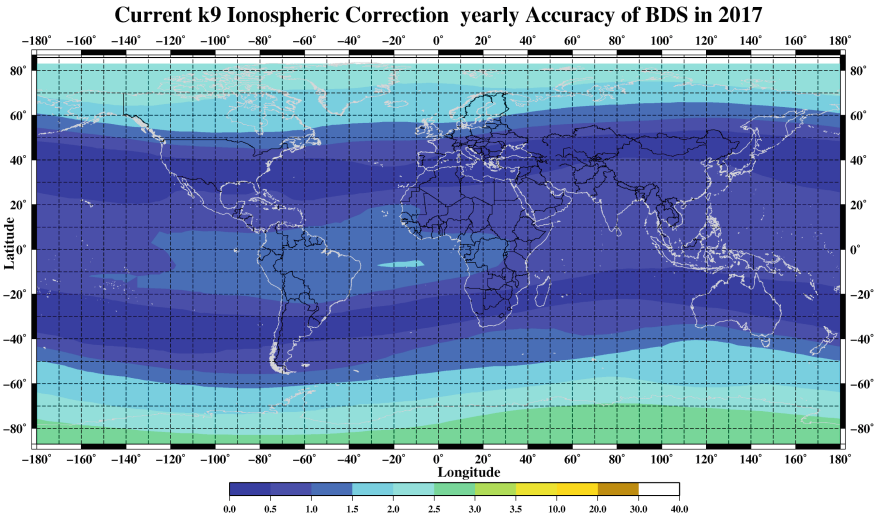

Fig. 9. Global ionospheric model correction accuracy (BDS-K9)

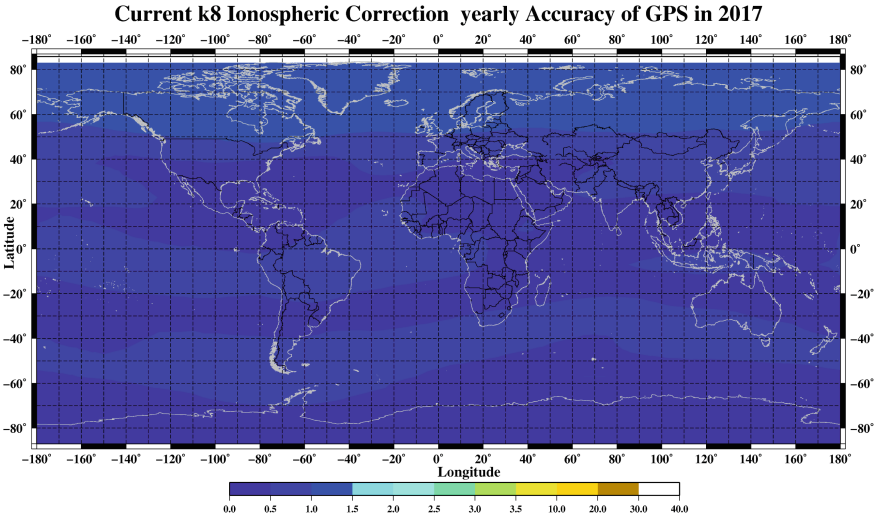

Fig. 10. Global ionospheric model correction accuracy (GPS-K8)

European region, where the largest regional correction error below 0.5 m. In the southern hemisphere, the correction rate of GPS-k8 model decreases gradually with the increase of southern latitude. As can be seen from Fig. 11, the global correction precision of NeQuick model is low compared with GPS - K8 model in the southern hemisphere longitude between the regions of 80–150°.

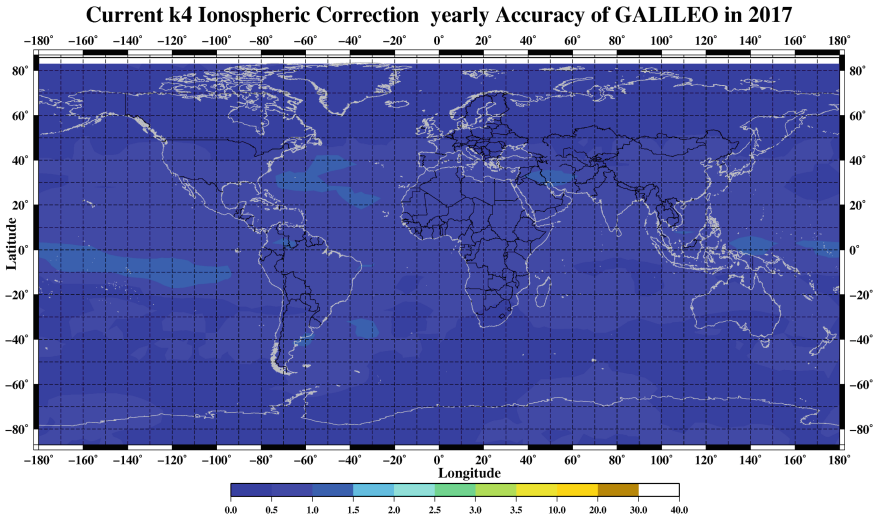

Fig. 11. Global ionospheric model correction accuracy (NeQuick2)

Compared the ionospheric model correction precision of four models, we can see that as a global ionospheric correction model, GPS-K8 in the regions of 20° to 45° mid-latitude has high precision, but the precision becoming low in other latitude regions in the world. The global correction precision of GPS-K8 and NeQuick is uniform and smooth.

4 Conclusions

Ionospheric delay error is an important source of error in the field of satellite navigation. In this paper, GNSS observation data of the year of 2017 provided by the iGMAS monitoring and evaluation center are used to evaluate and analyze the parameters of the single-frequency ionospheric model used by GPS, BDS and Galileo system. The accuracy of single-frequency ionospheric correction parameters of K8 and K9 models in BDS navigation messages, K8 model correction parameters in GPS navigation messages, and NeQuick model correction parameters in Galileo navigation messages are evaluated. And the final CODE global ionospheric grid diagram is adopted as the evaluation benchmark. The analysis results show that the accuracy of BDS-k9 model and parameters are basically the same as that of GPS-k8 in China and surrounding areas. The accuracy of BDS-k9 model is obviously improved compared with that of BDS-k8 model. As a global ionospheric correction model, the correction precision of GPS-K8 is highest in the regions of 20° to 45° N mid-latitude. But the southern hemisphere correction accuracy is low. The global correction precision of NeQuick is uniform and smooth.

Acknowledgments. The author would like to thank the Monitoring and Assessment Center (MAC) of International GNSS Monitoring and Assessment System (iGMAS) for their help in acquiring data.

References

1. Hofman-Wellenhof B, Lichtenegger H, Collins J (2001) GPS-theory and pratice, 5th edn. Springer, New York
2. Wang N (2017) Study on GNSS differential code biases and global broadcast ionospheric models of GPS, Galileo and BDS. Acta Geodaetica Cartogr Sin 46(8):1069
3. Wang N, Yuan Y, Li Z et al (2017) Performance analysis of different NeQuick ionospheric model parameters. Acta Geodaetica Cartogr Sin 46(4):421–429
4. Klobuchar J (1987) Ionsphere time-delay algorithm for single-frequency GPS user. IEEE Trans Aerosp Electron Syst 23(6):325–331
5. Zhang H et al (2006) Brief review of the ionospheric delay models. Prog Astron 24(1):16–26
6. Wu X, Hu X, Wang G (2012) Evaluation of COMPASS ionospheric model in GNSS positioning. Adv Space Res 51(6):959–968
7. China Satellite Navigation Office (2013) BeiDou navigation satellite system signal in space interface control document (2.0ver)
8. Nava B, Coisson P, Radicella SM (2006) Topside electron density in IRI and NeQuick: features and limitations. Adv Space Res 37:937–942
9. Lu H, Sun G et al (2017) Analysis of Different Ionospheric Model on the Accuracy of BDS Common-View. Navig Position Timing 01:53–59
10. Nava B, Coisson P, Radicella SM (2008) A new version of the nequick ionosphere electron density model. J Atmos Solar Terr Phys 70(15):1856–1862
11. Wu X, Han C, Ping J (2013) Monitoring and analysis of regional ionosphere with GEO satellite observations. Acta Geodaetica Cartogr Sin 42(1):13–18

Performance Evaluation of Beidou-3 On-Board Atomic Clock

Bo Zhang[1], Fuping Sun[1], Xiaolin Jia[2(✉)], Hailiang Dai[1], and Kai Xiao[1(✉)]

[1] Information Engineering University, Zhengzhou, China
izbo@mail.com
[2] Xi'an Research Institute of Surveying and Mapping, Xi'an, China
13891907401@139.com

Abstract. The performance of on-board atomic clock directly affects the accuracy of navigation and positioning for users. Evaluating the performance of on-board atomic clock is an important part of the construction and monitoring of satellite navigation systems. With the deployment of the Beidou-3, it is necessary to evaluate the performance of the new generation of on-board rubidium atomic clocks and hydrogen atomic clocks carried by Beidou-3 satellites. In this paper, the performance of the on-board atomic clock is evaluated by three indicators: frequency accuracy, drift rate and stability. From the experimental results, the frequency accuracy of Beidou-3 satellites on-board atomic clock is on the order of E-12–E-11, the drift rate of the rubidium clock is on the order of E-13, and the drift rate of the hydrogen clock is on the order of E-14. The stability of days is on the order of E-14, and the stability of the on-board hydrogen clock is on the order of E-15. Compared with the on-board atomic clock, the hydrogen clock is more prone to large phase jumps, but this jump has little effect on the accuracy index.

Keywords: Beidou-3 · On-board clock · Performance · Evaluation

1 Introduction

The key to navigation and positioning of satellite navigation systems lies in the high precision, high stability on-board atomic clock. As the on-board time reference for navigation signal generation and system ranging, the on-board navigation system payload, and its performance directly determines the user's navigation and positioning accuracy [1]. With the deployment of the Beidou global system, a new generation of on-board rubidium clock and hydrogen clock are gradually put into use, and the evaluation of the on-orbit performance of the new generation of on-board atomic clock is of great significance to the construction of the Beidou-3 system.

J. Sun et al. (Eds.): CSNC 2019, LNEE 563, pp. 368–375, 2019.
https://doi.org/10.1007/978-981-13-7759-4_33

Commonly used atomic clock performance evaluation indicators are: frequency accuracy, drift rate and frequency stability. Accuracy and drift rate reflect the exact nature of the atomic clock, and stability reflects the predictability of the clock [2]. Starting from these three indicators, this paper uses the post-precision clock data obtained by the calculation of Panda software with observation data from the International GNSS Monitoring and Assessment System (iGMAS) and Multi-GNSS Experiment (MGEX). The data starts and ends from October 25, 2018 to November 19, for a total of 26 days, with an interval of 30 s. The on-orbit performance of on-board atomic clock of Beidou-3 satellites were evaluated.

2 Indicator Calculation Method

The frequency accuracy of the on-board clock is calculated from the clock difference data. The clock difference model uses the quadratic model [3]:

$$\tau = \tau_0 + At + at^2/2 \tag{1}$$

In the formula, τ for the clock difference, t is the duration, τ_0 for the initial clock difference, a for the drift rate, A is the frequency accuracy of the on-board clock.

Assume T_0 the clock difference, at the moment is initial clock difference τ_0, T_1 the clock difference at the moment τ_1, T_2 clock difference at the moment is τ_2, From T_0 to T_1 the duration of t_1. From T_1 to T_2 the duration of t_2, there are:

$$\tau_1 - \tau_0 = A_1 t_1 + at_1^2/2 \tag{2}$$

$$\tau_2 - \tau_1 = A_2 t_2 + at_2^2/2 \tag{3}$$

A_1 for the atomic clock from T_0 to T_1 average accuracy between times. A_2 for the atomic clock from T_1 to T_2 average frequency accuracy between times. a for linear drift rate.

$$A_2 = A_1 + at_2 \tag{4}$$

Substituting (4) into (3) gives:

$$\tau_2 - \tau_1 = (A_1 + at_2)t_2 + at_2^2/2 \tag{5}$$

In equations (2) and (5), τ_0, τ_1, τ_2, t_1, t_2 are 是 known, only A_1 and a is unknown. In fact we only care A_1. Therefore, the solution of (2) and (5) can be obtained.

$$A_1 = \left(3\Delta\tau_1 t_2^2 - \Delta\tau_2 t_1^2\right)/\left(3t_1 t_2^2 - t_1^2 t_2\right) \tag{6}$$

In the formula, $\Delta\tau_1 = \tau_1 - \tau_0$, $\Delta\tau_2 = \tau_2 - \tau_1$
The drift rate is generally the least squares method [4]:

$$\mathrm{D} = \sum_{i=1}^{N} (f_i - \bar{f})(t_i - \bar{t}) / \sum_{i=1}^{N} (t_i - \bar{t})^2 \tag{7}$$

Among them, $\bar{f} = \sum_{i=1}^{N} f_i/N$, $\bar{t} = \sum_{i=1}^{N} t_i/N$
The stability assessment uses Hadamard variance estimation formula [5].

$$\mathrm{H}\sigma_y^2(\tau) \approx \sum_{i=1}^{M-2} [f_{i+2} - 2f_{i+1} + f_i]^2/6(M-2) \tag{8}$$

3 On-Board Clock Performance Evaluation

3.1 Clock Difference Data Preprocessing

During the epoch period, the Beidou-3 satellite that solves the clock data has 12 satellites, C20, C21, C22, C23, C24, C25, C26, C27, C29, C30, C32 and C33, C20, C21, C22, C23, C24, C32, and C33 satellites are equipped with a rubidium atomic clock, hydrogen atoms used in C25, C26, C27, C29, and C30 satellites. Meanwhile, G08 (cesium atomic clock, 2015.07 launched), G24 (cesium atomic clock, 2012.10 launched), G10 (rubidium atomic clock, 2015.10 launched) and G18 (rubidium atomic clock, 2014.10 launched) from GPS are evaluated to compare with clocks of Beidou-3 satellites.

Because the on-board atomic clock is sometimes affected by changes in its own characteristics and the complex space electromagnetic environment, abnormal disturbances [6] may occur, causing abnormal clock data. Therefore, abnormal data such as gross errors need to be processed before evaluation. Figure 1 shows the clock data of each on-board clock.

It can be seen from Fig. 1 that the satellites of the C27, C29 and C30 have large phase jumps in addition to the gross errors due to the phase adjustment of the operational control system or the phase jump of the satellite atomic clock.

Here, the phase jump data is not processed temporarily, and the phase data is converted into frequency data, and the gross error is eliminated by 5 times the error.

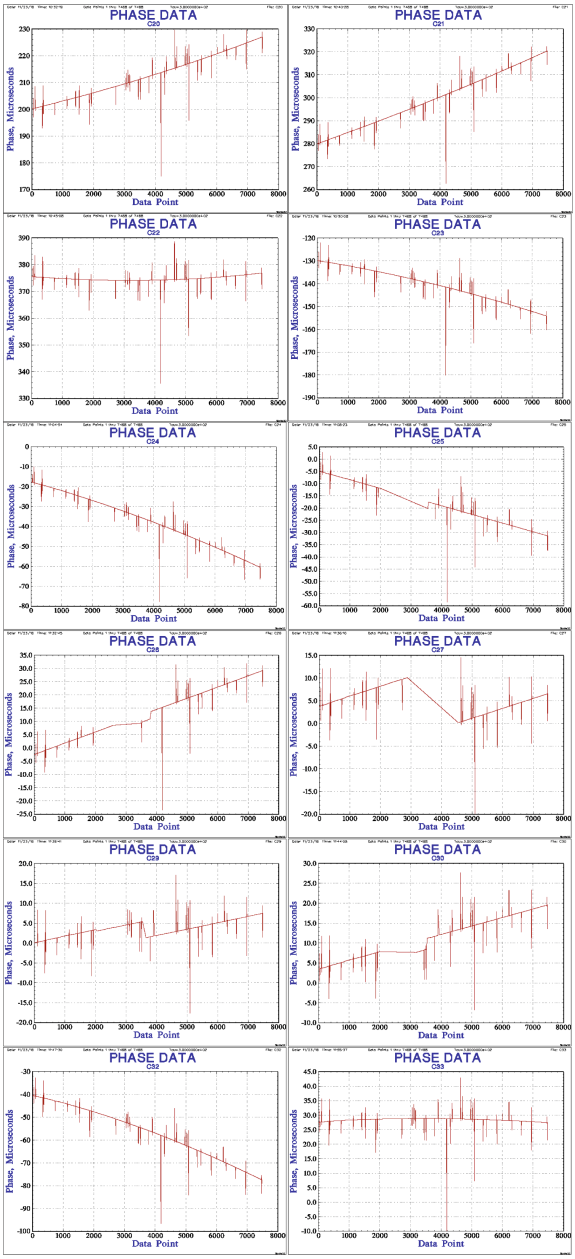

Fig. 1. Clock error data of Beidou-3 satellites

3.2 Frequency Accuracy Assessment

According to formula (6), the average frequency accuracy of the celestial clocks of the epochs is calculated, as shown in Table 1.

Table 1. Accuracy of on-board clock error frequency

PRN	C20	C21	C22	C23
Accuracy	1.50E-11	2.07E-11	4.41E-12	1.28E-11
PRN	C24	C25	C26	C27
Accuracy	2.20E-11	1.09E-11	1.50E-11	8.15E-12
PRN	C29	C30	C32	C33
Accuracy	6.28E-12	7.98E-12	2.00E-11	9.26E-13
PRN	G08	G24	G10	G18
Accuracy	2.80E-13	4.71E-13	3.13E-12	5.07E-12

From the results, the frequency accuracy of the Beidou-3 on-board clock is in the range of 9.26E-13–2.20E-11, which is basically in the order of E-12–E-11. The most of Beidou-3 clocks are inferior to the E-12 order of rubidium atomic clock and E-13 order of cesium atomic clock from GPS.

3.3 Frequency Drift Rate Assessment

According to formula (7), the frequency drift rate of the celestial clock is calculated, as shown in Table 2.

Table 2. Drift rate of on-board clock error frequency

PRN	C20	C21	C22	C23
Drift rate	1.87E-13	1.31E-13	2.55E-13	2.77E-13
PRN	C24	C25	C26	C27
Drift rate	3.95E-13	2.97E-14	2.38E-14	3.17E-14
PRN	C29	C30	C32	C33
Drift rate	3.10E-14	2.82E-14	4.03E-13	1.26E-13
PRN	G08	G24	G10	G18
Drift rate	7.77E-15	5.90E-15	2.05E-14	5.80E-15

From the results, the frequency drift rate of the Beidou-3 on-board clock is in the range of 2.38E-14–4.03E-13. The hydrogen atomic clock is basically in the E-14 magnitude, and rubidium atomic clock is E-13. The hydrogen atomic clocks slightly better than the rubidium atomic clock. Both of the atomic clocks are inferior to the GPS.

3.4 Frequency Stability Assessment

According to formula (8), the frequency stability of the epoch star clock is calculated, as shown in Table 3.

Table 3. Stability of on-board clock error frequency

PRN	C20	C21	C22	C23
Stability	4.17E-14	3.49E-14	2.68E-14	2.27E-14
PRN	C24	C25	C26	C27
Stability	1.16E-13	9.11E-15	1.14E-14	3.68E-14
PRN	C29	C30	C32	C33
Stability	5.20E-14	3.82E-14	3.24E-14	2.92E-14
PRN	G08	G24	G10	G18
Stability	5.50E-13	2.98E-13	8.31E-14	4.29E-13

From the results, the frequency stability of the Beidou-3 on-board clock is in the range of 9.11E-15–1.16E-13, which precede the GPS slightly.

3.5 Segment Performance Evaluation

It can be seen from Fig. 1 that there are phase jumps in the clock data of the C25, C26, C27, C29 and C30 satellites carrying the hydrogen atomic clock, and the clock skew of the C27, C29 and C30 satellites is more significant. Therefore, the clock data segmentation of the three satellites was evaluated. The segmentation of this paper is based on avoiding the epoch of the clock hopping period, and each segment is taken before (A) and (B) before the hopping period, as shown in Fig. 2.

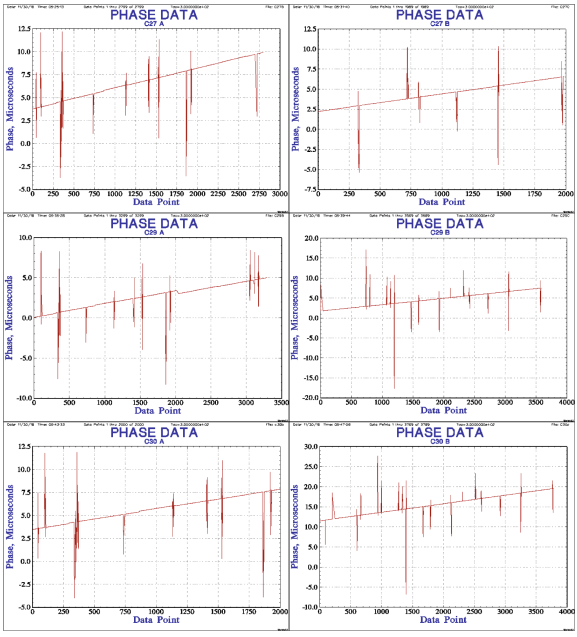

Fig. 2. Part of on-board clock error data selected

Calculate the three indicators of the selected clock error data for statistics (Tables 4, 5 and 6):

Table 4. Comparison of accuracy by different epoch arcs

PRN	C27	C29	C30
Full arc	8.15E-12	6.28E-12	7.98E-12
A arc	8.14E-12	6.28E-12	7.96E-12
B arc	8.12E-12	6.24E-12	7.92E-12

Table 5. Comparison of drift rate by different epoch arcs

PRN	C27	C29	C30
Full arc	3.17E-14	3.10E-14	2.82E-14
A arc	1.12E-15	1.37E-15	6.71E-15
B arc	1.24E-16	2.58E-15	5.44E-15

Table 6. Comparison of stability by different epoch arcs

Full arc	PRN	C27	C29	C30
	Stability	3.68E-14	5.20E-14	3.82E-14
A arc	PRN	C27	C29	C30
	Stability	2.13E-14	9.38E-15	8.20E-15
B arc	PRN	C27	C29	C30
	Stability	1.94E-14	1.54E-14	1.41E-14

From the statistics of the three indicators, whether the segmentation has almost no effect on the frequency accuracy; it is beneficial to the drift rate and stability performance improvement, and the performance improvement of the day and second is significantly stable in the tens of seconds. After the segmentation, the drift rate and stability of the on-board hydrogen atomic clock are better than the rubidium atomic clock.

4 Conclusion

As for atomic clock evaluation indicators, the frequency accuracy and drift rate of Beidou-3 on-board clocks are inferior to the GPS except the stability. The current frequency accuracy of the Beidou-3 satellite on-board clock is on the order of E-12–E-11, the drift rate of the cuckoo clock is on the order of E-13, and the drift rate of the hydrogen clock is on the order of E-14. The tens of seconds and days and seconds stability are on the order of E-14, and the space-second stability of the on-board hydrogen clock can reach the E-15 level. Compared with the on-board atomic clock,

the space-borne hydrogen clock is more prone to large phase jumps. This jump has little effect on the accuracy index evaluation, but has a greater impact on the evaluation of drift rate and stability performance. Perhaps because the performance of the on-board atomic clock is usually stable after six months of satellite launch [7], the performance of the new generation Beidou-3 satellite on-board atomic clock is not significantly better than the Beidou-2 satellite, but I believe that with the Beidou With the commissioning and stable operation of the No. 3 system, the performance advantages of the new generation of atomic clocks on-board will gradually become prominent.

References

1. Gu Y, Chen Z, Shuai P (2008) Development of satellite atomic clocks for navigation satellites abroad. Space Int 10:12–16
2. Guo H (2006) Study on the analysis theories and algorithms of the time and frequency characterization for atomic clocks of navigation satellites. Information Engineering University
3. Wang Y (2017) Research on modeling and prediction of the satellite clock bias and performance evaluation of GNSS satellite clocks. Information Engineering University
4. Guo H, Yang S, He H (2007) Analyse of frequency drift characteristic for atomic clocks of navigation satellites. GNSS World China 32(6):5–10
5. Sun D (2016) Research on the performance analysis of GNSS on-board clock. Chang'an University
6. Schmidt LS (2003) Atomic clock models using fractionally integrated noise processes. Metrologia 40(3):S305–S311
7. Liu S, Jia X, Sun D (2017) Performance evaluation of GNSS on-board atomic clock. Geomat Inf Sci Wuhan Univ 42(2):277–284

Quality Analysis of GNSS Data in Polar Region

Xiang Yao(✉), Mingjian Chen, Jianguang Wang, and Rui Chen

Geospatial Information Institute, Information Engineering University, Zhengzhou, China
yaoxiang30303@126.com

Abstract. Due to the special geographical and spatial meteorological characteristics in the polar region, we deeply studies the influence of this feature on the quality of GNSS observation data. In this paper, 12 MGEX stations and 2 IGMAS stations are used to test the data quality, such as the number of visible satellites, PDOP value, SNR and multipath delay. BDS-3 is also used for simulation test. The test results show that: (1) the number of GPS satellites in the polar region is significantly more than the number of BDS satellites. The BDS satellite has a large or zero PDOP value at some sites; (2) The SNR of the GPS and GLONASS satellites at the L1 frequency is better than the SNR at the L2 frequency. The SNR of the BDS satellite at the B3 frequency is better than the SNR of the B1 and B2. The SNR of GEO satellites is lower than that of IGSO and MEO satellites. The multipath effect of GEO satellites is obvious, and is greater than IGSO and MEO satellites. (3) The simulation results show that BDS-3 has more satellite numbers, better spatial geometry and better navigation accuracy.

Keywords: Polar region · Multipath delay · SNR · The number of visible satellites · PDOP

1 Introduction

With the full completion of the BDS-3 (Beidou three-generation system), global navigation and positioning services will be provided by the end of 2020. Due to the special geographical location at the ends of the Earth, the Beidou system has poor coverage in polar region. With the development of BDS-3 and GNSS (Global Navigation Satellite System), satellite numbers and geometric spatial structure of satellites are more optimized, which is of great significance for navigation and positioning in polar region. The observational conditions in the polar region lead to the observational characteristics of the observed GNSS data that are definitely different from those in the middle and low latitudes. At the same time, the analysis of GNSS observation data quality is a necessary prerequisite for high-precision positioning. Lv analyzes the data quality of GPS in Antarctic [1]. Zhou studies and analyzes the influence of data quality on BDS (BeiDou System, BDS) PPP (precise point positioning, PPP) [2]. Based on the special conditions of the polar region, Zuo proposes a feasible polar quality control strategy for data quality analysis [3]. In order to better understand the GNSS data quality in polar region, this paper studies and analyzes the number of visible satellites, PDOP [4] (Position Dilution of Precision) value, SNR (Signal-to-noise Ratio) and

J. Sun et al. (Eds.): CSNC 2019, LNEE 563, pp. 376–388, 2019.
https://doi.org/10.1007/978-981-13-7759-4_34

multipath delay [5], which provide reference for further polar positioning in polar region. We also perform simulation tests on BDS-3 for CAS1, CUT0, METG, and REYK sites. The number of visible satellites, PDOP and navigation accuracy are simulated, and good experimental results are obtained.

2 Data Processing and Analysis

2.1 Data

This experiment uses 12 MGEX stations and 2 IGMAS stations in the polar region. The test data is 24 h and the time interval is 30 s. The time is on the 4th day in 2016. The data observed by the GNSS receiver includes GPS, GLONASS and BDS. Due to the differences in the equipment of the station, the observed data may not contain the multi-system complete data. Based on the actual situation of each site, the number of visible satellites and PDOP values of each site are statistically analyzed. The number of visible satellites and the PDOP value are important indicators for measuring the spatial geometry of satellites and the spatial distribution of satellites [6].

2.2 Number of Visible Satellites

With the progress of GPS, GLONASS and BDS modernization plans, the visible number of satellites is constantly increasing [7]. For polar region, enough visible satellite numbers are guaranteed to ensure the reliability and stability of navigation and positioning accuracy [8]. The coordinates of the stations required for the test are shown in Table 1.

Table 1. Station coordinates

Sites	Position		
	Latitude/°	Longitude/°	Height/m
CAS1	−66.28	110.52	22.55
METG	60.24	24.38	59.67
DAV1	−68.57	77.97	44.4
DUM1	−66.67	140.00	−1.4
KIRU	67.86	20.97	391.1
MAW1	−67.61	62.87	59.1
MCM4	−77.84	166.67	98
CUT0	−32.004	115.89	24.0
OHI3	−63.32	−57.9	32.15
PALM	−64.78	295.95	31.1
REYK	64.14	−21.96	93.1
SYOG	−69.01	39.58	50
CNYR	78.92	11.93	/
ZHON	−69.37	76.38	/

The test results can be obtained by counting the number of visible satellites of the selected 12 MGEX stations and 2 IGMAS stations, as shown in Figs. 1, 2, 3 and 4.

Figure 1 shows the minimum, the mean and the maximum value of the number of visible satellites of GPS observation data for all stations. In Fig. 1, it can be known that the GPS satellites of all stations have a minimum value of 8 or more, and the average value is greater than 10. The GPS satellite can meet the minimum number of satellites required for positioning, which provides a basis for polar positioning.

Figure 2 shows the minimum, mean and maximum value of the number of visible satellites for GLONASS observations for all stations. It can be seen from Fig. 2 that the minimum number of visible satellites of all stations is greater than or equal to four, and the average value of all stations is greater than eight, which can meet the needs of polar positioning.

Figure 3 shows the minimum, mean and maximum value of the number of visible satellites for BDS observations for all stations. It can be seen from Fig. 3 that the visible number of BDS satellites is less than GPS and GLONASS, and the CAS1, CUT0, KIRU, METG, REYK, CNYR and ZHON stations in Fig. 3 have BDS observation data. Among them, the minimum value of visible satellites at KIRU, METG, REYK and CNYR stations is less than 4, and the mean value of REYK and CNYR are less than 4. The number of satellites at CUT0, CAS1 and ZHON sites is relatively good, which can be prioritized when performing BDS PPP.

Figure 4 shows the visible number of satellites of all stations, all of which is more than 15. Therefore, in the process of multi-system fusion navigation and positioning, the number of satellites can be seen to meet the requirement.

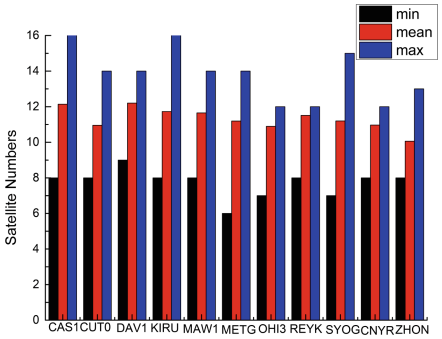

Fig. 1. Satellite numbers of GPS

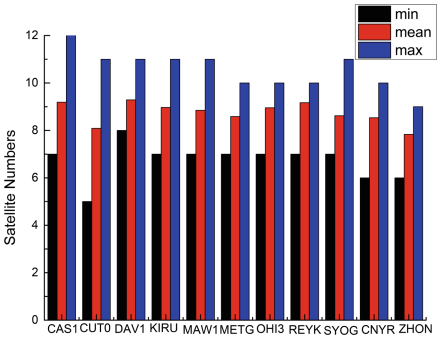

Fig. 2. Satellite numbers of GLONASS

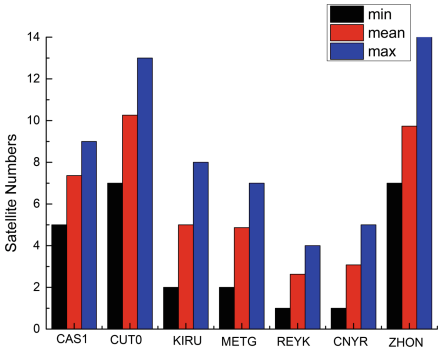

Fig. 3. Satellite numbers of BDS

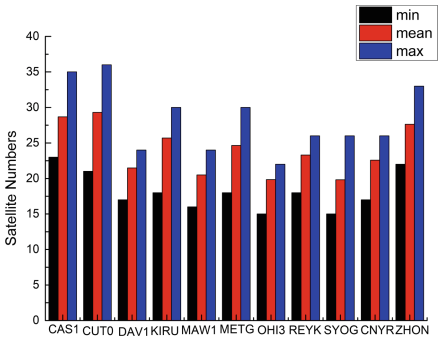

Fig. 4. Satellite numbers of GPS/GLONASS/BDS

The visible satellites of each station are counted, as shown in Table 2.

Table 2. Statistics of satellite numbers

Sites	Satellite numbers											
	GPS			GLONASS			BDS			SUM		
	Min	Mean	Max	Min	Mean	Max	Min	Mean	Max	Min	Mean	Max
CAS1	8	12.1399	16	7	9.1865	12	5	7.3622	9	23	28.68	35
CUT0	8	10.951	14	5	8.0854	11	7	10.2604	13	21	29.3	36
DAV1	9	12.2028	14	8	9.2854	11	/	/	/	17	21.4882	24
DUM1	6	9.914	12	/	/	/	/	/	/	6	9.914	12
KIRU	8	11.7285	16	7	8.9688	11	2	4.9979	8	18	25.6951	30
MAW1	8	11.6493	14	7	8.8479	11	/	/	/	16	20.4972	24
MCM4	8	10.9028	12	/	/	/	/	/	/	8	10.9028	12
METG	6	11.1972	14	7	8.5837	10	2	4.8649	7	18	24.6458	30
OHI3	7	10.8944	12	7	8.9569	10	/	/	/	15	19.8514	22
PALM	7	10.5212	12	/	/	/	/	/	/	7	10.5212	12
REYK	8	11.5094	12	7	9.1674	10	1	2.6278	4	18	23.3045	26
SYOG	7	11.2017	15	7	8.6191	11	/	/	/	15	19.8208	26

Table 2 summarizes the minimum, mean, and maximum values of visible satellites for GPS, GLONASS, BDS, and sum for 12 MGEX sites. It can be seen from Table 2 that the minimum number of GPS observation data is greater than the number of satellites required for the positioning solution; at the same time, it can be known that there are only GPS observation data in the three stations DUM1, MCM4 and PALM. DAV1, MAW1, OHI3 have GPS and GLONASS observation data, and the remaining stations have three-system observation data. According to the statistics in Table 2, the maximum, mean and minimum results of GPS, GLONASS and BDS of the number of visible satellites can be obtained, as shown in Fig. 3. The Figure does not include DUM1, MCM4 and PALM is only with single GPS observation data.

Table 2 summarizes the minimum, mean, and maximum values of the number of visible satellites near the polar region. According to the chart analysis, it can be known that the number of satellites that can be used for positioning in the polar region is less than the middle and low latitudes.

2.3 PDOP

The experiment uses RTKLIB software for calculation, and the test results can be obtained by statistical analysis. It can be seen as Table 3.

Table 3. Statistics of PDOP value

Sites	PDOP											
	GPS			GLONASS			BDS			SUM		
	Min	Mean	Max	Min	Mean	Max	Min	Mean	Max	Min	Mean	Max
CAS1	1	1.4778	2.4	1.1	1.6407	2.9	1.8	3.7021	13.8	0.7	0.832	1
CUT0	1.1	1.3943	2.2	1.3	1.8811	2.9	1.5	2.2	4	0.7	0.8475	1.1
DAV1	1.1	1.4789	2.5	1.2	1.6219	2.2	/	/	/	0.9	1.024	1.4
DUM1	1.3	2.0542	15.8	/	/	/	/	/	/	1.3	2.0542	15.8
KIRU	1	1.5576	3	1.2	1.7026	2.6	0	9.1329	98.3	0.8	0.9477	1.3
MAW1	1.1	1.5677	2.7	1.2	1.7299	2.9	/	/	/	0.9	1.0738	1.7
MCM4	1.4	1.8678	3.8	/	/	/	/	/	/	1.4	1.8678	3.8
METG	1.1	1.5267	3.7	1.3	1.7522	2.5	0	7.1182	97.4	0.8	0.9417	1.2
OHI3	1.2	1.612	2.3	1.2	1.6486	2.8	/	/	/	0.9	1.0818	1.5
PALM	1.2	1.7454	3.2	/	/	/	/	/	/	1.2	1.7454	3.2
REYK	1.1	1.5178	2.6	1.2	1.6014	2.3	0	3.3105	92.2	0.8	0.988	1.4
SYOG	1.2	1.7345	3.5	1.2	1.8524	3.3	/	/	/	0.9	1.1623	1.7
CNYR	1.4	1.9794	3.6	1.4	1.9016	3.4	0	7.8846	99	1	1.1906	1.8
ZHON	1.4	2.0325	4.7	1.5	2.1336	5.6	1.6	3.3073	6.8	0.8	0.9456	1.1

From the statistics in Table 3, the maximum, mean and minimum GDOP results of GPS, GLONASS and BDS at all sites can be obtained, as shown in the Figs. 5, 6, 7 and 8.

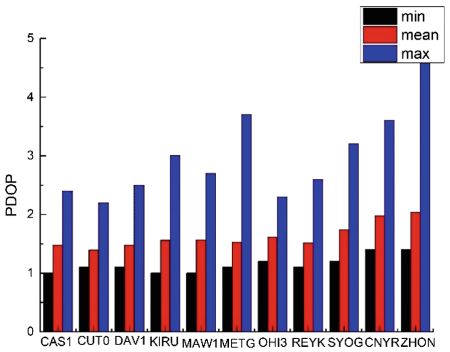

Fig. 5. Result of GPS

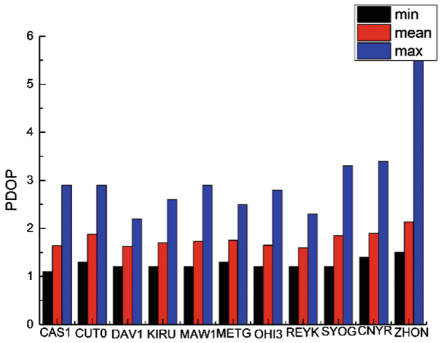

Fig. 6. Result of GLONASS

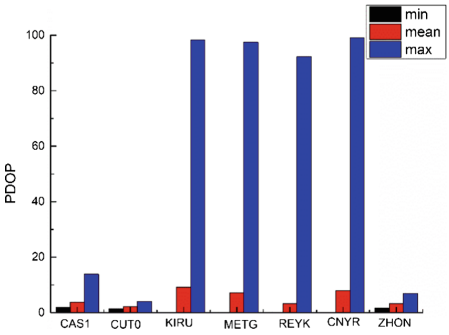

Fig. 7. Result of BDS

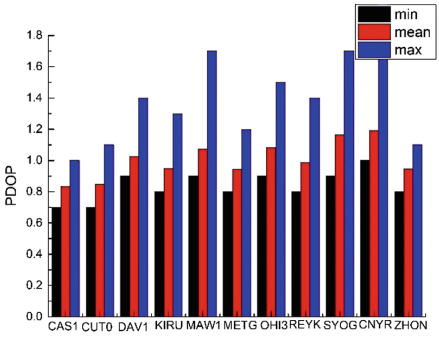

Fig. 8. Result of GPS/GLONASS/BDS

The observations of the DUM1, MCM4, and PALM stations only have GPS observations, seven sites with only BDS observations are counted as shown in the Fig. 7.

Figure 5 shows the minimum, mean and maximum of the PDOP values for all IGS stations near the polar region. From the statistical results in Table 3, it can be known that the maximum PDOP of GPS at the DUM site reaches 15.8 and average PDOP reaches 2.0542. The result is due to the loss of lock of individual satellite signals on the day. The maximum PDOP value of other statistical sites is less than 5.0, and the average PDOP is less than 2.1. The spatial structure of the GPS system performs better in all stations of the statistics.

Figure 6 shows the minimum, mean and maximum value of the PDOP values of GLONASS at sites near the polar region. Combined with Figs. 7 and 6, it can be seen that the PDOP value of the ZHON site can reach 5.6, and the average PDOP of each site is less than 2.1. Near the polar region, the spatial satellites of the GLONASS satellites are well distributed.

Figure 7 shows the minimum, mean, and the maximum value of the PDOP values of the BDS of the stations near the polar region. It can be seen from Fig. 3 that the spatial satellite geometry of the CAS1, CUT0 and ZHON stations is superior, and the maximum PDOP of the CAS1 station is 13.8. The minimum satellite of the CAS1 station is 5, because the satellites are less visible, so the satellite geometry is poor. The PDOP of the KIRU, METG, REYK, and CNYR sites can reach a maximum of 100, and even some epochs cannot be located.

Figure 8 shows the PDOP value maximum, mean and maximum for all GNSS satellites near the polar region. The PDOP average for all stations near the polar region is less than 1.2 and the PDOP value is less than 1.8. It can be seen from Table 3 that PDOP value of the BDS in the polar region is worse than that of GPS and GLONASS. The spatial geometry of the multi-system satellite combination in the polar region is significantly better than the single-system. The positioning of multiple system combinations in the vicinity of the polar region is significantly better than the single system positioning.

2.4 SNR

After statistics on the number of visible satellites and the value of PDOP, the sites with multiple systems satisfying the positioning requirements include CAS1, CUT0, METG, KIRU, and REYK. And the SNR analysis is performed. In the process of multipath delay, the five sites are mainly analyzed. The SNR describes the ratio of the active and noise components in the signal. The larger the SNR, the smaller the noise component in the signal, and vice versa [9]. The test results are tested by the selected sites, and the RMS statistics of the SNR are shown in Tables 4 and 5.

Table 4. Statistics of SNR RMS/(dB)

Sites	GPS			GLONASS		
	SNR1	SNR2	SNR5	SNR1	SNR2	SNR5
CAS1	44.3745	29.6371	/	42.6526	40.5605	/
CUT0	44.3386	31.8823	/	44.0146	40.6183	/
METG	44.8279	33.6824	/	45.2431	41.8659	/
KIRU	44.5939	41.6839	/	46.4236	41.0738	/
REYK	47.9345	41.4152	/	46.4263	41.0738	/

Table 5. Statistics of BDS SNR RMS/(dB)

Sites	GEO			IGSO			MEO		
	SNR1	SNR2	SNR3	SNR1	SNR2	SNR3	SNR1	SNR2	SNR3
CAS1	36.078	/	39.309	42.5201	/	43.8612	43.4361	/	45.026
CUT0	39.1453	/	42.87	44.9098	/	44.8963	44.3098	/	45.7815
METG	35.7065	38.2974	39.0172	42.4679	42.6085	46.6329	45.2869	42.6644	47.2672
KIRU	33.5771	/	36.0567	43.3476	/	44.4952	45.5856	/	47.1208
REYK	/	/	/	40.5196	/	43.4477	43.2552	/	47.2854

The statistics in Table 4 are the RMS values of GPS and GLONASS at five sites, such as CAS1. SNR1 represents the SNR of the observed values at the L1 frequency, SNR2 represents the SNR of the observed values at the L2 frequency, and SNR5 represents the L5 frequency. The SNR of the observed values. Table 4 shows that the SNR of GPS on L1 is between 40 and 50. The SNR at the L2 frequency is significantly lower than that at the CAS1, CUT0, METG and ZHON stations. The SNR of GPS at the L1 frequency, which is related to the latitude of the station. The latitude of these four stations is relatively high, and the satellite altitude angle is low. The SNR of GLONASS at L1 and L2 frequencies is between 40 and 50 respectively. Compared with GPS, GLONASS has better SNR at L2 frequency, and lower SNR means better observation quality.

The statistics in Table 5 are the RMS values of the five stations such as CAS1, SNR1 is the SNR of the B1 frequency observation, SNR2 is the SNR of the observations at the B2 frequency, and SNR5 is the observation on the B3 frequency. It can be seen from Table 5 that the SNR of BDS GEO satellites at B1, B2 and B3 frequencies is between 30 and 40, which is significantly lower than the SNR of GPS at L1 frequency, due to the low SNR of GEO satellites. For BDS IGSO and MEO satellites, the SNR is between 40 and 50. The SNR of IGSO is comparable to that of GPS. The SNR of MEO is even better than that of GPS satellites.

2.5 Multipath Delay

Multipath delay is the error caused by the direct and reflected signals superimposed into the receiver and affecting the observations [10]. After counting the visible number of satellites and the PDOP value, all the stations have multiple systems. The sites required for positioning mainly include CAS1, CUT0, METG, KIRU, and REYK, for multipath delay analysis.

This experiment performs statistical analysis on multipath delays of five sites such as CAS1, CUT0, METG, KIRU and REYK. The RMS statistics of multipath are shown in Tables 6 and 7.

Table 6. Statistics of multipath RMS/(m)

Sites	GPS			GLONASS		
	Mp1	Mp2	Mp5	Mp1	Mp2	Mp5
CAS1	0.409	0.3489	/	0.4553	0.4146	/
CUT0	0.5824	0.4103	/	0.5825	0.4924	/
METG	0.3288	0.3537	/	0.4032	0.3854	/
KIRU	0.3755	0.2759	/	0.3461	0.2742	/
REYK	0.3262	0.2752	/	0.3461	0.2742	/

Table 7. Statistics of BDS multipath RMS/(m)

Sites	GEO			IGSO			MEO		
	Mp1	Mp2	Mp3	Mp1	Mp2	Mp3	Mp1	Mp2	Mp3
CAS1	0.4829	/	0.2867	0.3904	/	0.2971	0.5062	/	0.3727
CUT0	0.5349	/	0.3717	0.5231	/	0.3975	0.6219	/	0.4924
METG	0.4893	0.5241	0.5597	0.3582	0.24	0.2825	0.5291	0.391	0.4147
KIRU	0.3324	/	0.2564	0.4213	/	0.3682	0.3798	/	0.4291
REYK	/	/	/	0.296	/	0.3148	0.4096	/	0.3247

The statistics in Table 6 are the multipath RMS values of GPS and GLONASS at five sites, such as CAS1. Mp1 represents the multipath of the observations at the L1 frequency, Mp2 represents the multipath of the observations at the L2 frequency, and Mp5 represents the L5 frequency. It can be seen from Table 5 that the multipath Mp1 of the GPS at the L1 frequency is significantly higher than the multipath of the L2 frequency, and the multipath Mp1 of the GLONASS at the L1 frequency is significantly higher than the multipath of the L2 frequency.

The statistics in Table 7 are the RMS values of the five stations BDS such as CAS1, Mp1 is the multipath of the B1 frequency observation, Mp2 is the multipath of the observations at the B2 frequency, and Mp3 is the observation of the B3 frequency. It can be seen from Table 7 that the multipath of the GEO satellite is higher than the multipath of the IGSO satellite at the B1 frequency, but the statistical results show that the multipath of the MEO at the B1 frequency is higher than that of the GEO because as the latitude increases, the satellite's elevation angle decreases, and the GEO satellite is in a stationary position. As the satellite's elevation angle decreases, the multipath of the MEO satellite continues to grow. The results of the statistics at the B2 frequency point are small. It can be seen from the METG site that the multipath effect of the GEO satellite is the most obvious. The multipath effect of MEO satellites at B3 is stronger than GEO and IGSO.

At the same time, comparing the L1 frequency of GPS and the multipath of BDS at B1, we can know that the multipath of GEO satellite and MEO satellite is higher than that of GPS satellite. The multipath effect of GEO satellite is higher due to satellite height. As well as the reason for synchronizing with the Earth, the multipath of the MEO satellite is higher than that of the GPS satellite and has a certain relationship with the noise of the satellite and the receiver equipment.

2.6 BDS-3 Simulation

With the networking of the BDS-3 and the advancement of global positioning services, it is of great significance to study the navigation and positioning availability of the Beidou-3 global system in the Polar Region. This experiment is to obtain the satellite visible number, PDOP and navigation precision in the polar region by simulating the BDS-3 satellite constellation. By analyzing the polar region sites CAS1, CUT0, REYK and METG, the BDS-3 satellite is determined in the polar high-altitude region. Availability, providing a reference for polar navigation positioning. Because the BDS-3 satellite orbit parameters cannot be accurately obtained, this paper uses STK to carry out simulation experiments according to the BDS-2 GEO/IGSO/MEO orbit parameters [11]. The experimental simulation of the satellite constellation 3GEO+3IGSO+24MEO hybrid configuration, the satellite orbit parameters are shown in Table 8.

Table 8. Satellite orbit parameters

Orbit parameters	GEO	IGSO	MEO
Semi major axis/km	62164	42164	27878
Eccentricity	0	0	0
Inclination/°	0	55	55
RAAN	158.75°E, 180°E, 210.5°E, 240°E, 260°E	218°E, 98°E, 338°E	0, 120°E, 240°E
Argument of Perigee/°	0	0	0
Mean anomaly	0	0(218°E), 120°(98°E), 240°(338°E)	The first satellite of each track set as 0, and the rest is increased by 45°
Satellite numbers	3	3	24
Track surface	1	3	3

The experiment simulated the BDS-3 satellite constellation from January 9, 2019 to January 10, 2019. The experimental results mainly include satellite visible number, PDOP and navigation accuracy, as shown in Figs. 9, 10 and 11.

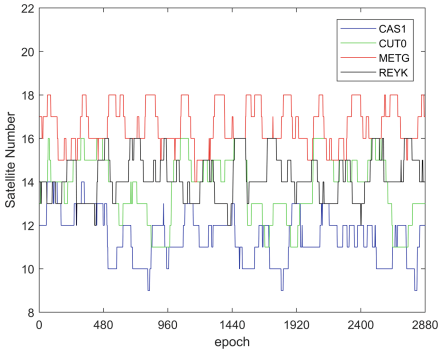

Fig. 9. Satellite numbers

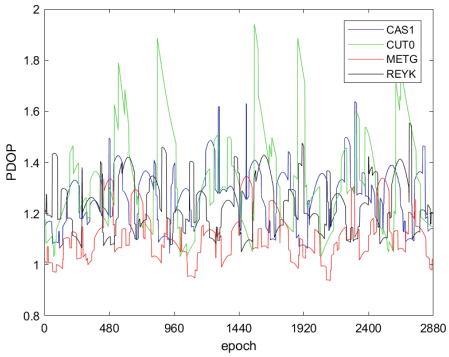

Fig. 10. PDOP

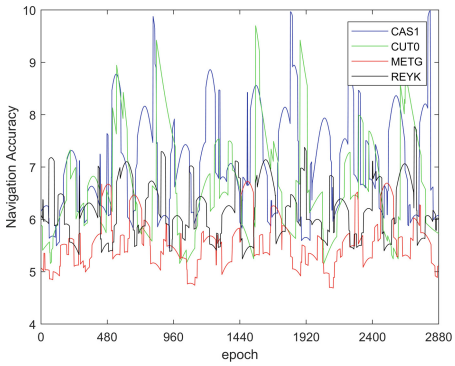

Fig. 11. Navigation accuracy

According to the simulation results, the PDOP, Satellite Numbers and Navigation Accuracy obtained from the experiment are statistically analyzed. The statistical results are shown in Table 9.

Table 9. Statistics of simulation result

Station	PDOP			Satellite numbers			Navigation accuracy/(m)		
	Max	Mean	Min	Max	Mean	Min	Max	Mean	Min
CAS1	1.637	1.265	1.042	14	11.5024	9	9.989	7.0925	5.4548
CUT0	1.94	1.3297	1.031	16	13.7627	11	9.6993	6.6485	5.1568
METG	1.345	1.1129	0.937	18	16.5337	14	6.7254	5.5646	4.6871
REYK	1.554	1.238	1.049	16	14.1992	12	7.7704	6.1902	5.244

Table 9 shows the PDOP, Satellite Numbers and Navigation Accuracy of CAS1, CUT0, METG and REYK sites. Figure 9 shows the satellite time series of CAS1, CUT0, KIRU and METG sites, all of which has better observation conditions. The number of minimum observation satellites at the METG site reached 14, and the average number of observation satellites reached more than 16. The observation conditions of the CAS1 station are slightly worse. The number of minimum observation satellites is 9 and the number of average observation satellites is more than 11 to meet the number of satellites for navigation and positioning.

Figure 10 shows the PDOP time series of CAS1, CUT0, KIRU and METG stations. It can be seen from the figure that all four stations have better satellite space geometry, and the PDOP of CUT0 station is worse than the other three stations. It is 1.031, the average is 1.3297, the maximum is 1.94, and the PDOP of all stations is less than 2, which has better satellite geometry in the Polar Region.

Figure 11 shows the Position accuracy time series of CAS1, CUT0, KIRU and METG stations. The navigation accuracy is affected by the number of visible satellites and PDOP values. It is consistent with the number of visible satellites and PDOP

values. The navigation accuracy of CAS1 and CUT0 stations is consistent. The average values are 7.0925 m and 6.6485 m, respectively, and the maximum is less than 10 m.

The results of the Satellite Number, PDOP and Navigation Accuracy tests were carried out on the BDS-3 using four polar stations. The results show that the BDS-3 global system has good coverage and availability in the polar region. Navigation and positioning can provide sufficient protection.

3 Conclusions

By conducting experiments on satellite visible numbers, PDOP values, SNRs, and multipath delays in sites in the polar region, statistics can be obtained based on the test results, and the following conclusions can be obtained:

1. By analyzing the number of visible satellites and PDOP value of 14 stations near the polar region, five sites with multiple system observations such as CAS1, CUT0, METG, KIRU and REYK were selected to meet the Multi-System positioning requirements.
2. The SNR and multi-path analysis were carried out on the six selected sites. From the statistical results, it can be known that the SNR of the GPS and GLONASS satellites at the L1 frequency is better than the SNR at the L2 frequency. The SNR of the B1 and B2 frequencies of the BDS satellite is not much different, and the SNR of the B3 frequency is better than the SNR of the B1 and B2 frequencies. The SNR of GEO satellites is lower than that of IGSO and MEO satellites. At the same time, it can be known from the statistical analysis of multipath of six stations that the multipath of the L1 frequency of GPS and GLONASS satellites is higher than that of the L2 frequency. For BDS satellites, the multipath effect of GEO satellites is obvious. The path delay error is greater than the multipath error delay of the IGSO and MEO satellites.
3. Simulation experiments show that BDS-3 has better visible satellite number, PDOP and navigation accuracy in polar region, and can provide sufficient basic guarantee for navigation and positioning in polar region.

References

1. Lv C, Zhang S, Dongchen E et al (2011) Analysis of GPS data in polar. Geodesy Geodyn 31 (2):117–120
2. Zhou R (2017) Research on precise point positioning technology based on BDS in polar region
3. Zuo Z (2018) Quality control methodology for BDS precise point positioning in polar region
4. Li Z, Zhang X (2009) New techniques and precise data processing methods of satellite navigation and positioning. Wuhan University Press, Wuhan
5. Van Nee RDJ (1991) Multipath effects on GPS code phase measurements. In: International technical meeting of the satellite division of the institute of navigation, ION GPS-1991. Proceedings of the 4th international technical meeting of the satellite division of the institute of navigation

6. Huang D et al (2015) Principle of satellite navigation and positioning. Wuhan University Press, Wuhan
7. Alkan RM, Karaman H, Sahin M (2005) GPS, GALILEO and GLONASS satellite navigation systems & GPS modernization. In: International conference on recent advances in space technologies. IEEE
8. Wu L, Sun Y, Yu X et al (2009) Research on GPS/GLONASS/CALILEO multi-constellation integrated navigation system. Chin Space Sci Technol 29(3):23–28
9. Yin Z, Chen M, Yan J et al (2017) Correlation analysis for GNSS multipath and SNR. Geomatics Spat Inf Technol 19(1):109–112
10. Wang G, De Jong K, Zhao Q et al (2015) Multipath analysis of code measurements for BeiDou geostationary satellites. GPS Solutions 19(1):129–139
11. Yang Y, Xu J (2016) Navigation performance of BeiDou in polar area. Geomatics Inf Sci Wuhan Univ 41(1):15–20

Precision Analysis of BDS-3 Satellite Orbit by Using SLR Data

Ding Li[3(✉)], Xue Cheng[3], Xiaolin Jia[1,2(✉)], and Wuzhao Yang[3]

[1] State Key Laboratory of Geo-Information Engineering, Xi'an 710054, Shanxi, China
13891907401@139.com
[2] Xi'an Research Institute of Surveying and Mapping, Xi'an 710054, Shanxi, China
[3] College of Geology Engineering and Geomantic, Chang'an University, Xi'an 710054, Shanxi, China
1343542911@qq.com

Abstract. The accuracy of satellite ephemeris directly affects the accuracy of navigation and positioning. The BDS-3 under construction in China is based on the BDS-2 system, and the Beidou global satellite navigation system with global service capability is built. The BDS-3 system is in operation before and after the official operation. The accuracy of satellite ephemeris needs to be analyzed to provide a reference for its builders and users. As a high-precision external evaluation method, satellite laser ranging (SLR) can be used to check the Beidou satellite orbit. This paper discusses the principle of using SLR to check the Beidou satellite orbit. The SLR observation data from August to October 2018 is used to evaluate the satellite broadcast ephemeris orbit and precision ephemeris orbit of the BDS-3 network. The results show that the radial accuracy of C20, C21, C29 and C30 satellite broadcast ephemeris orbitals are 12.92 cm, 15.08 cm, 8.53 cm and 10.74 cm, respectively, and the radial accuracy of the precision orbit are about 7 cm.

Keywords: Beidou global satellite navigation system · Satellite laser ranging (SLR) · Satellite orbit · Accuracy assessment

1 Introduction

Beidou Satellite Navigation system (BeiDou Navigation Satellite System, BDS) is a self-developed and independently operated global satellite navigation system in China. In 2012, Beidou Satellite Navigation system began to provide positioning and navigation to the Asia-Pacific region [1]. China successfully launched two BDS-3 Global Networked satellites in November 2017, marking the beginning of Beidou Satellite Navigation system entering the era of global networking [2]. At present, the BDS-3 system is being constructed quickly and 13 BDS-3 Global Networked satellites have been launched by October 2018. Planning to build a Beidou global system by 2020, to provide global services [2, 3]. Four MEO satellites, such as C20, C21, C29, C30 and so on, are equipped with laser reflectors and participate in the observation mission of the

J. Sun et al. (Eds.): CSNC 2019, LNEE 563, pp. 389–399, 2019.
https://doi.org/10.1007/978-981-13-7759-4_35

International Laser ranging Service Organization (ILRS), which provides the conditions for the precision evaluation of the Beidou satellite's precise orbit and broadcast ephemeris orbit.

Satellite navigation message is the data base used by users to locate and navigate, which mainly includes satellite ephemeris, clock correction, ionospheric delay correction, working state information and so on. The reliability and accuracy of satellite ephemeris directly affect the accuracy of navigation and positioning [4, 5]. Some domestic scholars have studied the accuracy of Beidou satellite orbit [6–10]. The results show that the accuracy of laser observation data is higher, usually better than 2 cm. The satellite laser ranging (SLR) can be used as an independent external reference with high precision. Applied to Beidou navigation satellite orbit determination, inspection and accuracy evaluation [8]. But most of the research is about the satellites launched before 2017, and the newly launched BDS-3 network satellite is not concluded. In this paper, the laser observations from August to October 2018 are used to check the broadcast ephemeris and precise orbits of some BDS-3 satellites. A certain conclusion has been drawn.

2 Principle of Accuracy Evaluation of Satellite Orbit

2.1 Assessment Methodology

Satellite laser ranging (SLR) can be used as an independent verification method for satellite orbit. The basic principle is to compare the error corrected laser observations with the satellite ephemeris calculated distance between satellite and earth, and to analyze the difference between them. Evaluation of satellite orbit accuracy [10]. In this paper, the mean (MEAN), standard deviation (STD) and the root mean square error (RMS).) are calculated respectively.

2.2 Calculation of SLR Observations and Space-Earth Distance

The basic principle of satellite laser ranging (SLR) is to determine the round trip time t of laser pulse signal from SLR observation station to satellite laser reflector and to obtain the distance between SLR observation station and satellite.

$$p = \frac{ct}{2} \tag{1}$$

In the formula, p is the distance between the stars and the earth, t is the round trip time of the laser pulse signal, c is the speed of light [11]. The error correction of laser observation is mainly the correction of tropospheric error, the correction of relativistic effect, and the correction of satellite centroid compensation.

The theoretical distance between laser observation station and satellite can be calculated by precise coordinates and satellite ephemeris.

$$p_i = \sqrt{(x - x_i)^2 + (y - y_i)^2 + (z - z_i)^2} \tag{2}$$

In the formula, P_i is the space distance, (x, y, z) is the position vector of the satellite, (x_i, y_i, z_i) is the position vector of the first station. At this point, the distance between the stars and the earth needs to be reduced to the center of mass of the satellite.

The difference between the satellite and earth distances observed by laser and those calculated by satellite ephemeris are laser residuals, which can be expressed as:

$$\Delta p = p - p_i \tag{3}$$

In the formula, ΔP is the laser residuals, P is the spaceground distance observed by laser, and Pi is the satellite ephemeris and the exact coordinates of the laser station. The laser residuals of the same satellite at different epochs and different stations are statistically analyzed to check the satellite orbit.

2.3 Corrective Model

The correction model in this paper mainly includes the pretreatment of laser observations and the coordinate correction of laser observation stations. The corrections of the original laser observations have been described above. The corrections in the coordinates of the laser observation stations include the correction of tidal displacement, the correction of crustal movement [12]. The error correction models are shown in Table 1.

Table 1. Correction models for SLR data processing

Correction	Model
Tropospheric delay	Mendes-Pavlis [12]
General relativity effect	Shapiro delay [12]
Tidal displacement	extreme tide, solid tide, tide [12]
Crustal movement	SLRF2018

3 Example Analysis

3.1 Broadcast Ephemeris

The SLR observation data from August to October 2018 was used to check the broadcast ephemeris orbits of four satellites BD-3, C20, C21, C29 and C30. The Beidou Broadcast Ephemeris used in this paper is from the multi-system hybrid ephemeris provided by MGEX. The coordinates of the laser station are provided by the International Laser Ranging Service [13]. From August to October 2018, a total of 18 laser stations observed BDS-3 satellites. The observation statistics of SLR stations are shown in Fig. 1. The distribution of stations is shown in Fig. 2. The basic information of each station is shown in Table 2. See the ILRS website for details. In the data processing, the wild value is eliminated according to the error principle of 3 times.

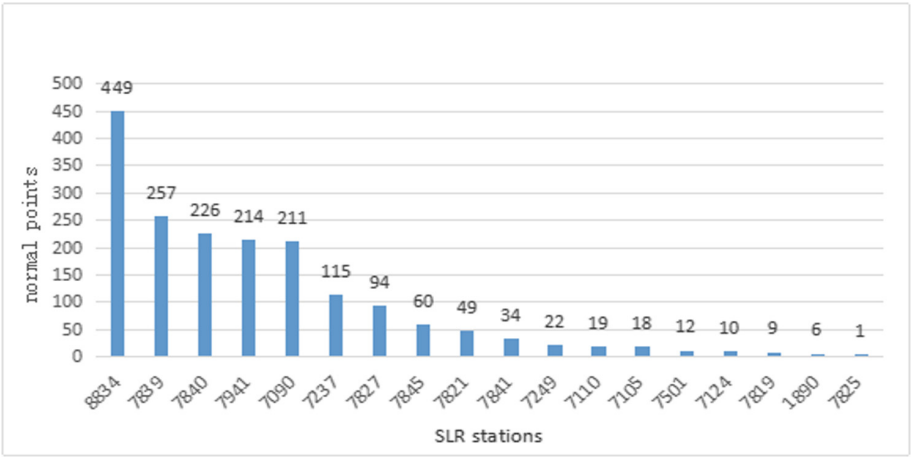

Fig. 1. SLR observations of BDS-3

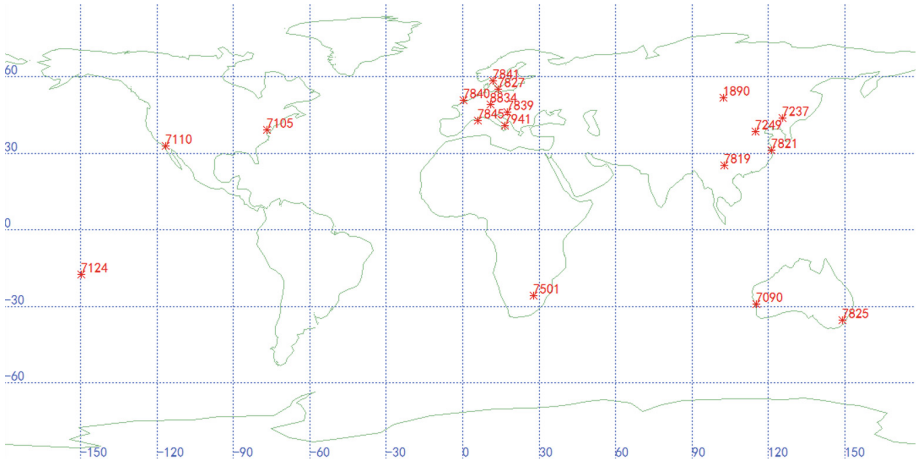

Fig. 2. Geographic locations of SLR stations

Using the SLR observation data from August to October 2018 to check the C20 satellite broadcast ephemeris, the mean (MEAN), standard deviation (STD) and the root mean square error (RMS).) are calculated respectively. Table 3 shows the laser residual time series of C20 satellite. The horizontal axis is the number of days since January 1, 2018, and the longitudinal axis is the laser check residual.

As can be seen from Fig. 3 and Table 3, from August to October 2018, 15 laser observation stations observed C20 satellites in Asia, Europe, North America, and Oceania. After eliminating the wild value, there are 544 laser standard point data. The laser observation is mainly concentrated in September and October. The laser residual

Table 2. Station information of track BDS-3

Monument	Location name	Country
7090	Yarragadee	Australia
7110	Monument Peak	California
7124	Tahiti	French Polynesia
7237	Changchun	China
7249	Beijing	China
7819	Kunming	China
7821	Shanghai	China
7825	Mt Stromlo	Australia
7827	Wettzell	Germany
7501	Hartebeesthoek	South Africa
7839	Graz	Austria
7840	Herstmonceux	United Kingdom
7841	Potsdam	Germany
7845	Grasse	France (LLR)
7941	Matera	Italy (MLRO)
8834	Wettzell	Germany
7105	Greenbelt	Maryland
1890	Badary	Russia

Table 3. Statistics of range residuals for C20

Monument	Normal points	Residuals/cm				
		MAX	MIN	MEAN	STD	RMS
7090	24	35.04	−2.46	16.8	9.95	19.53
1890	6	26.09	20.84	24.03	2.14	24.12
7110	19	23.83	−0.18	16.75	6.58	17.99
7124	6	15.09	13.99	14.52	0.36	14.53
7237	40	27.97	−9.23	11.05	10.5	15.25
7249	3	10.26	2.31	6.33	3.28	7.40
7819	4	22.53	9.36	15.86	6.42	17.11
7821	14	21.44	2.01	9.52	6.65	11.61
7827	29	18.31	−3.81	8.35	6.24	10.42
7839	83	27.79	−20.19	6.67	9.15	11.33
7840	89	35.81	−23.52	4.47	11.81	12.62
7841	16	12.85	4.06	9.10	3.06	9.60
7845	4	6.18	−16.3	−5.27	10.95	12.15
7941	63	22.26	−21.36	5.50	11.63	12.86
8834	144	25.04	−30.54	−2.39	10.85	11.11
Total	544	35.81	−30.54	5.39	11.74	12.92

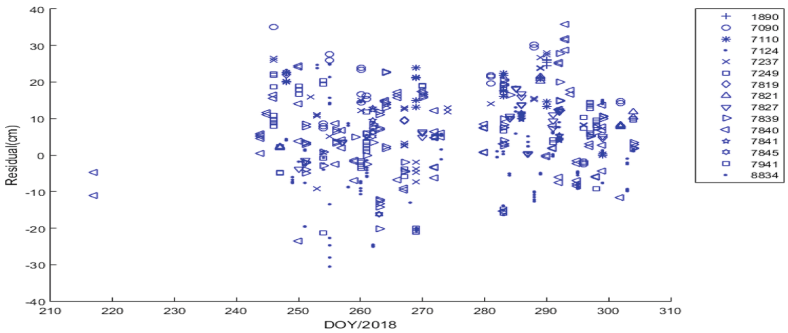

Fig. 3. Range residuals for C20

is distributed between −30.54 cm and 35.81 cm, with an average of 5.39 cm and an RMS of 12.92 cm. There is no obvious law of the laser residual distribution of each station, but the laser residual RMS of each station is basically between 10 cm–20 cm.

The SLR observation data is used to check the C21 satellite broadcast ephemeris orbit. The C21 satellite laser residual time sequence is shown in Fig. 4. The corresponding statistical information is shown in Table 4. As can be seen from Fig. 4 and Table 4, from August to October 2018, 11 laser observation stations observed C21 satellites, mainly in Asia, Europe, and Oceania. After removing the gross error, there are 233 laser standard point data, the laser residual is distributed between −17.98 cm–30.49 cm, the average value is 11 cm, and the laser residual RMS is 15.08 cm. The laser residual RMS of each station is basically the same, mostly between 10 cm–20 cm.

Table 4. Statistics of range residuals for C21

Monument	Normal points	Residuals/cm				
		MAX	MIN	MEAN	STD	RMS
7090	24	30.23	0.87	16.45	10.03	19.27
7237	37	30.49	−6.99	13.06	8.47	15.56
7249	9	20.08	7.71	15.01	4.72	15.74
7819	5	12.86	−1.62	7.26	6.44	9.71
7821	4	13.39	13.02	13.18	0.14	13.19
7827	19	26.14	−10.65	10.96	10.9	15.46
7839	74	29.43	−3.79	13.19	9.18	16.06
7840	18	20.73	−16.94	4.78	10.74	11.76
7841	4	1.53	−0.33	−0.86	0.44	0.96
7845	7	17.68	9.24	13.21	3.55	13.68
7941	32	20.62	−17.98	3.19	11.13	11.58
Total	233	30.49	−17.98	11.00	10.32	15.08

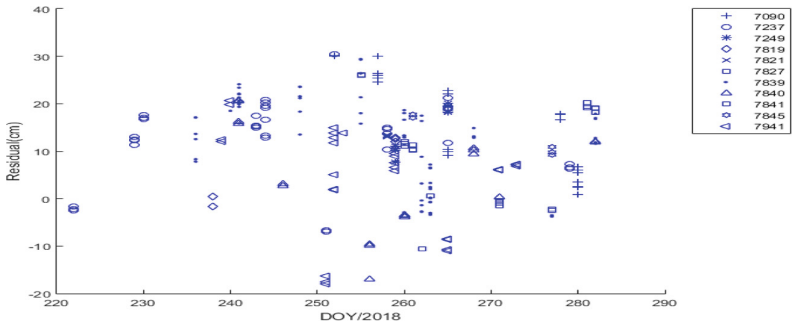

Fig. 4. Range residuals for C21

Based on the same method, the C29 and C30 satellite broadcast ephemeris are checked. The laser residual time series of C29 and C30 satellites are shown in Figs. 5 and 6. The corresponding statistical information is shown in Table 6 in Table 5.

Table 5. Statistics of range residuals for C29

Monument	Normal points	Residuals/cm				
		MAX	MIN	MEAN	STD	RMS
7090	94	32.64	−19.95	−2.81	10.06	10.44
7105	9	12.05	4.24	6.59	2.62	7.09
7124	4	−12.4	−14.24	−13.47	0.71	13.49
7237	23	21.32	−20.27	−1.93	10.49	10.67
7249	3	0.26	−1.55	−9.03	0.82	1.22
7501	6	4.45	−1.36	0.65	2.42	2.51
7821	19	6.10	−6.98	−1.03	3.87	3.99
7825	1	2.86	2.86	2.86	0	2.86
7827	27	10.86	−6.77	3.72	4.33	5.71
7839	46	22.02	−10.79	3.38	6.94	7.72
7840	64	27.22	−15.92	2.93	7.67	8.21
7841	8	12.63	4.87	8.02	2.19	8.31
7845	33	11.22	−13.45	0.20	7.21	7.22
7941	92	22.71	−14.41	0.79	7.90	7.94
8834	161	27.15	−31.53	−1.01	8.74	8.79
Total	590	32.64	−31.53	0.18	8.52	8.53

Statistics show that during this period, a total of 15 stations tracked and observed the C29 satellite. A total of 13 laser stations observed the C30 satellite. Compared with the C20 and C21 satellites, the C29 and C30 satellites have better laser data

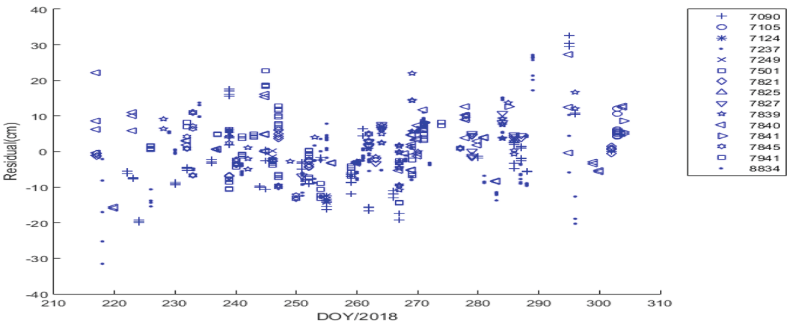

Fig. 5. Range residuals for C29

Table 6. Statistics of range residuals for C30

Monument	Normal points	Residuals/cm				
		MAX	MIN	MEAN	STD	RMS
7090	69	14.03	−32.28	−4.37	7.58	8.75
7105	9	−2.18	−5.10	−3.81	0.95	3.93
7237	15	8.63	−13.30	−5.02	6.7	8.38
7249	7	5.96	−11.65	−1.63	5.98	6.20
7501	6	−1.82	−18.66	−9.56	7.39	12.09
7821	12	−3.02	−15.55	−8.62	4.50	9.73
7827	19	13.06	−18.85	−3.23	10.91	11.37
7839	54	19.27	−17.82	1.82	10.43	10.59
7840	55	23.71	−33.07	2.34	11.76	11.99
7841	6	6.16	1.09	3.09	1.61	3.49
7845	16	11.54	−10.23	1.16	6.53	6.63
7941	27	8.04	−16.71	−2.26	8.56	8.85
8834	144	29.79	−33.20	−2.06	12.34	12.51
Total	439	29.79	−33.20	−1.68	10.60	10.74

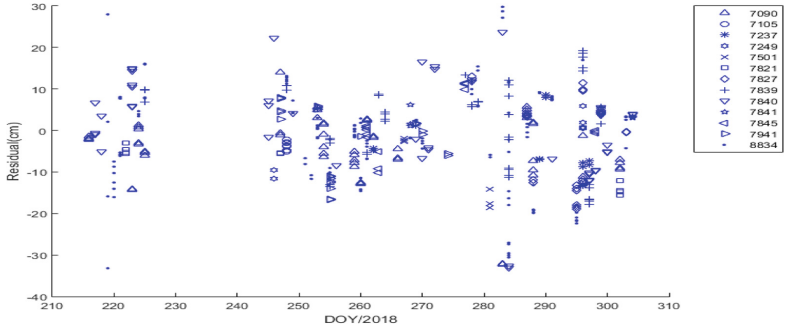

Fig. 6. Range residuals for C30

distribution. The stations are more widely distributed and distributed in Asia, Europe, North America, Africa, and Oceania, and can be covered globally. The C29 satellite laser observation data volume is relatively large, and the distribution is relatively uniform in August and September. The laser residual RMS is relatively small, about 8.53 cm. The laser residual RMS of each station is basically the same, mostly between 0–10 cm. There are 439 laser standard point data after the C30 satellite rejection. The laser residual is distributed between −33.20 cm and 29.79 cm, the average value is −1.68 cm, and the laser residual RMS is 10.74 cm.

The SLR observations from August to October 2018 were used to check the C20, C21, C29, and C30 satellite broadcast ephemeris. The results show that the C20, C21, C29, and C30 satellite broadcast ephemeris radial precisions are 12.92 cm, 15.08, 8.53 cm and 10.74 cm, overall, the C29 and C30 satellites are slightly better than the C20 and C21 satellites.

3.2 Precise Ephemeris

Based on the precision orbit provided by the IGMAS Analysis Center of Xi'an Institute of Surveying and Mapping, the SLR observation data from August 1st to October 17th, 2018 is used to check the four satellites of BD-3 C20, C21, C29, C30 precision ephemeris orbit. After the 3 times error principle is removed, the accuracy of laser detection residuals of each satellite is shown in Table 7. Figure 7 shows the sequence of the precision ephemeris laser residual.

Table 7. Statistics the accuracy of SLR check precise orbit

prn	Normal points	Stations	Residual/cm		
			MEAN	STD	RMS
C20	492	15	1.97	6.79	7.07
C21	279	12	5.93	4.84	7.65
C29	707	14	−3.35	5.93	6.81
C30	469	14	−4.47	6.02	7.49

The analysis shows that the C20, C21, C29 and C30 satellite lasers check the precision ephemeris orbit RMS within 10 cm, respectively 7.07 cm, 7.65 cm, 6.81 cm, 7.49 cm, and there is little difference between the satellites. The SLR check residual is the projection of the satellite orbit error in the direction of the line of sight of the laser station. It mainly refers to the radial error of the orbit, but it also includes the trajectory error of the tangential direction and the normal direction.

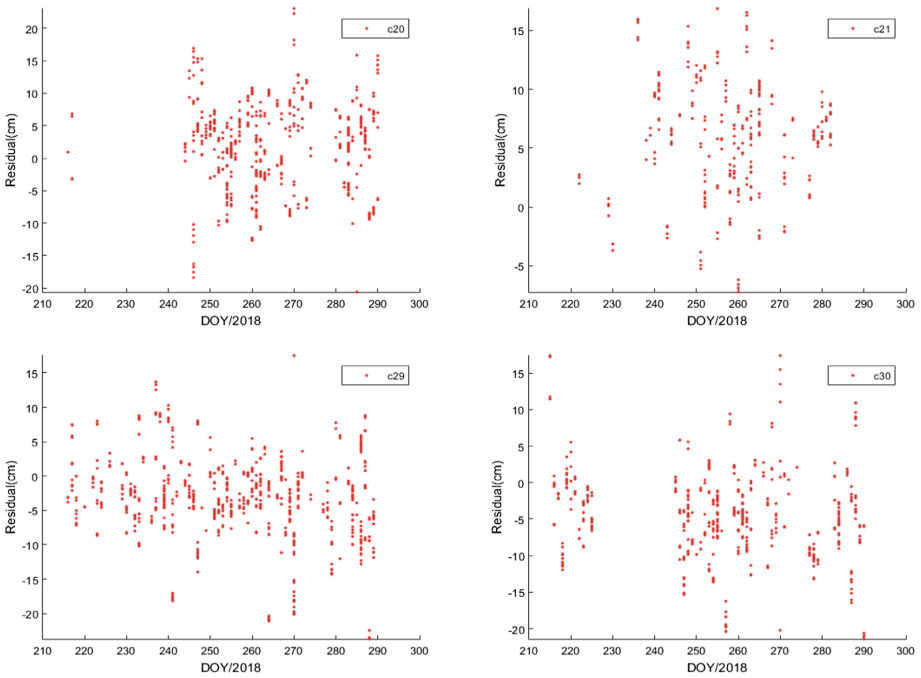

Fig. 7. Range residuals for C20, C21, C29, C30

4 Summary

This paper examines some satellite broadcast ephemeris orbits and precise ephemeris orbits of BDS-3 based on laser observation data from August to October 2018. The results show that BDS-3 participates in C20, C21, C29, C30 satellites of international laser joint measurement. The radial residual RMS of the broadcast ephemeris is 12.92 cm, 15.08 cm, 8.53 cm, 10.74 cm, respectively. Compared with the BDS-2 satellite [10], the accuracy is obviously improved. At the same time, the radial residual RMS of the laser inspection precision ephemeris orbit is about 7 cm, and there is little difference between the satellites. At present, the BDS-3 satellite laser observation data is less, and the amount of laser observation data will increase, which will be further analyzed.

Acknowledgement. Thanks to the data and technical support provided by the ILRS Data Center and the IGMAS Analysis Center.

Funding Information. This document is funded by the funded project (41874014).

References

1. Yang Y, Li J, Wang A et al (2014) Preliminary assessment of the navigation and positioning performance of BeiDou regional navigation satellite system. Sci China Earth Sci 57(1):72–81
2. Mao Y, Wang Q, Hu C et al (2018) Precision analysis of BeiDou satellites broadcast ephemeris. J Astronaut (09):1013–1021
3. Tan S (2018) The anticipated BeiDou global satellite navigation system. Chin Sci Bull 63 (27):2802–2803
4. Hong H (2011) A new cascade improvement coding plan of navigation message. In: Proceedings of the second China satellite navigation academic annual conference, pp 100–105
5. Shuai P, Chen D, Jiang Y (2004) Errors of GPS broadcast ephemeris and their effects on navigation and positioning accuracy. J Data Acquis Process (01):107–110
6. Geng T, Su X, Xu X et al (2015) Research on precise and broadcast ephemeris orbit of BeiDou navigation satellite system. China Sci Paper 10(09):1023–1026+103
7. Peng H, Yang Y, Wang G et al (2016) Performance analysis of BDS satellite orbits during eclipse periods: results of satellite laser ranging validation. Acta Geodaetica et Cartographica Sinica 45(06):639–645
8. Zhang Z, Cheng Z, Zhang H et al (2017) Global laser ranging observation of BeiDou satellites and data application. Chin J Lasers 44(04):164–172
9. Zhu Y, Li B, Yu L et al (2014) Analysis of BeiDou satellite broadcast ephemeris accuracy based on precise ephemeris. GNSS World China 39(01):1–4
10. Kong Y, Sun B, Yang X et al (2017) Precision analysis of BeiDou broadcast ephemeris by using SLR data. J Wuhan Univ 42(06):831–837
11. Qin X, Yang Y, Jiao W et al (2004) Determination of navigation satellite clock difference by using SLR and pseudo-distance data. Acta Geodaetica et Cartographica Sinica 3:205–209
12. Petit G, Luzum B (2010) IERS Conventions (2010). Bureau International des Poids et Mesures Severes, France
13. Pearlman MR, Degnan JJ, Bosworth JM (2002) The international laser ranging service. Adv Space Res 30(2):135–143

Accuracy Assessment and Improvement of GNSS Precise Point Positioning Under Ionospheric Scintillation

Zhenlong Fang[1], Wenfeng Nie[1], Tianhe Xu[1,2(✉)], Zhizhao Liu[3], and Shiwei Yu[3]

[1] School of Space Science and Physics, Shandong University, Weihai, China
thxugfz@163.com
[2] State Key Laboratory of Geo-Information Engineering, Xi'an, China
[3] Department of Land Surveying and Geo-Informatics, Hong Kong Polytechnic University, Hong Kong, China

Abstract. We focus on the accuracy analysis and improvement of multi-GNSS precise point positioning (PPP) during ionospheric scintillation. By using the observation data from Hong Kong Satellite Positioning Reference Station Network (SatRef) on 18 and 19, October 2015, the performance of kinematic PPP under the ionospheric scintillation condition is analyzed. The first day corresponds to the day of year 291, which is under the non-scintillation condition ($S_4 < 0.2$) while the second day corresponds to the day of year 292, which is under the scintillation condition ($S_4 > 1.0$). The results show that the GPS-only kinematic PPP solution is seriously influenced when scintillation occurs while the GPS/BDS/GLONASS combined solution can present a robust solution. Statistics results show that the root-mean-square (RMS) values of the single GPS and GPS/BDS/GLONASS combined kinematic PPP solution for the day of October 18 are stable and comparable, which are better than 5 cm. However, the RMS of positioning results in single GPS kinematic PPP solution for October 19 is 0.273 m, which is much worse than that of October 18. When using GPS/BDS/GLONASS combined solution, the positioning accuracy is 0.051 m, with an improvement of 81.3% compared to the result of the GPS-only solution. This indicates that multi-GNSS is an efficient way to overcome the impact of ionospheric scintillation on positioning result.

Keywords: Ionospheric scintillation · Precise Point Positioning (PPP) · Multi-GNSS

1 Introduction

Ionospheric scintillation refers to the phenomenon that ionospheric irregularities in the Earth's atmosphere layer, which can lead to rapid fading of the received signal power levels as well as the phase changing [1, 2]. The distortions on amplitude and phase are usually referred to as amplitude and phase scintillation. Most scintillations are likely to occur in the post sunset period, the nightside auroral oval and dayside cusp and the region around the polar cap at all local times [3, 4]. It can be frequently observed in

J. Sun et al. (Eds.): CSNC 2019, LNEE 563, pp. 400–411, 2019.
https://doi.org/10.1007/978-981-13-7759-4_36

equatorial and polar region of the Earth. In high latitudes, phase scintillation seems more severe than amplitude scintillation [5–8]. Around equator, both amplitude and phase scintillation can occur. Amplitude scintillation, however, is generally more severe than phase scintillation [9, 10].

Both amplitude and phase scintillation can degrade the Global Navigation Satellite System (GNSS) positioning performance by increasing the tracking errors from delay locked loop (DLL) and phase locked loop (PLL), causing cycle slips and even loss of lock [11]. With the increase of Ionospheric scintillation intensity, amplitude scintillation in general leads to the loss of signal locking, and the phase scintillation increases the occurrence of cycle slips, thus affecting the positioning performance of the receiver. This effect cannot be mitigated by the ionosphere-free combination of the dual-frequency observable that is effective at mitigating the ionospheric delay. Therefore, ionospheric scintillation is one of the most challenging threats for GNSS, especially for the users in the near equatorial and polar regions.

The effects of the ionospheric scintillation on GNSS can be classified into three aspects: the user receivers, the reference stations and the satellite datalinks. Specifically, the ionospheric scintillation can degrade the quantity and quality of the user measurements as well as those of the reference stations. In addition, it can disrupt the communication from Satellite Based Augmentation Systems (SBAS) geostationary satellite (GEO) to the user receiver. This contribution focuses on the effects of the ionospheric scintillation on the user receivers. And the influence of this effect depends on the severity of the scintillation. Xu et al. found that the largest Global Positioning System (GPS) PPP error can increase to more than 34 cm in the vertical and more than 20 cm in the horizontal components under the impact of severe ionospheric scintillations on 9 July 2012 when the S_4 index is greater than 1.0 [12]. Luo et al. presented that the three-dimension root-mean-square (RMS) of BeiDou Navigation System (BDS) PPP is 1.842 m under scintillation on 19 October 2015, which is much larger than that for non-scintillation condition as 0.155 m [13]. To improve the positioning performance, Conker et al. proposed the methods to determine the effects of ionospheric scintillation on the DLL and PLL of the GPS/SBAS receivers, now known as "Conker model". In this model, the tracking error variance of DLL and PLL for L1 and L2 signals were presented [11]. Further, Aquino et al. improved the GNSS positioning stochastic model of the least square equations according to the "Conker model" in the presence of ionospheric scintillation [5]. Focusing on the performance improvement of PPP during ionospheric scintillation, Zhang et al. proposed an improved approach based on a robust iterative Kalman filter with careful quality control for rejecting observables and detecting cycle slips. The horizontal errors can still reach to 0.1–0.2 m while the vertical errors 0.2–0.3 m [14].

In this contribution, the impact of introducing data from multi-GNSS systems in the traditional kinematic PPP is analyzed. In the case of kinematic PPP, the geometry of the satellite being tracked has strong influence on the performance of PPP. The kinematic positioning performance degrades when a small number of satellites are tracked, which occurs, for instance, under ionospheric scintillation. According to the severity of the ionospheric scintillation, more satellites are advantageous to present robust positioning

results, especially when the scintillation is low and moderate. Therefore, the GPS/GLONASS/BDS combined kinematic PPP experiments under ionospheric scintillation are employed in this contribution.

The data used in the PPP processing in this contribution are from Hong Kong Satellite Positioning Reference Station Network (SatRef) [15]. The receivers can track multi-frequency GPS, GLONASS and BDS signals in 2015. And the software GAMP is used to process the PPP experiments [16]. Besides, one Septentrio PolaRxS Pro ionospheric scintillation receiver, which is installed at Hok Tsui(22°12′N,114°15′E), south of Hongkong, is used to produce the S_4 and σ_φ index. The paper is organized as follows. Section 2 presents the methodology including the PPP model and scintillation index. Then the space weather indexes are shown, followed by the PPP results and analysis. Finally, the summary and conclusions are drawn.

2 Data and Methodology

2.1 PPP Model

In this study, we investigate different effects of strong ionospheric scintillation events on GPS-only and GPS/BDS/GLONASS dual kinematic PPP. The linearized equations of original pseudorange and carrier phase observations are written as following [16, 17]:

$$\begin{aligned} p_{r,j}^{s,T} &= \mathbf{u}_r^{s,T} \cdot \mathbf{x} + dt_r - dt^{s,T} + M_W \cdot Z_W \\ &+ \gamma_j^T \cdot I_{r,1}^{s,T} + \left(d_{r,j}^{s,T} - d_j^{s,T} \right) + \varepsilon_{r,j}^{s,T} \end{aligned} \tag{1}$$

$$\begin{aligned} l_{r,j}^{s,T} &= \mathbf{u}_r^{s,T} \cdot \mathbf{x} + dt_r - dt^{s,T} + M_W \cdot Z_W \\ &- \gamma_j^T \cdot I_{r,1}^{s,T} + \lambda_j^{s,T} \cdot \left(N_{r,j}^{s,T} + b_{r,j}^{s,T} - b_j^{s,T} \right) + \xi_{r,j}^{s,T} \end{aligned} \tag{2}$$

where indices s, r, and j (j = 1,2) refer to the satellite, receiver and carrier frequency band, respectively; T denotes satellite system; $p_{r,j}^{s,T}$, and $l_{r,j}^{s,T}$ represent observed minus computed (OMC) values of pseudorange and carrier phase observables, respectively; $\mathbf{u}_r^{s,T}$ is the unit vector of the component from the receiver to the satellite; $\mathbf{x}$ is the vector of the receiver position increments relative to the a priori position; dt_r and $dt^{s,T}$ are the receiver and satellite clock offsets, respectively; M_W is the wet mapping function; Z_W is the zenith wet delay; $I_{r,1}^{s,T}$ is the line-of-sight (LOS) ionospheric delay on the frequency $f_1^{s,T}$; γ_j^T is the frequency-dependent multiplier factor ($\gamma_j^T = \left(f_1^{s,T} / f_j^{s,T} \right)^2$), which is independent of the satellite pseudorandom noise (PRN) code; $d_{r,j}^{s,T}$ is the frequency-dependent receiver uncalibrated code delay (UCD) with respect to satellite s; $d_j^{s,T}$ is the frequency-dependent satellite UCD; $\lambda_j^{s,T}$ is the carrier wavelength on the frequency band j; $N_{r,j}^{s,T}$ is the integer phase ambiguity; $b_{r,j}^{s,T}$ and $b_j^{s,T}$ are the frequency-dependent receiver and satellite uncalibrated phase delays (UPDs); $\varepsilon_{r,j}^T$ and $\xi_{r,j}^T$ are the sum of

measurement noise and multipath error for pseudorange and carrier phase observations. Note that all the variables in (1) and (2) are expected in meters except the ambiguity and UPDs in cycles. For the combined processing of GLONASS system with the pattern of FDMA, both the inter-frequency bias (IFB) and the inter-system bias (ISB) should be carefully dealt with. More details can be seen in [16, 18].

For PPP processing, we select GNSS observations with an interval of 30 s, and GNSS products (orbits and clocks) generated by GFZ [19]. Data processing techniques and implementations for GNSS dual-frequency PPP are summarized in Table 1. For comparison, we calculate precise coordinate of the 4 SatRef stations through the GPS-only static PPP solution over 7 days under quiet ionospheric condition with the Bernese v5.2 GNSS scientific software [20].

Table 1. Summary of data processing techniques and implementations for GNSS dual-frequency PPP

Item	Techniques and implementations
Observations	GPS, GLONASS and BDS dual-frequency code and phase observations
Sampling interval	30 s
Elevation mask angle	7°
Cycle-slip detection	Geometry-free and Melbourne-Wubbena combination
Satellite orbit	Fixed with the MGEX products from GFZ
Satellite clock	Fixed with the MGEX products from GFZ
Phase center offset	igs08.atx
Ionospheric delay	First-order effect eliminated by ionospheric-free linear combination
Differential code bias	Corrected by CAS DCBs
Tropospheric delay	ZTD Estimated as parameter
Tide correction	Solid earth tide, ocean tide loading and pole tide

2.2 Ionospheric Scintillation

Scintillation can be monitored by the amplitude and phase scintillation indices, respectively S_4 and σ_φ. The S_4 index can be calculated from the satellite signal power or signal intensity (SI) tracked by the receiver, and can be interpreted as a normalized standard deviation around the intensity average.

From the receiver output data, the amplitude scintillation index S_4 can be computed as [21]:

$$S_4^2 = \frac{\langle SI^2 \rangle - \langle SI \rangle^2}{\langle SI^2 \rangle} \tag{3}$$

where SI represents the receiver power, and $\langle\rangle$ represents the average value over the interval of 60 s for sampling rate of 50 Hz. The basic formula of SI is

$$SI = \frac{NBP - WBP}{(NBP - WBP)_{lpf}} \tag{4}$$

where NBP and WBP are narrow and wide bandwidth power; $(NBP - WBP)_{lpf}$ is the low-frequency portion of the $NBP - WBP$. To obtain a stable S_4, $(NBP - WBP)_{lpf}$ is calculated from the average value of $NBP - WBP$ over 1 min in this study.

The phase scintillation index σ_φ is the standard deviation of the carrier phase, and is averaged over intervals of 10, 30 and 60 s, based on 50 Hz measurements made over very 1 min. Most researchers use the 60 s version of σ_φ, also referred to as Phi60, for analysis. The Phi60, which is characterized by the standard deviation φ of the detrended phase, can be given as [22]:

$$\sigma_\varphi^2 = \langle \varphi^2 \rangle - \langle \varphi \rangle^2$$

The S_4 and Phi60 indices are normally computed and recorded by the ionospheric scintillation monitoring receivers (ISMR), such as the Septentrio PolaRxS Pro ionospheric scintillation receiver. The experiments described here and after are based on the SatRef stations as well as the ISMR receiver, and the results are presented in the following section.

3 Ionospheric Scintillation

To study the performance of GNSS dual-frequency PPP under scintillation at low-latitude regions, GNSS data collected by 4 SatRef stations on October 18 and 19, 2015 (day of year (DOY) 291 and 292) are using in our experiments, and the geographical distribution of these stations is shown as Fig. 1. In the following, the space weather conditions on October 18 and 19, 2015 are firstly presented. Then the performance of different satellite system using kinematic PPP under ionospheric scintillation is analyzed.

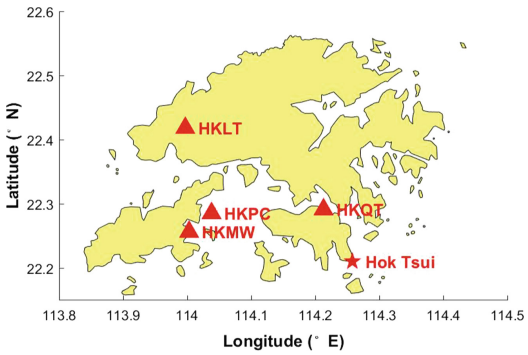

Fig. 1. Geographical locations of the 4 SatRef GNSS stations and the ISMR station in Hong Kong

3.1 Space Weather Indices

The time series of solar wind speed, Bz component of the interplanetary magnetic field, the disturbance storm time index, and Kp index from October 15 to 25 (DOY 288 to DOY 298), 2015 are presented in Fig. 2.

As depicted in Fig. 2, we can find that the solar wind speed in a moderate speed from October 15 to 25, 2015, the speed, however descend dramatically in DOY 292 and 295, 2015. Meanwhile, the Bz component of the interplanetary magnetic field varied from −10 to 5nT, fluctuating dramatically around DOY 291. The disturbance storm time (Dst, Kyoto Dst) index, which gives information about the strength of the ring current around Earth caused by solar protons and electrons [23], was mainly negative from DOY 288 to DOY 298, 2015, indicating that Earth's magnetic field is weakened and affected by solar storms in all probability. Similar to Dst index, the Kp index, which can measure solar particle radiation by its magnetic effects, is under quiet condition most of time in the figure, except moderate and high activity observed on DOY 290, DOY 291, DOY 294 and DOY 297, 2015.

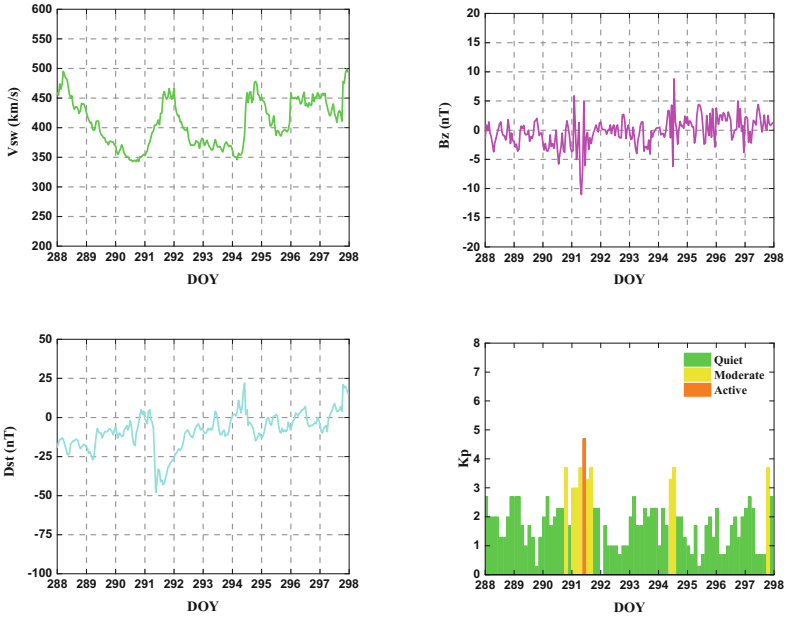

Fig. 2. Velocity of solar wind, Bz component of the interplanetary magnetic field, Disturbance storm time index, and Kp index from DOY 288 to DOY 298, 2015

Besides, Figs. 3 and 4 present the time series of S_4 and Phi60 index for GPS satellites observed at station Hok Tsui on October 18 and 19, 2015 (DOYs 291 and 292). It can be seen from Fig. 3 that the time series of S_4 and Phi60 are in a lower level and run smoothly over the period of 24 h on DOY 291, which means no ionospheric scintillation occurring on this day. However, it's obvious that a strong scintillation

event was happen on DOY 292 from 12:00 to 18:00 UTC, since a significant fluctuate can be seen in Fig. 4 over this period of time. From Fig. 4, we can find that the amplitude and phase scintillation appeared simultaneously from 12:00 to 18:00.

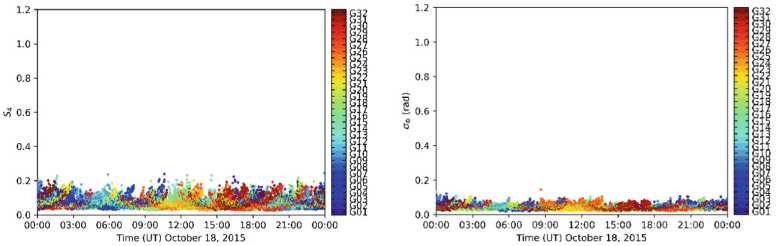

Fig. 3. Scintillation S_4 and Phi60 index for GPS on DOY 291, 2015

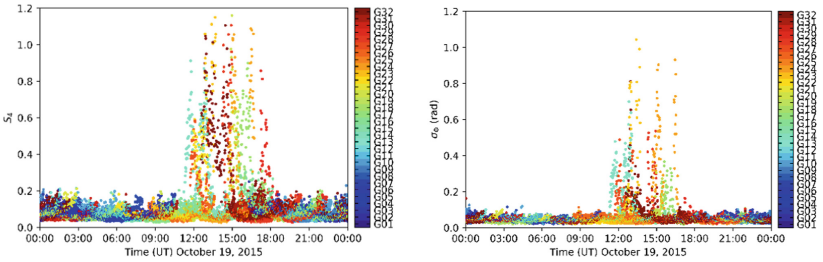

Fig. 4. Scintillation S_4 and Phi60 index for GPS on DOY 292, 2015

3.2 PPP Processing Results

To study the performance of PPP with different GNSS under ionospheric scintillation, we use GAMP to process multi-GNSS datasets in kinematic modes under the quiet and disturbed ionospheric condition, respectively.

Figures 5 and 6 show the time series of kinematic PPP errors using GPS-only and multi-GNSS (GPS/BDS/GLONASS) measurements collected by station HKQT as an example of 4 SatRef stations on October 18 and 19, 2015 (DOYs 291 and 292), respectively. The statistical results of the four SatRef stations are shown in the Tables 3 and 5. Since the kinematic PPP in the first 2 h (0:00–2:00 UTC) are in the state of convergence, the maximum of positioning errors and the root-mean-square (RMS) errors shown here are computed based on the positioning errors in the period 2:00–24:00 UTC.

3.2.1 GPS-Only PPP

Figure 5 shows kinematic PPP errors of station HKQT by using GPS-only on October 18 and 19, 2015. It can be seen that the accuracy and reliability of the kinematic PPP solution for DOY 291 and DOY 292 show a significant difference in the presence of

scintillation. On DOY 291, the kinematic positioning accuracy for each station in experiment is stable, which is better than 5 cm except those in the convergence time (0:00–2:00 UTC). However, since the presence of ionospheric scintillation during 12:00–18:00 UTC on DOY 292, the errors of GPS-only kinematic PPP for 4 SatRef stations show significant fluctuations. The maximum of GPS dual-PPP errors in east, north and up directions is 1.153, 0.466 and 1.966 m at station HKQT, and it's horizontal RMS, vertical RMS, 3D-RMS are 0.175, 0.208 and 0.272 m, respectively. These four stations' maximum positioning errors are shown in Table 2 and RMS values are shown in Table 3.

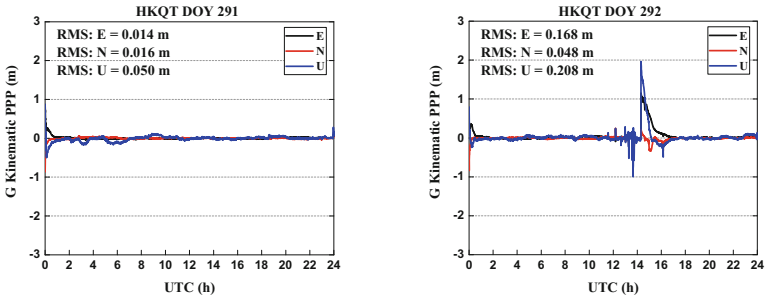

Fig. 5. Time series of GPS-only kinematic PPP errors for stations HKQT, on October 18 and 19, 2015

Table 2. Maximum of positioning errors of GPS-only PPP kinematic solution at HKLT, HKMW, HKPC and HKQT under the scintillation condition on October 19, 2015

Station	E/m	N/m	U/m
HKLT	2.809	3.995	9.832
HKMW	−1.090	2.842	2.769
HKPC	−2.036	−1.799	5.497
HKQT	1.153	−0.466	1.966

Table 3. RMS of GPS-only PPP kinematic positioning solution at HKLT, HKMW, HKPC and HKQT under the scintillation condition on October 19, 2015

Station	Horizontal-RMS/m	Vertical-RMS/m	3D-RMS/m
HKLT	0.179	0.235	0.296
HKMW	0.162	0.209	0.265
HKPC	0.122	0.230	0.260
HKQT	0.175	0.208	0.272

3.2.2 GPS/BDS/GLONASS PPP

Figure 6 presents kinematic PPP errors of station HKQT by using GPS/BDS/GLONASS combined solution on October 18 and 19, 2015. It's obvious that the positioning results of kinematic PPP for DOY 292 show a stable situation under the scintillation condition when using GPS/BDS/GLONASS combined solution comparing with GPS-only solution. Table 4 shows the maximum of GPS/BDS/GLONASS dual-PPP errors in east, north and up directions for HKQT is −0.163, −0.165 and −0.208 m, respectively. From Table 5, we can see that the results of kinematic positioning computed by multi-GNSS (GPS/BDS/GLONASS) data have higher accuracy than the results computed by GPS-only data in the scintillation environment, and the 3D RMS using GNSS data positioning can be degraded to about 5 cm under the scintillation condition.

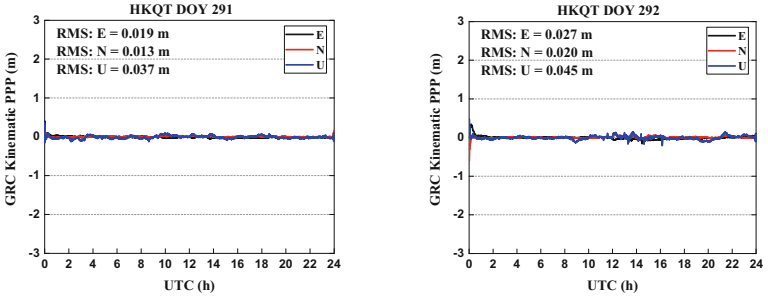

Fig. 6. Time series of GRC kinematic PPP errors for station HKQT on October 18 and 19, 2015

Table 4. Maximum of positioning errors of GPS/BDS/GLONASS PPP kinematic solution at HKLT, HKMW, HKPC and HKQT under the scintillation condition on October 19, 2015

Station	E/m	N/m	U/m
HKLT	−0.097	0.110	0.246
HKMW	−0.066	−0.235	−0.313
HKPC	−0.147	−0.180	−0.241
HKQT	−0.163	−0.165	−0.208

Table 5. RMS of GPS/BDS/GLONASS PPP kinematic positioning solution at HKLT, HKMW, HKPC and HKQT under the scintillation condition on October 19, 2015

Station	Horizontal-RMS/m	Vertical-RMS/m	3D-RMS/m
HKLT	0.020	0.043	0.047
HKMW	0.026	0.042	0.049
HKPC	0.030	0.042	0.051
HKQT	0.034	0.045	0.056

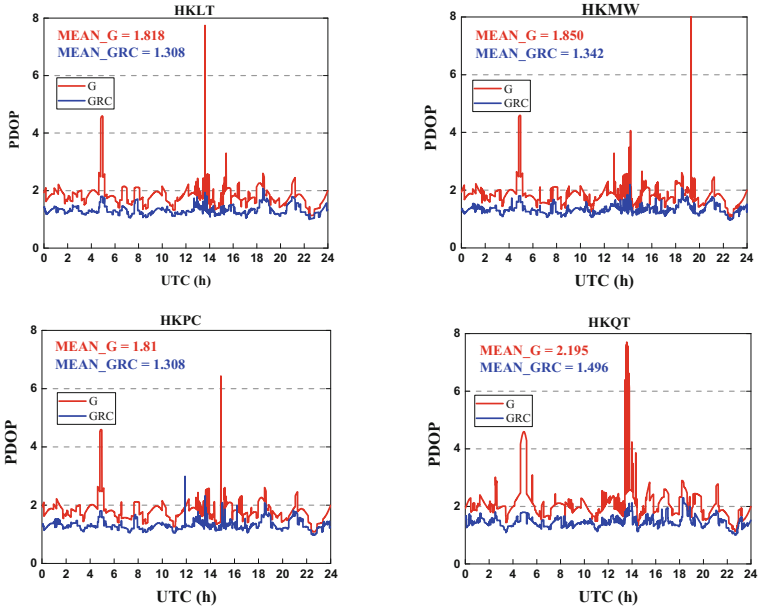

Fig. 7. Time series of PDOP for station HKLT, HKMW, HKPC and HKQT on October 19, 2015

Figure 7 shows time series of PDOP at station HKLT, HKMW, HKPC and HKQT on October 19, 2015. The mean value of PDOP is calculated in the period of 12:00–18:00 since most scintillation events are found in that time for the Hong Kong region. From these four pictures of Fig. 7, we can find a common character that there is a big variation of PDOP at about 5:00 UTC. However, we can see from Fig. 4 that there is no scintillation occurrence during this time since S_4 and Phi60 index are smaller 0.2 during 4:00–6:00 UTC. After checking the raw measurements, we find that the number of GPS satellites is small and the amount of utilizable satellites decreased from 7 to 6 and then recovered to 7 at around 5:00 UTC. It can be seen from the Fig. 7 that using GPS/BDS/GLONASS combination solution can strengthen geometry, and avoid scintillation disturbing. Therefore, from Figs. 6 and 7, we can conclude that using multi-GNSS measurements can improve the accuracy of kinematic positioning under the ionospheric scintillation.

4 Conclusions

The ionospheric scintillation has impacts on the GNSS positioning performance, especially when the scintillation is strong. We analyze the improvement of the kinematic PPP performance using multi-GNSS in the presence of the ionospheric scintillation. With more satellites, the performance of the kinematic PPP, which depends strongly on the geometry of the satellites tracked, should be more robust to reduce the effects of the ionospheric scintillations.

The GNSS observation data collected from 4 SatRef stations in Hong Kong on DOY 291 and DOY 292, 2015 are analyzed. Results demonstrate that:

(1) Under the ionospheric scintillation condition, the absolute maximum values of positioning errors for GPS-only kinematic PPP can reach 2.809, 3.995 and 9.832 m in east, north and up directions, however, the values for multi-GNSS (GPS/BDS/GLONASS) are 0.163, 0.235 and 0.313 m, respectively.
(2) In the scintillation environment, the average RMS values of positioning errors using GPS-only solution for 4 SatRef stations in horizontal, vertical and 3D are 0.16, 0.221 and 0.273 m, whereas the corresponding values from multi-GNSS solution are 0.028, 0.043 and 0.051 m, with an improvement of 82.5%, 80.5% and 81.3% in horizontal, vertical direction and 3D compared to GPS-only solution.

The results indicates that multi-GNSS is a good choice for GNSS users at low-latitude regions to improve the performance of kinematic positioning under ionospheric scintillation. Our further study will focus on the receiver autonomous integrity monitoring for the multi-GNSS positioning during the ionospheric scintillation.

Acknowledgements. The study is funded by National Key Research and Development Program of China (2016YFB0501902), National Natural Science Foundation of China (41574013, 41731069, 41874032 and 41574025) and State Key Laboratory of Geo-Information Engineering (SKL-GIE2015-M-2-2). The authors would like to acknowledge the Lands Department of the Government of Hong Kong. The Hong Kong Polytechnic University is thanked for providing the ISMR data. And we would like to thank GFZ for providing precise orbit and clock products.

References

1. Crane RK (1977) Ionospheric scintillation. Proc IEEE 65(2):180–199
2. Aarons J (1975) Global morphology of ionospheric scintillations. Proc IEEE 59(2):159–172
3. Basu S, Mackenzie E, Basa S (1988) Ionospheric constraints on VHF/UHF communication links during solar maximum and minimum periods. Radio Sci 23(3):363–378
4. Béniguel Y, Romano V, Alfonsi L et al (2009) Ionospheric scintillation monitoring and modelling. Ann Geophys 52(3–4):391–416
5. Aquino M, Monico JFG, Dodson AH et al (2009) Improving the GNSS positioning stochastic model in the presence of ionospheric scintillation. J Geodesy 83(10):953–966
6. Jiao Y, Yu M, Taylor S et al (2013) High latitude ionosphere scintillation characterization
7. Ngwira CM, Mckinnell LA, Cilliers PJ (2010) GPS phase scintillation observed over a high-latitude Antarctic station during solar minimum. J Atmos Solar Terr Phys 72(9):718–725
8. Spogli L, Alfonsi L, Franceschi GD et al (2009) Climatology of GPS ionospheric scintillations over high and mid-latitude European regions. Ann Geophys 27(9):3429–3437
9. Forte B (2016) Analysis of strong ionospheric scintillation events measured by means of GPS signals at low latitudes during disturbed conditions. Radio Sci 47(4):RS4009
10. Gwal A, Dubey S, Wahi R et al (2006) Amplitude and phase scintillation study at Chiang Rai, Thailand. Adv Space Res 38(11):2361–2365
11. Conker RS, El-Arini MB, Hegarty CJ et al (2003) Modeling the effects of ionospheric scintillation on GPS/satellite-based augmentation system availability. Radio Sci 38(1):1-1–1-23

12. Xu R, Liu Z, Li M et al (2012) An analysis of low-latitude ionospheric scintillation and its effects on precise point positioning. J Glob Position Syst 11(1):22–32
13. Luo X, Lou Y, Xiao Q et al (2018) Investigation of ionospheric scintillation effects on BDS precise point positioning at low-latitude regions. GPS Solutions 22(3):63
14. Zhang X, Guo F, Zhou P (2014) Improved precise point positioning in the presence of ionospheric scintillation. GPS Solutions 18(1):51–60
15. Hong Kong Satellite Positioning Reference Station Network. https://www.geodetic.gov.hk/sc/satref/downv.aspx. Accessed 26 Nov 2018
16. Zhou F, Dong D, Li W et al (2018) GAMP: an open-source software of multi-GNSS precise point positioning using undifferenced and uncombined observations. GPS Solutions 22(2):33
17. Leick A, Rapoport L, Tatarnikov D (2015) GPS satellite surveying, 4th edn. Wiley, Hoboken
18. Li X, Zhang X, Ren X et al (2014) Precise positioning with current multi-constellation global navigation satellite systems: GPS, GLONASS, Galileo and BeiDou. Sci Rep 5:8328
19. German Research Centre for Geosciences (GFZ). ftp://ftp.gfz-potsdam.de/GNSS/products/mgex/. Accessed 26 Nov 2018
20. Dach R, Lutz S, Walser P et al (2015) Bernese GNSS software version 5.2
21. Briggs BH, Parkin IA (1963) On the variation of radio star and satellite scintillations with zenith angle. J Atmos Terr Phys 25(6):339–366
22. Van Dierendonck AJ, Klobuchar J, Hua Q (1993) Ionospheric scintillation monitoring using commercial single frequency C/A code receivers. In: Proceedings of ION GPS 93, Salt Lake City, UT, 22–24 September, pp 1333–1342
23. Geomagnetic Equatorial Dst index Home Page. http://wdc.kugi.kyoto-u.ac.jp/dstdir/. Accessed 26 Nov 2018

Analysis of BDS-3 Satellite System Characteristics Based on "GaoJing-1" Self-designed GNSS Receiver

Ying Yang, Xiaohui Ba, Jian Li, and Jie Chen(✉)

Institute of Microelectronics of Chinese Academy of Sciences,
#3 Beitucheng West Road, Chaoyang District, Beijing, China
{yangying, jchen}@ime.ac.cn

Abstract. In our country's global navigation system, namely BDS-3, 19 satellites (18 MEO satellites and 1 GEO satellite) have been launched in the period from November 2017 to November 2018. The basic system of BDS-3 has been set up and is going to provide essential navigation service for the countries and districts in "the Belt and Road" starting from the end of 2018. The signal features of B1I/B1C, system visibility and performance of the navigation system are thoroughly studied based on self-designed "GaoJing-1" multi-mode multi-frequency receiver. Through analyzing the measurement results, the receiver can observe the 5 experimental satellites and all the satellites of BDS-3 except GEO-1(PRN59) and MEO-8(PRN48). Although the BDS-3 system is still in the debugging phase, the health flag is 1 for signal B1I, and 1 or 2 for B1C, which means that the receiver should not use the signals from B1I and B1C for positioning. However, we still try to get the positioning. The experiment results indicate that, utilizing the almanac with intermediate precision broadcast by B1C, when the cut-off angle is 10° and 20°, the minimum number of visible satellites in 24 h at Beijing for BDS-3 is 6 and 5 respectively, and the success rate of positioning is 100%. And the BDS-3 provides a better positioning accuracy than BDS-2. When using the signal B1I and B1C of BDS-3, the standard deviation of positioning error is 21% and 28% lower than that of BDS-2 respectively. When using the combined positioning of BDS-2 and BDS-3, the positioning error is 45% than that of BDS-2, and 31% lower than that of BDS-3.

Keywords: GNSS receiver · BDS-3 · B1I · B1C · Positioning precision

1 Introduction

By November 19th, 2018, BDS-3 has launched a total of 19 satellites, including eighteen MEO satellites and one GEO satellites. The basic system has been set up and is going to provide essential navigation services for the countries and districts in "the Belt and Road" [1]. BDS-3 uses a hybrid constellation composed of three orbital satellites. Compared with other satellite navigation systems, BDS-3 has more high-orbit satellites and stronger anti-occlusion ability. Secondly, BDS-3 provides navigation signals at multiple frequencies, which can improve service accuracy through multi-frequency signal combination.

J. Sun et al. (Eds.): CSNC 2019, LNEE 563, pp. 412–421, 2019.
https://doi.org/10.1007/978-981-13-7759-4_37

With the deployment of the basic constellation of BDS-3, system tuning and performance evaluation become the main tasks at present. In this paper, the signal characteristics, system visibility and positioning performance of BDS-3 are analysed through "GaoJing-1" the multi-mode multi-frequency GNSS receiver self-designed by the Institute of Microelectronics, Chinese Academy of Sciences (IMECAS).

This paper is organized as follows. In Sect. 2, the signal characteristics of BDS-3 satellite are analysed. In Sect. 3, the technical parameters of "GaoJing-1" multi-mode multi-frequency GNSS receiver are introduced, and BDS-3 related designs are described in detail. Based on "GaoJing-1" receiver, signal B1I and B1C tracking results, BDS-3 system visibility and positioning performance are presented in Sect. 4, and this work is concluded in Sect. 5.

2 Characteristics of the BDS-3 Open Service Signals

BeiDou Satellite Navigation System Signal In Space Interface Control Document (ICD) defines the open service signals provided by BDS-3: B1C is a new signal, B2a will replace B2I, both of them are broadcast on MEO and IGSO satellites, signal B1I and B3I are broadcast on all satellites [2–5]. All the signals are summarized in Table 1.

Table 1. Signal structure of BDS-3

Signal	Carrier frequency (MHz)	Code rate (Mcps)	Modulation mode	Code length
B1I	1561.098	2.046	BPSK(2)	2046
B1C	1575.42	1.023	BOC(1,1) QMBOC(6,1,3/44)	10230
B2a	1176.45	10.23	QPSK(10)	10230
B3I	1268.52	10.23	BPSK(10)	10230

BDS-3 not only enhances its global coverage, but also achieves performance improvement and service expansion in terms of technical system. The newly added signal B1C uses BOC modulation to realize compatible and interoperable operation with other GNSS signals at L1 frequency, which is 1575.42 MHz, and is able to improve the code tracking accuracy. Both code lengths of signal B1C and B2a are 10230, which have better anti-cross-correlation performance, and both signals designed separated pilot component and data component to improve tracking sensitivity. Both B1C and B2a NAV messages adopt non-binary LDPC coding to enhance the BER performance.

3 "GaoJing-1" Multi-mode Multi-frequency GNSS Receiver

"GaoJing-1" is a multi-mode multi-frequency GNSS receiver independently developed by Institute of Microelectronics, Chinese Academy of Sciences. The baseband chip is implemented in a 55 nm CMOS process, working with the MAXIM 2769 RF chipset.

3.1 Overview of "GaoJing-1" Receiver

The "GaoJing-1" receiver can receive signals of GPS, BDS-2, BDS-3, GLONASS, Galileo (GAL), QZSS and SBAS satellite systems. It supports multi frequencies, and as a result, achieves lane-level accuracy outdoors using the high-precision positioning RTK algorithm. Specific technical parameters are shown in Table 2.

Table 2. Technical parameters of "GaoJing-1" receiver

Tech parameters	
Received signals	GPS: L1C/A, L1C, L2C, L5
	BeiDou-2: B1I, B2I
	BeiDou-3: B1I, B1C, B2a
	GLONASS: L1OF, L2OF
	GALILEO: E1B/C, E5a, E5b
	QZSS: L1C/A, L1C, L1-SAIF, L2C, L5
	SBAS: L1C/A
Sampling frequency	16.368 MHz @ low IF 32.736 MHz @ zero IF

As can be seen from Table 2, the "GaoJing-1" receiver can support almost every open service signal of existing GNSS systems. The "GaoJing-1" test board is given in Fig. 1, and the baseband chip is in the lower circular frame and the MAXIM 2769 RF chipset is in the upper rectangular frame.

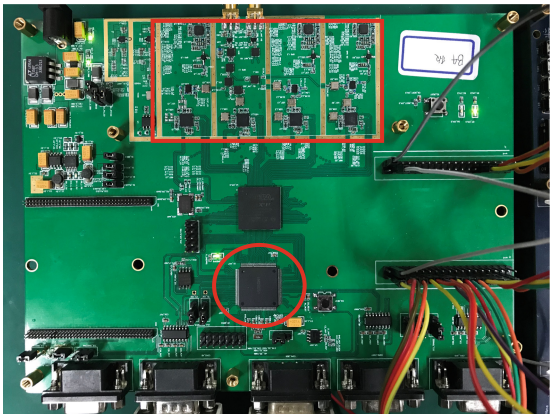

Fig. 1. "GaoJing-1" multi-mode multi-frequency GNSS receiver

3.2 Design for BDS-3 Signals

The "GaoJing-1" implements an acquisition engine based on large-scale correlator arrays and FFT structure to achieve parallel acquisition in the frequency domain and the code domain. The number of equivalent correlators exceeds 1 million. It can also achieve fast acquisition for the B1C and B2a signals with 10230 code length.

The primary and secondary code of the new signal B1C are both generated from truncating Weil codes with different lengths. Weil codes are generated based on Legendre sequences. The "Gaojing-1" tracking engine realizes the reuse of Legendre sequences and as a result saves memory space. Like the B1I signal, the primary code of B2a signal is Gold code. For the signal B1C with BOC modulation mode, 2-N correlation channel [6] is adopted to avoid the possibility of code phase error locking caused by the multi-peaks of autocorrelation. At the same time, the energy of upper and lower sidebands is used to improve the tracking sensitivity. This method makes full use of the characteristics of BOC modulation with higher code tracking accuracy to improve the pseudo-range single-point positioning accuracy.

Dealing with the Non-Binary LDPC encoded NAV messages of B1C and B2a signal, a LDPC decoder based on normalized minimum sum algorithm [7] is implemented in the "GaoJing-1" receiver, which can be applied for decoding B1C signal subframe 2, subframe 3 and B2a signal compatibly.

4 Performance Evaluation of BDS-3 System

In this section, the performance of BDS-3 is investigated. Specifically, the real B1I and B1C signals broadcasted by BDS-3 satellites are captured, tracked, decoded and used to deduce positioning through the "GaoJing-1" receiver. Based on several experimental results, the signal quality, system visibility and positioning accuracy of the B1I and B1C signals are evaluated and analyzed. The external GNSS measuring antenna AT-35101H located on the laboratory building roof of IMECAS is used in the experiment, which ECEF coordinates are [−2175028.38, 4384595.06, 4076047.15] m. Working with the MAXIM 2769 RF chip, "GaoJing-1" receiver carries out acquisition and tracking for B1I and B1C signals. The intermediate frequency is zero, the sampling rate is 32.736 MHz, and the ADC output has 2 bits of I and 2 bits of Q respectively.

In order to evaluate the performance of the system more comprehensively, the experiment was conducted several times from November 13th, 2018 to November 24th, 2018. According to the results, all BDS-3 satellites except GEO-1 (PRN59) and MEO-8 (PRN48) can be observed by "GaoJing-1", including the five previously launched BDS-3S experimental satellites. GEO-1 (PRN59) is the first geostationary orbit satellite of BDS-3, which code generator has not been open to the public in the existing ICD files, so it is impossible to be captured and tracked. MEO-8 (PRN48) has not been observed on MGEX platform of IGS [8] as well.

4.1 Signal Quality Evaluation

On November 23th, 2018, the B1I and B1C signals of BDS-3 were received by the "GaoJing-1" receiver. During the observation period, nine BDS-3 and BDS-3S satellites broadcast signal B1I and six BDS-3 satellites broadcast signal B1C. The received carrier-to-noise ratio (CN0) and tracking Doppler estimation of signal B1I/B1C are shown in Figs. 2 and 3 respectively. Particularly, the CN0 of signal B1C presented here is for the pilot component.

As can be seen from Figs. 2 and 3, the PRN corresponding to B1I signal includes C16/C18/C19/C23/C24/C26/C32/C34/C35, and the PRN corresponding to B1C signal includes C23/C24/C26/C32/C34/C35. According to the information released by MGEX platform on IGS website [8], C16/C18/C19/C35 are broadcast by the BDS-3S experimental satellites I1-S, I2-S, M1-S and M3-S. C23/C24/C26/C32/C34 are broadcast by the BDS-3 satellites MEO-5, MEO-6, MEO-11, MEO-13 and MEO-15. It can be seen that BDS-3 satellite satisfies that the B1C signal broadcasting on MEO/IGSO satellites,

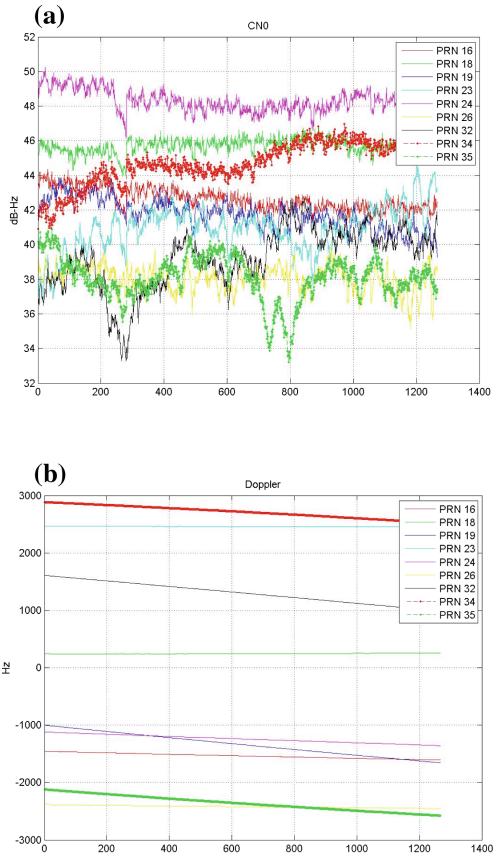

Fig. 2. (a) Tracking CN0 for BDS-3 B1I signal, (b) Tracking Doppler for BDS-3 B1I signal

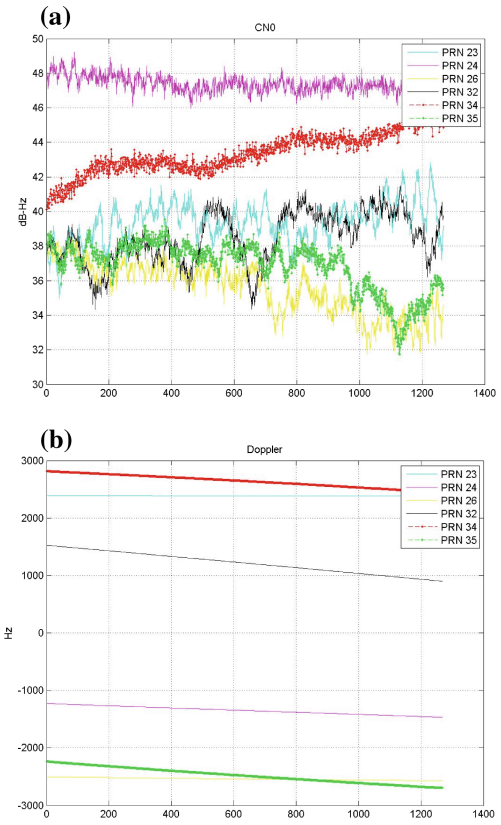

Fig. 3. (a) Tracking CN0 for BDS-3 B1C signal, (b) Tracking Doppler for BDS-3 B1C signal

and B1I signal broadcasting on all types of satellites [2]. However, the BDS-3S experimental satellites C16/C18/C19 only broadcast B1I signal at present, but does not broadcast B1C signal.

4.2 System Visibility Evaluation

According to ICD, the B1I signal broadcasts D1 navigation message on MEO/IGSO satellite, including PRN1-PRN30 almanac information on 1–24 pages of subframe 4 and 1–6 pages of subframe 5. The B1C signal broadcasts B-CNAV1 navigation message, including midi almanac on four pages of subframe 3.

On November 24th, 2018, the almanac information broadcast by B1I and B1C signals was decoded by the "GaoJing-1" receiver. According to the calculated satellite elevation angle based on the almanac information, 24 satellites which are PRN16/18/19/28/35, PRN20-27, PRN29/30, PRN32-34, PRN36/37, PRN47/48, PRN59/63, can be observed in Beijing. The 24 h elevation changes are shown in Fig. 4. Furthermore, if the almanac broadcast by B1I signal and the midi almanac

broadcast by B1C signal can be decoded simultaneously for some satellite, the elevation of the satellite can be compared and the results are consistent.

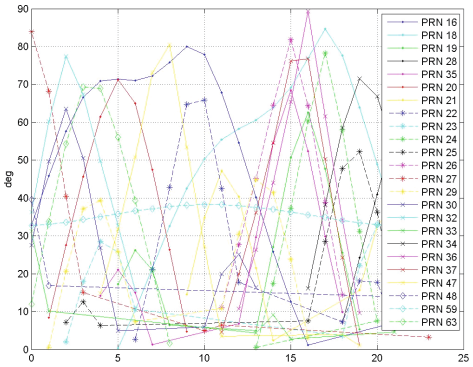

Fig. 4. Change of BDS-3 satellites elevation at 24 h

Figure 4 shows 24 h elevation variations for all BDS-3 and BDS-3S satellites in Beijing. As the only BDS-3 GEO satellite launched at present, PRN59 can be seen all day, with elevation between 30 and 40°; PRN16 and PRN18 can be seen most of the time as IGSO satellites.

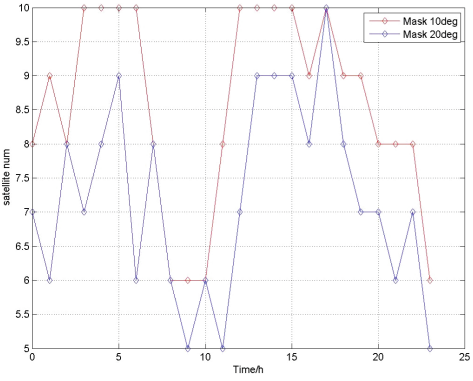

Fig. 5. Number of satellites with elevation of 10 and 20°

Figure 5 shows the number of BDS-3 and BDS-3S satellites that can be observed in Beijing at 10 and 20° of elevation. The minimum number of visible satellites is six and five in 24 h when the cut-off angle is 10° and 20° respectively, producing the 100% positioning rate.

4.3 Positioning Performance Evaluation

From the analysis of the navigation message, it can be seen that the autonomous health sign of B1I signal of BDS-3 is 1, which means that the satellite is not available; and the satellite health status of B1C signal is 1 which means that the satellite is unhealthy or in the test, or 2 which means reserved. In theory, satellites with poor health cannot be used for positioning, but in actual experiments, using the B1I and B1C signals have the opportunity to get the correct positioning solution.

On November 15th, 16th and 20th, 2018, the "GaoJing-1" receiver was used to track B1I signal and calculate the least squares single-point solution. The results of BDS-2, BDS-3 and combination positioning of BDS-2 and BDS-3 are shown in Table 3.

It can be seen that BDS-3 has better B1I positioning accuracy than BDS-2 although it has fewer available satellites. The standard deviation of BDS-3 decreases by 21% on average, which is related to the fact that BDS-3 can use fewer satellites to obtain good DOP values. The combination positioning of BDS-2 and BDS-3 effectively reduces the

Table 3. Results of B1I positioning

Data	SPP mode	ECEF	std (m)	std (m)	Number of SV
2018/11/15	BDS-2	X Y Z	3.641 6.545 1.899	7.726	9
	BDS-3	X Y Z	2.882 3.677 4.914	6.780	4
	BDS-2 + 3	X Y Z	1.877 2.621 1.722	3.655	13
2018/11/16	BDS-2	X Y Z	2.899 5.196 2.502	6.455	9
	BDS-3	X Y Z	2.086 2.817 4.378	5.609	4
	BDS-2 + 3	X Y Z	2.302 3.542 1.938	4.647	13
2018/11/20	BDS-2	X Y Z	4.360 7.726 3.128	9.407	8
	BDS-3	X Y Z	2.703 3.927 3.959	6.197	4–7
	BDS-2 + 3	X Y Z	1.967 3.140 2.173	4.296	12–15

standard deviation, getting the best positioning accuracy. Compared with the BDS-3 or BDS-3, the positioning standard deviation decreases by 45% and 31%, respectively. The results indicate that in the transitional stage of the coexistence of the BDS-2 and BDS-3 satellites, combination positioning should be considered to improve the positioning performance.

On November 13th and 24th, 2018, the signal B1C tracking and least squares positioning were performed by the "GaoJing-1" receiver. The results are shown in Table 4. From Tables 3 and 4, it can be seen that B1C signal can still achieve higher positioning accuracy than BDS-2, with an average reduction of 28% in standard deviation even under fewer available satellites. This is related to the better ranging code performance of BOC modulation and the better DOP construction ability of BDS-3.

Table 4. Results of B1C positioning

Date	ECEF	std (m)	std (m)	Number of SV
2018/11/13	X	2.768	5.655	4
	Y	3.485		
	Z	3.489		
2018/11/24	X	2.602	5.744	4
	Y	4.244		
	Z	2.580		

5 Conclusions

At present, the basic constellation of BDS-3 system is deployed and it is scheduled to operate at the end of 2018, providing navigation services to the countries and districts of "The Belt and Road". In this paper, the signal tracking and positioning performance of BDS-3 satellite are analyzed through "GaoJing-1" the multi-mode, multi-frequency GNSS receiver self-designed by IMECAS, in order to provide a reference for evaluating the performance of BDS-3 system. The results show that all BDS-3 satellites and BDS-3S experimental satellites except GEO-1 (PRN59) and MEO-8 (PRN48) can be observed by the receiver. In Beijing area, the minimum number of visible satellites is six and five in 24 h when the cut-off angle is 10° and 20° respectively, producing the 100% positioning rate. Users can employ BDS-3 satellites to locate independently, and can also locate combining with the BDS-2 satellites. When using the B1I and B1C signals of BDS-3, the positioning standard deviation are 21% and 28% lower than that of BDS-2 respectively. When the combination positioning of BDS-2 and BDS-3 is applied, the number of visual satellites increases, and the DOP value is improved. Compared with the positioning results of BDS-2 and BDS-3, the standard deviation is reduced by 45% and 31% respectively.

Acknowledgments. This paper is funded by CAS Interdisciplinary Innovation Team and National Program on Key Basic Research Project (2015CB352103).

References

1. China's BeiDou Navigation Satellite System, The State Council Information Office of the People's Republic of China, June 2016
2. BeiDou Navigation Satellite System Signal In Space Interface Control Document Open Service Signal (Version 2.1), China Satellite Navigation Office, November 2016
3. BeiDou Navigation Satellite System Signal In Space Interface Control Document Open Service Signal B3I (Version 1.0), China Satellite Navigation Office, February 2018
4. BeiDou Navigation Satellite System Signal In Space Interface Control Document Open Service Signal B1C (Version 1.0), China Satellite Navigation Office, December 2017
5. BeiDou Navigation Satellite System Signal In Space Interface Control Document Open Service Signal B2a (Version 1.0), China Satellite Navigation Office, December 2017
6. Fante RL Unambiguous tracker for GPS binary offset carrier signals. The MITRE Corporation
7. Wang J, Li J, Ni S, Ou G (2013) LDPC decoder for GPS L1C signal. J Natl Univ Defence Technol 35(1)
8. http://mgex.igs.org/IGS_MGEX_Status_BDS.php. Accessed 24 Nov 2018

Performance Evaluation of Galileo Precise Point Positioning

Zongpeng Pan(✉), Hongzhou Chai, Rui Wang, Chunhe Liu, Mingchen Shi, and Wenlong Qi

Institute of Surveying and Mapping, Information Engineering University, Zhengzhou 450001, China
panzongpeng@yeah.net

Abstract. Galileo Satellite Navigation System has been put into trial operation at the end of 2016. Whether Galileo Satellite Navigation System can be used independently for navigation and positioning needs to be analyzed and evaluated because it is not yet in full constellation, especially the performance of Galileo Precision Point Positioning is worth studying. This paper evaluates the global positioning performance of Galileo Precision Point Positioning. The Galileo satellite visibility, average DOP value, convergence speed and positioning accuracy of PPP in different regions are evaluated by experiments with MGEX observation data. The experimental results show that in the initial operation stage of Galileo, the convergence speed of Galileo PPP is slower due to fewer visible satellites, but the positioning accuracy of static PPP is comparable to that of GPS PPP. At the same time, the positioning accuracy and convergence speed of GPS/Galileo PPP is better than that of Galileo PPP.

Keywords: Galileo · Precise point positioning · Performance evaluation

1 Introduction

Galileo is a global satellite navigation system designed and constructed by the European Union. The constellation consists of 30 satellites (27 of them are working satellites and 3 are standby satellites). These satellites are evenly distributed on three orbit planes, with 9 working satellites and 1 backup satellite on each orbit plane [1]. Galileo Satellite Navigation System has completed the system test phase and on-orbit verification phase, and entered the initial operation phase in December 2016. At present, there are 26 satellites in orbit, 20 of which provide services [2]. Compared with GPS and GLONASS, Galileo not only has global navigation and positioning functions, but also has global search and rescue functions. At the same time, it adds system differential and integrity monitoring functions, which makes the system have the better performance of positioning accuracy, availability and continuity. When the system is completed, Galileo will be compatible and interoperable with GPS at L1 and L5 frequencies [3].

Galileo Satellite Navigation System has been in initial operation since the end of 2016. Whether it can be used independently for navigation and positioning needs to be analyzed and evaluated, especially how the performance of Galileo Precise Point

J. Sun et al. (Eds.): CSNC 2019, LNEE 563, pp. 422–434, 2019.
https://doi.org/10.1007/978-981-13-7759-4_38

Positioning (PPP) is worth researching. At present, several MGEX analysis centers have released Galileo's precise orbit and clock error products [4], such as ESA/ESOC, GFZ and CODE, which can provide precise ephemeris correction information for Galileo's precise point positioning. Because Galileo has fewer visible satellites at present, the existing research mainly focuses on the precise positioning performance of combined Galileo and other satellite navigation systems, and analyses the improvement of positioning accuracy, convergence speed and reliability of PPP by including Galileo [5, 6], but lacks the research of precise point positioning performance by Galileo alone.

Therefore, this paper evaluates the performance of Galileo precise point positioning and the contribution of Galileo to combined GPS/Galileo PPP. The Galileo satellite visibility, average DOP value, convergence time and positioning accuracy of PPP are analyzed by experiments with the MGEX observation data. The second part is the precise point positioning model. The third part is the experimental analysis. Finally, the conclusion of this paper is given.

2 Mathematical Model of Precision Point Positioning

2.1 PPP Observation Equation

The original pseudo-range and carrier phase observation equation of GNSS can be expressed as [7]

$$P_{i,r}^{s,j} = \rho_r^{s,j} + \delta t_r^s - \delta t^{s,j} + d_{orb}^{s,j} + T_r^{s,j} + \gamma_i I_{1,r}^{s,j} + d_{i,r}^s - d_i^{s,j} + \varepsilon(P_{i,r}^{s,j}) \quad (1)$$

$$L_{i,r}^{s,j} = \rho_r^{s,j} + \delta t_r^s - \delta t^{s,j} + d_{orb}^{s,j} + T_r^{s,j} - \gamma_i I_{1,r}^{s,j} + b_{i,r}^s - b_i^{s,j} + \lambda_i^s N_{i,r}^{s,j} + \varepsilon(L_{i,r}^{s,j}) \quad (2)$$

Where, $L_{i,r}^{s,j}$ and $P_{i,r}^{s,j}$ are the original carrier phase and pseudo-range observations, in meters; the superscript j is a satellite number, the s is a satellite navigation system, and the subscript r for station number, i for the frequency number. $\rho_r^{s,j}$ is geometric component which include geometric distance between satellite and receiver, δt_r^s and $\delta t^{s,j}$ for clock error of receiver and satellite, respectively, $d_{orb}^{s,j}$ is the satellite orbit error, $T_r^{s,j}$ is troposphere delay, $I_{1,r}^{s,j}$ is ionosphere path delay on the frequency L1. $\gamma_i = f_1^2/f_i^2$, $d_{i,r}^s, d_i^{s,j}$ are hardware delays in code observations of receiver and satellite. $b_{i,r}^s$, $b_i^{s,j}$ are hardware delays in phase observations of receiver and satellite., $N_{i,r}^{s,j}$ is phase ambiguity which include initial phase bias. $\varepsilon(L_{i,r}^{s,j})$, $\varepsilon(P_{i,r}^{s,j})$ are carrier phase and code measurement noise and other un-modeled errors.

$\rho_r^{s,j}$ is geometric distance of satellite and receiver and can be expressed as

$$\rho_r^{s,j} = \sqrt{(x^j - x_r)^2 + (y^j - y_r)^2 + (z^j - z_r)^2} \quad (3)$$

Where, $(x^j, y^j, z^j)^T$ is the position of the satellite and can be obtained from the precise ephemeris, $(x_r, y_r, z_r)^T$ indicating the position of the receiver.

In order to eliminate the influence of the first order term of the ionosphere, the ionosphere-free combination is usually used in the above equation. At the same time, the pseudo-range hardware delay at the receiver and satellite cannot be separated directly from other parameters, and can be combined with the receiver clock error and satellite clock error parameters respectively. In PPP model, the carrier observation contains ambiguity parameter, which is linearly related to the receiver clock error parameter. Therefore, the initial value of the receiver clock error parameter in the carrier observation equation is estimated by the pseudo-range observation. At this time, the pseudo-range hardware delay will be introduced into the carrier observation equation with the receiver clock error parameter. The hardware delay in carrier phase is classified into ambiguity parameters. Taking L1 and L2 dual-frequency ionosphere-free combination as an example, the pseudo-range and carrier observation equations are expressed as follows.

$$\begin{aligned} P_{IF,r}^{s,j} &= \frac{f_1^2 \cdot P_{1,r}^{s,j} - f_2^2 \cdot P_{2,r}^{s,j}}{f_1^2 - f_2^2} \\ &= \rho_r^{s,j} + (\delta t_r^s + d_{IF,r}^s) - (\delta t^{s,j} + d_{IF}^{s,j}) + d_{orb}^{s,j} + T_r^{s,j} + \varepsilon(P_{IF,r}^{s,j}) \end{aligned} \tag{4}$$

$$\begin{aligned} L_{IF,r}^{s,j} &= \frac{f_1^2 \cdot L_{1,r}^{s,j} - f_2^2 \cdot L_{2,r}^{s,j}}{f_1^2 - f_2^2} \\ &= \rho_r^{s,j} + (\delta t_r^s + d_{IF,r}^s) - (\delta t^{s,j} + d_{IF}^{s,j}) + d_{orb}^{s,j} + T_r^{s,j} \\ &\quad + [b_{IF,r}^s - d_{IF,r}^s + d_{IF}^{s,j} - b_{IF}^{s,j} + \lambda_{IF}^s N_{IF,r}^{s,j}] + \varepsilon(L_{IF,r}^{s,j}) \end{aligned} \tag{5}$$

where, the subscript *IF* denotes the ionosphere-free combination, and the other symbols are the same as the preceding one.

$$\delta\hat{t}_r^s = \delta t_r^s + d_{IF,r}^s,\ \delta\hat{t}^{s,j} = \delta t^{s,j} + d_{IF}^{s,j} \tag{6}$$

$$\lambda_{IF}^s B_{IF,r}^{s,j} = b_{IF,r}^s - d_{IF,r}^s + d_{IF}^{s,j} - b_{IF}^{s,j} + \lambda_{IF}^s N_{IF,r}^{s,j} \tag{7}$$

$\delta\hat{t}_r^s$ and $\delta\hat{t}^{s,j}$ for the receiver clock error and satellite clock error with pseudo-range hardware delay, $B_{IF,r}^{s,j}$ for the ambiguity parameter with pseudo-range and phase hardware delay error. In this case, the ionosphere-free combination equation can be simplified to

$$P_{IF,r}^{s,j} = \rho_r^{s,j} + \delta\hat{t}_r^s - \delta\hat{t}^{s,j} + d_{orb}^{s,j} + T_r^{s,j} + \varepsilon(P_{IF,r}^{s,j}) \tag{8}$$

$$L_{IF,r}^{s,j} = \rho_r^{s,j} + \delta\hat{t}_r^s - \delta\hat{t}^{s,j} + d_{orb}^{s,j} + T_r^{s,j} + \lambda_{IF}^s B_{IF,r}^{s,j} + \varepsilon(L_{IF,r}^{s,j}) \tag{9}$$

In the above equation, satellite orbit error and clock error can be corrected by precise ephemeris. Because the precise satellite clock error provided by MGEX analysis center is generated by the ionosphere-free combination observations, the precise clock error product contains the hardware delay of ionosphere-free combination [8], which is consistent with the satellite clock error in the ionosphere-free combination

PPP model. In ionosphere-free combination PPP model, the precise clock error product can be directly corrected, otherwise the corresponding DCB correction should be carried out. The tropospheric delay is corrected by a prior model (such as Sasstamoinen model), and the remaining zenith wet delay is estimated. Finally, the antenna phase center correction, relativistic effect correction, phase windup correction, earths tide correction, DCB correction and other PPP errors need to be taken into account [9]. The pseudo-range and carrier observation equation of PPP can be further simplified as

$$\tilde{P}_{IF,r}^{s,j} = \boldsymbol{\mu}_r^{s,j}\boldsymbol{r} + \delta\hat{t}_r^s + M_r^{s,j} \cdot \ d_{trop,r} \tag{10}$$

$$\tilde{L}_{IF,r}^{s,j} = \ \boldsymbol{\mu}_r^{s,j}\boldsymbol{r} + \ \delta\hat{t}_r^s + M_r^{s,j} \cdot \ d_{trop,r} \ + \ \lambda_{IF}^s B_{IF,r}^{s,j} \tag{11}$$

In the formula, $\boldsymbol{\mu}_r^{s,j} = \left(\alpha^j, \beta^j, \gamma^j\right), \boldsymbol{r} = (\delta x_r, \delta y_r, \delta z_r)^T$ is the correction vector of coordinate components, $d_{trop,r}$ is the zenith tropospheric wet delay (ZWD), and $M_r^{s,j}$ is the mapping function of the tropospheric wet delay. In this case, the parameters to be estimated in the equation are

$$\boldsymbol{X} = [\ \boldsymbol{r},\ \delta\hat{t}_r^s,\ d_{trop,r},\ B_{IF,r}^{s,1}, \cdots, B_{IF,r}^{s,m}] \tag{12}$$

The parameters in the $\boldsymbol{X}$ are station coordinate correction, receiver clock difference, zenith tropospheric wet delay and ambiguity parameters. When GPS/Galileo PPP is used, the system time bias parameter should also be added. For the linearized equation of precise point positioning, Kalman filter can be used to estimate the parameters [10].

2.2 Stochastic Model of Observation and Processing Method of Parameters

In PPP model, the stochastic model of pseudo-range and carrier phase measurements can be quantified by elevation-based model.

$$\sigma^2 = \frac{\sigma_0^2}{2\sin(E)} \tag{13}$$

where, E is the elevation of the satellite, σ_0 is the standard deviation of the observed noise. The accuracy of original pseudo-range and carrier observations of GPS and Galileo is shown in Table 1. The accuracy of combined observations of ionosphere-free can be obtained by the law of error propagation.

Table 1. Accuracy of original pseudo-range and carrier observations (unit: meter)

GPS		Galileo	
Code	Phase	Code	Phase
0.3	0.003	0.3	0.003

The parameters of PPP model can be estimated by extended Kalman filter, and process noise should be set up properly. Detailed estimation strategies of parameters and initial filtering values are shown in Table 2, which also gives the treatment strategies of observation values and errors.

Table 2. PPP parameter configuration

Processing items	Processing methods
Observations	Ionosphere-free pseudo-range and carrier observations
Elevation cutoff angle	10°
Satellite DCB	DCB Product Released by CODE and MGEX
Antenna phase center correction	Antenna phase center correction of satellite and receiver: igs_14.atx model
Phase windup	Model corrected
Earth tides	Solid tide, sea tide and polar tide correction
Relativistic effects	Model corrected
EOP	Fixed to IERS release results
Satellite position and clock error	Using GBM products provided by GFZ
Station coordinates	Station coordinates are estimated as constants in static mode, and random walk process with process noise as 10000 m^2 in kinematic mode
Receiver clock error	White noise with process noise variance of 8.1 $e^7 m^2/s \times \Delta t$ Initial value estimated by code observations and initial variance is 9 $e^6 m^2$
Tropospheric delay	Dry component provided by UNB3 model Wet component is modeled by random walk process and estimated, with process noise variance of 3 $e^{-8} m^2/s \times \Delta t$ Initial value provided by UNB3 and initial variance is 0.25 m^2
ISB	ISB is modeled by random walk process, with process noise variance of $1.0e^{-3} m^2/s \times \Delta t$ Initial value is zero and initial variance is $1.0e^2 m^2$
Ionospheric delay	First order term of Ionosphere is removed by ionosphere-free combination
Ambiguity	Ambiguity is estimated as a constant and is reset when cycle slip

3 Experiments and Results Analysis

3.1 Experimental Data and Processing Strategies

In order to evaluate the performance of Galileo PPP and Galileo/GPS combined PPP, 30 MGEX stations with global distribution are selected for experimental analysis. The distribution of stations is showed in Fig. 1. The data sampling interval is 30 s, the observation time is at the day of year 288 in 2018. The multi-system precise satellite orbit and clock error products are provided by the GFZ. The 'ground truth' of the stations are provided by GFZ network solution.

Firstly, the number of visible satellites and PDOP of each MGEX station are compared and analyzed; secondly, the positioning accuracy of static and kinematic Galileo PPP, GPS PPP and Galileo/GPS combined PPP is analyzed, and the performance of current Galileo PPP is evaluated. Extended Kalman filter (EKF) is used to estimate the parameters of PPP. The random model of the observation is described in Sect. 2.2. At the same time, the antenna phase center correction, relativistic effect correction, phase windup correction, earth tides correction, DCB correction and other PPP error correction should be taken into account. Finally, the convergence time of Galileo PPP, GPS PPP and Galileo/GPS PPP are analyzed.

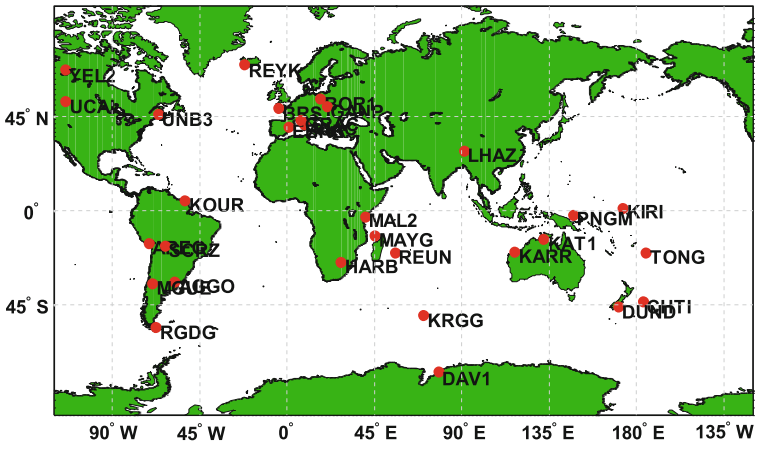

Fig. 1. Station distribution

3.2 Visible Satellites and DOP Value Analysis

The convergence of PPP parameters takes a certain time. It usually needs 30 min of continuous observation to ensure the convergence of position parameters to 10 cm [11]. Therefore, the key to ensure the convergence of position parameters is to ensure the continuous visibility of satellites. At present, the Galileo satellite navigation system only achieves the initial operating conditions. Although the number of satellites in orbit is 26, the actual number of satellites in operation is 20. Therefore, the visible satellites and DOP of Galileo satellite are compared with GPS. Figures 2 and 3 show the Galileo and GPS visible satellites at CHTI Station, respectively. The elevation cutoff angle is 10°. Figures 4 and 5 show the Galileo and GPS visible satellite numbers and PDOP at CHTI station, respectively.

It can be seen from the Figs. 2 and 3 that the number of GPS visible satellites at CHTI station is obviously more than that of Galileo, which is related to the number of satellites in the current two systems. At the same time, it can be seen from Figs. 4 and 5 that the number of GPS visible satellites at CHTI station is more than 7, while that of Galileo satellites is only more than 4. Moreover, because of the large number of GPS satellites, the change of PDOP of GPS is relatively stability, while that of Galileo is obviously fluctuating, mainly due to the number of Galileo satellites.

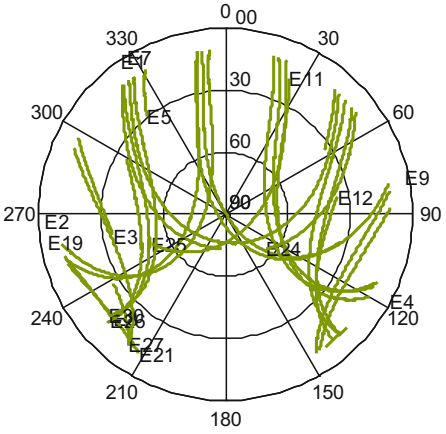

Fig. 2. Galileo visible satellites at CHTI station

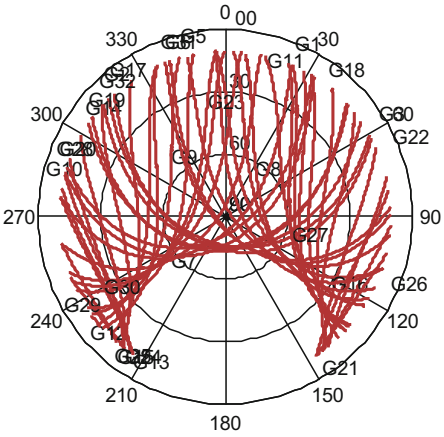

Fig. 3. GPS visible satellites at CHTI station

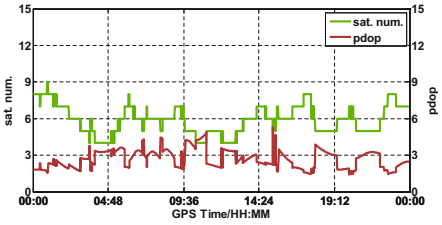

Fig. 4. Galileo satellite visibility and PDOP

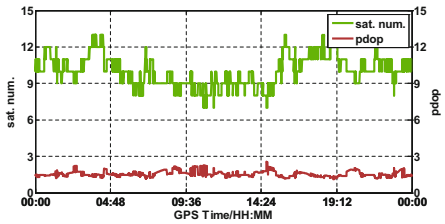

Fig. 5. GPS satellite visibility and PDOP

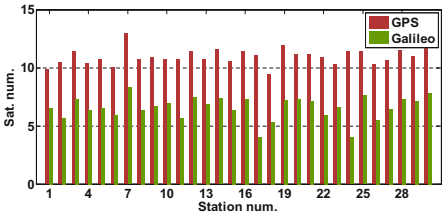

Fig. 6. Average visible satellite number of all station

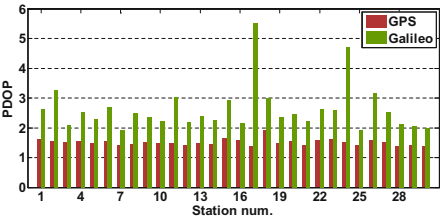

Fig. 7. Average PDOP of all station

Figures 6 and 7 show the average number of visible satellites per day and the average PDOP for all MGEX stations. As can be seen from the figure, the average number of GPS visible satellites at all stations is larger than that of Galileo. Among them, the number of GPS visible satellites at each station is between 9 and 12, with an average of 11, while the average number of Galileo visible satellites is between 5 and 8.

Meanwhile, the average PDOP value of GPS in all stations is also less than that of Galileo, in which the average PDOP value of GPS is 1.52, and the average PDOP value of Galileo is 2.62. The stations with larger PDOP values in Fig. 7 are mainly due to the number of Galileo satellites.

3.3 Analysis of Positioning Accuracy

The data from 30 stations around the world are applied to analysis the performance of Galileo PPP, GPS PPP and Galileo/GPS combined PPP in static and kinematic modes. The 'ground truth' of the stations are provided by GFZ network solution. The parameters of station coordinate are estimated as a random walk in the kinematic positioning, and the process noise variance is 10000 m^2.

(1) Static positioning results

Table 3 gives the positioning bias of PPP hourly solutions in N, E, U and 3D component for all stations (Note that we take absolute value of the positioning bias before conducting average). It can be seen from the table that the positioning bias of GPS PPP hourly solution is slightly better than Galileo PPP hourly solution. The main reason is that the number of Galileo visible satellites, which leads to a slightly longer convergence time of PPP, so its short-time positioning accuracy is not as good as GPS PPP. The positioning accuracy of the GPS/Galileo PPP is the best, mainly because the multi-system combination can provide more visible satellites in the convergence stage of the PPP, which makes the strength of the PPP model better than that of the single system, so the positioning result is better.

Table 3. The average positioning bias of static PPP hourly solution (Unit: cm)

	N	E	U	3D
Galileo	5.49	4.87	8.09	10.92
GPS	1.94	6.01	6.07	8.76
GPS/Galileo	1.66	4.44	3.83	6.10

Figure 8 shows the comparison of positioning bias of GPS and Galileo PPP daily solution in horizontal and vertical direction for all stations, and Fig. 9 shows comparison of positioning bias of GPS and GPS/Galileo PPP daily solution in horizontal and vertical direction for all stations. Analysis of Figs. 8 and 9 shows that for PPP daily solution, the positioning accuracy of GPS, Galileo and GPS/Galileo combination PPP are the same. The positioning accuracy in horizontal direction is mostly better than 1 cm, and that in vertical direction is mostly better than 3 cm. The horizontal positioning accuracy of GPS/Galileo PPP is slightly better than that of GPS PPP, which can be seen more clearly from Table 4. Table 4 shows the mean values, STD and RMS of static positioning solutions for all stations. It can be seen from the table that the positioning accuracy of GPS, Galileo and GPS/Galileo PPP daily solution is millimeter in horizontal direction and 1–2 cm in elevation direction, and there is little difference

between Galileo static PPP daily solution and GPS PPP daily solution, which shows that the positioning accuracy of Galileo static PPP daily solution is comparable to that of GPS.

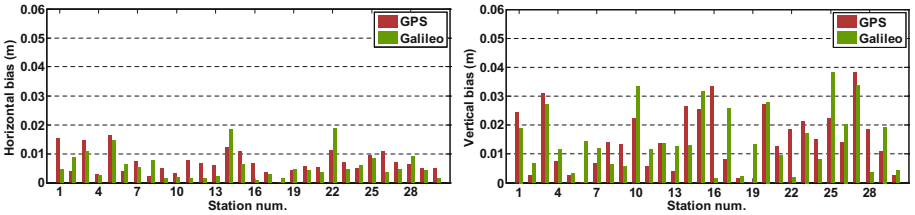

Fig. 8. Comparison of positioning bias of GPS and Galileo PPP daily solution in horizontal and vertical direction

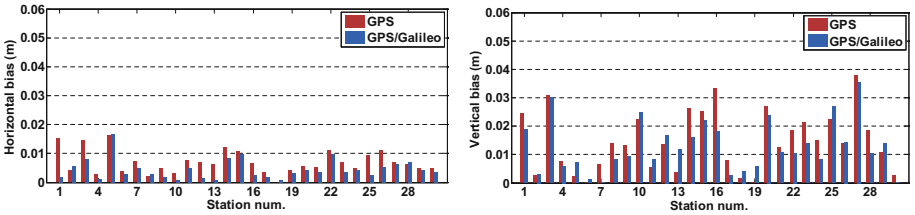

Fig. 9. Comparison of GPS and GPS/Galileo PPP daily solution in horizontal and vertical direction

Table 4. Positioning bias statistic of static PPP daily solution for all stations (unit: cm)

	Mean			std			rms		
	N	E	U	N	E	U	N	E	U
GPS	−0.01	−0.47	−0.69	0.43	0.51	1.69	0.42	0.68	1.80
Galileo	−0.21	−0.14	−0.58	0.34	0.63	1.75	0.39	0.63	1.82
GPS/Galileo	−0.07	−0.07	−0.64	0.36	0.43	1.44	0.36	0.43	1.56

(2) kinematic positioning results

Figure 10 shows the number of Galileo visible satellites and PDOP of MAL2 station. Figure 11 shows the positioning bias time series of Galileo kinematic PPP. As can be seen from the figure, PDOP changes smoothly when Galileo has more visible satellites. The positioning bias time series of Galileo kinematic PPP is relatively stable. The STD of positioning bias in N, E, U direction is centimeter. Comparing the GPS and GPS/Galileo kinematic PPP bias time series of Fig. 12, we can see that the stability of

positioning bias of GPS kinematic PPP is better than that of Galileo kinematic PPP. At the same time, the positioning bias of GPS/Galileo kinematic PPP is more stable, mainly because of the more visible satellites in the combination systems and the good spatial geometry of satellites, so the positioning bias time series is more stable.

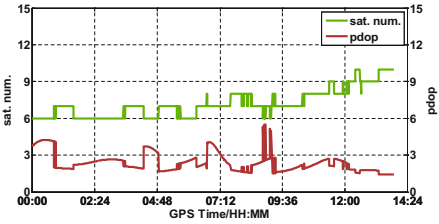

Fig. 10. Galileo satellite visibility and PDOP

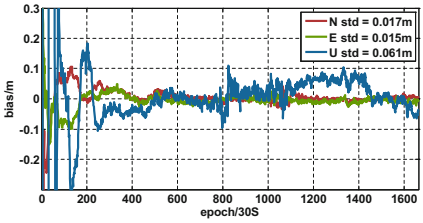

Fig. 11. The positioning bias series of Galileo kinematic PPP

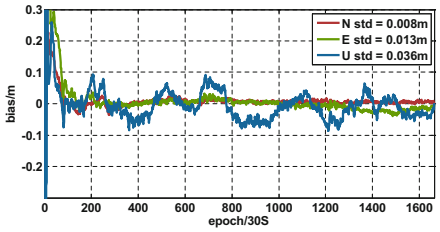

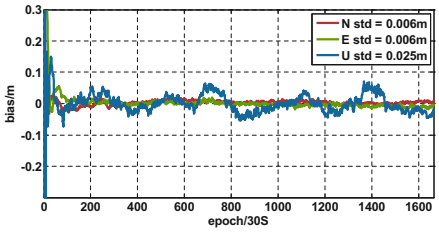

Fig. 12. The positioning bias series of GPS and GPS/Galileo kinematic PPP.

3.4 Convergence Time Analysis

In order to analyze the convergence time of PPP, Kalman filter is re-initialized every two hours during the filtering process (PPP will re-converge at this case). The convergence time of Galileo PPP, GPS PPP and Galileo/GPS combination PPP is counted, and the results are compared with those of Galileo single system PPP. The convergence condition is that the bias of the three components of NEU are less than 10 cm and the following 5 min all satisfy the condition [12, 13]. It is assumed that PPP can converge to 10 cm in two hours, otherwise this section of data will not participate in statistics. Figure 13 shows the positioning bias time series of PPP for different satellite navigation systems at KIRI station. The jump occurring every two hours in the figure is caused by filter reset.

As can be seen from Fig. 13, the convergence speed of positioning bias of Galileo/GPS PPP is the fastest, which is obviously better than that of Galileo PPP. At the same time, the convergence speed of GPS PPP is faster than that of Galileo PPP. The convergence speed of Galileo PPP is relatively slow because of its satellite number. In order to further compare and analyze the convergence time of PPP for different satellite navigation systems, the observation time required for all stations

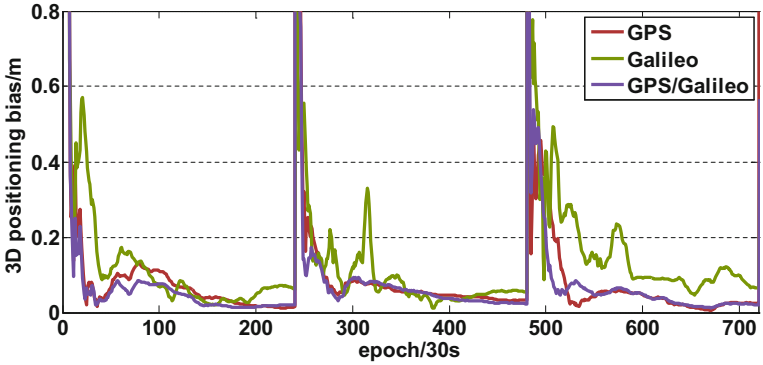

Fig. 13. The position time series of static PPP at KIRI station

to meet the convergence conditions is counted. Figure 14 shows the statistic of convergence time of static PPP at all stations. Table 5 shows the average convergence time of static PPP at all stations and the percentage decrease of convergence time relative to Galileo PPP.

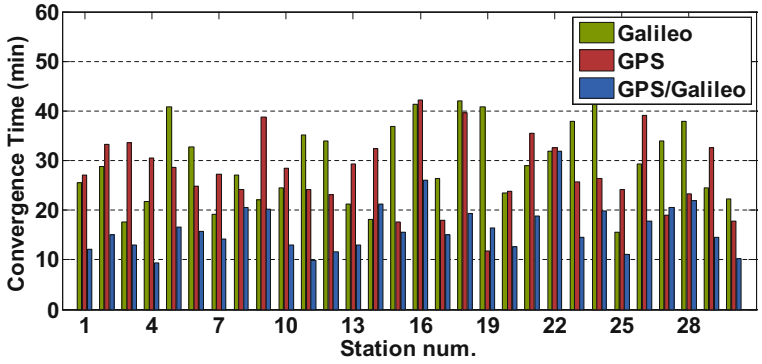

Fig. 14. Convergence time of static PPP for all stations

From Fig. 14 and Table 5, it can be concluded that the Galileo PPP cost a lot of convergence time at most stations, averaging 29.65 min, and the convergence time of GPS PPP is shorter than that of Galileo PPP, averaging 27.81 min. The convergence time of GPS/Galileo PPP is the shortest, only 16.39 min, which is 44.74% less than that of Galileo PPP.

Table 5. Comparison of convergence time of PPP in static mode

	Galileo	GPS	GPS/Galileo
Convergence time (min)	29.65	27.81	16.39
Reduction (%)	\	6.20	44.74

Figure 15 shows the mean position bias of PPP in different time periods for all stations. It is also clear from Fig. 15 that Galileo PPP converges slowly in the first four hours, so its positioning bias is large. However, with the increase of observation time, the positioning accuracy of PPP converges gradually, and the positioning bias of different systems tends to be consistent. The above analysis shows that at present, in the initial operation stage of Galileo, the convergence time of Galileo PPP is long because of the number of visible satellites, but the positioning accuracy of static PPP is comparable to GPS PPP. With the increase of Galileo satellites, the convergence speed of Galileo PPP is expected to accelerate.

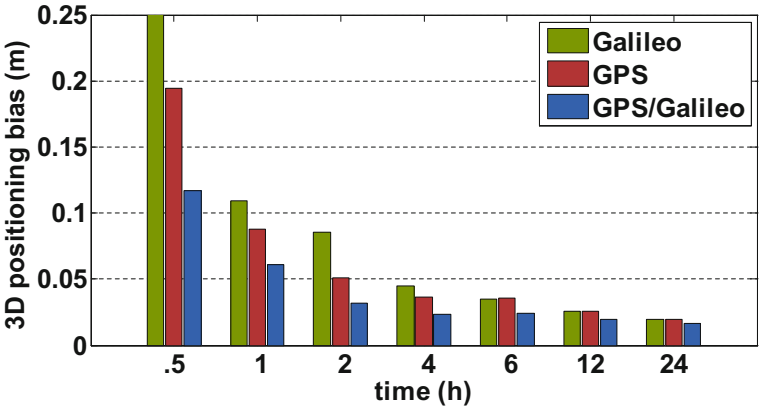

Fig. 15. Mean position bias of PPP in different time periods for all stations

4 Conclusion

In the initial operation stage of Galileo satellite navigation system, this paper studies the performance of Galileo precise point positioning and the contribution of Galileo to combined GPS/Galileo PPP. The Galileo satellite visibility, average DOP value, convergence time and positioning accuracy of PPP are analyzed by experiments with the MGEX observation data. The experimental results show that, firstly, under the current Galileo constellation, the average number of Galileo visible satellites in all stations is less than the average number of GPS visible satellites. Among them, the number of GPS visible satellites in each station is between 9 and 12, with an average of 11, while the average number of Galileo visible satellites is between 5 and 8. Meanwhile, the average PDOP of GPS in all stations is also less than that of Galileo, in which the average PDOP of GPS is 1.52, and the average PDOP of Galileo is 2.62. Secondly, under static mode, the positioning accuracy of GPS, Galileo and GPS/Galileo PPP daily solution is millimeter, and the vertical component is 1–2 cm, and the Galileo static PPP daily solution is comparable to GPS PPP daily solution. Finally, the

convergence speed of Galileo PPP is slower due to fewer visible satellites, and the performance of GPS/Galileo PPP is better than that of Galileo PPP. Both the positioning accuracy and the convergence speed of GPS/Galileo PPP are improved with respect to Galileo PPP.

Acknowledgments. This work was supported by National Natural Science Foundation of China (Grant No. 41604013, No. 41574010) and State Key Laboratory of Geo-information engineering (No. SKLGIE2015-Z-1-1).

References

1. Li Z, Huang J (2016) GPS surveying and data processing. Wuhan University Press, Wuhan
2. Chai H, Pan Z, Cui Y (2016) Review of combined multi-system precision positioning. Hydrogr Surv Charting 36(4):21–26
3. http://mgex.igs.org/IGS_MGEX_Status_GAL.php
4. Guo F, Li X, Zhang X et al (2017) Assessment of precise orbit and clock products for Galileo, BeiDou, and QZSS from IGS multi-GNSS experiment (MGEX). GPS Solut 21 (1):1–12
5. Li X, Zhang X, Ren X et al (2014) Precise positioning with current multi-constellation global navigation satellite systems: GPS, GLONASS, Galileo and BeiDou. Sci Rep 5:8328
6. Li X, Ge M, Dai X et al (2015) Accuracy and reliability of multi-GNSS real-time precise positioning: GPS, GLONASS, BeiDou, and Galileo. J Geodesy 89(6):607–635
7. Leick A, Rapoport L, Tatarnikov D (2014) GPS satellite surveying, 4th edn. Wiley, Hoboken
8. Bock H, Dach R, Yoon Y et al (2009) GPS clock correction estimation for near real-time orbit determination applications. Aerosp Sci Technol 13(7):415–422
9. Kouba J (2009) A guide to using international GNSS service (IGS) products. Maryland Biol Stream Survey Data 4(3):106
10. Yang Y (2006) Adaptive navigation and kinematic positioning. Survey Press, Beijing, pp 56–59
11. Geng J, Teferle FN, Shi C et al (2009) Ambiguity resolution in precise point positioning with hourly data. GPS Solu 13(4):263–270
12. Jokinen A, Feng S, Schuster W et al (2013) GLONASS aided GPS ambiguity fixed precise point positioning. J Navig 66(03):399–416
13. Pan Z, Chai H, Kong Y (2017) Integrating multi-GNSS to improve the performance of precise point positioning. Adv Space Res 60(12):2596–2606

User Terminal Technology

An Improved Geometric Factor-Based Searching and Positioning Algorithm for CGL

Aogen Dong[1], Ying Xu[2(✉)], Wenbo Wang[1], Yuwei Shi[2], Zhihui Song[3], and Shiyang Yuan[3]

[1] University of Chinese Academy of Sciences, No. 19(A) Yuquan Road, Shijingshan District, Beijing 100049, China
[2] Aerospace Information Research Institute, Chinese Academy of Sciences, No. 9 Dengzhuang South Road, Haidian District, Beijing 100049, China
nadinexy@aoe.ac.cn
[3] Beijing Information Science and Technology University, No. 12 xiaoying East Road, Haidian District, Beijing 100192, China

Abstract. The concept of cooperative group localization (CGL) scheme, based on the measurements of time of arrival (TOA), is to solve the ill-conditioned cellular localization. In the light of CGL's traditional searching and positioning algorithm, the paper proposes an improved geometric factor-based searching and positioning algorithm for CGL. In the suggested algorithm, the mobile terminals (MTs) which communicate with a new base station are supposed to be selected preferentially when choosing the next one for positioning. The geometric relationship between MT and its reference terminals (other MTs or base stations) is first put forward as an essential reference index to choose the successor positioning MT. The relationship between the geometric factor and positioning accuracy is completely proved in the theory in this paper. The simulation results indicate that the improved algorithm enjoys higher positioning accuracy than the traditional algorithm at a lower complexity.

Keywords: Cooperative Group Localization · TOA · Geometric factor

1 Introduction

As for the traditional TOA-based cellular localization, if one MT is supposed to be accurately positioned, the fundamental prerequisite condition is to make sure that the MT connects well with at least three BSs. However, the condition is very difficult to provide satisfaction in practical scenarios. For instance, if the MT is in ill-conditioned positioning scenarios such as indoor and urban areas, the TOA measurement will be corrupted due to a large non-line of sight (NLOS) error, or MT will fail to establish an excellent connection with at least three BSs in the rural and city valley areas [1–3]. These ill-conditioned scenarios are likely to result in a positioning failure or reduced accuracy. In recent years, the cooperative localization has been put forward to solve the above problems. It aims to address the lack of effective measurement information by utilizing the distance measurement between MTs with the peer-to-peer communication to ensure the convergence of the algorithm and to improve the positioning accuracy [4].

J. Sun et al. (Eds.): CSNC 2019, LNEE 563, pp. 437–449, 2019.
https://doi.org/10.1007/978-981-13-7759-4_39

Along with the vision that foresees the mobile communication system, which will support short-range communication among its mobile terminals, Refs. [5] and [6] propose two geolocation schemes that combine long-range and short-range location information respectively. The schemes are able to improve the location accuracy concerning the hybrid cellular solutions. Literatures [7, 8] proposed a semi-difinite programming (SDP) cooperative localization method, which has good performance in wireless networks with different topologies and achieve high robustness.

Literature [9] proposes a cooperative localization scheme, named as the cooperative group location (CGL), to solve the positioning problem in ill-conditioned scenarios. Instead of the traditional iterative algorithm, a searching and positioning algorithm presented in the literature is applied to solve the issue caused by the positions of MTs in the CGL scheme in consideration of reducing the computational complexity [10]. The searching and positioning algorithm is a localization algorithm aiming at maximizing the positioning ability of the cellular localization network to deal with the poor performance of the trilateration localization in ill conditions, while the algorithm still has some defects need to be further improved, such as convergence speed and positioning accuracy.

In this paper, an improved geometric factor-based searching and positioning algorithm for CGL is proposed, which first introduces the geometric factor to optimize the candidate MT selection strategy to improve the positioning accuracy at a lower computational complexity.

2 The Original Searching and Positioning Algorithm for CGL

In the CGL scheme, the distance between adjacent mobile terminals can be measured via peer-to-peer (P2P) communication, which is also the prerequisite for cooperative localization. The terminal group refers to a group of MTs connecting with each other through P2P cooperative communication. It is assumed that the location of each MT is unknown, and the distances between some certain MT pairs are known to represent a general situation. Even if each MT in the TG cannot be positioned based on the

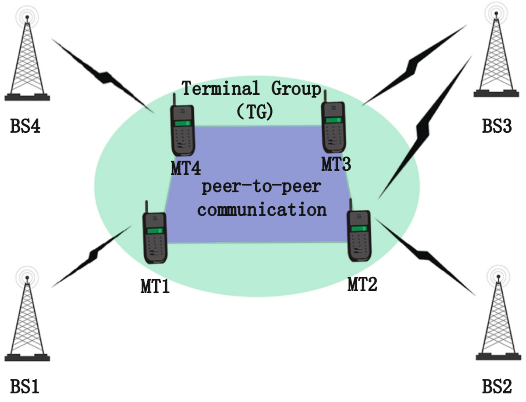

Fig. 1. The topology structure for CGL in the real scenario

trilateration, as shown in Fig. 1, the locations of all MTs are able to be calculated by using the searching and positioning algorithm.

If all MTs in the TG form a loop according to mutual measurement information, as shown in Fig. 2, the algorithm will calculate the candidate positions of MTs one by one. Meantime, impossible candidate positions are supposed to be deleted through trilateral detection in the end of algorithm execution, and every MT can be positioned accurately. The specific method includes following steps:

Step 1: Initialization: selecting an MT connecting well with at least two BSs and denote as H, calculating the two candidate positions of H: H_1 and H_2 on the basis of the known positions of BS A and BS D, and defining the candidate positions as set $H = \{H_1, H_2\}$.

Step 2: Searching for the neighbors of the MT of H on the loop (including E, F, K). E is supposed to be selected. If E and H connect with the same BS to measure the distance, then skip to Step 3; otherwise, performing the following trilateral detection: supposing that d_1, d_2, d_3 denote the distances between E and A, E and H, A and H_1 respectively. If the length of d_1, d_2, d_3 cannot form a triangle, then remove H_1 from the set of H. H_2 is verified in the same way.

Step 3: (i) Choosing one element from the set H. On the basis of the known positions A and H_i, calculating the candidate positions of E: $E_{i,1}$ and $E_{i,2}$, and defining the candidate position as set $E = \{E_{i,1}, E_{i,2}\}$; (ii) Performing the same process described in **Step 2**; (iii) repeating **Step 3** until all candidate positions have been detected.

Step 4: Searching the neighbors of E on the loop. K is supposed to be selected. Then, repeating **Step 2** until all the MTs have been found and positioned. Or else the algorithm terminates.

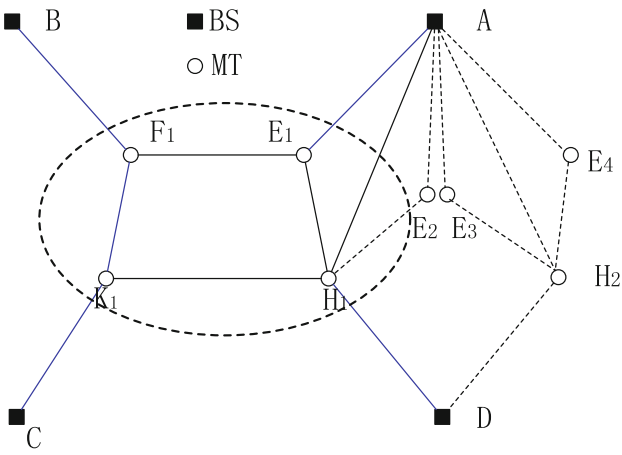

Fig. 2. The solutions to the positions of MTs in the searching and positioning algorithm

The binary tree can be used to illustrate the searching and positioning algorithm clearly, as shown in Fig. 3. Each node in the binary tree denotes a potential candidate position, and all the nodes on the same layer only represent the candidate positions of the same MT. The algorithm starts at the top of the tree and ends at the leafages, forming a clear path. The path will be terminated early if Step 2 figures out that d1, d2, d3 cannot form a triangle. The paths looping through all layers in the tree are the potential paths. The final estimated positions of all MTs are determined by selecting the most favorable path from the candidate paths. The choice is done by the following maximum likelihood detection:

$$(i,j) = \min abs\{||p_i(H) - p_j(K)|| - d(H,K)\} \tag{1}$$

where abs{.} denotes the absolute value. ‖.‖ stands for the Euclidean distance between two positions, $p_i(H)$ represents the i^{-th} possible position of MT H, and d(H, K) represents the measured distance between MT H and K. Once the last node of the path is determined, the algorithm completes the localization of all the MTs.

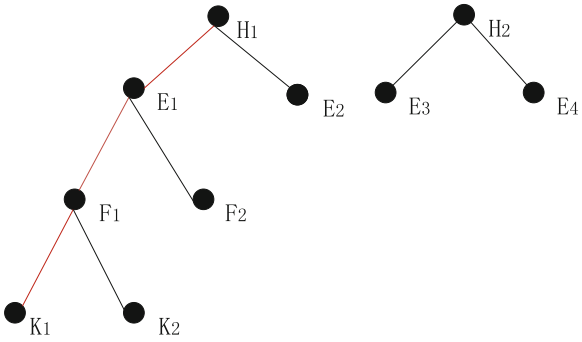

Fig. 3. Binary tree for the searching and positioning algorithm

3 Improved MTs' Selection Strategy

Some MTs are located according to measurement information with two reference terminals (RTs). That is to say, a searching and positioning algorithm for CGL has lower complexity at the cost of acceptable certain positioning accuracy loss. However, the algorithm does not consider the influence of the geometric relationship between the MT and its RTs on the positioning accuracy in the MTs' selection strategy. This paper proposes an improved geometric factor-based searching and positioning algorithm for CGL, which first highlights the geometric relationship between the MT and its RTs as an important basis for selecting which MT is the next one that needs to be positioned to improve the positioning accuracy.

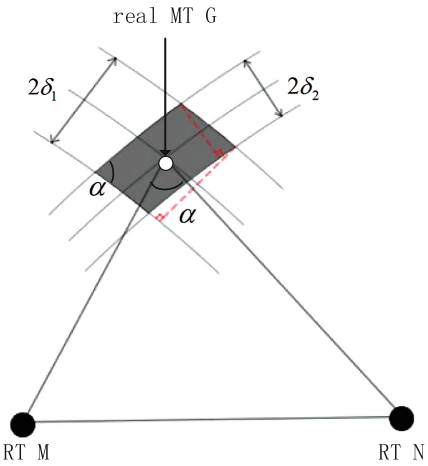

Fig. 4. The geometric relationship between MT with RTs

Considering that the essence of cooperative localization in the CGL is a hybrid positioning of bilateral and trilateral measurements, the angle α formed by the two lines between the MT and its two RTs is harnessed to characterize their geometric relationship in the improved algorithm for the bilateral ranging location, as shown in Fig. 4. The two additional half rings formed by three-section arcs separately denote the possible location areas of MT G caused by the ranging errors δ_1 and δ_2 respectively. The shadow area S represents the set of positions of MT G that are obtained in the light of the ranging information within the scope of allowed errors, which reflects the positioning accuracy of the MT G. The shadow area S is regarded as a diamond, whose area is formulated as

$$S = \frac{4\delta_1 \cdot \delta_2}{\sin \alpha} \ (0^\circ < \alpha < 180^\circ) \tag{2}$$

It is not difficult to find out that the positioning accuracy of one MT is only related to ranging errors and the angle between the MT and its RTs. In other words, when the ranging errors δ_1 and δ_2 are determined, the closer the value of $\sin \alpha$ is to 1, the smaller the shadow area is, and the higher the positioning accuracy is. While it is hard to calculate the value of directly, can be obtained easily by applying the cosine theorem. Based on the following two important trigonometric function formulas, the conclusions is drawn as follows:

(i) The smaller the absolute value of $\frac{a^2+b^2-c^2}{2ab}$ is, the closer the value of $\cos \alpha$ is to 0, and the better the geometric relationship is;

(ii) When the relationship between the values of a, b and c satisfies $a^2 + b^2 = c^2$, the degree of the angle α formed by the two lines between the MT and its two RTs respectively is equal to 90°, and the positioning result is the best, as shown in Fig. 5.

$$\sin^2 \alpha + \cos^2 \alpha = 1 \tag{3}$$

$$\cos \alpha = \frac{a^2 + b^2 - c^2}{2ab} \tag{4}$$

where a, b, and c denote the distances between MT G and RT M, MT G and RT N, RT M and N.

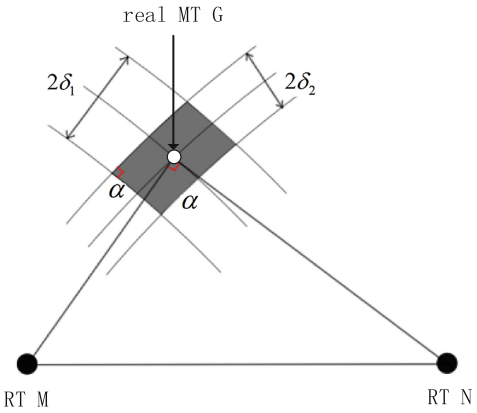

Fig. 5. The best geometric relationship between MT with RTs

The fact remains that Fig. 4 can only represent the general situation. As Fig. 6 shows, when the MT and RTs are on the same straight line, the shadow area can not be approximated as a diamond. The theory mentioned above works equally, that is to say, the positioning result is the worst when the degree of the angle α is close to 0° or 180°.

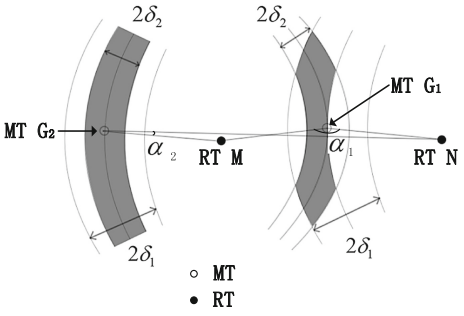

Fig. 6. The worst geometric relationship between MT with RTs

In order to speed up the convergence of the algorithm, the MT communicating with a new base station is supposed to be selected first when choosing the next one to positioning in the improved algorithm. If the condition does not work, the MT which

has a better geometric relationship will be chosen. Compared with the original algorithm, on the basis of MT H's position, MT F and K have a higher positioning priority than E in the improved algorithm because they connect with new BS B and C respectively except A and D. On the same basis, MT K has a higher priority than F due to the geometric relationship. In the improved algorithm, the new MTs location sequence is: H, K, F, E, as shown in Fig. 7.

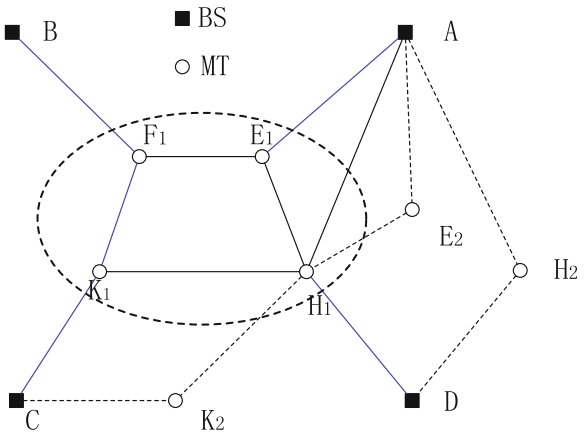

Fig. 7. Solve the positions of MTs in the improved algorithm

Meanwhile, the corresponding binary tree of the improved algorithm is shown in Fig. 8. By comparing Figs. 3 and 8, it is obvious that the improved algorithm has a simpler binary tree. If each none-leaf node is treated as a calculation process, concerning the calculation for H, the improved algorithm performs four calculations, which is less than the five calculations of the original one.

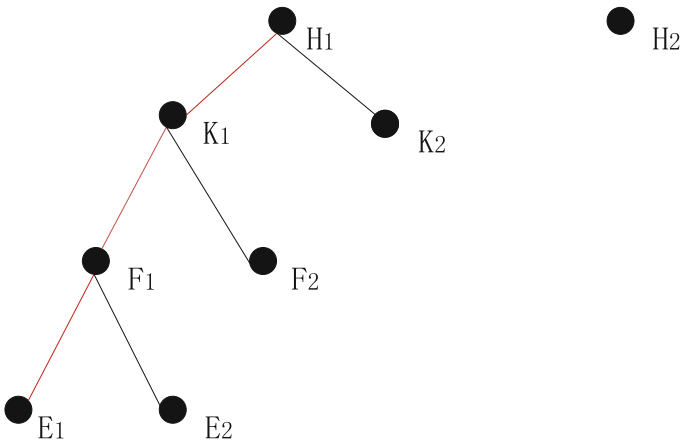

Fig. 8. Binary tree for the improved algorithm

4 Simulation Results

4.1 Mapping Relationship Between Geometric Factor and Positioning Accuracy

The factors that influence positioning accuracy of the MT are the position error of RTs, the geometric relationship, and the ranging errors between MT and RTs [11, 12]. In this paper, only the geometric relationship in the bilateral measurement positioning is discussed. In the improved algorithm, least squares are employed to estimate the positions of the MT. It is necessary to mention that there will be two initial positions of the MT on the both sides of the line between its RTs if the MT only connects with two RTs whose positions are known. For the sake of analysis, I suppose the given position of the RTs is accurate, and the ranging errors between the MT and its RTs are Gaussian white noise with a mean of zero and a root mean square error of 5 m. It is assumed that all the MTs are stationary or in low speed mobile status.

Figure 9 shows the simulation results of the relationship between the MT's positioning accuracy, the MT's position, and the distances between the MT and its RTs when the ranging errors and the angle α formed by the two lines between the MT and its two RTs respectively remain unchanged. The positioning error in the MT is calculated by the average of 1000 independent Monte Carlo simulations, and the number of horizontal axis indicates the number of the MTs that are evenly distributed on a semicircle with diameters between A and B to make sure that keep unchanged. The MTs numbered from 1 to 10 and from 990 to 1000 are ignored because they are so close to one RT that the distances are smaller than the measurement errors, which may

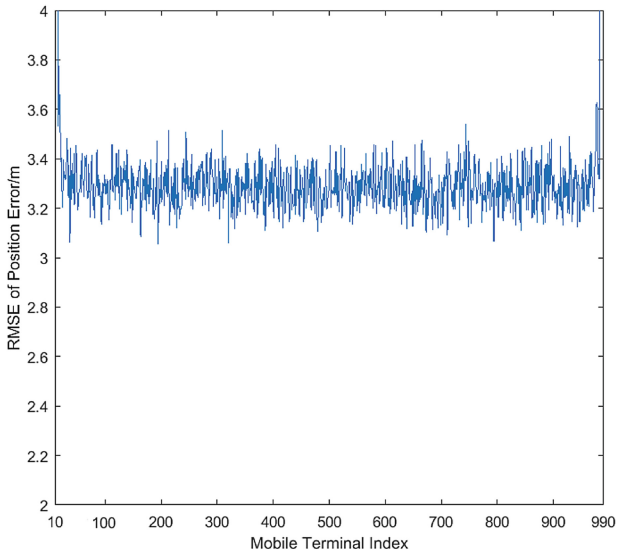

Fig. 9. The relationship between the MT's positioning accuracy and both of MT's position and the distances between the MT and its RTs

cause unreasonable location accuracy loss. When the number of MT is between 15 and 985, the result tends to be stable. In Fig. 9, it is obvious that the MT's positioning accuracy is not relevant to the MT's position and the distances between the MT and its RTs. And by calculation the variance of RMSE of position errors is equal to 0.08 m which also supports the conclusion.

Figure 10 shows the mapping relationship between the geometric factor and accuracy when the ranging errors remain unchanged. It is clear that the closer α is to 90°, the better the geometric relationship is, and the higher the positioning accuracy of the MT.

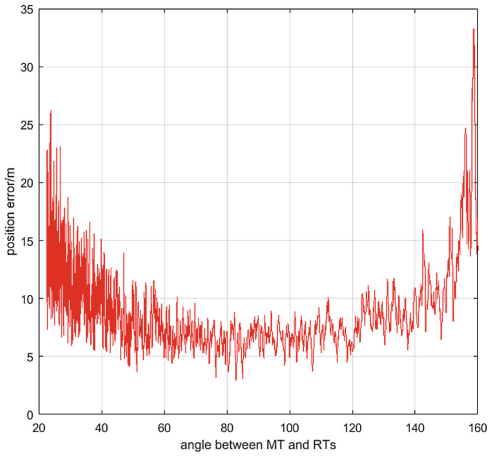

Fig. 10. Mapping relationship between the geometric factor and accuracy

4.2 Performance Comparison of the Improved and the Original Algorithms

In order to facilitate the analysis, the simplified topology structure of the CGL is applied to verify the impact of introducing the geometric factor in the MTs' selection strategy on the positioning accuracy of the MTs, as shown in Fig. 11. In the light of the known position of H, the MT that has a better geometric relationship with its RTs are chosen first. The location sequence in the original algorithm is: H, F, and K, and the new location sequence is: H, K, and F in the improved one.

When it comes to the typical requirement in real wireless networks, the simulation scene is set up in the two-dimensional area of 1500 m * 1500 m where there are four BSs and their MTs whose real position coordinates are: A[1400, 1200], B[200, 1200], C[200, 200], D[1400, 200], H[900, 6500], F[750, 900], and K[350, 700]. The simulation parameters are the same in Fig. 8 in ranging errors and the number M of Monte Carlo trials (M = 1000), but the positioning errors are described by Root Mean Square Error (RMSE).

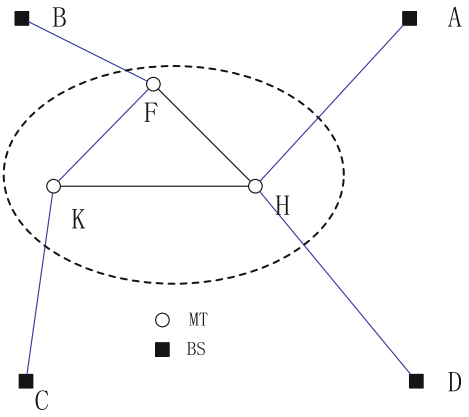

Fig. 11. The simplified topology structure for CGL

Figure 12 explains the two-dimensional scatter plots of positioning results in two algorithms. The green circles denote the real position of the MTs, and the blue squares represent the real position of the BSs. While the red area shows the possible positions of three MTs calculated by the original algorithm, the blue one indicates the possible positions calculated by the improved algorithm. Table 1 presents the means and the standard deviations of the positioning errors in the X and Y directions in two algorithms, where algorithm I indicates the original algorithm, and algorithm II denotes the improved one. It is obvious that the improved algorithm has a better performance on positioning MT F and K, except for MT H whose order does not change. Also, Table 1 shows the means of positioning error for MT F calculated by the improved algorithm, which are at least 0.13 m, and the standard deviations decrease by at least 1.9 m in both X and Y directions, whereas the improvement in MT K is not obvious enough.

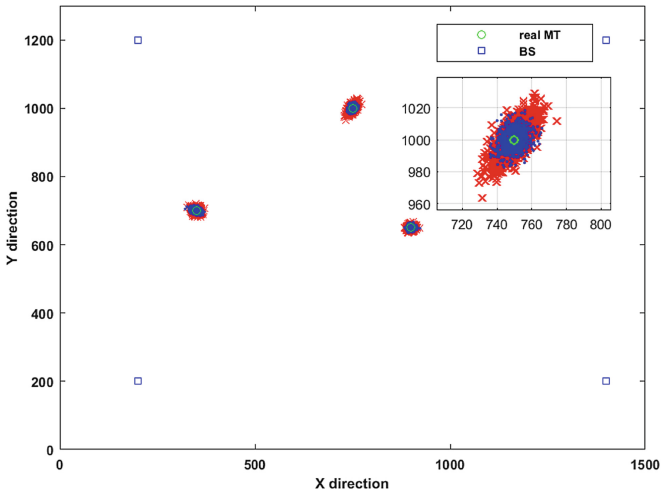

Fig. 12. The scatter plots of positioning results

Table 1. Means and variance of the positioning errors of three MTs in the X and Y directions/m

	MT H	MT F	MT K
Algorithm I x mean ± std	−0.2522 ± 5.2289	−0.3060 ± 7.0586	−0.4637 ± 6.5709
Algorithm II x mean ± std	−0.2522 ± 5.2289	−0.1705 ± 5.0962	−0.3698 ± 7.4063
Algorithm I y mean ± std	−0.3258 ± 5.0130	−0.6387 ± 9.3529	−0.2942 ± 6.5856
Algorithm II y mean ± std	−0.3258 ± 5.0130	−0.4629 ± 5.8874	−0.2619 ± 5.5851

Figure 12 shows the comparison of the positioning performance of the original algorithm and the improved algorithm under different variance δ of BS-TOA measurement error when the MT-MT TOA measurement error ε keeps unchanged, where δ is set as [5, 10, 15, 20, 25]. The value selections of δ and ε refer to the literature [10] where the original algorithm is put forward. The RMSE of MT F between the real MTs' position $p_F(i)$ and the estimated location $p'_F(i)$ is:

$$E_{RMSE(F)} = \sqrt{\frac{\sum_{i=1}^{M} ||p_F(i) - p'_F(i)||_2^2}{M}} \tag{5}$$

where M is the number of Monte Carlo trials.

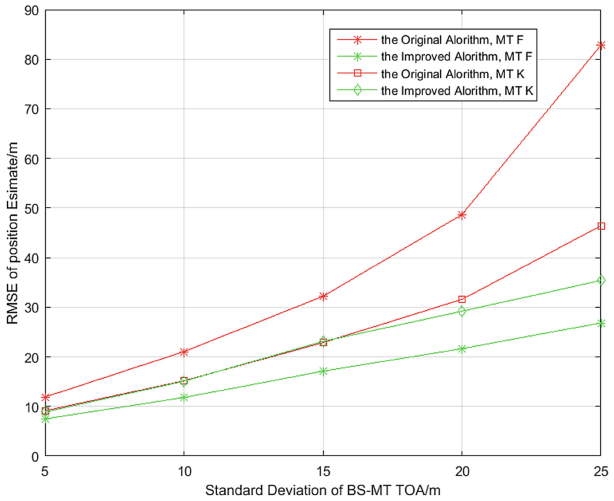

Fig. 13. The positioning performance comparison under different MT-BS measure error

From Fig. 13, it can be seen that the improved algorithm outperforms the original one under the same δ, especially for MT F. Though the improvement in MT K is not obvious until the δ has been over 15 m, the positioning performance of MT H is not taken into consideration because of its particularity. The simulation results are not difficult to be understood. When the MT F' position is estimated by applying the least

square method, the improved algorithm introduces a new effective measurement information from K, which explains why the improved algorithm outperforms the original one. When the MT K' position is calculated, the new measurement information about F in the original algorithm is not useful for positioning because of the poor geometric relationship between MT F and its RTs. On the contrary, the measurement of F may reduce the positioning accuracy of MT K if MT F' position accuracy is very poor, as shown in Fig. 13.

5 Conclusion

This paper has proposed an improved geometric factor-based searching and positioning algorithm for the CGL to solve the problem of ill-conditioned location with insufficient measurement information. Compared with the original algorithm, the proposed algorithm has higher positioning accuracy at a lower complexity. In the paper, the work only focuses on the theoretical verification of the relationship between the geometric factor and positioning accuracy. However, some problems need to be further considered. For instance, in real positioning scenarios, the TOA measurement error is, to some extent, related to the distance if the signal attenuation is under consideration. What's more, MTs are supposed to be rest or move slowly, so that the impact of the MTs' mobility on the accuracy is not discussed in the paper. The above-mentioned issues are the focus of future work.

Acknowledgments. This work is supported by Beijing Municipal Science & Technology Commission 5G special project (No. 100003218009), innovation project of Academy of Opto-Electronic, Chinese Academy of Sciences (No. Y80B08A1BY) and Youth Innovation Promotion Association, Chinese Academy of Sciences (No. Y50301A1BY).

References

1. Tayal M (2005) Location services in the GSM and UMTS networks. In: IEEE international conference on personal wireless communications. IEEE Xplore
2. Zhao Y (2002) Standardization of mobile phone positioning for 3G systems. Commun Mag IEEE 40(7):108–116
3. Sayed AH, Tarighat A, Khajehnouri N (2005) Network-based wireless location: challenges faced in developing techniques for accurate wireless location information. IEEE Sig Process Mag 22(4):24–40
4. Mensing C, Nielsen JJ (2010) Centralized cooperative positioning and tracking with realistic communications constraints. In: Workshop on positioning navigation & communication. IEEE Xplore
5. Frattasi S, Monti M, Prasad R (2006) Cooperative mobile user location for next-generation wireless cellular networks. In: IEEE international conference on communications. IEEE, pp 5760–5765
6. Cui Q, Liu J, Tao X et al (2007) A novel location model for 4G mobile communication networks. In: IEEE vehicular technology conference. IEEE

7. Biswas P, Ye Y (2004) Semidefinite programming for ad hoc wireless sensor network localization. In: International symposium on information processing in sensor networks. IEEE
8. Zou Y, Liu H, Xie W et al (2017) Semidefinite programming methods for alleviating sensor position error in TDOA localization. IEEE Access PP(99):1
9. Cui Q, Zhang X (2013) Research analysis of wireless localization with insufficient resources for next-generation mobile communication networks. Int J Commun Syst 26(9):1206–1226
10. Zhang Y, Cui Q, Tao X (2009) Cooperative group localization for the 4G wireless networks. In: Vehicular technology conference fall. IEEE
11. Tseng PH, Feng KT, Lin YC et al (2009) Wireless location tracking algorithms for environments with insufficient signal sources. IEEE Trans Mob Comput 8(12):1676–1689
12. Brown B, Aaron M (2001) The politics of nature. In: Smith J (ed) The rise of modern genomics, 3rd edn. Wiley, New York

Tracking Error Analysis and Performance Evaluation Method for GNSS Non-coherent Vector Tracking Loop

Zhibin Luo, Lin Zhao(✉), Jicheng Ding(✉), and Mouyan Wu

College of Automation, Harbin Engineering University, Harbin 150001, China
zhaolin@hrbeu.edu.cn, aaron.heu@163.com

Abstract. It is hard to accurately analyze the performance of non-coherent (NC) Global Navigation Satellite System (GNSS) vector tracking loop (VTL) according to tracking error because of tracking error propagation between tracking channels and the non-linear nature of NC-VTL. To solve this problem, this paper first analyzes NC-VTL algorithms and proposes a vector code loop control algorithm, which can be easily implemented in both hardware and software GNSS receiver. Secondly, the tracking error propagation of NC-VTL is analyzed in detail. The mathematic formula, that describes the relationship between tracking error and navigation error, timing error, ephemeris error, satellite clock bias error, atmospheric correction error, ionosphere correction error is deduced. Thirdly, according to these equations, the performance evaluation method based on semi-analytic framework for NC-VTL is established. This method can flexibly set simulation scene, NC-VTL parameters and accurately calculate the signal tracking error and navigation error. The mixing and correlation operation are discarded in this method with realistic simulation for NC-VTL's running reserved. Thus this method provides a flexible, fast way to accurately and reliably access the performance of NC-VTL. In the end, a sample evaluation result is displayed to verify the effectiveness of this evaluation method.

Keywords: Non-coherent vector tracking · Tracking error propagation · Semi-analytic framework · Performance evaluation

1 Introduction

GNSS vector tracking is considered to be one of the key techniques of the GNSS receiver of next generation [1]. Compared with classical scalar tracking loop, it can increase the tracking sensitivity, dynamic performance, bridge the signal after transient signal lost by fully exploiting the aiding among all GNSS satellites in view. The non-coherent vector tracking loop (NC-VTL) structure utilizes the traditional discriminator to estimate the tracking error. The discriminator outputs are then used to update the navigation filter (NF) and NF generates the feedback command for carrier and code tracking [2]. Compared with coherent vector tracking loop, the non-coherent version makes less changes to scalar tracking loop, consumes less computational resources and provides satisfactory performance. Thus NC-VTL is on the top priority for hardware implement of GNSS vector tracking loop.

J. Sun et al. (Eds.): CSNC 2019, LNEE 563, pp. 450–462, 2019.
https://doi.org/10.1007/978-981-13-7759-4_40

The performance evaluation of vector tracking loop has attracted a lot of attention of researchers all over the world. Their research methods can be divided into two categories. The first one is actual test. The GNSS intermediate frequency (IF) signal under various scenes are collected, and then processed by GNSS scalar and vector tracking receivers to show the advantage of vector structure. These scenes include weak signal, dense foliage, and urban canyon, etc. [3–5]. However, it is hard to flexibly change the signal environment and tracking loop parameters, and rapidly accomplish the performance evaluation in actual test. The processing of real IF signal consumes long simulation time for non-real-time GNSS software receiver, which has widely been used by many researchers. The second method is theoretical analysis. The concepts of "vector transfer function" and "equivalent noise bandwidth matrix" are introduced to explain the tracking error propagation between tracking channels in NC-VTL [7, 8]. It can be concluded that the performance of vector tracking is related with geometric distribution of GNSS satellites, parameters of NF and signal strength. However, tracking error of vector tracking loop is not accurately analysed and the nonlinear nature of tracking loop is ignored. The analytical expression of tracking error is derived and exploited to analyse the performance of NC-VTL [8]. However, the nonlinear nature of NC-VTL is not considered thus the analysis results cannot manifest its true performance. For classical scalar tracking loop, the tracking error under different signal strength and relative acceleration (or jerk) can be analysed by theoretical formula under linear hypothesis. There also exists the open source software "SATLSim" for fast loop performance evaluation under the real non-linear condition [9]. However, performance evaluation method of this kind for NC-VTL does not exist as far as we are concerned.

This paper is organized as follows: the NC-VTL algorithm is first designed. Then the mathematical formulas that describe tracking error propagation are derived. Based on these equations, the designing philosophy and software implementation of performance evaluation method is presented. Finally, a sample result is displayed to show its effectiveness.

2 Tracking Error Propagation of Non-coherent Vector Tracking Loop

2.1 Navigation Filter Update and Tracking Loop Control Algorithms

The NC-VTL algorithms can be divided into two part: the NF update and the carrier/code tracking loop control. The NF is implemented as Kalman Filter (KF), and its state variables are:

$$\delta \boldsymbol{X}_k = [\delta x_k \; \delta y_k \; \delta z_k \; \delta \dot{x}_k \; \delta \dot{y}_k \; \delta \dot{z}_k \; \mathrm{c} \cdot \delta(\delta t_{\mathrm{u},k}) - \lambda \cdot \delta(\delta f_{\mathrm{u},k})]^{\mathrm{T}} \tag{1}$$

where subscript k represents the update epoch; $\delta x, \delta y, \delta z$ represent position error in earth centered earth fixed coordinate [m]; $\delta \dot{x}, \delta \dot{y}, \delta \dot{z}$ represent the velocity error [m/s]; $\delta(\delta t_{\mathrm{u}})$ represents the estimation error for receiver clock bias δt_{u} [m] while $\delta(\delta f_{\mathrm{u}})$ represents the estimation error for receiver clock drift δf_{u} [Hz]; c represents the speed of light [m/s]; λ is the wavelength of carrier signal [m]. It should be noted that the constant

velocity (CV) model is utilized in this paper. The constant acceleration (CA) model, constant jerk (CJ) model can also be used. That depends on the motion state of the receiver. The actual state variables that the NF tries to estimate are:

$$\begin{aligned} \boldsymbol{X}_k &= [\, x_k \quad y_k \quad z_k \quad \dot{x}_k \quad \dot{y}_k \quad \dot{z}_k \quad c \cdot \delta t_{\mathrm{u},k} \quad -\lambda \cdot \delta f_{\mathrm{u},k} \,]^{\mathrm{T}} \\ &= [\boldsymbol{P}_{\mathrm{u},k} \qquad\qquad \boldsymbol{V}_{\mathrm{u},k} \qquad\qquad \boldsymbol{T}_{\mathrm{u},k} \qquad\qquad] \end{aligned} \tag{2}$$

where $\boldsymbol{P}_{\mathrm{u}} = [x; y; z]$; $\boldsymbol{V}_{\mathrm{u}} = [\dot{x}; \dot{y}; \dot{z}]$; $\boldsymbol{T}_{\mathrm{u}} = [c \cdot \delta t_{\mathrm{u}}; -\lambda \cdot \delta f_{\mathrm{u}}]$. The two quadrant arctangent (ATAN) frequency discriminator and normalized non-coherent Early-minus-Late envelope (NC-EMLE) code discriminator are used to respectively estimate the carrier frequency tracking error and code phase tracking error. The measurements for NF are:

$$\mathbf{Z}_k = [\, \delta\tau_{1,k} \quad \ldots \quad \delta\tau_{\mathrm{N},k}, \quad \delta f_{1,k} \quad \ldots \quad \delta f_{\mathrm{N},k} \,]^{\mathrm{T}} \tag{3}$$

where the first number in subscript represents tracking channel number; N represents the total number of tracking channels; $\delta\tau$ represents the code phase tracking error [chip]; δf represents the carrier frequency tracking error [Hz]. The update equations of NF in k-th epoch are displayed as follows:

$$\hat{\boldsymbol{X}}_k^- = \boldsymbol{A} \cdot \hat{\boldsymbol{X}}_{k-1} \tag{4}$$

$$\boldsymbol{P}_k^- = \boldsymbol{A} \cdot \boldsymbol{P}_{k-1}\boldsymbol{A}^{\mathrm{T}} + \boldsymbol{Q}_k \tag{5}$$

$$\boldsymbol{K}_k = \boldsymbol{P}_k^- \boldsymbol{H}_k^T (\boldsymbol{H}_k \boldsymbol{P}_k^- \boldsymbol{H}_k^T + \boldsymbol{R}_k)^{-1} \tag{6}$$

$$\delta\hat{\boldsymbol{X}}_k = \boldsymbol{K}_k \cdot \mathbf{Z}_k \tag{7}$$

$$\hat{\boldsymbol{X}}_k = \hat{\boldsymbol{X}}_k^- + \delta\hat{\boldsymbol{X}}_k \tag{8}$$

$$\boldsymbol{P}_k = (\boldsymbol{I}_{8\mathrm{x}8} - \boldsymbol{K}_k \boldsymbol{H}_k)\boldsymbol{P}_k^- \tag{9}$$

where the superscript $\hat{}$ represents the estimation value for the NF states; the superscript $^-$ represents priori estimate; δ represents the estimation error; $\boldsymbol{A}$ represents the state-transition matrix; $\boldsymbol{H}$ represents the measurement matrix; $\boldsymbol{P}$ represents the covariance matrix of state estimation error; $\boldsymbol{Q}$ represents the covariance matrix of system noise; $\boldsymbol{R}$ represents the covariance matrix of measurement noise; $\boldsymbol{I}_{8\mathrm{x}8}$ represents the unit matrix. These matrixes have been discussed in a lot of literatures and their value will not be displayed in this paper [10].

After $\hat{\boldsymbol{X}}_k$ is obtained, $\hat{\boldsymbol{X}}_{k+1}^-$ can be calculated and exploited to generate the feedback control command of tracking loop at k + 1-th epoch. The $\hat{\boldsymbol{X}}_{k+1}^-$ is:

$$\hat{\boldsymbol{X}}_{k+1}^- = \boldsymbol{A} \cdot \hat{\boldsymbol{X}}_k \tag{10}$$

The relationships between true NF state variables and carrier/code frequency are:

$$f_{\text{carr},k+1} = f_{\text{IF}} - \frac{(\boldsymbol{V}_{\text{s},k+1} - \boldsymbol{V}_{\text{u},k+1}) \cdot \boldsymbol{l}}{\lambda} + \delta f_{\text{u},k+1} \tag{11}$$

$$f_{\text{code}} = f_{\text{codeB}} + \beta \cdot (f_{\text{carr}} - f_{\text{IF}}) \tag{12}$$

where f_{carr} represents the frequency of local carrier [Hz]; f_{code} represents the frequency of local code [Hz]; f_{codeB} represents the nominal code frequency [Hz]; f_{IF} represents the analog IF frequency [Hz]; $\boldsymbol{V}_{\text{s}}$ represents the satellite velocity [m/s]; $\boldsymbol{V}_{\text{u}}$ represents the receiver velocity [m/s]; $\boldsymbol{l}$ represents the unit line-of-sight (LOS) vector between receiver and GNSS satellites; β represents the conversion factor that converts nominal carrier frequency to nominal code frequency. The relationship between signal transmit time at k + 1-th epoch and true NF state variables is

$$t_{\text{tr},k+1} = t_{\text{u},k+1} - \delta t_{\text{u},k+1} + \delta t_{\text{s},k+1} - \frac{\left|\boldsymbol{P}_{\text{s},k+1} - \boldsymbol{P}_{\text{u},k+1}\right| + I + T - \Delta \boldsymbol{P}_{\text{s}} \cdot \boldsymbol{l}}{\text{c}} \tag{13}$$

where t_{tr} represents the signal transmit time [s]; t_{u} represents the time of receiver clock in format of seconds of week (SOW) [s]; δt_{s} represents the satellite clock bias [s]; $\boldsymbol{P}_{\text{s}}$ represents the position of satellite; $\boldsymbol{P}_{\text{u}}$ represents the position of the receiver; I is ionospheric delay [m]; T is tropospheric delay [m]; $\Delta \boldsymbol{P}$ represents the satellite movement vector in signal travel time Δt and can be calculated as follow:

$$\Delta t = \frac{\left|\hat{\boldsymbol{P}}_{\text{s},k+1} - \hat{\boldsymbol{P}}^{-}_{\text{u},k+1}\right|}{c} \tag{14}$$

$$\mathbf{C}(\Delta t) = \begin{bmatrix} \cos(\Omega_{\text{ie}} \cdot \Delta t) & \sin(\Omega_{\text{ie}} \cdot \Delta t) & 0 \\ -\sin(\Omega_{\text{ie}} \cdot \Delta t) & \cos(\Omega_{\text{ie}} \cdot \Delta t) & 0 \\ 0 & 0 & 1 \end{bmatrix} \tag{15}$$

$$\Delta \boldsymbol{P}_{\text{s}} = \boldsymbol{P}_{\text{s},k+1} - \boldsymbol{C}(\Delta t) \cdot (\boldsymbol{P}_{\text{s},k+1} - \boldsymbol{V}_{\text{s},k+1} \cdot \Delta t) \tag{16}$$

where Ω_{ie} represents the rotational angular velocity of the earth [rad/s]. Because the scalar tracking loop has initialized the vector tracking loop before vector mode starts, the signal transmit time at k + 1-th epoch can be locked (estimated) by receiver baseband part as $\tilde{t}_{\text{tr},k+1}$. Thus the increment of code phase adjustment is:

$$\Delta \tau_{k+1} = (t_{\text{tr},k+1} - \tilde{t}_{\text{tr},k+1}) \cdot f_{\text{codeB}} \tag{17}$$

where $\Delta\tau$ is code phase increment [chip]. $\Delta\tau$ should be added in local code phase to accomplish the code phase adjustment of NC-VTL. If $\tilde{t}_{\text{tr},k+1}$ cannot be obtained because of the failure of sub-frame synchronization or navigation data demodulation, the NC-VTL can also use the following two equations to calculate $\Delta\tau_{k+1}$:

$$\Delta\tau_{k+1} = \tau_{k+1} - \tilde{\tau}_{k+1} \tag{18}$$

$$\tau_{k+1} = \left(\frac{t_{\mathrm{tr},k+1}}{t_{\mathrm{code}}} - \left[\frac{t_{\mathrm{tr},k+1}}{t_{\mathrm{code}}} \right] \right) \cdot l_{\mathrm{code}} \tag{19}$$

where $[\cdot]$ represents floor division operator, e.g. $[4.6] = 4$; t_{code} represents code period [s]; l_{code} represents code length [chip], $\tilde{\tau}_{k+1}$ is the local code phase locked by receiver baseband part at $k + 1$ epoch. Equation (19) actually transforms signal transmit time $t_{\mathrm{tr},k+1}$ to the value of code phase τ_{k+1}. The delay between NF update and feedback command write-back are tolerable by adding the code phase increment to local code phase in order to adjust the local code phase to the set value. Equations (11)–(17) represent the relation between true NF state and GNSS signal parameters. The true value of NF states cannot be known accurately and should be replaced by priori estimate of NF when generating the feedback control command for carrier and code tracking loop, as follows:

$$\hat{f}_{\mathrm{carr},k+1} = f_{\mathrm{IF}} - \frac{(\hat{\boldsymbol{V}}_{\mathrm{s},k+1} - \hat{\boldsymbol{V}}^{-}_{\mathrm{u},k+1}) \cdot \boldsymbol{l}}{\lambda} + \delta f^{-}_{\mathrm{u},k+1} \tag{20}$$

$$\hat{f}_{\mathrm{code},k+1} = f_{\mathrm{codeB}} + \beta \cdot (\hat{f}_{\mathrm{carr},k+1} - f_{\mathrm{IF}}) \tag{21}$$

$$\hat{t}_{\mathrm{tr},k+1} = t_{\mathrm{u},k+1} - \delta\hat{t}^{-}_{\mathrm{u},k+1} + \delta\hat{t}_{\mathrm{s},k+1} - \frac{\left| \hat{\boldsymbol{P}}_{\mathrm{s},k+1} - \hat{\boldsymbol{P}}^{-}_{\mathrm{u},k+1} \right| + \hat{I} + \hat{T} - \Delta\boldsymbol{P}_{\mathrm{s}} \cdot \boldsymbol{l}}{c} \tag{22}$$

$$\Delta\hat{\tau}_{k+1} = (\hat{t}_{\mathrm{tr},k+1} - \tilde{t}_{\mathrm{tr},k+1}) \cdot f_{\mathrm{codeB}} \tag{23}$$

It should be noted that the estimation error for $\Delta\boldsymbol{P}_{\mathrm{s}}$ can be ignored and thus this variable is not expressed as $\Delta\hat{\boldsymbol{P}}_{\mathrm{s}}$ in Eq. (22).

2.2 The Propagation of Navigation Error to Code Phase Tracking Error

The code tracking error is defined as how much chips local code is delayed with respect to received code. Actually, another equivalent definition of code tracking error is the difference between the estimated signal transmit time and true signal transmit time as follow:

$$\delta\tau_{k+1} = (t_{\mathrm{tr},k+1} - \hat{t}_{\mathrm{tr},k+1}) \cdot f_{\mathrm{codeB}} \tag{24}$$

Subscribe Eq. (13) and Eqs. (22) to (24), the code tracking error at $k + 1$-th epoch is

$$\begin{aligned} \delta\tau_{k+1} = & -\frac{f_{\mathrm{codeB}}}{\mathrm{c}} \delta\boldsymbol{P}_{\mathrm{u},k+1} \cdot \boldsymbol{l} + \frac{f_{\mathrm{codeB}}}{\mathrm{c}} \cdot [\mathrm{c} \cdot \delta(\delta t_{\mathrm{u},k+1})] \\ & + \frac{f_{\mathrm{codeB}}}{\mathrm{c}} \delta\boldsymbol{P}_{\mathrm{s},k+1} \cdot \boldsymbol{l} + \frac{f_{\mathrm{codeB}}}{\mathrm{c}} \delta I + \frac{f_{\mathrm{codeB}}}{\mathrm{c}} \delta T - f_{\mathrm{codeB}} \cdot \delta(\delta t_{\mathrm{s},k+1}) \end{aligned} \tag{25}$$

where

$$\delta \boldsymbol{P}_{\mathrm{u},k+1} = \hat{\boldsymbol{P}}^{-}_{\mathrm{u},k+1} - \boldsymbol{P}_{\mathrm{u},k+1} \tag{26}$$

$$\delta(\delta t_{\mathrm{u},k+1}) = \delta \hat{t}^{-}_{\mathrm{u},k+1} - \delta t_{\mathrm{u},k+1} \tag{27}$$

$$\delta(\delta t_{\mathrm{s},k+1}) = \delta \hat{t}^{-}_{\mathrm{s},k+1} - \delta t_{\mathrm{s},k+1} \tag{28}$$

$$\delta \boldsymbol{P}_{\mathrm{s},k+1} = \hat{\boldsymbol{P}}_{\mathrm{s},k+1} - \boldsymbol{P}_{\mathrm{s},k+1} \tag{29}$$

$$\delta I = \hat{I} - I \tag{30}$$

$$\delta T = \hat{T} - T \tag{31}$$

It can be concluded from Eq. (25) that, if the proposed code loop control algorithm is employed, the true code tracking error would contain the LOS projection of receiver position error, LOS projection of satellite position error, ionospheric correction error δI; troposphere correction error δT; receiver clock bias estimation error $\delta(\delta t_{\mathrm{u}})$; satellite clock bias estimation error $\delta(\delta t_{\mathrm{s}})$. It also should be noted that the second term in Eq. (25) is not in its simplified form. That is because the term "$\mathrm{c} \cdot \delta(\delta t_{\mathrm{u}})$" is actually the state variable of NF and this form can clearly show the error propagation from NF state variables to code tracking. The NC-EMLE discriminator output includes the true tracking error shown in Eq. (25) and estimation noise. Code tracking error sources appear to be white noise and can be filtered by NF except δI and δT. δI and δT would result in bias term in position error and receiver clock bias error. Meanwhile, the sum of position error LOS projection and clock bias error would in turn counteract a portion of $\delta I + \delta T$ in Eq. (25), thus reduces the effect of atmosphere delay correction error in code phase tracking. In experiment part, it can be shown that the sensitivity of NC-VTL depends on the more vulnerable carrier tracking loop. The code tracking bias caused by atmosphere delay correction error can be ignored. The NC-VTL which uses position increment between adjacent epochs to close the code loop usually requires the initial code tracking error and initial position error to be very small [5]. However, NC-VTL algorithms proposed in this paper can reduce the requirement for initial conditions. Even though the initial position error and code tracking error is relatively large, it has the ability to decrease the error with NF updating. The price is a few code tracking bias introduced by atmosphere delay correction error.

2.3 The Propagation of Navigation Error to Carrier Frequency Tracing Error

The carrier frequency tracking error is defined as the difference between received carrier frequency and local carrier frequency as follows:

$$\delta f_{k+1} = f_{\mathrm{carr},k+1} - \hat{f}_{\mathrm{carr},k+1} \tag{32}$$

Subscribe Eq. (11) and Eqs. (20) to (32), the true carrier frequency tracking error can be derived:

$$\delta f_{k+1} = -\frac{1}{\lambda}\delta \boldsymbol{V}_{\mathrm{u},k+1} \cdot \boldsymbol{l} + \frac{1}{\lambda}[-\lambda \cdot \delta(\delta f_{\mathrm{u},k+1})] + \frac{1}{\lambda}\delta \boldsymbol{V}_{\mathrm{s},k+1} \cdot \boldsymbol{l} \tag{33}$$

where

$$\delta \boldsymbol{V}_{\mathrm{u},k+1} = \hat{\boldsymbol{V}}^{-}_{\mathrm{u},k+1} - \boldsymbol{V}_{\mathrm{u},k+1} \tag{34}$$

$$\delta \boldsymbol{V}_{\mathrm{s},k+1} = \hat{\boldsymbol{V}}^{-}_{\mathrm{s},k+1} - \boldsymbol{V}_{\mathrm{s},k+1} \tag{35}$$

$$\delta(\delta f_{\mathrm{u},k+1}) = \delta\hat{f}^{-}_{\mathrm{u},k+1} - \delta f_{\mathrm{u},k+1} \tag{36}$$

It can be concluded form Eq. (33), if carrier loop control algorithm is employed, the true carrier frequency tracking error would contain the LOS projection of receiver velocity error, the LOS projection of satellite velocity error, the receiver clock drift estimation error. Similarly, the second term in Eq. (33) is not in its simplified form. That is because the term "$-\lambda \cdot \delta(\delta f_{\mathrm{u}})$" is actually the state variable of NF and this form can clearly show the error propagation from NF state variables to carrier frequency tracking. Similarly, the ATAN discriminator outputs would include the true carrier frequency tracking error and estimation noise.

3 Performance Evaluation Method for Non-coherent Vector Tracking Loop

3.1 Design Philosophy of Performance Evaluation Method

The analytical model of In-phase/Quadrature (I/Q) correlation value is [9]:

$$I + jQ = A \cdot R(\delta\tau) \cdot \mathrm{sinc}(\delta f \cdot T_{\mathrm{coh}}) \exp(j \cdot \delta\varphi) + \eta_{\mathrm{n}} \tag{37}$$

where A is signal amplitude; I and Q represent the correlation value outputted by I-branch and Q-branch of integration and dump (I&D) blocks; $\delta\tau$ represents the code phase tracking error; T_{coh} represents the coherent integration time [s]; η_{n} is the noise component in correlation value and $\eta_{\mathrm{n}} \sim \mathrm{N}(0, \sigma_{\mathrm{n}}^2)$. If the carrier-to-noise power spectrum ratio ($\mathrm{C/N_0}$) of the signal is c/n_0 [dB]. The relation between A and c/n_0 is:

$$\sigma_{\mathrm{n}} = \sqrt{2 \cdot c/n_0 \cdot T_{\mathrm{coh}}} \tag{38}$$

After the above analysis, the navigation computation and signal tracking are coupled in one set of algorithm in NC-VTL. The priori navigation solutions are used to close the signal tracking loop, thus navigation error would propagate to tracking error and the tracking error estimates from discriminator can be used to update NF. The propagation of navigation error to tracking error is explicit according to Eqs. (25), (33),

and the I/Q correlation value is a function of tracking error according to Eq. (38). Thus I/Q correlation value generated by I&D blocks can be simulated by their analytical models instead of doing the intact mixing and correlation operation with IF signal according to Eqs. (25), (33) and (38). That is, the discriminator algorithms (nonlinear block), NF update algorithms in NC-VTL can be accomplished by real numerical calculation, while the loop control algorithms and coherent integration in NC-VTL can be described by their analytical mathematical model, which is the design philosophy of performance evaluation method. This method can also be termed as "Semi-Analytic framework". In Eq. (38), the initial value of $\delta\varphi$ can be arbitrary. The $\delta\varphi$ is actually the mean carrier tracking error in coherent integration interval. Thus the $\delta\varphi$ of adjacent coherent integration interval, m and $m + 1$, can be modeled as:

$$\delta\varphi_{m+1} = \delta\varphi_m + 0.5 \cdot T_{\text{coh}} \cdot (\delta f_m + \delta f_{m+1}) \tag{39}$$

3.2 Software Implementation of Performance Evaluation Method

The performance evaluation software should be initialized before running. The initializing parameters mainly include: (1) Simulation time. (2) Satellite number; satellite elevation (θ) and azimuth angle (ψ); the unit LOS vectors of all satellites. (3) the true navigation and time parameters of receiver, including time tags, the receiver position, receiver velocity, receiver clock bias and drift. The receiver motion can be modeled by CP, CV, CA model. Other motion trajectories can also be used. The receiver clock-related error can be modeled by CV model. In this paper the real GNSS receiver clock bias and drift data, outputted by a real GNSS receiver with temperature compensated crystal oscillator (TCXO) in it, are exploited to make the evaluation convictive. (4) correlator spacing d (d is set to 1 chip in this paper); coherent integration time; update interval of NF. It should be noted that the NF update interval can be longer than coherent integration time and multi-outputs of discriminator can be averaged before they are sent to NF.

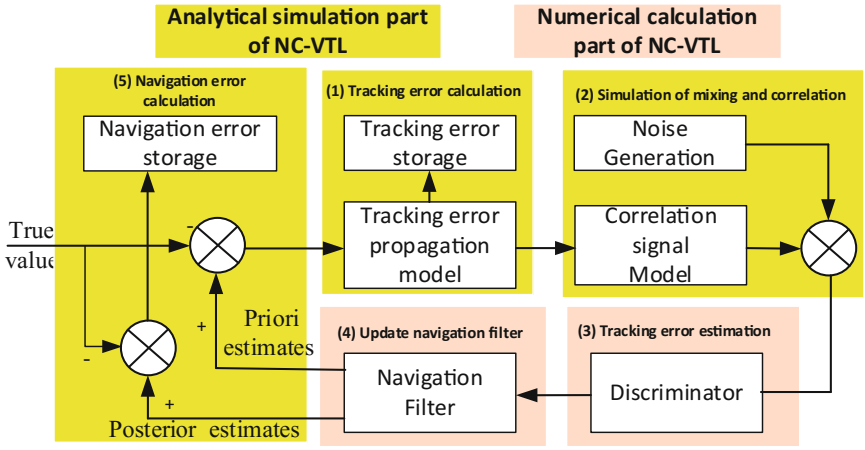

Fig. 1. Performance evaluation software scheme

After the initialization, the evaluation software can enter the performance evaluation phase. Figure 1 displays the scheme and running process of this software. The NC-VTL algorithm is divided into two parts: analytical simulation part and numerical calculation part. The software running steps are described as follows:

Step 1: Calculate and storage the real tracking error. The difference between the priori estimate of NF and their true value set in initialization phase can be calculated, thus $\delta \boldsymbol{P}_{\mathrm{u}}$, $\delta(\delta t_{\mathrm{u}})$, $\delta \boldsymbol{V}_{\mathrm{u}}$, $\delta(\delta f_{\mathrm{u}})$ can be obtained. It should be noted that these errors are priori estimation error. The final navigation error is actually the posterior estimation error and can be obtained after the NF update. $\delta \boldsymbol{P}_{\mathrm{s},k+1} \cdot \boldsymbol{l}$, $\delta \boldsymbol{V}_{\mathrm{s},k+1} \cdot \boldsymbol{l}$, $\delta(\delta t_{\mathrm{s}}) \cdot \mathrm{c}$ can be modeled as white Gaussian noise as follows:

$$\delta \boldsymbol{P}_{\mathrm{s}} \cdot \boldsymbol{l} \sim \mathrm{N}(0, 1^2\ \mathrm{m}) \tag{40}$$

$$\delta \boldsymbol{V}_{\mathrm{s}} \cdot \boldsymbol{l} \sim \mathrm{N}(0, 0.01^2\ \mathrm{m/s}) \tag{41}$$

$$\delta(\delta t_{\mathrm{s}}) \cdot \mathrm{c} \sim \mathrm{N}(0, 1^2\ \mathrm{m}) \tag{42}$$

δI and δT are modeled as follows:

$$\delta I = (1 + 16 \cdot (0.53 - \frac{\theta}{\pi})^3)\delta I_z \tag{43}$$

$$\delta T = \frac{\delta T_z}{\sin(\theta^2 + (\frac{2.5 \cdot \pi}{180})^2)} \tag{44}$$

where δI_z represents the correction error for ionosphere delay of zenith direction [m]; and δT_z represents the correction error for troposphere delay of zenith direction [m]. In this paper, δI_z is set to 1 m while δT_z is set to 0.1 m. Even though the real atmospheric effect is hard to accurately be modeled by Eqs. (43) and (44), these two equations are still enough for us to study the code tracking bias introduced by atmospheric delay correction error. Subscribe the relevant value to Eqs. (25) and Eq. (33). The real tracking error can be obtained and stored.

Step 2: Simulate the correlation values. The six correlation values, $I_{\mathrm{E}} + j \cdot Q_{\mathrm{E}}, I_{\mathrm{P}} + j \cdot Q_{\mathrm{P}}, I_{\mathrm{L}} + j \cdot Q_{\mathrm{L}}$, can be simulated using the real tracking error calculated in Step 1 according to Eq. (37). The subscript E, P, L indicates the correlation value correlated with local generated Early (E), Prompt (P), Late (L) pseudo-random noise (PRN) code.

Step 3: Estimate tracking error through discriminator. The ATAN discriminator and NC-ELME discriminator are employed to respectively estimate the carrier frequency tracking error and code phase tracking error from six correlation values.

Step 4: Update NF. The discriminator outputs are used to update the NF, as shown in Eqs. (4)–(9). The covariance matrix of observation noise ($\boldsymbol{R}$) is calculated according to method proposed in the literature [11].

Step 5: Calculate and storage the real navigation error. After NF update, difference between the posterior estimate of NF and true value set in initialization phase can be calculated. Thus the navigation error can be obtained and stored.
Step 6: Determine the simulation time. If the simulation time has not reached the limit, the software would go back to Step1 and continue the processing. If the simulation time has reached the limit, the software would jump out of the loop and calculate the root mean square value of real tracking error and real navigation error obtained in Step 1 and Step 5 for NC-VTL.

4 Sample Results

4.1 Simulation Setup

The sample is designed to evaluate the tracking error and navigation error of NC-VTL in the designed scene through the performance evaluation software. Figure 2 shows the sky plot of simulated satellites. The geometric dilution of precision (GDOP) is 1.60, position dilution of precision (PDOP) is 1.40. The coherent integration time is 20 ms while update interval of NF is 100 ms. The motion of receiver is modeled as CV model and the velocity of receiver is 10 m/s. The total simulation number is 10000 with the assumption that the NF converges to steady states after 1000 times of NF update. The performance of NC-VTL are evaluated in the C/N_0 range of [10 dB-Hz, 45 dB-Hz] with 1 dB-Hz step size.

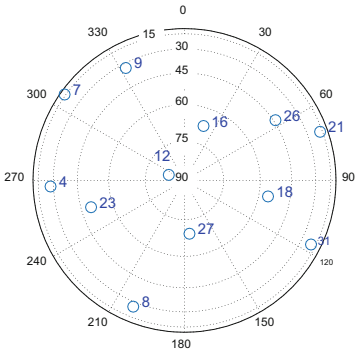

Fig. 2. Sky plot of simulated satellites

4.2 Tracking Error Evaluation

Figure 3(a) and (b) respectively shows the root mean square (RMS) value of code phase tracking error and carrier frequency tracking error for PRN 7, PRN 12 and PRN 18. When C/N_0 is less than 16 dB-Hz, the tracking error increases suddenly which

indicates the NC-VTL cannot keep lock for GNSS signal. Thus the sensitivity of NC-VTL is 16 dB-Hz in the designed scenario. With the C/N_0 decreasing, the tracking error increases. That is because measurements noise would increase and then propagates to the navigation error, which subsequently propagates to tracking error of all tracking channels. In addition, the tracking error of different satellite is not same, even tracking channels share a set of vector tracking algorithm, which could be explained by Eqs. (25) and (33). Near the C/N_0 value of 16 dB-Hz, the carrier frequency tracking error reaches the frequency tracking threshold (2.08 Hz) while code tracking error is significantly less than the code tracking threshold (0.167 chip). Thus the sensitivity of NC-VTL mainly depends on the carrier tracking capacity. And code tracking bias introduced by atmospheric correction error can be ignored.

It also should be noted that all the tracking channels fails to lock the GNSS signal when C/N_0 = 16 dB-Hz. That is because tracking error in one channel would propagate to that of other channels. If one tracking channel lose lock, the tracking error of that channel would be large, and causes failure in code and carrier tracking of other channels. There are quite large spaces of performance improvement for NC-VTL by further adjusting $\boldsymbol{P}, \boldsymbol{Q}, \boldsymbol{R}$ of NF and implementing fault detection algorithms. This software provides a flexible and efficient solution for performance evaluation, parameters tuning of NC-VTL.

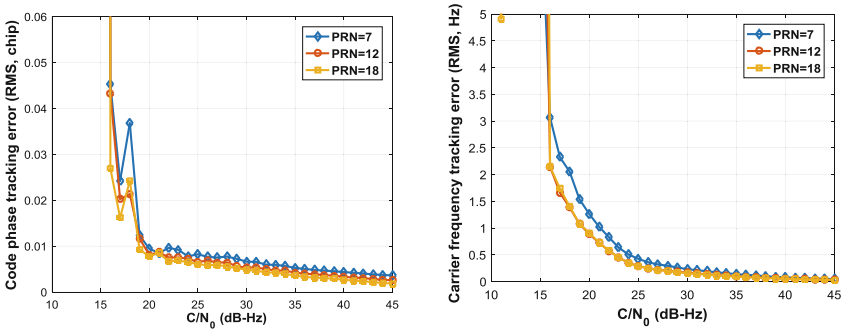

Fig. 3. (a) The code phase tracking error (b) The carrier frequency tracking error

4.3 Navigation Error Evaluation

Figure 4(a) and (b) respectively shows navigation error and timing error under different C/N_0. When C/N_0 is below 16 dB-Hz, the navigation error dramatically increases for NC-VTL cannot keep lock for the GNSS signal. When C/N_0 belongs to the range of [21, 45 dB-Hz], the position error is not markedly increasing with C/N_0 falls, which shows noise depression ability of vector tracking loop. There exists biases of 4 m and 5 m respectively for position RMS error and clock bias RMS error in this C/N_0 range because the atmosphere delay correction error is set in the software, which simulates the real signal propagation environment. Atmosphere delay correction errors feature in

bias characteristic and would propagate to the position error and clock bias error. Unlike other tracking error sources in NC-VTL, they cannot be filtered by Kalman filter because they are not white noise.

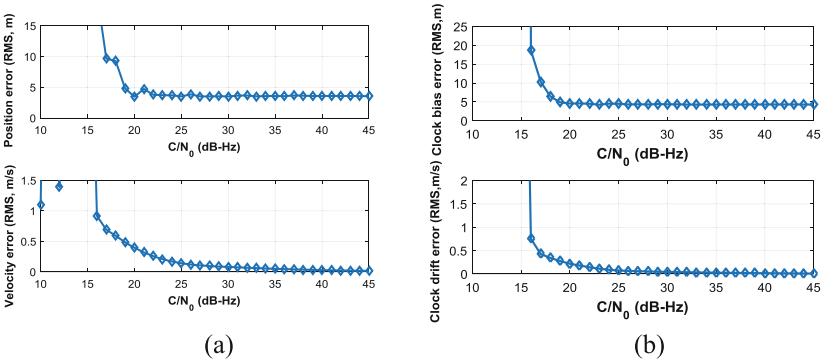

Fig. 4. (a) Position and velocity determination error (b) Clock bias and drift determination error

5 Conclusion

This paper focuses on the accurate analysis for tracking error and navigation error for NC-VTL. Firstly, a vector code tracking algorithm, which exploits the absolute position, instead of position increment, to close the code tracking loop, is proposed. This algorithm is easy to implement in both hardware and software and reduces the dependence on initial condition (initial position error and initial code tracking error) for NC-VTL. The proposed NC-VTL has the ability to correct the error when initial position error and code tracking error is relatively large, with a price that a bias would be introduced in code phase tracking. Even though code tracking bias are introduced by the atmospheric delay correction error, this effect can be ignored. Secondly, this paper derives the formulas that describe tracking error propagation of NC-VTL. According to error propagation formulas, performance evaluation method based on semi-analytic framework is designed to accurately calculate the real tracking error and navigation error in designed scene. The core idea of semi-analytic framework lies in that the discriminator algorithms (nonlinear block), NF update algorithms in NC-VTL are accomplished by real numerical calculation, while the loop control algorithms and coherent integration in NC-VTL are described by their analytical mathematical model. Performance evaluation for NC-VTL can be done in flexibly designed scenes without processing the real GNSS IF signals. The non-linear effect is considered in this method to simulate what really happens in NC-VTL. Thus performance evaluation method based on semi-analytic framework provides a flexible, fast way to accurately and reliably access the performance of NC-VTL through tracking error and navigation error. A sample results is displayed to show the effective of this method. Besides, if atmosphere delay correction error is set to zero, this method can also evaluate the

performance of NC-VTL whose code phase adjustment is based on position increment between adjacent epoch. This method also has the ability to be extended to evaluate the performance of coherent vector tracking loop with minor modification.

In the future, the study for parameter selection, fault detection, satellite selection algorithms in NC-VTL will be conducted based on this performance evaluation method. Besides, the hardware implementation of proposed NC-VTL is also the future work.

Acknowledgement. This research was jointly funded by the National Natural Science Foundation of China (Nos. 61633008, 61773132, 61803115), the 7th Generation Ultra Deep Water Drilling Unit Innovation Project sponsored by Chinese Ministry of Industry and Information Technology, the Heilongjiang Province Science Fund for Distinguished Young Scholars (No. JC2018019), and the Fundamental Research Funds for Central Universities (No. HEUCFP201768).

References

1. Misra P (2011) Global positioning system: signals, measurements, and performance. Ganga-Jamuna Press
2. Groves P, Mather C, Macaulay A (2007) Demonstration of non-coherent deep INS/GPS integration for optimized signal-to-noise performance. In: ION GNSS 2007, pp 2627–2638
3. Lashley M, Bevly DM, Hung JY (2009) Performance analysis of vector tracking algorithms for weak GPS signals in high dynamics. IEEE J Sel Top Sig Process 3(4):661–673. https://doi.org/10.1109/JSTSP.2009.2023341
4. Zhao S, Akos D (2011) An open source GPS/GNSS vector tracking loop - implementation, filter tuning, and results. In: Institute of navigation - international technical meeting, pp 3453–3467
5. Zhao S, Lu M, Feng Z (2011) Implementation and performance assessment of a vector tracking method based on a software GPS receiver. J Navig 64(S1):S151–S161. https://doi.org/10.1017/S0373463311000440
6. Bhattacharyya S, Gebre-Egziabher D (2010) Development and validation of parametric models for vector tracking loops. Navigation 57(4):275–295. https://doi.org/10.1002/j.2161-4296.2010.tb01783.x
7. Bhattacharyya S (2018) Vector loop transfer functions and noise bandwidths. Navigation 65 (3) https://doi.org/10.1002/navi.219
8. Lashley M, Bevly DM (2011) Comparison in the performance of the vector delay/frequency lock loop and equivalent scalar tracking loops in dense foliage and urban canyon. In: Proceedings of international technical meeting of the satellite division of the institute of navigation, pp 1786–1803
9. Borio D, Anantharamu PB, Lachapelle G (2011) SATLSim: a semi-analytic framework for fast GNSS tracking loop simulations. GPS Solut 15(4):427–431. https://doi.org/10.1007/s10291-011-0221-0
10. Xu, D, Morton YJ, Jiao Y, Rino C, Yang R (2018) Implementation and performance evaluation of a vector-based receiver during strong equatorial scintillation on dynamic platforms. In: Proceedings of the 31st international technical meeting of the satellite division of the institute of navigation (ION GNSS + 2018), Miami, Florida, September 2018, pp 3611–3622
11. Luo Z, Ding J, Zhao L et al (2017) An enhanced non-coherent pre-filter design for tracking error estimation in GNSS receivers. Sensors 17(11). https://doi.org/10.3390/s17112668

Design and Performance Analysis of Doppler-Aided Beidou B1C/B2a Joint Tracking Algorithm

Mouyan Wu, Lin Zhao(✉), Jicheng Ding(✉), Yingyao Kang, and Zhibin Luo

College of Automation, Harbin Engineering University, Harbin, China
zhaolin@hrbeu.edu.cn, aaron.heu@163.com

Abstract. With the development of the third-generation Beidou system (Beidou-3), the new generation B1C and B2a signals have been transmitted, which have many characteristics such as BOC/QMBOC modulation types and data/pilot channel structures. This paper firstly reviews the signal properties of B1C and B2a, including the transmit power, the tracking and observation noise. Then, the B1C data/pilot joint tracking are designed by using pseudo-correlation-function based unambiguous tracking technology. In order to reduce the tracking noise and improve the tracking sensitivity and robustness of B1C, the Doppler-aided B1C/B2a joint tracking loop is proposed. A wide bandwidth tracking loop of B2a pilot channel is adopted to tracking the signal dynamics whereas both the B1C data and pilot channels use narrow tracking bandwidth to reduce signal noises and interferences. The traditional and joint tracking loop are compared by the field experiments. Experiment results show that the proposed method can keep tracking under step jamming with a sudden CN_0 decrease over 10 dB and also reduce the tracking noise especially for code loop tracking. Moreover, the proposed method can keep tracking at lowest CN_0 about 15.68 dB-Hz for B1C data component and 19.58 dB-Hz for B1C pilot component when a fading B2a pilot signal is used as the aiding information, and even keep tracking at lowest CN_0 about 9.83 dB-Hz for B1C data component and 15.91 dB-Hz for B1C pilot component when a good B2a pilot signal is used as the aiding information.

Keywords: B1C/B2a · Doppler-aided · Joint tracking · Tracking noise · Sensitivity · Robustness

1 Introduction

With the development of the third-generation Beidou system (Beidou-3), the new generation Beidou-3 satellites have been launched since November 2017 and the civil B1C and B2a signals have been transmitted, which greatly accelerate the construction of Beidou-3 system. The B1C signal uses 1575.42 MHz as the carrier frequency and Quadrature Multiplexed BOC (QMBOC) as the modulation type. The autocorrelation function of QMBOC cancels the cross-correlation parts of BOC(1,1) and BOC(6,1), which highly benefits the power allocation and the polarity selection of B1C [1].

J. Sun et al. (Eds.): CSNC 2019, LNEE 563, pp. 463–476, 2019.
https://doi.org/10.1007/978-981-13-7759-4_41

Besides, the B2a signal is transmitted with 1176.45 MHz as the carrier frequency and BPSK-R(10) as the modulation type to replace the B2I signal gradually, which can improve the ranging performance with the higher code rate [2].

The autocorrelation function of BOC has multiple side peaks, which will cause the ambiguity problem of B1C signal's acquisition and tracking. In order to cancel the ambiguity of the BOC signals, some unambiguous tracking algorithms has been proposed, such as the Bump-Jump method [3], dual estimate technology [4], ASPeCT method [5] and PUDLL [6] and so on. The B1C unambiguous tracking can be designed based on these methods with proper parameters.

Besides, like other modernized GNSS signals, both the B1C and B2a signals are also designed as two components, i.e., data and pilot components, which can further improve the ranging and navigation bit decoding performance. In order to improve the tracking performance of the Beidou receiver, it is necessary to explore the advantages the modernized architecture and some technologies such as data/pilot joint tracking architectures can be designed for B1C and B2a signals.

It is well known that any GNSS signal is susceptible to interference e.g. signal blocking or attenuation in fading and weak environment and even the intentional interference such as jamming and spoofing, which will extremely decrease the tracking performance of the receiver and even cause the lost lock of the signals. However, both B1C and B2a signals come from the same satellite which means that they have the same signal source and common geometrical feature between the satellite and user. Based on these features, the joint tracking of B1C and B2a signals from the same satellite can be designed to improve the tracking robustness and sensitivity of the receiver in challenging signal environment, especially for the individual signal interference.

In this paper, the signal specifications of B1C and B2a are firstly reviewed, including the transmit power, the tracking and observation noise. Then, we propose the Doppler-aided B1C/B2a joint tracking loop. The B1C data/pilot joint tracking loop is designed with side peak cancellation technology. In order to reduce the tracking noise and improve the tracking sensitivity and robustness of B1C, a wide bandwidth tracking loop of B2a pilot channel is adopted to tracking the signal dynamics whereas both the B1C data and pilot channels use narrow tracking bandwidth to reduce signal noises and interferences. Finally, the field experiments are conduct to access the proposed algorithm and the conclusion is addressed.

2 Beidou B1C and B2a Civil Signal Specifications

2.1 Beidou B1C and B2a Signal

As shown in Table 1, the BOC(1,1) and QMBOC(6,1,4/33) modulation are used for B1C data component and pilot component respectively. The power ratio of the data component to the pilot component is 1:3. The QMBOC(6,1,4/33) is composed of a BOC(1,1) subcarrier and a BOC(6,1) subcarrier, which are in phase quadrature with each other and have a power ratio of 29:4.

The complex envelope of the B1C signal can be expressed as:

$$s_{\mathrm{B1C}}(t) = s_{\mathrm{B1C\_data}}(t) + j \cdot s_{\mathrm{B1C\_pilot}}(t) \tag{1}$$

where $s_{\mathrm{B1C\_data}}(t)$ is the data component and $s_{\mathrm{B1C\_pilot}}(t)$ is the pilot component.

The BPSK(10) modulation are used for both B2a data component and pilot component. The power ratio of the data component to the pilot component is 1:1.

The complex envelope of the B1C signal can be expressed as:

$$s_{\mathrm{B2a}}(t) = s_{\mathrm{B2a\_data}}(t) + j \cdot s_{\mathrm{B2a\_pilot}}(t) \tag{2}$$

where $s_{\mathrm{B2a\_data}}(t)$ $s_{\mathrm{B1C\_data}}(t)$ is the data component and $s_{\mathrm{B2a\_pilot}}(t)$ is the pilot component.

Table 1. Beidou B1C and B2a civil signal specifications

Signal component	Carrier frequency (MHz)	Modulation	Primary code length (chip)	Primary code frequency (MHz)	Minimum received power (dBW)	Received power difference (dB)
B1C data component	1575.42	BOC(1,1)	10230	1.023	MEO: −159 ISGO: −161	0
B1C pilot component	1575.42	QMBOC (6,1,4/33)	10230	1.023		≈ +4.77
B2a data component	1176.45	BPSK(10)	10230	10.23	MEO: −156 IGSO: −158	≈ +6.02
B2a pilot component	1176.45	BPSK(10)	10230	10.23		≈ +6.02

2.2 Theory Analysis of B1C and B2a Tracking Performance

2.2.1 Carrier Phase Tracking Performance

It is known that the total tracking noise of the phase lock loop (PLL) can be calculated as [7]:

$$\sigma_{\varphi} = \sqrt{\sigma_{t-\varphi}^2 + \sigma_v^2 + \theta_A^2} + \frac{\theta_e}{3} \ [\mathrm{deg}] \tag{3}$$

where $\sigma_{t-\varphi}$ is 1-sigma thermal noise in degrees, σ_v is 1-sigma vibration-induced oscillator jitter in degrees, θ_A is Allan variance-induced oscillator jitter in degrees and θ_e is dynamic stress error in the PLL tracking loop in degrees.

As for data channels of B1C and B2a, the ATAN phase discriminator is be used and the thermal noise jitter of an ATAN PLL is computed as follows:

$$\sigma_{t-\varphi} = \frac{360}{2\pi}\sqrt{\frac{B_n}{C/N_0}\left(1+\frac{1}{2TC/N_0}\right)}\ [\text{deg}] \tag{4}$$

In order to improve the sensitivity of the tracking loop, the ATAN2 phase discriminator is be used for pilot channels of B1C and B2a and the thermal noise jitter of an ATAN2 PLL is computed as follows:

$$\sigma_{t-\varphi} = \frac{360}{2\pi}\sqrt{\frac{B_n}{C/N_0}}\ [\text{deg}] \tag{5}$$

where B_n is the carrier loop noise bandwidth in Hz, T is the predetection integration time in seconds, C/N_0 is carrier to noise power expressed as a ratio in Hz and λ is the carrier wavelength of B1C or B2a in meters.

The simulation parameters of B1C and B2a carrier phase tracking are set as follows:

The third-order ATAN PLL is used for B1C and B2a's data channel while the third-order ATAN2 PLL is used for B1C and B2a's pilot channel. The carrier loop noise bandwidths for all PLLs are set to 10 Hz, the predetection integration times are set to 10 ms and the maximum light-of-sight (LOS) acceleration dynamics are set to 1 g/s.

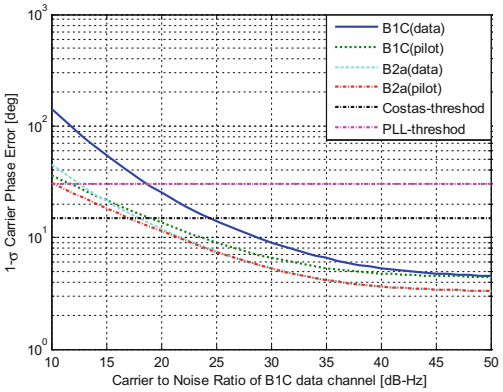

Fig. 1. Carrier phase tracking noise of B1C and B2a

Figure 1 shows the carrier phase tracking noise of B1C and B2a. It is noted that we set different C/N_0 values for B1C and B2a signals during the simulation analysis due to received power differences between the B1C and B2a signals and also their own data and pilot channels as shown in Table 1. The x-axis of Fig. 1 represents the C/N_0 values of the data channel of B1C. It can be seen that both B1C and B2a's pilot channel reach a higher tracking sensitivity due to the pure PLLs are used compare to their data channel (Costas PLLs). The pilot channel of B2a achieves about 6 dB improvement in signal tracking threshold compared to the data channel of B2a. Moreover, due to a

higher power ratio of the pilot channel of B1C, it achieves about 12 dB improvement in signal tracking threshold compared to the data channel of B1C. We can see from Fig. 1 that the pilot channel of B2a can achieve the best tracking sensitivity while the data channel of B1C is most vulnerable.

2.2.2 Code Phase Tracking Performance

The thermal noise is the main noise source in the delay lock loop (DLL). The non-coherent early minus late envelope DLL can be used for B1C and B2a's code tracking. The thermal noise jitter of the DLL is computed as follows [7]:

$$\sigma_{tDLL} = \sqrt{\frac{B_n D}{2C/N_0}\left(1 + \frac{2}{(2-D)T_{coh}C/N_0}\right)} \tag{6}$$

where B_n is the code loop noise bandwidth in Hz, T is the predetection integration time in seconds, C/N_0 is carrier to noise power expressed as a ratio in Hz and D is the early-to-late correlator spacing in chips.

The simulation parameters of B1C and B2a code phase tracking are set as follows:

The second-order DLL is used for B1C and B2a. The code loop noise bandwidths for all DLLs are set to 1 Hz, the predetection integration times are set to 10 ms and the early-to-late correlator spacing is set to 0.2.

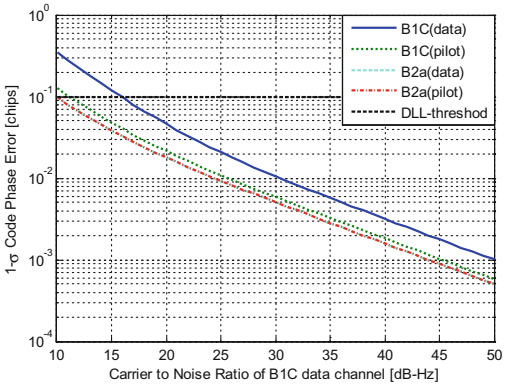

Fig. 2. Code phase tracking noise of B1C and B2a

Figure 2 shows the code phase tracking noise of B1C and B2a. The x-axis of Fig. 2 represents the C/N_0 values of the data channel of B1C. We can also see that both the data and pilot channel of B2a can achieve the best tracking sensitivity while the data channel of B1C is most vulnerable.

3 Design of Doppler-Aided Beidou B1C/B2a Joint Tracking Algorithm

It can be seen from Sect. 2 that B2a signal has a higher transmit power and also achieves the best tracking sensitivity especially for the pilot channel of B2a. Therefore, we will design the B2a Doppler-aided B1C/B2a joint tracking algorithm in this section.

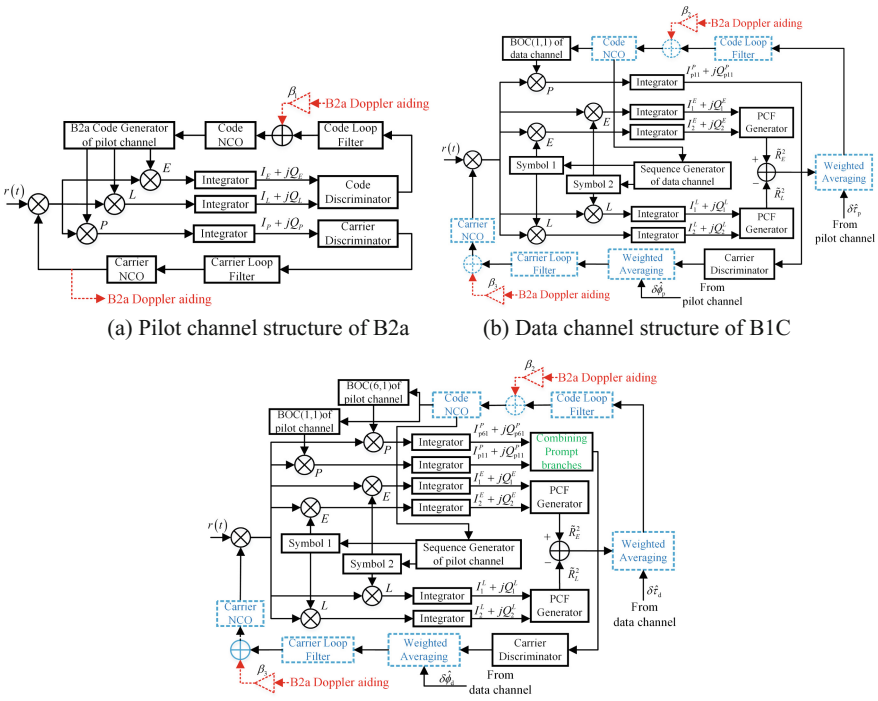

(a) Pilot channel structure of B2a

(b) Data channel structure of B1C

(c) Pilot channel structure of B1C

Fig. 3. B1C/B2a joint tracking architecture

The B1C/B2a joint tracking architecture is shown in Fig. 3. Figure 3(a) indicates pilot channel structure of B2a. The B2a's code loop is aided by its carrier Doppler frequency to reduce the dynamic stress of the code loop. Figures 3(b) and (c) indicate the data and pilot channel structures of B1C respectively. The tracking loop of B1C is designed as data/pilot joint structure, which uses the common NCO and loop filter for both code and carrier loop. Besides, the pseudo-correlation-function based unambiguous tracking method is adopted for BOC tracking. Moreover, in order to improve the tracking robustness and sensitivity of B1C, the Doppler aiding information from B2a is also feedback to both the code and carrier tracking loop of B1C. The design details of the B1C/B2a joint tracking architecture are given in the following subsections.

3.1 Unambiguous Tracking Method of B1C Signal

Firstly, in order to cancel the ambiguity of B1C's tracking, the pseudo-correlation-function based unambiguous tracking method is adopted [6]. As shown in Figs. 3(a) and (b), both the data and pilot channels of B1C have two local modulated symbol whose shape vector $\boldsymbol{d}$ can be described as [6]:

$$\begin{cases} \boldsymbol{d}_1(\kappa) = \left(\sqrt{M/(1+\kappa^2)}, 0, \ldots, 0, \kappa\sqrt{M/(1+\kappa^2)}\right)^T \\ \boldsymbol{d}_2(\kappa) = \left(\kappa\sqrt{M/(1+\kappa^2)}, 0, \ldots, 0, \sqrt{M/(1+\kappa^2)}\right)^T \end{cases} \tag{7}$$

where M is the modulation order of BOC signal, i.e., $M = 2$ for B1C data component and $M = 12$ for B1C pilot component. Besides, the shapes are identified by the parameter κ, and $\kappa \in [0, 1)$ [6].

After carrier wipe off, the intermediate frequency (IF) signals of B1C are correlated with both $\boldsymbol{d}_1$ and $\boldsymbol{d}_2$ in their own early and late branches respectively and then operate the integrate and dump process. After that, the pseudo-correlation functions can be obtained by [6]:

$$\begin{cases} \tilde{R}_E = \sqrt{\left(I_1^E\right)^2 + \left(Q_1^E\right)^2} + \sqrt{\left(I_2^E\right)^2 + \left(Q_2^E\right)^2} - \sqrt{\left(I_1^E + I_2^E\right)^2 + \left(Q_1^E + Q_2^E\right)^2} \\ \tilde{R}_L = \sqrt{\left(I_1^L\right)^2 + \left(Q_1^L\right)^2} + \sqrt{\left(I_2^L\right)^2 + \left(Q_2^L\right)^2} - \sqrt{\left(I_1^L + I_2^L\right)^2 + \left(Q_1^L + Q_2^L\right)^2} \end{cases} \tag{8}$$

Finally, the code phase error of B1C can be calculated as:

$$\varepsilon(\tau) = \tilde{R}_E^2 - \tilde{R}_L^2 \tag{9}$$

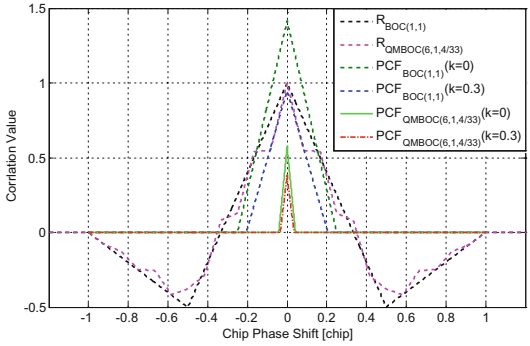

Fig. 4. B1C's pseudo-correlation function v.s. auto-correlation function

Figure 4 shows the pseudo-correlation function and the auto-correlation function curves of B1C. We can see that the side-peaks of the both auto-correlation functions of

B1C data and pilot components are all be canceled by the pseudo-correlation function based method. Therefore, the ambiguity of B1C tracking can be avoided. Besides, although increasing the κ, the noise mitigation performance of the loop will increase, but as shown in Fig. 4, the width and peak value of the main-peak, the slope and sharp features will decrease. Therefore, we choose $\kappa = 0$ in this paper.

3.2 Design of B1C/B2a Joint Tracking Architecture

As mentioned above, the Doppler aiding information is given by the pilot channel of B2a as shown in Fig. 3(a). The Doppler aiding information is fed back to B2a's code loop in one side to reduce the dynamic stress and also to both carrier loop and code loop of B1C in the other side to enhance B1C signal tracking. The ratio rates of the aiding information are calculated as:

$$\left\{ \beta_1 = \frac{f_{c\_B2a}}{f_{L\_B2a}},\ \beta_2 = \frac{f_{c\_B1C}}{f_{L\_B2a}},\ \beta_3 = \frac{f_{L\_B1C}}{f_{L\_B2a}} \right\} \tag{10}$$

where f_{c_B2a} and f_{c_B1C} are the primary code rate of B2a and B1C respectively. f_{L_B2a} and f_{L_B1C} are the carrier frequency of B2a and B1C respectively.

A wide bandwidth tracking loop of B2a (25 Hz for PLL and 2 Hz for DLL) is adopted to tracking the signal dynamics whereas the B1C use narrow tracking bandwidth (2 Hz for PLL and 0.01 Hz for DLL) to reduce signal noises and interferences.

The ATAN2 phase discriminator is used for the carrier phase loop of B2a's pilot channel:

$$\delta\widehat{\phi}_{B2a\_p} = \arctan 2(Q_{B2a\_P}, I_{B2a\_P}) \tag{11}$$

Besides, the noncoherent early minus late envelope discriminator is used for the code phase loop of B2a's pilot channel:

$$\delta\widehat{\tau}_{B2a\_p} = (1-\mathrm{d})\frac{\sqrt{I_{B2a\_E}^2 + Q_{B2a\_E}^2} - \sqrt{I_{B2a\_L}^2 + Q_{B2a\_L}^2}}{\sqrt{I_{B2a\_E}^2 + Q_{B2a\_E}^2} + \sqrt{I_{B2a\_L}^2 + Q_{B2a\_L}^2}} \tag{12}$$

where I_{B2a_E}, I_{B2a_P}, I_{B2a_L}, Q_{B2a_E}, Q_{B2a_P} and Q_{B2a_L} are in-phase and quadrature-phase of the correlator outputs in early, prompt and late branches of B2a respectively. d is the correlator spacing.

Figures 3(b) and (c) show the data and pilot channel structures of B1C respectively. The blue dashed parts are the common parts of the joint data/pilot structure. The carrier phase errors are calculated by discriminators from the data and pilot channels respectively and then are combined with different weight values to generate the common carrier phase error. The code phase errors have the similar processing.

In order to achieve the optimal tracking performance, the matching receiving method is used to track B1C signals [8]. According to the phase relationship of BOC

(1,1) and BOC(6,1) in the pilot component of B1C, the correlator outputs of B1C pilot channel in prompt branch are denoted as:

$$\begin{cases} I_{\mathrm{B1C\_P}} = \sqrt{29/33} \cdot Q_{\mathrm{B1C\_p11}} - \sqrt{4/33} \cdot I_{\mathrm{B1C\_p61}} \\ Q_{\mathrm{B1C\_P}} = -\sqrt{29/33} \cdot I_{\mathrm{B1C\_p11}} - \sqrt{4/33} \cdot Q_{\mathrm{B1C\_p61}} \end{cases} \tag{13}$$

where $I_{\mathrm{B1C\_p11}}$ and $Q_{\mathrm{B1C\_p11}}$ are the in-phase and quadrature-phase correlator outputs of BOC(1,1) components while $I_{\mathrm{B1C\_p61}}$ and $Q_{\mathrm{B1C\_p61}}$ are the in-phase and quadrature-phase correlator outputs of BOC(6,1) components in the B1C pilot channel respectively.

The ATAN2 phase discriminator is used for the carrier phase loop of B1C's pilot channel:

$$\delta\widehat{\phi}_{\mathrm{B1C\_p}} = \arctan 2(Q_{\mathrm{B1C\_P}}, I_{\mathrm{B1C\_P}}) \tag{14}$$

Besides, the ATAN phase discriminator is used for the carrier phase loop of B1C's data channel:

$$\delta\widehat{\phi}_{\mathrm{B1C\_d}} = \arctan(Q_{\mathrm{B1C\_d}}/I_{\mathrm{B1C\_d}}) \tag{15}$$

where $I_{\mathrm{B1C\_P}}$ and $Q_{\mathrm{B1C\_P}}$ are the in-phase and quadrature-phase correlator outputs of the whole B1C pilot channel respectively.

Then, the combined carrier phase error is weighted by [9]:

$$\delta\widehat{\phi}_{\mathrm{B1C}} = 1/4 \cdot \delta\widehat{\phi}_{\mathrm{B1C\_d}} + 3/4 \cdot \delta\widehat{\phi}_{\mathrm{B1C\_p}} \tag{16}$$

The code phase tracking loops of both B1C data and pilot channel are designed by the pseudo-correlation-function based unambiguous tracking method mentioned in Subsect. 3.1. After outputting the code phase errors, the combined code phase error is calculated by the lowest Cramér-Rao threshold of the code tracking error, which can be denoted as:

$$\delta\widehat{\tau}_{\mathrm{B1C}} = \alpha\delta\widehat{\tau}_{\mathrm{B1C\_d}} + (1-\alpha)\delta\widehat{\tau}_{\mathrm{B1C\_p}} \tag{17}$$

where $\delta\widehat{\tau}_{\mathrm{B1C\_d}}$ is the code phase error of B1C data channel while $\delta\widehat{\tau}_{\mathrm{B1C\_p}}$ is the code phase error of B1C pilot channel. The weight factor of α can be calculated as [9]:

$$\alpha = \frac{11 \cdot \eta_{\mathrm{d}} \cdot \beta^2_{\mathrm{RMS\_d}}}{11 \cdot \eta_{\mathrm{d}} \cdot \beta^2_{\mathrm{RMS\_d}} + 33 \cdot \eta_{\mathrm{p}} \cdot \beta^2_{\mathrm{RMS\_p}}} \tag{18}$$

where $\beta_{\mathrm{RMS\_d}}$ and $\beta_{\mathrm{RMS\_p}}$ are the root-mean-square (RMS) bandwidth of B1C data and pilot components respectively. η_{d} and η_{p} are the remain power of B1C data and pilot components after passing the receiver's front-end filter respectively.

4 Experiments and Performance Analysis

This section verifies the effectiveness of the proposed method through field experiments in the scene of dynamic vehicle tests at Harbin Engineering University on October 19, 2018. The data set was collected by the NUT4NT IF collector manufactured by Amungo Inc.

In the first test, the step jamming experiment was carried out to test the tracking robustness performance.

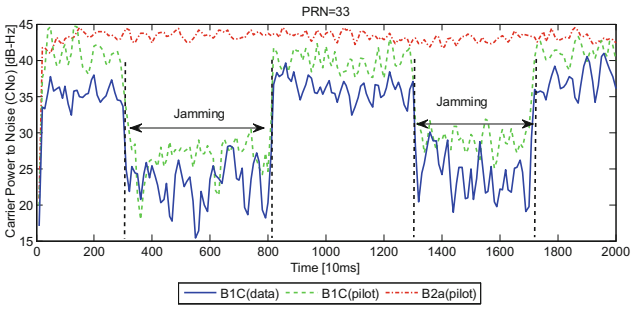

Fig. 5. Carrier power to noise ratio (CN_0) values of B1C and B2a

The CN_0 values of PRN 33 for B1C and B2a signals are shown in Fig. 5. We introduce the artificial noise interference during the period [3–8] s and [13–17] s to the field data in order to decrease the signal quality of B1C. It can be seen that the B2a pilot component has the highest CN_0 values during the whole test. The B1C pilot component achieves the suboptimal signal quality while the B1C data component has the lowest CN_0 values. This is due to their receiving power differences.

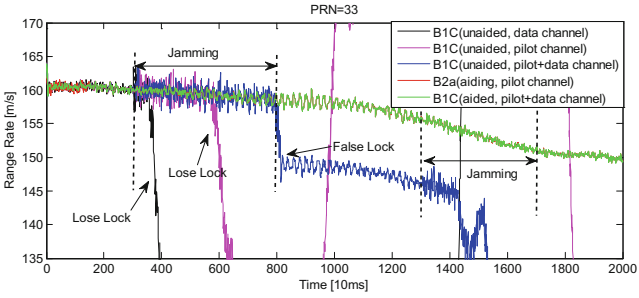

Fig. 6. Range rate values of B1C and B2a

Figure 6 compares the range rate values of B1C and B2a using different tracking methods for PRN 33. It can be seen that the carrier tracking loop loses lock when the unaided B1C data or pilot channel is used. Although the unaided B1C data/pilot joint

tracking loop maintains the lock, the carrier tracking noises increase extremely during the interference and even cause the false lock. However, when the proposed B1C/B2a joint tracking loop is used, the B1C loop keeps lock well and achieves the lowest tracking noises even during the interference period.

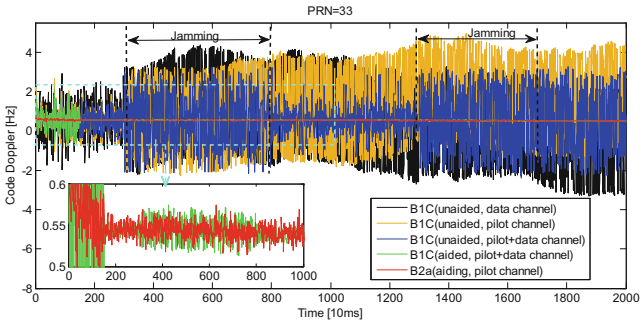

Fig. 7. Code Doppler values of B1C and B2a

Figure 7 compares the code Doppler values of B1C and B2a (convert to the aiding frequency for B1C by the scaling factor) using different tracking methods PRN 33. Similar to the carrier tracking loop, it can be seen that the code tracking loop loses lock when the unaided B1C data or pilot channel is used. The unaided B1C data/pilot joint tracking loop maintains lock during [3–8] s, but the code tracking noises increase extremely during the interference and even loses lock during [13–17] s. However, when the proposed B1C/B2a joint tracking loop is used, the B1C loop keeps tracking well and achieves the lowest tracking noises even during the interference period. This is due to the Doppler aiding information coming from B2a pilot channel and the narrow bandwidth of the B1C tracking loop is used. These results indicate that the proposed method can keep tracking under step jamming with a sudden CN_0 decrease over 10 dB and even lower to 20 dB-Hz, and also reduce the tracking noise especially for code loop tracking.

In the second test, the signal fading experiment was carried out to assess the tracking sensitivity performance. The continuously stronger noise interference was added to PRN 24 during [3–20] s in the field data (i.e. the CN_0 decreased gradually with the time). In this test, we focus on the carrier tracking loop since it is more vulnerable than code loop. Figure 8 shows the tracking results of the experiment.

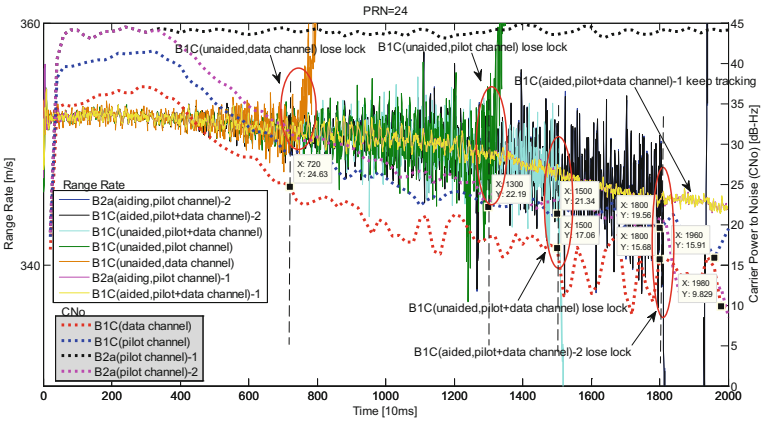

Fig. 8. Range rate values and CN_0 values of B1C and B2a

As shown in Fig. 8, the CN_0 values of both B1C data and pilot signal decrease gradually. Besides, there are two cases of the B2a pilot signal's CN_0 values, i.e. no noise interference (denoted as B2a (pilot channel)-1) and continuously stronger noise interference (denoted as B2a (pilot channel)-2). Five different tracking methods are compared, i.e. the B1C (unaided, data channel), B1C (unaided, pilot channel), B1C (unaided, data + pilot channel), B1C (aided, data + pilot channel) aided by B2a (aiding, pilot channel)-1 and B1C (aided, data + pilot channel) aided by B2a (aiding, pilot channel)-2.

Table 2. B1C and B2a tracking results of the continuously stronger noise interference experiment

Tracking method	B2a (aiding, pilot channel)-1	B2a (aiding, pilot channel)-2	Tracking CN_0 threshold (dB-Hz)	
			B1C data	B1C pilot
B1C (unaided, data channel)	no	no	24.63	/
B1C (unaided, pilot channel)	no	no	/	22.19
B1C (unaided, data + pilot channel)	no	no	17.06	21.34
B1C (aided, data + pilot channel)	no	yes	15.68	19.58
B1C (aided, data + pilot channel)	yes	no	9.83	15.91

Table 2 indicates B1C and B2a tracking results of the continuously stronger noise interference experiment. We can see that the B1C (unaided, data channel) method keeps tracking at lowest CN_0 about 24.63 dB-Hz while 22.19 dB-Hz for B1C (unaided, pilot channel) method. Besides, the B1C (unaided, data + pilot channel) method can further keep tracking at lowest CN_0 about 17.06 dB-Hz for data component and 21.34 dB-Hz for pilot component. However, the proposed B1C (aided, data + pilot

channel) can keep tracking at lowest CN_0 about 15.68 dB-Hz for data component and 19.58 dB-Hz for pilot component when the fading B2a (aiding, pilot channel)-2 signal is used as the aiding information. Moreover, the proposed B1C (aided, data + pilot channel) can even keep tracking at lowest CN_0 about 9.83 dB-Hz for data component and 15.91 dB-Hz for pilot component when the good B2a (aiding, pilot channel)-1 signal is used as the aiding information.

5 Conclusions

This paper analyzes the signal specifications of B1C and B2a. Then, the Doppler-aided B1C/B2a joint tracking algorithm is proposed. The B1C data/pilot joint tracking are design with the pseudo-correlation-function based unambiguous tracking method. In order to reduce the tracking noise and improve the tracking sensitivity and robustness of B1C, the Doppler aiding information from B2a is fed back to B1C tracking loop. A wide bandwidth tracking loop of B2a is adopted to tracking the signal dynamics whereas the B1C uses narrow tracking bandwidth to reduce noises and interferences. Experiment results show that the proposed B1C/B2a joint tracking method can keep tracking under step jamming with a sudden CN_0 decrease over 10 dB and also reduce the tracking noise especially for code loop tracking. Moreover, the proposed method can keep tracking at lowest CN_0 about 15.68 dB-Hz for B1C data component and 19.58 dB-Hz for B1C pilot component when the fading B2a pilot signal is used as the aiding information, and even keep tracking at lowest CN_0 about 9.83 dB-Hz for B1C data component and 15.91 dB-Hz for B1C pilot component when the good B2a pilot signal is used as the aiding information.

Acknowledgements. This research was funded by the National Natural Science Foundation of China (Nos. 61633008, 61773132, 61803115), the Heilongjiang Province Science Fund for Distinguished Young Scholars (No. JC2018019), the Fundamental Research Funds for Central Universities (No. HEUCFP201768) and the China Scholarship Council Foundation (No. 201806680008).

References

1. China Satellite Navigation Office (2017) BeiDou Navigation Satellite System Signal in Space Interface Control Document Open Service Signal B1C (Version 1.0)
2. China Satellite Navigation Office (2017) BeiDou Navigation Satellite System Signal in Space Interface Control Document Open Service Signal B2a (Version 1.0)
3. Fine P, Wilson W (1999) Tracking algorithm for GPS offset carrier signal. In: Proceedings of Institute of Navigation NTM, pp 671–676
4. Hodgart MS, Blunt PD (2007) Dual estimate receiver of binary offset carrier modulated signals for global navigation satellite systems. Electron Lett 43(16):877–878. https://doi.org/10.1049/el:20071101
5. Julien O, Macabiau C, Cannon ME et al (2007) ASPeCT: unambiguous sine-BOC(n, n) acquisition/tracking technique for navigation applications. IEEE Trans Aerosp Electron Syst 43(1):150–162. https://doi.org/10.1109/TAES.2007.357123

6. Yao Z, Cui X, Lu M et al (2010) Pseudo-correlation-function-based unambiguous tracking technique for Sine-BOC signal. IEEE Trans Aerosp Electron Syst 46(4):1782–1796. https://doi.org/10.1109/TAES.2010.5595594
7. Kalpan ED, Hegarty CJ (2006) Understanding GPS: principles and applications. Artech House, Norwood
8. Yao Z, Lu M (2016) Principle and implementation technology of the new generation satellite navigation system signal design. Electronic Industry Press, Beijing
9. Li Y, Shivaramaiah N, Akos D (2018) Design and implementation of an open source BDS-3 B1C/B2a SDR receiver. GPS Solutions (accepted)

PNT System and Multi-source Fusion Navigation

The GNSS/Acoustic One-Step Positioning Model with Attitude Parameters

Yingcai Kuang[1], Zhiping Lǔ[1(✉)], Junting Wang[2], and Fangchao Wang[1]

[1] Information Engineering University, Zhengzhou 450001, China
ssscenter@126.com
[2] Institute of Space Science, Shandong University, Weihai 264209, China

Abstract. Compared with the current multi-step method to solve the coordinate of the transponder, the combined solution of GNSS observation data and acoustic observation data is more consistent with the actual operation state, but if the error of attitude angle cannot be eliminated in the process of coordinate transformation, the accuracy of the transponder positioning will be seriously affected. Aiming at this shortcoming, based on the proposed GNSS/acoustic joint positioning model in this paper, the attitude angle is used as the parameter to be estimated to participate in the filtering solution, and the filtering effect of the new model is verified by simulation and experimental data in this paper. The results show that: after the attitude parameters' adding into the filtering model for estimation, the results of the three-dimensional coordinate error of the transponder are improved in varying degrees, and when the range of attitude error is larger, the improvement effect is more obvious.

Keywords: GNSS/acoustic · Coordinate change · The attitude error · Transponder position · Filtering effect

1 Introduction

To plan the ocean, safeguard maritime rights and interests, and achieve the goal of building a maritime power requires the support of the marine geodetic control network, one of the important basic work is to determine the precise position of the Marine control point. At present, the most effective method is to provide high-precision sea surface datum for underwater positioning with the help of the rapidly developing global satellite positioning technology [1–4]. The method can be expressed as follows: on the sea surface, the shipborne antenna is used to receive satellite observation data, and the acoustic pulse response can be established between the transducer mounted on the bottom of the vessel and the transponder mounted on the bottom of the vessel. In this way, the absolute coordinates of the seabed control point can be determined by real-time position of the vessel. This method is of low cost and simple implementation [5].

In the data processing stage, limited by the underwater positioning technology with unbreakable accuracy, the dynamic positioning on the sea is carried out in the traditional method firstly, then the solved position coordinates, regarded as the known intermediate quantity, participate in the underwater positioning. However, the above

J. Sun et al. (Eds.): CSNC 2019, LNEE 563, pp. 479–489, 2019.
https://doi.org/10.1007/978-981-13-7759-4_42

process is not consistent with the actual operation state. In addition, on the one hand, due to the influence of Marine environmental factors, the vessel is not moving smoothly on the sea surface, and the vessel itself, as well as the onboard GNSS antenna, transducer and other sensors have instantaneous attitude changes; On the other hand, there is a position offset between the transducer coordinates and the GNSS antenna central geographic coordinates obtained by dynamic positioning. When the attitude angle error exists and cannot be ignored, the datum on the sea surface will have a large displacement, which will affect the position of the transponder.

Different from the traditional method of independent solution on the sea surface and underwater, coordinate transformation is required before the processing of underwater data. In this paper, the original GNSS data and acoustic data are put together for position, and the attitude angle is taken as the parameter to be estimated to participate in the filtering solution, so that the GNSS/acoustic joint positioning process can be described more accurately.

2 Change of Hull Attitude

2.1 Definition of Attitude Angle

The attitude change of hull mainly includes roll, pitch and heading changes.

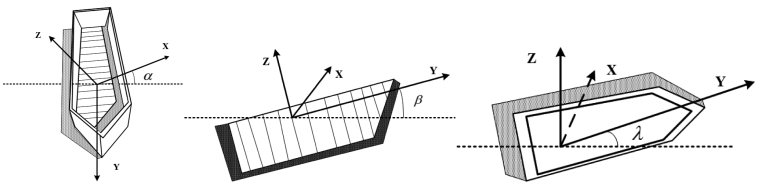

Fig. 1. Three hull attitude angles. X, Y and Z denote the axes of three directions in the hull's coordinate system. α in the left panel denotes the roll angle. β in the middle panel denotes the pitch angle. λ in the right panel denotes the heading angle

From the three panels of Fig. 1, the three attitude changes can be defined as follows:

Roll: the hull's sway from side to side. It is agreed that when the port deck of the hull tilts downward, it is positive; when the starboard deck tilts downward, it is negative.

Pitch: the pitch is generally expressed as the rising and sinking of the hull. It is agreed that the pitch is positive when the bow sinks and negative when the bow rises.

Heading: the horizontal deviation from the hull's direction. It is agreed that when the direction of the bow is on the right side of the heading line, it is positive, otherwise, it is negative.

According to the definition of three attitude changes, the specific form of attitude rotation matrix can be given as follows:

$$\begin{cases} \boldsymbol{R}_{\text{heading}} = \begin{bmatrix} \cos(-\lambda) & \sin(-\lambda) & 0 \\ -\sin(-\lambda) & \cos(-\lambda) & 0 \\ 0 & 0 & 1 \end{bmatrix} \\ \boldsymbol{R}_{pitch} = \begin{bmatrix} \cos(\beta) & 0 & -\sin(\beta) \\ 0 & 1 & 0 \\ \sin(\beta) & 0 & \cos(\beta) \end{bmatrix} \\ \boldsymbol{R}_{roll} = \begin{bmatrix} 1 & 0 & 0 \\ 0 & \cos(-\alpha) & \sin(-\alpha) \\ 0 & -\sin(-\alpha) & \cos(-\alpha) \end{bmatrix} \end{cases} \tag{1}$$

2.2 The Effect of Attitude Error on the Instantaneous Coordinate of Transducer

Effect of roll angle error: the instantaneous roll angle is α, the roll angle error is assumed to be $\Delta\alpha$, the transducer actually rotates at an angle of $\alpha + \Delta\alpha$ around the Y-axis in XOZ plane, and the effect on the coordinate of the transducer during attitude correction is:

$$\begin{bmatrix} X_t \\ Y_t \\ Z_t \end{bmatrix} = \begin{bmatrix} 1 & 0 & 0 \\ 0 & \cos(\alpha+\Delta\alpha) & -\sin(\alpha+\Delta\alpha) \\ 0 & \sin(\alpha+\Delta\alpha) & \cos(\alpha+\Delta\alpha) \end{bmatrix} \begin{bmatrix} X \\ Y \\ Z \end{bmatrix}$$
$$\Rightarrow \begin{bmatrix} \Delta X_t \\ \Delta Y_t \\ \Delta Z_t \end{bmatrix}_{roll} = \begin{bmatrix} 0 \\ -(Y\ \sin\alpha + Z\ \cos\alpha)\Delta\alpha \\ (Y\ \cos\alpha - Z\ \sin\alpha)\Delta\alpha \end{bmatrix} \tag{2}$$

According to Eq. (2), the roll angle error has an impact on the coordinate of the transducer in the Y and Z directions, but not in the X direction.

Effect of pitch angle error: the instantaneous pitch angle is β, because of the pitch angle error $\Delta\beta$, the transducer actually rotates around the X axis at the Angle $\beta + \Delta\beta$ in the YOZ plane, and the effect on the coordinate of the transducer during attitude correction is:

$$\begin{bmatrix} X_t \\ Y_t \\ Z_t \end{bmatrix} = \begin{bmatrix} \cos(\beta+\Delta\beta) & 0 & -\sin(\beta+\Delta\beta) \\ 0 & 1 & 0 \\ \sin(\beta+\Delta\beta) & 0 & \cos(\beta+\Delta\beta) \end{bmatrix} \begin{bmatrix} X \\ Y \\ Z \end{bmatrix}$$
$$\Rightarrow \begin{bmatrix} \Delta X_t \\ \Delta Y_t \\ \Delta Z_t \end{bmatrix}_{pitch} = \begin{bmatrix} -(X\ \sin\beta + Z\ \cos\beta)\Delta\beta \\ 0 \\ (X\ \cos\beta - Z\ \sin\beta)\Delta\beta \end{bmatrix} \tag{3}$$

According to Eq. (3), pitch angle error has an effect on the coordinates of the transducer in the X and Z directions, but not in the Y direction.

Effect of heading Angle error: the instantaneous heading angle is λ, due to the existence of heading angle error $\Delta\lambda$, the transducer actually rotates at the angle of $\lambda+\Delta\lambda$ around Z axis in XOY plane, and the effect of attitude correction on the coordinate of the transducer is:

$$\begin{bmatrix} X_t \\ Y_t \\ Z_t \end{bmatrix} = \begin{bmatrix} \cos(\lambda+\Delta\lambda) & -\sin(\lambda+\Delta\lambda) & 0 \\ \sin(\lambda+\Delta\lambda) & \cos(\lambda+\Delta\lambda) & 0 \\ 0 & 0 & 1 \end{bmatrix} \begin{bmatrix} X \\ Y \\ Z \end{bmatrix}$$
$$\Rightarrow \begin{bmatrix} \Delta X_t \\ \Delta Y_t \\ \Delta Z_t \end{bmatrix}_{heading} = \begin{bmatrix} -(X\ \sin\lambda + Y\ \cos\lambda)\Delta\lambda \\ (X\ \cos\lambda - Y\ \sin\lambda)\Delta\lambda \\ 0 \end{bmatrix} \tag{4}$$

According to Eq. (4), pitch angle error has an influence on the coordinates of the transducer in the X and Y directions, but not in the Z direction.

In the actual motion of the vessel, several errors usually exist together, and the combined effects on the coordinate of the transducer is as follows:

$$\begin{bmatrix} X_t \\ Y_t \\ Z_t \end{bmatrix} = \boldsymbol{R}_{\text{heading}}(\lambda+\Delta\lambda)\cdot\boldsymbol{R}_{pitch}(\beta+\Delta\beta)\cdot\boldsymbol{R}_{roll}(\alpha+\Delta\alpha)\begin{bmatrix} X \\ Y \\ Z \end{bmatrix}$$
$$\begin{bmatrix} \Delta X_t \\ \Delta Y_t \\ \Delta Z_t \end{bmatrix} = \begin{bmatrix} \frac{\partial X_t}{\partial\alpha}\Delta\alpha + \frac{\partial X_t}{\partial\beta}\Delta\beta + \frac{\partial X_t}{\partial\lambda}\Delta\lambda \\ \frac{\partial Y_t}{\partial\alpha}\Delta\alpha + \frac{\partial Y_t}{\partial\beta}\Delta\beta + \frac{\partial Y_t}{\partial\lambda}\Delta\lambda \\ \frac{\partial Z_t}{\partial\alpha}\Delta\alpha + \frac{\partial Z_t}{\partial\beta}\Delta\beta + \frac{\partial Z_t}{\partial\lambda}\Delta\lambda \end{bmatrix} \tag{5}$$

In order to reflect the effects of three main attitude errors on the coordinates of the transducer more directly, the deviation is simulated by using the measured data of Lingshan island. The dynamic PPP module of Bernese software is used for the preliminary calculation of GNSS data, and the high-precision positioning result is obtained as the GNSS antenna central coordinate of each epoch. The three kinds of measured attitude angle are combined with random errors artificially, the errors range in [−0.1°, 0.1°]. According to the Eqs. (2), (3) and (4), the effect of attitude errors on the coordinates of transducers in X, Y and Z direction is analyzed:

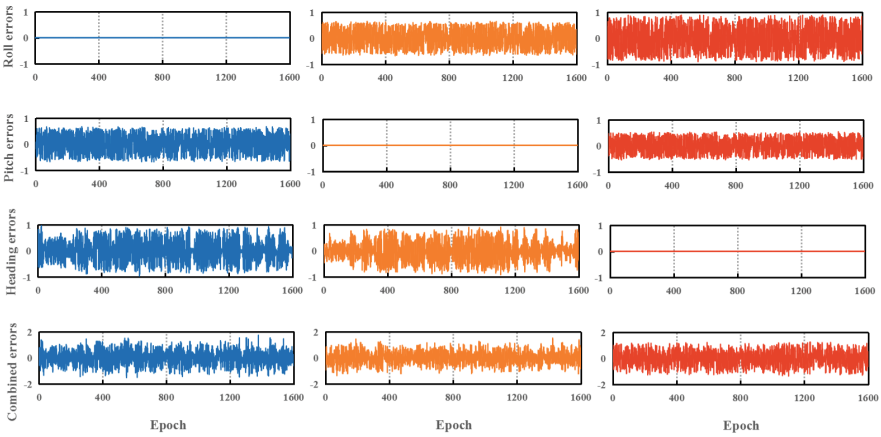

Fig. 2. The effect of attitude angle errors on the transducers coordinates in three directions (m). *Blue curves* in the *left* panels denote the effect in X direction. *Orange curves* in the *middle* panels denote the effect in Y direction. *Red curves* in the *right* panels denote the effect in Z direction.

The following conclusions can be drawn from the analysis of Fig. 2:

(1) When the three attitude errors exist alone, the deviation on the transducer coordinate are within 1 m, while under the combined effects of all attitude errors, the coordinate deviation of the transducer is close to 2 m.

(2) If only a single error is considered, the roll angle error has no effect in the X direction, and the pitch angle error has no effect in the Y direction. In both directions, the heading angle error has a greater impact on coordinates and the error sequence fluctuates more violently. In the Z direction, the roll angle error has the most significant influence on coordinates, while heading angle error has no effect. The longitudinal comparison results show that the roll angle error has a greater impact on the Z-direction coordinate than the Y-direction coordinate, the pitch angle error has a greater impact on the X-direction coordinate than the Z-direction coordinate, and the heading angle error has a greater impact on the X-direction coordinate than the Y-direction coordinate.

(3) In the actual operation, the three kinds of attitude error often affect transducer coordinate together. It can be found that the error interval in the simulation has resulted in the nonnegligible deviation of the converted coordinates. If such coordinates are used in the subsequent underwater solution, the accuracy of the result will be greatly reduced, so it is necessary to take the appropriate method to reduce the attitude error effect.

3 The GNSS/Acoustic One-Step Positioning Model with Attitude Parameters

3.1 Traditional Data Processing Methods

At present, when the absolute coordinates of the seafloor transponder are obtained through data processing, it is generally believed that the observation accuracy of GNSS on the sea is much higher than that of underwater signals. Therefore, the two parts are often separated and adjusted independently. ① Using the observation data between the satellite and the shipborne GNSS antenna on the sea to implement the dynamic positioning, then the absolute coordinates of the shipborne antenna in the WGS84 coordinate system can be obtained; ② Based on the attitude parameters provided by the shipborne attitude and direction finding sensor, the conversion matrix is constructed to transform the positioning coordinate from the GNSS antenna center to the transducer center; ③ By using the transducer coordinates and the observation signal between shipborne transducer and seafloor transponder underwater, the adjustment is carried out to obtain the absolute coordinates of the seafloor transponder. In this paper, this method is called "step-by-step method". With the development of measuring equipment and technical means, underwater acoustic positioning has been able to achieve the accuracy of decimeter or higher [6, 7]. The decrease of accuracy difference between the two positioning means provides a new way to calculate the seafloor point. On this basis, this paper proposes an "one-step method" to solve the positioning of seafloor points, that is, GNSS positioning and underwater positioning are combined to solve the problem as a whole.

3.2 The Function Model of "One-Step Method"

According to the principle of positioning on the sea and underwater, corresponding observation equations can be given. The original data received on the sea includes GNSS pseudo-range data and carrier phase data, both observations are combined to eliminate ionospheric delays, as shown in the following equation:

$$\begin{cases} P = \sqrt{(x_{sat}-x)^2+(y_{sat}-y)^2+(z_{sat}-z)^2} + cdT + M_w zpd_w + \varepsilon_P \\ \Phi = \sqrt{(x_{sat}-x)^2+(y_{sat}-y)^2+(z_{sat}-z)^2} + cdT + M_w zpd_w + N\lambda + \varepsilon_\Phi \\ \rho = \sqrt{(x_t-x_\rho)^2+(y_t-y_\rho)^2+(z_t-z_\rho)^2} + \delta\rho_d + \delta\rho_v + \varepsilon \end{cases} \tag{6}$$

Where, P, Φ and ρ respectively represent the pseudo-range observation, carrier phase observation and the calculated distance of acoustic signal from transducer to transponder; $(x_{sat}, y_{sat}, z_{sat})$ is the coordinate of GNSS satellite, (x, y, z) is the coordinate of shipborne antenna, (x_ρ, y_ρ, z_ρ) is the coordinate of responder and (x_t, y_t, z_t) is the coordinate of transducer; cdT and $zpd_w M_w$ respectively represent the influence of clock offset on the receiving device of the vessel and the influence of tropospheric zenith path delay, λN represent the influence of the integer ambiguity, $\delta\rho_d$ represent the systematic error caused by the receiving time delay of the transducer, and $\delta\rho_v$ represent

the systematic error caused by the space-time change of the sound velocity structure. ε_P, ε_Φ and ε respectively represent the unmodeled errors of the two parts.

After linearization of Eq. (6), the error equation can be written as follows:

$$\begin{bmatrix} \boldsymbol{V}_P \\ \boldsymbol{V}_\Phi \\ \boldsymbol{V}_\rho \end{bmatrix} = \begin{bmatrix} \boldsymbol{A}_P \\ \boldsymbol{A}_\Phi \\ \boldsymbol{A}_\rho \end{bmatrix} \delta \boldsymbol{X} - \begin{bmatrix} \boldsymbol{L}_P \\ \boldsymbol{L}_\Phi \\ \boldsymbol{L}_\rho \end{bmatrix} \tag{7}$$

This is the error equation of GNSS/acoustic one-step method calculation model. Where $\boldsymbol{V} = [\boldsymbol{V}_P \quad \boldsymbol{V}_\Phi \quad \boldsymbol{V}_\rho]^{\mathrm{T}}$, $\boldsymbol{L} = [\boldsymbol{L}_P \quad \boldsymbol{L}_\Phi \quad \boldsymbol{L}_\rho]^{\mathrm{T}}$ respectively represent residual and free terms of the error equation, and the specific form of the parameters to be estimated is $\delta \boldsymbol{X} = \left[\delta x \quad \delta y \quad \delta z \quad \delta t_r \quad \delta zpd_w \quad \delta x_\rho \quad \delta y_\rho \quad \delta z_\rho \quad \delta N^i_{(i\in[1,nsat])} \right]^{\mathrm{T}}$.

3.3 Introduction of Attitude Parameters

In the actual data processing, GNSS positioning can only obtain the GNSS antenna central geographic coordinates, which cannot be directly used as the surface datum for underwater positioning. In the traditional "step-by-step method", coordinate transformation is carried out before underwater positioning. In order to describe the "one-step method" function model more accurately, this paper proposes to take attitude parameters as estimated parameters to participate in the joint adjustment.

To get the error equation with attitude parameters, we can start from the process of coordinate transformation. As shown in Fig. 3, GNSS dynamic positioning can obtain the GNSS antenna central geographic coordinates in the WGS-84 coordinate system. After the coordinate transformation, the final need is the transducer geographic coordinates in the WGS-84 coordinate system. This process is also accompanied by the coordinate offset caused by the attitude changes of the hull at any time (mainly referring to the influence of roll, pitch and heading angle).

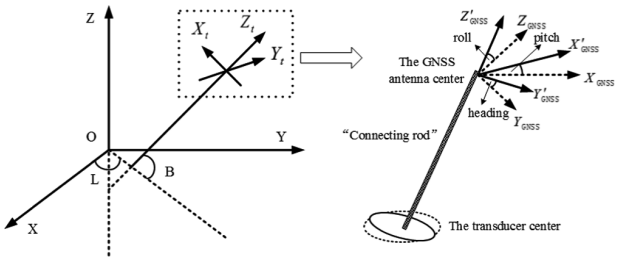

Fig. 3. Coordinate transformation

From the analysis above, coordinate transformation includes two steps [8]. First, it is necessary to solve the problem of coordinate transformation of the same point in different coordinate systems. To make better use of the obtained GNSS antenna coordinates, the subsequent hull coordinate system will be defined with the GNSS

antenna center point as the ordinate origin instead of the gravity point of the hull. After some axis rotation (including the opposite of the Y-axis, a rotation around the reverse Y-axis and the Z-axis), the transducer coordinates in the hull coordinate system can be transformed into the WGS-84 coordinate system. However, considering the attitude change, there are also coordinate offsets in the inner hull system. To solve this problem, an un-deformable "connecting rod" is assumed to connect the GNSS antenna center and the transducer center. When the initial relative positions of various sensors are calibrated before departure, its lengths can be obtained. Then, when the hull's attitude changes, the "connecting rod" can play a transmission role. The coordinate offset of GNSS antenna center is reflected by the coordinate offset of the transducer. Formula (8) can be used to summarize the above coordinate transformation process:

$$\begin{bmatrix} x_t \\ y_t \\ z_t \end{bmatrix} = \boldsymbol{R}_L \cdot \boldsymbol{R}_B \cdot \begin{bmatrix} 1 & & \\ & -1 & \\ & & 1 \end{bmatrix} \cdot \boldsymbol{R}_{heading} \cdot \boldsymbol{R}_{pitch} \cdot \boldsymbol{R}_{roll} \cdot \begin{bmatrix} 0 \\ 0 \\ l \end{bmatrix} + \begin{bmatrix} x \\ y \\ z \end{bmatrix} \tag{8}$$

where L is longitude, B is latitude, *head* is heading angle, *pitch* is pitch angle, *roll* is roll angle, l is the assumed length of "connecting rod".

According to Eq. (8), the underwater observation equation can be rewritten as:

$$\rho = \sqrt{\left[x + \Delta x) - x_\rho\right]^2 + \left[(y + \Delta y) - y_\rho\right]^2 + \left[(z + \Delta z) - z_\rho\right]^2} + \delta\rho_d + \delta\rho_v + \varepsilon \tag{9}$$

$\Delta x(roll, pitch, heading)$, $\Delta y(roll, pitch, heading)$ and $\Delta z(roll, pitch, heading)$ are coordinates increments determined by three attitude parameters jointly. Based on Eq. (7), three attitude parameters are added to the estimated parameters. The results of partial derivatives of attitude parameters are obtained according to Eq. (9), and the corresponding terms of each attitude parameter are added to the coefficient matrix. Then the GNSS/acoustic "one-step" positioning model with attitude parameters can be obtained.

4 Experiments and Results Analysis

In order to evaluate the effect of attitude error on the results of seafloor transponder positioning, and the application effect of GNSS/acoustic joint filtering with attitude parameters, a group of measured data are used in the subsequent experiments based on the software GNSSer under the different conditions of error ranges.

The data was measured in the waters of Lingshan island on December 1, 2017. Carrying sensors such as Applanix's POS-MV positioning system, the sound velocity profiler, etc., the ship made about 75 min of observations on the sea. The depth in the area is about 25 m, and the sampling interval of all the observed data is preprocessed to 2 s. The surface sound velocity of the transducer is obtained by gradient formula each epoch, and the initial incident angle is obtained by iteration using the method in literature [9]. In advance, Bernese software was used for the preliminary calculation of the GNSS observations. In addition, the coordinate of the transponder is determined by

the equal-gradient sound velocity tracking algorithm in the same layer [10], which is used as the reference value for the comparison of experimental results

In subsequent experiments, the three kinds of measured attitude angles are added with random errors in each epoch, the errors range in [−0.02°, 0.02°], [−0.03°, 0.03°], [−0.05°, 0.05°], [−0.08°, 0.08°] and [−0.1°, 0.1°], corresponding to scheme 1, 2, 3, 4 and 5 respectively. The 3D coordinate errors of the experimental results are obtained by using the formula $3D = \sqrt{\Delta X^2 + \Delta Y^2 + \Delta Z^2}$. The comparison results are shown as follows:

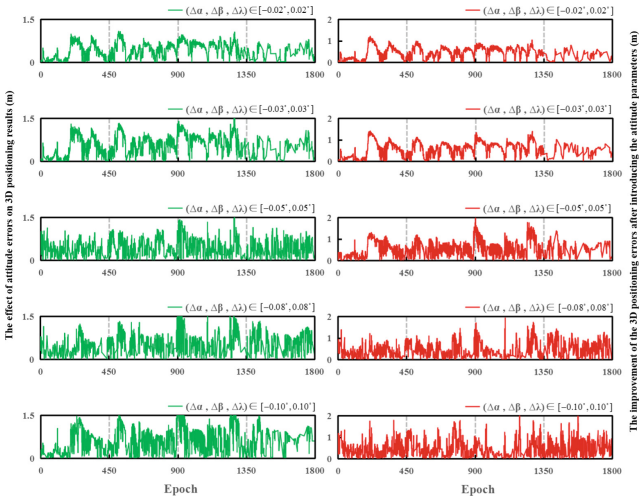

Fig. 4. The comparison results of the three-dimensional (3D) positioning errors under different conditions of attitude error ranges. *Green curves* in the *left* panels denote the effect of attitude errors on 3D positioning results, which is the deviation sequence between the situation with attitude errors and the original positioning results. *Red curves* in the *right* panels denote the improvement of positioning effect after the introduction of attitude parameters, which is the deviation sequence between the new model's positioning results and the situation with attitude errors.

As shown in Fig. 4:

(1) With the addition of random attitude errors, the three-dimensional coordinate errors of the transponder in each scheme are significantly increased. When the change of the attitude error range within [−0.03°, 0.03°], the amplified errors compared with the results without attitude errors has exceeded 1.5 m in some epochs. This is consistent with the conclusions in Sect. 2.2.

(2) After the attitude parameters are added to the filtering model for estimation, the 3D transponder coordinate error results of each scheme are improved to varying degrees due to the more realistic description of the inner function relations and the more accurate description of the motion state. and the greater the variation interval of the attitude error is, the more obvious the improvement effect is. Besides, when

the range of attitude error is larger, the improvement effect is more obvious. When the change of the attitude error range within [−0.1°, 0.1°], the three-dimensional point position accuracy of the transponder can be improved by nearly 2 m in some epochs.

In addition, the STD value and RMS value of positioning deviation in scheme 1 to scheme 5 are counted, and the results are shown in the following table:

Table 1. The STD and RMS values of the deviation results under different schemes in three directions. ① Denotes the difference between the positioning results with the introduction of attitude errors and the reference value. ② Denotes the statistical results of the deviation between the positioning results of the model proposed this paper and the reference value.

		STD/m			RMS/m		
		ΔX	ΔY	ΔZ	ΔX	ΔY	ΔZ
Scheme 1	①	0.9577	0.7153	1.5645	0.9719	0.7304	1.5698
	②	0.8633	0.6952	1.4947	0.8777	0.7111	1.4998
Scheme 2	①	1.0080	0.7051	1.5947	1.0291	0.7211	1.5977
	②	0.8722	0.6960	1.5057	0.8872	0.7119	1.5108
Scheme 3	①	1.0980	0.8489	1.8374	1.1208	0.8667	1.8427
	②	0.8800	0.6879	1.5102	0.8959	0.7035	1.5152
Scheme 4	①	1.1726	0.8215	1.8687	1.1992	0.8393	1.8716
	②	0.8808	0.6699	1.5017	0.8972	0.6850	1.5068
Scheme 5	①	1.1703	0.8757	1.9325	1.1962	0.8937	1.9374
	②	0.8854	0.6672	1.5108	0.9017	0.6820	1.5161

By analyzing the results in Table 1, it can be seen that:

(1) With the expansion of attitude error range, the STD value and RMS value of GNSS/acoustic joint positioning results also show a trend of gradual increase. When the random errors range within [−0.1°, 0.1°], the RMS value of deviation results of transponder coordinates in X, Y and Z direction is close to 1.2 m, 0.9 m and 2 m respectively;

(2) After the introduction of attitude parameters, the STD value and RMS value in three directions are reduced to different degrees in each scheme. This indicates that the fluctuation and the obvious jumps of filtering result sequence decreases, the result is relatively more stable and the positioning effect is significantly improved. Among them, the improvement effect of scheme 5 is the most obvious. In terms of positioning stability, it has been improved by 24.34%, 23.81% and 21.82% in X, Y and Z direction respectively. In terms of positioning accuracy, it has been improved by 24.62%, 23.69% and 21.75% in X, Y and Z direction respectively. The above results show that introducing attitude parameters into the estimation can make the function model more accurate and the result of transponder positioning more precise.

5 Conclusion

One of the important factors affecting the accuracy of dynamic positioning is the adequacy of the assumptions of the motion model. The GNSS/acoustic joint positioning model considering attitude parameters is more reasonable and realistic to describe the information of motion state, especially when there are attitude errors in the movement process. The model proposed in this paper can effectively reduce the influence of gross errors, obtain more stable filtering result sequence and higher accuracy of the transponder coordinate. Precision in X and Y direction is within 1 m, which can reach about 1.5 m in Z direction.

Acknowledgements. The team of researcher Liu Yanxiong from oceanographic institute is appreciated for providing the observed data for this paper.

References

1. Spiess FN (1985) Analysis of a possible sea floor strain measurement system. Mar Geodesy 9(4):385–398
2. Xu P, Ando M, Tadokoro K (2005) Precise, three-dimensional seafloor geodetic deformation measurements using difference techniques. Earth Planets Space 57(9):795–808
3. Sato M, Fujita M, Matsumoto Y et al (2013) Improvement of GPS/acoustic seafloor positioning precision through controlling the ship's track line. J Geodesy 87(9):825–842
4. Nishimura T, Sato M, Sagiya T (2014) Global positioning system (GPS) and GPS-acoustic observations: insight into slip along the subduction zones around Japan. Annu Rev Earth Planet Sci 42(1):653–674
5. Linyang L, Zhiping L, Yang C (2018) Summary of the research progress of seafloor geodetic control network. Bull Surv Mapp 1:8–13
6. Liu Y, Peng L, Wu Y et al (2006) Calibration of transducer and transponder positions. Geomatics Inf. Sci Wuhan Univ 31(7):610–612
7. Cai Y (2007) Investigations on integration of underwater GPS positioning system. Liaoning Technical University
8. Wang Y (2014) Research on algorithms of high-precision underwater positioning in petroleum exploration. China University of Petroleum (East China)
9. Ling S (2015) Research on the method of sound speed correction in underwater acoustic positioning. China University of Petroleum (East China)
10. Zhao J, Liu J (2008) Multi-beam sounding and image data processing. Wuhan University Press

Unscented Kalman Filter Based Attitude Estimation with MARG Sensors

Zeliang Zhang[1], Zebo Zhou[1(✉)], Shuang Du[1], Changgan Xiang[2], and Changhong Kuang[2]

[1] The School of Aeronautics and Astronautics, University of Electronic Science and Technology of China (UESTC), Chengdu 611731, China
klinsmann.zhou@gmail.com

[2] Sichuan Jiuzhou Beidou Navigation and Location Service Co., Ltd., Chengdu 611731, China

Abstract. This paper focuses on the approach to attitude estimation. When describing the attitude of a dynamic object, the quaternion has a better numerical continuity and stability compared with other conventional Euler angles' methods. However, acceleration observation vector has a nonlinear relation to attitude quaternion and as a result, the representative linear methods e.g. Kalman filter (KF) and complementary filter (CF) are no longer applicable. In addition, the disturbances of accelerometers and magnetometers also greatly degrade the attitude estimation reliability, leading to solution biased even divergence. In this contribution, the general heterogeneous MARG data fusion strategy is proposed, to minimize the noises influences of nonlinear system imposing on the attitude estimation of MARG sensors. To overcome the nonlinear estimation problem, the unscented Kalman filter (UKF) for attitude determination is proposed based on the unscented transformation. Furthermore, a real-time disturbance detection rules are established for the external acceleration and magnetic field distortion. Finally, the real experiments are carried out to evaluate performances of our proposed attitude estimation method.

Keywords: Attitude estimation · MARG · Unscented Kalman filter · Magnetometer

1 Introduction

Characterized by lost cost, low consumption and lightweight, Micro-electro-mechanical systems (MEMS) magnetic angular rate and gravity (MARG) sensors have been widely applied in the industrial fields and scientific research to provide the location and attitude information (Lee and Jung 2012; Luinge et al. 2005; Odry et al. 2018; Zhou et al. 2018). It has many advantages by combining tri-axial magnetometers, gyroscopes and accelerometers into a MARG module where the accumulated errors of attitude angles derived from inertial sensors can be well suppressed. It can continuously provide the real-time, accurate and reliable orientation even can endure a long period.

J. Sun et al. (Eds.): CSNC 2019, LNEE 563, pp. 490–502, 2019.
https://doi.org/10.1007/978-981-13-7759-4_43

To improve the attitude estimation accuracy and reliability, many fusion methods have been developed in the past few decades. One of the representative approaches is complementary filter (CF), which consumes less computation time and is east-to-run on the low-cost hardware platforms (Wang et al. 2014; Wu et al. 2016b; Yang et al. 2018). Generally, the basic structure of complementary filter is to combine information from gyroscope and accelerometer, which have complementary frequency characteristics (Li and Li 2017; Kottath et al. 2017). In addition, the yaw angle can be corrected further with magnetometer (Ghasemi-Moghadam and Homaeinezhad 2018). Recently, the quaternion-type complementary filter is also designed by Wu et al. (2016a). However, CF can only provide suboptimal estimation. To achieve more accurate attitude estimation, another popular fusion method centralized Kalman Filter (CKF) is utilized, which produces an optimal recursive solution in the sense of minimum mean square estimation in the fusion center (Feng 2017; Jalali et al. 2017; Zhou et al. 2013). In addition, Gao et al. (2017), Suh (2010) and Hemerly et al. (2012) propose the indirect Kalman filter to estimate the quaternion error state subsequently correcting the attitude quaternion. In the base of Wu's Fast Liner quaternion Attitude Estimation (2018), we proposed the FLAE-based KF recently to reduce the computation burdens and generate the virtual-gyro output in the case of gyroscope failures. (Zhang et al. 2018). However, similar to other KF- and CF-based methods, the attitude estimation is accomplished based on the liner relation. Obviously, there is a non-linear relationship between acceleration observation vector and attitude quaternion, and as a result, the representative linear methods KF and CF are no longer available thus the nonlinear filter should be applied.

Furthermore, the attitude estimation accuracy of MARG is easily affected by the non-gravity acceleration and magnetic field disturbances which frequently occurs on a moving platform in the time-variant observation environments. The result of the interference is that the observational errors cannot satisfy the assumption of Kalman filtering, and therefore, the attitude estimates will be biased or even divergent (Bird and Arden 2011; Koo et al. 2009; Lee et al. 2012). To solve these problems, the detection rules should be established, so that the information of sensors is introduced only in the absence of interference.

To achieve robust attitude estimation, the paper proposed the unscented Kalman filter (UKF) based attitude estimation method. By establishing real-time detection rules for the external acceleration and magnetic field distortion, the general heterogeneous MARG data fusion strategy is proposed to minimize the noises influences of nonlinear system imposing on the attitude estimation of MARG sensors. The rest of paper is organized as follows: Sect. 2 depicts the principle of attitude determination with KF. UKF based attitude estimation strategy is proposed in Sect. 3. The detection rules of external acceleration and magnetic field disturbance is presented in Sect. 4. Experiments and analysis are given in Sect. 5 and finally, conclusions Sect. 6.

2 MARG System Model and Its Linear Kalman Filter Solution

The rotation relationship between the body frame (denoted as b-frame, right-front-up) and the navigation frame (denoted as n-frame, east-north-up, i.e. ENU) can be represented by the quaternion, composed of a real number and three imaginary units. Its complex form is as follows:

$$\boldsymbol{q} = q_0 + q_1\boldsymbol{i} + q_2\boldsymbol{j} + q_3\boldsymbol{k} \tag{1}$$

where, $\boldsymbol{i}, \boldsymbol{j}, \boldsymbol{k}$ are the unit vectors corresponding to the three axis of the vector coordinate system, and the quaternion differential equation is as follows:

$$\dot{\boldsymbol{q}} = \frac{1}{2}\boldsymbol{q} \otimes \boldsymbol{\omega} \tag{2}$$

where ω is quaternion type angular rate vector, i.e. $\boldsymbol{\omega} = 0 + \omega_x\boldsymbol{i} + \omega_y\boldsymbol{j} + \omega_z\boldsymbol{k}$, and $\omega_x, \omega_y, \omega_z$ are angular rate of x, y and z axis, respectively. $\otimes$ represents the quaternion product. The matrix form of (2) is given by

$$\begin{gathered} \tfrac{d\boldsymbol{q}}{dt} = \tfrac{1}{2}[\boldsymbol{\Omega}\times]\boldsymbol{q} \\ \begin{pmatrix} \dot{q}_0 \\ \dot{q}_1 \\ \dot{q}_2 \\ \dot{q}_3 \end{pmatrix} = \tfrac{1}{2}\begin{pmatrix} 0 & -\omega_x & -\omega_y & -\omega_z \\ \omega_x & 0 & \omega_z & -\omega_y \\ \omega_y & -\omega_z & 0 & \omega_x \\ \omega_z & \omega_y & -\omega_x & 0 \end{pmatrix}\begin{pmatrix} q_0 \\ q_1 \\ q_2 \\ q_3 \end{pmatrix} \end{gathered} \tag{3}$$

Discretized equation can be modelled as:

$$\boldsymbol{q}_k = \left(\boldsymbol{I}_4 + \frac{1}{2}\delta t[\boldsymbol{\Omega}\times]_k\right)\boldsymbol{q}_{k-1} + \boldsymbol{w}_k \tag{4}$$

where subscript k denotes the time epoch index. δt represents sampling interval and w_k denotes the zero-mean process noise with variance of $\boldsymbol{Q}_{\mathbf{w}_k}$.

The observation vectors of accelerometers $\boldsymbol{a}$ and magnetometers $\boldsymbol{m}$ related to the transformation between b- and r-frames can be established as follows:

$$\begin{cases} \boldsymbol{a}^{\mathrm{b}} = \boldsymbol{C}_{\mathrm{n}}^{\mathrm{b}}\boldsymbol{a}^{\mathrm{n}} \\ \boldsymbol{m}^{\mathrm{b}} = \boldsymbol{C}_{\mathrm{n}}^{\mathrm{b}}\boldsymbol{m}^{\mathrm{n}} \end{cases} \tag{5}$$

In which

$$\begin{cases} \boldsymbol{a}^{\mathrm{b}} = \begin{bmatrix} a_x^{\mathrm{b}} & a_y^{\mathrm{b}} & a_z^{\mathrm{b}} \end{bmatrix}^{\mathrm{T}} \\ \boldsymbol{a}^{\mathrm{n}} = \begin{bmatrix} 0 & 0 & -g \end{bmatrix}^{\mathrm{T}} \\ \boldsymbol{m}^{\mathrm{b}} = \begin{bmatrix} m_x^{\mathrm{b}} & m_y^{\mathrm{b}} & m_z^{\mathrm{b}} \end{bmatrix}^{\mathrm{T}} \\ \boldsymbol{m}^{\mathrm{n}} = \begin{bmatrix} 0 & m_N & m_U \end{bmatrix}^{\mathrm{T}} \end{cases}$$

where superscript b and n represent the vector in b-frame and n-frame respectively. g is the norm of local gravity; m_N and m_U are the magnetic field strength in north and up in n-frame respectively. The transformation matrix $\boldsymbol{C}_n^b$ represents the rotation from the n-frame to the b-frame, and it can be expressed as follows:

$$\boldsymbol{C}_n^b = \begin{pmatrix} q_0^2+q_1^2-q_2^2-q_3^2 & 2(q_1q_2+q_0q_3) & 2(q_1q_3-q_0q_2) \\ 2(q_1q_2-q_0q_3) & q_0^2-q_1^2+q_2^2-q_3^2 & 2(q_2q_3+q_0q_1) \\ 2(q_1q_3+q_0q_2) & 2(q_2q_3-q_0q_1) & q_0^2-q_1^2-q_2^2+q_3^2 \end{pmatrix} \tag{6}$$

Our previous work solves the Eqs. (5–6) through FLAE-KF (Zhang et al. 2018), in which attitude quaternion is invoked for parameterization of orientation in the filter. The system state model is established with (4) and the corresponding observation model is constructed by

$$\boldsymbol{l}_k = \boldsymbol{H}\boldsymbol{q}_k + \boldsymbol{\varepsilon}_k \tag{7}$$

Where the observation vector $\boldsymbol{l}_k$ is the quaternion solution of (4) derived from FLAE, $\boldsymbol{H}$ connecting the state vector with the observation vector becomes unit identity matrix $\boldsymbol{I}$ with the dimension of 4 × 4; ε_k is Gaussian distributed with the variance of $\boldsymbol{Q}_{\varepsilon_k}$.

Then the predicted state and its covariance matrix are respectively computed by:

$$\bar{\boldsymbol{x}}_k = \boldsymbol{\Phi}_{k,k-1}\hat{\boldsymbol{x}}_{k-1} \tag{8}$$

$$\boldsymbol{Q}_{\bar{x}_k} = \boldsymbol{\Phi}_{k,k-1}\boldsymbol{Q}_{\hat{x}_{k-1}}(\boldsymbol{\Phi}_{k,k-1})^{\mathrm{T}} + \boldsymbol{Q}_{w_k} \tag{9}$$

in which $\boldsymbol{\Phi}_k = \boldsymbol{I}_4 + \frac{1}{2}\delta t[\boldsymbol{\Omega}\times]_k$.

The time update set of KF equations are:

$$\boldsymbol{K}_k = \boldsymbol{Q}_{\bar{x}_k}\boldsymbol{H}_k^{\mathrm{T}}(\boldsymbol{H}_k\boldsymbol{Q}_{\bar{x}_k}\boldsymbol{H}_k^{\mathrm{T}})^{-1} + \boldsymbol{Q}_{\varepsilon_k} \tag{10}$$

$$\hat{\boldsymbol{x}}_k = \bar{\boldsymbol{x}}_k + \boldsymbol{K}_k(\boldsymbol{l}_k - \boldsymbol{H}_k\bar{\boldsymbol{x}}_k) \tag{11}$$

$$\boldsymbol{Q}_{\hat{x}_k} = (\boldsymbol{I} - \boldsymbol{K}_k\boldsymbol{H}_k)\boldsymbol{Q}_{\bar{x}_k} \tag{12}$$

where $\hat{\boldsymbol{x}}_k = \hat{\boldsymbol{q}}_k$ and $\boldsymbol{Q}_{\hat{\mathbf{x}}_k} = \boldsymbol{Q}_{\hat{\mathbf{q}}_k}$ are KF estimate and its covariance, respectively and $\boldsymbol{K}_k$ is so-called gain matrix.

3 Nonlinear Kalman Filtering for Attitude Estimation

During the FLAE-KF, the observation vector is obtained with the Wahba's solution of (4). In order to avoid the linearization error during the calculation, the measurement equation can be established directly with (4), where the observation vectors are:

$$\boldsymbol{z}_k = \begin{bmatrix} \boldsymbol{y}_{a_k}^{\mathrm{T}} & \boldsymbol{y}_{m_k}^{\mathrm{T}} \end{bmatrix}^{\mathrm{T}}$$

in which $\boldsymbol{y}_{a_k}$ and $\boldsymbol{y}_{m_k}$ denote accelerometer and magnetometer outputs at epoch k respectively.

Apparently, the observation vectors are a nonlinear function of state quaternion. To achieve the better attitude accuracy, the unscented transformation (UT) is introduced to estimate the nonlinear Kalman filter.

As there is a liner relationship in the state equation, the predicted state and its covariance matrix can still be computed by (9) and (10) respectively.

Then a set of weighted Sigma points are obtained based on (9) and (10):

$$\begin{cases} \xi_{i,k} = \bar{\boldsymbol{x}}_k & i = 0 \\ \xi_{i,k} = \bar{\boldsymbol{x}}_k + a\left(\sqrt{n\boldsymbol{Q}_{\bar{x}_k}}\right)_i & i = 1, 2, \cdots, n \\ \xi_{i,k} = \bar{\boldsymbol{x}}_k - a\left(\sqrt{n\boldsymbol{Q}_{\bar{x}_k}}\right)_i & i = n+1, n+2, \cdots, 2n \end{cases} \tag{13}$$

where a is the adjustment parameter to regulate the Sigma points distribution around $\bar{\boldsymbol{x}}_k$; n denotes the dimension of $\bar{\boldsymbol{x}}_k$ and $\left(\sqrt{n\boldsymbol{Q}_{\bar{x}_k}}\right)_i$ is the i-th column of root mean square of the matrix $n\boldsymbol{Q}_{\bar{x}_k}$.

The Sigma points after UT of nonlinear observation Eq. (4) (denoted as $f(\cdot)$) are as follows:

$$\gamma_{i,k} = f\left(\xi_{i,k}\right)(i = 0, 1, \ldots, 2n) \tag{14}$$

and then calculate the predicted observation and its covariance by

$$\hat{\boldsymbol{z}}_k = \sum_{i=0}^{2n} p_i \gamma_{i,k} \tag{15}$$

$$\boldsymbol{Q}_{\hat{z}_k} = \sum_{i=0}^{2n} p_i (\gamma_{i,k} - \hat{\boldsymbol{z}}_k)(\gamma_{i,k} - \hat{\boldsymbol{z}}_k)^{\mathrm{T}} + \boldsymbol{Q}_{\varepsilon_k} \tag{16}$$

with

$$\begin{cases} p_i = 1 - \frac{1}{a^2} & i = 0 \\ p_i = \frac{1}{2na^2} & i = 1, 2, \cdots, 2n \end{cases}$$

The cross-correlation between predicted state and predicted observation is computed through

$$\boldsymbol{Q}_{\bar{x}_k\hat{z}_k} = \sum_{i=0}^{2n} p_i(\xi_{i,k} - \bar{x}_k)(\gamma_{i,k} - \hat{z}_k)^{\mathrm{T}} \tag{17}$$

Finally, the quaternion state and its variance are estimated by following equations:

$$\boldsymbol{K}_k = \boldsymbol{Q}_{\bar{x}_k\hat{z}_k}\boldsymbol{Q}_{\hat{z}_k}^{-1} \tag{18}$$

$$\hat{\boldsymbol{x}}_k = \bar{\boldsymbol{x}}_k + \boldsymbol{K}_k(\boldsymbol{z}_k - \hat{\boldsymbol{z}}_k) \tag{19}$$

$$\boldsymbol{Q}_{\hat{x}_k} = \boldsymbol{Q}_{\bar{x}_k} - \boldsymbol{K}_k\boldsymbol{Q}_{\hat{z}_k}\boldsymbol{K}_k^{\mathrm{T}} \tag{20}$$

4 Disturbance Detection Rules for External Acceleration and Magnetic Field Distortion

For a moving platform in the time-variant observation environments, the attitude estimation accuracy of MARG is quite easily affected by disturbances due to the external acceleration and magnetic field distortion. While, compared with accelerometer and magnetometer, gyroscope has the smallest risk suffering from the outer environment influences. Therefore, it can be used to detect the abnormality of observation vector pairs of accelerometer and magnetometer models. The disturbance detection rules are given as follows (Table 1):

It should be pointed out that: *Condition* 1 is used to detect the abnormality of acceleration norm. The threshold τ_1 is set based on 3σ-criterion according to the variance of accelerometer noises. Once the Condition 1 is satisfied, the *Condition* 2 is triggered for detecting the external acceleration. The threshold relation between τ_1 and τ_{ax}, τ_{ay} τ_{az} is

$$\tau_1 = \sqrt{\tau_{ax}^2 + \tau_{bx}^2 + \tau_{cx}^2} \tag{21}$$

Where $\tau_{ax} = 3\sqrt{\mathrm{Q}_{a_x}}$, $\tau_{ay} = 3\sqrt{\mathrm{Q}_{a_y}}$ and $\tau_{az} = 3\sqrt{\mathrm{Q}_{a_z}}$, in which $\mathrm{Q}_{a_x}, \mathrm{Q}_{a_y}$ and Q_{a_z} are the acceleration variances of x, y and z axis respectively. Similarly, the threshold τ_2 for detecting magnetic field distortion is given by

$$\tau_2 = \sqrt{\tau_{mx}^2 + \tau_{mx}^2 + \tau_{mx}^2} \tag{22}$$

Where $\tau_{mx} = 3\sqrt{\mathrm{Q}_{m_x}}$, $\tau_{my} = 3\sqrt{\mathrm{Q}_{m_y}}$ and $\tau_{\mathrm{mz}} = 3\sqrt{\mathrm{Q}_{m_z}}$, in which $\mathrm{Q}_{m_x}, \mathrm{Q}_{m_y}$ and Q_{m_z} are the magnetic field strength variances of x, y and z axis respectively.

Based on the rules mentioned above, the observation model can be real-time switched with the four system working modes for latter UKF estimating.

Table 1. The profile of disturbance detection at time epoch k

Acquired observations and state information
The outputs of MARG sensor at time epoch k: $\boldsymbol{y}_a, \boldsymbol{y}_\omega, \boldsymbol{y}_m$
Attitude quaternion solution at time epoch k-1: $\hat{\boldsymbol{q}}_{k-1}$
Detection rules
IF *Condition* 1 ($\left\|\left\|\boldsymbol{y}_a\right\| - g\right\| < \tau_1$) is satisfied, calculate $\hat{\boldsymbol{a}}^{\mathrm{b}} = \boldsymbol{C}_{\mathrm{n}}^{\mathrm{b}}(\hat{\boldsymbol{q}}_{k-1})\boldsymbol{a}^{\mathrm{n}}$
IF *Condition* 2 ($\left\|\boldsymbol{y}_{\mathrm{a}} - \hat{\boldsymbol{a}}^{b}\right\| < \left[\tau_{ax} \quad \tau_{ay} \quad \tau_{az}\right]^{\mathrm{T}}$) is satisfied, accelerometer observation is valid
ELSE Accelerometer observation is invalid
ELSE Accelerometer observation is invalid
IF *Condition* 3 ($\left\|\left\|\boldsymbol{y}_m\right\| - \left\|\boldsymbol{m}^{\mathrm{n}}\right\|\right\| < \tau_2$)is satisfied, calculate: $\hat{\boldsymbol{m}}^{\mathrm{b}} = \boldsymbol{C}_{\mathrm{n}}^{\mathrm{b}}(\hat{\boldsymbol{q}})\boldsymbol{m}^{\mathrm{n}}$
IF *Condition* 4 ($\left\|\boldsymbol{y}_m - \hat{\boldsymbol{m}}^{b}\right\| < \left[\tau_{mx} \quad \tau_{my} \quad \tau_{mz}\right]^{\mathrm{T}}$) is satisfied, no magnetic field disturbance and then magnetometer observation is valid
ELSE Magnetometer observation is invalid
ELSE Magnetometer observation is invalid
IF Both of accelerometer observation and magnetometer observation are invalid, select **Mode** 1
ELSE IF Accelerometer observation is valid and magnetometer observation is invalid, select **Mode** 2
ELSE IF Accelerometer observation is invalid and magnetometer observation is valid, select **Mode** 3
ELSE (Both of accelerometer observation and magnetometer observation are valid) select **Mode** 4
System working mode selection
Mode 1 Gyro: attitude updating with gyroscope only
Mode 2 Gyro + Acc: the observation model $\boldsymbol{y}_a = \boldsymbol{C}_{\mathrm{n}}^{\mathrm{b}}\boldsymbol{a}^{\mathrm{n}} + \boldsymbol{\varepsilon}_a$
Mode 3 Gyro + Mag: the observation model $\boldsymbol{y}_m = \boldsymbol{C}_{\mathrm{n}}^{\mathrm{b}}\boldsymbol{m}^{\mathrm{n}} + \boldsymbol{\varepsilon}_m$
Mode 4 Gyro + Acc +Mag: the observation model $\begin{pmatrix} \boldsymbol{y}_a \\ \boldsymbol{y}_m \end{pmatrix} = \begin{pmatrix} \boldsymbol{C}_{\mathrm{n}}^{\mathrm{b}} & \boldsymbol{0} \\ \boldsymbol{0} & \boldsymbol{C}_{\mathrm{n}}^{\mathrm{b}} \end{pmatrix} \begin{pmatrix} \boldsymbol{a}^{\mathrm{n}} \\ \boldsymbol{m}^{\mathrm{n}} \end{pmatrix} + \begin{pmatrix} \boldsymbol{\varepsilon}_a \\ \boldsymbol{\varepsilon}_m \end{pmatrix}$

5 Experimental Results and Analysis

The proposed UKF based attitude estimation method is compiled on the Uranus 2, which is equipped with tri-axial accelerometer, magnetometer, and gyroscope. The commercial software output is used as the reference value. After calibrated beforehand, the MARG module is mounted on the top of the shoe to collect walking data and one set of raw data is shown in Fig. 1:

It can be seen that periodically external accelerations during the walking process. In this section, three methods are computed for comparison purposes:

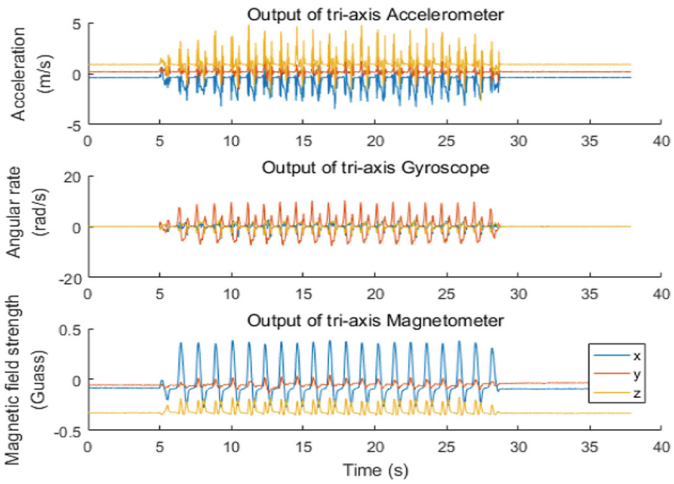

Fig. 1. Raw data of MARG sensors

(1) UKF based attitude estimation with disturbance detection (AD-UKF);
(2) UKF based method without disturbance detection (ND-UKF)
(3) FLAE-KF based method without disturbance detection (FLAE-KF)

In AD-UKF, with the aid of acceleration and magnetic field disturbance detection rules, the system working mode changes as the disturbance occurs. The system working mode flag is shown in Fig. 2 and the attitude estimation results are drawn in Fig. 3.

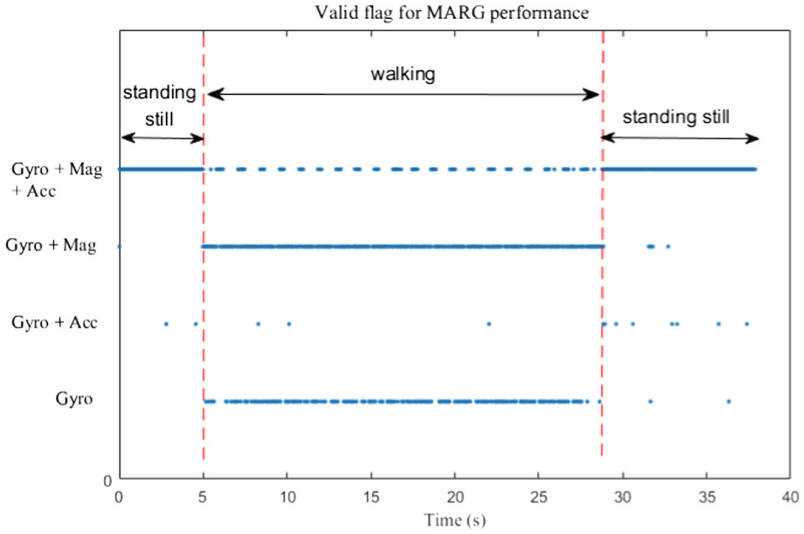

Fig. 2. Detection result of the external acceleration and magnetic field disturbance

Seen from Fig. 2, when the platform is in static, the attitude is estimated with all sensors at most of time. While during walking process, the external accelerations are detected thus the accelerometer outputs will not be incorporated into the filter.

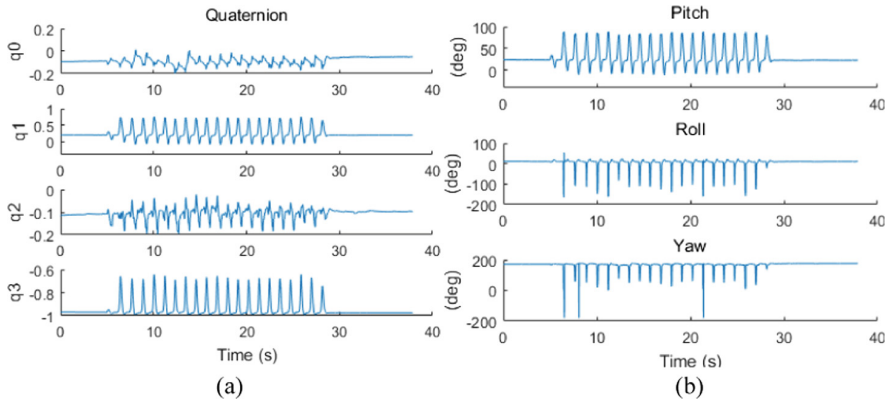

Fig. 3. Attitude estimation results of MARG based on AD-UKF (quaternion and Euler angle)

To show the efficiency of the proposed UKF based method, we compute the results of AD-UKF and FLAE-KF with the standing still dataset which is free of external acceleration and magnetic field disturbances. The attitude errors and statistic results are presented in Fig. 4 and root mean square errors (RMSE) are shown in Table 2. It can be inferred from Fig. 4 and Table 2 that UKF always outperforms the FLAE-KF. This is because the unscented transformation achieves the better stochastic model during the filtering progress. On the contrary, the FLAE-KF does not take into account the influences by nonlinear model imposing on the stochastic model. Therefore, AD-UKF is superior to FLAE-KF in MARG sensors nonlinear fusion.

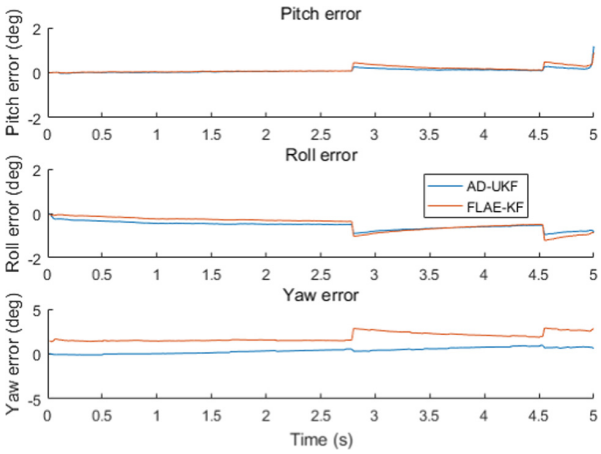

Fig. 4. Attitude Euler angle errors of AD-UKF and FLAE-KF

Table 2. RMSE of AD-UKF and FLAE-KF (unit: degree)

	Pitch	Roll	Yaw
AD-UKF	0.27	0.94	0.97
FLAE-KF	0.47	1.21	2.89

In order to validate disturbance detection rules, we further compute and analyze the results of AD-UKF and ND-UKF (see Fig. 5 and Table 3). It shows that the Euler angle estimation errors of AD-UKF is much smaller, indicating that the disturbance detection is efficient and significantly minimize the unexpected influences on the estimation results.

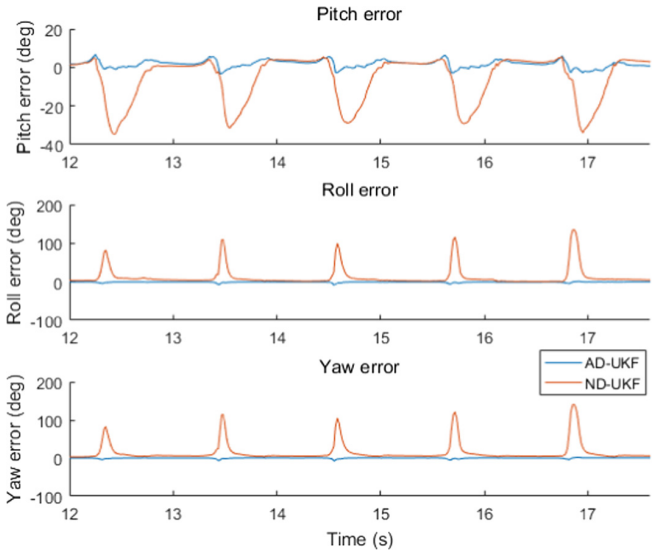

Fig. 5. Attitude estimation errors of AD-UKF and ND-UKF

In addition, we test the implementation efficiency of our proposed method. The MARG attitude estimation program is implemented (Inter i5 1.70-GHz CPU, 4G-RAM, MATLAB R2016a). The execution time for AD-UKF and FLAE-KF is shown in Fig. 6. It is worthy of pointing out that FLAE has been proven to be a very efficient attitude estimation method which outperforms many representative methods (Choukroun et al. 2002; Markley 1993; Shuster and Oh 1981). Compared with FLAE-KF, our proposed method only has a slightly higher time-consumption (Average time consumptions of AD-UKF and FLAE-KF are 5.4510×10^{-4} s and 5.2382×10^{-4} s, respectively). This can meet the computation requirements of low-cost hardware platform.

Table 3. RMSE of AD-UKF and ND-UKF (unit: degree)

	Pitch	Roll	Yaw
AD-UKF	6.83	7.94	7.83
ND-UKF	33.90	135.80	140.90

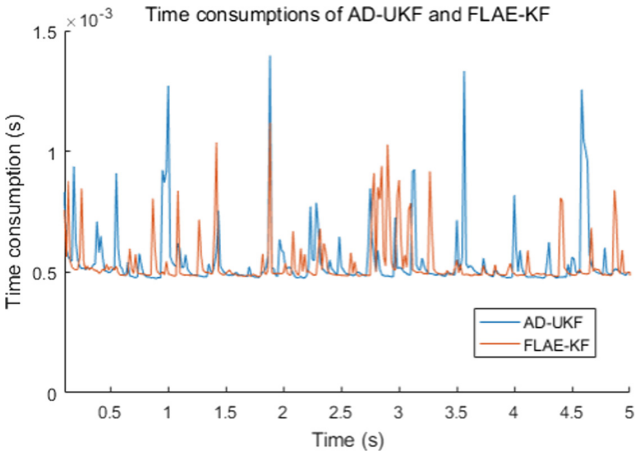

Fig. 6. Time consumptions of AD-UKF and FLAE-KF

6 Conclusion

Based on the unscented Kalman filter (UKF) theory, the nonlinear attitude estimation for MARG sensors is investigated. By establishing the real-time disturbance detection rules of the platform acceleration and magnetic field disturbance, the robust heterogeneous data fusion method is proposed to minimize the influences their influences imposing on the attitude estimation of the MARG systems. The experiment results show that the nonlinear observation models degrade the accuracy of conventional KF. In contrast, with the aid of unscented transformation, AD-UKF produces the better estimation accuracy and exhibit the robustness in the case of outer disturbances occurs.

Acknowledgment. This work is supported by the National Natural Science Funds of China (No. 41604025 and 41704029), the State Key Laboratory of Geodesy and Earth's Dynamics (Institute of Geodesy and Geophysics, CAS, SKLGED2018-3-2E), Sichuan Province Science and Technology Project (No. 2018CC0018; 2018SZ0364) and the Fundamental Research Funds for the Central Universities under Grant ZYGX2018J080.

References

Bird J, Arden D (2011) Indoor navigation with foot-mounted strap down inertial navigation and magnetic sensors emerging opportunities for localization and tracking. Wirel Commun IEEE 18(2):28–35

Choukroun D, Bar-Itzhack IY, Oshman Y (2002) Novel quaternion Kalman filter. IEEE Trans Aerosp Electron Syst 42(1):174–190

Gao N, Wang M, Zhao L (2017) A novel robust Kalman filter on AHRS in the magnetic distortion environment. Adv Space Res 60(12):2630–2636

Feng K, Li J, Zhang X, Shen C, Bi Y, Zheng T, Liu J (2017) A new quaternion-based Kalman filter for real-time attitude estimation using the two-step geometrically-intuitive correction algorithm. Sensors 17(9):2146

Ghasemi-Moghadam S, Homaeinezhad MR (2018) Attitude determination by combining arrays of MEMS accelerometers, gyros, and magnetometers via quaternion-based complementary filter. Int J Numer Model-Electron Netw Devices Fields 31(3):e2282

Hemerly EM, Maciel BCO, Milhan ADP, Schad VR (2012) Attitude and heading reference system with acceleration compensation. Aircr Eng Aerosp Technol 84(2):87–93

Jalali M, Hashemi E, Khajepour A, Chen SK, Litkouhi B (2017) Integrated model predictive control and velocity estimation of electric vehicles. Mechatronics 46:84–100

Koo W, Sung S, Lee YJ (2009) Development of real-time heading estimation algorithm using magnetometer/IMU. ICCAS-SICE, pp 4212–4216

Kottath R, Narkhede P, Kumar V, Karar V, Poddar S (2017) Multiple model adaptive complementary filter for attitude estimation. Aerosp Sci Technol 70:644

Lee JK, Park EJ, Robinovitch SN (2012) Estimation of attitude and external acceleration using inertial sensor measurement during various dynamic conditions. IEEE Trans Instrum Meas 61 (8):2262–2273

Lee H, Jung S (2012) Balancing and navigation control of a mobile inverted pendulum robot using sensor fusion of low cost sensors. Mechatronics 22(1):95–105

Li X, Li Q (2017) External acceleration elimination for complementary attitude filter. In: IEEE international conference on information and automation, pp 208–212

Luinge HJ, Veltink PH (2005) Measuring orientation of human body segments using miniature gyroscopes and accelerometers. Med Biol Eng Compu 43(2):273–282

Markley FL (1993) Attitude determination from vector observations: a fast optimal matrix algorithm. J Astronaut Sci 41(2):261–280

Shuster MD, Oh SD (1981) Three-axis attitude determination from vector observations. J Guidance Control Dyn 4(1):70–77

Suh YS (2010) Orientation estimation using a quaternion-based indirect Kalman filter with adaptive estimation of external acceleration. IEEE Trans Instrum Meas 59(12):3296–3305

Odry Á, Fullér R, Rudas IJ, Odry P (2018) Kalman filter for mobile-robot attitude estimation: novel optimized and adaptive solutions. Mech Syst Sig Process 110:569–589

Wang Y, Li N, Chen X, Liu M (2014) Design and implementation of an AHRS based on MEMS sensors and complementary filtering. Adv Mech Eng. https://doi.org/10.1155/2014/214726

Wu J, Zhou Z, Chen J, Fourati H, Li R (2016a) Fast complementary filter for attitude estimation using low-cost MARG sensors. IEEE Sens J 16(18):6997–7007

Wu J, Zhou Z, Gao B, Li R, Cheng Y, Fourati H (2018) Fast linear quaternion attitude estimator using vector observations. IEEE Trans Autom Sci Eng 15(1):307–319

Wu Z, Sun Z, Zhang W, Chen Q (2016b) A novel approach for attitude estimation based on MEMS inertial sensors using nonlinear complementary filters. IEEE Sens J 16(10):3856–3864

Yang Q, Sun L, Yang L (2018) A fast adaptive-gain complementary filter algorithm for attitude estimation of an unmanned aerial vehicle. J Navig 71(6):1477

Zhang Z, Zhou Z, Wu J, Du S, Fourati H (2018) Fast linear attitude estimation and angular rate generation. Indoor Positioning Indoor Navig. https://doi.org/10.1109/ipin.2018.8533736

Zhou Z, Li Y, Liu J, Li G (2013) Equality constrained robust measurement fusion for adaptive Kalman filter based heterogeneous multi-sensor navigation. IEEE Trans Aerosp Electron Syst 49(4):2146–2157

Zhou Z, Wu J, Wang J, Fourati H (2018) Optimal recursive and sub-optimal linear solutions to attitude determination from vector observations for GNSS/Accelerometer/Magnetometer orientation measurement. Remote Sens 10(3):1–28

A Modified TDCP/INS Tightly Coupled Navigation

Wanli Jian, Yi Dong, Dingjie Wang, and Jie Wu(✉)

National University of Defense Technology, Changsha, China
850944852@qq.com, dy_nudt2013@hotmail.com,
wangdingjiell@nudt.edu.cn, Wujie_nudt@sina.com

Abstract. Nowadays, the navigation systems, such as phone-based and vehicle navigation, are developing, and techniques of GNSS/INS loosely and tightly coupled navigation are under widely used. Compared with loosely coupled navigation, the tightly coupled navigation shows more and more superiorities in urban canyons, because it can provide continuous integrated navigation solution even with less than four satellites. Conventional tightly coupled navigation only use pseudo range and Doppler observations, while the time-differenced carrier phase (TDCP)/Inertial navigation system (INS) tightly coupled navigation uses an extra TDCP observation; this can provides higher attitude accuracy than the conventional tightly coupled navigation. However, the mathematical model of the conventional TDCP/INS tightly coupled navigation makes difference between the reference epoch and current epoch, this creates poor real-time. To improve the accuracy and reduce the computation burden, this paper presents a modified TDCP/INS tightly coupled navigation method, infers a modified mathematical model of TDCP, which can make difference between the current 0.1 s epoch. The experimental results show that, compared with the loosely coupled navigation, the modified TDCP/INS tightly coupled navigation method provides higher accuracy of position, velocity and attitude. As expected, compared with the conventional tightly coupled navigation, the attitude accuracy is significantly improved, meanwhile the accuracy of position and velocity are slightly improved. In the face of few observable satellites and turning, the modified TDCP/INS tightly coupled navigation method shows a clear advantage.

Keywords: Tightly coupled navigation · TDCP · Kalman filter · Attitude accuracy · Real-time

1 Introduction

In recent years, the GNSS/INS loosely and tightly coupled navigations are under widely used in many applications, such as vehicle navigation and mobile phone navigation. Compared with the loosely coupled navigation system, the GNSS/INS tightly coupled navigation system can work smoothly even when the number of observed GNSS satellites drops below 4. In the traditional tightly coupled navigation system, pseudo range and Doppler are the main observations. However, the high noise of pseudo range makes the positioning result of the traditional tightly coupled navigation close to the precision of single point positioning (SPP). Compared with the pseudo

J. Sun et al. (Eds.): CSNC 2019, LNEE 563, pp. 503–512, 2019.
https://doi.org/10.1007/978-981-13-7759-4_44

range, carrier phase observation information is more accurate, it can take the tightly coupled navigation system to centimeter-level positioning, speed accuracy and higher attitude accuracy [6].

When the carrier phase observation information is used in the tightly coupled navigation system, correcting the ambiguity is always a difficult problem. To avoid complex calculations, the time-differenced carrier phase (TDCP) technique emerged. Due to the carrier phase ambiguity which can remain unchanged when there is no cycle jump between two continuous GNSS moments, the application of TDCP can avoid correcting the ambiguity. Theoretically, the TDCP technique could achieve centimeter-level, even millimeter-level positioning accuracy [1], and the attitude accuracy could improve significantly. However, the TDCP information is a relative measurement. When the TDCP information is taken as the only observation quantity in GNSS/IMU tightly coupled navigation system, the absolute positioning information will be lost [1], resulting in a large position drift. In order to restrain the position drift, pseudo range should be extended as the observation information in Kalman filter to achieve absolute position estimation. To further improve the accuracy of the TDCP/INS tightly coupled navigation, scholars have done a lot of research and made some achievements. Han et al. [6] designed a further two-speed Kalman filter, and Ding et al. [3] proposed a two-step correction method. However, the absolute position accuracy of these two methods is only slightly better than SPP, there is no helpful to improve the accuracy of speed and attitude. For this reason, Zhao et al. [1] proposed a further method. In the further method, the TDCP measurement equation is derived based on speed error, and the difference is between the current epoch and reference epoch, so the position drift could be avoid, then the position accuracy could be improved. However, when the carrier enters urban streets, canyons and woods, the satellite signal is often blocked. Then lots of weekly jumps make the reference epoch change frequently. That greatly limits the accuracy of TDCP/INS tightly coupled navigation system. In fact, when the satellite signal is often blocked, if the TDCP measurement equation can be derived based on the position error, and the difference is between the current 0.1 s epoch, the TDCP/INS tightly coupled navigation system could work effectively. Then the calculation speed and accuracy could be higher [1].

Inspired by the above traditional TDCP/INS tightly coupled navigation methods, a modified TDCP/INS tightly coupled navigation method is proposed in the first half of this paper, and a modified TDCP equation is derived. In order to verify the effectiveness and advantages of the modified method, the latter part of this paper designs a comparative test for the modified TDCP/INS tightly coupled navigation, loosely coupled navigation and traditional tightly coupled navigation.

2 Scheme Design and Mathematical Modeling

2.1 Overall Scheme

The modified TDCP/INS coupled navigation method uses satellites-difference pseudo range, satellites-difference Doppler and satellites-difference TDCP as the observation information. The observation equations of satellites-difference pseudo range and

Doppler are referred to literature [2]. In this paper, the modified satellites-difference TDCP observation equation is mainly studied.

The error state vector $\delta \boldsymbol{X}$ could be selected as follows:

$$\delta \boldsymbol{X}_{15\times 1}=\left[\delta \boldsymbol{r}_{3\times 1}, \delta \boldsymbol{v}_{3\times 1}, \delta \boldsymbol{\theta}_{3\times 1}, \delta \boldsymbol{\omega}^{b}_{ib,3\times 1}, \delta \boldsymbol{f}^{b}_{,3\times 1}\right]^{\mathrm{T}} \tag{1}$$

Where $\delta \boldsymbol{r}_{3\times 1}$ is the difference between the predicted value and true value of the position vector in WGS84 coordinates, and it include latitude error (rad), longitude error (rad) and elevation error (m). $\delta \boldsymbol{v}_{3\times 1}$ is the difference between the predicted value and true value of the velocity vector (m/s) in navigation frame (North-East-Down), $\delta \boldsymbol{\theta}_{3\times 1}$ is misalignment angle error vector between the true navigation frame $\tilde{n}$ and predicted navigation frame n, and it include $\delta\theta_x$, $\delta\theta_y$ and $\delta\theta_z$ (rad). $\delta \boldsymbol{\omega}^{b}_{ib,3\times 1}$ is the difference between the predicted value and true value of the gyro zero deviation error vector (rad/s), $\delta \boldsymbol{f}^{b}_{,3\times 1}$ is the difference between the predicted value and true value of the accelerometer zero deviation error vector (m/s^2).

A low-cost MIMU (STIM300) is used to collect inertial data, and the bias instability of accelerometer noise characteristics is 0.05 mg.

2.2 The Modified TDCP Mathematical Modeling

In the GPS/IMU tightly coupled navigation system, due to the GPS sampling rate which can be up to 10 Hz, the TDCP can be made within 0.1 s. In fact, within the time of 0.1 s, the variation of tropospheric delay error and ionospheric delay error is in the same order as the measurement error of carrier phase. Then the tropospheric and ionospheric delay error can be ignored in the modified TDCP. Therefore, the modified TDCP equation deriving is shown as follows:

$$\begin{aligned}\lambda\varphi^{j}(t_2)-\lambda\varphi^{j}(t_1) &= \left(\boldsymbol{r}^{j}(t_2)\cdot\boldsymbol{e}^{j}(t_2)-\boldsymbol{r}^{j}(t_1)\cdot\boldsymbol{e}^{j}(t_1)\right)\\ &\quad-\left(\boldsymbol{r}_{k}(t_1)\cdot\boldsymbol{e}^{j}(t_2)-\boldsymbol{r}_{k}(t_1)\cdot\boldsymbol{e}^{j}(t_1)\right)\\ &\quad-\left(r_{k}(t_2)-r_{k}(t_1)_{k}\right)\cdot\boldsymbol{e}^{j}(t_2)+c\cdot\delta t_{u}-c\cdot\delta t^{j}_{21}+\Delta\xi^{j}\end{aligned} \tag{2}$$

Where δt_u represents the variation of the clock difference between the ephemeris of a receiver, then the error state $\boldsymbol{x}(t)$ expands from 15 to 16 dimensions. Due to the variation of clock difference which is the same for all satellites, the TDCP equation could eliminate the estimated parameters δt_u for faster calculating by differentiating between satellites.

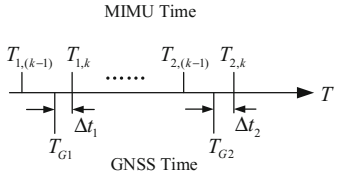

Fig. 1. GNSS and IMU measurement time

Figure 1 shows the GNSS and IMU measurement time not same. Considering that, the observable $y_{\phi 12}^{ji}$ need be modified as follows:

$$\begin{aligned} y_{\phi 12}^{ji} \triangleq \phi_{12}^{ji} - \frac{1}{\lambda}\left\{ \begin{array}{l} \left|\vec{r}^{\,i}\left(T_{G2}^{i}\right) - \left[\vec{r}_{g0}\left(T_{2,k}\right) - \vec{v}_{g0}\left(T_{2,k}\right) \bullet \Delta t_2\right]\right| \\ -\left|\vec{r}^{\,i}\left(T_{G1}^{i}\right) - \left[\vec{r}_{g0}\left(T_{1,k}\right) - \vec{v}_{g0}\left(T_{1,k}\right) \bullet \Delta t_1\right]\right| \end{array} \right\} \\ + \frac{1}{\lambda}\left\{ \begin{array}{l} \left|\vec{r}^{\,j}\left(T_{G2}^{j}\right) - \left[\vec{r}_{g0}\left(T_{2,k}\right) - \vec{v}_{g0}\left(T_{2,k}\right) \bullet \Delta t_2\right]\right| \\ -\left|\vec{r}^{\,j}\left(T_{G1}^{j}\right) - \left[\vec{r}_{g0}\left(T_{1,k}\right) - \vec{v}_{g0}\left(T_{1,k}\right) \bullet \Delta t_1\right]\right| \end{array} \right\} \\ + f_0 \bullet \left[\delta t^i\left(T_{G2}^{i}\right) - \delta t^i\left(T_{G1}^{i}\right)\right] \\ - f_0 \bullet \left[\delta t^j\left(T_{G2}^{j}\right) - \delta t^j\left(T_{G1}^{j}\right)\right] \end{aligned} \tag{3}$$

Where the meanings of related parameters are referred to the literature [10]. Where $\vec{r}_{g0}$ and $\vec{v}_{g0}$ represent the position and speed of GNSS antenna center, they need calculate from the predicted value of MIMU antenna center by compensating the lever arm vector. That can be show as follows:

$$\delta\vec{r}_g\left(T_k\right) = \delta\vec{r}_m\left(T_k\right) + \left[\left(C_b^n\vec{l}^b\right)\times\right] \bullet \delta\vec{\theta} \tag{4}$$

In view of $\delta\vec{x}\left(T_{1,k}\right) = \Phi_{1,2} \bullet \delta\vec{x}\left(T_{2,k}\right)$, where $\Phi_{1,2}$ is the error state transition matrix from time $T_{2,k}$ to time $T_{1,k}$, and $\Phi_{1,2(15\times15)} = \Phi_{2,1(\mathrm{IMU})}^{-1}$.

At last, the Eq. (2) is modified as follows:

$$\begin{aligned} y_{\phi 12}^{ji} = \frac{1}{\lambda} \bullet \left[\left[\vec{e}^{\,ji0}\left(T_{2,k}\right)\right]^T \bullet \mathrm{C}_n^e \bullet A\left(T_{2,k}\right) - \left[\vec{e}^{\,ji0}\left(T_{1,k}\right)\right]^T \bullet \mathrm{C}_n^e \bullet A\left(T_{1,k}\right) \bullet \Phi_{1,2}\right] \\ \bullet \delta\vec{x}\left(T_{2,k}\right) + \varepsilon_{\nabla\Delta\phi}^{ji} \end{aligned} \tag{5}$$

Where $\sigma_{\nabla\Delta\phi} = 0.03\ cycle$, and

$$A_{3\times15} = \begin{bmatrix} R_M + H & 0 & 0 & & & \\ 0 & (R_N + H)\cos B & 0 & 0_{3\times3} & \left(C_b^n\vec{l}^b\right)\times & 0_{3\times6} \\ 0 & 0 & -1 & & & \end{bmatrix} \tag{6}$$

3 Comparative Test

In order to verify the effectiveness and advantages of the modified TDCP/INS tightly coupled navigation method, this paper designs a comparative experiment. The experimental data is about 30 min from the off-road vehicle. In this test, the low-cost MIMU (STIM300) comes from Sensonor Company, and the sampling frequency is 125 Hz. The GNSS receiver is multi-frequency measuring antenna based on nanometer antenna

array LiDAR, which is used to store and process GNSS data of reference station or mobile station. The GNSS data update rate is 10 Hz. The standard data come from the POS system based on high precision laser gyro LD-A15 of Wuhan University. The movement is "Z" shape, and the carrier speed is not exceeding 72 km/h. Figure 2 shows the real route.

The test objects are loosely coupled navigation and traditional tightly coupled navigation from literature [2], and the modified TDCP/INS tightly coupled navigation of this paper. All the three coupled navigation systems use mobile station data for navigation calculation. The traditional tightly coupled navigation system uses the satellites-difference pseudo range and satellites-difference Doppler as the observation information for measurement update. The modified TDCP/INS tightly coupled navigation not only uses the satellites-difference pseudo range and satellites-difference Doppler observation information, but also uses the modified satellites-difference TDCP for measurement update, as Eq. (5).

Fig. 2. Experimental actual route

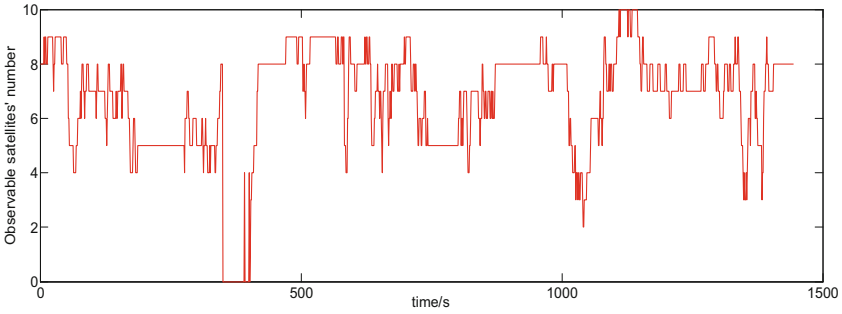

Fig. 3. The number of observable satellites

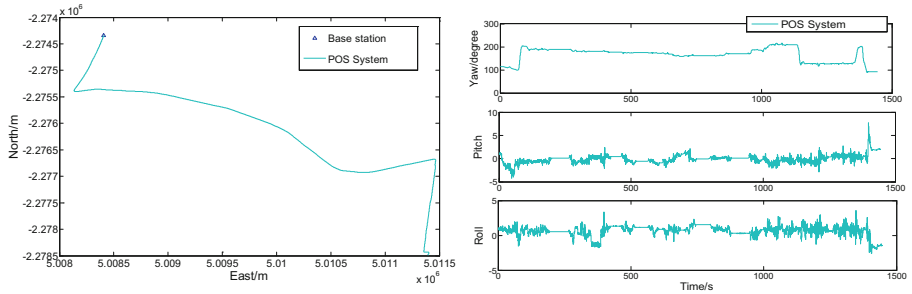

(a) Plane position result of POS system in WGS84 coordinates (b) Attitude result of POS system

Fig. 4. Result benchmarks of integrated navigation (Position, Attitude)

To make the result clear, this paper delete the initial alignment range and the first 800 s data. Then only the later 1500 s data is retained for the result analysis. During this period, the number of satellites is shown in Fig. 3. It is not difficult to find there are two cases of satellites fewer than 4 from 300 s to 1100 s, and longest one lasts about 30 s around 300 s. Figure 4 shows the position and attitude results drawn by the POS system data. Figure 4(a) shows the plane position trajectory is consistent with the real trajectory in Fig. 2. Figure 4(b) shows that the carrier makes three large turns around 70 s, 1200 s and 1400 s.

3.1 Result Analysis of Position Errors

The 3D position error curve Fig. 5(a) shows the position error of the modified TDCP/INS tightly coupled navigation is smoother and smaller than the other methods. Combined with the statistical data in Table 1, it can be seen that the 3D position error mean of the modified TDCP/INS tightly coupled navigation is significantly less than the loosely coupled navigation, slightly less than the traditional tightly coupled navigation. Figure 5(b) shows, in any direction, the position error mean, error standard deviation and RMSE of the modified TDCP/INS tightly coupled navigation are smallest. The positioning accuracy of the modified TDCP/INS tightly coupled navigation is highest, within 1 m.

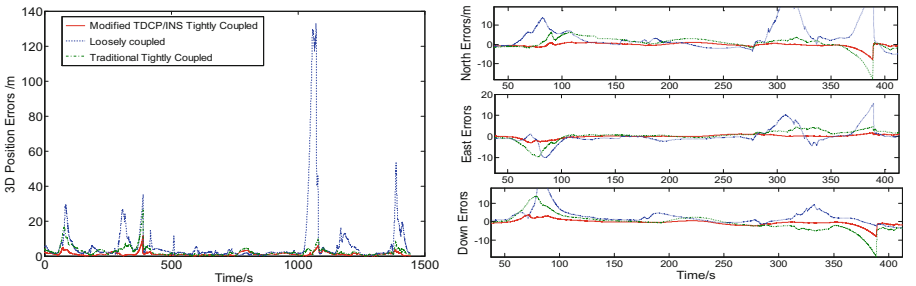

(a) Overall comparison of three-dimensional position errors (b) Partial view of position errors in three directions

Fig. 5. Comparison of position errors from the three integrated navigation methods

Figure 5(b) shows that, in the period of 300 s–400 s, too few observable satellites could lead to the increase of positioning error of the three methods. But the modified TDCP/INS tightly coupled navigation shows better positioning than the others. The blue line shows that loosely coupled navigation has largest positioning error, because its' measurement updating needs the SPP results of satellites, so the number of effective satellites can be not less than 4. To its credit, the tightly coupled navigation does not rely on SPP, even if the number of effective satellites is less than four, can also work.

Figure 4(b) shows, around 70 s, the carrier makes a big turn. Then Fig. 5(b) shows that the positioning error of the modified TDCP/INS tightly coupled navigation method is almost same and close to zero, while the error of loosely combination and traditional tightly coupled navigation is significantly increased.

Table 1. Statistical table of position and velocity error results from the three integrated navigation methods

Form	Direction	Error mean		Error standard deviation		RMSE	
		Position (m)	Velocity (m/s)	Position	Velocity	Position	Velocity
The loosely coupled navigation	North	1.837	−0.0657	9.602	1.04	17.8710	1.5372
	East	1.271	−0.1333	10.51	1.083		
	Down	−0.7186	0.02048	10.55	0.2907		
	3D	6.926	0.9912	16.47	1.175		
The traditional tightly coupled navigation	North	0.01875	−0.0194	2.008	0.2658	3.7140	0.6315
	East	−0.1257	0.03308	1.671	0.459		
	Down	0.04058	0.03865	2.636	0.3383		
	3D	2.492	0.4665	2.754	0.4256		
The modified TDCP/INS tightly coupled navigation	North	−0.3395	−0.0132	0.786	0.1313	1.6188	0.2516
	East	−0.3382	0.00911	0.712	0.1615		
	Down	0.1302	0.01201	1.118	0.14		
	3D	1.207	0.1843	1.079	1.156		

3.2 Result Analysis of Velocity Errors

The 3D velocity error curve Fig. 6(a) shows the modified TDCP/INS tightly coupled navigation has lower velocity error than the other methods. Combined with the statistical data in Table 1, it can be seen that the velocity error mean, error standard deviation and RMSE of the modified TDCP/INS tightly coupled navigation is significantly smaller than these of the loosely coupled navigation, slightly smaller than these of the traditional tightly coupled navigation. The modified TDCP/INS tightly coupled navigation can achieve a speed accuracy level of 1 cm/s in any direction.

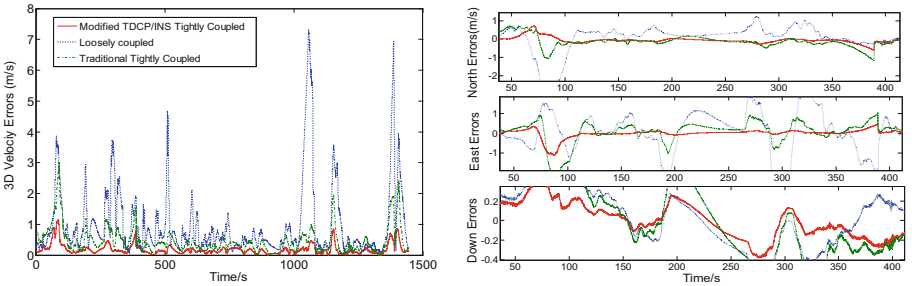

(a) Overall comparison of three-dimensional velocity errors (b) Partial view of velocity errors in three directions

Fig. 6. Comparison of velocity errors from the three integrated navigation methods

Figure 4(a) and (b) shows, in the 300 s to 400 s, the carrier is going eastward. Figure 6(b) shows, in the 300 s to 400 s, the east velocity error changes obviously. These show that the velocity errors of the three methods are increased with the serious reduction of observation satellites. But the modified TDCP/INS tightly coupled navigation can offer smaller change of velocity error than the other methods.

In the turning process around 70 s, Fig. 6(b) shows that the speed errors of the three methods are increasing, but the speed error of the modified TDCP/INS tightly coupled navigation is still significantly smaller than the other methods.

3.3 Result Analysis of Attitude Errors

The attitude error curve Fig. 7 is drawn based on the misalignment angle. The 3D attitude error curve Fig. 7(a) shows, combined with the loosely coupled navigation and traditional tightly coupled navigation, that the attitude error of modified TDCP/INS tightly coupled navigation reduces obviously. From the statistical data in Table 2, it can be seen that the attitude error mean of the modified TDCP/INS tightly coupled navigation is significantly smaller than the other two methods, the 3D attitude error standard deviation and RMSE of the modified TDCP/INS tightly coupled navigation are also smaller than the other two methods. Those also show the three directions attitude accuracy of the modified method can reach 1 degree level far better than other methods.

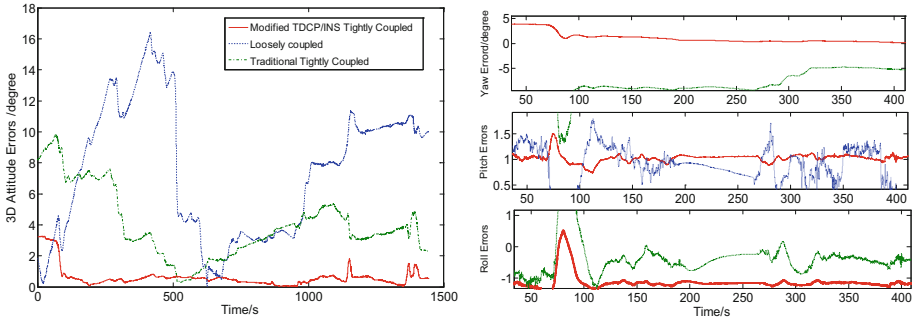

(a) Overall comparison of three-dimensional attitude errors (b) Partial view of attitude errors in three directions

Fig. 7. Comparison of attitude errors from the three integrated navigation methods

The carrier attitude changes mainly displayed in the yaw angle, so the yaw angle error of the coupled navigation changes most. Figure 7(b) shows that the yaw angle error of the modified TDCP/INS tightly coupled navigation is obviously smaller than the other methods. During 300 s to 400 s, when the observable satellite number goes down to less than 4, the yaw Angle error of three methods has little change, but the yaw Angle of the modified TDCP/INS tightly coupled navigation is lowest, the yaw angle error of the loosely coupled navigation is highest.

In the turning process around 70 s, Fig. 7(b) shows that the attitude errors of the three methods are changing, while the modified TDCP/INS tightly coupled navigation changes least, close to zero.

Table 2. Statistical table of attitude errors results from the three integrated navigation methods

Form	Attitude direction	Error MEAN (degree)	Error standard deviation	RMSE
The loosely coupled navigation	Yaw	−10.85	8.546	8.5897
	Pitch	1.11	0.605	
	Roll	2.369	0.623	
	3D attitude	7.463	4.253	
The traditional tightly coupled navigation	Yaw	−1.818	4.537	4.5764
	Pitch	2.628	0.3228	
	Roll	−0.5364	0.5051	
	3D attitude	4.005	2.214	
The modified TDCP/INS tightly coupled navigation	Yaw	0.843	0.8516	0.8927
	Pitch	1.025	0.1945	
	Roll	−1.094	0.1841	
	3D attitude	0.6187	0.6435	

4 Conclusions

In order to further improve the accuracy and calculation speed of the tightly coupled navigation based on TDCP, a modified TDCP/INS tightly coupled navigation method is proposed in this paper, and a modified TDCP equation is derived. Then the system doesn't have to calculate the state matrix multiplication of velocity integral, and the mathematical modeling is easier than before. In order to verify the effectiveness of the modified method, this paper designs a comparative test for loosely coupled navigation, traditional tightly coupled navigation, and modified TDCP/INS tightly coupled navigation. The test results show that the attitude accuracy of the modified TDCP/INS tightly coupled navigation is obviously superior to the other two methods. The position and speed accuracy of the modified method is obviously better than the loosely coupled navigation, slightly better than the traditional tightly coupled navigation. These results

verify the effectiveness of the modified method in this paper. At the same time, the test results also show that the modified TDCP/INS tightly coupled navigation has obvious advantages, when the number of visible satellites is less than 4, or the attitude of carrier changes significantly. Therefore, the proposed method of this paper is suitable for Real-time navigation for vehicles and small autonomous carrier. This method has extremely high application value and potential, especially in the environment with poor satellite signal (such as urban streets, canyons and woods), or when the attitude of the carrier changes greatly. It can bring better position, speed and attitude accuracy for the real-time coupled navigation system.

In order to ensure the accuracy and reliability of the modified TDCP/INS tightly coupled navigation, it is necessary to detect and eliminate the gross errors in the next step.

Acknowledgements. The successful completion of this paper cannot be achieved without the help of my teacher Wu Jie, thanks for his hard education to me. The first author is also grateful to teachers from the GPS center of Wuhan University for their instructive help in test site and the POS system.

References

1. Zhao Y (2017) Applying time - differenced carrier phase in nondifferential GPS/IMU tightly coupled navigation systems to improve the positioning performance. IEEE Trans Veh Technol 66(2):992–1003
2. Wu J, An X, Zheng W (2015) Technology of Positioning and Navigation for Vehicle. National Defense Industry Press, Beijing, pp 135–152
3. Ding W (2008) Optimal integration of GPS with inertial sensors: modelling and implementation. M.S. thesis, Faculty Engineering, University New South Wales, Sydney, NSW, Australia
4. Chen Q, Niu X, Zhang Q, Cheng Y (2015) Railway track irregularity measuring by GNSS/INS integration. Navig: J Inst Navig 62(1):83–93
5. Wang D (2014) Research on the real-time information fusion algorithm for GNSS/MIMU integrated navigation system. In: Proceedings of 2014 IEEE Chinese guidance, navigation and control conference
6. Han S (2010) A novel initial alignment scheme for low-cost INS aided by GPS for land vehicle applications. J Navig 63(4):663–680
7. Wendel J, Meister O, Schlaile C (2006) An integrated GPS/MEMS-IMU navigation system for an autonomous helicopter. Aerosp Sci Technol 10(6):527–533
8. Shin E-H (2001) Accuracy improvement of low cost INS/GPS for land applications. Master Degree thesis, UCGE Reports Number 20156, University of Calgary, Canada, pp 35–46
9. Wang D, Chen L, Wu J (2016) Novel in-flight coarse alignment of low-cost strapdown inertial navigation system for unmanned aerial vehicle applications. Trans JSASS 59(1):1–8 (in press)
10. Li C (2017) Research on GNSS/SINS Tightly Coupled Integration Approach with Receiver Autonomous Integrity Monitoring. College of Aerospace Science and Engineering, National University of Defense Technology

An Image-Guided Autonomous Navigation System for Multi-rotor UAVs

Weiqi Liu, Danping Zou(✉), Daniele Sartori, Ling Pei, and Wenxian Yu

Shanghai Key Laboratory of Navigation and Location-Based Services, School of Electronic Information and Electrical Engineering, Shanghai Jiao Tong University, Shanghai 200240, China
dpzou@sjtu.edu.cn

Abstract. Multi-rotor UAVs have been highly valued in both military and civilian applications for its low cost and excellent maneuverability in recent year. Most multi-rotor UAVs rely on Global Navigation Satellite System (GNSS) for navigation and the commands from ground station for control. However, there are many environments with difficulty in receiving GNSS signals or remote control commands. To deal with such cases, we implement an autonomous navigation system based on visual information. The proposed navigation system is divided into two parts - state estimations and UAV control. The first part is the state estimation, which is responsible for estimating the position by fusing the data from an IMU and a forward-looking camera and the velocity from the optical flow of the image sequence captured by a downward-looking camera. In addition, an Extended Kalman Filter (EKF) is applied to fuse the information from both sides. The second part is UAV control. We introduce a velocity control loop in traditional PID system to obtain the desired acceleration that is then converted to desired attitude. During the task of object searching, we propose to use the pixel difference between the image center and the object center to control the UAV. We conducted several experiments in both simulation and real environment to evaluate our algorithms. The results show that our system is feasible to complete tasks relying solely on onboard computing in autonomous mode.

Keywords: State estimation · Extended Kalman Filter · UAV control · Autonomous navigation system

1 Introduction

Multi-rotor UAV is a kind of unmanned helicopter capable of vertical taking-off and landing without the need of runway and it has been widely used in many areas for its excellent characteristics, including its simple structure, low cost and so on. Nowadays, most professional products rely on Global Navigation Satellite System (GNSS) for navigation in outdoor environments, but there are many environments with difficulty in receiving GNSS signals. In addition, the UAVs also rely heavily on user's involvement by manually sending remote control signals to complete the missions, although in most applications, they are supposed to perform the pre-set missions automatically, even

J. Sun et al. (Eds.): CSNC 2019, LNEE 563, pp. 513–526, 2019.
https://doi.org/10.1007/978-981-13-7759-4_45

independent of external position systems (e.g. GNSS signals or motion capture systems). Due to that, in this paper, we present an autonomous navigation system composing of a state estimator and a controller that enables a vision-based vehicle to fulfil tasks without any external aids.

The methods used to localize and navigate for flying robotics can be simply classified into two types, using GNSS signals or using vision-based algorithms in GNSS-denied environments. To the best of our knowledge, vision-based techniques, whether they are vision-only [1–3] or vision-inertial [4, 5], are subject to the lighting condition and texture of the scene. Therefore, in this paper, we use the extended Kalman filter [6, 7] to fuse multiple-source navigation information to provide an accuracy and stable state estimation for the control system in case one of the positioning method fails. We estimate the position of the drone with an IMU and a forward-looking camera and calculate the velocity from the optical flow of the video stream captured by a downward-looking camera. All the measurements are used to update the EKF state and covariance.

As for control part, the inner-loop control of UAVs refers to the design of the attitude control algorithms according to its dynamic model [8, 9]. By aligning the current attitude with desired attitude, the vehicle can execute different flight maneuvers. We look at the outer loop flight control merely and it is reasonable because there are many excellent autopilots able to execute the inner control. Based on the classic PID control algorithm, we introduce a velocity control loop into the controller to obtain desired accelerations which is converted to the desired attitude with the dynamic model of the drone. In addition, when performing the tasks of object searching, we make use of the pixel difference between the image center and the object center to calculate the desired attitude. This is also one of the contributions of this work to UAV control algorithm.

The remainder of this paper is organized as follows. Section 2 introduces the method to estimate pose of drone in weak GNSS environment. Section 3 firstly introduces the dynamical model of UAVs, and then describes the proposed control algorithm. Section 4 shows and discusses the experimental results. Finally, we draw the conclusions of this paper.

2 State Estimation

To facilitate the description of our state estimation and controller algorithms, we clarify the notations used in this paper firstly. We express the vectors of different coordinate system as ${}^{x}e$, where $x = b$ or w denotes body and world coordinate systems respectively. $E(\cdot)$ denotes the mean operation and $a \otimes b$ describing the cross multiplication of two vectors a and b. Furthermore, we describe the position and velocity and acceleration of the drone in the world coordinate system as $P = [x \quad y \quad z]^{\mathrm{T}}$, $V = [v_x \quad v_y \quad v_z]^{\mathrm{T}}$ and $a = [a_x \quad a_y \quad a_z]^{\mathrm{T}}$. $R = [r_1 \quad r_2 \quad r_3]$ are used to represent the attitude while

$W = [\, w_1 \quad w_2 \quad w_3 \,]^{\mathrm{T}}$ indicates the angular speed. Note that vectors are expressed in the world coordinate system if not specified.

2.1 State Estimator Based on Extended Kalman Filter

It is challenge to estimate the motion state of the flying robotics accurately if relying solely on a single sensor system. To obtain the optimal state estimation, integrating the multi-sensor data is the most intuitive method. Since the Extended Kalman Filter can deal with the problem of state estimation with multi-variable and multi-sensor and its computational and storage are much smaller than the optimized methods, which makes it suitable for UAV platforms with limited computing power. By assuming that the noises and states meet the Gaussian noise requirements and are independent of each other, the mathematical forms of propagating the EKF state and covariance is derived as [10]

$$
\begin{aligned}
&\widehat{x}(t+1|t+1) = \widehat{x}(t+1|t) + \mathrm{K}(t+1)\varepsilon(t+1) \\
&\widehat{x}(t+1|t) = \Phi\widehat{x}(t|t) \\
&\varepsilon(t+1) = y(t+1) - \mathrm{H}\widehat{x}(t+1|t) \\
&\mathrm{K}(t+1) = \mathrm{P}(t+1|t)\mathrm{H}^{T}[\mathrm{H}P(t+1|t)\mathrm{H}^{T} + \mathrm{R}]^{-1} \\
&\mathrm{P}(t+1|t) = \Phi\mathrm{P}(t|t)\Phi^{T} + \mathrm{Q} \\
&\mathrm{P}(t+1|t+1) = [I_n - \mathrm{K}(t+1)\mathrm{H}]\mathrm{P}(t+1|t) \\
&\widehat{x}(0|0) = \mu_0 \\
&\mathrm{P}(0|0) = p_0
\end{aligned}
\tag{1}
$$

where μ_0, p_0 are the initial state and initial covariance, Q, R denote the noise matrix of prediction and measurement, respectively, H is measurement matrix, Φ is state-transition matrix and P is covariance matrix.

2.1.1 Height Compensation by the Attitude of UAVs

We make use of a LiDAR Lite v3 range sensor to estimate the height and velocity in vertical direction. The principle of the infra-red sensor can be write as $2s = ct_s$, s is the measured value, c indicates the speed of light, t_s is the time difference between the moment of sending the light waves and that moment of receiving the reflection. While executing flight maneuvers, the LiDAR sensor will tilt along with the body of vehicle, causing the measured value deviating from the truth value, as shown in Fig. 1. Therefore, we make compensation for the vertical height. Let $H = [\, 0 \quad 0 \quad \bar{z} \,]$ be the measurement vector from LiDAR sensor and R be the attitude observed by the IMU (see Sect. 2.1.3), then the rectified vector H_{rec} can be derived from the attitude and the measurement vector.

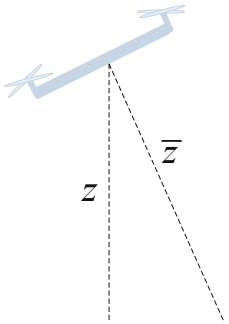

Fig. 1. Effects of the UAVs' attitude on LiDAR measurement

$$H_{rec} = RH = [0 \quad 0 \quad z] \tag{2}$$

2.1.2 Position Estimation

The EKF state is denoted by the vector $\widehat{x}$

$$\widehat{x} = [\, x \quad y \quad z \quad v_x \quad v_y \quad v_z \,] \tag{3}$$

Since the velocity of the vehicle can be approximately treated as a constant within a small time interval, we use the smooth-motion model to obtain a priori estimation, in the meantime, it will introduce errors n because of the low possibility of maintaining a uniform motion strictly for the drone.

$$n_{6\times1} = \left[0.5a \cdot dt^2 \quad a \cdot dt\right]^{\mathrm{T}} \tag{4}$$

Q is the covariance matrix of the noise vector n and can be computed as

$$Q = E(nn^T) \cdot I_{6\times6} \tag{5}$$

From the motion law of constant motion, the state transition matrix Φ can be constructed as

$$\Phi = \begin{bmatrix} 1 & 0 & 0 & dt & 0 & 0 \\ 0 & 1 & 0 & 0 & dt & 0 \\ 0 & 0 & 1 & 0 & 0 & dt \\ 0 & 0 & 0 & 1 & 0 & 0 \\ 0 & 0 & 0 & 0 & 1 & 0 \\ 0 & 0 & 0 & 0 & 0 & 1 \end{bmatrix}$$

dt is the time interval between two consecutive frames and I is an unit matrix. Note that we have obtained the EKF prediction state and covariance, then the update step should follow.

The visual information from the forward-looking camera and the inertial information from IMU are aligned by interpolation. After that the method introduced in [4] is implemented to estimate the position and velocity of the drone, which is applied to get the corrected state and covariance after aligning with the world coordinate system. To simplify the subsequent description, we take the outputs for observed value from sensor A, with a measurement matrix H_A. Meanwhile, we make use of the sum of absolute difference (SAD) block matching algorithm to compute the optical flow from the image sequence captured by a downward-looking camera. The horizontal velocity expressed in the body coordinate system is then calculated from the optical flow by

$$^{b}V_{xy} = \frac{Flow_{xy}z}{f} \tag{6}$$

f denotes the focal length. Similarity to sensor A, we have to transform the velocity from body frame to world frame using the current attitude R and consider the velocity as measurement information from sensor B, with a measurement matrix H_B.

The method in [4] requires a robust procedure for estimation initialization and then takes the initial point as original, which makes the measurement in vertical direction not equal to the altitude of the drone with respect to ground. On the other hand, the optical flow is solely calculated in the horizontal direction. Therefore, the data from sensor A and sensor B are both used to update the position and velocity in horizontal direction but not in vertical. We use the measurements of LiDAR sensor to correct the vertical estimated. The measurement matrices of the three sensors are designed as

$$H_A = \begin{bmatrix} 1 & 0 & 0 & 0 & 0 & 0 \\ 0 & 1 & 0 & 0 & 0 & 0 \\ 0 & 0 & 0 & 1 & 0 & 0 \\ 0 & 0 & 0 & 0 & 1 & 0 \end{bmatrix}$$

$$H_B = \begin{bmatrix} 0 & 0 & 0 & 1 & 0 & 0 \\ 0 & 0 & 0 & 0 & 1 & 0 \end{bmatrix}$$

$$H_{lidar} = \begin{bmatrix} 0 & 0 & 1 & 0 & 0 & 0 \end{bmatrix}$$

2.1.3 Attitude Estimation

The attitude estimator on the PX4 [11] fuses the gyroscope and acceleration measurements to get the current estimation and as described in [11], the accuracy and frequency of it satisfy the requirements of control system. Thus, we directly use the attitude estimates from the PX4 to control the drone and compensate in height (described in Sect. 2.1.1).

3 UAV Control

3.1 Dynamical Model of UAVs

We build the dynamical model of UAVs under several assumptions: the quadrotor is a rigid body which means its center of gravity is consistent with the geometric center and the quadrotor subjects to the thrusts from four motors and the gravity, ignoring the influence of air resistance. Noted that the collective motor thrust is always parallel to the normal vector of the rotor plane. The model of quadrotor is illustrated in Fig. 2.

Firstly, we use $W = \{{}^{w}e_x, {}^{w}e_y, {}^{w}e_z\}$ to represent the world coordinate frame in right-handed system and $B = \{{}^{b}e_x, {}^{b}e_y, {}^{b}e_z\}$ to represent the body frame in right-handed system. The transformation from world to body frame can be described as

$$[{}^{b}e_x\ {}^{b}e_y\ {}^{b}e_z] = R \cdot [{}^{w}e_x\ {}^{w}e_y\ {}^{w}e_z] \tag{7}$$

The mathematic equations of dynamic model of a quadrotor are derived from the total force:

$$T = \sum_{i=1}^{4} T_i = m^{b}a \tag{8}$$

$$\dot{V} = g^{w}e_z - \frac{T}{m} R^{w}e_z \tag{9}$$

Similarly, we establish the attitude dynamic model in the body coordinate system as

$$\dot{W} = J^{-1}\tau - J^{-1}({}^{b}W \times J^{b}W) \tag{10}$$

where T is the collective thrust and m is the mass of the quadrotor, ${}^{b}a$ is the acceleration generated by rotor thrusts, $g = -9.8\,\mathrm{m/s^2}$ is the acceleration of gravity, $\tau \triangleq [\tau_x \quad \tau_y \quad \tau_z]$ denotes the torque and $J \in \mathbb{R}^{3\times3}$ indicates the moment of inertia matrix of the quadrotor.

According to the law of kinematics, we get the following equations

$$\dot{P} = V \tag{11}$$

$$\dot{R} = R \cdot \Lambda({}^{b}W) \tag{12}$$

the skew-symmetric matrix $\Lambda(W)$ is defined as:

$$\Lambda(W) \triangleq \begin{bmatrix} 0 & -w_3 & w_2 \\ w_3 & 0 & w_1 \\ -w_2 & w_1 & 0 \end{bmatrix}$$

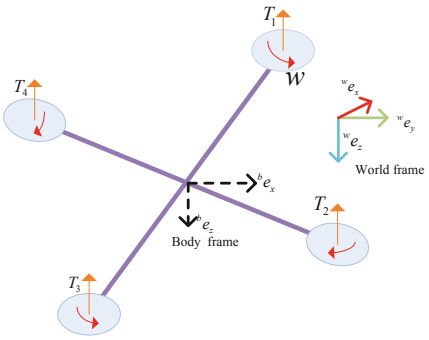

Fig. 2. Model of the quadrotor

3.2 Position Control of UAVs

Our position controller takes a reference position $P_{des} = [x_{des} \quad y_{des} \quad z_{des}]$ and an estimated position $P = [x \quad y \quad z]$ as inputs, then outputs the desired attitude, which is finally sent to the inner loop control. The structure is illustrated in Fig. 3(a) and outputs are computed as

$$u = k_p E(t) + k_i \int_0^t E(\tau)d\tau + k_d \dot{E}(t) \tag{13}$$

where k_p is the proportional gain, k_i is the integral gain and k_d is the derivative gain. A high k_p would have the effect of reducing the rise time but would cause oscillation. k_i term can reduce the steady state error caused by the noises in feedback measurements. k_d term decreases oscillations and yields large influence when the error changes rapidly.

3.2.1 Position-Velocity Controller

The controller described above computes the desired attitude in position loop directly. It usually lets the drone to fly with frequent velocity changes and not so easy to tune a precise control performance. Previous work [12] has shown that introducing a velocity loop into the controller before attitude controller can improve the control precision and stability. The velocity control loop takes a desired velocity as input, which is obtained from the position control loop described in Sect. 2.1.2. Unlike in [12], we use the output of velocity loop for the desired acceleration a_{des} instead of the desired attitude R_{des} and compute the desired attitude from the desired acceleration and the dynamic model of quadrotor. The position-velocity control structure is illustrated in Fig. 3(b).

Noted that the collective motor thrusts have to be parallel to the normal vector of the rotor plane, which forces the direction of the desired acceleration to be same with the desired body z axis, namely, ${}^be_{z,des} = D(a_{des})$. Furthermore, to get full desired attitude, the world frame should rotate around its z axis by the remaining heading error θ, by which a intermediate coordinate system m is derived. The projection of the desired body z axis in world frame has to lie in the plane spanned by ${}^me_x$ and ${}^we_z$. Since that, ${}^be_{x,des}$ should be perpendicular to both ${}^me_y$ and ${}^be_{z,des}$, we can construct the desired body x and y axis and then the desired attitude, respectively, as

$$^{b}e_{x,des} = D(^{m}e_{y} \otimes {}^{b}e_{z,des}) \tag{14}$$

$$^{b}e_{y,des} = D(^{b}e_{x,des} \otimes {}^{b}e_{z,des}) \tag{15}$$

$$R_{des} = \begin{bmatrix} ^{b}e_{x,des} & ^{b}e_{y,des} & ^{b}e_{z,des} \end{bmatrix} \tag{16}$$

3.2.2 Image-Guided Controller

The controller described in Sect. 3.2.1 improves the control performance with both precision and stability and can be used to command the drone when there is no strict requirement in control accuracy. In the cases that require high control accuracy, such as landing in designated area or flying through narrow gaps, a more accurate controller is required. Here, we propose an image-guided control method (Table 1).

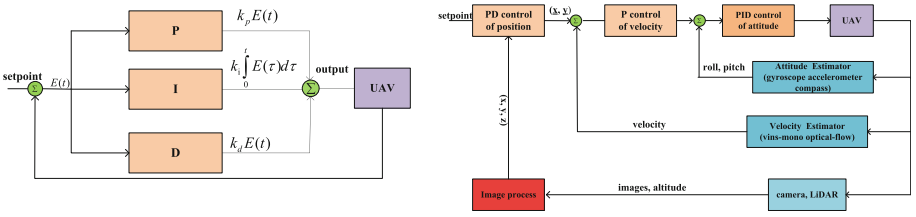

(a) PID controller (b) Position-velocity PID controller

Fig. 3. UAV controller

Suppose the transformation between the center of the camera and quadrotor is calibrated as long as the camera is installed. Therefore, we can obtain the rotation $\tilde{R}$ and translation $\tilde{t}=[\Delta x \quad \Delta y \quad \Delta z]^{T}$ in advance. Without loss of generality, let the rotation matrix $\tilde{R}$ be an identity matrix, which can be easily satisfied by a designed installation. The coordinates $p_{uav}(u, v)$ of the quadrotor in the image coordinate system is calculated by

$$p_{uav}(u,v) = \begin{bmatrix} u \\ v \\ 1 \end{bmatrix} = \frac{1}{\Delta z} \begin{bmatrix} f_x & 0 & c_x \\ 0 & f_y & c_y \\ 0 & 0 & 1 \end{bmatrix} \begin{bmatrix} \Delta x \\ \Delta y \\ \Delta z \end{bmatrix} = \frac{1}{\Delta z} K\tilde{t} \tag{17}$$

where K is the camera intrinsic matrix.

When the target is detected, the image processing module outputs the coordinates of the target center in the image coordinate system, represented as $p_{object}(\bar{u}, \bar{v})$. From the $p_{uav}(u, v)$ and $p_{object}(\bar{u}, \bar{v})$, we can compute the desired attitude using (13) but set the integral gain to zero. If the desired attitude is within a reasonable range, we update the command sent to attitude controller. An example of the image-guided controller is show in Fig. 4. In Fig. 4(a), the quadrotor detects the circular gate and switches the control mode from position-velocity to image-guided mode. As shown in Fig. 4(d), the quadrotor has reached the desired pose and can fly through the circular gate with the maximum safe distance of the drone to the edge of the gate.

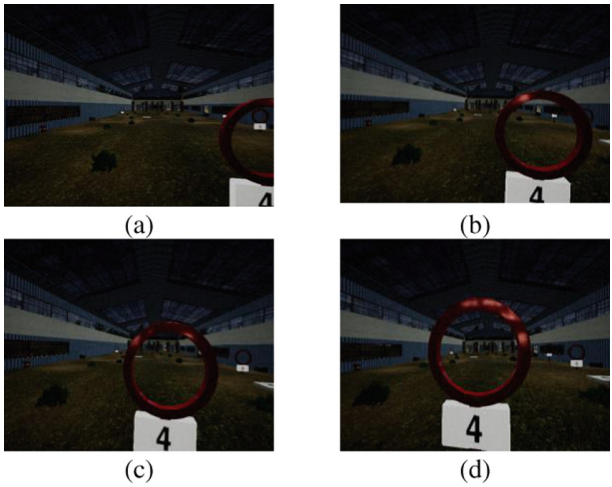

Fig. 4. Example of image-guided UAV controller

Table 1. Image-guided UAV control algorithm

Algorithm：Image-guided UAV control algorithm

Input: image sequence I_i , odometry measures U_i
Output: reference accelerations for each pose

```
    UavMassCenter ⟵ getUavMassCenter ()
    InitController()

for t = 1: n do
  // object detected
  if Obj ⟵ ObjectDetect(I_i)
   ObjectCenter ⟵ getObjectCenter(I_i)
   Error ⟵ ComputeError(UavMassCenter, ObjectCenter )
   ReferenceAcc ⟵ PIDcontroller(Error)
  end
  else
  UAVstate ⟵ getOdometryMeasurement()
  UAVReferenceStae ⟵ getReferenceState()
  ErrorXYZ ⟵
      ComputeError(UAVReferenceStae.pos, UAVstate.pos)
  ErrorVxVyVz ⟵ Comput-
    eError(UAVReferenceStae.vel,PIDcontroller(ErrorXYZ))

     ReferenceAcc ⟵ PIDcontroller(ErrorVxVyVz)
    end
end
```

4 Experiments

This section describes the experiments we designed to evaluate our state estimation and control algorithms, followed by the analysis of experimental results.

4.1 Experimental Platform

We built our UAV platform using the airframe of DJI F550 and the matched motors and propellers. PX4 autopilot is used for attitude stabilization control. To estimate the state of the drone as described in Sect. 2, we make use of a forward-looking camera, Intel Realsense ZR300, which consists of an IMU and a fish-eye camera. The range sensor LiDAR lite v3 as well as the downward-looking color camera with 640*480 resolution are installed in the bottom of the drone. State estimation and controlling are done on an onboard computer (Intel NUC) where the Ubuntu 16.04 LTS system is installed. The framework of our system is based on the Robot Operating System (ROS). The platform is illustrated in Fig. 5.

Fig. 5. The six-rotor UAV platform used in the experiments

In addition, we evaluate our autonomous navigation system in a simulation environment by completing a competition task from the 2nd National Intelligent Perception of UAVs Competition. In the competition, a drone is required to identify serval numbered landing fields, automatically land on and take off in turn according to the recognized numbers and fly through the circular gates as fast as possible. The competition organizing committee built the simulation platform based on Airsim simulator. They added noises to the camera and IMU sensors in order to be more realistic and exposed APIs to retrieve data from barometer, IMU, a downward-looking camera as well as a forward-looking RGB-D camera with measurement distance up to 5 m. Moreover, a control API that takes the desired attitude and thrust as inputs is also available.

4.2 State Estimation and Control Performance Evaluation

To evaluate the performance of the state estimator, we conducted experiments in a small room equipped with a Vicon system, which is used for ground truth. Figure 6(a) shows the position estimates in the X-Y axis direction (corresponding to the North and East directions, respectively). The root-mean-square error (RMSE) is $[0.2125, 0.2703]$ m, satisfying the requirements of the positioning accuracy in most applications. 4.2 (b) shows the speed estimates in the X-Y axis direction. Compared with the velocity directly obtained from the optical flow, the filtered value is closer to the true value and smoother with a small noise variance. Since we introduce the velocity loop into our controller, if the estimate is noisy, it could greatly weaken the stability of the control and even ruins the control completely. Similarly, Fig. 7 shows the position and velocity estimates in vertical direction and the RMSE of height is 0.0704 m.

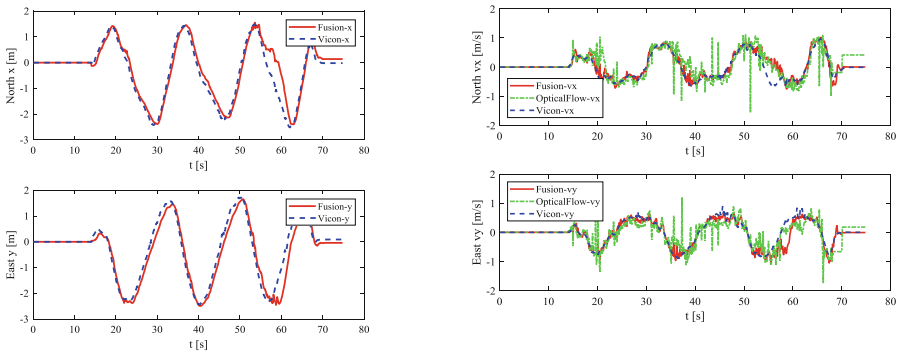

(a) Position estimates result (b) Velocity estimates result

Fig. 6. Estimates in X-Y direction from vision pipeline

Due to the size limitation in indoor environment, we perform only the hover and set-points tracking tests using position-velocity controller. In simulation environment, we demonstrate that our autonomous navigation system enables the drone to fulfill tasks described in Sect. 4.1. Figure 8(a) shows the result of the hover test. The point with coordinates (0, 0, 0.7) (in meter) is the target point. The hover trajectory is in a circle with a radius of 0.07 m centered at the target point. That is to say, the accuracy of the controller can reach the level of centimeter, which meets the accuracy requirement of control for most applications. In addition, it should be noted that an initial thrust value is needed in vertical direction for balancing gravity and it is normalized to 0.36 from the hover experiment for our drone.

Figure 8(b) shows the result of tracking several reference points. The coordinates are $(-0.2, -0.3), (-0.1, -1), (-0.8, -1.4), (-1.6, -0.55), (-1, -0.2), (-1.5, 0.0)$.

Similarly, the drone can reach at these points accurately.

Figure 9(a) shows the global 2D map of simulation environment fused with images acquired by the downward-looking camera, details are in [13]. As it is shown, there are seven numbered landing fields and four red circular gates in the simulation environment.

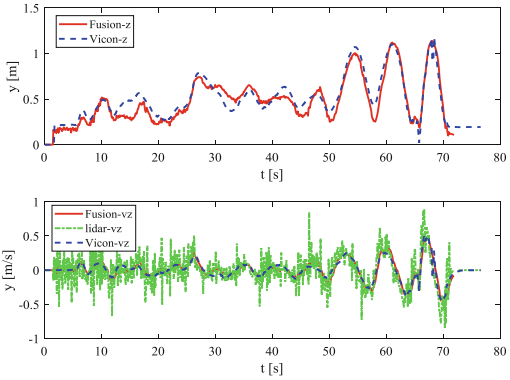

Fig. 7. State estimates in Z direction from LiDAR+ EKF

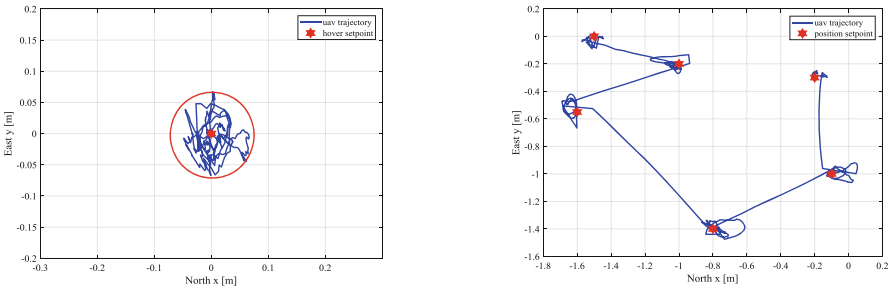

(a) hover trajectory (b) Setpoints following trajectory

Fig. 8. UAV trajectory

Figure 9(b) shows the trajectory when the drone performing the competition tasks in the simulation environment automatically. Our quadrotor finished the tasks within 684 s, ranking the first among all teams, proving that the proposed system is feasible to complete complex tasks relying solely on onboard computing in autonomous mode.

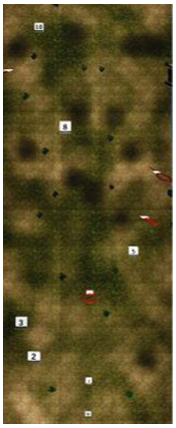

(a) 2D map of the experimental scene.

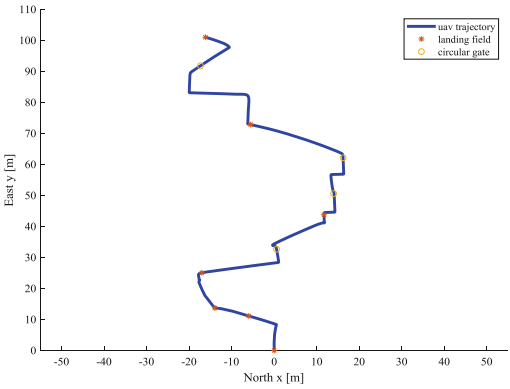

(b) The trajectory of our quadrotor when performing tasks

Fig. 9. Autonomous navigation test

5 Conclusion

In this paper, firstly, we make use of the Extended Kalman Filter to fuse the information from different sensors to estimate the UAVs' state in GNSS signals denied environment. Secondly, the dynamic model of quadrotor as well as the PID control algorithm are introduced. We add a velocity control loop in the control system using the velocity feedback from the filter, which improves the performance of position control of the Multi-rotor UAV. Moreover, as for the applications requiring high precision of control, we propose an image-guided control algorithm, whose main idea is using the pixel difference between the image center and the object center to control the UAV. Lastly, we conduct several experiments and analyze the results. The results demonstrate that the performance of the state estimator and control algorithms meets the requirements of autonomous tasks.

Acknowledgement. This work was mainly supported by the Adv. Res. Proj. of EDD (61405180104), partially by the National Sci. & Tec. Major Program (2017ZX01041101-003), NSFC (61873163), and Shanghai Sci. & Tec. Comm. (grant 17DZ1100803).

References

1. Mur-Artal R, Montiel JMM, Tardos JD (2015) ORB-SLAM: a versatile and accurate monocular SLAM system. IEEE Trans Rob 31(5):1147–1163
2. Forster C, Pizzoli M, Scaramuzza D (2014) SVO: fast semi-direct monocular visual odometry. In: 2014 IEEE international conference on robotics and automation (ICRA), pp 15–22. IEEE
3. Engel J, Schöps T, Cremers D (2014) LSD-SLAM: large-scale direct monocular SLAM. In: European Conference on Computer Vision, pp 834–849. Springer, Cham

4. Qin T, Li P, Shen S (2018) VINS-Mono: a robust and versatile monocular visual-inertial state estimator. IEEE Trans Rob 34(4):1004–1020
5. Leutenegger S, Lynen S, Bosse M, Siegwart R, Furgale P (2015) Keyframe-based visual–inertial odometry using nonlinear optimization. Int J Rob Res 34(3):314–334
6. Bloesch M, Burri M, Omari S, Hutter M, Siegwart R (2017) Iterated extended Kalman filter based visual-inertial odometry using direct photometric feedback. Int J Rob Res 36 (10):1053–1072
7. Sun K, Mohta K, Pfrommer B, Watterson M, Liu S, Mulgaonkar Y, Taylor CJ, Kumar V (2018) Robust stereo visual inertial odometry for fast autonomous flight. IEEE Rob Autom Lett 3(2):965–972
8. Faessler M, Franchi A, Scaramuzza D (2018) Differential flatness of quadrotor dynamics subject to rotor drag for accurate tracking of high-speed trajectories. IEEE Robot Autom Lett 3(2):620–626
9. Faessler M, Fontana F, Forster C, Scaramuzza D (2015) Automatic re-initialization and failure recovery for aggressive flight with a monocular vision-based quadrotor. In: IEEE international conference on robotics and automation (ICRA), pp 1722–1729. IEEE
10. Zili D, Xin W, Yuan G (2007) Modeling and Estimator. Beijing
11. PX4 Dev Team (2017) Open Source for Drones-PX4 Pro Open Source Autopilot. https://px4.io/
12. Zhe S et al (2015) Vision-based pose control and autonomous return for an unmanned aerial vehicle
13. Ruochen Y et al (2018) Vision-based navigation and sensing system for an unmanned aerial vehicle. In: China high resolution earth observation conference (CHREOC)

An Efficient Simulation Platform for Testing and Validating Autonomous Navigation Algorithms for Multi-rotor UAVs Based on Unreal Engine

Xinglong Yang, Danping Zou(✉), Ling Pei, Daniele Sartori, and Wenxian Yu

Shanghai Key Laboratory of Navigation and Location-Based Services, School of Electronic Information and Electrical Engineering, Shanghai Jiao Tong University, Shanghai 200240, China
{yangxinglong0319,dpzou}@sjtu.edu.cn

Abstract. Developing autonomous navigation algorithms without using extern positioning signals is the key to allow Multi-rotor UAVs to fly in complex environments where the GNSS signals are week or invalid. However, it is an expensive and time consuming process to develop and test autonomous navigation algorithms with real UAV platforms in the real world. It becomes even more difficult when developing autonomous navigation algorithms based on deep learning techniques, since it requires to collect a large amount of annotated training data. To address such problem, we developed a simulation platform based on Unreal Engine, providing physically and visually realistic simulations, to validate and test navigation algorithms for Multi-rotor UAVs.

Keywords: Autonomous navigation · Multi-rotor UAVs · Simulation platform · Unreal Engine

1 Introduction

Multi-rotor UAVs have been widely used and developed rapidly in recent years due to its simple structure, low cost and excellent maneuverability, especially in the fields of investigation and rescue [1], irrigated farmland [2], bridge and circuit maintenance [3], and aerial photography. Typically, UAVs use global positioning system (GPS) for autonomous navigation and positioning. However, GPS requires an outdoor environment, which limits the application of UAVs. At present, autonomous navigation algorithms based on visual information and depth information has become more and more popular for UAVs. Autonomous flight of rotorcraft UAVs can be realized by using the visual simultaneous localization and mapping (SLAM) algorithms. This method is generally simple in construction and low in cost, but requires to be extensively tested before real application.

J. Sun et al. (Eds.): CSNC 2019, LNEE 563, pp. 527–539, 2019.
https://doi.org/10.1007/978-981-13-7759-4_46

One approach to test those autonomous navigation algorithms is fly the real drone in a real-world environment. However it is a time-consuming task with extremely low efficiency. The situation becomes even worse when machine learning based methods are developed, since it requires to collect a large amount of annotated data for training. To address above mentioned issues, we developed a simulation platform based on the Unreal game engine for verification and testing autonomous navigation algorithms for UAVs. The platform is able to simulate the physical motion of the quadcopter and generate the data of on-board sensors in real time, while providing complex virtual scenarios with high fidelity.

To build a high-fidelity virtual environment, firstly, we employ an accurate dynamic model of the multi-rotor UAV. Secondly, we model typical complex environments in the real world, such as roads, trees, buildings and electricity towers, etc., and include high-quality rendering with fine details, such as lighting, reflection, and so on. Currently, simulation platforms commonly used in the robot field include Gazebo [4], Hector [5], RotorS [6], and jMavSim [7]. All of them provide rich functions such as sensor models, 3D scene modelling, mechanical simulation, robot mobility simulation, etc., but none of them are able to provide large-scale, complex and visually rich simulation environments of high fidelity. In our simulation platform, we create a highly realistic and complex simulation environment based on the Unreal Engine, and develop a more accurate dynamic model and sensor model based on Microsoft's open source AirSim [8]. Finally, we expose APIs that are convenient for developers to quickly implement and test algorithms. Since those APIs are independent of real hardwires, the users can easily migrate their implementation of algorithms from the simulation platform to the real drone platform.

2 Platform Architecture

The entry point of the simulation platform is the drone flight control system (flight controller), which also serves as the connection point between the simulation platform and the real drone. The simulation platform is designed on the principle of modularity. The core modules can be divided into environment model, drone model, physics engine module, sensor model and API layer. The structure diagram is shown in Fig. 1.

In a real UAV system, the flight controller calculate the current state of the drone from the sensors data after receiving input data from various sensors. At the same time, the flight controller also receives the target state and calculate the difference between the target state and the current state estimated from the sensor data. The difference is converted into PWM signals that are directly used to regulate the motor speed of each blade, which drives the drone to turn, climb, subduction and roll, finally makes the drone to reach the target state steadily. Popular flight controller firmware includes PX4 [9], ROSFlight [10] and related flight controller firmware developed by DJI Company. Since the flight controller of DJI Company has not been open sourced, we chose the open source PX4 flight controller, which has been used by a large number of users.

In the simulation environment, after receiving the sensors data from the platform, the flight controller calculates the power signal and sends it to the drone model. The drone model will take the friction, gravity, air resistance and other factors into account

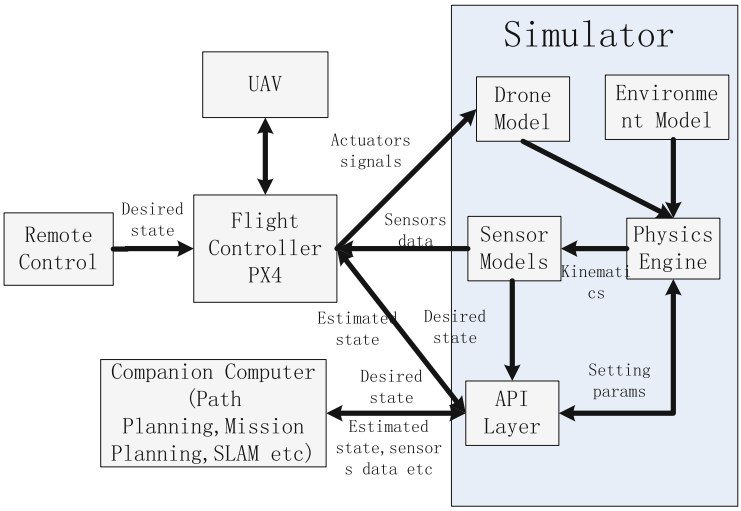

Fig. 1. The structure diagram of simulation platform

to calculate the thrust and torque that the drone can generate under the current power signal. Finally, the physics engine uses the thrust and torque to calculate the position and state of the drone at the next moment. The environmental model in the simulation platform also provides the physical data such as barometric pressure, GPS and magnetometer signals. After the sensor module, the optimized noise model will be added, and finally used as the input data of the flight controller.

There are two ways to input the target position and target attitude. The user can use the remote control to input through the model of hardware in the loop simulation, or input it through an external computation board. The computation board runs the autonomous navigation and high-level control algorithms, such as such as SLAM algorithms, path planning, and collision avoidance. Those algorithms acquire the sensor data of the simulation environment and the current state of the drone, and sends control commands to the virtual drone through the platform APIs.

The APIs provided in our platform is kept as close as to those provided in the real UAV platforms, which enables the algorithm implementation and testing to be seamlessly switched between the simulation and the real world. Since most existing SLAM algorithms are running under the Linux platform, while the Unreal Engine works best under the Windows platform, we add RPC network communication at the API layer, to make the algorithm and the simulation platform to be able to run on different platforms, and let the speed of data transmission meet the real-time requirements of the SLAM algorithms.

Next, we present the detail of each module.

2.1 Environment Model

In the simulation platform, we design virtual 3D scenes with great texture details and make them as close as possible to the real world scenes. Meanwhile those scenes are optimized as much as possible to meet the requirements of real-time rendering. In the real world, drones are exposed to various physical phenomena at all times. Our environment model of the simulation platform focuses on four main simulation models: magnetic field, gravity field, air pressure and visual scene.

2.1.1 Air Pressure and Density

The model of air pressure and density are mainly based on international standards. There are many different layers in the atmosphere and each layer has its own characteristics. The relationship between altitude and air pressure is therefore segmented into different layers. The international standard atmospheric pressure model of 1976 [12] is used below 51 km. Another model [13] is used between 51 km–86 km. From the standard temperature T and the standard pressure P, we can calculate Air density ρ in each model:

$$\rho = \frac{P}{R \bullet T} \tag{2.1}$$

Where R is the fixed constant of the gas. According to the specific environmental information in the simulation scenario, we set it to 8314.3 J (mol.k).

2.1.2 Magnetic Field

Accurately simulating the magnetic field of a complex object like the Earth is a computationally expensive task. For the real-time requirements, we adopted a simplified version of the tilt dipole model [14]. We assume that the earth is a dipole sphere, ignoring the first-order term of the magnetic field estimation derived from the spherical geometry. This model allows us to simulate changes in the magnetic field. Given the geographic latitude θ, longitude ϕ, and altitude h (relative to the Earth's surface), we first calculate the magnetic latitude θ_m:

$$\cos\theta_m = \cos\theta\cos\theta^0 + \sin\theta\sin\theta^0\cos(\phi - \phi^0) \tag{2.2}$$

Where θ^0, ϕ^0 represent the latitude and longitude of the magnetic north pole. The total intensity of the magnetic field can be expressed as:

$$|B| = B_0\left(\frac{R_e}{R_e + h}\right)^3\sqrt{1 + 3\cos^2\theta_m} \tag{2.3}$$

B_0 represents the average value of the magnetic field at the equator and R_e represents the radius of the Earth. Next, we use α, β to define the dip:

$$\tan\alpha = 2\cot\theta_m$$

$$\sin\beta = \begin{cases} \sin(\phi - \phi^0)\frac{\cos\theta^0}{\sin\theta_m}, \cos\theta_m > \sin\theta\sin\theta^0 \\ cos(\phi - \phi^0)\frac{\cos\theta^0}{\sin\theta_m}, \text{others} \end{cases} \tag{2.4}$$

Finally, we can calculate the magnetic field strength in the horizontal direction (H), and also the field strengths in the latitude (X) and longitude (Y) directions, as well as the vertical direction (Z):

$$\begin{aligned} H &= |B|\cos\alpha \quad Z = |B|\sin\alpha \\ X &= H\cos\alpha \quad Y = H\sin\alpha \end{aligned} \tag{2.5}$$

2.1.3 Gravity

In existing simulation platforms, the gravity is represented by a constant value, and the error for doing this is negligible when the simulation platform is used for ground and low-altitude applications. However, considering that the drone may fly at high altitude, we adopt the gravity model proposed by GRACE [11], using the binomial theorem of Newton's law of gravity, ignoring the higher power, and approximating the gravitational acceleration g at height h:

$$\mathrm{g} = g_0 \bullet \frac{R_e^2}{(R_e + h)^2} \approx g_0 \bullet (1 - 2\frac{h}{R_e}) \tag{2.6}$$

Which R_e represents the radius of the Earth and g_0 represents the constant gravity of the Earth's surface.

2.1.4 Virtual Scenes

Many autonomous navigation algorithms rely on visual information. It therefore requires rich and complex visual scenes with high fidelity provided by the simulation platform. Aiming at the specific scenes currently targeted by real drone applications, we construct texture-rich indoor and outdoor scenes, including trees, buildings, and electricity towers, as well as sophisticated lighting conditions, to mimic reflection, shadows happened in real life. We use the Unreal engine to render those scenes and the realistic pictures generated in real time is shown in Fig. 2.

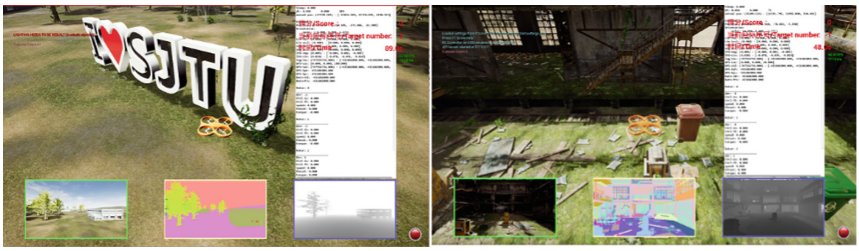

Fig. 2. Example diagrams of indoor and outdoor scenarios

Considering that it is necessary for machine learning to collect data under different conditions, we randomly generate 300 different settings by randomly arranging different objects and changing their appearances. The setting can be configured by setting one variable in the configuration file, which is convenient for developers to choose the specific scene.

2.2 Sensor Model

The sensor models of the simulation platform are mainly constructed according to the sensors that are usually seen on the real drone. Those sensors include GNSS receivers, accelerometers, magnetometers, gyroscopes, barometers and cameras. For each sensor we add one noise model. The sensor model and the environmental model are independent of each other. All sensors model are declared and implemented in relevant C++ files, where old sensors can be replaced and new sensors can be added.

2.2.1 Gyroscope and Accelerometer

The gyroscopes and accelerometers are the core components of an inertial measurement unit (IMU). We model these by adding white noise and bias drift over time to the ground truth. For gyroscope, when given the true angular velocity in the body coordinate system, the specific formula ω is:

$$\omega^{out} = \omega + \eta_a + b_t \quad \eta_a \sim N(0, r_a)$$
$$b_t = b_{t-1} + \eta_b \quad \eta_b \sim N\left(0, \mathrm{b}_0 \sqrt{\frac{dt}{t_a}}\right) \tag{2.7}$$

The ω^{out} represents output values of the gyroscope, parameters r_a, deviations b_0, and the time constant for drift deviations t_a can be obtained from the gyroscope manufacturer's datasheet. Accelerometers are calculated in a similar way, we obtain the real linear acceleration in the world coordinate system from the simulation platform. After subtracting the gravity, the result is converted into the coordinate system of the body. Finally, the white noise and drift deviation are added. The highest frequency of IMU data acquisition can be set to 1000 Hz by the API.

2.2.2 Magnetometer

According to the description in Sect. 2.1.2, we know that if latitude and longitude are known, we can calculate the component of the magnetic field strength in each component direction. Similarly, we can calculate the magnetic field strength at the current time by transforming the coordinate system. Finally, we also add white noise to the data to produce the final outputs. The upper limit of the output frequency of the magnetometer data is set to 500 Hz in our APIs.

2.2.3 Barometer

According to the description in Sect. 2.1.1, the air pressure output in the environmental model is the actual pressure on the ground, but the real barometer measurement has accumulated errors. We use a Markov process to simulate the error and set the deviation error at the current moment as b_k. The accumulative error model can be expressed as:

$$b_{k+1} == w \bullet b_k + (1 - w) \bullet \eta$$
$$w = e^{-\frac{dt}{\tau}} \eta \bullet N\left(0, s^2\right) \tag{2.8}$$

Where τ represents a time constant. We set it to 1 h in our simulation platform. η represents a standard Gaussian distribution [15]. The mean is zero and the variance is 0.0135. Based on the above noise model and the true value of the barometric pressure value, we can calculate the output value h of the barometer:

$$h = \frac{T_0}{a}\left[\left(\frac{p}{p_0}\right)^{-\left(\frac{a \bullet R}{g}\right)} - 1\right] \tag{2.9}$$

Where T_0 is the constant 15/C, a is $-6.5 * 10^{-3}$, g is gravity, R is the gas constant, p_0 is the current sea level pressure value, p is the barometric pressure value added the noise.

2.2.4 Global Positioning System (GPS)

The GPS data in the simulation platform is converted according to the coordinate system of the sphere. We set the current latitude and longitude according to the origin in the simulation platform. The GPS coordinates of the origin in the simulation platform is set to be 31° north latitude, 121° east longitude, and 10 m altitude. The coordinates in the simulation platform coordinate system are converted into latitude and longitude according to the conversion relationship of the sphere. At the same time, our GPS model simulates the transmission delay (200 ms). The sensor data update frequency in the API interface is as fast as 10 Hz. Considering the difference of latitude and longitude, we adopted different Gaussian noise models for longitude and latitude. The mean values of longitude and latitude directions were all zero, among which, the variance in longitude direction was 0.000004, and the error in dimension direction was 0.0000047. The attenuation rate was parameterized separately by first-order low-pass filter.

2.2.5 Camera

In the simulation platform, the process of the virtual camera to capture images is very different from that of the real camera. The real camera will always encounter interference, noise and other situations. In order to make the picture rendered by the 3D engine fit the real situation, we add random noise and horizontal line distortion noise to the acquired picture. The noise model is set to: the noise speed of random noise is set to

0.16 (up to 1, indicating full fluctuation, the lowest is 0, indicating no fluctuation). For the overall display effect of the image, we set a noise value for every 1000 pixels. Horizontal noise is divided into three types, horizontal line area noise, horizontal line fluctuation noise, and horizontal bump distortion. Horizontal bump distortion is to increase the flicker, ghost and horizontal bulge of the image. We set the intensity to 0.08 (the highest intensity is 1, the lowest intensity is 0), the convex effect affects the upper and lower pixels; the horizontal noise is mainly set to how many pixels are affected on the horizontal line and how many lines of the image are affected, we set the parameters to 64 pixels per line, a total of 240 lines; horizontal line fluctuation noise, we set the intensity of the noise fluctuation to 0.002 (the highest intensity is 1, the lowest intensity is 0). At the same time, we open the setting interface of the above parameters to the script file of the scene, which is convenient for developers to set up autonomously. The result of effect is shown in Fig. 3:

Fig. 3. Contrast the original image (left) with the image added noise (right)

In addition, visual SLAM algorithms require camera calibration parameters. To simulate the calibration process, we placed a calibration board in the scene, as shown in Fig. 4. The developer can obtain the camera's internal and external parameters by collecting images of the calibration board in the simulation environment. In addition, the camera's real parameters are provided along with the scene, which is available through the API and the developers can use them to compare the results of their own calibration.

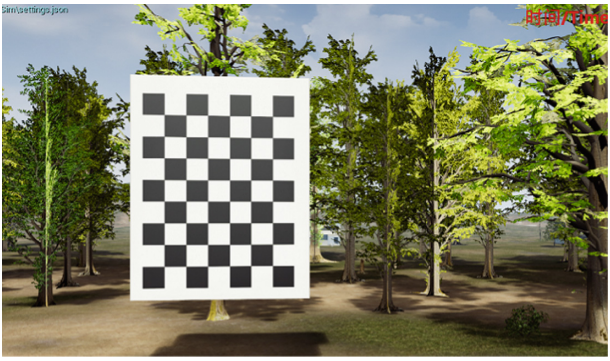

Fig. 4. Calibration board

We placed a front camera and a bottom camera on the drone. Each camera can capture both color images and depth images. In order to mimic the performance of the real-world depth sensor, we limit the range of the captured depth image to 5 m.

3 Experimental Results

The simulation platform is designed for the fast implementing and testing the visual navigation algorithms of UAV. In the experimental stage, we first compare the sensor in the simulation platform with the real sensor. Next, we realize the indoor project from the second Smart UAV IntelliSensing Technical Competition [16] in the simulation platform. In the project, the drone needs to fly autonomously in indoor scenes, to land on the parking pads and pass through obstacle circles in the correct order by recognizing the printed numbers. After that, the drone starts to search for the printed ArUco codes in the fake woods, and finally returns to the starting point. We use the simulation platform to refine and optimize the relevant recognition and location algorithms and migrate the codes to the real drone platform in the end.

3.1 Sensor Model Comparison

Our hardware platform for sensors model comparison is PixhawkV2.4.8 [17]. In this hardware platform, the IMU model is MPU9250, the barometer model is MS5611, and the magnetometer model is LSM303D. The GPS signal is not included in comparison as we are focusing on visual navigation algorithms.

The comparison test results of the accelerometer and the gyroscope are shown in Table 1. The gyroscope error unit is rad^2/s^2 the accelerometer error unit m^2/s^2.

Table 1. Sensor comparison experiment results

sensors	simulation	real
gyroscope	$3.12e^{-7}$	$5.43e^{-7}$
accelerometer (static)	$1.5e^{-4}$	$1.7e^{-4}$
accelerometer (move)	$2.6e^{-3}$	5.19

As can be seen from the above table, the large difference of accelerometer may be caused by the vibration effect during the movement of the drone. As we can see, in the static state, the noise model of virtual sensors is similar to that of real sensors. But the noise model differs much from that of real world because of the vibrations when the drone is flying. We leave this issue to be addressed in the future.

In the experiment of comparison of noise models for the magnetometer and the barometer, the actions of the UAV in the simulation platform are kept consistent with those of real drones equipped with the PX4 flight controller. Firstly, we rotated the drone 90° on the ground and rotated it four times, and rotated it back to its original state, for comparing the changes of the magnetometer data. Secondly, the drone took off and stayed at an altitude of two meters. We then compared the changes of the barometer data during this process. In this process, we found that the trend and variance of the simulation platform are basically the same as the real hardware platform.

3.2 SLAM Algorithm Implementation

The virtual scene for the projects in The Second Smart UAV IntelliSensing Technical Competition is shown in Fig. 5, where the aprons, obstacle circles can be seen.

Fig. 5. Indoor simulation scene

In the simulation platform, the texture of visual scene is rich and many feature points are available. We use the monocular ORB-SLAM [18] algorithm for positioning. The effect diagram of ORB-SLAM is shown in Fig. 6:

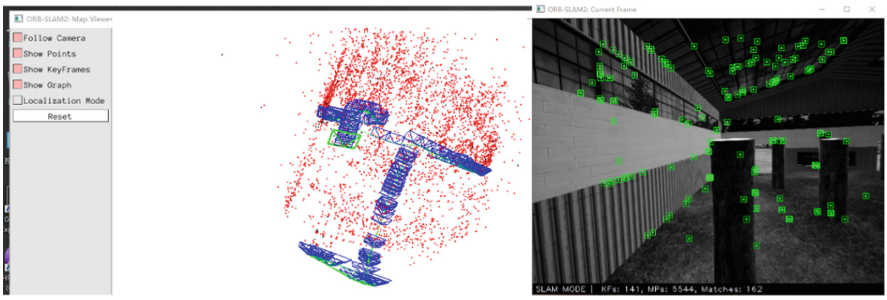

Fig. 6. Results of ORB-SLAM

With reliable visual positioning, we add the recognition and detection algorithms, and successfully complete the project task. At last, the trajectory of the UAV in the simulation platform is shown in Fig. 7.

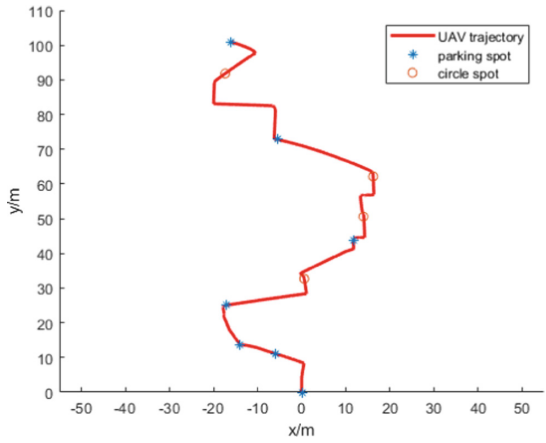

Fig. 7. UAV trajectory map

The * mark indicates the real position of the apron, and the o mark indicates the actual position of the obstacle circle. The red trajectory is the flight path of the drone successfully completing the tasks of autonomous landing and passing through circles.

3.3 Algorithm Migration

In the second Smart UAV IntelliSensing Technical Competition, the venue of the real drone competition is shown in Fig. 8:

Fig. 8. Offline venue

It can be seen that the entire competition venue is very close to the simulation platform. The recognition and detection algorithms and the positioning algorithms can still be used after a simple modification according to the real environment.

We use the DJI F550 and PixhawkV2.4.8 flight controller to build our quadrotor. The on-board sensors include the front and bottom color cameras, liteLiarV3 module. The layout of the hardware platform is basically the same as the drone in the simulation platform.

The trained networks and optimized algorithms in the simulation environment can be quickly migrated to real drones. It hence reduces the probability of drone damage and injury during debugging the algorithms in real platforms.

4 Conclusion and Future Work

Developing autonomous navigation algorithms requires a lot of tasks of debugging and testing. It is an expensive and time consuming process to do such tasks with real UAV platforms in the real world. To address such issue, we present a simulation platform based on Unreal Engine to quickly validate and test navigation algorithms for Multi-rotor UAVs. The platform can simulate the movement of UAV and the generation of sensor data in real time, and provide realistic and complex virtual scenes for algorithm verification and testing.

In future work, we will further improve sensor models and expand the types of flight controllers in the simulation platform. At present, the types of simulation platform sensors are mainly for commercial drones. We will increase the types of sensors, such as the Intel RealSense camera, the ZED binocular camera and so on, which are commonly used by autonomous drones. At the same time, we will further enrich the visual scenes and build visual scenes to meet special tasks. We will update and maintain the simulation platform on the website regularly (http://drone.sjtu.edu.cn/contest/).

Acknowledgements. This work was mainly supported by the Adv. Res. Proj. of EDD (61405180104), partially by the National Sci. & Tec. Major Program (2017ZX01041101-003), NSFC (61873163), and Shanghai Sci. & Tec. Comm. (grant 17DZ1100803).

References

1. Li Y, Xu W, Wu W (2011) Application research on aviation remote sensing UAV for disaster monitoring. J Catastrophol 26(1):138–143
2. Jiangtao J, Feifei H, Zhitao H (2013) The application of quad-rotor UAV in farmland information acquisition. J Agric Mechanization 35(2):1–4
3. Zhang Y, Yuan X, Fang Y et al (2017) UAV low altitude photogrammetry for power line inspection
4. Koenig N, Howard A (2004) Design and use paradigms for gazebo, an open-source multi-robot simulator. In: 2004 Proceedings of IEEE/RSJ international conference on intelligent robots and systems, IROS 2004, vol 3. IEEE, pp 2149–2154
5. Meyer J, Sendobry A, Kohlbrecher S, Klin-gauf U, Von Stryk O (2012) Comprehensive simulation of quadrotor UAVs using ROS and Gazebo. In: International conference on simulation, modeling, and programming for autonomous robots. Springer, Heidelberg, pp 400–411
6. Quigley M, Conley K, Gerkey B, Faust J, Foote T, Leibs J, Wheeler R, Ng AY (2009) ROS: an open-source robot operating system. In: ICRA workshop on open source software, Kobe, vol 3, p 5
7. Furrer F, Burri M, Achtelik M, Siegwart R (2016) Rotorsa modular Gazebo MAV simulator framework. In: Robot operating system (ROS). Springer, Heidelberg, pp 595–625
8. Shah S, Dey D, Lovett C, Kapoor A (2017) AirSim: high-fidelity visual and physical simulation for autonomous vehicles. In: Field and service robotics
9. Meier L, Tanskanen P, Fraundorfer F, Pollefeys M (2011) Pixhawk: a system for autonomous flight using onboard computer vision. In: ICRA. IEEE, pp 2992–2997
10. Jackson J, Ellingson G, McLain T (2016) Rosflight: a lightweight, inexpensive MAV research and development tool. In: ICUAS, pp 758–762. https://doi.org/10.1109/icuas.2016.7502584
11. Tapley B, Ries J, Bettadpur S, Chambers D, Cheng M, Condi F, Poole S (2007) The GGM03 mean earth gravity model from grace. In: American Geophysical Union, G42A-03
12. Stull R (2015) Practical Meteorology: An Algebra-based Survey of Atmospheric Science. University of British Columbia
13. Braeunig R (2014) Atmospheric models. http://www.braeunig.us/space/atmmodel.htm
14. Lanza R, Meloni A (2006) The Earth's Magnetism: An Introduction for Geologists. Springer, Heidelberg (2006)
15. Burch D, Burch T (2014) Mariner's Pressure Atlas: Worldwide Mean Sea Level Pressures and Standard Deviations for Weather Analysis. Starpath School of Navigation
16. http://drone.sjtu.edu.cn/contest/?p=891
17. Babushkin A Jmavsim. https://pixhawk.org/dev/hil/jmavsim
18. Mur-Artal R, Tardós JD (2016) ORB-SLAM2: an open-source SLAM system for monocular, stereo and RGB-D cameras. ArXiv preprint arXiv:1610.06475

Anti-interference and Anti-spoofing Technology

GNSS Anti-jamming Receiving Technology Based on Batch Processing According to CDMA Signals Intensity

Rong Shi(✉) and Yu Du

Science and Technology on Electronic Information Control Laboratory, Chengdu, China
jasminewyx@sina.com

Abstract. The code division multiple access (CDMA) is widely used in GNSS. Although its spectrum utilization efficiency is high, serious multiple access interference is caused by strong deception jamming signals, which make it difficult for navigation receivers to capture real satellite navigation signals with weak power. So the anti-deception receiving and processing are very impracticable. In order to solve these problems, the batch processing method based on CDMA signals intensity is proposed. Firstly, the strong signals are captured and tracked, and their waveforms are reconstructed by the de-spread and demodulated results of each strong signal. Then the strong signals are eliminated by subtracting the reconstructed signals out of the mixed ones. Through above processing, the satellite navigation receiver can reduce the additional suppression effect caused by deception signals with strong power, and find out the real satellite navigation signals which are concealed by the deception ones. It provides more complete measurement data for the deception signals identification and elimination, as well as the pseudo-range measurement and positioning solution based on the real navigation satellite signals. The validity and practicability of the above method is verified by simulations. It provides a new technique approach for GNSS anti-jamming and anti-deception processing.

Keywords: Satellite navigation · Code division multi access · Interference from multi access · Navigation deception jamming · Anti-jamming receiving · Signal reconstruction · Deception signal recognition · Batch processing according to intensity

1 Introduction

GPS, BD and Galileo are typical CDMA systems in the four major GNSS. Although the combination of FDMA and CDMA is used in GLONASS now, it is gradually evolving to the CDMA main system for modern advancement and signal interoperability [1, 2]. There are many advantages in the CDMA system, such as high spectrum efficiency and high communication capacity by different pseudo-codes, and so on. But its cross correlation interference is a major inherent shortcoming. This often occurs in the third generation terrestrial mobile communication systems, also known as multiple access interference of CDMA signals [3]. In order to diminish interference among

J. Sun et al. (Eds.): CSNC 2019, LNEE 563, pp. 543–552, 2019.
https://doi.org/10.1007/978-981-13-7759-4_47

CDMA signals, many restrictions are introduced in the overall design for navigation systems. For example, the beamforming of the satellite transmitting antenna makes the gain of the main beam centre lower and the edge gain slightly higher, like a crescent shape. In this way, the intensity of received signals can be approximately equal when the satellite signals reach the earth surface. On the other hand, the transmitting power of each satellite must be strictly limited within a certain range to avoid interfering with each other. Because of above measures, the normal PNT services are guaranteed in GNSS. But under the deception jamming conditions, whether it is self-produced or repeated, the deception signals have the same pseudo-code sequences as the navigation satellites and they also become legitimate CDMA signal components in GNSS [4–6]. At this time, the intensity of deception signals is much greater than that of normal navigation satellite signal. It makes the strong jamming signal suppress the weak normal signal in CDMA system. The navigation receiver can not capture and track the real satellite navigation signal with weak power according to the traditional procedure [7]. In this paper, the anti-jamming receiving technology based on batch processing according to CDMA signals intensity is proposed. The capture and tracking of CDMA navigation signals are completed in two batches. The satellite navigation receiver can eliminate the additional suppression effect caused by the deception jamming signals with strong power, and discover the real navigation satellite signals which are concealed by jamming. It will benefit for the recognition and elimination of deception jamming, as well as the pseudo range measurement and positioning calculation based on the real navigation satellite signals.

2 CDMA Multiple Access Interference in Satellite Navigation System

There are N signals with different pseudo-codes, which complex baseband components are denoted as $S_i(t)$, $i = 1, 2, \cdots, N$. The N signals are completely orthogonal to each other in the ideal state. That is to say, the cross correlation, $R_{i,j}(t)$, between any two signals is zero.

$$R_{i,j}(t) = \int_T S_i(t) \cdot S_j^*(t) dt = 0 \tag{1}$$

Where "*" represents the conjugate operation, and T is the cross correlation integral time. In practical applications, Eq. (1) is only approximate, which means that the signals emitted by navigation satellites have no ideal cross correlation characteristics with zero, $R_{i,j}(t) \approx 0$. For example, the C/A code of GPA is a GOLD code. The peak cross correlation level difference between any two codes is −24 dB when the Doppler frequency is zero. With the increase of Doppler frequency, the cross correlation level becomes higher sometimes. It is only −21.1 dB in the worst period with 1 kHz Doppler frequency difference. The maximum cross correlation peaks are summarized in the Table 1 for all 32 C/A codes of GPS [8]. The unit in the Table 1 is dB, and the Doppler frequency difference delta increment is 1 kHz.

Table 1. Maximum cross correlation peak of C/A codes with various Doppler frequency differences

Probability	△ = 1 kHz	△ = 2 kHz	△ = 3 kHz	△ = 4 kHz	△ = 5 kHz
0.1%	−21.1	−21.1	−21.6	−21.1	−21.9
2%	−24.2	−24.2	−24.2	−24.2	−24.2
10%	−26.4	−26.4	−26.4	−26.4	−26.4
40%	−30.4	−30.4	−30.4	−30.4	−30.4

If in the whole CDMA signal set, there is a very strong signal, $S_{big}(t)$, which power is at least 30 dB stronger than weak signals, $S_{small}(t)$, the cross correlation level between other weak signals and this strong one will be much higher than the auto-correlation level of weak signals, as shown below.

$$\left\| \int_T S_{big}(t) \cdot S^*_{small}(t) dt \right\| > \int_T \|S_{small}(t)\|^2 dt \tag{2}$$

So in the capture process, it is always impossible to capture weak signals effectively. This is the typical effect of strong signal suppressing weak one in satellite navigation systems using CDMA. Whether it is self-generated or repeated, the deception jamming signals have the same pseudo-code sequences as the real navigation satellite signal. Therefore, the deception signal will enter the subsequent correlation processing for signal capture and tracking. The transmission power of the jammer is very stronger. Moreover, the jamming distance is much shorter than that between the navigation satellite and the receivers. So the deception jamming signal intensity is usually much higher than that of the real one. In this way, the deception jamming signals have the suppression effect on the normal satellite navigation signals, so that the receivers are forced to capture and track the deception signals and neglect the real ones.

3 Batch Processing Method for Signals

(1) Capture, tracking and waveform reconstruction for the first batch of signals

The real navigation satellite signals and the deception jamming signals are received together to form the mixture signal, which complex baseband component is denoted by $H_1(t)$. It is processed for capture and tracking the pseudo-code phase, carrier frequency and phase. It is obvious that the strong signals with high power, $S_{g,k}(t)$, $k = 1, 2, \cdots, M$, can be captured and tracked firstly, where M is the number of the first batch of processing signals. The demodulation data of these signals entering the pseudo-code tracking stage are denoted by $b_k(t)$ respectively. Through the code sequence $PN_k(t)$ by the code tracking loop, the Doppler frequency offset f_k outputted by the frequency-locked loop and the phase value ϕ_k outputted by the phase-locked loop, the signal can be reconstructed as follows, denoted by $\hat{S}_{g,k}(t)$.

$$\hat{S}_{g,k}(t) = A_k \cdot b_k(t) \cdot PN_k(t) \cdot \exp(j(2\pi f_k t + \phi_k)) \tag{3}$$

Where A_k is the estimation of the signal amplitude. It is determined by the correlation peak of the capture and tracking loop.

(2) The second batch of signals processing after the strong signal elimination

After reconstructing M strong signals, these signals are removed out of the mixed signal $H_1(t)$, and the output signal $H_2(t)$ is expressed as follows.

$$H_2(t) = H_1(t) - \sum_{k=1}^{M} \hat{S}_{g,k}(t) \tag{4}$$

Then $H_2(t)$ goes into correlative receiving channels for capture and tracking of pseudo-code phase, carrier frequency and phase, so that the receiver can find the relatively weak navigation satellite signals, denoted by $S_{s,l}(t)$, $l = 1, 2, \cdots, L$, where L is the number of the second tracking signals.

There is a step delay between signal reconstruction and strong signal cancellation in the above two batches of capture and tracking processes. Because complete signal reconstruction requires bit values after de-spreading and demodulation, the signal can be accurately reconstructed only after a datum bit is fully received. For example, the modulation rate of the navigation message is 50 bps for GPS and one bit datum can be demodulated every 20 ms. Due to the different distances of the navigation satellites or Deception Jammers and the receiver, the flip of the navigation message bits in each signal does not occur synchronously. In order to ensure the reconstruction of all the received strong signals, the interval of 25–40 ms is necessary between the first batch and the second batch. This can ensure high probability to reconstruct and cancel strong signals effectively and completely.

(3) Analysis on the degree of strong signal cancellation

In the theory, if a signal is reconstructed completely and accurately, the signal can be entirely eliminated from the mixed signal. However, in practical engineering applications, the parameters estimation accuracy for the strong signal determines the accuracy of the signal reconstruction. After the receiver captures and tracks a strong signal $S_{g,k}(t)$, due to the relative motion between the platform and the jammer, the carrier phase ϕ_k becomes the parameter which has a great influence on signal reconstruction. The parameter estimation error is denoted by $\Delta\zeta_k$. The residual δ_k of the reconstructed signal due to this error is expressed as follows.

$$\delta_k = \int_{t\in\tau} [A_k(\sin(t + \Delta\zeta_k) - \sin(t))]^2 dt/\tau \approx A_k^2(1 - \cos\Delta\zeta_k) \tag{5}$$

Where τ is integral time. Theoretically, when the carrier phase estimation error $\Delta\zeta_k = 0$, the strong signal can be completely cancelled. When $\Delta\zeta_k \neq 0$, there will be

some residual signals due to the signal reconstruction error. So the cancellation ratio γ_k (unit dB) is expressed by the following formula.

$$\gamma_k = 10 \cdot \log_{10}\left(\frac{A_k^2}{\delta_k}\right) = -10 \cdot \log_{10}(1 - \cos\Delta\zeta_k) \tag{6}$$

The relationship between the phase estimation error of the reconstructed signal and the cancellation ratio is shown in Fig. 1. It can be seen that the cancellation ratio could reach more than 20 dB, when $\Delta\zeta_k < 8^o$.

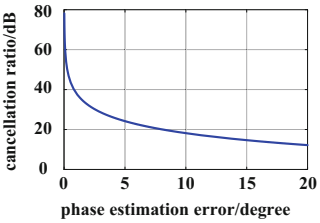

Fig. 1. Relationship between phase estimation error and cancellation ratio

4 Detection and Elimination of Deception Jamming Signals Based on Intensity

In satellite navigation applications, a typical beam pattern of a receiver antenna is shown in Fig. 2, where the gain (unit dB) is normalized.

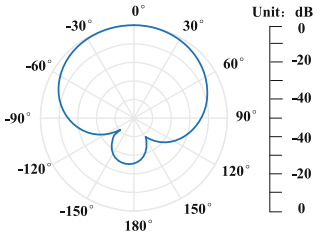

Fig. 2. A typical beam pattern of a satellite navigation receiver antenna

In Fig. 2, the gain difference in the whole angle range is about 9 dB, when the receiving elevation angle is higher than 15°. Despite this difference, the beam patterns of the transmitting antennas for various navigation satellites have been specially shaped during the overall design of the GNSS. The gain of the central main beam is low and the gain of edge is high so as to compensate the attenuation during the low elevation angle receiving [2]. On the other hand, the power transmitted by each navigation satellite is basically equal. For example, in GPS the power level of C/A code signal

received by ground-based navigation receivers at L1 frequency is generally between −127 dBm and −130 dBm, and the power level of P code signal received at L1 frequency is between −130 dBm and −133 dBm. Moreover, the signal power of each navigation satellite is max at the initial stage of the satellites operation. With the increase of the satellites working period, the signal power will be reduced year by year, but the maximum of reduction will not exceed 8 dB. If the intensity of the navigation satellite signal is measured within a week or a month, it is usually relatively stable.

So the signal intensity is accurately measured in the receiving process for the satellite navigation signal which has been captured and tracked. In the above two batches signal processing, the power of the corresponding signal can be measured, either in the first stage for strong signals or in the second stage for weak ones, as follows.

$$P_i = 0.5A_i^2 \tag{7}$$

Then a decision threshold, P_{th}, is set up. If the intensity of received signals exceeds this threshold, these signals can be judged as deception jamming ones. Although they are also captured and tracked by the navigation receiver, the pseudo-range measurement will not be carried out. Therefore, even if the deception jamming signal enters the navigation reception and the signal tracking loop, it will not affect any subsequent positioning solution.

For the remaining navigation signals whose intensity is less than the threshold, further detection and identification for deception are needed. A lot of research results in various literatures have been published in this field, and we can refer these results. After identifying and eliminating the deception jamming signals, the pseudo-ranges are measured with the remaining navigation satellite signals, and the positioning equations are solved. So the accurate position coordinates of the receivers can be finally obtained.

5 Simulations

The simulation scene is set up as follows. The simulation time is set at 10:00 a.m. on September 20, 2018. A satellite navigation jammer generates signals of four independent GPS satellites for a GPS C/A code receiver at the Changsha Experimental Station in China. The azimuth angle θ_{az}, elevation angle θ_{el} of each real GPS signal, its relative power P_{re} and Doppler frequency f_{d} of the signals arriving at the receiver are shown in Table 2. Here PRN represents the pseudo-code number of the GPS satellite signal, and the relative power of the received signal is normalized by the largest one, denoted by 0 dB.

Table 2. PRN, azimuth angle, elevation angle, relative power and Doppler frequency of the visible GPS satellites

No.	PRN	θ_{az}/°	θ_{el}/°	P_{re}/dB	f_d/kHz
1	5	107.6	10.0	−12	2.195
2	10	309.6	18.1	−9	−1.636
3	12	141.7	6.3	−14	1.727
4	13	48.7	13.8	−11	−2.399
5	15	29.0	50.1	−2	−1.350
6	20	323.3	42.8	−3	−0.299
7	21	273.2	61.7	−1	1.470
8	24	108.2	70.8	0	−0.991
9	29	200.9	6.1	−14	2.845
10	32	254.5	10.9	−12	−0.207

We can see from Table 2 that the elevation angles of four satellites with PRN 15, 20, 21 and 24 are all over 50°, and their signal powers are relatively larger. The navigation deception jammer produces C/A signals of above four GPS satellites to deceive the navigation receiver. The relative signal power $P_{re,J}$ of these four deception signals (referring to the signal with PRN = 24 in Table 2) and the modulated Doppler shift $f_{d,J}$ are shown in Table 3.

Table 3. PRN, relative power and Doppler frequency of deception jamming signals

No.	PRN	$P_{re,J}$/dB	$f_{d,J}$/kHz
1	15	12	2.6
2	20	12	−1.8
3	21	12	−2.0
4	24	12	1.6

The GPS navigation receiver implements the capture of C/A code signals by the traditional method, and the results are shown in Fig. 3.

We can see from Fig. 3 that GPS signals with PRN 15, 20, 21 and 24 can be captured by traditional methods, but all these four signals are deception jamming ones, and none of the real satellite navigation signals is captured. As shown in Table 3, the powers of deception jamming signals are 12 dB higher than the maximum of the normal one. Due to the multiple access interference effect of CDMA, the strong deception jamming signal suppresses the weak real ones, and the receiver cannot receive the real signals at all. This suppressing effect has a strong negative impact on the anti-jamming and anti-deception operations.

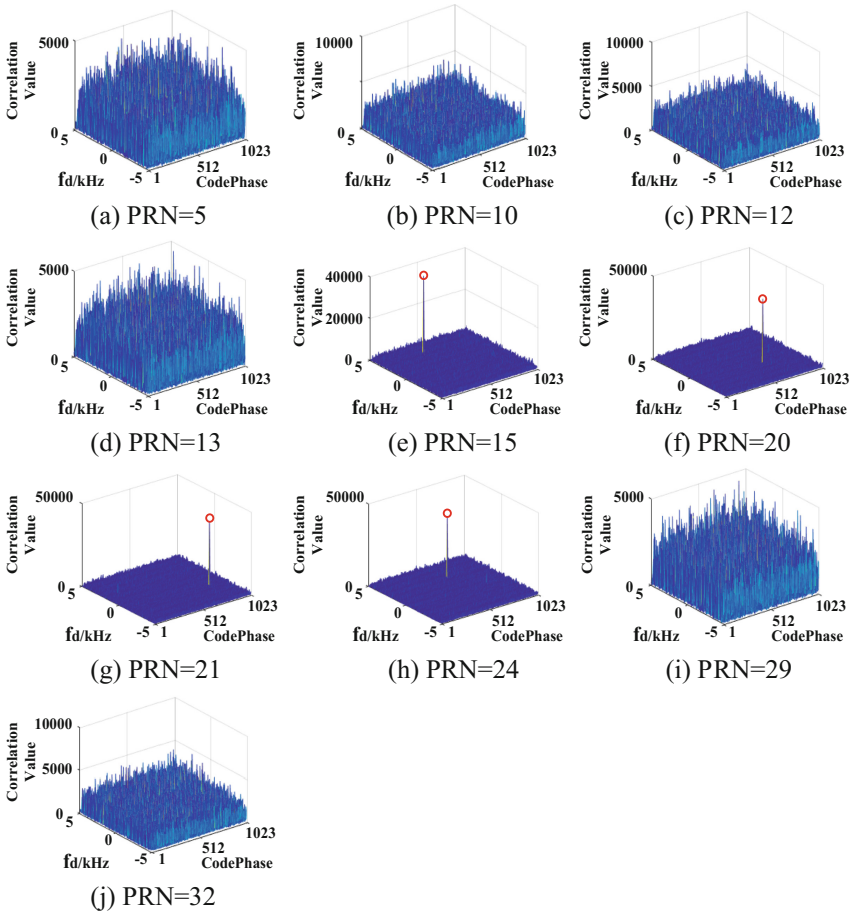

Fig. 3. Capture results of time-frequency correlation by traditional methods

According to the method proposed in this paper, four strong signals captured in the first batch are tracked, de-spread and demodulated. Their waveforms are reconstructed. Then they are subtracted out of the received signals. After strong signal elimination, the second batch of signal capture is performed, and the correlated processing results are shown in Fig. 4.

Comparing with Fig. 4 and Fig. 3, the ten weaker real satellite navigation signals have been all captured after strong ones elimination. In this way, not only four deception jamming signals captured in the first batch can be identified by intensity parameters, but also ten real GPS satellite signals captured in the second batch can be used for pseudo range measurement and positioning calculation, so that the real position coordinates of the satellite navigation receiver can be obtained in the end.

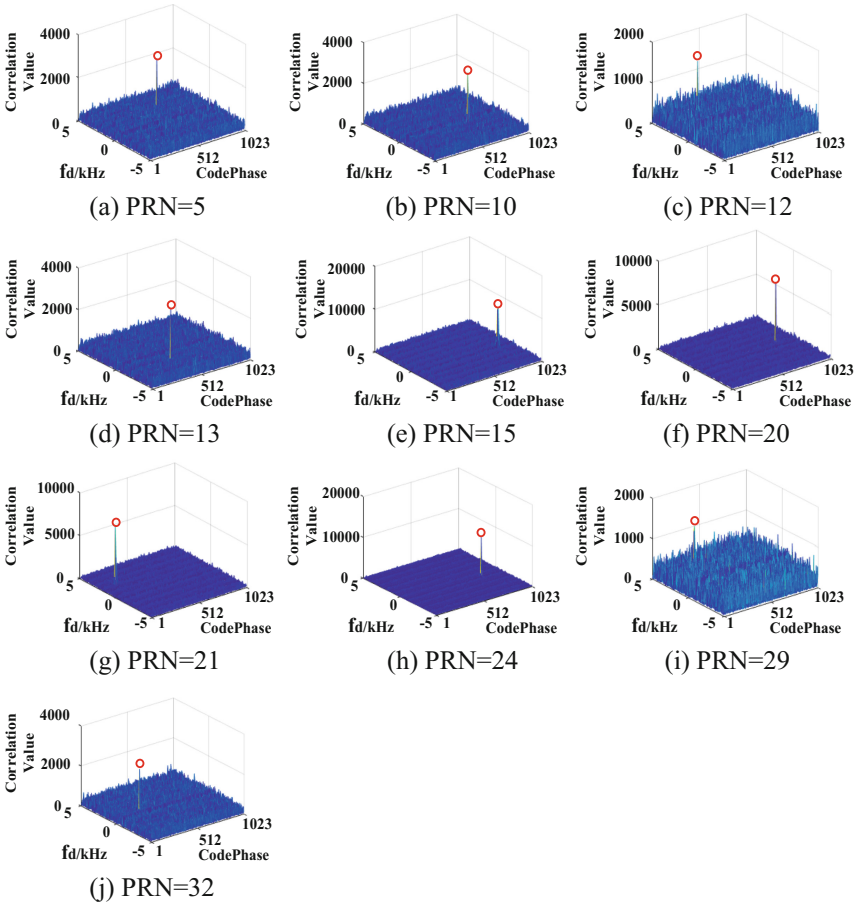

Fig. 4. The second capture results of time-frequency correlation after strong signals elimination

6 Conclusions

A novel method of batch processing based on CDMA signal intensity is proposed in the paper, which eliminates the additional suppression effect caused by the strong deception jamming signal in CDMA GNSS and extracts the weak real satellite navigation signals concealed by strong one. It benefits on the identification and rejection of deception jamming signals, the pseudo range measurement and location calculation based on the real navigation satellite signals. The validity and practicability of the method are verified by simulations. It provides a new technical approach for GNSS anti-jamming and anti-deception process.

References

1. Holmes JK (2007) Spread spectrum systems for GNSS and wireless communications. Artech House, Inc., Norwood
2. Teunissen P, Montenbruck O (2017) Handbook of global navigation satellite systems. Springer, Germany
3. Yading C, Youxi T, Shaoqian L (2003) Channel estimation and multiple access interference in CDMA system. J UEST China 32(5):583–587
4. Long H, Zhicheng L, Feixue W (2012) Spoofing pattern research on GNSS receiver. J Astronaut 33(7):884–890
5. Shi R, Liu J (2018) Detection on navigation deception signals based on INS and GNSS attitude measurement. In: CSNC 2018, Harbin China, 1–5
6. Shi R, Jiantao X, Yan J (2017) Detection on navigation deception signals based on direction finding by nulling antenna and angle contrast. Modern Navig 8(3):193–198
7. Li-an G, Kai Y, Ying L et al (2005) The performance analysis of MAI in DS-CDMA system Based on multi-user number. J Projectiles Rockets Missiles Guidance 25(4):216–218
8. Kaplan ED, Hegarty CJ (2006) Understanding GPS principles and applications, 2nd edn. Artech House Inc., Norwood

Detection on Satellite Navigation Deception Signals Based on Multi Platforms Cooperation

Rong Shi(✉) and Chang Liu

Science and Technology on Electronic Information Control Laboratory, Chengdu, China
jasminewyx@sina.com

Abstract. Effective detection on deception signals in satellite navigation is the important foundation and premise for subsequent deception signal rejection and location based on real navigation signals. At present, most of the proposed methods are based on the single platform application. Due to various reasons, the further improvement of effectiveness and applicability is difficult. In order to solve above problems, a conical constraint condition of two platforms is established by using the advantage of multi platforms networking cooperation and the time difference measurement of the received signals. Then the direction of signal arrival in the coordinate system of multi platforms spatial configuration is obtained by several conical constraint equations. The cross-angle matrix of signals direction can be gotten naturally. At the same time, the cross-angle matrix of standard signals direction is obtained from the known navigation satellite almanac. Therefore, the difference between the actual matrix and the reference one is contrasted to detect navigation deception signals. Finally, the validity and practicability of this method are verified by simulations. It provides a new technical approach for satellite navigation deception signals recognition and anti-deception processing.

Keywords: Satellite navigation · Navigation deception · Detection on deception signals · Multi platforms cooperation · Direction finding based on time difference · Almanac · Angle constraint condition · Cross-angle contrast

1 Introduction

After detecting and eliminating deception jamming components from the received satellite navigation signals, the authenticity-verified signals can be used to implement pseudo-range measurement and position process. This is one of the important methods for anti-deception and positioning credibility improvement of satellite navigation [1]. In recent years, many detection methods on navigation deception jamming have been proposed in various kinds of public literatures, such as: deception jamming suppression based on cross-correlation projection [2], carrier phase difference of antenna array [3], clock frequency drift test [4], the shortest transmission path and signal strength [5], main beam pointing and null constraint optimization for satellite navigation nulling antenna [6]. All above methods are only suitable for the single platform application.

J. Sun et al. (Eds.): CSNC 2019, LNEE 563, pp. 553–561, 2019.
https://doi.org/10.1007/978-981-13-7759-4_48

Because of the platform space constraint conditions, the effectiveness and applicability of these methods are difficult to further improve. In this paper, a new method about detection on navigation deception signals based on multi platforms cooperation has been proposed, in which the data links with information exchange and time synchronization are equipped. It has many advantages of high measurement accuracy, good low elevation-angle characteristics and wide applications. It is very helpful for detection and recognition of deception signals in satellite navigation.

2 Conical Constraint Condition Based on Time Difference Measure

The data links with capability of information transmission and exchange, distance measurement and time synchronization, are the bases of multi platform cooperative networking. In this system, the distance between any two platforms, denoted by A1 and A2 respectively, is known, and the whole network has a uniform clock. The spatial connection between A1 and A2 constitutes a baseline, which length is denoted by $l_{1,2}$. The satellite navigation receivers on the platforms measure the time difference of arrival for the captured navigation signals with the same pseudo-random code sequence, and the arrival time of A1 minus that of A2 is denoted by $\tau_{1,2}$. Since the distance from the navigation satellite to the platform is much longer than that between these two platforms, it is an approximate plane wave. The distance difference $d_{1,2}$ can be derived from the time difference measurement expressed in the following formula.

$$d_{1,2} = \mathrm{c} \cdot \tau_{1,2} \tag{1}$$

Where $\mathrm{c} = 3 \times 10^8\,\mathrm{m/s}$ is the velocity of electromagnetic wave propagation. The above spatial measurement scene is shown in Fig. 1.

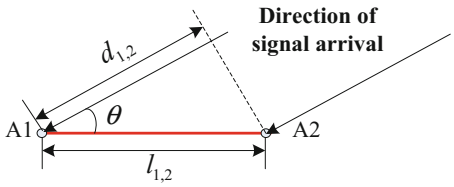

Fig. 1. Time difference measurement for two platforms

The baseline $l_{1,2}$ between the two platforms is the bevel edge, and the distance difference line $d_{1,2}$ is the right-angled edge in the triangle in Fig. 1. Therefore, the angle between the direction of the signal arrival and the baseline can be calculated by the following formula.

$$\theta = \cos^{-1}\left(d_{1,2}/l_{1,2}\right) \tag{2}$$

If we observe in three-dimensional space, the direction of signal arrival is located on a conical surface with A1 as the vertex, the line between A1 and A2 as the rotation axis, and θ as the half-cone angle. It is shown in Fig. 2. This is the spatial conical constraint condition formed by the time difference measurement between the two platforms.

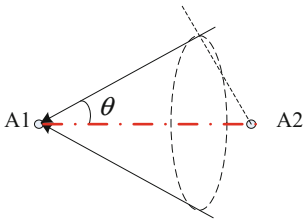

Fig. 2. Space conical constraint condition

3 Direction Finding Based on Multi Conical Constraint Equations

From the above analysis, we know that a conical constraint condition can be formed by time difference measurement between any two platforms. If there are three platforms denoted by A1, A2 and A3, two spatial cones with A1 as the common vertex, A1, A2 and A1, A3 as the rotation axis, can be formed by two time difference measurements of signals arrival. Their half conical angles are denoted by θ_1 and θ_2 respectively. The two conical surfaces with the common vertex will produce one or two intersecting lines in three-dimensional space through the vertex A1, which is the direction of signal arrival, as shown in Fig. 3.

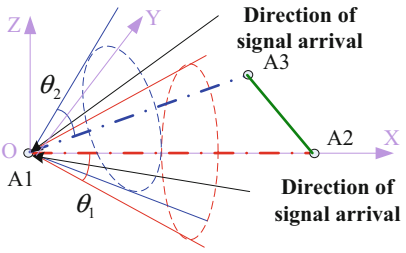

Fig. 3. Two space conical constraint conditions from 3 platforms

When two conical surfaces are tangent, only one intersecting line is formed, and this line is in the plane determined by A1, A2 and A3. Otherwise, two intersecting lines are formed, and they are symmetrical up and down on this plane. To show the above spatial geometry more clearly, two conical surfaces with the common vertices are projected from point A1 to the direction of the signal arrival as shown in Fig. 4. The just tangent case of two conical surfaces is in Fig. 4(a) and the intersecting case is in Fig. 4(b).

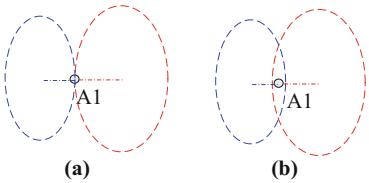

Fig. 4. Projection of two space conical surfaces

In Fig. 3, the OXYZ Cartesian coordinate system is established with A1 point as the origin and A1A2 as X axis forward. The Y axis and the X axis are located in the plane determined by A1, A2 and A3. The Z axis is perpendicular to the plane and forms a right Cartesian coordinate system with the X and Y axes. The coordinate system is also known as the multi platform spatial coordinate system, in which the unit direction vector of A1 to A2 is $\vec{n}_{1,2} = (1, 0, 0)$, the unit direction vector of A1 to A3 is $\vec{n}_{1,3} = (\cos\phi, \sin\phi, 0)$, and the angle ϕ can be obtained by the cosine theorem.

$$\phi = \cos^{-1}\left(\frac{d_{1,2}^2 + d_{1,3}^2 - d_{2,3}^2}{2d_{1,2}d_{1,3}}\right) \tag{3}$$

Where $d_{1,2}$, $d_{1,3}$ and $d_{2,3}$ are the distances among platforms, which are measured in real time through the data links. The pitch angle of the direction of signal arrival relative to the XOY plane is denoted by α, and the projection angle relative to the X positive direction is denoted by β. Then the unit vector of the direction of signal arrival is $\vec{n}_s = (\cos\alpha\cos\beta, \cos\alpha\sin\beta, \sin\alpha)$. From the above analysis of spatial geometry, $\vec{n}_{1,2}$, $\vec{n}_{1,3}$ and $\vec{n}_s$ satisfy the following relations.

$$\begin{cases} \vec{n}_s \bullet \vec{n}_{1,2} = \cos\theta_1 \\ \vec{n}_s \bullet \vec{n}_{1,3} = \cos\theta_2 \end{cases} \tag{4}$$

Where "•" represents the dot product between two vectors. α and β can be solved from formula (4). Thus, the arrival direction of signal received by the satellite navigation receiver in the OXYZ coordinate system can be determined.

There are probably two solutions in formula (4): one is the real solution and the other is the mirror solution, which can be removed according to additional constraints,

such as more platforms for the same application, or applying boundary conditions. In this way, time difference of arrival for the signal with the same pseudo-random code sequence is measured by three platforms, and the direction can be determined. Similarly, this operation is repeated for the different signals and then the spatial multi conical constraint equations for each signal, similar to Eq. (4), can be established. Then the direction of signal arrival is obtained. If the number of platforms involved in the measurement is more, the constraint equation will be more increased, and the more accurate angle of arrival can be obtained by the least square method. These angle values are important data for subsequent satellite navigation deception signal detection.

4 Deception Signals Identification by Cross-Angle Contrast

In the overall design of GNSS, in order to achieve higher positioning accuracy under the limited number of navigation satellites, the satellite constellations and orbit parameters are carefully designed to ensure better GDOP conditions at any point on the earth surface. In fact, the cross-angle between directions of signal arrival for any two navigation satellites can be calculated by the almanac for an observation point on the earth at a certain time. The almanac can be publicly downloaded on the Internet. Therefore, the true or deception navigation signal can be identified by the cross-angle contrast. On the other hand, the calibration of absolute direction of arrival is avoided in this method. As long as all signals are in the same coordinate system, the cross-angle can be easily calculated by using the relative direction of arrival.

(1) Calculation of reference direction for the satellite navigation signal.

The position coordinates of N navigation satellites in the earth geostationary coordinate system at the certain time can be calculated from the previously downloaded almanac, which are denoted as $(x_j, y_j, z_j), j = 1, 2, \cdots, N$. If the position coordinates of platform A1 at the current moment are (x_{A1}, y_{A1}, z_{A1}), the unit vector $\vec{n}_{r,j} = (\gamma_{x,j}, \gamma_{y,j}, \gamma_{z,j})$ of the direction of signal arrival for the j th navigation satellite can be calculated by the following formula.

$$\begin{cases} \gamma_{x,j} = (x_j - x_{A1})/r_j \\ \gamma_{y,j} = (y_j - y_{A1})/r_j \\ \gamma_{z,j} = (z_j - z_{A1})/r_j \\ r_j = \sqrt{(x_j - x_{A1})^2 + (y_j - y_{A1})^2 + (z_j - z_{A1})^2} \end{cases} \tag{5}$$

The current position coordinates of platform A1 need to be used in the Eq. (5), which can be provided by other sensors with a very rough estimation. The platform is on the earth surface. The distance between the platform and the navigation satellite is very far, almost 20,000 km or more. If the coordinate error of A1 reaches the order of 100 km, the error of the direction of arrival from Eq. (5) does not exceed 0.005 rad.

After obtaining the direction of arrival for the above N navigation satellite signals in the earth geostationary coordinate system, a $N \times N$ dimensional cross-angle matrix

M_{ref} can be generated. The element $m_{k1,k2}$ in the matrix represents the cross-angle between the direction of the k_1th signal and that of the k_2th signal, $k_1, k_2 \in \{1, 2, \cdots, N\}$, and it can be expressed by the following formula.

$$m_{k1,k2} = \cos^{-1}\left(\gamma_{\text{x},k_1} \cdot \gamma_{\text{x},k_2} + \gamma_{\text{y},k_1} \cdot \gamma_{\text{y},k_2} + \gamma_{\text{z},k_1} \cdot \gamma_{\text{z},k_2}\right) \tag{6}$$

It is obvious that the cross-angle matrix M_{ref} is symmetrical, i.e. $m_{k1,k2} = m_{k2,k1}$, and the elements on the diagonal are all zeros, i.e. $m_{k1,k1} = 0$. Therefore, the number of independent components in M_{ref} is $N \times (N-1)/2$.

(2) Calculation of the direction angle of actual signals arrival.

According to the method proposed in the previous section, the direction of arrival for each received signal in the multi platform spatial coordinate system can be obtained through time difference measurement and multi conical constraint equations in the networking cooperative application. Its unit direction vector is denoted by $\vec{n}_{\text{s},j} = (\zeta_{\text{x},j}, \zeta_{\text{y},j}, \zeta_{\text{z},j})$. In the same way, the $N \times N$ dimension cross-angle matrix R_{M} for the actual signals can be obtained too. The element $r_{k1,k2}$ in the matrix represents the cross-angle between the direction of the k_1th signal and that of the k_2th signal, and it can be expressed by the following formula.

$$r_{k1,k2} = \cos^{-1}\left(\zeta_{\text{x},k_1} \cdot \zeta_{\text{x},k_2} + \zeta_{\text{y},k_1} \cdot \zeta_{\text{y},k_2} + \zeta_{\text{z},k_1} \cdot \zeta_{\text{z},k_2}\right) \tag{7}$$

The cross-angle matrix R_{M} formed by the actual signals is also symmetrical, and the diagonal elements are all zero. The number of independent components is $N \times (N-1)/2$.

(3) Deception signal recognition based on cross-angle contrast.

The cross-angle matrix M_{ref} from the almanac is obtained in the earth geostationary coordinate system. The cross-angle matrix R_{M} for the actual signals is calculated in the multi platform spatial coordinate system. Although these two coordinate systems are different, the cross-angle between the directions of arrival does not change. Therefore, if the N received signals are all from the real navigation satellites, and the measurement and approximate calculation error are neglected, it is absolutely $R_{\text{M}} = M_{\text{ref}}$ in theory. The deception jamming signals can be detected by the difference between R_{M} and M_{ref}. The absolute value matrix G_{diff} of the difference between these two matrices can be expressed as following.

$$G_{\text{diff}} = |R_{\text{M}} - M_{\text{ref}}| \tag{8}$$

The judgment threshold T_{s} is set. If the element $g_{k1,k2}$ in G_{diff} is greater than the threshold, the cross-angle is abnormal. The abnormal element in matrix is denoted by 1 and the other is denoted by 0. In this way, a new binary matrix H_{diff} is formed, in which each element $h_{k1,k2}$ is expressed as follows.

$$h_{k1,k2} = \begin{cases} 0 & g_{k1,k2} < T_s \\ 1 & g_{k1,k2} \geq T_s \end{cases} \tag{9}$$

The number of ones in every column of H_{diff} is counted up, and the most abnormal column with maximum is found. The signal corresponding to this column can be judged as deception jamming signal. Then the corresponding row and column are deleted from H_{diff} to form a new matrix $H_{\text{diff},1}$ with dimension $(N-1) \times (N-1)$. By counting the number of ones in each column of $H_{\text{diff},1}$, the column with maximum is found. The corresponding signal of this column can be judged as deception jamming signal. Then the corresponding row and column are deleted from $H_{\text{diff},1}$ to form a new matrix $H_{\text{diff},2}$ with dimension $(N-2) \times (N-2)$. The process is repeated until the remaining elements in the matrix are all zeros. The signals corresponding to the zero matrix are all from the real navigation satellites, and the other signals are the deception ones. Based on these real signals for pseudo-range measurement and location calculation, the real coordinate positions of each platform can be obtained in the end.

5 Simulations

Simulation Scene: Four UAVs are flying in Changsha, China, at 8:00 a.m. on September 12, 2018. The location of the airspace is about 113° east longitude, 28° north latitude and 806 m altitude. The GPS satellite almanac downloaded from the Internet on September 9, 2018 is used to calculate the direction of visible GPS satellites signal arrival in the earth geostationary coordinate system at the current time, as shown in Table 1. The PRN in the Table 1 represents the pseudo-code number of the GPS satellite. It is obvious that the above four UAVs can receive signals from 8 GPS satellites at this time.

Table 1. The direction of GPS satellite signals from the UAV view

NO.	PRN	Azimuth angle/°	Pitch angle/°	NO.	PRN	Azimuth angle/°	Pitch angle/°
1	2	120.4302	46.3273	5	21	315.7177	12.1702
2	5	40.2070	44.8216	6	24	178.7720	10.6525
3	13	63.5891	76.7717	7	29	270.6242	49.0662
4	15	228.6458	56.5698	8	30	57.7486	13.0538

At this time, two jammers send out the navigation deception jamming signals from 352°, 5°, 95° and 8° of azimuth and pitch angles respectively. They imitate the signals of PRN = 21, 30 for deception jamming. In the eight signals captured by the four UAVs, there are six signals from real navigation satellites and two signals from deception jammers. The four UAVs (denoted by A1, A2, A3, A4, respectively) fly at the same altitude (806 m) in a diamond fleet to the east by 30° north, as shown in Fig. 5.

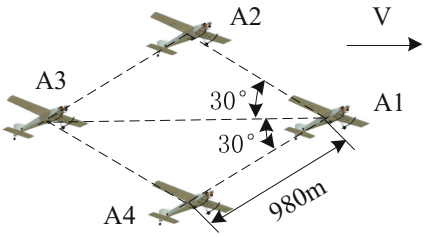

Fig. 5. Four-UAV fleet flying diagram

In Fig. 5, the distance between two adjacent UAVs in the fleet is 980 m, which can be measured by the inter-aircraft data link. It also forms a unified timing clock too.

The angle between A1A2 and A1A3 is 30° and the angle between A1A3 and A1A4 is also 30°.

According to the above method, A1A2, A1A3 and A1A4 are used as three baselines to measure the time difference of eight currently captured satellite navigation signals. The measurement results are shown in Table 2.

Table 2. Time difference measurement results of UAV fleet for each signal

NO.	PRN	A1A2/ns	A1A3/ns	A1A4/ns	NO.	PRN	A1A2/ns	A1A3/ns	A1A4/ns
1	2	2264	1698	1132	5	21	3002	2792	2582
2	5	424	1309	2193	6	24	1666	63	−1540
3	13	405	579	753	7	29	−1856	−1840	−1825
4	15	−580	−1164	−1748	8	30	−1836	−225	1386

By using the measurements in Table 2 for formulas (1) and (2), the angles between the directions of the eight signals captured by the navigation receivers and the baselines can be calculated. Then, the direction of these signals arrival in the spatial coordinate system of UAV platforms can be obtained by formula (4). Next, the cross-angle matrix R_M of the actual signals is calculated from the formula (7). Based on the data in Table 1, the cross-angle matrix M_{ref} of the reference signals in the region at this time is obtained. Then the absolute value matrix G_{diff} of the difference between R_M and M_{ref} can be gotten from formula (8) as follows (unit: degree).

$$G_{diff} = \begin{bmatrix} 0.00 & 0.22 & 0.29 & 0.22 & 74.87 & 0.08 & 0.00 & 44.83 \\ 0.22 & 0.00 & 0.02 & 0.17 & 14.62 & 0.33 & 0.06 & 18.19 \\ 0.29 & 0.02 & 0.00 & 0.23 & 8.54 & 0.09 & 0.36 & 13.05 \\ 0.22 & 0.17 & 0.23 & 0.00 & 27.95 & 0.10 & 0.28 & 8.41 \\ 74.87 & 14.62 & 8.54 & 27.95 & 0.00 & 51.13 & 72.43 & 2.37 \\ 0.08 & 0.33 & 0.09 & 0.10 & 51.13 & 0.00 & 0.13 & 43.66 \\ 0.00 & 0.06 & 0.36 & 0.28 & 72.43 & 0.13 & 0.00 & 31.19 \\ 44.83 & 18.19 & 13.05 & 8.41 & 2.37 & 43.66 & 31.19 & 0.00 \end{bmatrix}$$

The judgment threshold is set to $T_s = 1.2°$. Through the formula (9), the two-valued matrix H_{diff} can be expressed as follows.

$$H_{\text{diff}} = \begin{bmatrix} 0 & 0 & 0 & 0 & 1 & 0 & 0 & 1 \\ 0 & 0 & 0 & 0 & 1 & 0 & 0 & 1 \\ 0 & 0 & 0 & 0 & 1 & 0 & 0 & 1 \\ 0 & 0 & 0 & 0 & 1 & 0 & 0 & 1 \\ 1 & 1 & 1 & 1 & 0 & 1 & 1 & 1 \\ 0 & 0 & 0 & 0 & 1 & 0 & 0 & 1 \\ 0 & 0 & 0 & 0 & 1 & 0 & 0 & 1 \\ 1 & 1 & 1 & 1 & 1 & 1 & 1 & 0 \end{bmatrix}$$

It is obvious that after removing the fifth and eighth columns and rows of H_{diff}, a 6×6 dimensional zero matrix can be obtained. This shows that the two signals captured by UAVs, which PRNs are 21 and 30, are abnormal. They can be judged as deception jamming signals. In this way, the satellite navigation deception jamming signal can be detected effectively through UAVs cooperation mode. After removing two deception jamming signals with PRN of 21 and 30, pseudo range measurement and positioning calculation are implemented in the satellite navigation receivers on the UAVs. The real and accurate positions are obtained in the end.

6 Conclusions

In this paper, the satellite navigation deception jamming signal detection method based on multi platforms cooperation is put forward, and the advantages of networking cooperation are fully utilized. After the direction finding by time difference measurement among platforms for signals arrival, the deception jamming signals can be effectively detected by contrasting the cross-angle matrix of the received signals and that of standard reference signals. The simulation results show the validity and practicability of this technique, which provides a new approach for the deception jamming signal identification and anti-deception processing in the satellite navigation.

References

1. Teunissen P, Montenbruck O (2017) Handbook of global navigation satellite systems. Springer, Germany
2. Wang C, Zhang L (2016) Spoofing mitigation method for navigation receiver based on cross correlation and projection. J Electron Inf Tech 38(8):1984–1990
3. Zhang X, Pang J, Su Y et al (2014) Spoofing detection technique on antenna array carrier phase double difference. J Natl Univ Defense Technol 36(4):55–60
4. Hu Y, Cao K, Bian S et al (2015) GNSS spoofing detection algorithm based on clock frequency drift monitoring. Syst Eng Electron 37(7):1629–1632
5. Shi R, He J, Xu J (2017) Detection on repeater deception signal based on the shortest transmission path and signal power. In: CSNC 2017, Shanghai, China, 1–5
6. Shi R (2018) Main beam pointing and null constraint optimization for satellite navigation nulling antenna. In: CSNC 2018, Harbin, China, no 3, pp 279–288

The Navigation Anti-jamming Resource Optimization Algorithm Implemented Based on Wiener Filtering Structure

Chanchan Ren(✉), Zhenxing Xu, Jiaojiao Zhu, and Shengdian Liu

Space Star Technology Co., Ltd., Beijing 102209, China
rcchjl23@163.com

Abstract. Adaptive antenna array technology used to improve the anti-jamming ability of navigation receiver now. Inversion process in adaptive antenna array anti-jamming is complicated in FPGA, which takes up a lot of hardware resources and increases the power consumption of the system. The navigation anti-jamming resource optimization algorithm, which implemented base on wiener filtering (WF) structure, is presented to solve this problem. Firstly, taking the four-channel signal as an example, the model of the traditional power inversion (PI) algorithm is introduced. The fourth-order covariance matrix is inversed by matrix decomposition when power inversion algorithm implements on FPGA. Then, a wiener filtering structure is proposed, which same order as power inversion algorithm. When implementing the wiener filtering algorithm, we only need to use the matrix decomposition to invert the third-order covariance matrix to filter the four-channel signals. Wiener filtering algorithm reduces dimensions of the weight calculation in the matrix inversion, and simplifies the calculation. Numerical simulations show that, power inversion algorithm and wiener filtering structure solve the optimal weight in navigation anti-jamming has equivalence. Moreover, through resource comparison after synthesize and implement, it can be seen that all resources in FPGA have been significantly reduced.

Keywords: Wiener filtering · Satellite navigation · Anti-jamming · Resource optimization · FPGA

1 Introduction

The fragility of satellite signals makes navigation receivers highly vulnerable to human and natural interference. At present, the adaptive antenna array processing technology is relatively mature, but the process of weight calculation is complicated, which has always been one of the main problem of this technology [1]. In paper [2], the space-time navigation anti-jamming technology is studied. Based on the power inversion constraint optimal weight, the beamforming algorithm of feedback orientation information is introduced. The algorithm improves the anti-jamming performance by about

J. Sun et al. (Eds.): CSNC 2019, LNEE 563, pp. 562–571, 2019.
https://doi.org/10.1007/978-981-13-7759-4_49

15 dB. In paper [3], a normalized power inversion algorithm for tracking random features of interference is proposed. The optimal parameters of the low-pass filter are determined by adaptively adjusting the loop step. The algorithm converges quickly and forms a deeper depression, making GPS receiver is more adaptable to complex electromagnetic environments. The main research target of the paper [4] is weak signal interference. The subspace projection method is introduced in the process of interference suppression using the power inversion algorithm, but it will inevitably bring more computational complexity. It can be seen from the paper [2–4] that the power inversion algorithm has been widely used in navigation anti-jamming technology, but the algorithm has a large amount of computation and storage in the process of engineering implementation. The wiener filtering structure can physically reduce the dimensionality and the degree without loss the freedom of the algorithm. In the process of image denoising using BM3D algorithm, the paper [5] uses the wiener filtering structure for dimensionality reduction, which simplifies the calculation process while ensuring the optimal performance of the image denoising algorithm. In paper [6], frequency hopping technology is used to improve the anti-jamming performance of the system, but the tracking accuracy is reduced. To solve this problem, the loop structure of wiener filtering is introduced. This structure reduces the number of filtering coefficients and makes tracking speed has increased by 3 times. Both the paper [5] and the paper [6] use the wiener filtering structure to reduce the number of filtering coefficients in the optimization algorithm proposed in their respective fields, and obtain the dimensionality reduction processing and system performance improvement. In paper [7], a novel wiener structure named Poisson non-local wiener filter (PNL-Winner) is proposed for the image damaged by noise. The filter estimation parameters are degraded. The weight of the estimation function is calculated by a random sequence of images, which enables the image edges and details to be better processed.

This paper establishes a system model for anti-jamming algorithm resources optimization in adaptive array processing technology. Firstly, in the navigation anti-jamming, the theory and algorithm implementation process of solving the optimal weight by power inversion is given. Then, the wiener filtering structure with wide application range, easy to understand and use is proposed instead of power inversion algorithm. When the algorithm is implemented, the dimension can go down and the storage and computing resources in the FPGA can be reduced.

2 Power Inversion Algorithm

2.1 Algorithm Model

The power inversion algorithm is used to filter the four-channel signal, and the schematic diagram is shown in Fig. 1.

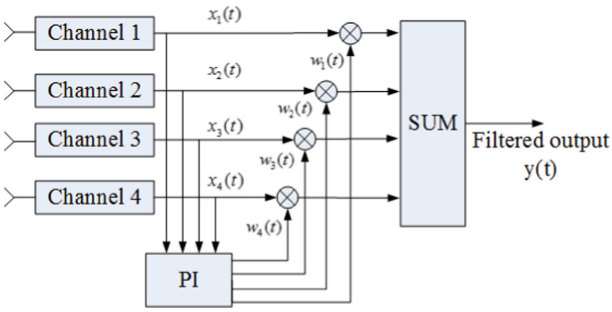

Fig. 1. Schematic diagram of power inversion algorithm

At time t, assume that the signal received by the four channels is given by

$$X(t) = [x_1(t), x_2(t), x_3(t), x_4(t)]^T \tag{1.1}$$

Where "T" indicates transposition.

The covariance matrix of the received signal can be expressed as

$$R_{XX} = \sum_{k=1}^{K} X(t)X^T(t) \tag{1.2}$$

Where K is the number of snapshots.

According to the linear constraint minimum variance criterion, under the constraint of the steering vector S, the optimal weight is given by

$$W_{opt}^{PI} = \frac{R_{XX}^{-1}S}{S^H R_{XX}^{-1}S} \tag{1.3}$$

In the above formula, the steering vector S selects the first channel to be constrained. To reflect the equivalence, the wiener filtering structure below also selects the first channel as the main channel.

The output after filtering the four-channel signal is given by

$$y(t) = W_{opt}^{PIH}X(t) \tag{1.4}$$

2.2 Implementation Steps

Figure 2 shows the process of solving the optimal weight on the FPGA using the power inversion algorithm.

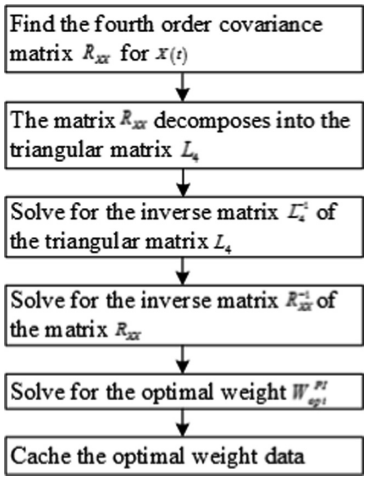

Fig. 2. Power inversion algorithm implementation process

3 Wiener Filtering Algorithm

3.1 Algorithm Model

The four-channel signal is filtered by the wiener filtering algorithm, and its structure is shown in Fig. 3.

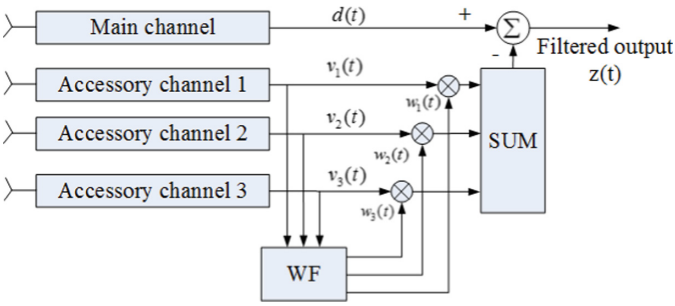

Fig. 3. Schematic diagram of wiener filtering algorithm

Suppose all signals received at time t are given by

$$D(t) = [d(t), v_1(t), v_2(t), v_3(t)]^T \tag{1.5}$$

The signal can be divided into two parts, $d(t)$ is the signal received by the main channel, and the signal received by the accessory channel can be recorded as

$$V(t) = [v_1(t), v_2(t), v_3(t)]^T \tag{1.6}$$

From the structural model of the algorithm, it can be concluded that the signal on the accessory channel is weighted by the optimal weight and summed with the main channel signal. The filtered output is given by

$$z(t) = d(t) - W_{opt}^{WFH} V(t) \tag{1.7}$$

It can be seen from Eq. (1.7) that the filtered output is obtained by subtracting the weighted sum of the weight vector and the accessory channel signal from the main channel. It can be considered that the main channel signal contains the useful signal and interference, and the accessory channel signal is only subjected to interference after weighted summation. Eliminating the interfering signal from the main channel signal can output the desired signal.

Using the Least Mean Square (LMS), the output power after cancellation of the primary and secondary channels is given by

$$\begin{aligned} P_{res} &= E\left[|z(t)|^2\right] \\ &= E\left[\left(d(t) - W_{opt}^{WFH} V(t)\right)\left(d^*(t) - V^H(t) W_{opt}^{WF}\right)\right] \\ &= E\left[|d(t)|^2\right] - W_{opt}^{WFH} r_{Vd} - r_{Vd}^H W_{opt}^{WF} + W_{opt}^{WFH} R_{VV} W_{opt}^{WF} \end{aligned} \tag{1.8}$$

In the above formula, R_{VV} is the covariance matrix of the accessory channel signal, expressed as

$$R_{VV} = \sum_{k=1}^{K} V(t) V^T(t) \tag{1.9}$$

r_{Vd} is the cross-correlation matrix of the main channel and the accessory channel signal, expressed as

$$r_{Vd} = \sum_{k=1}^{K} V(t) d^*(t) \tag{1.10}$$

In order to minimize the power, the Eq. (1.8) is respectively subjected to gradients for W_{opt}^{WF}.

$$\nabla_{W_{opt}^{WF}}(P_{res}) = 2R_{VV} W_{opt}^{WF} - 2r_{Vd} \tag{1.11}$$

The above formula is equal to zero, we can get

$$R_{VV} W_{opt}^{WF} - r_{Vd} = 0 \tag{1.12}$$

Solving the above Wiener-Hopf equation matrix, the optimal weight of the accessory channels can be obtained.

$$W_{opt}^{WF} = R_{VV}^{-1} r_{Vd} \tag{1.13}$$

3.2 Implementation Steps

The process of solving the optimal weight on the FPGA using the wiener filtering algorithm is shown in Fig. 4.

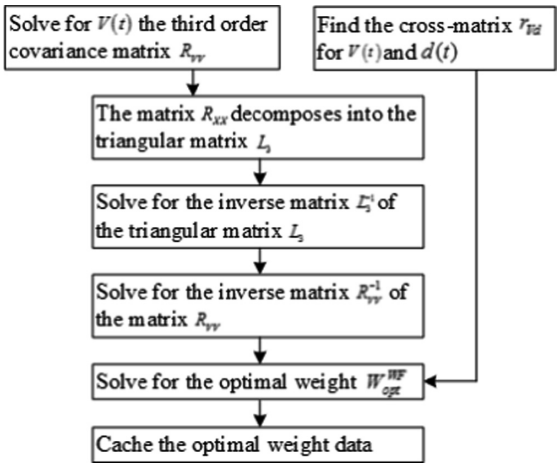

Fig. 4. Wiener filtering algorithm implementation process

Compared with the power inversion algorithm, there are three main differences between the optimal weight calculations using the wiener filtering algorithm.

(a) The order of the covariance matrix R changes from four to three, and the solution of the cross-correlation matrix r_{Vd} is added.
(b) The computational resources and storage resources used in the matrix decomposition and inversion process are changed from fourth to third.
(c) The computational complexity of the weight matrix is reduced.

The following describes the implementation process of each module in the wiener filtering algorithm.

Step1. R_{VV} and r_{Vd}

Select the channel that is constrained by the steering vector S in the power inversion algorithm as the main channel. The covariance matrix of the accessory channel and the cross-correlation matrix of the main and accessory channels are obtained by using the formula $R_{VV} = \sum_{k=1}^{K} V(t)V^T(t)$ and the formula $r_{Vd} = \sum_{k=1}^{K} V(t)d^*(t)$, respectively. An example, the fourth channel as the main channel, can get the following formula

$$R_{VV} = \begin{bmatrix} v_1 \\ v_2 \\ v_3 \end{bmatrix} \begin{bmatrix} v_1 & v_2 & v_3 \end{bmatrix}^H = \begin{bmatrix} v_1 v_1^H & v_1 v_2^H & v_1 v_3^H \\ v_2 x_1^H & v_2 v_2^H & v_2 v_3^H \\ v_3 v_1^H & v_3 v_2^H & v_3 v_3^H \end{bmatrix} \tag{1.14}$$

$$r_{Vd} = \begin{bmatrix} v_1 \\ v_2 \\ v_3 \end{bmatrix} v_4^H = \begin{bmatrix} v_1 v_4^H \\ v_2 v_4^H \\ v_3 v_4^H \end{bmatrix} \tag{1.15}$$

From formula (1.14), R_{VV} is a Hermit matrix, so R_{VV} and r_{Vd} can be written as

$$R_{VV} = \begin{bmatrix} r_{11} & r_{12} & r_{13} \\ r_{12}^H & r_{22} & r_{23} \\ r_{13}^H & r_{23}^H & r_{33} \end{bmatrix} \qquad r_{Vd} = \begin{bmatrix} r_{14} \\ r_{24} \\ r_{34} \end{bmatrix} \tag{1.16}$$

Step2. R_{VV} matrix decomposition

Decompose the covariance matrix into $R_{VV} = L_3 L_3^H$, where L_3 is the lower triangular matrix, denoted as

$$L_3 = \begin{bmatrix} l_{11} & 0 & 0 \\ l_{21} & l_{22} & 0 \\ l_{31} & l_{32} & l_{33} \end{bmatrix} \tag{1.17}$$

Step3. Lower triangular matrix inversion

Inverting the lower triangular matrix L_3, the inverse matrix can be recorded as

$$L_3^{-1} = \begin{bmatrix} l'_{11} & 0 & 0 \\ l'_{21} & l'_{22} & 0 \\ l'_{31} & l'_{32} & l'_{33} \end{bmatrix} \tag{1.18}$$

Step4. Covariance matrix inversion

According to the inverse matrix L_3^{-1} of the lower triangular matrix, we can get the following formula

$$R_{VV}^{-1} = \left(L_3^{-1}\right)^H L_3^{-1} = \begin{bmatrix} l_{11}'^H & l_{21}'^H & l_{31}'^H \\ 0 & l_{22}'^H & l_{32}'^H \\ 0 & 0 & l_{33}'^H \end{bmatrix} \begin{bmatrix} l_{11}' & 0 & 0 \\ l_{21}' & l_{22}' & 0 \\ l_{31}' & l_{32}' & l_{33}' \end{bmatrix}$$
$$= \begin{bmatrix} l_{11}'^H l_{11}' + l_{21}'^H l_{21}' + l_{31}'^H l_{31}' & l_{21}'^H l_{22}' + l_{31}'^H l_{32}' & l_{31}'^H l_{33}' \\ l_{22}'^H l_{21}' + l_{32}'^H l_{31}' & l_{22}'^H l_{22}' + l_{32}'^H l_{32}' & l_{32}'^H l_{33}' \\ l_{33}'^H l_{31}' & l_{33}'^H l_{32}' & l_{33}'^H l_{33}' \end{bmatrix} \tag{1.19}$$
$$\triangleq \begin{bmatrix} R_{11}' & R_{12}' & R_{13}' \\ R_{21}' & R_{22}' & R_{23}' \\ R_{31}' & R_{32}' & R_{33}' \end{bmatrix}$$

Step5. Multiplication module

The stored R_{VV}^{-1} and r_{Vd} data are read, and the optimal weight is obtained after multiplication.

$$W_{opt}^{WF} = R_{VV}^{-1} \bullet r_{Vd} = \begin{bmatrix} R_{11}' r_{14} + R_{12}' r_{24} + R_{13}' r_{34} \\ R_{21}' r_{14} + R_{22}' r_{24} + R_{23}' r_{34} \\ R_{31}' r_{14} + R_{32}' r_{24} + R_{33}' r_{34} \end{bmatrix} \triangleq \begin{bmatrix} w_1 \\ w_2 \\ w_3 \end{bmatrix} \tag{1.20}$$

4 Numerical Simulations

Firstly, the equivalence between the power inversion algorithm and the wiener filtering algorithm is verified. Then, the effects of the two algorithms on the interference performance are compared. Finally, the resource usage of the two algorithms in the FPGA is compared. In the simulation, the number of signal channels $N = 4$, the first channel is selected as the main channel, and a wideband interference signal with interference-signal ratio (ISR) of 70 dB is added to the signal data. The optimal weights obtained by the two algorithms are compared as follows.

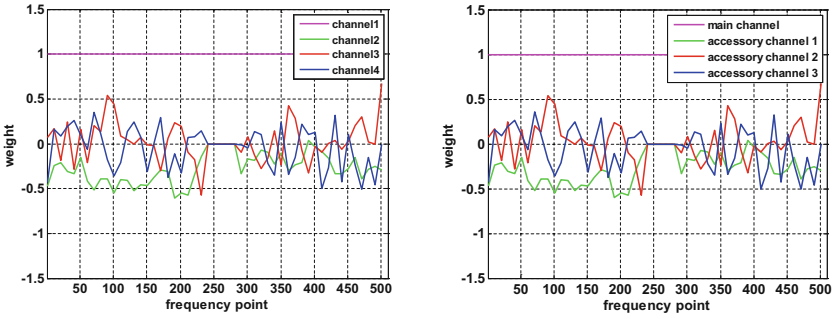

a) Power inversion **b)** Wiener filtering

Fig. 5. Contrast of the real part of the optimal weight

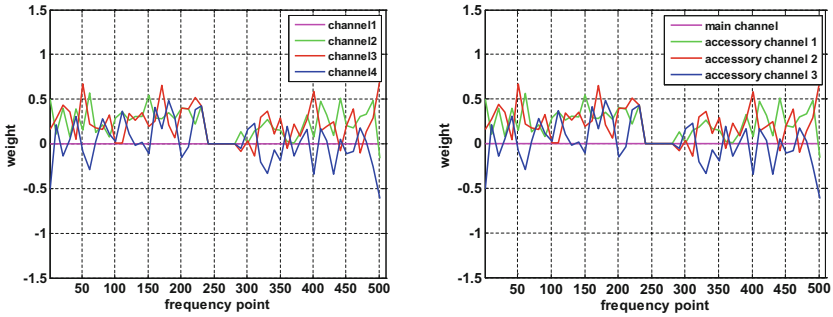

a) Power inversion **b)** Wiener filtering

Fig. 6. Contrast of the imaginary part of the optimal weight

It can be seen from the comparison between Figs. 5 and 6 that the real and imaginary values of the optimal weight obtained by the power inversion and wiener filtering algorithms are the same. The optimal weight of the two algorithms are consistent, indicating that the two algorithms are equivalent.

In order to compare the anti-jamming performance of power inversion and wiener filtering, Fig. 7 shows the energy contrast of the two algorithms after filtering under different ISR. The simulation data is added to a wideband interference signal, which ISR is 40 dB, 50 dB, 60 dB, and 70 dB, respectively. It can be seen from Fig. 7, after the anti-jamming filtering process, the signal residual energy of the two algorithms is the same magnitude when the ISR is the same, that is, the anti-jamming performance of the two algorithms is consistent.

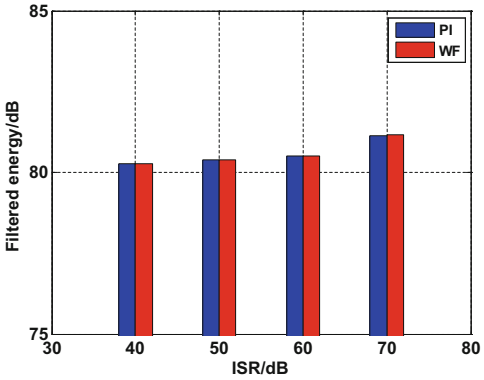

Fig. 7. Energy contrast under different ISR

The power inversion algorithm and the wiener filtering algorithm are respectively coded on the FPGA. The FPGA model is XC7K410T. The resource usage is shown in Table 1.

Table 1. Resource usage of implementation on FPGA

Resource	Estimation		Available		Utilization	
	PI	WF	PI	WF	PI	WF
FF	89053	80157	508400	508400	18%	16%
LUT	78763	68174	254200	254200	31%	27%
Memory LUT	6381	6027	90600	90600	7%	7%
BRAM	230	202	1590	1590	14%	13%
DSP48	460	393	1540	1540	30%	26%

Table 1 shows the statistics of resource usage after synthesis and implementation on the FPGA. It can be seen that after the wiener filtering algorithm, the FF resource is reduced from 18% to 16%, the LUT resource is reduced from 31% to 27%, the BRAM resource is reduced from 14% to 13%, and the DSP48 resource is reduced by 30% to 26%.

5 Summary

The adaptive antenna array processing technology can effectively against the high power interference when receiving satellite signals. Firstly, this paper introduces the filtering algorithm model and implementation process with traditional power inversion. Secondly, the process of anti-jamming filtering using wiener filtering algorithm structure is researched without loss of freedom. The numerical simulation results show that the optimal weight obtained by wiener filtering and power inversion is equivalent to the multi-channel signal filtering, and the implementation resource by the wiener filtering algorithm proposed in this paper is reduced. The practical performance of the FPGA has been improved.

References

1. Gupta IJ, Moore TD (2004) Space-frequency adaptive processing (SFAP) for radio frequency interference mitigation in spread-spectrum receivers. IEEE Trans Antennas Propag 52 (6):1611–1616
2. Li FN, Xu JN, Li HP et al (2015) Design for a dual-system satellite navigation anti-jamming receiver. Appl Mech Mater 3843(744):1674–1679
3. Meng DW, Feng ZM, Lu MQ (2008) Anti-jamming with adaptive arrays utilizing power inversion algorithm. Tsinghua Sci Technol 13(6):796–799
4. Zhao F, Lang R, Li W (2017) Anti-jamming algorithm of power inversion satellite navigation based on subspace projection. Mod Navig 10(5):323–327
5. Hasan M, El-Sakka MR (2018) Improved BM3D image denoising using SSIM-optimized Wiener filter. EURASIP J Image Video Process 1:1–12
6. Qian H, Guang Zhi W, Yan Jun W (2014) Tracking optimization of FH signal based on Wiener filtering. Adv Mater Res 3326(989):4038–4041
7. Bindilatti AA, Vieira MAC, Mascarenhas NDA (2018) Poisson Wiener filtering with non-local weighted parameter estimation using stochastic distances. Signal Process 144:68–76

Extended Kalman Filter-Based GNSS Signal Tracking Method to Counter Spoofing Attacks

Shuai Yue, Rui Xu(✉), Qianjun Yan, and Jianye Liu

Navigation Research Centre, Nanjing University of Aeronautics and Astronautics, Nanjing, China
{yueshuai123, ruixu}@nuaa.edu.cn

Abstract. Under spoofing attacks, the positioning results of GNSS receivers will be towed away. In this study, based on the correlation results of mixed signals, a novel processing model for Kalman Filter-based GNSS code delay tracking loop is proposed. The proposed tracking loop aims to estimate the two sets of correlation peaks and code delays of both GNSS authentic signals and spoofing signals. In the observing model, different from the common KF-based GNSS tracking loop, the measurements are the coherent integrations rather than the DLL discriminator output. Experimental results show that the proposed method is able to estimate the parameters of both authentic signals and counterfeited signals simultaneously. The method can obtain information about the spoofing signal in time, which improves the anti-interference ability of GNSS receiver.

Keywords: GNSS receiver · Anti-spoofing method · GNSS tracking loop · Extended kalman filter

1 Introduction

In the past few years, Global Navigation Satellite System (GNSS) has been increasingly applied in military and civil fields. However, since the power of the received GNSS signal on Earth surface is weak, GNSS receivers are susceptible to various radio wave signals, such as spoofing signals, which have the similar signal structure to the authentic signals. Spoofing signals are able to mislead GNSS receiver, resulting in an erroneous position, velocity and time (PVT) solution.

Anti-spoofing technique is a potential direction and research hotspots in the field of navigation and positioning. It is generally carried out at the RF front end and the baseband signal processing part of the receiver. After the estimation of the spoofing signal and the authentic signal, the identification and culling of the spoofing signal can be finally realized. The GNSS spoofing detection technique based on monitoring carrier-to-noise ratio is given by [1]. Such methods can be easy to implement as they are software-defined, but they cannot achieve the identification results of the spoofing signals. They cannot suppress the spoofing signals, either. The multi-antenna defense strategy is proposed in [2]. Assuming that the spoofing signals are transmitted from the same direction, the spoofing device is unique and stationary; the strategy can partially detect and suppress the spoofing signals [3]. However, it weakens the useful signals in

J. Sun et al. (Eds.): CSNC 2019, LNEE 563, pp. 572–581, 2019.
https://doi.org/10.1007/978-981-13-7759-4_50

the same direction. Multipath mitigation techniques, represented by multipath estimating delay locked loop (MEDLL), have attracted widespread attention to be used for anti-spoofing technology [4]. Through using maximum likelihood estimation, it can estimate the parameters of direct path and multipath signals simultaneously. In order to estimate the parameters of spoofing signals, the observation information must be as complete as possible. Multi-correlator structure can meet the above requirements. In Dierendonck [5], it has been proved that multi-correlator structure with narrow code chip spacing is an effective measure to weaken the multipath effect. The conventional Kalman filter-based receiver cannot detect spoofing signals and has no anti-spoofing capability [6], because it does not consider the existence of spoofing signals in the filtering model. This makes the application scenario of the Kalman filter-based receiver limited.

In this paper, a novel GNSS signal tracking loop based on Extended Kalman Filter (EKF) is proposed. The algorithm aims to estimate the correlation peak and code delay of the GNSS signals and the spoofing signals when they are mixed. Different from the general KF-based GNSS tracking loop [7–9], the proposed tracking loop can simultaneously estimate the parameters of the GNSS signals and the spoofing signals, which has a significant contribution to the suppression of the spoofing signals.

This paper consists of five sections. A brief overview of the KF-based GNSS tracking loop is given in Sect. 2. The model of spoofing signal is presented in Sect. 3. The core principle of the tracking loop based on EKF is presented in Sect. 4. The results of spoofing signal tracking experiments are presented in Sect. 5. Finally, a short conclusion and further works are given in Sect. 6.

2 GNSS Tracking Loop Based on Kalman Filter

The receiver uses the traditional Delay Lock Loop (DLL) to track the C/A code and solve the accurate code delay. However, due to the weak GNSS signal power, the classical second/third-order tracking loop has insufficient ability to suppress the jitter noise. In order to solve the problem, there exists a common method to estimate the GNSS signal parameters using the Kalman filter.

The block diagram of DLL, which exploits the Kalman filter, is depicted in Fig. 1, where the measurements are represented by values of the DLL discriminator.

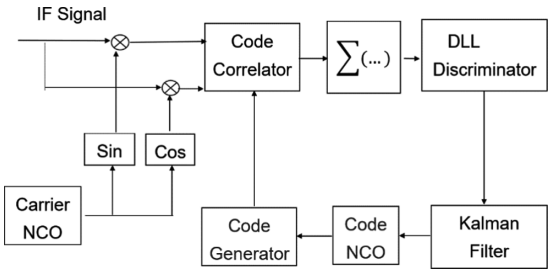

Fig. 1. Block diagram of a KF-based delay tracking loop

In Fig. 1, the output of the DLL discriminator is the only observation of the Kalman filter. By filtering white noise in the observation band more effectively, the Kalman filter achieves a higher estimation accuracy of the C/A code delay error than traditional tracking loop.

In order to keep the loop steady, the dynamic model of the system must be established accurately. The discrete code phase model is a second-order model, according to the following formula:

$$\boldsymbol{x_k} = \begin{bmatrix} \Delta\tau_k \\ f_k \end{bmatrix} = \begin{bmatrix} 1 & T \\ 0 & 1 \end{bmatrix} \begin{bmatrix} \Delta\tau_{k-1} \\ f_{k-1} \end{bmatrix} + \begin{bmatrix} -T \\ 0 \end{bmatrix} \dot{\Delta}\tau_{k-1}^{re} + \boldsymbol{w} \tag{1}$$

where $\boldsymbol{x_k}$ is state vector, $\Delta\tau_{k-1}$ is the code delay error, f_{k-1} is the rate of change of code delay at the start of the (k − 1)-th update interval, and T is predetection integration time (PIT) in unit of seconds, which is nominally 0.001 s. The item $\dot{\boldsymbol{\Delta}}\boldsymbol{\tau}_{\boldsymbol{k-1}}^{\boldsymbol{re}}$ is the reconstructed code Doppler rate, and w is the process noise vector, which satisfies the form of AWGN (Additive White Gaussian Noise).

The measurement model is written as:

$$\boldsymbol{y_k} = \left[1 - \frac{1}{2}T\right] \begin{bmatrix} \Delta\tau_k \\ f_k \end{bmatrix} + \frac{1}{2}T\dot{\Delta}\tau_{k-1}^{re} + v \tag{2}$$

where $\boldsymbol{y_k}$ is the code phase error, measured from the DLL discriminator, and v is observation noise vector. The value of the noise variance is related to the type of the discriminator.

The core of the traditional KF-based GNSS tracking loop is to reduce the effects of the jitter noise of the receiver. However, due to the indirectness of the observation and the loss of correlation result, it is impossible to estimate the parameters of the spoofing signals. The observation source of KF-based GNSS tracking loop is the original DLL discriminator output instead of the correlation output. A commonly used DLL discriminator function satisfies the following formula:

$$\delta_{cp} = \left(E^2 - L^2\right) / \left(E^2 + L^2\right) \tag{3}$$

Essentially, it attempts to lock the code delay of the GNSS signal only through two correlators, which is feasible and efficient in the case of pure GNSS signal. Nevertheless, if the receiver tracks the spoofing signal at the same time, the discriminator will lead to incorrect estimation for code delay. Under spoofing attacks, E and L are changed by the spoofing signals and contain both correlation values of the local replica with authentic signals and spoofing signals. However, the traditional phase discriminator is unable to cancel the spoofing signal-induced change. Therefore, it is necessary to replace the original phase discriminator and take into account the impact of the spoofing signal on the correlation result with a new structure. The KF will be a good choice. The KF-based tracking loop will be introduced in Sect. 5 in detail.

3 Spoofing Signal Model

The input of the GNSS tracking loop $s_{IF}(t)$ can be modeled as:

$$s_{IF}(t) = \sqrt{2P(t)}C(t)D(t)sin(2\pi ft + \theta_{IF}) + w(t). \quad (4)$$

where P(t) is GNSS signal power, C(t) is C/A code, D(t) is navigation data; f is the local carrier frequency, which consists of the IF signal frequency and the Doppler frequency in Hz, θ_{IF} is carrier phase; and w(t) is the additive white Gaussian noise (AWGN).

The structure of the spoofing signals is similar to that of the GNSS signals, but the spoofing signals have different code time delay and signal power. Under spoofing attack, the target receiver will receive mixed signals of authentic signals and spoofing signals transmitted from the spoofer. In this case, the mixed signal received by the target receiver can be expressed as:

$$s(t) = \sqrt{2P_{au}(t)}C(t)D(t)sin(2\pi ft + \theta_{IF}) + \sqrt{2P_{sp}(t)}C(t-\alpha)D(t)sin(2\pi ft + \theta_{IF}). \quad (5)$$

where, the subscript au refers to the GNSS authentic signal, and the subscript sp identifies the spoofing signal.

After the IF signal being mixed with the local carrier replica and correlated with the local code replica, a small part of the final correlation result is also the input of the code phase discriminator. The correlation result of mixed signal is given in Fig. 2.

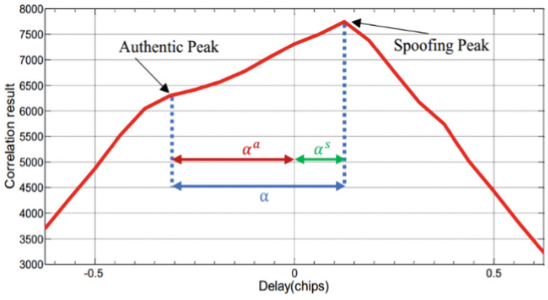

Fig. 2. Correlation result of received signal and the local repeat under spoofing attack

From Fig. 2, the spoofing signal power is usually higher than the authentic signal power, which can be inferred from the comparison results of the peak values of the two signals. The estimating code delay distance α between authentic and spoofing signals can be seen from Fig. 2. α^a is the code chip offset between GNSS signal and the specific code chip delay of mixed signal,and α^s is the code chip offset distance between spoofing signal and the specific code chip delay of mixed signal. The correlation peak of the mixed signal will be dragged from that of the authentic signal to that of the

spoofing signal. The process will not stop until the output of code phase discriminator chatters around 0.

To study the influence of the spoofing signal, the influence of other error sources and the additive white Gaussian noise are simplified. The In-phase $I^{\delta i}$ and the Quadra phase $Q^{\delta i}$ of the correlation output under spoofing for i-th channel is modeled as:

$$I^{\delta i} = [A^a R(\delta_i, \alpha^a) + A^s R(\delta_i, \alpha^s)] D \cos(\Delta\phi) \tag{6}$$

$$Q^{\delta i} = [A^a R(\delta_i, \alpha^a) + A^s R(\delta_i, \alpha^s)] D \sin(\Delta\phi) \tag{7}$$

where δ_i is the i-th code delay space from Prompt code, which is determined by multi-correlator structure. A^a and A^s are the amplitude of correlation peak of authentic and counterfeited signal, respectively. D is navigation data, the items of $R(\delta_i, \alpha^a)$ and $R(\delta_i, \alpha^s)$ are the code correlation function of authentic and spoofing signal; and $\Delta\phi$ is the carrier phase error.

4 EKF-Based Tracking Loop to Estimate Spoofing Parameters

The EKF-based tracking loop is improved through the KF-based tracking loop's modeling framework. Compared to the KF-based tracking loop, the new tracking loop discards the traditional phase discriminator. By directly observing the results of the coherent integration, the EKF-based tracking loop can expand the dimension of the state vector so that the parameters of the two signals can be tracked simultaneously.

Figure 3 shows the block diagram of the signal-tracking loop based on Extended Kalman Filter, where the measurements are derived from the multi-correlator structure.

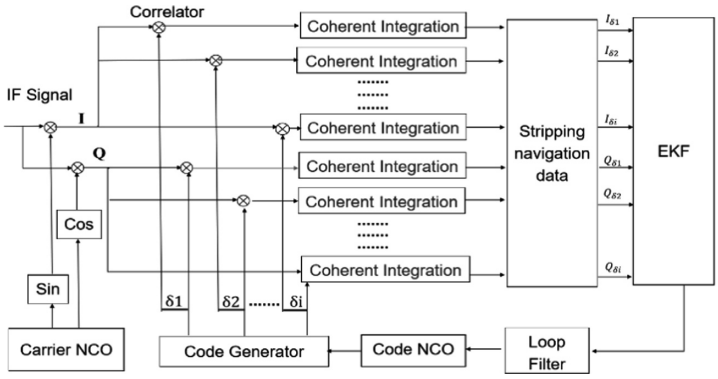

Fig. 3. Block diagram of the EKF-based tracking loop

The time update equation is given by the following equation:

$$\boldsymbol{X_{k+1}} = \boldsymbol{F}\boldsymbol{X_k} + \boldsymbol{B}\boldsymbol{U_k} + \boldsymbol{Q} \tag{8}$$

where the state column vector $\boldsymbol{X} = \begin{bmatrix} \Delta\tau & \dot{\Delta}\tau & A^a & A^s & \alpha^a & \alpha^s \end{bmatrix}^T$ comprises the code delay error $\Delta\tau$, the code Doppler rate $\dot{\Delta}\tau$, amplitude of correlation peak of GNSS signal A^a, amplitude of correlation peak of spoofing signal A^s, the code chip offset between GNSS signal and the specific code chip delay of mixed signal α^a, and the code chip offset distance between spoofing signal and the specific code chip delay of mixed signal α^s.

The value of the state transition matrix F is:

$$\boldsymbol{F} = \begin{pmatrix} 1 & T_{coh} & 0 & 0 & 0 & 0 \\ 0 & 1 & 0 & 0 & 0 & 0 \\ 0 & 0 & 1 & 0 & 0 & 0 \\ 0 & 0 & 0 & 1 & 0 & 0 \\ 0 & 0 & 0 & 0 & 1 & 0 \\ 0 & 0 & 0 & 0 & 0 & 1 \end{pmatrix} \tag{9}$$

The state transition matrix $\boldsymbol{F}$ is used to update the value of the $\boldsymbol{X_k}$ state across PIT. Moreover, $\boldsymbol{Q}$ is the process noise. T_{coh} is predetection integration time (PIT) in unit of seconds. The value of the control-input matrix $\boldsymbol{B}$ is:

$$\boldsymbol{B} = [-T_{coh}0\,0\,0\,0\,0]^T \tag{10}$$

B is applied to the control vector $\boldsymbol{U_k}$. And $\boldsymbol{U_k}$ comprises the reconstructed code Doppler rate $\Delta\tau^{re}$. At time $k + 1$, the observation of the true state $\boldsymbol{X_k}$ is made according to:

$$\boldsymbol{Z_{k+1}} = h(\boldsymbol{X_k}) + \boldsymbol{R_k}. \tag{11}$$

where h is the function which can calculate the predicted measurements $\boldsymbol{Z}$ from predicted state vector $\boldsymbol{X}$. The measurement update equations can be modeled by:

$$\tilde{I}_{k+1}^{\delta i} = \left[A_k^a R(\delta_i, \Delta\tau_k, \alpha_k) + A_k^s R\left(\delta_i, \Delta\tau_k, \alpha_k^s\right)\right] \cdot cos(\Delta\phi_k) + R_{\delta ki}^{wi} \tag{12}$$

$$\tilde{Q}_{k+1}^{\delta i} = \left[A_k^a R(\delta_i, \Delta\tau_k, \alpha_k) + A_k^s R\left(\delta_i, \Delta\tau_k, \alpha_k^s\right)\right] \cdot sin(\Delta\phi_k) + R_{\delta ki}^{wq} \tag{13}$$

where the measurement $\tilde{I}_k^{\delta i}$, $\tilde{Q}_k^{\delta i}$ is derived from $I^{\delta i}, Q^{\delta i}$ after culling navigation data. The dimension of the observation vector is determined by multi-correlator structure. $R_{\delta ki}$ is the observation noise.

5 Experiments and Analysis

5.1 Experiment Method and Environment

In order to test the performance of the proposed tracking loop, the simulation verification work was implemented. The GNSS signal was generated by the GNSS Receiver on the roof of college of automation engineering, NUAA, on July 2017.

The specification of the target receiver and signals are shown in Table 1.

Table 1. The specification of the GNSS receiver

Parameter	Value
Intermediate frequency	4.123968 MHz
Sampling frequency	16.3676 MHz
PLL bandwidth	25 Hz
DLL bandwidth	2 Hz
Predetection integration time	1 ms
Correlator chip spacing	0.0625 chip

To elaborate on the performance of the proposed EKF-based tracking loop, the case of the mixed signal with a ISR of 6.02 dB (The signal strength of spoofing signal was set to be 6.02 dB stronger than the GNSS signal, in other words, The former is twice that of the latter.) and a code delay offset of 0.5 chip was simulated and used in detail. Then the paper uses the same analysis steps to test other types of spoofing signals, and gives statistical results of EKF estimation ability. In the final test, this paper will test with LOA (Lift-of-aligned) using the proposed method.

5.2 Simulation Verification and Analysis

Figure 4 shows the spoofing and GNSS signal parameter estimation results of PRN 28 from the mixed signal using the proposed tracking loop.

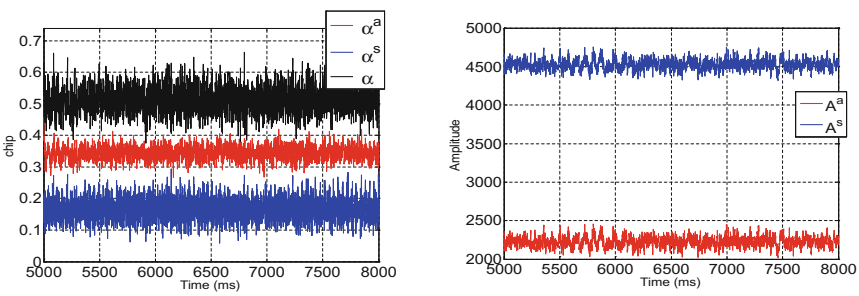

(a) Code delay estimation of mixed signal (b) Amplitude estimation of mixed signal

Fig. 4. Parameter estimation results of EKF-based tracking loop

In order to obtain a mixed signal correlation model, the EKF is introduced into the loop at 5000 ms. As shown in Fig. 4(a), the average estimated value of α^a was 0.166 chip, and the average estimated value of α^s was 0.329 chip. Based on the above results, the estimated code chip offset can be obtained, about 0.494 chip. Figure 4(b) shows the spoofing and the authentic signal amplitude of correlation peak estimation of PRN 28 from the mixed signal using the proposed tracking loop. As shown in Fig. 4 (b), the value of GNSS and spoofing signals' coherent integration amplitudes are estimated by EKF. Based on the above results, the estimated ISR can be obtained, about 5.872 dB. In other words, the amplitude ratio of spoofing signal to GNSS signal is about 1.966.

Based on the same analysis steps, Fig. 5 shows the statistical curves of EKF's estimation accuracy for the two parameters (amplitude ratio and code delay) as they change.

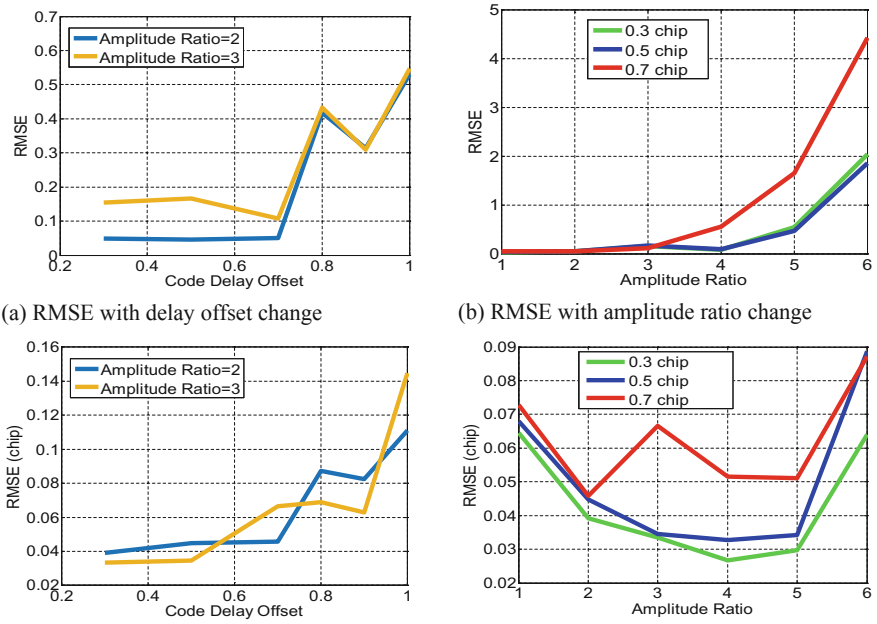

(a) RMSE with delay offset change

(b) RMSE with amplitude ratio change

(c) RMSE(chip) with delay offset change

(d) RMSE(chip) with amplitude ratio change

Fig. 5. Extended Kalman Filter estimation accuracy statistical results

The data in Fig. 5 shows that the EKF-based GNSS tracking loop can estimate the parameters of the spoofing signal relatively accurately, although it is a biased estimate. For a spoofing signal with a preset spoofing distance between 0.3 and 0.7 chip and an amplitude ratio between 1 and 4, EKF-based GNSS tracking loop has high estimation accuracy.

For LOA, EKF also has a certain estimation effect. For the spoofing signal with a traction rate of 0.1 chip/s and an initial code delay offset of 0.4 chip, the parameter estimation results of EKF are shown in Fig. 6.

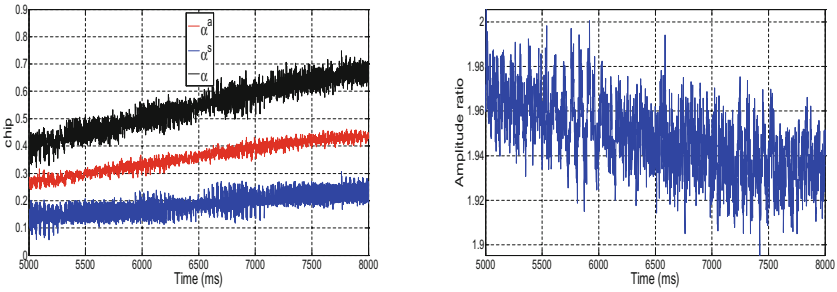

(a) Code delay offset estimation of LOA (b) Amplitude ratio estimation of LOA

Fig. 6. LOA parameter estimation results

As shown in Fig. 6(a), after 3000 ms of EKF estimation, the code delay gradually changed from a value of about 0.4 chip to about 0.7 chip at a certain rate, which is consistent with the preset value. Figure 6(b) shows the amplitude ratio estimation of the spoofing signal to GNSS signal. Compared with the preset value of 2, the amplitude ratio has a certain deviation from the estimation and has a certain change trend, which may be related to the LOA's own traction rate and external interference.

6 Conclusion

In this paper, an innovative GNSS tracking loop based on extended Kalman filter with increased dimensions to estimate the amplitude of correlation peak and code delay of the spoofing signal is presented. Compared to the traditional KF-based tracking loop, the proposed method can additionally estimate the code chip offset between GNSS and mixed signal. After obtaining the estimated amplitude of correlation peak and code delay of the spoofing signal, the receiver will be able to avoid the influence of the spoofing signal through calculating the pseudoranges of the authentic signals.

Future work will focus on exploring the coupling relationship between the amplitude of correlation peak and code delay. Based on the relationship, the proposed EKF-based loop can reduce the number of dimensions and calculations. Designing the feedback is also a promising research point. It makes the tracking loop gradually re-track the GNSS signal after getting the parameters of the spoofing signal by EKF. After that, converting the observation model of the EKF allows the loop to stably track the GNSS signals.

References

1. Zhang Z, Trinkle M, Qian L et al (2013) Quickest detection of GPS spoofing attack. In: Military communications conference. IEEE
2. Montgomery P, Humphreys T, Ledvina B (2009) A multi-antenna defense: receiver-autonomous GPS spoofing detection

3. Nielsen J, Broumandan A, Lachapelle G (2011) GNSS spoofing detection for single antenna handheld receivers. Navigation 58(4):335–344
4. Townsend BR, Fenton PC, Dierendonck KJV et al (1995) Performance evaluation of the multipath estimating delay lock loop. Navigation 42(3):502–514
5. Dierendonck AJV, Fenton P, Ford T (1992) Theory and performance of narrow correlator spacing in a GPS receiver. Navigation 39(3):265–283
6. Psiaki ML (2001) Smoother-based GPS signal tracking in software receiver. In: Proceedings of the ION GPS/GNSS 2001, 11–14 September, Salt Lake City, UT, pp 2900–2913
7. Huang B, Yao Z, Lu M et al (2013) A code phase measurement method for snap-shot GNSS receiver. In: China satellite navigation conference (CSNC), 2013 Proceedings. Springer, Heidelberg
8. Won JH, Pany T, Eissfeller B (2012) Characteristics of Kalman filters for GNSS signal tracking loop. IEEE Trans Aerosp Electron Syst 48(4):3671–3681
9. Tang X, Falco G, Falletti E et al (2017) Complexity reduction of the Kalman filter-based tracking loops in GNSS receivers. GPS Solutions 21(2):685–699

Fast Interference Detection Aided Notch Filter and Switched Tracking Loop for Mitigating Pulsed CWI in GNSS Receiver

Qianjun Yan(✉), Rui Xu(✉), Shuai Yue, Mengyu Ding, Ya Qi, Ruiqi Tang, and Jianye Liu

Nanjing University of Aeronautics and Astronautics, Nanjing 210016, China
{qianjunyan, ruixu}@nuaa.edu.cn

Abstract. The GNSS signals are vulnerable to radio frequency interferences. Among these interferences, continuous wave interferences (CWIs) are able to jam the GNSS signals. After pulse-modulation, the CWIs further cause the useful signal losses. To smooth the effects of useful signal losses, a notch filter with detection algorithm based on power switching tracking loop is proposed. The algorithm uses a time domain detector in order to reduce the computation cost. What's more, the periodically switches of the notch filter and the tracking loop are able to smooth the fluctuations of the Doppler frequencies and positioning estimation. A series of tests show that the method mitigates the effects of pulsed CWIs and improves the anti-jamming capability of the receiver.

Keywords: GNSS receiver · Notch filter · Pulsed CWIs · Anti-jamming technique · Blanket jamming

1 Introduction

GNSS receivers have become fundamental instrument since they provide accurate positioning service. However, due to the low power (−130 dBm) of the GNSS signals, the receivers are vulnerable to in-band radio frequency (RF) interferences [1–3]. Among different RF interferences, pulsed Continuous Wave Interferences (CWIs) strongly affect the tracking loops, resulting in reduction of correlator outputs, abnormal fluctuations of Doppler frequencies and even loss of lock.

To mitigate pulsed CWIs, various methods based on space, time and frequency domain are proposed. Within them, space domain methods are effective for mitigating most interferences [4–6]. However, the methods also attenuate the useful signals from the similar direction of the jammer. Their anti-interference performances are superior to the time and frequency domain methods. For example, the space domain methods aid receivers keep signal tracking under −70 dBm interference [7], while most time and frequency domain methods mitigate the effects of CWIs with power ≤ -75 dBm [8–10]. However, time and frequency domain methods are easy to implement without requirement of multiple antennas of antenna array [9, 11, 12]. They indeed keep signals in all directions. In the two types of methods, the time domain methods provide lower improve ratio compared with the frequency domain methods [13]. Thus, the frequency

J. Sun et al. (Eds.): CSNC 2019, LNEE 563, pp. 582–592, 2019.
https://doi.org/10.1007/978-981-13-7759-4_51

domain methods become optimal alternatives. The notch filter is the most known frequency domain method. It effectively suppresses the CWIs but hardly smoothes the abnormal periodic fluctuations of Doppler frequencies under pulsed CWIs.

To improve the anti-interference performances of the receivers under pulsed CWIs, a fast interference detector is proposed to control the states of the notch filter and tracking loops. Besides, a switched tracking loop is exploited to substitute the traditional closed tracking loop. The detector compares the signal magnitude with its normal level. If the signal magnitude significantly exceeds the level, it is considered that the receiver is under interference. Once the interference detected, the notch filter begins working and the closed tracking loop switches to the open tracking loop. When the interference leave, the open loop returns to the closed loop and the notch filter stops working. The notch filter and the switched tracking loop together smooth the abnormal periodic fluctuations of Doppler frequencies and hence eliminate the possibilities of loss of lock.

The signal model and mathematical analysis is presented in Sect. 2. The structure of the algorithm is introduced in Sect. 3. The performance of the algorithm is analyzed in Sect. 4, and the conclusion is given in the final Section.

2 Signal Model and Mathematical Analysis

The signal $r(t)$ is the input of the receiver. It can be modeled as the sum of the GNSS signal $S^i(t)$, the pulsed CWI $J^i(t)$ and the noise $n(t)$, and written as

$$r(t) = \sum_{i=1}^{L} S^i(t) + J^i(t) + n(t) \tag{2.1}$$

where i is Pseudo Random Noise (PRN) number and L is total number of the available satellites.

The GNSS signal $S^i(t)$ can be expressed by

$$S^i(t) = \sqrt{2P_G^i}c^i\left(t-\tau_G^i\right)d^i\left(t-\tau_G^i\right)sin\left[2\pi\left(f_{L1}+f_{dop}^i\right)\left(t-\tau_G^i\right)+\theta_G^i\right] \tag{2.2}$$

where P_G^i is power of the i-th satellite signal; c^i is C/A code of the i-th satellite; τ_G^i is signal-reference code phase difference in code chips; f_{L1} is frequency of L1 carrier; f_{dop}^i is frequency of the estimated Doppler frequency; d^i is the navigation message of the i-th satellite; and, θ_G^i is initial phase of the GPS L1 carrier.

The jamming signal $J^i(t)$ can be expressed by

$$J^i(t) = \begin{cases} \sqrt{2P_J^i}sin\left[2\pi f_{LJ}^i\left(t-\tau_J^i\right)+\theta_J^i\right], t \in (n, nT \cdot DC) \\ 0, t \notin (n, nT \cdot DC) \end{cases} \tag{2.3}$$

where P_J^i is power of jamming signal; f_{LJ}^i is frequency of pulsed CWI, equaling to the nominal center frequency of carrier wave; τ_J^i is interference-reference code phase

difference in code chips; θ_J^i is initial phase of the jamming signal; and, T is pulse repetition period, DC is duty cycle of the pulsed CWI.

In the front-end, the RF signal is down-converted to intermediate frequency (IF) signal by mixing with local oscillator. When $t \in (n, nT \cdot DC)$, the IF signal can be expressed by

$$\begin{aligned} S_{IF}^i(t) = &\frac{1}{2}A_{LO}\sqrt{2P_G^i}c^i\left(t-\tau_G^i\right)d^i\left(t-\tau_G^i\right)cos\left(2\pi\left(f_{L1}+f_{dop}^i-f_{LO}\right)t+\theta_G^i-\theta_{LO}\right) \\ &+\frac{1}{2}A_{LO}\sqrt{2P_J^i}cos\left(2\pi\left(f_{LJ}^i-f_{LO}\right)t+\theta_J^i-\theta_{LO}\right) \end{aligned} \tag{2.4}$$

where f_{LO} is frequency of the local oscillator; θ_{LO} is initial phase of the local oscillator.

After baseband processing, the IF signal is converted to in-phase and quadrate components and can be expressed by

$$\begin{aligned} r_p^i(t) = &a_G^i R_0\left(\tau_G^i\right)sinc\left(\Delta f_G^i T_{coh}\right)e^{j\left(2\pi\Delta f_G^i\left(t+\frac{T_{coh}}{2}\right)+\theta_G^i\right)} \\ &+a_J^i(1/N)sinc\left(\Delta f_J^i T_{coh}\right)e^{j\left(2\pi\Delta f_J^i\left(t+\frac{T_{coh}}{2}\right)+\theta_J^i\right)} \end{aligned} \tag{2.5}$$

where N is number of sample; T_{coh} is integration period; t is initial time of integration period; $R_0\left(\tau_G^i\right)$ is the cross correlation of the received C/A code and the receiver estimate of the code; $a_G^i = (1/2)A_{LO}\sqrt{2P_G^i}$; $a_J^i = (1/2)A_{LO}\sqrt{2P_J^i}$; $\Delta f_G^i = f_{L1} + f_{dop}^i - f_{LO}$ and $\Delta f_J^i = f_{LJ}^i - f_{LO}$.

Take a derivative with respect to discriminator output and the fluctuations of the Doppler frequencies can be expressed by

$$\Delta f_d^i(t) = \frac{A\left(cos\left(2\pi\Delta f_G^i(t+T_{coh}/2)+\theta_G^i\right)+A\right)}{1+2Acos\left(2\pi\Delta f_G^i(t+T_{coh}/2)+\theta_G^i\right)+A^2}\Delta f_J^i \tag{2.6}$$

where $A = (1/N)\sqrt{P_J^i/P_G^i}sinc\left(\Delta f_J^i T_{coh}\right)$.

3 Proposed Algorithm

In this section, an algorithm designed for mitigating the effects of the pulsed CWIs on positioning is proposed.

3.1 Architecture of Detector Aided Interference Mitigation Algorithm

As is shown in Eq. (2.6), the pulsed CWIs can lead to abnormal fluctuations of Doppler frequencies in the traditional closed tracking loop. Different from the closed tracking loop, the open tracking loop is able to keep the Doppler frequencies the same as the input. Therefore, during the pulse period, the notch filter works and the normally used closed tracking loop switches to open tracking loop. The point which is noticeable is

that the input frequency of the open loop is the estimated frequency of the previous moment, since the Doppler frequency changes little in a short pulse period. Moreover, when the pulsed CWIs leave, the open tracking loop returns to the closed loop and the notch filter stops working.

The algorithm with low complexity can provide the references for engineering applications. The structure of the algorithm is shown in Fig. 1.

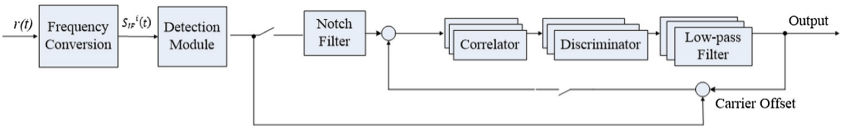

Fig. 1. The structure of the algorithm.

3.2 Fast Detection Module

The common detector based on Fast Fourier Transform (FFT) causes large amounts of computation. To improve the efficiency of the interference detection, a time domain detector is exploited. The detector determines interference occurrence by comparing the signal magnitude with the normal level. Since the integration period of the tracking loop is 1 ms, if the signal magnitude integrated in 1 ms exceeds its normal level, the CWI is detected. The normal level $\left(1.8 \times 10^6\right)$ is obtained from normal signals, as is shown in Fig. 2.

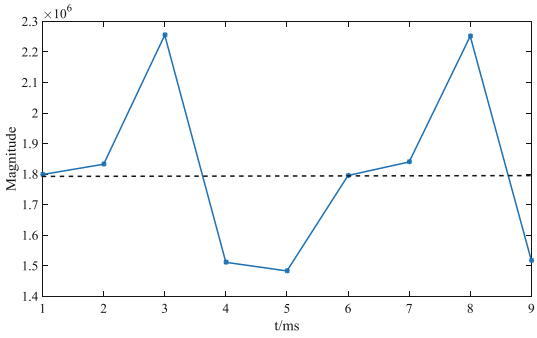

Fig. 2. Result of time domain detection method.

The result of the time domain detection method is compared with that of the time-frequency distribution of the interfered signal based on the short-time Fourier transform (STFT), as is shown in Fig. 3.

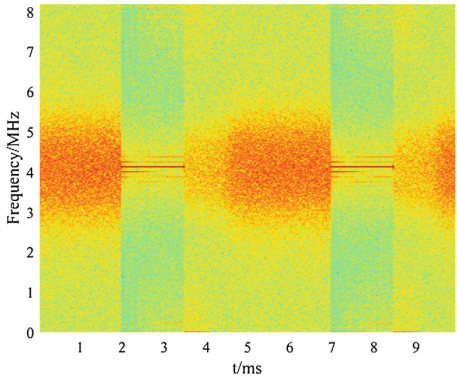

Fig. 3. Time-frequency distribution of the interfered signal.

Both Figs. 2 and 3 show that the CWI appears at the 2nd, 3rd, 7th and 8th ms. The consistency between two detection methods indicate that the time domain detector accurately detects the CWI. The time domain method requires less computational complexity than the FFT method for no need of Fourier Transform.

3.3 Structure of Notch Filter

Notch filter can attenuate the power of the signal at certain frequency. The ideal frequency response of the notch filter is:

$$\left|H\left(e^{j2\pi f_0}\right)\right| = \begin{cases} 1, f \neq f_0 \\ 0, f = f_0 \end{cases} \tag{3.1}$$

where f_0 is the notch frequency.

The Z-domain transfer function of the notch filter is characterized by:

$$H(z) = \frac{1 - 2Re\{z_0\}z^{-1} + |z_0|^2 z^{-2}}{1 - 2k_\alpha Re\{z_0\}z^{-1} + k_\alpha^2 |z_0|^2 z^{-2}} \tag{3.2}$$

where $Re\{z_0\}$ represents the real part of the parameter z_0, the parameter k_α influences the bandwidth B and the trap depth of the notch filter. The parameter z_0 is determined by the notch frequency and can be expressed as

$$z_0 = exp(2\pi f_0) = exp(2\pi f_{IF}) \tag{3.3}$$

where f_{IF} is the nominal frequency of GNSS carrier wave. Notch filter is used to remove the pulsed CWI and its notch frequency should be equal to CWI's center frequency. Commonly, CWI has the same frequency to the nominal frequency of GNSS carrier wave. Hence, notch frequency equals the GNSS IF frequency.

The parameter k_α should be adjusted according to the bandwidth and the trap depth of the notch filter. It can be estimated by using −3-dB bandwidth B and can be expressed by

$$k_\alpha = \frac{1 - tan(B/2)}{1 + tan(B/2)} \tag{3.4}$$

Figure 1 shows the frequency response of the notch filter. When k_α decreases, the bandwidth becomes wider and the trap depth becomes deeper (Fig. 4).

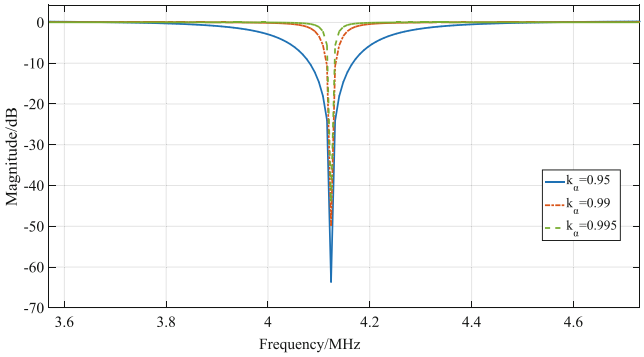

Fig. 4. Frequency characteristic of the notch filter with different parameter k_α.

In order to filter out the pulsed CWI and retain the useful signal, the bandwidth of the notch filter must be narrow and the trap depth of the notch filter should be adjusted. Tests are conducted to obtain the optimal parameter k_α.

4 Experiments and Tests

To test the performance of the algorithm for mitigating pulsed CWIs, experiments based on actual signals were conducted.

4.1 Experiment Environment

The actual signals are collected on September 26th. Figure 5 shows the hardware setup for experiments. The jammer generates pulsed CWIs with different power $\left(P_J^i\right)$, duty cycle (DC) and pulse repetition period (T). The GNSS signals received by an antenna were mixed with the pulsed CWIs via a combiner. The mixed signals were connected to a signal sampler. The output of the sampler is transmitted to a GNSS receiver.

Pulsed CWIs with different parameters have different influences on receivers [14]. In the case of T = 10 ms, when $P_J^i < -60$ dBm, the Root Mean Square Error (RMSE) of Doppler frequencies is smaller than 2 Hz. However, when $P_J^i \geq -60$ dBm, the RMSE increases 3 Hz. To smooth the abnormal fluctuations of the Doppler

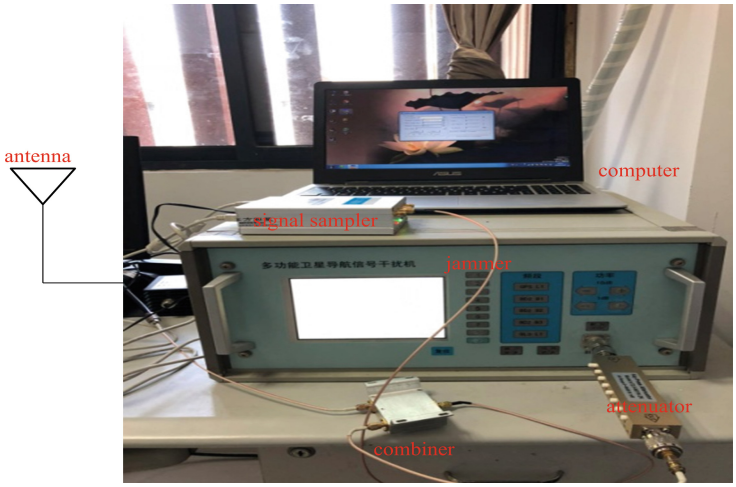

Fig. 5. The picture of the physical equipment connected.

frequencies, an algorithm is proposed and its performance is tested based on the software receiver. Parameters of the receiver are given in Table 1.

Table 1. Parameters of GNSS receiver.

Symbol	Quantity
Center frequency	1575.42 MHz
Sampling rate	16.367667 MHz
Bandwidth	2 MHz
Quantization bits	2bit
IF of GNSS signal	4.123968 MHz
PLL bandwidth @ integral time	20 Hz@1 ms
DLL bandwidth @ integral time	1 Hz@1 ms

During pulse period, the frequency spectrogram of the IF signal is shown in Fig. 6. The notch filter removes the interference and the useful signal maintains. The performance of the notch filter depends on k_α. The optimal parameter $(k_\alpha = 0.99)$ is determined by a series of tests.

4.2 Performance of the Algorithm for Mitigating Pulsed CWIs

Figure 7 shows the Doppler frequencies estimated by the receiver without any anti-interference algorithm, with notch filer, and with the proposed algorithm, under −60 dBm pulsed CWIs with different DC.

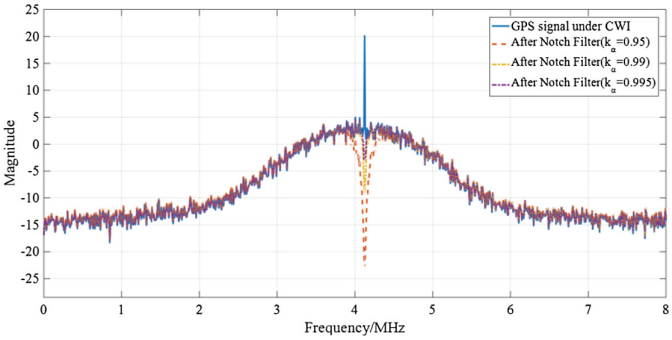

Fig. 6. Spectrogram of IF signal interfered by pulsed CWI and filtered by notch filter.

As is shown in Fig. 7, the Doppler frequencies fluctuate periodically. In the case that T remains unchanged, the fluctuation frequency increases when DC increases. Moreover, the RMSE of the Doppler frequencies of the signals under CWIs is approximately 5 Hz; meanwhile the maximum value of the fluctuations reaches 18 Hz. After notch filtering, the fluctuation decreases but still exists. The RMSE decreases to 3.5 Hz. With the assistance of the open tracking loop, the fluctuation is significantly eliminated. The RMSE decreases to 1.5 Hz and the maximum value of the fluctuations greatly reduced to about 2 Hz. Generally, the RMSE and the maximum value of the Doppler frequencies of the protected signals under −60 dBm CWIs are the same as those of the normal signals.

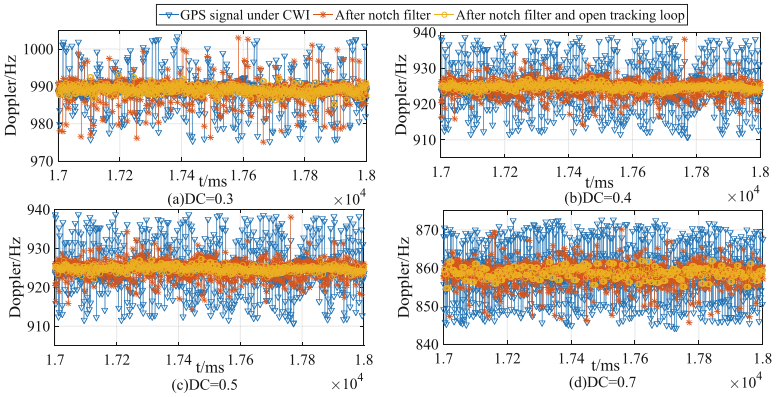

Fig. 7. Doppler frequencies estimated by the receiver without any anti-interference algorithm, with notch filer, and with proposed algorithm, under −60 dBm pulsed CWIs with different DC.

As is shown in Eq. (2.5), the Doppler fluctuations induce the adverse phase of the in-phase correlator outputs.

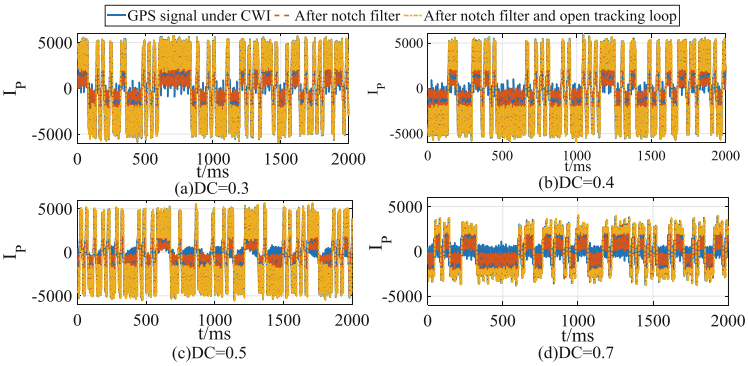

Fig. 8. In-phase correlator outputs of GNSS signals without any anti-interference algorithm, with notch filer, and with proposed algorithm, under −60 dBm pulsed CWIs with different DC.

As is shown in Fig. 8, under the CWIs, the signs of some in-phase correlator outputs change about. When DC increases, the changes become more severely. Since the adverse phase frequently happens, some satellites become unavailable and when the number of the available satellites is smaller than 4, the GNSS receivers cannot position. After notch filtering, the incorrect sign changes are partly modified and the receivers can achieve correct positioning results. With the assistance of the switched tracking loop, the incorrect sign changes are further modified. When the positioning errors of the filtered signals are higher than that of the normal signals, the errors can be decreased by the algorithm in the paper.

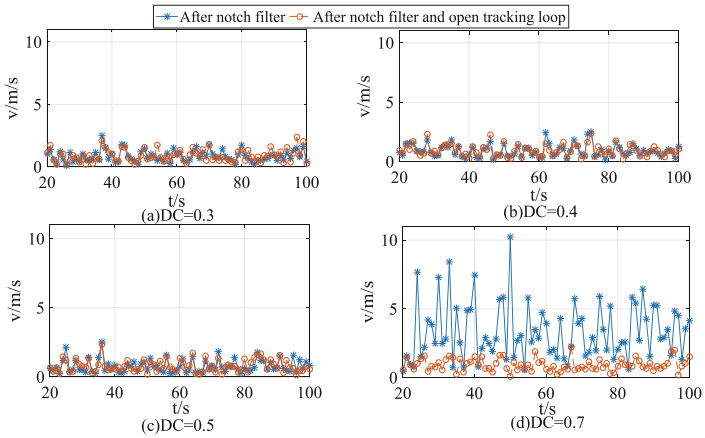

Fig. 9. Positioning velocities of GNSS signal with notch filer, and with the proposed algorithm, under −60 dBm pulsed CWIs with different DC.

As is show in Fig. 9, the GNSS receivers cannot position due to the adverse phase of the in-phase correlator outputs. After notch filtering, in the case of $DC < 0.7$, the positioning velocities are smaller than 2 m/s. When DC = 0.7, the positioning velocities are larger than 5 m/s, and the maximum value reaches 10 m/s. With the assistance of the switched tracking loop, the positioning velocities decrease by 8 m/s. Generally, the notch filter and the switched tracking loop together enable the positioning velocities less than 2 m/s.

5 Conclusions

Strong interferences cause the Doppler fluctuations and increase the changes of the signs of some in-phase correlator outputs of the victim receiver. The notch filter is able to improve the robustness of the GNSS receiver, while the proposed algorithm improves the accuracy of Doppler frequency estimation and significantly reduces the adverse phase of the in-phase correlator outputs under strong pulsed CWIs $\left(P_J^i = -60\,\text{dBm},\ \text{DC} = 0.3 - 0.7\right)$. The proposed method also keeps the velocity estimation error within 2 m/s under the pulsed CWIs $\left(P_J^i = -60\,\text{dBm},\ \text{DC} = 0.3 - 0.7\right)$.

The present work is just a preliminary demonstration of the suitability of the algorithm in mitigating the effects of the pulsed CWIs on the GNSS signals. Future work will focus on a more thorough statistical analysis and more methods for mitigating the effects of many other jamming signals on receivers.

References

1. Ioannides RT, Pany T, Gibbons G (2016) Known vulnerabilities of global navigation satellite systems, status, and potential mitigation techniques. Proc IEEE 104(6):1174–1194
2. Laitinen E (2017) Physical Layer Challenges and Solutions in Seamless Positioning via GNSS, Cellular and WLAN Systems. Tampere University of Technology. Publication, 1470
3. Qu Z, Yang J, Chen J (2015) Continuous wave interference effects on ranging performance of spread spectrum receivers. Wireless Pers Commun 82(1):473–494
4. Vagle N (2016) Interference Mitigation and Measurement Quality Assessment for Multi-Antenna GNSS Receivers. University of Calgary
5. Marathe T (2016) Space-Time Processing Methods to Enhance GNSS Signal Robustness under Electronic Interference. University of Calgary
6. Li M, Dempster AG, Balaei AT et al (2011) Switchable beam steering/null steering algorithm for CW interference mitigation in GPS C/A code receivers. IEEE Trans Aerosp Electron Syst 47(3):1564–1579
7. Dai X, Nie J, Chen F et al (2017) Distortionless space-time adaptive processor based on MVDR beam former for GNSS receiver. IET Radar Sonar Navig 11(10):1488–1494
8. Schmidt E, Ruble ZA, Akopian D et al (2018) A reduced complexity cross-correlation interference mitigation technique on a real-time software-defined radio GPS L1 receiver. In: ION. IEEE, pp 931–939
9. Zhao H, Hu Y, Sun H et al (2018) A BDS interference suppression technique based on linear phase adaptive IIR notch filters. Sensors 18(5):1515

10. Mosavi MR, Moghaddasi MS, Rezaei MJ (2016) A new method for continuous wave interference mitigation in single-frequency GPS receivers. Wireless Pers Commun 90 (3):1563–1578
11. Chien YR, Chen PY, Fang SH (2017) Novel anti-jamming algorithm for GNSS receivers using wavelet-packet-transform-based adaptive predictors. IEICE Trans Fundam Electron Commun Comput Sci 100(2):602–610
12. Chien YR (2015) Design of GPS anti-jamming systems using adaptive notch filters. IEEE Syst J 9(2):451–460
13. Mao WL (2017) Robust set-membership filtering techniques on GPS sensor jamming mitigation. IEEE Sensors J 17(6):1810–1818
14. Balaei AT, Dempster AG, Presti LL (2009) Characterization of the effects of CW and pulse CW interference on the GPS signal quality. IEEE Trans Aerosp Electron Syst 45(4): 1418–1431

Research on the Random Traversal RAIM Method for Anti-spoofing Applications

Jianfeng Li, Hong Li(✉), Chenxi Peng, Jian Wen, and Mingquan Lu

Department of Electronic Engineering, Tsinghua University,
Beijing 100084, China
lihongee@tsinghua.edu.cn

Abstract. Spoofing attack is one of the main security threats faced by Global Satellite Navigation System (GNSS). If the spoofing signal is regarded as the fault satellite signal, the conventional Receiver Autonomous Integrity Monitoring (RAIM) algorithm can be used for spoofing detection, but its performance is limited by the number of spoofing signals. In this paper, a random traversal RAIM method is proposed for anti-spoofing applications. In the method, the conventional RAIM algorithm is used as the core, and spoofing signals are detected and eliminated by random signal removal and iteration. When there are more than four real signals, the method can effectively eliminate spoofing signals and get correct positioning results by using real signals. So it solves the problem effectively that conventional RAIM algorithm can only detect but not eliminate spoofing signals to get correct positioning results. Finally, simulation and actual signal test results verify the effectiveness of the proposed method.

Keywords: GNSS · Spoofing detection · RAIM · Random traversal

1 Introduction

With the rapid development of GNSS, navigation and positioning services have been widely used in transportation, energy, communication, agriculture and other fields. However, with the increase of security threats such as jamming and spoofing, people pay more and more attention to the security of navigation and positioning. Jamming will make the GNSS receiver unavailable, while spoofing will make the GNSS receiver get wrong positioning results, which will lead to more serious consequences [3, 4].

If the spoofing signal is regarded as a fault satellite signal, the spoofing detection can be realized by using the RAIM algorithm. The conventional RAIM algorithm is mainly applied to fault detection and elimination (FDE). It detects faults and excludes them by detecting the consistency among the measured values of each satellite's pseudorange [2]. The performance of conventional RAIM is influenced by the redundancy of satellites and the geometric distribution of satellites [5, 8]. When the number of satellites is greater than or equal to 6 and there is only one satellite fault, the conventional RAIM can detect and eliminate the fault [9]. When there are multiple satellite faults, the conventional RAIM algorithm can only detect whether there are faults. The probability of a single satellite fault is relatively little, while the probability of two or more satellites faults at the same time is much less. So the application of

J. Sun et al. (Eds.): CSNC 2019, LNEE 563, pp. 593–605, 2019.
https://doi.org/10.1007/978-981-13-7759-4_52

conventional RAIM algorithm in satellite fault detection is feasible. However, unlike satellite faults, spoofing attacks can have multiple spoofing signals at the same time, and generally there is a good synergy among spoofing signals. So the performance of the conventional RAIM algorithm in spoofing detection and elimination (SDE) will be very limited.

Since the RAIM algorithm has been put forward, there have been many researches on its development and optimization. The weighted RAIM algorithm proposed by Walter and Enge in 1995 effectively improves positioning accuracy and integrity by using the prior information to weight different satellite's information [11]. The author analyses the performance of RAIM when two-satellite faults occur simultaneously in the paper [6]. An iterative RAIM algorithm is proposed, which can be well applied to the occurrence of simultaneous two-satellite faults [10]. The method and performance analysis of detecting multiple satellite faults through RAIM features on different epochs are described in detail in the paper [7].

So aiming at spoofing detection and mitigation, the paper proposed a random traversal RAIM method which takes the conventional RAIM algorithm as the core. The basic idea is that the conventional RAIM algorithm will be invoked in each iteration. If the conventional RAIM algorithm is effective, the traversal will end and the correct positioning result is got. On the contrary, the traversal iteration will continue by removing the signal randomly. In this paper, the conventional RAIM algorithm is considered as effective if it can detect and mitigate spoofing to get the correct positioning result. The introduction of the random traversal method will improve the application scope of RAIM algorithm, so that it has a strong ability of SDE. If the number of real signals is more than 4 and spoofing signals are not entirely consistent, the algorithm can get the correct positioning result by randomly removing the signal, traversing and iteration. To satisfy the requirement of entirely consistency, the number of spoofing signals is more than four and more than four of all spoofing signals can be solved to obtain a spoofing location that makes conventional RAIM effective. In addition, the performance and complexity of the random traversal RAIM method are affected by the number of real signals and spoofing signals. The article has carried on the detailed theory analysis and the discussion on this issue.

The following chapters are organized as follows. At first, we introduce in detail the implementation of the random traversal RAIM method in Sect. 2. Then in Sect. 3, the algorithm complexity of the method is analysed. In Sect. 4, the simulation results about the performance of the random traversal RAIM method and the actual signal test results are given. Finally, the paper is summarized in Sect. 5.

2 The Random Traversal RAIM Method

2.1 Introduction to Conventional RAIM

The conventional RAIM uses the redundant information of the measured values to detect the consistency among all pseudorange values. In GNSS receiver, only 4 visible satellites are enough to achieve positioning and timing. However, when the conventional RAIM algorithm is implemented effectively, the receiver needs to observe at

least five satellites at the same time. In the paper, the least square residual method proposed by Parkinson is used to introduce the conventional RAIM theory [8].

The pseudorange residual observations in the GNSS receiver are as follows:

$$\mathbf{y} = (\mathbf{d} - \boldsymbol{\rho} - c\triangle t * \mathbf{1}) = \mathbf{G}\mathbf{x} + \boldsymbol{\varepsilon} \tag{1.1}$$

where $\mathbf{d}$ is a $n \times 1$ vector. Its i^{th} element represents the distance between the i^{th} visible satellite position and the user position. $\boldsymbol{\rho}$ is a $n \times 1$ vector. Its i^{th} element represents the pseudorange value of the i^{th} visible satellite. $\triangle t$ is the receiver clock error while c is the speed of light. $\mathbf{1}$ is a $n \times 1$ vector and each element is 1. $\mathbf{x}$ is the 4×1 state vector. $\boldsymbol{\varepsilon}$ is a $n \times 1$ vector, representing the measurement error, and each element obeys the independent Gauss distribution. $\mathbf{G}$ is the geometric matrix.

Further, the least squares estimate $\hat{\mathbf{x}}$ of $\mathbf{x}$ can be obtained:

$$\hat{\mathbf{x}} = (\mathbf{G}^T\mathbf{G})^{-1}\mathbf{G}^T\mathbf{y} \tag{1.2}$$

$\hat{\mathbf{y}}$, the estimation of $\mathbf{y}$, can be obtained based on $\hat{\mathbf{x}}$:

$$\hat{\mathbf{y}} = \mathbf{G}(\mathbf{G}^T\mathbf{G})^{-1}\mathbf{G}^T\mathbf{y} \tag{1.3}$$

The pseudorange residual error vector is the pseudorange residual observation minus the pseudorange residual estimation and its expression is as follows:

$$\mathbf{w} = \mathbf{y} - \hat{\mathbf{y}} = \mathbf{S}\mathbf{y} \tag{1.4}$$

where $\mathbf{S}$ matrix is:

$$\mathbf{S} = \mathbf{I} - \mathbf{G}(\mathbf{G}^T\mathbf{G})^{-1}\mathbf{G}^T \tag{1.5}$$

$\mathbf{I}$ is a identity matrix of order n.

The detection statistic SSE is the sum of the squares of pseudorange residual errors. It can be expressed as:

$$SSE = \mathbf{w}^T\mathbf{w} \tag{1.6}$$

In the case of no satellite fault, each element of $\boldsymbol{\varepsilon}$ obeys independent and identical Gauss distribution which is zero-mean. SSE obeys the chi square distribution and its degree of freedom is $N - 4$, where N is the number of visible satellites. Therefore, the detection threshold T_{SSE} of the conventional RAIM algorithm can be determined according to the false alarm probability P_{fa}. If the detection statistic obtained from GNSS receivers is larger than the detection threshold, satellite faults are considered to exist, and vice versa.

In the case of only one satellite fault, the conventional RAIM can also be used for fault elimination [1]. The following method is included.

$$FDE = \arg \max_{1 \le i \le N} \left\{ \frac{w_i^2}{s_{ii}} \right\} \tag{1.7}$$

where *FDE* indicates the satellite pseudorandom noise code (PRN) number that will be excluded. N is the number of visible satellites. w_i represents the i^{th} element of the $\mathbf{w}$ vector while s_{ii} represents the i^{th} element on the diagonal line of the $\mathbf{S}$ matrix.

Assuming that there are $N(N \ge 5)$ visible satellites, the process of conventional RAIM algorithm is summarized as follows:

(1) The value of the detection statistic *SSE* is calculated and compare it with the detection threshold T_{SSE}. If $SSE < T_{SSE}$, there is no satellite fault and the algorithm comes to an end. Conversely, there is a satellite fault and the alarm is given.
(2) If $N = 5$, the algorithm will be finished. If $N > 5$, *FDE* is calculated and the corresponding satellite is labeled as the fault satellite.
(3) The remaining $N - 1$ visible satellites are used to position, velocity and time (PVT) solution and *SSE* is calculated. If $SSE < T_{SSE}$, it indicates that only one satellite fault exists and is successfully eliminated. Conversely, it indicates that there are multiple satellite faults, and RAIM fails to eliminate fault satellites.

In the paper, effective cRAIM (conventional RAIM) is defined as: when there is no satellite fault, it can output PVT results normally; when there is a satellite fault, it can eliminate the fault and output PVT results normally.

2.2 The Random Traversal RAIM Method

Due to the limitation of cRAIM in the case of multiple-spoofing signals, the paper proposes a random traversal RAIM method. In the method,the conventional RAIM algorithm is used every iteration as the core, and spoofing signals are detected and eliminate by random signal removal and iteration.

The method performs cRAIM verification every time, and if the cRAIM is effective, then the method will be finished. If the cRAIM is invalid, partial signals are randomly removed and the method continues. Removing signals is a traversal process. So as long as there are more than four real satellite signals, there must be a traversal situation to make cRAIM effective, and then the correct PVT results can be obtained. When the number of visible satellite is greater than 4, the random traversal RAIM method is enabled (Fig. 1).

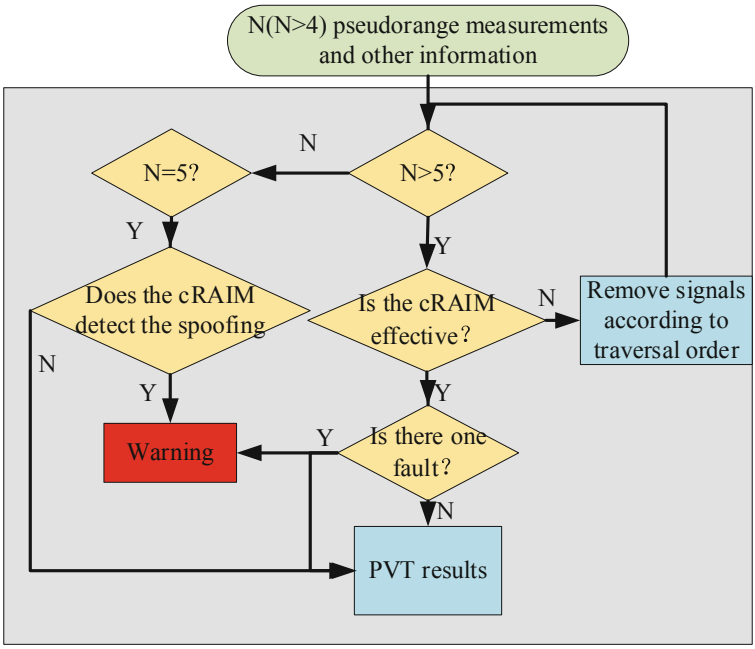

Fig. 1. Flow chart of the random traversal RAIM method

The method removes the signal by the traversal sequence shown below:

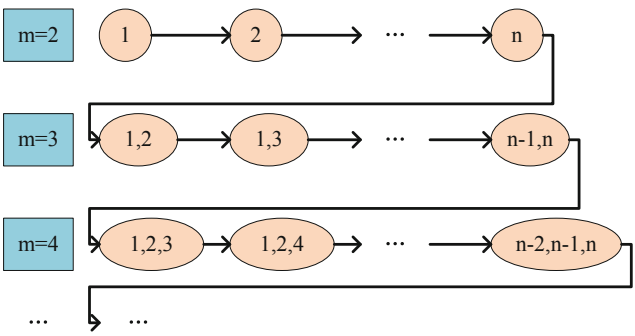

Fig. 2. Traversal sequence diagram

In the Fig. 2, n is the number of visible satellites while m is the number of spoofing signals, and n visible satellites are numbered $1, 2, \cdots, n$. The arrow direction is the traversal order. The removed satellite signal numbers are showed in the ellipse for this traversal period. When there are two spoofing signals, the traversal ends at the first level; when there are three spoofing signals, the traversal ends at the second level; and so on.

3 The Complexity Analysis of the Random Traversal RAIM Method

In the chapter, we mainly analyze the complexity of the random traversal RAIM method. The complexity of random traversal RAIM method is mainly affected by traversal times. The cRAIM algorithm is used once in each traversal. Therefore, the paper takes the number of calling the cRAIM algorithm (traversal times) as the measurement of random traversal RAIM method's complexity.

Suppose the number of visible satellite is n, of which there are m spoofing signals. Because cRAIM can eliminate a spoofing signal when it is valid, the traversal will end at the $(m-1)^{th}$ level. According to the theory of permutation and combination, we can figure out that the traversal number of the $(m-1)^{th}$ layer in Fig. 2 is $q = C_n^{m-1}$. If the traversal ends at the $(m-1)^{th}$ level, there will be $p = C_m^{m-1}$ combinations that make the cRAIM effective. The minimum, maximum and mathematical expectation of traversal times are derived and given below.

$$\begin{aligned} S_{\min} &= 1 + n + \cdots + C_n^{m-2} + 1 = \sum_{k=0}^{m-2} C_n^k + 1 \\ S_{\max} &= 1 + n + \cdots + C_n^{m-1} - C_m^{m-1} + 1 = \sum_{k=0}^{m-1} C_n^k - m + 1 \end{aligned} \tag{1.8}$$

where $S_{\min}, S_{\max}$ represent the minimum and maximum of traversal times respectively. In the Eq. (1.8), the first 1 on the right side of the equal sign denotes a cRAIM done before signals removal, n denotes the n cRAIM done when traversing the first level in Fig. 2, and so on. In the best case, the cRAIM takes effect after traversing the first position of the $(m-1)^{th}$ layer. So it only needs to add one time on the basis of traversing the first $m-2$ layers. In the worst case, the cRAIM is effective only after traversing all the combinations in the $(m-1)^{th}$ layer that will make the cRAIM ineffective. So the number of traversals in the $(m-1)^{th}$ layer is $C_n^{m-1} - C_m^{m-1} + 1$.

According to the knowledge of permutation and combination, we can see that the probability of traversing k times on the $(m-1)^{th}$ level is C_{q-k}^{p-1}/C_q^p. So the mathematical expectation $E_{m-1}(p,q)$ of traversal times for traversing the $(m-1)^{th}$ level is derived as follows:

$$\begin{aligned} E_{m-1}(p,q) &= 1 * \frac{C_{q-1}^{p-1}}{C_q^p} + 2 * \frac{C_{q-2}^{p-1}}{C_q^p} + \cdots + (q-p+1) * \frac{C_{p-1}^{p-1}}{C_q^p} \\ &= (C_q^p + C_{q-1}^p + \cdots + C_p^p)/C_q^p = C_{q+1}^{p+1}/C_q^p \\ where, q &= C_n^{m-1}, p = C_m^{m-1} = m \end{aligned} \tag{1.9}$$

We further derive the mathematical expectation of traversal times $E(S)$:

$$E(S) = \sum_{k=0}^{m-2} C_n^k + C_{C_n^{m-1}+1}^{m+1} / C_{C_n^{m-1}}^{m} \tag{1.10}$$

where $\sum_{k=0}^{m-2} C_n^k$ is the mathematical expectation of traversal times for the first $m-2$ layers.

The traversal times under some common scenarios are listed in Table 1.

Table 1. Index table for the traversals times in common scenarios

(n, m)	$S_{\min}$	$S_{\max}$	$E(S)$
(7, 2)	2	7	3.667
(8, 2)	2	8	4
(9, 2)	2	9	4.333
(8, 3)	10	35	16.25
(9, 3)	11	44	19.25
(10, 3)	12	54	22.5
(9, 4)	47	127	63
(10, 4)	57	173	80.2
(11, 4)	68	229	100.2
(10, 5)	177	382	211.167
(11, 5)	233	558	287.167

Approximately, with the increase of n, the number of traversals increases with a growth rate of the power function, and with the increase of m, the number of traversals increases with the a growth rate of the exponential function. Therefore, although the effectiveness of the method is not limited by the number of spoofing signals, the computational complexity of the method will increase significantly.

4 Simulation and Actual Signal Test Results

In the chapter, we will show a pseudorange spoofing deviation model. Further, the influence of the number of spoofing signals, the pseudorange spoofing deviation and the difference of pseudorange spoofing deviation among different satellite signals on detection performance is analyzed by the simulation experiments. Finally, the random traversal RAIM method is implemented on the hardware receiver, and the feasibility of the method is verified by the actual GNSS signal.

4.1 The Simulation Data Description

In the paper, the Global Positioning System (GPS) ephemeris in February 23, 2018 is downloaded. According to the GPS ephemeris, the positions of all GPS satellites are calculated and saved every 10 min. The coordinates of the GPS receiver in World Geodetic System (WGS)-84 is $(40.001487^\circ\ \mathrm{N}, 116.330482^\circ\ \mathrm{E}, 96.69\ \mathrm{m})$. Ten visible satellites are randomly selected from the stored GPS position data and the corresponding pseudorange data are calculated. Gaussian noise is added to pseudorange and the corresponding data are saved. Generally speaking, the size of the pseudorange spoofing deviation will affect the performance of the cRAIM algorithm, and then affect the performance of the random traversal RAIM method. At the same time, the difference of pseudorange spoofing deviation among different satellite signals may also affect the detection performance. A recursive RAIM method proposed in [10] is used to deal with spoofing scenarios where two satellite faults exist simultaneously. When the size of two pseudorange spoofing deviations are basically the same, the detection performance will decrease.

So the pseudorange deviation of spoofing signal is modeled as:

$$\begin{aligned} \rho_s^{(i)} &= \rho_a^{(i)} + d^{(i)} \\ d^{(i)} &= d_s + d_d * rand(1)^{(i)} \end{aligned} \tag{1.11}$$

where $\rho_a^{(i)}$ represents the authentic pseudorange value of the i^{th} satellite while $\rho_s^{(i)}$ represents the false pseudorange value of the i^{th} satellite. $d^{(i)}$ is the pseudorange spoofing deviation of the i^{th} satellite. d_s is the same deviation, which is used to measure the influence of the spoofing deviation on the detection results. $rand(1)$ can generate random numbers which conform to the uniform distribution between 0 and 1. d_d is the difference deviation, which is used to measure the influence of different pseudorange spoofing deviations on the detection results.

4.2 The Simulation Result One

The effect of the same deviation on the detection performance is simulated in this part. d_s takes the eight values of $[50, 100, 200, 400, 800, 1600, 3200, 6400]$. Monte Carlo simulation experiments are carried out for 1000 times, in which d_d is 400 m and cRAIM sets the threshold according to false alarm rate of one in a thousand. If the random traversal RAIM can eliminate all spoofing signals and get the correct positioning results, the method is considered to be successful in SDE. The SDE rate is the ratio of successful spoofing detection and elimination in all Monte Carlo simulation experiments. The simulation results are shown below:

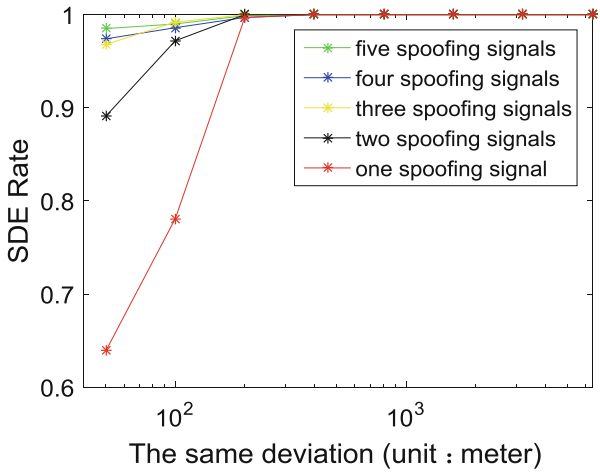

Fig. 3. Trend chart of the same deviation's influence on detection performance

Simulation results show that the successful SDE probability increases rapidly with the increase of d_s. When d_s increases to nearly 200 m, the successful SDE probability is basically near 1. When d_s is small, its influence on the positioning results is relatively small, and *SSE* calculated may be less than the threshold, resulting in missed detection. From the simulation results, the number of spoofing signal has a great impact on the successful SDE probability when d_s is small and the impact is very small when d_s is large. However, the essence is that the number of satellites is different when the last cRAIM is effective, rather than the number of spoofing signals is different. In conclusion, the size of the pseudorange spoofing deviation will affect the performance of the proposed method, while the number of spoofing signals will affect the computational complexity.

4.3 The Simulation Result Two

The effect of the difference deviation on the detection performance is simulated in this part. d_d takes the eight values of $[50, 100, 200, 400, 800, 1600, 3200, 6400]$. Monte Carlo simulation experiments are carried out for 1000 times, in which d_s is 180 m and cRAIM sets threshold according to false alarm rate of one in a thousand. The simulation results are shown below (Fig. 4):

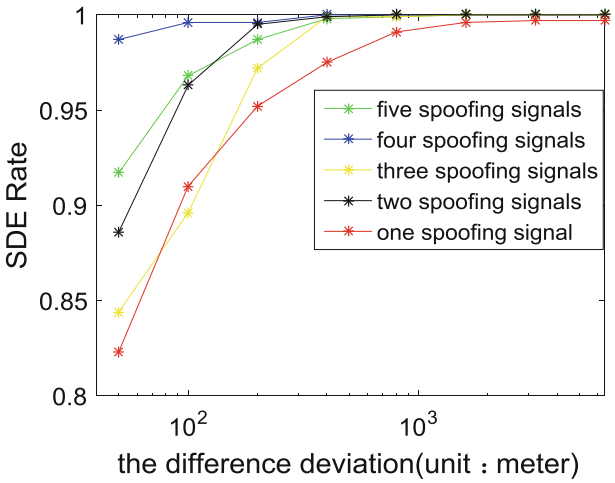

Fig. 4. Trend chart of the difference deviation's influence on detection performance

Simulation results show that the successful SDE probability increases rapidly with the increase of d_d. When d_d increases to nearly 500 m, the successful SDE probability is basically near 1. When d_d increases, the probability of smaller pseudorange deviation becomes smaller. And the speed of the successful SDE probability's increase is slower than it in Fig. 3. From the simulation results, the number of spoofing signal has a great impact on the successful SDE probability when d_d is small and the impact is relatively small when d_d is large. Its essence is the influence of pseudorange spoofing deviations on detection performance because the size of d_d affects the size of $d^{(i)}$ indirectly. The difference of pseudorange spoofing deviations among different satellite has little effect on detection performance. And with the increase of the false satellites number, the complexity of the proposed method will increase greatly.

4.4 The Experimental Design and Result Verification

In this part, the random traversal RAIM method is implemented on the hardware receiver and tested in the actual GNSS signal environment, compared with the cRAIM algorithm.

In the experiment, three satellite signals are randomly selected to transmit by the receiver-based spoofer in Fig. 5. Then the transmitted GPS signals are transmitted to the sky by up-converter, power amplifier and transmitting antenna. The receiving antenna in Fig. 5 can receive real GPS signal and transmitted GPS signal in the sky at the same time, and process them in the GPS receiver after down conversion. The coordinates of the receiver antenna in WGS-84 is $(40.001487^\circ\ \mathrm{N}, 116.330482^\circ\ \mathrm{E}, 96.69\ \mathrm{m})$.

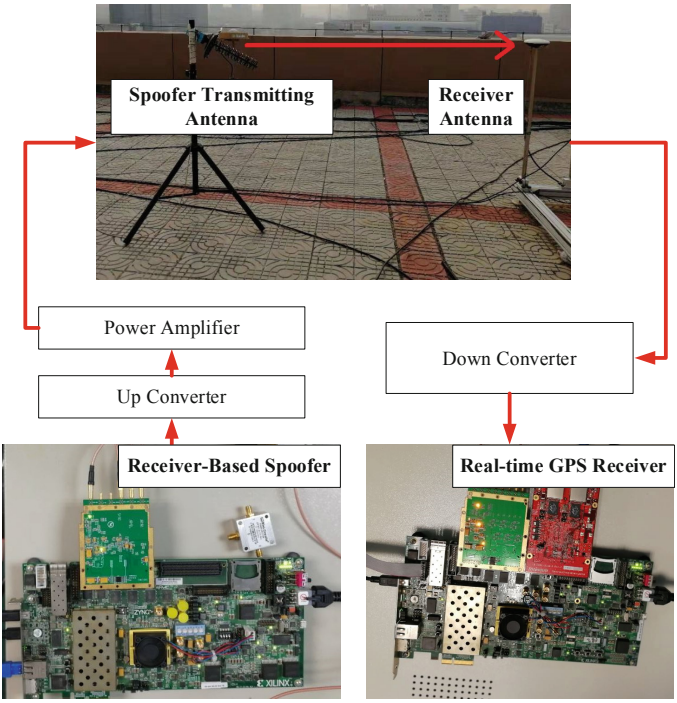

Fig. 5. The experimental platform and signal environment

In the experiment, the signals of satellites PRN 14, 18 and 20 are transmitted, with the delay of about 3 us. The left part in Fig. 6 is the result of applying the cRAIM algorithm, which results in the wrong position. The detection statistic *RaimSSE* is 1399.607339, much larger than the threshold. So the cRAIM can detect that the spoofing exists, but it can't recognize and eliminate spoofing signals to get the correct positioning results. The position obtained is more than one kilometer different from the real location. The right part in Fig. 6 is the result of applying the random traversal RAIM method. *FaultsNum* indicates that the identified spoofing signals are in channel 2, 3 and 4, corresponding to the satellite PRN 14, 18 and 20, respectively. This shows that spoofing signals can be effectively identified. After identifying the spoofing signals, the residual real signals are used to PVT solution, and the positon is basically consistent with the real position. The experimental results show that the random traversal RAIM proposed in the paper is effective, and can detect and identify spoofing and further get the correct positioning results.

The conventional RAIM

```
Chan  PRN  C/N0  TransTime
  0   10    45   376865545781.919861
  1   12    45   376865542628.053406
  2   14    50   376865544356.939575
  3   18    50   376865534622.007324
  4   20    51   376865539353.978577
  5   31    42   376865543207.650696
  6   25    43   376865546147.563049
  7   32    48   376865547464.585510

----------PVT Results-----
Latitude:  40.001336
Longitude: 116.333379
Height:    1399.607339
Time:  2018.11.29  16.41.5
NumView:  8
RaimSSE:  1267.082060
EffecFlag:3
FaultsNum: -1, -1, -1
```

The random traversal RAIM

```
Chan  PRN  C/N0  TransTime
  0   10    44   376776645880.263611
  1   12    45   376776642693.270813
  2   14    50   376776644223.297424
  3   18    50   376776634676.678955
  4   20    50   376776639525.120239
  5   31    45   376776643043.346802
  6   25    44   376776646087.279785
  7   32    48   376776647383.757568

----------PVT Results------
Latitude:  40.001415
Longitude: 116.330249
Height:    100.491615
Time:  2018.11.29  16.39.36
NumView:  8
RaimSSE:  0.330546
EffecFlag:-1
FaultsNum: 2, 3, 4
```

Fig. 6. Comparison of experimental results under the scenario of three spoofing signals

5 Conclusion

The paper proposes a random traversal RAIM method, where the cRAIM algorithm is used as the core, and spoofing signals are detected and eliminate by random signal removal and iteration. In each traversal, the cRAIM algorithm is invoked until it is effective. As long as there are more than four real signals and spoofing signals are not entirely consistent, the method can eliminate the spoofing signals and get the correct location results through PVT calculation, solving the limitation of cRAIM algorithm in the spoofing environment. Through simulation and experimental demonstration, the validity of random traversal RAIM method is verified.

If spoofing signals are entirely consistent, the method in the paper may converge to the false location. In this case, we need further identification of the positioning results by other anti-spoofing methods. At the same time, when the number of spoofing signals is relatively large, the complexity of the method will increase dramatically, which requires receivers to have a good computing power.

Acknowledgments. This work was supported by the National Natural Science Foundation of China (Grant No. 61571255).

References

1. Brown A, Sturza M (1990) The effect of geometry on integrity monitoring performance. In: 46th annual meeting of the institute of navigation
2. Brown RG (1992) A baseline GPS RAIM scheme and a note on the equivalence of three RAIM methods. Navigation 39(3):301–316
3. Carroll JV (2003) Vulnerability assessment of the U.S. transportation infrastructure that relies on the global positioning system. J Navig 56(2):185–193

4. Jafarnia-Jahromi A, Broumandan A, Nielsen J et al (2012) GPS vulnerability to spoofing threats and a review of antispoofing techniques. Int J Navig Obs 2012(9)
5. Kalafus RM, Chin GY Performance measures of receiver-autonomous GPS integrity monitoring. In: Institute of Navigation, pp 223–229
6. Liu J, Lu M, Cui X et al (2007) Theoretical analysis of RAIM in the occurrence of simultaneous two-satellite faults. IET Radar Sonar Navig 1(2):92–97
7. Martini I, Hein GW (2006) An integrity monitoring technique for multiple failures detection. In: IEEE/ION Position, Location, and Navigation Symposium, pp 450–467
8. Parkinson BW, Axelrad P (1988) Autonomous GPS integrity monitoring using the pseudorange residual. Navigation 35(2):255–274
9. Sturza MA (1988) Navigation system integrity monitoring using redundant measurements. Navigation 35(4):483–501
10. Tao H, Li H, Zhang W et al (2015) A recursive receiver autonomous integrity monitoring (recursive-RAIM) technique for GNSS anti-spoofing. In: Institute of navigation ITM, pp 738–744
11. Walter T, Enge P (1995) Weighted RAIM for precision approach. In: Proceedings of the ION GPS-1995

Time Domain Differential RAIM Method for Spoofing Detection Applications

Yimin Wei, Hong Li(✉), Chenxi Peng, and Mingquan Lu

Department of Electronic Engineering, Tsinghua University,
Beijing 100084, China
lihongee@tsinghua.edu.cn

Abstract. With modern society's increasing dependence on Global Navigation Satellite System (GNSS), the potential harm caused by spoofing attacks on GNSS is also increasing. In order to effectively resist possible spoofing threats, a series of anti-spoofing algorithms have been developed. The Receiver Autonomous Integrity Monitoring (RAIM) is a commonly used anti-spoofing method and has been widely used in various fields. The algorithm exploits the consistency among satellites and utilizes the transmit time of each navigation signal to perform spoofing detection. However, RAIM only focuses on the code phase information of the navigation signal and does not utilize the carrier portion. In some scenarios, it is feasible and effective to utilize the information held in the carrier. In this paper, carrier doppler check are integrated with RAIM by using time-domain difference method, which makes the algorithm applicable to more spoofing scenarios. Simulation and field test verify the effectiveness of the algorithm in different spoofing scenarios.

Keywords: Receiver spoofing detection · Autonomous Integrity Monitoring · Time domain difference

1 Introduction

With the advancement of technology and the development of economy, globalization has gradually become a major trend. In such context, the importance of Global Navigation Satellite Systems (GNSS) is becoming increasingly apparent, and the possible damage caused by GNSS interference are increasing. Among GNSS interference methods, GNSS spoofing has become the focus of research because of its good concealment and strong interference ability.

As a typical representative of anti-spoofing algorithm, the Receiver Autonomous Integrity Monitoring method (RAIM) has been widely used in various fields. It detects spoofing through checking the consistency of the pseudoranges between receiver and satellites. Many other anti-spoofing algorithms based on RAIM have been designed and proposed. For example, reference [1] replaces the pseudorange measurement used in RAIM with carrier smoothed pseudorange; reference [2] uses carrier integral doppler as an alternative to pseudorange measurement; reference [3] takes information collected by IMU as redundant observation to perform spoofing detection.

J. Sun et al. (Eds.): CSNC 2019, LNEE 563, pp. 606–614, 2019.
https://doi.org/10.1007/978-981-13-7759-4_53

In fact, the utilization of carrier doppler in spoofing detection can be meaningful: firstly, as described in reference [4], when the spoofer attempts to align spoofing signal with the authentic signal, the code doppler and the carrier doppler of spoofing signal will not be consistent anymore; secondly, the non-ideality of spoofer components will also cause inconsistency between code doppler and carrier doppler. However, the instantaneous carrier doppler measurement contains non-ignorable noise [5] and it is time varying because of receiver's movement, thus the change of carrier phase over a period of time is adopted in this paper instead of the instantaneous carrier doppler.

In this paper, a receiver autonomous integrity detection method based on time domain difference is designed and proposed. It utilizes pseudoranges at two adjacent moments and the integral carrier doppler during this period of time. This method can detect inconsistency between code doppler and carrier doppler as small as 0.3 Hz. Based on the principle of statistical inference, the solution to the problem of judging the existence of spoofing signal will also be given in this paper. The validity of this method is verified by simulation and field test.

The content of this paper is arranged as follow: the second section will introduce RAIM briefly; the third section will introduce the time domain difference based RAIM method proposed in this paper; the fourth section will provide the simulation and field test results; the fifth section comprises summary and outlook.

2 Traditional RAIM

Traditional RAIM method performs spoofing detection by exploiting the consistency among pseudoranges of each satellite. As is shown in Eq. (1).

$$\mathbf{y} = \mathbf{H}\mathbf{x} + \mathbf{w} + \mathbf{b} \tag{1}$$

In the equation above, $\mathbf{y}$ represents the difference between the observed pseudoranges and the estimated one; $\mathbf{H}$ denotes the line-of-sight matrix between receiver and satellites; $\mathbf{x}$ represents the increment of user position and clock bias; $\mathbf{w}$ represents the observation noise; $\mathbf{b}$ denotes the offset introduced by spoofer.

One can detect spoofing using the residual shown in Eq. (2).

$$\mathbf{f} = \left(\mathbf{I} - \mathbf{H}\mathbf{H}^{\dagger}\right)\mathbf{y} \tag{2}$$

Where $\mathbf{H}^{\dagger}$ represents the pseudo inverse of $\mathbf{H}$. In the absence of spoofing, the magnitude of the residual should satisfy the centralized chi-square distribution, while in the presence of spoofing, the magnitude of the residual satisfies the decentralized chi-square distribution with the same degree of freedom. Therefore, the corresponding detection threshold can be designed according to the preset false alarm probability.

More details about traditional RAIM can be found in reference [6].

3 RAIM Method Based on Time Difference

As described in introduction, the transmit time $\tau_{k,i}^{(s)}$ and carrier integral doppler $\Delta\varphi_{k,i}$ are utilized to conduct spoofing detection, where subscript k stands for the measurement moment and subscript i stands for the identifier of satellite. Pseudorange $\rho_{k,i}$ can be drawn from corresponding transmit time $\tau_{k,i}^{(s)}$, as shown in Eq. (3).

$$\rho_{k,i} = c \cdot \left(\tau_k^{(u)} - \tau_{k,i}^{(s)}\right) \tag{3}$$

Where c represents the speed of light; $\tau_k^{(u)}$ represents the reading of receiver clock at time k. It should be noticed that the pseudorange measurement contains errors caused by clock bias, ionospheric delay, tropospheric delay, etc.

Under the condition of stable signal tracking, the pseudorange measurement of each satellite at two adjacent moment and the change of carrier phase over the period of time can be integrated to obtain the overall observation as shown in Eq. (4).

$$\left[\boldsymbol{\rho}_\mathbf{0}^\mathbf{T}, \boldsymbol{\rho}_\mathbf{1}^\mathbf{T}, \boldsymbol{\Delta\varphi}^\mathbf{T}\right]^\mathbf{T} \tag{4}$$

As is shown in traditional RAIM, the pseudorange and integrated carrier doppler in Eq. (4) are associated with receiver's position and its clock parameters.

Take the position of the GNSS receiver at time k as $\mathbf{x}_k^{(u)}$, the clock bias of the receiver as δt, and the clock drift of the receiver as δf, the Jacobian matrix of the observation shown in Eq. (4) to variables introduced above can be shown in Eq. (5).

$$\mathbf{H} = \begin{pmatrix} \mathbf{1}_{M\times 1} & \mathbf{0}_{M\times 1} & \mathbf{G_0} & \mathbf{0} \\ \mathbf{1}_{M\times 1} & cT\mathbf{1}_{M\times 1} & \mathbf{0} & \mathbf{G_1} \\ \mathbf{0}_{M\times 1} & -\alpha cT\mathbf{1}_{M\times 1} & \mathbf{G_0} & -\mathbf{G_1} \end{pmatrix} \begin{pmatrix} \delta t \\ \delta f \\ \mathbf{x}_0^{(u)} \\ \mathbf{x}_1^{(u)} \end{pmatrix} \tag{5}$$

Where T is the time interval between two measurement moments; α represents the effect of clock drift on the integral doppler measurement; $\mathbf{G_0}, \mathbf{G_1}$ represent the line-of-sight matrix between receiver and satellites; $\mathbf{1}, \mathbf{0}$ represent matrix with all one and all zero; M represents the number of available satellites.

The error terms in pseudorange measurements include DLL error, multipath error, ephemeris error, tropospheric delay error, ionospheric delay error, etc. The error terms contained in integrated carrier doppler measurements include PLL error, RF down conversion error, phase cycle slip error, etc. The covariance matrix of these error terms can be obtained as:

$$\mathbf{C} = \mathbf{E}\left[\mathbf{w}\mathbf{w}^T\right] = \begin{pmatrix} \sigma_{DLL}^2\mathbf{I} + \sigma_{EPH}^2\mathbf{I} & \sigma_{EPH}^2\mathbf{I} & \mathbf{0} \\ \sigma_{EPH}^2\mathbf{I} & \sigma_{DLL}^2\mathbf{I} + \sigma_{EPH}^2\mathbf{I} & \mathbf{0} \\ \mathbf{0} & \mathbf{0} & \sigma_{PLL}^2\mathbf{I} + \sigma_{RF}^2\mathbf{1} \end{pmatrix} \tag{6}$$

In Eq. (6), σ_{DLL} corresponds to time-uncorrelated errors in pseudorange measurements such as DLL error and multipath error; σ_{EPH} corresponds to time-correlated errors such as ionospheric delay error, tropospheric delay error and ephemeris error; σ_{PLL} corresponds to time-uncorrelated errors in integrated carrier doppler measurements, e.g. PLL error and phase cycle slip error; σ_{RF} corresponds to error caused by RF down converter.

The whitening matrix can be obtained through covariance matrix in Eq. (6).

$$\mathbf{W} = \mathbf{C}^{-\frac{1}{2}} \tag{7}$$

Whitening both sides of Eq. (1) obtains:

$$\tilde{\mathbf{y}} = \tilde{\mathbf{H}}\mathbf{x} + \tilde{\mathbf{w}} + \tilde{\mathbf{b}} \tag{8}$$

Where $\tilde{\mathbf{y}}, \tilde{\mathbf{H}}, \tilde{\mathbf{w}}, \tilde{\mathbf{b}}$ correspond to the whitening result of $\mathbf{y}, \mathbf{H}, \mathbf{w}, \mathbf{b}$. The residual can be obtained by applying weighted least square algorithm iteratively:

$$\mathbf{f} = \mathbf{P}\mathbf{P}^{T}\left(\tilde{\mathbf{w}} + \tilde{\mathbf{b}}\right) \tag{9}$$

Matrix $\mathbf{P}$ corresponds to the projection matrix on null space of matrix $\tilde{\mathbf{H}}$ and $\mathbf{P^T}\tilde{\mathbf{w}}$ is of standard Gaussian distribution. The variable used for spoofing detection can be drawn from the residual as:

$$\mathbf{t} = \mathbf{P^T}\mathbf{f} = \mathbf{P^T}\tilde{\mathbf{w}} + \mathbf{P^T}\mathbf{W}\mathbf{b} \tag{10}$$

As can be seen from Eq. (10), the variable $\mathbf{t}$ is in fact a linear combination of $\mathbf{b}$, which is the offset introduced by spoofing signals.

Through Eq. (10), the spoofing detection problem can be simplified as a hypothesis test problem:

$$\begin{aligned} \mathcal{H}_0 &: \mathbf{b} = \mathbf{0} \\ \mathcal{H}_1 &: \mathbf{b} \neq \mathbf{0} \end{aligned} \tag{11}$$

Where $\mathcal{H}_1$ declares the existence of spoofing while $\mathcal{H}_0$ declares the opposites. By making use of Generalized Likelihood Ratio Test (GLRT), the test statistic of spoofing detection problem can be drawn as:

$$\gamma = \|\mathbf{t}\|^2 \tag{12}$$

The distribution of the test statistic under two hypotheses are:

$$\begin{aligned} \mathcal{H}_0 &: \gamma \sim \boldsymbol{\chi}^2(0, 3M - 8) \\ \mathcal{H}_1 &: \gamma \sim \boldsymbol{\chi}^2(\left\|\mathbf{P^T}\mathbf{W}\mathbf{b}\right\|^2, 3M - 8) \end{aligned} \tag{13}$$

Based on distribution shown in Eq. (13), the detect threshold corresponding to the preset false alarm rate can be determined.

4 Simulation and Experiment

4.1 Simulation

The simulation is conducted based on real data collected by GNSS receiver and spoofing is simulated by manually modification. The data was collected at 15:10 on September 28, 2018. 7 satellites are available at that time and the PRN numbers are 5, 13, 15, 20, 21, 24, and 29 respectively.

The parameters of the algorithm is shown in Table 1.

Table 1. Parameters of the anti-spoofing algorithm

T	60 s
σ_{DLL}	5 m
σ_{EPH}	5 m
σ_{PLL}	1 m
σ_{RF}	9 m

Firstly, the spoofing detection performance of the algorithm is simulated. Signal transmitted by satellite 13, 15 and 20 is supposed to be spoofing signal and different spoofing scenarios are simulated by changing the carrier doppler. On this basis, the amplitude of test statistic is shown in Fig. 1.

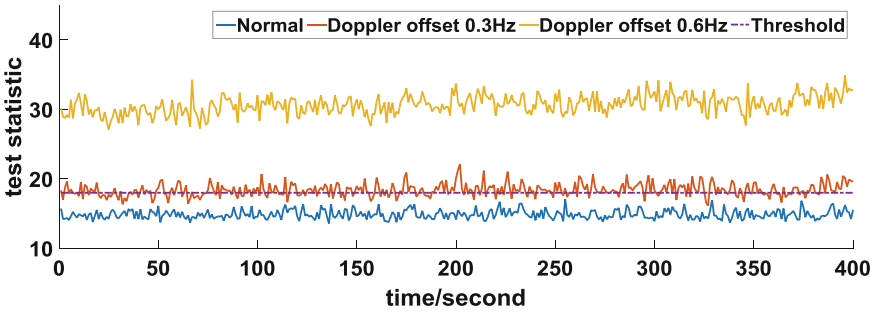

Fig. 1. Simulation results of test statistic for spoofing detection

It can be seen from Fig. 1 that the algorithm can detect offset in carrier doppler sensitively: when the carrier doppler frequency offset reaches 0.3 Hz, the algorithm can detect spoofing at most times; when the carrier doppler frequency offset reaches 0.6 Hz, the corresponding test statistics are far beyond the detection threshold.

To verify the improvement of this algorithm over RAIM algorithm, signal transmitted by satellite 15 are supposed to be spoofing signal and the Receiver Operating Characteristic (ROC) are compared, which is shown in Fig. 2.

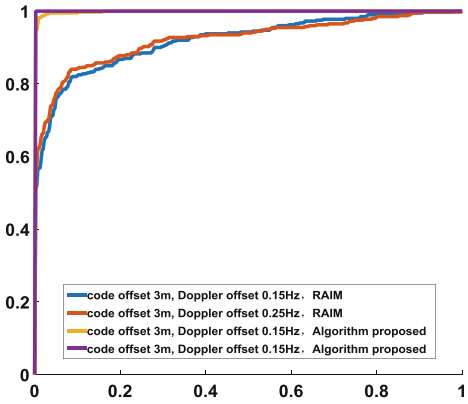

Fig. 2. Comparison of spoofing detection performance between RAIM and proposed algorithm

The method presented in this paper can improve the detection probability obviously with the carrier frequency deviation of spoofing signal. From Figs. 1 and 2, it can be seen that the algorithm proposed in this paper improves the traditional RAIM method by integrating sensitive carrier doppler detection, which can detect carrier doppler offset as small as 0.3 Hz.

4.2 Experiment

The spoofing detection algorithm introduced in this paper is deployed on the hardwire platform and experiments are performed with the existing spoofing signal generator, as can be seen in Fig. 3.

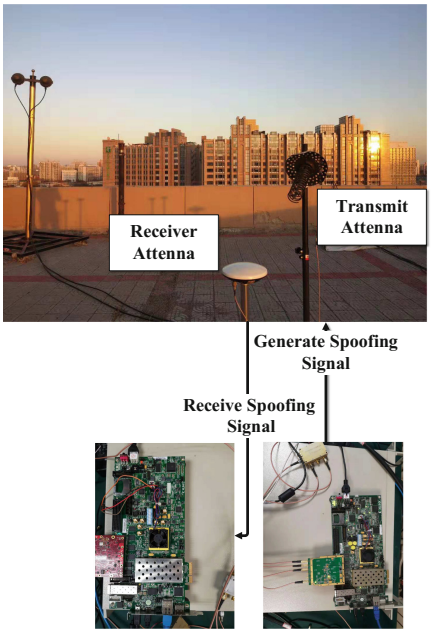

Fig. 3. Spoofing experiment

The experiment is carrier out at 20:21 on November 1, 2018. There are 7 satellites available and the PRN numbers are 10, 14, 22, 25, 26, 31 and 32, respectively. The satellite signals with PRN number 14 and 25 are generated by the spoofing signal generator. The code phase of the spoofing signal is controllable and varies during the experiment. The experiment result are shown in Figs. 4 and 5.

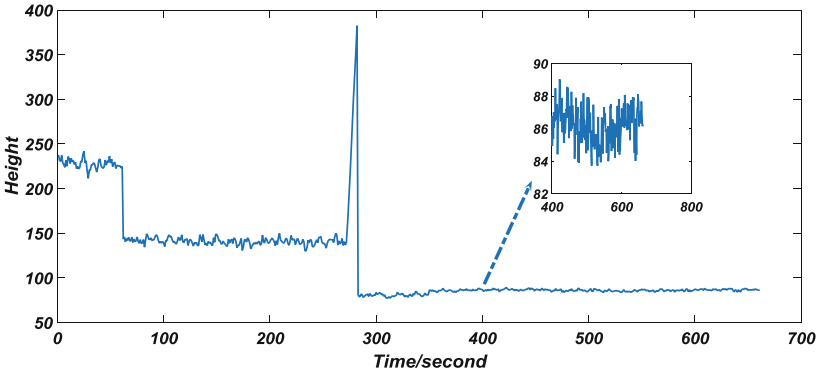

Fig. 4. Height solution during experiment

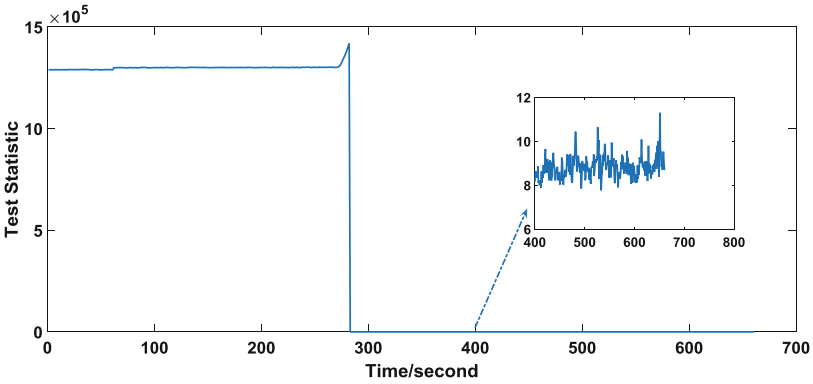

Fig. 5. Detection statistic during experiment

The spoofer started transmitting spoofing signals before receiver start up and stopped transmitting at the 280 s. The receiver is placed at 85 m height. It can be seen from Fig. 4 that the positioning height of the receiver changes when spoofing signal exists. Meanwhile, the test statistic obtained by the spoofing detection algorithm far exceeds the threshold, as can be seen in Fig. 5. The positioning height returns to 85 m after the spoofer stops transmitting spoofing signals, and the test statistic obtained by the spoofing detection algorithm also returns below the detection threshold, which illustrates the effectiveness of the proposed algorithm in dealing with spoofing attacks in actual scenarios.

5 Conclusion

The association between pseudorange, integrated carrier doppler and receiver states are exploited to develop a RAIM method based on time domain difference. The method integrates carrier doppler detection into traditional RAIM method and can detect carrier doppler offset as small as 0.3 Hz. The simulation and field test results further verify its spoofing detection performance.

Acknowledgments. This work was supported by the National Natural Science Foundation of China (Grant No. 61571255).

References

1. Salgueiro F, Sanguino J, Rodrigues A, Hernandez FA (2012) Weighted total least squares RAIM algorithm using carrier phase measurements. In: 2012 6th ESA workshop on satellite navigation technologies (Navitec 2012) & European workshop on GNSS signals and signal processing, Noordwijk, pp 1–6
2. Kirkko-Jaakkola M, Traugott J, Odijk D, Collin J, Sachs G, Holzapfel F (2009) A RAIM approach to GNSS outlier and cycle slip detection using L1 carrier phase time-differences. In: 2009 IEEE workshop on signal processing systems, Tampere, pp 273–278

3. Tanıl Ç, Khanafseh S, Joerger M, Pervan B (2018) An INS monitor to detect GNSS spoofers capable of tracking vehicle position. IEEE Trans Aerosp Electron Syst 54(1):131–143
4. Yuan D, Li H, Wang F, Lu M (2018) A GNSS acquisition method with the capability of spoofing detection and mitigation. Chin J Electron 27(1):213–222
5. Juang J, Chen Y (2009) Phase/frequency tracking in a GNSS software receiver. IEEE J Sel Top Sig Process 3(4):651–660
6. Sturza MA (1988) Navigation system integrity monitoring using redundant measurements. Navigation 35(4):483–501

Research of Intermediate Spoofing Without Precise Target Information

Chenxi Peng, Hong Li(✉), Jian Wen, and Mingquan Lu

Department of Electronic Engineering, Tsinghua University, Beijing 100084, China
lihongee@tsinghua.edu.cn

Abstract. Intermediate spoofing is capable of converting receiver's tracking loop from locking on genuine signal to spoofing signal without disturbing normal working state. This kind of attack requires precise target information, which is difficult to meet in actual attack scenario. In order to improve the feasibility of intermediate spoofing, factors affecting intermediate spoofing such as power, carrier frequency and code phase will be evaluated through theoretical analysis combined with experimental verification. Besides, we will analyze the reasons for loss of lock in intermediate spoofing. Based on the above analysis, we developed an intermediate spoofing attack device and successfully perform wireless spoofing attack against commercial u-blox receiver without knowing its accurate information.

Keywords: Intermediate spoofing · Tracking loop · Carrier frequency

1 Introduction

The Global Positioning System (GPS) is now playing an increasingly important role in our life due to its widely application. However, civilian GPS signals have been facing serious spoofing threats for its public signal structure and low signal power. Since GPS spoofing attack was proposed [1] and demonstrated [2] for the first time, various spoofing attacks have emerged. They can be roughly divided into meaconing and autonomous generation. These spoofing attacks are easy to launch, but generally rely on high power jamming to trigger loss of lock. Spoofing signal will be tracked by receiver after re-acquisition due to its power advantage. Abnormal jamming may alert target receiver to spoofing attacks.

While intermediate spoofing which works in tracking stage can effectively avoid this defect and achieve covert spoofing. Humphreys first proposed the concept of intermediate spoofing [3] and carried spoofing attack against smart grid and UAV [4, 5]. He pointed out that after knowing the precise position and velocity information of target receiver, a low power spoofing signal synchronized with genuine signal can be generated. Power of spoofing signal is then gradually increased to control the tracking loop of target receiver. This spoofing attack utilizes the characteristics of tracking loop, thus achieving high performance in both concealment and efficiency. However, in some application scenarios, parameters of spoofing signal deviate from real signal for lacking

J. Sun et al. (Eds.): CSNC 2019, LNEE 563, pp. 615–624, 2019.
https://doi.org/10.1007/978-981-13-7759-4_54

accurate state information, which may result in loss of lock instead of taking over without being detected [6, 7].

To this end, the application scenario of intermediate spoofing must be expanded. In this paper, we will review the basic principle of intermediate spoofing, study the influence of various signal parameters through simulation attack on software GPS receiver and elaborate how parameter error causes receiver to lose lock. On the basis of previous results, we will further research intermediate spoofing attack under the circumstance when accurate target information is unknown and exploit the developed spoofing attack device to conduct spoofing attack against commercial u-blox receivers.

2 Basic Principles of Intermediate Spoofing

2.1 Principle Introduction

Before analyzing intermediate spoofing without accurate target information, let's first review the basic principles of intermediate spoofing.

Inside GPS receiver, RF GPS signal is down-converted, sampled and quantized. Resulting digital signal is multiplied by local carrier and then correlated with different local C/A code. To synchronize local signal with GPS signal, local carrier NCO and pseudo code generator are adjusted in real time according to correlation results. When receiver is tracking real signal, it is equivalent to filtering received signal on the frequency and code phase of real signal. Only when the parameter deviation of spoofing signal is within a certain range can it enters tracking loop and affects correlation value, thus achieving control of tracking loop.

In the presence of spoofing signal, the output of P correlator can be expressed as follows:

$$\begin{aligned} I_p &= \sqrt{P_a} D_a R(\tau_{pa}) \sin c(f_{ea} T_{coh}) \cos(\varphi_{ea}) \\ &+ \sqrt{P_s} D_s R(\tau_{ps}) \sin c(f_{es} T_{coh}) \cos(\varphi_{es}) + \eta_I \end{aligned} \tag{1}$$

$$\begin{aligned} Q_p &= \sqrt{P_a} D_a R(\tau_{pa}) \sin c(f_{ea} T_{coh}) \sin(\varphi_{ea}) \\ &+ \sqrt{P_s} D_s R(\tau_{ps}) \sin c(f_{es} T_{coh}) \sin(\varphi_{es}) + \eta_Q \end{aligned} \tag{2}$$

where P is signal power, D stands for navigation message, R represents code auto-correlation function, τ_p and f_e indicate code phase deviation and carrier frequency offset respectively, T_{coh} is coherent integration time, φ_e is carrier phase tracking error, η_I, η_Q represents Gaussian noises on I and Q channel, subscript a and s denote real signal and spoofing signal. Output values of E and L correlator are similar to above formula except for code phase deviation.

With precise information of target receiver's position and motion, we can generate the spoofing signal whose carrier frequency and code phase are consistent with real signal. Power of spoofing signal is set higher than real signal, so as to dominate E, P, L correlators and consequently tracking loop of target receiver. The code phase of

spoofing signal is then adjusted to move off genuine signal to achieve complete control of target receiver.

2.2 Analysis of Influencing Factors

For navigation message D, it remains constant during coherent integration and can be accurately predicted after short time observation. Ephemeris part of navigation message repeats every 30 s and updates every 2 h. While repetition period of almanac part is 12.5 min, it is renewed once a week [8]. After collecting ephemeris and almanac data, the next message bit can be conveniently predicted. For carrier phase control of spoofing signal, it is required to measure the position and speed of target receiver at cm level. On the other hand, carrier phase error of spoofing signal leads to randomly dispersing of signal energy on both I and Q channel, which can be compensated by increasing signal power. If the receiver adopts non-coherent phase discrimination formula, energy dispersed in I, Q channels will be collected, thus leaving no effect on the success rate of spoofing attack.

Therefore, we will mainly analyze other factors such as power, carrier frequency and code phase in the following part and carry out simulation attack on software GPS receiver. A recorded IF GPS signal is used here as real signal. Signal parameters are calculated in advance to generate different spoofing scenarios. Tracking loop parameters of software receiver are as follows. The coherent integration time is 1 ms. DLL uses the non-coherent early minus late power method for phase discrimination with 0.5 chips correlator space and 10 Hz bandwidth. PLL adopts a third-order phase-locked loop with 20 Hz bandwidth. Non-coherent code loop reduces the dependence of code loop on carrier loop and avoids being influenced by PLL phase discrimination fluctuation during spoofing process.

Considering that different receivers have their own criterion for loss of lock, we adopt PLL loop lock value that characterizes the energy concentration on I channel to quantify the degree of locking on GPS signal. The formula is shown in Eqs. (3) and (4). Calculation of I_{pll} adopts an iterative form. I_p is the newly obtained I correlation value after each integration. The calculation of Q_{pll} is similar.

$$I_{pll} = I_{pll}\frac{255}{256} + I_p\frac{1}{256} \tag{3}$$

$$L = \frac{I_{pll}^2 - Q_{pll}^2}{I_{pll}^2 + Q_{pll}^2} \tag{4}$$

The loop lock value L is between 0 and 1. The closer the value is to 1, the better the degree of locking on GPS signal. We don't set any condition for loss of lock here but use the minimum PLL lock value during spoofing attack to compare the impact of different attack scenarios on tracking loop. Smaller PLL lock value indicates that target receiver is easier to lose lock during spoofing attack.

3 Simulation Test

3.1 Power Effect

Power control is a crucial part in intermediate spoofing. High spoofing signal power turns target receiver from tracking genuine signal to spoofing signal during spoofing process. However, abnormal high power signal will be perceived as potential threat. Since the effect of power is influenced by code phase offset and carrier frequency deviation, power setting of intermediate spoofing will be analysed together with carrier and pseudo-code in the subsequent section.

3.2 Code Phase Effect

GPS C/A code consists of 1023 chips and repeats every 1 ms. If the precise position of target receiver is unknown, code phase of real signal at the target receiver and transmission delay of the spoofing signal cannot be estimated, making it impossible to align the code phase of spoofing signal with genuine signal. Considering the periodicity of civilian GPS signal, if the code phase of spoofing signal is adjusted in a certain direction relative to real signal, namely, scan all the possible code phase of real signal, it will inevitably collide with real signal, and thus achieve successful control of target receiver.

The method of code phase scanning is slightly different from aligning code phase and then increasing signal power. When the code phase of spoofing signal is within 1.5 chips of real signal, correlation value of early correlator or late correlator will increase under the influence of spoofing signal. According to phase discrimination formula, code loop will adjust local code to approach and eventually lock on spoofing signal before the correlation peaks completely overlap. In order to study the influence of spoofing strategies on carrier loop, we set up the following simulation scenario. The spoofing authentic power ratio (SAR) is 3 dB. Code pulling rate is 4 Hz, that is, the code rate of spoofing signal is 4 Hz higher than real signal. Code rate is modified here to adjust the relative code phase between spoofing signal and real signal. The duration of modifying code rate, which we called pulling time here, is set to 1 s. Initially, the code phase of spoofing signal lags real signal by 2 chips. Therefore, it can be calculated that the code phase of spoofing signal leads real signal by 2 chips when the attack is completed.

Table 1. Minimum PLL lock value under different spoofing strategy

Frequency offset	0 Hz	10 Hz	20 Hz	30 Hz	40 Hz	50 Hz
Spoof strategy						
Aligned	0.906	0.668	0.664	0.550	0.552	0.395
Scan	0.918	0.622	0.633	0.636	0.342	0.450

Simulation results are shown in Table 1. Spoofing signal took control of target receiver successfully in all spoofing scenario. But with the increase of carrier frequency offset, target receiver is more likely to lose lock in the process of taking over. In

general, under different strategies, the probability of losing lock caused by carrier frequency offset are almost the same.

The pull-in range of code loop is generally 0.5 chips. Considering code phase measurement error and dynamic stress error, the relative offset of pseudo code in one integration cannot exceed 0.5 chips. In order to avoid consistency check between code Doppler and carrier Doppler [9], code pulling rate should also be as low as possible. Therefore, we discussed the effects of power and code pulling rate here. Following experiment is designed. Initially, the code phase of spoofing signal lags real signal by 2 chips. Carrier frequency is aligned with real signal.

Table 2. Response to different code rate and SAR

Code pulling rate	2 Hz	8 Hz	16 Hz	24 Hz	32 Hz	42 Hz
SAR						
2 dB	S	S	S	A	A	A
3 dB	S	S	S	S	A	A
5 dB	S	S	S	S	S	A
8 dB	S	S	S	S	S	A
10 dB	S	S	S	S	S	S

Experimental results are shown in Table 2. "A" indicates that target receiver keeps tracking real signal, while "S" represents that target receiver is under the control of spoofing signal. It can be seen from Table 2 that as the code pulling rate increases, it gets more difficult for target receiver to lock on spoofing signal. But for spoofing signal with higher SAR, even if there exists certain code phase difference between real signal and spoofing signal, correlation value at EPL correlator of spoofing signal may still be higher than that of real signal. Wider affecting range of correlation peak of spoofing signal results in higher allowable code pulling rate, so increasing signal power can increase the success rate under high code pulling rate.

3.3 Carrier Frequency Effect

The carrier Doppler of GPS signal can be expressed as follows:

$$f_d = \frac{(v - v^{(s)}) \bullet 1^{(s)}}{\lambda} = \frac{v \bullet 1^{(s)}}{\lambda} - f_s \tag{5}$$

Where $1^{(s)}$ stands for line-of-sight vector, v and $v^{(s)}$ represent velocity vector of receiver and satellite respectively, f_s represents Doppler frequency due to satellite motion. The altitude of GPS navigation satellite is about 20,000 km. Therefore, position change of receiver has little influence on $1^{(s)}$. After deriving $v^{(s)}$ from ephemeris, f_s can be accurately calculated using roughly estimated receiver position. The uncertainty of carrier frequency mainly lies on motion of target receiver. In order to research the influence of carrier frequency offset, we set up the spoofing experiment with 4 Hz code pulling rate and 1 s pulling time. Initially, the code phase of spoofing signal lags real signal by 2 chips.

Table 3. Minimum PLL lock value under different intermediate spoofing attack

Frequency offset	0 Hz	10 Hz	20 Hz	30 Hz	40 Hz	50 Hz
SAR						
2 dB	0.918	0.659	0.503	0.584	0.642	0.398
3 dB	0.918	0.653	0.621	0.646	0.579	0.449
5 dB	0.918	0.622	0.678	0.619	0.503	0.325
8 dB	0.918	0.664	0.586	0.575	0.441	0.315
10 dB	0.918	0.602	0.673	0.607	0.293	0.225

According to the experimental results in Table 3, the possibility of losing lock in intermediate spoofing attack is determined by carrier frequency deviation between spoofing signal and real signal. As the frequency offset increases, target receiver gets more vulnerable to loss of lock. From the overall trend, response of carrier loop during the pulling process is independent of SAR. In the pulling process, spoofing signal gains control of code loop through code phase scanning. Response of carrier loop falls slightly behind code loop. Once code loop is under the control of spoofing signal, EPL correlation value and consequent phase discrimination result of carrier loop is dominated by spoofing signal. Carrier loop will gradually change the frequency of local carrier from real signal to spoofing signal. Frequency adjustment gets carrier loop into an unstable state. Therefore, as frequency deviation increases, carrier loop needs more time to adjust itself to tracking spoofing signal and undergo longer unstable state, leading to higher probability of declaring loss of lock. Carrier loop adjusts its carrier frequency according to phase discrimination result influenced by relative magnitude of I and Q correlation values instead of absolute power, so power has little effect on carrier loop during the pulling process.

Continue to increase the carrier frequency deviation of spoofing signal, we studied relock time under different carrier frequency offsets here. Time elapsed from PLL fluctuation to finally tracking spoofing signal is defined as relock time. SAR is set to 3 dB in this experiment.

Table 4. PLL relock time under different frequency offset

Frequency offset/Hz	75	90	105	120	135	150
Relock time/s	0.226	0.313	0.439	0.658	0.857	Inf

Experimental results in Table 4 demonstrate that when carrier frequency offset is within the pull-in range of PLL, PLL needs longer time to track spoofing signal as carrier frequency offset increases. However, if frequency offset exceeds pull-in range, such as the case of 150 Hz, PLL will not be able to track spoofing signal. Relock time of PLL also depends on parameters such as integration time, loop bandwidth, and loop gain.

4 Verification with Commercial Receiver

It can be concluded from the above analysis and simulation experiment that during intermediate spoofing, power advantage of spoofing signal should be matched with code pulling rate to ensure that code loop of target receiver can lock on spoofing signal. Meanwhile, carrier frequency offset should be kept within pull-in range for carrier to track spoofing signal. Moreover, smaller carrier frequency offset help mitigate the risk of losing lock during the attack. Based on the above analysis, we developed an intermediate spoofing device and carried out wireless attack against commercial u-blox receiver. The spoofing attack platform is shown in Fig. 1.

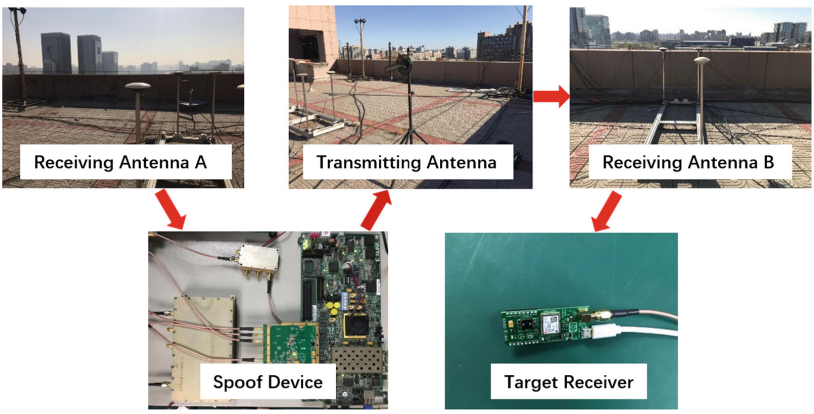

Fig. 1. Spoof platform

Spoofing device generates IF spoofing signal in real time according to solved real signal parameters and specific spoofing scenario. IF spoofing signal is up-converted and transmitted through transmitting antenna. Spoofing signal is mixed with real signal in the process of transmission and feed into target receiver.

For stationary target receiver whose accurate information is unknown, we can't calculate the code phase of real signal at target receiver. But the calculation of carrier frequency is feasible using approximate position of target receiver. When spoofing device is close to target receiver, carrier frequency solved by spoofing device can be directly used in generation of spoofing signal.

We first carried out the spoofing experiment with only one spoofing signal whose PRN is 31. Figure 2(a) shows the state of u-blox receiver before attack. At this time, pseudo-range residual of different satellites is nearly zero. Through manipulating of spoofing signal, we successfully complete spoofing attack. Result is shown in Fig. 2(b). Spoofing signal replaces real signal, but is not used for navigation because of its large pseudo-range residual. This indicates that the receiver has certain anti-spoofing ability.

SV	CN0	Residual	Nav	Qi	El	Az
G10	52	0.40	Y	7	73	208
G12	50	-0.60	Y	7	42	81
G14	46	0.20	Y	7	37	295
G15	36	0.90	Y	7	6	102
G18	41	-1.40	Y	7	14	303
G20	48	-0.10	Y	7	46	172
G24	41	1.00	Y	7	23	53
G25	48	-0.90	Y	7	45	135
G28	0	0.00	N	1	--	--
G31	45	1.00	Y	7	23	235
G32	51	-0.10	Y	7	56	312

(a)

SV	CN0	Residual	Nav	Qi	El	Az
G1	25	0.00	N	4	6	324
G10	52	0.10	Y	7	69	200
G12	49	-0.20	Y	7	42	75
G14	46	-0.30	Y	7	40	298
G15	0	0.00	N	1	3	104
G18	43	0.20	Y	7	14	299
G20	47	-0.70	Y	7	42	172
G24	44	0.60	Y	7	20	55
G25	48	-0.40	Y	7	49	130
G31	52	87.70	N	6	26	238
G32	50	-0.10	Y	7	59	317

(b)

Fig. 2. Response of u-blox receiver to single spoofing signal

From the results of above experiment, it can be seen that anti-spoofing algorithm may be used in u-blox receiver. In order to achieve effective spoofing, we simultaneously generate multiple spoofing signal. Strong synergy between different spoofing signals can effectively evade spoofing detection technique. When positioning result is controlled by spoofing signal, real signal will be excluded for large pseudo-range residual and no longer used in positioning.

In this spoofing attack experiment, six spoofing signals with PRN 2, 5, 13, 21, 29 and 30 are generated at the same time. In the beginning, multiple spoofing signal cooperates to locate target receiver in its estimated position, but is delayed compared with real signal. Then the code phase of multiple spoofing signal is controlled to slide relative to real signal. The sliding of code phase causes the transmission time of different spoofing signal to change uniformly. Positioning result of spoofing signal remains unchanged, but solved clock offset keeps changing. When spoofing signal get close to real signal in both code phase and transmitting time, they will take the place of corresponding real signal in target receiver. At this point, six spoofing signals cooperate with two genuine signal to local target receiver near its real position. As the adjustment of code phase continues, spoofing signal now deviates from real signal. Since the number of spoofing signals is dominant, target receiver will gradually be completely controlled by spoofing signals. The pseudo-range residuals of real signal are increased little by little and no longer used for positioning calculation. The state of the u-blox receiver before and after the attack is shown in Fig. 3(a) and (b).

Ch	SV	CN0	Residual	Nav	Qi	El	Az
0	G2	47	-0.82	Y	7	36	137
1	G5	53	-0.13	Y	7	57	54
2	G7	39	1.41	Y	7	8	37
3	G13	50	0.38	Y	7	77	141
4	G15	52	-0.24	Y	7	47	219
5	G29	52	-0.64	Y	7	44	253
6	G30	44	-0.88	Y	7	22	65

(a)

Ch	SV	CN0	Residual	Nav	Qi	El	Az
0	G2	51	4.83	Y	7	31	140
1	G5	51	3.44	Y	7	53	61
2	G7	33	-436.01	N	7	5	33
3	G13	51	7.31	Y	7	79	110
4	G15	48	-434.40	N	7	53	223
--	G20	0	0.00	N	0	2	278
7	G21	51	4.55	Y	7	26	312
--	G24	0	0.00	N	0	4	178
5	G29	51	10.45	Y	7	41	246
6	G30	51	1.58	Y	7	21	59

(b)

Fig. 3. Response of u-blox receiver to multiple spoofing signals

After being fully taken over, target receiver can be spoofed to any preset position. The ECEF X, Y, and Z coordinate values throughout the attack are shown in Fig. 4(a), (b), (c). Red vertical lines in the figure indicate value of 200 s and 1000 s in time

coordinate. At about 200 s, spoofing signal collides with real signal and achieve control of target receiver. From 200 s to 1000 s, spoofing signal competes with real signal for positioning result of target receiver, causing the positioning result to fluctuate. However, target receiver tends to trust spoofing signal for its numerical superiority. After 1000 s, spoofing signal took complete control of target receiver. According to preset spoofing position, spoofing device calculates the adjustment of different spoofing signal and applies corresponding code phase control until spoofing position is reached. During the entire spoofing attack, target receiver can continuously solve its position without being interrupted.

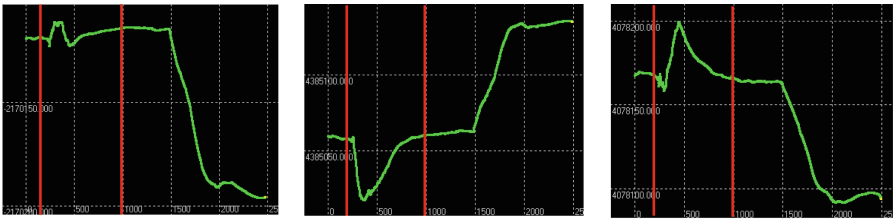

(a) (b) (c)

Fig. 4. Changes of ECEF coordinate in spoofing attacks

The ECEF coordinate of spoofing position is (−2170192.66, 4385133.93, 4078090.15). Figure 5(a), (b) presents the positioning result of u-blox receiver before and after spoofing attack. As can be seen from this figure, the spoofed positioning result is nearly the same as preset spoofing position.

(a) (b)

Fig. 5. ECEF coordinate before and after spoofing attack

5 Analysis and Conclusion

In this paper, we researched the requirements for power, pseudo code and carrier frequency of spoofing signal to successfully carry out intermediate spoofing attack. Further, we studied the impact of signal parameter error on intermediate spoofing when exact target information is unknown. It's found that code tracking loop is relatively independent of carrier tracking loop during the spoofing process. Because of its high power, spoofing signal is capable of controlling code tracking loop through code phase scanning, and then influences EPL correlation value. Carrier tracking loop adjusts the

frequency of local replica carrier according to correlation value and undergo an unstable state during this adjustment process. The larger the carrier frequency deviation of spoofing signal is, the longer the unstable state lasts, and the easier it is to be determined in the state of loss of lock. On the basis of the above conclusion, we developed the intermediate spoofing device, and successfully carried out spoofing experiment against commercial receiver without knowing its accurate information. The research results provide the basis for further research on intermediate spoofing and corresponding defensive measures.

References

1. Carroll JV, Van Dyke K, Kraemer JH et al (2001) Vulnerability assessment of the U.S. transportation infrastructure that relies on GPS. In: Proceedings of international technical meeting of the satellite division of the institute of navigation
2. Warner JS, Johnston RG (2002) A simple demonstration that the global positioning system (GPS) is vulnerable to spoofing. J Secur Adm 25(2):19–27
3. Humphreys TE, Ledvina BM, Psiaki ML et al (2008) Assessing the spoofing threat: development of a portable GPS civilian spoofer. In: Radio navigation laboratory conference proceedings
4. Shepard DP, Humphreys TE, Fansler AA (2012) Evaluation of the vulnerability of phasor measurement units to GPS spoofing attacks. Int J Crit Infrastruct Prot 5(3–4):146–153
5. Shepard DP, Bhatti JA, Humphreys TE et al (2012) Evaluation of smart grid and civilian UAV vulnerability to GPS spoofing attacks
6. Kerns AJ, Shepard DP, Bhatti JA et al (2014) Unmanned aircraft capture and control via GPS spoofing. J Field Robot 31(4):617–636
7. Tippenhauer NO, Rasmussen KB, Capkun S (2011) On the requirements for successful GPS spoofing attacks. In: ACM conference on computer and communications security, pp 75–86. ACM
8. Xie G (2012) Principles of GPS and receiver design. Publishing House of Electronics Industry, Beijing, pp 69–155
9. Gao Y, Li H, Lu M et al (2013) Intermediate spoofing strategies and countermeasures. Tsinghua Sci Technol 18(6):599–605

The Performance Testing and Evaluation of Anti-spoofing Techniques Using Single or Double Antenna

Zhiyuan Chen, Hong Li(✉), Jianfeng Li, Kexian Xiao, and Mingquan Lu

Department of Electronic Engineering, Tsinghua University, Beijing 100084, China
lihongee@tsinghua.edu.cn

Abstract. The miniaturization and low-cost of GNSS spoofing equipment have made the security of GNSS more concerned. The demand, research and application of anti-spoofing technology have also attracted more attention. For the spoofing signals transmitted by a single radiation source, it is a feasible anti-spoofing way to distinguish the authentic and counterfeit signals using the signal space characteristics. The anti-spoofing technology with single-antenna and dual-antenna are two typical representatives among them. This paper analyzes and compares the above two existing anti-spoofing technique. They are classified into two categories of spoofing detection and recognition algorithms, which are based on the correlation of amplitudes with single-antenna and the consistency of arrival time differences with dual-antenna. At the same time, this paper implements an anti-spoofing receiver architecture, and builds an experiment platform combined with sophisticated receiver-based spoofer. It is used to test and evaluate the performance of the above anti-spoofing technologies. A series of experiments were carried out with the single-antenna and dual-antenna anti-spoofing algorithms in different modes. Then the influence factors of performance and the advantages and disadvantages of the algorithms were analyzed and summarized. The results of this research have reference value for the development of anti-spoofing receiving equipment.

Keywords: GNSS · Anti-spoofing · Single-antenna · Correlation · Dual-antenna · Consistency

1 Introduction

The Global Navigation Satellite System (GNSS) provides a precise positioning and timing service for a large number of users. Since the civil navigation signal has an open structure and no encryption function, it is possible to spoof the positioning result of the ordinary targets. The University of Texas team has verified this with a series of spoofing attack tests. The tracking loop is captured and replaced when aligning the counterfeit signals with the authentic signals. The spoofing attack is successfully accomplished when the receiver is still locked. The drone is controlled by the counterfeit signal and the yacht is deviated from the predetermined route [1]. Therefore, the

J. Sun et al. (Eds.): CSNC 2019, LNEE 563, pp. 625–638, 2019.
https://doi.org/10.1007/978-981-13-7759-4_55

common commercial receiver is fragile and can be easily spoofed under the precisely designed spoofing attack. Even if the counterfeit signal, which is broadcasted by the GNSS signal simulator or the replay-with-delay device, can disturb the receiver output. The satellite navigation technology has been widely used, and the GNSS signal simulators can meet the demands of miniaturization and low cost. However, the positioning and timing service of the user segments in satellite navigation systems is confronted by a serious threat. The concept of 'navigation security' has attracted more and more attention from researchers. For the key areas of the national economy and national security, how to give correct and reliable positioning and timing results in the spoofing scene is an urgent problem to be solved.

In response to the above situation, various anti-spoofing algorithms have been proposed to spoofing countermeasures. At the present stage, the proposed anti-spoofing algorithms can be formed by the consistency of auxiliary information, the characteristics of signal structure, the signal spatial characteristics and so on. In terms of the characteristics of signal structure, the algorithm mainly includes signal power monitoring and signal quality monitoring [2]. In terms of signal spatial characteristics, it mainly includes the moving antenna method for space-time domain processing and the multi-antenna method for spatial domain processing [3]. In terms of the consistency of auxiliary information, the inertial measurement unit and the barometric altimeter are mainly sensors which are combined to form a RAIM algorithm with additional observations [4]. The algorithm, which is formed by signal spatial characteristics, can achieve better results in dealing with counterfeit signals emitted by a single source.

The single-antenna and dual-antenna anti-spoofing techniques are simpler and less expensive than the antenna array anti-spoofing techniques. At present, the proposed single-antenna anti-spoofing technology mainly includes the moving antenna method and the rotating antenna method. Analysing from the basic principle, the single-antenna users with these two modes both perform spoofing detection and recognition according to the correlation of signal amplitudes between different channels. Therefore, it is feasible to analyse these two methods using a unified model. The dual-antenna users perform spoofing detection and recognition according to the consistency of signal arrival time differences between different channels. Through theoretical analysis and experimental verification, the cumulative average of observation can be used to reduce the influence of noise and improve performance. The above techniques have not yet deployed and applied in receivers. Therefore, there is a lack of the performance testing and evaluation. Focusing on this problem, this paper constructs a spoofing and anti-spoofing test platform, and uses the authentic and counterfeit signal to conduct the experimental evaluation and comparison on the performance of the above two anti-spoofing technologies in different application environments. At the same time, we also designed and implemented an anti-spoofing receiver architecture, which can give correct positioning and timing results through grouping solution based on spoofing detection and recognition.

The rest of the paper is as follows: The second section is the model and analysis of the authentic and counterfeit signals, as well as the single-antenna and dual-antenna anti-spoofing detection techniques. The third section details the architecture of the anti-spoofing receiver and the spoofing and anti-spoofing test platform. The fourth section

analyses and evaluates the spoofing and anti-spoofing experiments. Then the advantages and disadvantages, such as the performance, cost, and so on, are compared and concluded. At last, the fifth section is the conclusion.

2 Single-Antenna and Dual-Antenna Anti-spoofing Technology

2.1 Authentic and Counterfeit Signal Model

In the outdoor environment where both the authentic and counterfeit signal exist, it is assumed that there are L^A authentic signals and L^S counterfeit signals. The global navigation satellite signal model is as follows:

$$\begin{aligned} r(t) = & \sum_{i=1}^{L^A} \alpha_i^A(t)\beta_i^A(t)A_i^A(t)c_i\left(t-\tau_i^A\right)e^{j\left[2\pi f_i^A\left(t-\tau_i^A\right)+\varphi_i^A\right]} \\ & + \sum_{i=1}^{L^S} \alpha_i^S(t)\beta_i^S(t)A_i^S(t)c_i\left(t-\tau_i^S\right)e^{j\left[2\pi f_i^S\left(t-\tau_i^S\right)+\varphi_i^S\right]} + u(t) \end{aligned} \tag{1.1}$$

where t represents time. The superscript A and S are used to distinguish the authentic signal from the counterfeit signal. The subscript i is used to represent the *i-th* channel signal. $\alpha(t)$ indicates the influence of path attenuation. $\beta(t)$ represents the influence of receiving antenna gain. $A(t)$ denotes the signal emission amplitude. $c(t-\tau)$ is the navigation message and the spreading code. τ represents the delay to arrive at the receiving antenna. f represents the Doppler frequency. φ represents the carrier phase. $u(t)$ represents the noise term.

The space-time domain information is obtained by single-antenna with translational motion or rotational motion, while the tracking correlation values can provide channel fading or antenna gain characteristics. The spatial domain information is obtained by the dual-antenna, while the carrier phase double differences between different signals can provide time differences of arrival. The detection statistic is generated and the detection algorithm is formed by the above observation. The single-antenna users utilize the correlation between signal amplitudes to detect and recognize the authentic and counterfeit signals. The dual-antenna users utilize the consistency between the signal arrival time differences to detect and recognize the authentic and counterfeit signals.

2.2 Correlation Detection of Signal Amplitudes with Single-Antenna

On the basis of the above signal model, after the *i-th* channel signal dispreading, the receiver output, tracking correlation value, is as follows:

$$I_i(n) = \alpha_i(t_n)\beta_i(t_n)A_i(t_n)R(\tau_{e_i})\left|\mathrm{sinc}(f_{e_i}T_{coh})\cos\left(\varphi_{e_i}\right)\right| + v_i(t_n) \tag{1.2}$$

where t_n represents the time corresponding to n. $R(\tau_e)$ represents the autocorrelation function of the pseudo code $c(t-\tau)$. τ_e represents the phase difference between the received and the local pseudo code, that is, the pseudo code loop tracking error, and f_e indicates the frequency difference between the received and the local carrier, that is, the carrier loop tracking error. T_{coh} represents the coherent integration time. φ_e represents the phase difference between the received and the local carrier, that is, the carrier phase-locked loop tracking error. $v(t_n)$ represents the noise term after dispreading.

Assuming that the impact of tracking error is small, $R(\tau_e)$ and $|\mathrm{sinc}(f_e T_{coh})\cos(\varphi_e)|$ can be considered as a stable item in a short time. Under the premise that the signal emission amplitude $A(t)$ remains stable, the tracking correlation values of the moving antenna and the rotating antenna vary with $\alpha(t)$ and $\beta(t)$, respectively.

When the antenna only undergoes translational motion without rotational motion [5], $\beta(t)$ can be regarded as a stable item in a short time. $\alpha_i(t_n)$ is a function of the variation which is affected by the *i-th* signal transmitter position $p_i(t_n)$ and the receiver position $p_r(t_n)$.

When the antenna only undergoes rotation motion without translational motion [6], $\alpha(t)$ can be regarded as a stable item in a short time. $\beta_i(t_n)$ is a function of the variation which is affected byss the *i-th* signal receiving azimuth $\mu_i(t_n)$ and pitch $\upsilon_i(t_n)$.

When the antenna is static without any translational or rotational motion, $\alpha(t)$ and $\beta(t)$ can be regarded as stable items in a short time. The tracking correlation values remain stable for a period of time.

The authentic signals have different propagation paths. This means that they have different path losses or antenna gains, as the antenna performs translational or rotational motion. The counterfeit signals have the same propagation path. This means that they have the same path losses or antenna gains. The correlation coefficient of the tracking correlation values is used as the correlation detection statistic to characterize the correlation of the two signal amplitudes. According to this, the spoofing detection and recognition works. The correlation detection statistic calculated according to the correlation coefficient is defined as:

$$\rho_{i,j} = \frac{\sum_{n=1}^{N} \left[I_i(n) - \overline{I_i}\right] \bullet \left[I_j(n) - \overline{I_j}\right]}{\sqrt{\sum_{n=1}^{N} \left[I_i(n) - \overline{I_i}\right]^2 \bullet \sum_{n=1}^{N} \left[I_j(n) - \overline{I_j}\right]^2}} \tag{1.3}$$

where $\overline{I_i} = \frac{1}{N}\sum_{n=1}^{N} I_i(n)$, N is the accumulation time of the tracking correlation values.

The single-antenna anti-spoofing algorithm uses the signal amplitude correlation to generate detection statistic, then uses it to detect and recognize the counterfeit signals. The correlation detection statistics are obtained with other different channels based on each channel. When the correlation detection statistics of more than one channel are greater than or equal to the threshold, that is $\rho_{i,j} \geq V_{corr,th}$, the *i-th* and *j-th* channel are marked as counterfeit signals. The remains whose correlation detection statistics are less than the threshold, are marked as authentic signals.

2.3 Consistency Detection of Signal Arrival Time Differences with Dual-Antenna

On the basis of the above signal model, after the *i-th* channel signal has been stably tracking, the receiver phase-locked loop output, carrier phase, is as follows:

$$\varphi_i(n) = \frac{1}{\lambda} d_i(t_n) + N_i + \frac{c}{\lambda}(\Delta T_i - \Delta T_r) + \frac{c}{\lambda}\left[\tau_{trop,i}(t_n) - \tau_{ion,i}(t_n)\right] + w_i(t_n) \tag{1.4}$$

where t_n denotes the time corresponding to n. $d(t_n)$ denotes the distance from the satellite to the receiver. λ denotes the signal wavelength, and N denotes the full-circumference ambiguity, which is an integer. c represents the speed of light. ΔT_i and ΔT_r represent the satellite clock and receiver clock, respectively. $\tau_{trop}(t_n)$ and $\tau_{ion}(t_n)$ represent the tropospheric and ionospheric delays, respectively. $w(t)$ represents the noise term of the carrier phase-locked loop.

The two antennas of dual-antenna are nearby and use the same clock. The carrier phase double difference [7] between the *i-th* and *j-th* channel is expressed as:

$$\begin{aligned} \Delta\varphi_{i,j}(n) &= \Delta\varphi_i(n) - \Delta\varphi_j(n) \\ &= \frac{b}{\lambda}\left[\cos\theta_i(t_n) - \cos\theta_j(t_n)\right] + \left(\Delta N_i - \Delta N_j\right) + \left[\Delta w_i(t_n) - \Delta w_j(t_n)\right] \end{aligned} \tag{1.5}$$

which can be denoted as $\Delta\varphi_i(n) = \frac{b}{\lambda}\cos\theta_i(t_n) + \Delta N_i + \Delta w_i(t_n)$. The symbol Δ indicates that the variables correspond to the two antennas are subtracted. b is the distance between the two antennas. It is the length of baseline. θ indicates the angle between satellite-to-receiver vector and dual-antenna baseline. The dual-antenna carrier phase double difference eliminates the satellite clock error and receiver clock error, as well as the effects of tropospheric and ionospheric delays, leaving the influence of satellite and receiver geometry, integer ambiguity and noise effects.

The authentic signals have different propagation paths with different angles of arrival respect to the baseline. It means that the arrival time differences are unequal. The spoofing signals have the same propagation paths and have the same angles of arrival respect to the baseline. It means that the arrival time differences are equal. The fractional part $\phi_{i,j}$ of the carrier phase double difference $\Delta\varphi_{i,j}$ is used as the consistency detection statistic to characterize the consistency of the two signal arrival time differences. It represents the relationship between the angles of arrival θ_i and θ_j. According to this, the spoofing detection and recognition works.

In order to further eliminate the influence of the Integer ambiguity in the carrier phase double difference, the single-point consistency detection statistic is obtained by taking the decimal frac$(\bullet)$ and limiting it to −0.5–0.5. Only the influence of the satellite and receiver geometry is preserved.

$$\begin{aligned} \phi_{i,j} &= \mathrm{frac}\left(\Delta\varphi_{i,j}\right) \\ &= \mathrm{frac}\left(\Delta B_{i,j}\right) + \mathrm{frac}\left(\Delta W_{i,j} - \mathrm{frac}\left(\Delta B_{i,j}\right)\right) \end{aligned} \tag{1.6}$$

In order to reduce the influence of measurement noise and further improve the detection performance, $\Delta\varphi_{i,j}$ can be averaged and recorded as $\overline{\Delta\varphi_{i,j}} = \overline{\Delta B_{i,j}} + \Delta N_{i,j} + \overline{\Delta W_{i,j}}$. Also, the average consistency detection statistic $\overline{\phi_{i,j}} = \mathrm{frac}\left(\overline{\Delta\varphi_{i,j}}\right)$ is obtained by take the decimal $\mathrm{frac}(\bullet)$ and limit it to −0.5–0.5.

The single-antenna anti-spoofing algorithm uses the signal amplitude correlation to generate detection statistic, then use it to detect and recognize the counterfeit signals. Calculating with other different channels based on each channel.

The dual-antenna anti-spoofing algorithm uses the arrival time difference to generate consistency detection statistic, then uses it to detect and recognize the counterfeit signals. The consistency detection statistics are obtained with other different channels based on each channel. When the absolute values which apply to the consistency detection statistics of more than one channel are less than or equal to the threshold, that is $\left|\phi_{i,j}\right| \le V_{cons,th}$, the *i-th* and *j-th* channel are marked as counterfeit signals. The remains are marked as authentic signals.

3 Spoofing and Anti-spoofing Platform

3.1 Spoofer and Scenarios

The counterfeit signal generated by a sophisticated receiver-based spoofer is transmitted through a single source antenna. The process of spoofing attack is mainly divided into two stages. The first stage is adjusting the counterfeit signal power to capture the target receiver's tracking loop. The second stage is adjusting the pseudo-range and Doppler shift of counterfeit signal in order to traction and deflection. The test carried out in this paper is mainly after the stage of traction and deflection.

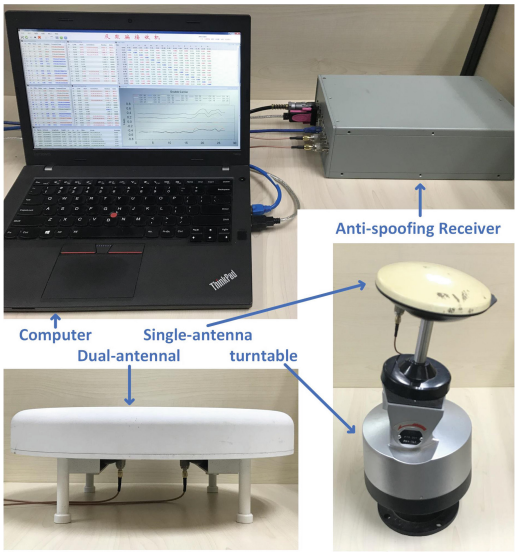

Fig. 1. Anti-spoofing receiver configurations

3.2 Anti-spoofing Receiver Architecture

The anti-spoofing receiver involved in the experiment can receive and process the B1I signal of the Beidou navigation satellite system. The anti-spoofing receiver, as well as the single-antenna and the dual-antenna, are shown in Fig. 1. Also, a turntable for rotating the antenna and a computer for running display and control software are included. The workflow for the anti-spoofing receiver architecture are as follows:

(a) Multi-peak acquisition and tracking. A multi-peak acquisition and tracking algorithm is used, that is, for each satellite number, not only the maximum peak but also the second largest peak channel is tracked [8].
(b) Multi-channel anti-spoofing strategy with the same radiation source. The anti-spoofing technology is used to detect and recognize the channel signal. When the detection statistics of multiple channel signals are not within the threshold, the channels are marked as spoofing signals, otherwise they are marked as authentic signals.
(c) Clustering and grouping strategy. The channels are clustered according to the label. The channels with the same label and the same satellite number are grouped into group $\{N\}$. The channels marked as counterfeit or authentic signals are grouped into group $\{S\}$ and group $\{A\}$.
(d) PVT estimation and detection. Using the pseudo-range of group $\{A\}$ and $\{S\}$ to obtain the PVT solutions R_A and R_S. If the PVT solutions pass the RAIM detection algorithm [9]. The pseudo-range residuals of group $\{N\}$ are calculated separately and then dropped into group $\{A\}$ or $\{S\}$. Finally, the PVT solutions are calculated again.

4 Experiment Analysis and Evaluation

When both authentic and counterfeit signals exist and the correlation peaks are separated, the anti-spoofing receiver can simultaneously receive and process the authentic and counterfeit signals. A series of experiments are designed for single-antenna and dual-antenna anti-spoofing techniques in order to test and evaluate the performance. The anti-spoofing technology in this paper can be divided into three categories: the correlation detection with stationary and moving single-antenna, the correlation detection with fixed point rotating antenna, and consistency detection with stationary and moving dual-antenna.

4.1 Correlation Detection with Stationary and Moving Single-Antenna

In this experiment, the test and analysis of static and moving single-antenna correlation detection are mainly carried out. The authentic signals are tracking in the channels including 2, 3, 7, 10, 13, 16, which amount to 6 channels. The counterfeit signals are tracking in the channels including 0, 1, 5, 8, 11, 12, 21, 23, which amount to 8 channels. The states of antenna motion are divided into two segments. The single antenna is stationary at 0 s–16 s, then the single antenna is moving at 20 s–60 s.

The tracking correlation value curves are shown in Fig. 2a. When the single-antenna is stationary, the tracking correlation values of all channels are relatively stable. When the single-antenna is in translational motion, the tracking correlation values of different counterfeit signal channels have similar fluctuations. The tracking correlation values of different authentic signal channels have different fluctuations.

When the single-antenna is stationary, the correlation detection statistics of both the authentic signal and counterfeit signal are under the threshold. The authentic and counterfeit signals cannot be recognized. The receiver can give neither correct grouping nor reliable positioning and timing results. However, the receiver can detect and alarm according to either the multi-correlation peak acquisition and tracking or the RAIM algorithm. When the single-antenna is in translational motion, the correlation detection statistics are shown in Fig. 2b. The correlation detection statistics of the counterfeit signals are above the threshold. Then, the counterfeit signals are marked in red, and the authentic signals are marked in green. At the same time, the receiver can give both correct grouping and reliable positioning and timing results.

(a)

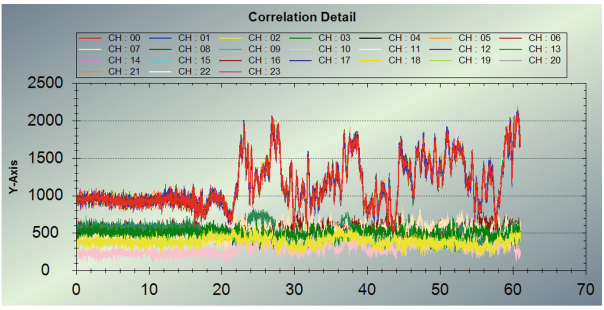

(b)

Main	0	1	2	3	5	7	8	10	11	12	13	16	21	23
0	0.00	0.99	0.11	-0.28	0.99	0.33	0.99	0.57	0.99	0.99	0.21	-0.09	0.99	0.99
1	0.99	0.00	0.11	-0.28	0.99	0.33	0.99	0.57	0.99	0.99	0.21	-0.09	0.99	0.99
2	0.11	0.11	0.00	0.10	0.11	-0.11	0.12	0.01	0.12	0.12	0.35	-0.28	0.12	0.12
3	-0.28	-0.28	0.10	0.00	-0.28	-0.19	-0.28	-0.27	-0.28	-0.28	-0.09	0.09	-0.28	-0.28
5	0.99	0.99	0.11	-0.28	0.00	0.33	0.99	0.57	0.99	0.99	0.21	-0.09	0.99	0.99
7	0.33	0.33	-0.11	-0.19	0.33	0.00	0.33	0.54	0.33	0.33	-0.17	0.01	0.33	0.33
8	0.99	0.99	0.12	-0.28	0.99	0.33	0.00	0.57	1.00	0.99	0.21	-0.09	0.99	0.99
10	0.57	0.57	0.01	-0.27	0.57	0.54	0.57	0.00	0.57	0.57	0.07	-0.11	0.57	0.57
11	0.99	0.99	0.12	-0.28	0.99	0.33	1.00	0.57	0.00	0.99	0.22	-0.09	0.99	0.99
12	0.99	0.99	0.12	-0.28	0.99	0.33	0.99	0.57	0.99	0.00	0.21	-0.10	0.99	0.99
13	0.21	0.21	0.35	-0.09	0.21	-0.17	0.21	0.07	0.22	0.21	0.00	-0.24	0.21	0.21
16	-0.09	-0.09	-0.28	0.09	-0.09	0.01	-0.09	-0.11	-0.09	-0.10	-0.24	0.00	-0.10	-0.08
21	0.99	0.99	0.12	-0.28	0.99	0.33	0.99	0.57	0.99	0.99	0.21	-0.10	0.00	0.99
23	0.99	0.99	0.12	-0.28	0.99	0.33	0.99	0.57	0.99	0.99	0.21	-0.08	0.99	0.00

Fig. 2. a. The tracking correlation value curves with stationary and moving single-antenna b. The correlation detection statistics with moving single-antenna

We found that the user-side influence factors of the correlation detection statistics with moving single-antenna mainly include the channel fading variation and accumulation time. The channel fading is usually caused by the motion antenna and changes in the surrounding environment. If the accumulation time is relatively small, the detection performance is poor. On the contrary, if the accumulation time is relatively large, the detection response is slow.

4.2 Correlation Detection with Fixed Point Rotating Antenna

In this experiment, the test and analysis of static and rotating single-antenna correlation detection are mainly carried out. The authentic signals are tracking in the channels including 3, 5, 7, 8, 13, 14, 17, 18, 19, 20, 22, which amount to 11 channels. The counterfeit signals are tracking in the channels including 0, 1, 2, 6, 9, 10, 12, 23, which amount to 8 channels. The single-antenna rotation period is 68 s and the single-antenna slope angle is 10°.

The tracking correlation value curves are shown in Fig. 3a. Due to the rotation of the single antenna, the tracking correlation values of the counterfeit signals incomed with the same direction have similar fluctuations. The tracking correlation values of authentic signals incomed with the different directions have different fluctuations. Using the correlation detection statistic in Fig. 3b to detect and recognize, the receiver can give correct grouping results, then provide reliable positioning and timing results.

Similar to the previous section, as the rotational motion mode is selected, the user-side influence factors of the correlation detection statistics mainly include slope angle and accumulation time. The slope angle determines the magnitude of the signal amplitude change, which directly affects the magnitude of the correlation detection statistic. However, when the signal amplitude changes too much, it will affect the performance of the receiver tracking loop. A better result can be obtained when the length of cumulative time and rotation period are the same.

(a)

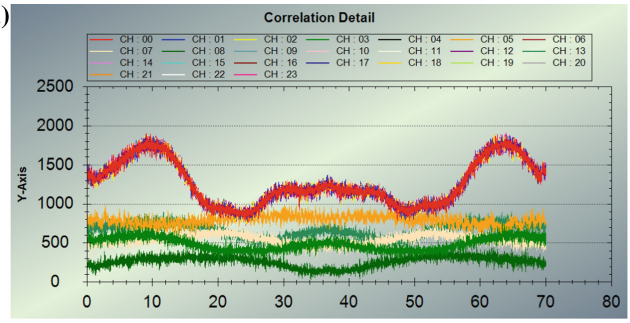

(b)

Main	0	1	2	3	5	6	7	8	9	10	12	13	14	17	18	19
0	0.00	0.99	0.99	0.90	-0.48	0.99	-0.65	-0.42	0.99	0.99	0.99	0.64	-0.80	0.85	0.93	-0.18
1	0.99	0.00	0.99	0.90	-0.48	0.99	-0.65	-0.42	0.99	0.99	0.99	0.64	-0.80	0.85	0.93	-0.19
2	0.99	0.99	0.00	0.90	-0.48	0.99	-0.65	-0.41	0.99	0.99	0.99	0.64	-0.80	0.85	0.93	-0.18
3	0.90	0.90	0.90	0.00	-0.35	0.90	-0.73	-0.54	0.90	0.90	0.90	0.58	-0.85	0.90	0.91	-0.37
5	-0.48	-0.48	-0.48	-0.35	0.00	-0.48	0.21	0.02	-0.48	-0.48	-0.45	-0.41	0.26	-0.28	-0.40	-0.17
6	0.99	0.99	0.99	0.90	-0.48	0.00	-0.64	-0.42	0.99	0.99	0.99	0.63	-0.79	0.86	0.92	-0.18
7	-0.65	-0.65	-0.65	-0.73	0.21	-0.64	0.00	0.61	-0.65	-0.65	-0.64	-0.34	0.82	-0.79	-0.74	0.58
8	-0.42	-0.42	-0.41	-0.54	0.02	-0.42	0.61	0.00	-0.42	-0.42	-0.41	-0.12	0.64	-0.62	-0.51	0.62
9	0.99	0.99	0.99	0.90	-0.48	0.99	-0.65	-0.42	0.00	0.99	0.99	0.64	-0.80	0.85	0.93	-0.19
10	0.99	0.99	0.99	0.90	-0.48	0.99	-0.65	-0.42	0.99	0.00	0.99	0.64	-0.80	0.85	0.93	-0.18
12	0.99	0.99	0.99	0.90	-0.45	0.99	-0.64	-0.41	0.99	0.99	0.00	0.64	-0.79	0.85	0.92	-0.18
13	0.64	0.64	0.64	0.58	-0.41	0.63	-0.34	-0.12	0.64	0.64	0.64	0.00	-0.46	0.52	0.64	0.19
14	-0.80	-0.80	-0.80	-0.85	0.26	-0.79	0.82	0.64	-0.80	-0.80	-0.79	-0.46	0.00	-0.90	-0.87	0.54
17	0.85	0.85	0.85	0.90	-0.28	0.86	-0.79	-0.62	0.85	0.85	0.85	0.52	-0.90	0.00	0.91	-0.50
18	0.93	0.93	0.93	0.91	-0.40	0.92	-0.74	-0.51	0.93	0.93	0.92	0.64	-0.87	0.91	0.00	-0.32
19	-0.18	-0.19	-0.18	-0.37	-0.17	-0.18	0.58	0.62	-0.19	-0.18	-0.18	0.19	0.54	-0.50	-0.32	0.00

Fig. 3. a. The tracking correlation value curves with fixed point rotating antenna b. The correlation detection statistics with fixed point rotating antenna

4.3 Consistency Detection with Stationary and Moving Dual-Antenna

The consistency detection with stational and moving dual-antenna is mainly tested and analysed in this experiment. The authentic signals are tracking in the channels including 3, 5, 6, 7, 8, 10, 11, 15, which amount to 8 channels. The counterfeit signals are tracking in the channels including 0, 1, 2, 4, 12, 14, 18, 23, which amount to 8 channels. The states of antenna motion are divided into three segments. The dual-antenna is randomly moving at 0 s–30 s, then the dual-antenna is stationary at 30 s–42 s. The dual-antenna is reciprocating moving at 42 s–52 s.

The carrier phase double difference curves are shown in Fig. 4a, and their values are the double differences between channel 1 and the others. The dual-antenna is whether stationary or moving does not affect the double differences between the counterfeit signal channels. The double differences between the counterfeit signal channels are concentrated near the zero. The double differences between the authentic signal channels are dispersed within the value range. Using the average consistency detection statistics in Fig. 4b to detect and recognize, the receiver can give correct grouping results, then provide reliable positioning and timing results.

In contrast, the user-side influence factors are mainly the length of dual-antenna baseline in the dual-antenna consistency experiment. The translational motion of the dual-antenna does not change the value of the consistency detection statistics, and the rotational motion does not change the statistical distribution of the consistency detection statistics. Thus, the dual-antenna anti-spoofing algorithm can ensure the effectiveness.

(a)

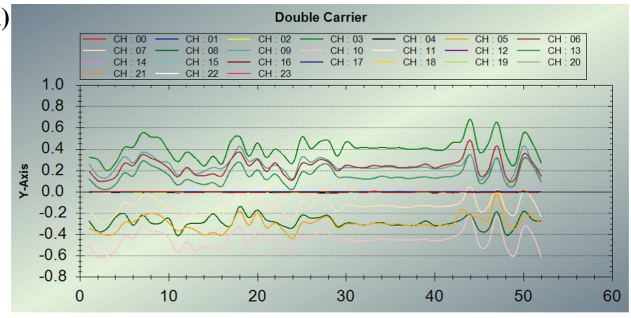

(b)

PRN		8	8	9	13	13	2	12	12	1	1	6	6	4	3	3
	chNo	0-24	10-34	1-25	2-26	7-31	3-27	4-28	15-39	5-29	14-38	6-30	23-47	8-32	11-35	12-36
8	0-24	0.000	0.265	0.002	0.000	-0.126	0.409	0.001	0.159	-0.284	0.001	0.240	0.000	-0.273	-0.441	0.001
8	10-34	-0.265	0.000	-0.263	-0.265	-0.390	0.144	-0.264	-0.106	0.451	-0.263	-0.025	-0.265	0.463	0.294	-0.264
9	1-25	-0.002	0.263	0.000	-0.002	-0.128	0.407	-0.001	0.157	-0.286	-0.001	0.238	-0.002	-0.275	-0.443	-0.001
13	2-26	0.000	0.265	0.002	0.000	-0.126	0.409	0.001	0.159	-0.284	0.001	0.240	0.000	-0.273	-0.441	0.001
13	7-31	0.126	0.390	0.128	0.126	0.000	-0.465	0.127	0.285	-0.159	0.127	0.366	0.126	-0.147	-0.315	0.126
2	3-27	-0.409	-0.144	-0.407	-0.409	0.465	0.000	-0.408	-0.250	0.307	-0.407	-0.169	-0.409	0.319	0.150	-0.408
12	4-28	-0.001	0.264	0.001	-0.001	-0.127	0.408	0.000	0.158	-0.285	0.001	0.239	-0.001	-0.274	-0.442	0.000
12	15-39	-0.159	0.106	-0.157	-0.159	-0.285	0.250	-0.158	0.000	-0.443	-0.158	0.081	-0.159	-0.432	0.400	-0.158
1	5-29	0.284	-0.451	0.286	0.284	0.159	-0.307	0.285	0.443	0.000	0.286	-0.476	0.284	0.012	-0.157	0.285
1	14-38	-0.001	0.263	0.001	-0.001	-0.127	0.407	-0.001	0.158	-0.286	0.000	0.239	-0.001	-0.274	-0.443	-0.001
6	6-30	-0.240	0.025	-0.238	-0.240	-0.366	0.169	-0.239	-0.081	0.476	-0.239	0.000	-0.240	0.487	0.319	-0.239
6	23-47	0.000	0.265	0.002	0.000	-0.126	0.409	0.001	0.159	-0.284	0.001	0.240	0.000	-0.273	-0.441	0.001
4	8-32	0.273	-0.463	0.275	0.273	0.147	-0.319	0.274	0.432	-0.012	0.274	-0.487	0.273	0.000	-0.168	0.273
3	11-35	0.441	-0.294	0.443	0.441	0.315	-0.150	0.442	-0.400	0.157	0.443	-0.319	0.441	0.168	0.000	0.442
3	12-36	-0.001	0.264	0.001	-0.001	-0.126	0.408	0.000	0.158	-0.285	0.001	0.239	-0.001	-0.273	-0.442	0.000

Fig. 4. a. The carrier phase double difference curves with stationary and moving dual-antenna b. The consistency detection statistics with stationary and moving dual-antenna

Monte Carlo simulation is used to reveal the performance of dual-antenna consistency detection affected by the length of baseline. It is assumed that the directions of satellite signal arrivals are independent of each other and subject to uniform distribution, $\theta_i \sim \mathcal{U}(-\pi, \pi)$. The carrier phase measurement errors of different channels are independent of each other and obey the Gaussian distribution, $w_i \sim \mathcal{N}(0, 0.004^2)$.

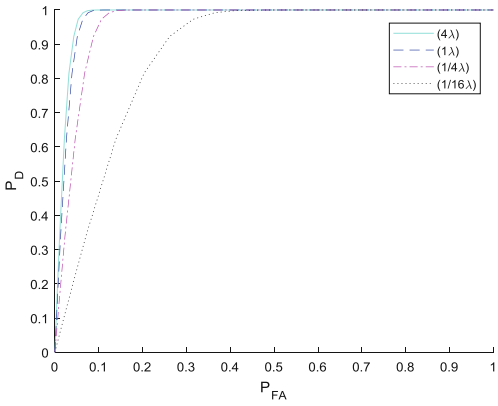

Fig. 5. The ROC curve of dual-antenna consistency detection

Figure 5 shows the ROC curves of single point consistency detection with different baseline lengths. As the baseline length increases, its detection performance increases. However, the performance increases gradually become slow. When the baseline length is greater than $1/4$ wavelength, the consistency detection statistic can be distributed between -0.5–0.5.

4.4 Performance of Technologies and Comparison of Advantages and Disadvantages

The correlation detection method of the single-antenna anti-spoofing technology has the advantages of low hardware and software implementation complexity, and the convenient of expansion on existing commercial receivers. However, the performance of the moving antenna anti-spoofing algorithm is heavily dependent on the channel fading variations caused by the motion mode and the surrounding environment. These features result in poor stability and reliability of detection and recognition. Moreover, this technique may be invalid, when the antenna is stationary. The rotating antenna anti-spoofing algorithm can solve the anti-spoofing demand of fixed point. The detection performance can be adjusted by changing the slope angle, and the response time can be adjusted by changing the rotation period. However, the signal amplitude changes with the rotation of antenna, there is a problem that the tracking of received

signal is unstable when the antenna slope angle is too large. The consistency detection method of the dual-antenna anti-spoofing technology has the advantages of stable and reliable performance, and no constraint on the motion of the user antenna. The average consistency detection has better performance than the single point consistency detection. However, compared to the single-antenna method, the dual-antenna method needs double the hardware and software resources, which increases the cost of implementation. The analysis and comparison of the above two anti-spoofing method are summarized in Table 1.

Table 1. The comparison of single-antenna and dual-antenna anti-spoofing technology

Anti-spoofing	Mode	Statistic	Influence factor		Advantages	Disadvantages
Single-antenna	Translational motion	Correlation detection statistic	Accumulation time	Motion channel fading	The algorithm is the easiest to implement, and it is convenient to obtain tracking correlation values	It requires the motion of antenna or the change of surrounding environment, which would cause channel fading variations. The stability and reliability of the algorithm is poor
	Rotational motion			Slope angle	This can handle fixed point antennas, and is further improved compared to the translational one	Need antenna turntable. The rotational variations affect the performance of tracking
Dual-antenna	Single-point	Single-point consistency detection statistic	Length of baseline	——	The adaptability of user environment is good. The detection performance is stable and reliable, and response time is short	The receiver is costly to implement and is required to provide carrier phase. The performance of single point is slightly worse than the average one
	Average	Average consistency detection statistic		Accumulation time	The adaptability of user environment is better. The performance of the average one is better than the single point one	The receiver implementation cost is high and the response time is long

5 Conclusions

This paper designs and implements an anti-spoofing receiver architecture, builds a spoofing and anti-spoofing test platform. Using the open area signal environment to evaluate the performance and capability of the existing single-antenna and dual-antenna anti-spoofing technology. It is found that the single-antenna correlation detection, which is contributed by signal amplitude, can be divided into two types: translational motion mode and rotational motion mode. The performance of single-antenna correlation detection with translational motion is mainly affected by the channel fading variation. The performance of single-antenna correlation detection in with rotational motion is mainly affected by the slope angle. The dual-antenna consistency detection, which is contributed by signal arrival time difference, includes the single point mode and the average mode. The detection performance in both modes is affected by the length of baseline. The performance of dual-antenna consistency detection with average mode is also affected by the accumulation time.

Finally, the paper also analyses the advantages and disadvantages of the above anti-spoofing technologies. The single-antenna anti-spoofing algorithm has the advantages of simplest to implement, and easy to obtain tracking correlation value. However, the stability and reliability of this algorithm are poor. The dual-antenna anti-spoofing algorithm has the stable and reliable performance of detection, but requires the receiver to provide carrier phase. The demand of double hardware and software resources means high cost. The results of this research have reference value for the development of anti-spoofing receiving equipment.

Acknowledgements. This work was supported by the National Natural Science Foundation of China (Grant No. 61571255).

References

1. Psiaki ML, Humphreys TE, Stauffer B (2016) Attackers can spoof navigation signals without our knowledge. Here's how to fight back GPS lies. IEEE Spectr 53(8):26–53
2. Jafarnia-Jahromi A, Broumandan A, Nielsen J, Lachapelle G (2012) GPS vulnerability to spoofing threats and a review of antispoofing techniques. Int J Navig Obs 2012:16
3. Broumandan A, Jafarnia-Jahromi A, Daneshmand S, Lachapelle G (2016) Overview of spatial processing approaches for GNSS structural interference detection and mitigation. Proc IEEE 104(6):1246–1257
4. Khanafseh S, Roshan N, Langel S, Chan FC, Joerger M, Pervan B (2014) GPS spoofing detection using RAIM with INS coupling. In: Proceedings of the position, location and navigation symposium—PLANS, vol 2014
5. Broumandan A, Jafarnia-Jahromi A, Dehghanian V, Nielsen J, Lachapelle G (2012) GNSS spoofing detection in handheld receivers based on signal spatial correlation. In: Position location and navigation symposium (PLANS), 2012 IEEE/ION. IEEE, pp 479–487
6. Wang F, Li H, Lu M (2017) GNSS spoofing countermeasure with a single rotating antenna. IEEE Access 5:8039–8047

7. Borio D, Gioia C (2015) A dual-antenna spoofing detection system using GNSS commercial receivers. In: Proceedings of the 28th international technical meeting of the satellite division of the institute of navigation (ION GNSS+), Tampa, Florida, pp 1–6
8. He L, Li H, Lu M (2017) A fundamental architecture of anti-spoofing GNSS receiver. In: China satellite navigation conference. Springer, Singapore, pp 899–909
9. Parkinson BW, Axelrad P (1988) Autonomous GPS integrity monitoring using the pseudorange residual. Navigation 35(2):255–274

Policies, Regulations, Standards and Intellectual Properties

Analysis on Intellectual Property Litigations and Countermeasures of Satellite Navigation Enterprises

Yuxuan Wang(✉)

China Industrial Control Systems Cyber Emergency Response Team, Electronic First Research Institute, Ministry of Industry and Information Technology, No. 35, Lugu Road, Beijing 100040, China
wangyuxuan@infoip.org

Abstract. At present, China's BDS has entered a new era of global networking, and the application industry has shown a rapid development trend. With the rapid development of BDS' global system construction and industrial development, Beidou's R&D and innovation activities increasing fast, international exchanges are becoming more frequent. As a technology highly concentrated industry, satellite navigation related companies will encounter a variety of IP litigations in this process. Enterprises face high IP risks in daily operations, international exchanges and corporate IPO. It is essential for the enterprises to pay attention in advance and respond appropriately. This paper searches the typical cases of IP lawsuits in satellite navigation enterprises, and analyses the problems that satellite navigation enterprises reflected in patent litigation, trademark litigation, software copyright litigation, trade secret litigation and IPO process. In combination with IP regulations and domestic & foreign litigation practices, strategies such as strengthen core patent R&D applications, attach importance to product trademarks and copyright rights, improve corporate IP management, attach importance to IP due diligence of core patents, apply overseas IP rights in advance, and explore ways to establish IP insurance system are listed. Thus, Satellite navigation enterprises can attach importance to and properly solve various IP issues, which enable IPR to safeguard the long-term development of satellite navigation enterprises.

Keywords: Satellite navigation enterprise · Intellectual property litigation · Countermeasures

1 Introduction

Since entering 2018, China's Beidou satellite has completed 11 launch missions and sent 20 satellites into the orbit. The intensive launch of the Beidou satellite marks the successful completion of the Beidou-III basic system constellation deployment and takes a "significant milestone" from the region to the world. On December 27 2018, Chengqi Ran announced that the basic system of the Beidou-III was completed and began to provide global services. With the construction of Beidou satellite navigation system, the basic products of satellite navigation in China are controllable, and a

J. Sun et al. (Eds.): CSNC 2019, LNEE 563, pp. 641–650, 2019.
https://doi.org/10.1007/978-981-13-7759-4_56

complete industrial chain has been formed. Beidou is gradually applied to various fields including national transportation, agriculture, forestry, fisheries, electric power, finance, public security, disaster prevention and mitigation, special population care, mobile phones and wearable devices, covering various fields of national economy and social development. According to the data disclosed in the "White Paper on the Development of China's Satellite Navigation and Location Services Industry in 2018", the total output value of China's satellite navigation and location service industry has reached 255 billion yuan in 2017. As of January 2018, the total number of satellite navigation and Beidou application-related listed companies (including New OTC Market) has reached 58. Along with the construction and application development of China's Beidou satellite navigation system, domestic satellite navigation and Beidou application-related enterprises will achieve rapid development, the industrial chain will improved increasingly. The industrial scale will continue to expand as well.

As a technology-highly concentrated industry, satellite navigation-related enterprises will inevitably incur intellectual property disputes as they own or use other people's patents, trademarks, copyrights and other intellectual property rights. According to the legal research result, satellite navigation related enterprises may encounter intellectual property lawsuits in daily operations, mergers and acquisitions, and IPOs. Some type of cases is commonplace. Through several typical cases analyzing and litigation countermeasures summarizing, we wish this could enhance the ability of satellite navigation enterprises to respond to intellectual property risks and promote the long-term development of enterprises.

2 Intellectual Property Litigations in the Daily Operation of Satellite Navigation Enterprises Introduction

After searching on the public network and judicial case database like Pkulaw.cn and China Judgments Online, etc., Beidou related enterprises face certain litigation risks in various types of IPR. The top priority of management work in satellite navigation-related enterprises is to prevent and cope with such IPR risks.

2.1 Patent Infringement Litigation

In satellite navigation industry, patents play a vital role in enterprises' development. Patent information can provide technical reference for enterprises, innovate the way of working, avoid duplication of research, prevent infringement disputes, warn competitors and protect intellectual property rights. Patent infringement disputes in the field of satellite navigation are also very common. Both the SIRF and Global Locate patent foreign litigation and the domestic Shenzhen SEG Navigation v. Toyota G-BOOK patent infringement litigation reflect the important value of the core patent for navigation companies.

In August 2010, SEG Navigation sued Guangzhou Automobile Toyota in Shenzhen Intermediate People's Court, claiming that the technology used in its G-BOOK system infringed SEG's "an interactive navigation and vehicle security system patent (Patent No.: ZL200610157027.7)". The court decided to conduct an infringement

judicial appraisal by the Shanghai Intellectual Property Judicial Appraisal Center. During this period, GAC Toyota applied to the court to declare the SEG navigation patent invalid, but it was not supported. In December 2013, after the long process of five trials, forensics, and third-party appraisal of the Toyota SEG case, the Shenzhen Intermediate People's Court ruled that the Toyota G-BOOK smart co-driver system was infringed. The focus of the dispute in this case is whether the alleged infringing product falls within the scope of patent protection of SEG Navigation. The current patent infringement judgement basis is mainly the provisions of Article 56 of the Patent Law. In practice, the determination of patent infringement is extremely complicated, and in the process of judgment, the court may need assistance from technical judgments such as the judicial appraisal center to draw a conclusion. This case enlightens satellite navigation enterprises to strengthen the patent layout, and to develop a reasonable litigation strategy when facing patent litigations (Fig. 1).

Time		Process
2010	August	SEG Navigation filed a Toyota G-BOOK patent infringement lawsuit in Shenzhen Intermediate People's Court
	September 10th	Toyota Company filed patent invalidation request for patent number ZL200610157027.7 (SEG owned) to the Patent Reexamination Board of the State Intellectual Property Office
	October 13th	First trial in the first instance
2011	May 19th	the Patent Reexamination Board of the State Intellectual Property Office made Decision No. 16536 on the Examination of Invalidation Requests to maintain the validity of the patent.
	June 2nd	the second trial added Beijing 95190 Information Technology Co., Ltd. as the defendant.
	July 21st	the third trial
	September 19th	the court decided to adopt Shanghai Intellectual Property Judicial Appraisal Center
	October 18th	Beijing First Intermediate People's Court heard the Toyota lawsuit and rejected its invalid patent request
	November 10 th	Beijing Guowei Intellectual Property Judicial Appraisal Center Appraisal: Toyota G-BOOK falls into the scope of SEG patent protection
2012	March 14th	Toyota applied patent invalidation request to the Patent Reexamination Board of the State Intellectual Property Office for the second time.
	June 26th	Toyota patent invalidation request was rejected
	November	Shanghai Intellectual Property Judicial Appraisal Center Appraisal: Toyota G-BOOK falls into the scope of SEG patent protection
2013	May 27th	2013 The fourth session, corss-examination of appraisal opinion
	December 20th	Shenzhen Intermediate People's Court ruled that Toyota G-BOOK was infringed

Fig. 1. SEG v. Toyota G-BOOK patent infringement case process map

2.2 Copyright Infringement Litigation

In the process of product production and operation, enterprises inevitably need to use the software or parts of upstream and downstream enterprises. If they neglect the intellectual property licenses in this process, they may bring infringement risks to themselves. Take Microsoft's and Unistrong's software copyright dispute case as an example, in 2011, Microsoft sued Beijing Unistrong Technology Co., Ltd. (hereinafter referred to as Unistrong) for software copyright infringement, because Microsoft found Windows CE 6.0 computer software used in Unistrong's car navigation devices was not authorize. According to the No. TX7-261-726 registration certificate of the US

Copyright Office, both the author and copyright applicant of the work "WindowsCE6.0" are all Microsoft. In this case, Unistrong did install Windows CE software in the car navigation system which it produced and sold, but Unistrong defended on the grounds of having a legitimate source. Microsoft Corporation recognizes that Lianqiang Corporation is one of its three authorized agents in Taiwan. However, the serial number of WindowsCE6.0 software is not reflected in the software license agreement. It is only recorded in the genuine label, and the evidence in the case cannot prove Unistrong's products have genuine labels and thus cannot prove it had legal sources. Therefore, the court found that it constituted a software copyright infringement, and sentenced Unistrong to stop the infringement and compensate Microsoft for more than 1.93 million yuan.

This case is a typical external source of intellectual property infringement cases. Enterprises need to pay more attention to software copyrights. The copyright produced by itself need to register while copyright from external sources must obtain legal authorization.

2.3 Trademark Reverse Confusion Litigation

The reverse confusion of trademarks means that trademark users in the post-production makes the trademarks have a high reputation, so that consumers will mistakenly believe that the products of former trademark users are derived from the post or there is a connection between the two. In the field of Beidou satellite navigation, there are well-known enterprises established earlier. In the process of development, they have gained high reputation through huge commercial investment and operation. At the same time, some well-known trademarks they own have often become objects of people who profit from litigation.

The "Ren Wo You" trademark case of Beijing Unistrong Technology Co., Ltd. endorsed by Yao Ming is a typical trademark litigation case in satellite navigation enterprises. On August 15, 2003, Zhang Chunlong, a natural person, applied for registration of the "Ren Yi You" trademark, which was approved in 2005. The trademark is approved to use on communication devices such as internet communication. In December 2006, Zhang Chunlong licensed Beijing Lakeway Company to use its trademark on GPS car navigation devices and other equipment. Zhang Chunlong alleged that the company found in the product sales that consumers would confuse the "Ren Yi You" communication products with the source of "Ren Wo You" navigation products, affecting the normal sales of their products, and believed that Unistrong's registering "Ren Wo You" trademark on similar products without permission constitutes trademark infringement. According to the investigation, the "Ren Yi You" trademark authorization time is April 14, 2005, and the "Ren Wo You" trademark authorization time is June 6, 2008. On this condition, Zhang Chunlong believes that the behavior of Unistrong constitutes a reverse confusion, which makes the relevant public mistakenly believe that the products of its authorized company are from Unistrong, which has affected the development of its trademarks and products. The current judging criteria of trademark infringement is whether the trademarks are the same or similar and whether the goods are the same or similar. In this case, the court held that the network communication equipment products and the vehicle navigation products do not

constitute similar goods in terms of functions, uses and consumption groups. And in the case, as the plaintiff does not regulate the use of registered trademarks, even if the relevant public has reverse confusion, the responsibility is also on the plaintiff. The court ruled that the plaintiff's claim was rejected.

The case is a typical case on the ground of reverse confusion. In the process of expanding, satellite navigation enterprises need to strengthen the operation and management of their brands and trademarks. In face of litigation, they must adopt proper litigation strategies to protect their legitimate rights and interests.

2.4 Trade Secret Infringement Litigation

For the core technology of enterprises, some choose to obtain protection through patent application, and some choose to protect their rights through method of trade secrets because they do not want to disclose technical solutions. The biggest risk of trade secret protection is leaking. For satellite navigation enterprises, if they choose to protect technical solutions by trade secrets, they need to pay special attention to the secret management.

In the 11th issue of the People's Justice Case in 2016, a case concerning infringement of trade secrets was announced. Defendants Zhang Yong and Ze Hong were the product division and R&D manager of Yiluo Company, a subsidiary of Beijing Unistrong Company. They signed an employee confidentiality contract when they joined the company. In 2010, as the core personnel, the two mastered the relevant technical secrets of the Yiluo GIS collector. In 2011, the two defendants joined the Haowei Company, and assembled the GIS data collector with the technical secrets and PCBA boards previously acquired, produced S10 and sold the products. The investigating agency entrusted the Judicial Appraisal Center to conduct the appraisal. The appraisal object is the E750 GIS data collector developed by Yiluo Company and the S10 and S12 GIS data collector PCBA board produced by Haowei Company. It is intended to identify whether the two are identical or substantive similar. Finally, it was identified that there is more than 95% similarity between the PCBA board of the two company, which could confirm the direct use of Yiluo Company's relevant trade secrets. The S12 type has 81.9% similarity with the PCBA board produced by Yiluo company and does not have independence. It can be determined that it is produced after using the relevant trade secrets of Yiluo Company. In the end, the court found that the two defendants had violated Yiluo's trade secrets rights and constituted a crime of trade secrets infringement. They were sentenced to fixed-term imprisonment (probation) and fined.

This case is a criminal lawsuit. The satellite navigation enterprises should strengthen the management of their own trade secrets, regulate the IPR ownership of the core technical personnel, service invention problems. On the other hand, they need to strengthen the provisions of the confidentiality agreement and the competition restriction agreement to prevent leakage.

3 Intellectual Property Litigation in Satellite Navigation Enterprises M&A

Enterprise M&A can realize the complementary and resource integration between enterprises, and can concentrate on the advantages and strengths to improve the competitive advantage of enterprises. In a certain sense, it is a shortcut for the development of enterprises. M&A cases in the field of satellite navigation are also commonplace. As satellite navigation enterprises have plenty of IPR, IP litigation often becomes a roadblock in mergers and acquisitions.

In the field of Beidou satellite navigation, a classic case of the industry is the acquisition of Huaxin Antenna Company by BDStar Navigation. In August 2014, BDStar Navigation announced that it intends to purchase 100% equity of Huaxin Antenna by means of issuing shares and paying cash to enter the antenna field of satellite navigation. The total value of the underlying assets of the transaction is expected to be 1.3 billion yuan. From September to December 2014, Huaying Ruixing Company issued a statement to the China Securities Regulatory Commission on "Wang Chunhua and Huaxin Antenna Violate Huaying Ruixing's Trade Secrets and Patent Rights" and sued Huaxin to the Shenzhen Intermediate People's Court on the ground of 9 antenna patent infringements and 1 patent application right infringement. The report and lawsuit of Huaying Ruixing Company led to the failure of the first merger application of BDStar Navigation. Afterwards, in response to the issue of intellectual property legal disputes, the parties of the dispute conducted full and effective communication, eventually eliminating disputes and reaching a settlement. After successfully resolving patent litigation and equity disputes, on March 23 2017, BDStar Navigation announced the succession of acquiring Shenzhen Huaxin Antenna Technology Co., Ltd., as a wholly-owned subsidiary which lasted for more than two years.

Merge and acquisition cases like BDStar Navigation occurs occasionally, this suggests that Beidou related enterprises should do a detailed job in IPR due diligence in the process of mergers and acquisitions.

4 Intellectual Property Litigation in the Process of Satellite Navigation Enterprises IPO

As a relatively new industry, BDS related enterprises require huge financial support for technology research and product operation. The capital chain is an extremely important part. Through IPO,enterprises can obtain stable and long-term financing channels for the company's sustainable development and improve corporate reputation and industrial competitiveness. Therefore, many satellite navigation enterprises choose to go public. However, the company's IPO process will also often be attacked by intellectual property such as patents.

In the satellite navigation post-installation market, there have been patent dispute cases arising from the IPO, which includes many issues such as corporate qualification review, patent stability and litigation strategies. For example, on March 18, 2015,

Wang Enhui sued Beijing StarNeto Technology Development Co., Ltd. (hereinafter referred to as "StarNeto") which was in the preparatory period for IPO for patent infringement, claiming that, on the purpose of production and operation, StarNeto has manufactured, used, sold and promised to sell models of XW-ETS2231 in-vehicle mobile devices and related systems without any permission. Those conducts have infringed its patent named as "GPS-based driving test system" (patent number ZL201110382103.5), thus she requires compensation for various economic losses totaling 10.5 million yuan. Two days later, Wang Enhui reported to the China Securities Regulatory Commission for a real name, requesting the suspension of the IPO review of StarNeto. StarNeto filed a request to the Patent Reexamination Board for invalidation of the patent. On September 16, 2015, the Patent Reexamination Board determined that all six patents held by Wang Enhui were not creative or novel, the patent in question was invalid and the plaintiff lost the case.

The victory of the patent litigation cleared the obstacles for the IPO of StarNeto and warned Beidou satellite navigation enterprises to figure out their own intellectual property rights before IPO and to ensure the validity of patents related to the main business.

5 Countermeasures for IP Litigation in Satellite Navigation Enterprises

As mentioned above, satellite navigation enterprises are facing litigation risks at the stages of production, operation, mergers and acquisitions, and IPO. In combination with intellectual property laws and regulations and litigation practices from home and abroad, satellite navigation enterprises can take the following measures to strengthen IPR risk management and to properly handle intellectual property litigation issues.

5.1 Strengthening Core Patent R&D and Patent Litigation Strategies

Take SEG as an example, SEG's patents are mainly improved innovations and the characteristics of such patents are generally high. After Toyota decided to terminate the cooperation with SEG, it should circumvent some technical features in product design to avoid infringement. However, the "big patent" Toyota did not take any measures which lead to the loss of the infringement case. Satellite navigation related enterprises should learn from the experience of this case. SEG Navigation successfully defended its rights with GAC Toyota through its own patents, warning some leading companies in the industry to maintain a certain number of core patents is the core competitiveness. Enterprises need to increase investment in technology research and development, form their own core patents as soon as possible. Strengthen patent layout, build patent pools and improve their ability to respond to intellectual property litigation are also essential for them. Patent litigations can be solved through the following aspects: First, conduct patent search to clarify the specific conditions and rights status of the plaintiff's patent; second, formulate a response strategy, properly arrange from personnel to procedures; third, review whether the conduct of the enterprise is considered as non-infringement; the fourth is trying to declare the other party's patent invalid; the fifth is to seek cross-licensing of intellectual property rights.

5.2 Pay Attention to Copyright and Trademark Protection

Enterprises have a certain advanced warning awareness of patent rights while often pay less attention to the copyrights and trademark rights that are generated during the production and development process. The software copyright dispute between Unistrong Company and Microsoft Corporation reminds relevant enterprises to strengthen their awareness of prevention when using other products and must confirm that the software has a legitimate source. At the same time, the software copyright developed by itself should be registered and protected as soon as possible. The status of the rights should be fixed in case of emergency. Cases involving software copyright like this one, should sign license agreement with the right holder, obtain authorization to use and develop. Besides, evidence of legitimate legal source and genuine software purchasing invoices should be retained.

As satellite navigation enterprises expanding quickly, cases such as brand-name and free-riding occurred from time to time. The typical case of Zhang Chunlong suing Unistrong Company has sounded the alarm for large-scale satellite navigation companies. Satellite navigation enterprises should strengthen the management of corporate brands and trademarks. First, when applying for a trademark, we should try to embody the distinctiveness of the trademark; second, we must prevent the trademark from being maliciously squatted; third, it is essential to actively use the trademark and preserve the valid evidence and renew it on time to prevent it from being revoked; fourth, try to avoid trademark fraud. Satellite navigation enterprises should clearly understand the number of trademarks, its rights status, licensing conditions, etc. of the enterprise. In case of others getting free ride, enterprises can also apply for partial defense trademarks to strengthen the defensiveness of their trademarks.

5.3 Intensifying the Protection of Trade Secrets and Improving Corporate Intellectual Property Management

Satellite navigation-related high-tech enterprises should set up intellectual property management departments, independently formulate their intellectual property management systems, and maintain long-term cooperation mechanisms with intellectual property agencies and law firms in the early stage of establishment. Beidou satellite navigation related enterprises should expand funding in intellectual property compliance work, establish a sound intellectual property management mechanism and incorporate intellectual property work into all aspects of enterprise such as product development, manufacturing, market development and asset management. First, enterprises should deepen the cultivation of patents and independent IPR, multiple the intellectual property reserves of enterprises, and form the core competitiveness of enterprises. Second, it is necessary to establish and complete business secret management, improve the provisions of confidentiality agreements, non-competition clauses, etc., and strengthen the management and restrictions on secret-related people. The third is to build cooperative intellectual property management system. In the external cooperation, the initial signing of the non-disclosure agreement must clarify the attribution of IPR; in the process of subsequent research, it is necessary to stipulate the right to apply for intellectual property and ownership matters, and pay attention to

relevant evidence such as who proves the technical plan or evidence of delivering data to the other party, etc. In addition, compliance and intellectual property risk reviews are required during technology development, software purchases, and product operations.

5.4 Prudently Promote IP Due Diligence: Focus on the Effectiveness of Key Patents

In the development of Beidou satellite navigation enterprises, corporate M&A and IPO transactions are common means. It can be seen from the above cases that patent litigation incurred by IPR due diligence will hinder the pace of enterprise development. In the process of mergers and acquisitions, Beidou satellite navigation related enterprises must first examine the impact of the transaction structure of mergers and acquisitions on the ownership, licensing and transfer of IPR; in addition, they should also examine the validity of IPR, analyze the real rights holders of IPR, and examine the scope of IPR. It needs to be determined whether the purpose of the merger and acquisition can be effectively implemented. Whether the target company has infringement of the intellectual property rights of others should also be examined. Taking the IPO of StarNeto Company as an example, in the process of IPO, satellite navigation enterprises must first ensure the validity of patents related to the main business. Meanwhile, it is necessary to ensure that the disclosed intellectual property information is in line with the facts. Whether the IPR owned by the company will bring litigation and whether the litigation has a significant impact on the main business should be valued. The intellectual property issues of internal sources especially between the parent company and the child company often play a big role.

Pay attention to possible risks of external licensing of IPR, properly resolve intellectual property issues of departing employees, and patent ownership issues in technology development contracts. To regulate corporate intellectual property management is necessary.

5.5 Applying Overseas Intellectual Property in Advance

China's Beidou-III basic system has been completed now, and global services have been provided since December 27, 2018. At the same time, the pace of "going out" of satellite navigation enterprises is accelerating. Under the background of the increasingly complete intellectual property protection around the world, special attention needs to be paid to the global layout of IPR. First, satellite navigation enterprises must choose the right time to apply for foreign patents. Most countries or regions currently follow the "first application principle", filing patent applications as early as possible will have a time advantage. Second, the target countries need to properly consider in the overseas layout. Enterprises need to consider how to obtain the most effective protection with limited investment. It can be laid out according to the enterprise's overseas business scope, such as the manufacturing country and the sales market country. Moreover, regional organizations can be selected for layout, and patent authorizations obtained in regional organizations can be effective in each member state, which simplifies the application process and reduces costs. Notable regional organizations include Eurasian Patent, African Regional Intellectual Property Organization (ARIPO), and African (French Country) Intellectual Property Organization (OAPI).

5.6 Exploring Intellectual Property Insurance System

Through the typical cases listed, we can found that the amount of intellectual property litigation claims faced by satellite navigation enterprises is often very significant. Once loss, it is a huge burden for enterprises, there are also expenses such as litigation costs. Enterprises should speculate how to share intellectual property litigation risks. At present, the United States has established an intellectual property insurance system to decentralize the costs of intellectual property disputes. The so-called intellectual property insurance is an insurance that uses intellectual property as the subject of insurance. US intellectual property insurance is mainly divided into intellectual property enforcement insurance and intellectual property infringement insurance. With the accelerating pace of China's satellite navigation enterprises going abroad, the number of overseas intellectual property litigations faced by enterprises will also increase, and the establishment of an intellectual property insurance system is a possible route. In the design of specific systems, efforts should be made to avoid the disadvantages of excessive premiums in the current US system and delays in litigation by large enterprises. Strive to share risks rationally and provide strong guarantee for the development of small and medium-sized enterprises.

6 Conclusion

The intellectual property risk runs through the whole process of satellite navigation enterprises' business activities. Enterprises should pay close attention to the risks and properly solve various intellectual property issues. Enterprises can explore the establishment of a sound IPR risk response system by strengthening patent R&D, attaching importance to trademark and copyright protection, improving corporate IP management, prudent IPR due diligence, and strengthening overseas distribution. At the policy level, intellectual property insurance system can be introduced to share risks. Through all the efforts above, it is promising that intellectual property rights may safeguard the long-term development of satellite navigation companies.

References

1. Pan Canjun J (2012) Investigation and assistance mechanism of overseas intellectual property disputes of enterprises in Zhejiang Province. Electron Intell Property 10:50–55
2. Yang Ying J (2009) Analysis on the defense strategies of intellectual property litigation in high-tech enterprises. Legal Syst Econ 2:70–73
3. Beidou Navigation Satellite System. OL (2018). http://www.beidou.gov.cn
4. GNSS & LBS Association of China, R/OL (2018) White Paper on the Development of China's Satellite Navigation and Location Service Industry in 2018
5. Unveiling the Overseas Distribution Strategy of Intellectual Property Rights. OL (2018) World Managers Magazine, 27 September 2018
6. Gao Liuzhi J (2006) The enlightenment of American intellectual property insurance system to China. Spec Econ Zone 2:297–299

The Method and Function of Obtaining Technology and Market Competitive Intelligence of Beidou Industry by Patent Analysis

Qiuyan Fan(✉)

School of Information, Renmin University of China, Beijing, China
vividus@sohu.com

Abstract. In the past 20 years, various innovative technology patents of BeiDou Navigation Satellite System (BDS) emerge in endlessly. Patent analysis is a practical method in enterprise strategy and competition analysis, serving decision-making. This paper describes how to use patent analysis method to process, compose and analyze the relevant patents of Beidou industry, convert these patent data into valuable technical information and market competition information. It provides supplementary means to formulate technological innovation, technology import plans and market strategy. Patent analysis technology is playing its potential as a management tool, which should be taken seriously.

Keywords: Beidou industry · Patent analysis · Competitive intelligence · Strategy decision

1 Introduction

Beidou (hereinafter referred to as BD) Satellite Navigation System (hereinafter referred to as BD System) is a global satellite navigation system independently developed and operated by our country. BD System has been open for civilian application for 15 years since 2003. BD industry has emerged from scratch, showing a flourishing development trend. BD system has been widely used in transportation, maritime, power, civil affairs, meteorology, fisheries, surveying and mapping, miner, public security, agriculture, forestry, land, water conservancy, finance and other industries. BD industry has become an important strategic emerging industry in China.

Throughout the development process of BD industry, technological innovation is the main means of development. With the promotion and policy support of the national science and technology innovation strategy, the technological innovation of BD industry in China is more active. The innovators actively transform the achievements of independent innovation into intellectual property rights, and carry out a comprehensive strategic layout around the BD industry chain. In recent years, the number of patent applications in BD area has increased dramatically in China. The number of patents related to BD has reached nearly 40,000 by searching the contents of patent specifications with the keyword "Beidou" on the website of the State Intellectual Property Office.

J. Sun et al. (Eds.): CSNC 2019, LNEE 563, pp. 651–661, 2019.
https://doi.org/10.1007/978-981-13-7759-4_57

Patentees (hereinafter mainly referred to as enterprises) protect their own technological innovation achievements and intellectual property rights through patents. At the same time, as an important and effective carrier of technological information, patent documents also reveal the technological strength of patentees to the outside world. Therefore, patents can be used as an important information resource for the technological competitiveness of enterprises, which can be deeply excavated to analyze and evaluate the technological competitiveness of enterprises. Patent analysis method is a unique and practical analysis method in enterprise strategy and competition analysis. Enterprises can constantly extract valuable competitive intelligence from patent data to serve enterprise decision-making.

With the continuous development and improvement of information technology, network technology and patent database since 1990s, patent analysis method has been applied to enterprise strategy and competition analysis, and gradually applied in other industries at home and abroad, but it has not attracted enough attention in many enterprises of BD industry yet.

This paper describes how to use patent analysis method to extract relevant patent information from a large number of patent data of BD industry, process, combine and analyze, and convert it into technical information with overall and predictive functions, further then judge the technical competitiveness, and predict related technological development trends. Through patent analysis, we can also get competitors' R&D ability, their technological innovation ability and so on, which can provide supplementary means for enterprises to formulate technological innovation and technology introduction plan, and competition plan based on new technology. Furthermore, it can predict the market competition information of BD industry and provide valuable reference information for the formulation of enterprise market strategy.

2 The Significance and Role of Patent Analysis in Enterprise Strategy

The statistics of the World Intellectual Property Organization show that 90–95% of the latest inventions and creations in the world can be retrieved in patent documents every year, and spread completely and rapidly through patent specifications. 70% of the technical contents have not been published in other non-patent documents. Although patent documents are timeliness from invention to publication, patent documents are the fastest and most authoritative source of information to understand invention and creation. Because the first report from any other channel will destroy the patentability of invention and creation, which means abandoning the monopoly of the market and abandoning the economic benefits of invention and creation. Therefore, the analysis of technology patents is an important means for enterprises to obtain technical information from industries and competitors.

The antennas, chips and boards in the upstream of BD industrial chain, the system integration and terminal integration in the midstream, and the operation services in the downstream have been fully matched. But in fact, due to the late start of BDS in China, domestic navigation chips and terminal manufacturers have less core technology and insufficient patent strength, mainly based on the U.S. GPS system. Therefore, some BD

technology pioneers do not have domestic references, GPS related patent technology literature is the best reference, we should use patent analysis method to absorb foreign advanced technology for our use.

Learning to carry out R&D activities on the shoulders of "giants" and make good use of relevant patent documents at home and abroad can effectively save research funds and research and development time. At the same time, the effective introduction of patented technology, in the fierce market competition, can quickly develop products needed by the market, and improve product function and performance. Patent analysis can also effectively avoid patent risks.

Beidou industry has great attraction. There has been lots of enterprises in Beidou industry, but many new enterprises still want to enter it every year. New entrepreneurs with a lot of capital and entrepreneurial courage can not be underestimated. How to stand out among lots enterprises, dominate and maintain the leading edge? Enterprises with core competitiveness of technology or market are often more invincible. There are many ways to improve the technology and market competitiveness of enterprises, but patent analysis can be an important auxiliary means. The analysis of patent literature on technology and market competition information can help enterprises evaluate competitors, grasp the competitive environment and industry development trend, and improve the pertinence and scientificity of enterprise competition strategy. Without a systematic understanding of competitors and industry technology development, technology strategy (technological innovation and technology introduction) falls into blindness and non pertinence. The application of patents to the analysis of technological factors in competition, related R&D and technological status of competitors can help formulate R&D strategies and market competition strategies.

3 Patent Data Source and Retrieval Analysis Method

Following is the introduction of data sources, analysis process and selection of retrieval objects for patent analysis.

3.1 Patent Retrieval and Analysis Process

The number of BD patents or reference patents applied at home and abroad is huge. How can we find the patents needed for analysis in a large number of patents? Patent retrieval for the purpose of obtaining competitive intelligence can be roughly divided into three steps:

Firstly, enterprises need to define the scope of analysis. Lock in international or domestic patents, and lock in the subdivision of the industry. For example, BD industry can be subdivided into chips, modules, terminals, system integration, terminal integration, operation services, etc. System integration, terminal integration and operation services can also continue to be subdivided according to the user scope of product services.

Secondly, we need to clarify the main technical fields. The scope of patent analysis for new entrants or existing old enterprises in the industry is different. New entrants of BD industry need to fully understand the technical status, technical hot spots and trends

of the industry, to find entry points and obtain long-term development. Existing enterprises need to regularly review their existing technological competitive position, competitors' technological status and technological trends in order to continuously improve existing products and enhance the core competitiveness of products. or conversely, enterprises need to consider how to set obstacles to competitors through patent means in the case of leading technology.

Finally, we use effective tools to make statistical analysis of patents. In addition to the website of the State Intellectual Property Office, there are many manufacturers who can provide patent retrieval and analysis, so it can be assisted by selecting appropriate retrieval and analysis tools.

3.2 Patent Retrieval Analysis Tools and Data Sources

To assist in illustration, the contents of the pictures and texts shown in this paper mainly depend on the results of Chinese retrieval statistics of the National Intellectual Property Office Network. The purpose of this paper is to illustrate the method and function of patent analysis applied to competitive intelligence of BD industry. Therefore, the retrieval tools, data sources and data retrieval results are not verified in detail.

3.3 Selection of Patent Retrieval Objects

Enterprises should select one or more retrieval objects according to their own needs and strive to be comprehensive when selecting technical topics for retrieval.

In order to assist the patent analysis method in this paper, the topic of BD Intelligent Agriculture, one of the current BD hot applications, will be selected in this paper. The retrieval time will be after BD Satellite Navigation System opened for civilian applications in 2003. With "BD Agriculture" as the key word, 289 patents were searched, including 182 invention patents and 107 utility model patents. The following patent analysis methods illustrate that all the data are taken as objects.

Of course, only using "BD Agriculture" as the search keyword will filter out the relevant technical patents in this field that do not contain this keyword, that is, the search will be incomplete. This article only selected the scope for illustrating the need. If "BD agriculture" is subdivided into "BD soil", "BD cultivation", "BD aquaculture" and other information, more comprehensive search results will be obtained.

4 Contents and Methods of Technology Patent Analysis in BD Industry

Patent analysis of BD industry includes: analysis of competitive environment of BD industry, analysis of competitive technology of BD industry, analysis of competitors of BD industry, analysis of technological competitiveness of enterprises themselves, analysis and mining of partners.

4.1 Analysis on Competitive Environment of BD Industry

When a new entrant tries to enter the BD industry or an existing enterprise tries to enter a new technology field, it is necessary to analyze the whole competitive environment of the technology field in the industry in order to understand the overall situation of the field. From the perspective of patent technology, the industry technology competition environment faced by enterprises mainly includes four aspects: current technology development trend, technology life cycle, technology situation of countries or regions, competitor identification and so on.

4.1.1 Analysis of Technology Development Trend

Through the analysis of the number of patents and the application trend in the specific technology field, we can understand the development situation and the overall trend of the industry technology.

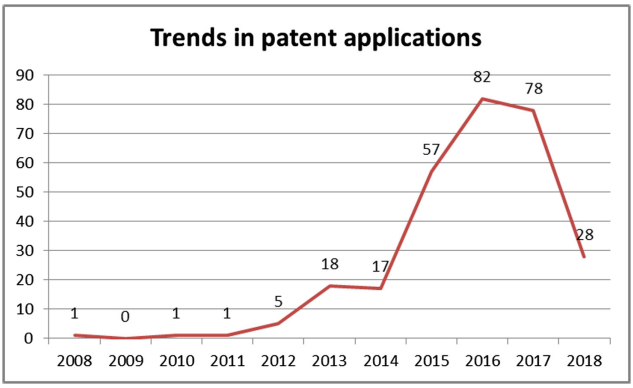

Fig. 1. Example: patent quantity trend of BDS in agricultural application

From the trend chart of BD's patent application in agriculture, it can be concluded that BD's research on agricultural application began in 2008, and made significant progress after 2013. The number of patent applications has increased year by year and is in the developing stage. From the number of patents, BD's agricultural application is still at a low level. Therefore, pioneer enterprises in this field need to further analyze foreign patents and learn from developed countries such as the United States, which has a small population and a wide area, how to use GPS satellite to assist agricultural production.

4.1.2 Patent Technology Life Cycle

Patent technology life cycle refers to the general periodic law between the number of patent applications and the number of patent applicants, which can be divided into germination period, development period, maturity period, recession period and recovery period. The number of patents or the number of patent applicants in different periods can represent the technological development of that period, showing the state of "appearing and a small amount", "gradually rising", "slowly growing or maintaining stability", "gradually declining until zero", "appearing a small amount again".

Understanding the development stage of technology is very helpful for a company to judge whether it should intervene in the business of this technology field. If a technology has entered a mature stage, it means that the space for technological development has been relatively small. It is difficult for enterprises to make technological breakthroughs. On the contrary, if the technology is in the development stage, it indicates that there is still a large space for R&D and the return of technological investment will be relatively large.

From the above "Fig. 1", it can be seen that BD's application in agriculture is still in its infancy (the annual patent application volume is maintained at 1–5 items in 2008–2013) and is entering the development period (the rapid increase year by year after 2013). The number of patent applications and the number of patent applications are small. China is a large agricultural country, limited by thousands of years of cultivation methods, agricultural mechanization level is low. With the increase of agricultural equipment, BD's application in agriculture should have a rapid development trend, which deserves the attention of new enterprises or industries.

4.1.3 Technical Distribution in Countries or Regions

Patent technology distribution in different countries or regions can be used as a technical index to measure regional innovation ability and competitiveness, and reflect the potential of market application.

We will continue to analyze the regional distribution of patented technology based on the search results of domestic BDS applied technology patents in agriculture, in order to determine which provinces and municipalities take the lead in the application of BDS in agriculture and whether the technology level in this region has advantages. It is concluded that the strong or weak distribution of patents serves enterprises in choosing market development decision-making. Of course, other market research methods are needed to draw a conclusion, but patent analysis can indeed be used as an effective supplementary means (Fig. 2).

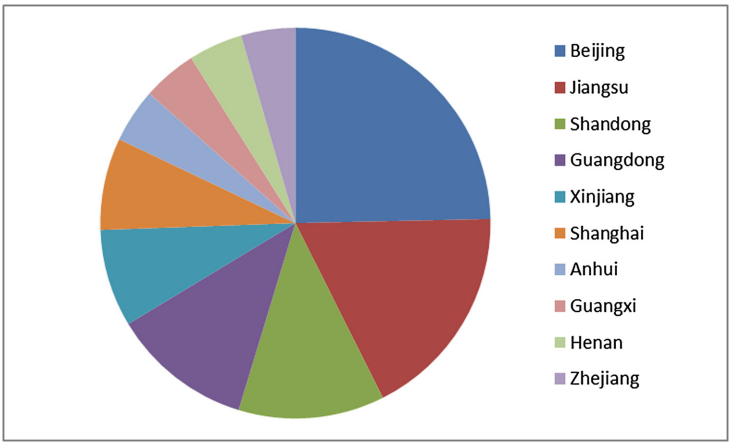

Fig. 2. Example: top ten regional contrast maps of BDS in agricultural application

4.1.4 Competitor (or Potential Competitor) Identification

Let's start with a list of the top ten patent applicants for BDS in agricultural applications in China (Fig. 3).

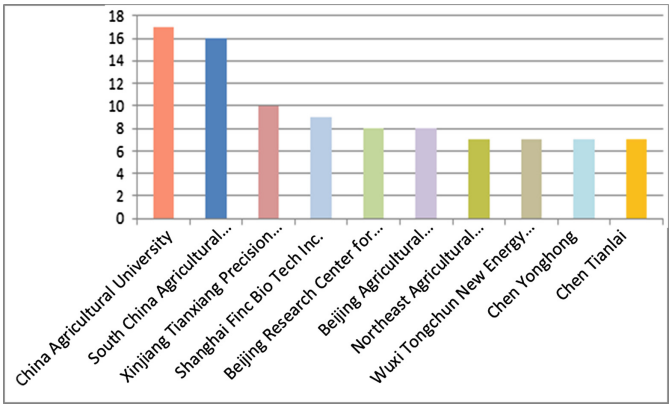

Fig. 3. Example: top ten patent applicants of BDS in agricultural application

The top 10 companies accounted for 33.2% of the total patent applications. Among them, there are 3 enterprises, 5 universities and scientific research institutes, and 2 individuals. Potential competitors may come from these three enterprises, and then through the following competitor analysis methods for in-depth analysis.

Taking "Wuxi Tongchun New Energy Technology Co., Ltd" as an example, through searching its patentee, we find that there are 90 patents applied for by the company, of which 50 are related to "BD" and 7 are related to "BD Agriculture". In fact, the company has adopted dozens of patents related to BD's application in agriculture, and no "agriculture" keywords have appeared. For example, wheat maturity monitoring with BDS belongs to agriculture. Therefore, in the detailed analysis, the patent analysis tools may not be accurate, and need manual addition and statistics.

Through a detailed analysis of the company's patents, the BD patents mainly focus on UAV agriculture, UAV fish swarm monitoring, UAV marine resources monitoring, UAV forest fire monitoring, UAV agricultural pest monitoring and so on. The company's patent layout mainly uses BDS high-precision positioning UAV applications, its core technology is BDS UAV applications, and still shows a strong development trend.

Through analysis, we can judge whether the enterprise has become a competitor of the enterprise.

4.2 Competitive Technology Analysis of BD Industry

The patent classification number of patent applications for invention and utility model is identified by IPC International Patent Classification Table. IPC is divided into departments, large groups, small groups, large groups and small groups. Each patent is assigned a patent classification number indicating the technical subject of the patent.

A patent may have a different classification number. Through the statistical analysis of patent classification number, we can know the technical hotspots of the industry and find out the competitive technology, that is, to understand the key technology, core technology and potential technology in the technical field, and to judge its development trend.

The distribution map of IPC reveals the distribution of patents in each IPC category in a technology field. The more patents clustered in a certain IPC category, the more important this type of technology is, and it belongs to the research hotspot, and vice versa. When making detailed analysis, the IPC distribution map should be as detailed as possible to large groups or groups. The more detailed the IPC distribution map is, the more favorable it will be for your analysis (Fig. 4).

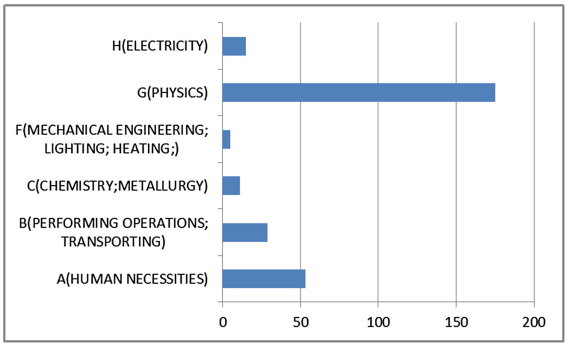

Fig. 4. Example: the patent IPC distribution map of BDS in agricultural application

4.3 Analysis of Competitors in BD Industry

Know the enemy and know yourself, and you can fight a hundred battles with no danger of defeat. In today's market economy of economic globalization, competition is becoming more and more fierce. Enterprises want to survive and develop, adopt effective competition strategy, understand the industry and market of enterprises and competitors, which can improve the success rate of decision-making.

Enterprises with strong technological strength in the industry are often the ones with strong competitive strength in this field, and they are the main competitors. Competition analysis includes many methods, and technology patent analysis can be used as an important auxiliary means. Through in-depth study and analysis of competitors'patents, we can understand competitors' technological layout and focus, technological trends, potential links between competitors, competitors'positioning and technological strength.

4.3.1 Analysis of Patent Layout of Competitors

Through the display and analysis of patented radar or function matrix diagrams in different technical fields of different competitors, we can understand the technological overlap and main technological layout among competitors, the technological emphasis

and strength difference between competitors, and analyze the technological strength difference between our enterprises and competitors, so as to provide support for technological strategy (Fig. 5).

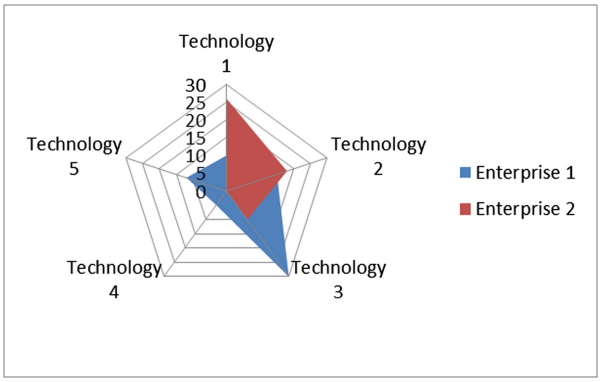

Fig. 5. Example: patent radar map of competitors

4.3.2 Analysis of Patent Layout of Competitors

When we lock in competitors, we can understand the development trend of competitors in the whole technology field by analyzing the trend of their patent applications (Fig. 6).

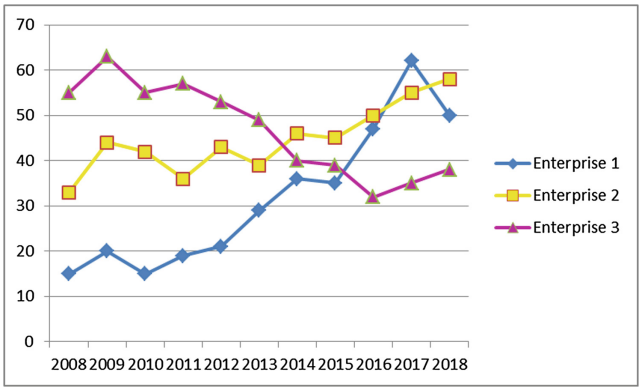

Fig. 6. Example: patent quantity trend of competitors

The technology trend map of a single competitor can also be detailed to each IPC classification or specific technology.

4.4 Analysis of Enterprise's Own Technical Competitiveness

Know the other and know yourself too. Through the patent analysis method, we can understand the technological competition pressure we are facing. At the same time, through the analysis of patent citation rate, we can understand the importance and intrinsic value of patent technology owned by our own enterprises, and help to judge the technological competition situation and technological development trend faced by our own enterprises (Fig. 7).

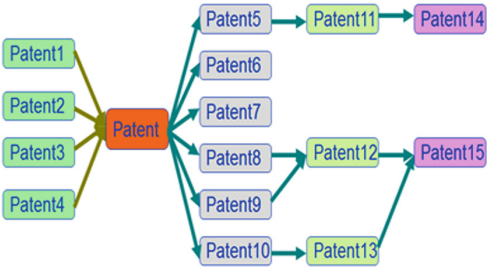

Fig. 7. Schematic diagram of the relationship between patent citation and citation

Patent citation rate can be divided into self-citation rate and cited rate. Self-citation rate describes the situation of subsequent patents citing their own patents. The higher the citation rate, the stronger the autonomy of R&D; the higher the citation rate, the higher the content of the technology.

4.5 Partner Analysis and Mining

Through the ranking of patent applicants in a certain technology field, we can find some universities, research institutes or individuals with technical strength. When enterprises try to enter this field, they can cooperate with them and introduce patented technology to quickly develop competitive products.

Through the list of patent inventors, we can find the most active people in the field of technology, and track their journal papers and technical activities, so that we can understand the development trend of technology more abundantly. Business managers can also seek partners or engage in headhunting activities.

At the same time, we can also find satisfactory partners by analyzing the patents of upstream suppliers and downstream customers.

5 Notices for Competition Analysis with Patents

The methods and functions of patent analysis in obtaining technology and market competition information in BD industry are described above. Through patent analysis, we can find out the technical status and development trend of competitors in the field, but not absolutely. Not all patents have commercial value and strategic guiding

significance, and need eye recognition. Patent analysts also need to have relevant industry knowledge, analysis and judgment ability, and a certain foreign language ability when analyzing international patents.

6 Concluding Remarks

At present, comprehensive patent database can be easily accessed through the Internet, and a large number of data can be effectively analyzed. Patent analysis technology is playing a more and more potential as a management tool, which should be taken seriously by enterprises in BD industry. By means of patent analysis, we can understand the situation and development trend in the field of technology, effectively formulate enterprise technology and market competition strategy, reduce the probability of blind duplication of R&D and failure, avoid waste of resources, and jointly promote the healthy and orderly development.

References

1. Wang X, Sun J Application of patent map in technological competition analysis, book and information work 53(53):79–82
2. Piao H (2016) Inner mongolia science technology & economy, No 23 (All No 369), December 2016
3. Zhou L, Li S, Yang S (2015) Analysis of patent status of Beidou satellite navigation industry and relevant suggestions. Chin Invent Pat 9:44–48

Patent Layout and Early Warning Advices of Satellite Navigation

Yuanyuan Wang(✉)

China Industrial Control Systems Cyber Emergency Response Team, Beijing, China
wangyuanyuan@infoip.org

Abstract. Satellite navigation industry has become a global new and high technology industry, which has achieved the cross-border integration in many livelihood fields and penetrated into every aspect of our lives, with the rapid development of beidou satellite navigation system, the beidou satellite navigation industry is facing great opportunities and challenges, although patent applications of beidou are growing fast, but the proportion of valid patents is not high, the number and layout of core patents are limited, most of enterprises are small scale, the ability of overseas risk management and response capacity are relatively weak, that are all urgent to sort out and plan beidou's related intellectual property work. This paper analyzed the present situation in the field of satellite navigation, and then explored the application trend, regional distribution, main applicants and industry application distribution, selected representative innovation applicant for analysis, including its patents situation, foreign layout, transfer and transformation work, acquisition, merge or listed situation etc., by analyzing the overall situation and detailed case, discussed the 'going out' intellectual property risk of beidou enterprises, put forward some corresponding countermeasures and suggestions as a reference for the development of satellite navigation autonomy and internationalization in China.

Keywords: Satellite navigation · Beidou · Patent layout · Risk prevention · Warning advices

1 Introduction

Global navigation satellite system (GNSS) is one of the national important infrastructures in the information era, common examples are America's Global Positioning System (GPS), China's Beidou System (BDS), Russian's GLONASS system (GLONASS), European's Galileo system (GALILEO), Japan's Quasi-Zenith Satellite System (QZSS) and India's Regional Navigation Satellite System (IRNSS) [1].

Beidou is a global satellite navigation system which independently build and operated by China, it can be compatible with other global satellite navigation systems. Beidou can provide all kinds of users with high-precision, high-reliable positioning, navigation and timing services around the world and at all hours of the day. Beidou is also capable of short message communication. In the late 20th century, China began to explore the development path of satellite navigation system suited to its national

J. Sun et al. (Eds.): CSNC 2019, LNEE 563, pp. 662–672, 2019.
https://doi.org/10.1007/978-981-13-7759-4_58

conditions, and a three-step development strategy has been gradually formed. By the end of 2000, the bds-1 was completed to provide services to China. By the end of 2012, the bds-2 was completed to provide services to the asia-pacific region. The bds-3 global system is scheduled to be completed around 2020. On the basis of bds-2, new functions such as high-precision service, satellite-based enhancement service, large-capacity RDSS service, mid-orbit search, rescue service and global location report will be added to broadcast better navigation signals and further enrich the functions of the satellite navigation system.

The "global" satellite navigation patent mentioned in this paper only refers to six country's relevant patents, including China, the United States, Europe, Russia, Japan and India. The deadline for patent searching and data update is June 30, 2018. The patent data comes from the Thomson Innovation database and Innojoy patent database.

2 Patent Layout of Global Satellite Navigation

2.1 Application Trend Analysis of Global Satellite Navigation

Figure 1 is the statistical graph of the annual development trend of global and Chinese patent applications in the field of satellite navigation (Chinese patent applications include foreign applications entered into China and domestic applications, the proportions are shown in Fig. 1). Up to the June 30, 2018, a total of 110,986 patent applications were applied for global satellite navigation. China has received a total of 54,350 satellite navigation patent applications, ranking first in the world. In 2016, China received 10,678 annual applications for satellite navigation, accounting for 80 percent of annual global applications that year.

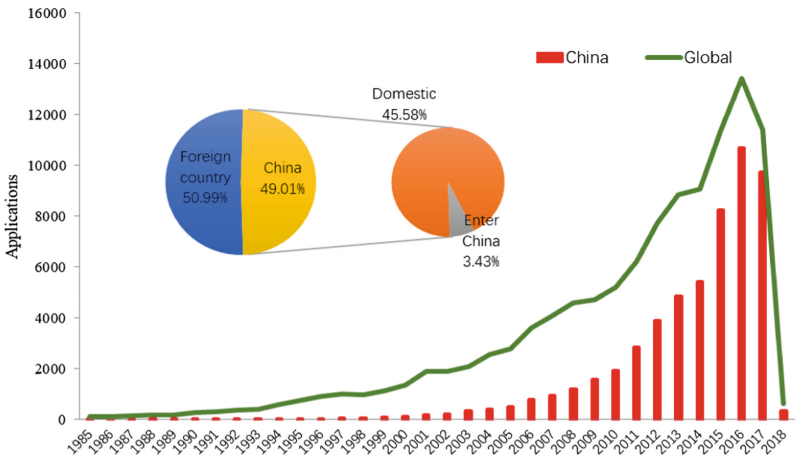

Fig. 1. Annual development trend of patent applications of global and China

Figure 2 shows the comparison of application and authorization amount in various countries around the world. As can be seen from this figure, the proportion of valid patents in China is not high (the number of granted and valid patents accounted for only 42% of the total number of applications), more patents are in the process of examination or not paid after authorization. However, the proportion of valid patents in the United States is up to 57%, indicating that the US patents' quality and practical value are relatively high.

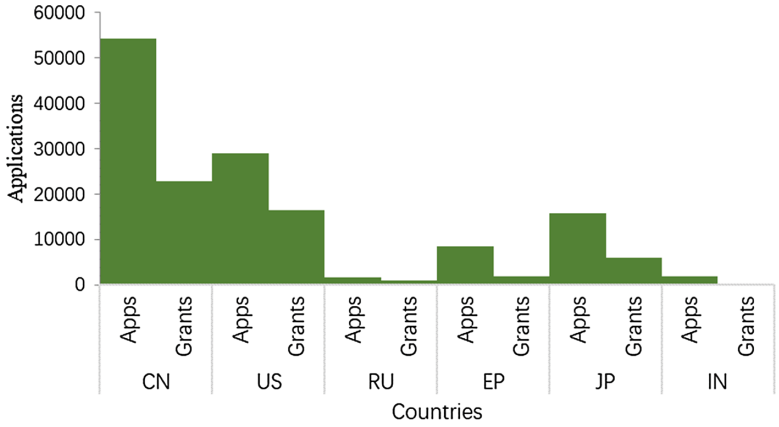

Fig. 2. Comparison of application and authorization amount

2.2 Layout Analysis of Main Applicants of Global Satellite Navigation

Based on the statistical analysis of the main applicants in the field of global satellite navigation, the ranking of the main applicants (the data was statistical of patent families) was obtained as shown in Fig. 3. It can be seen from the figure that the top ten innovation applicants include three American enterprises, four Japanese enterprises, two Korean enterprises and one Finnish enterprise.

These enterprises are all the leading enterprises in the field of satellite navigation, and most of them are traditional communication or internet enterprises, Chinese company did not enter the top 10 ranking, mainly due to that the satellite navigation enterprise in China started late and have not yet formed a certain scale, beidou enterprises will compete with traditional communication or internet companies in the market, enterprise scale and enterprise competitiveness need to be further improved.

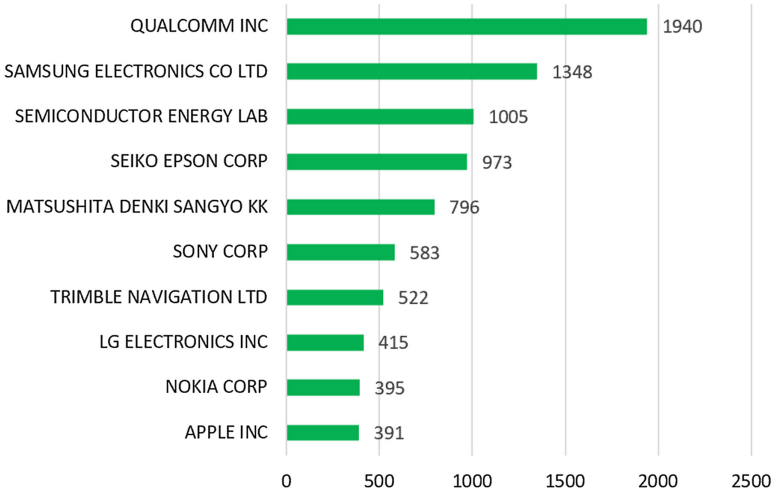

Fig. 3. Distribution of top10 applicants of global satellite navigation

On this basis, this is a further analysis on the main applicants that have been active in the satellite navigation markets of the world, and it has been discovered that:

Qualcomm inc. of the United States ranks in the forefront of satellite navigation in the world and enjoys an absolute advantage in this field. In addition to Qualcomm inc., the Japanese market is almost occupied by domestic enterprises, such as: Seiko Epson, Panasonic, Sony, Mitsubishi, Toshiba and so on, patent barrier is strong and the monopoly situation has been formed. Most of the major innovations subjects in the Indian market are American enterprises, the advantages of local applicants are not obvious. Major innovation subjects in China include some universities and some emerging enterprises, foreign innovation subjects and international manufacturers also have a certain market share. However, different from India, domestic applicants in China have a higher market share and obvious advantages, although they are small, dispersed and a monopoly situation have not been formed.

3 Patent Layout of Satellite Navigation in China

3.1 Application Trend Analysis of China Satellite Navigation

Patents in China in the field of satellite navigation include foreign applications entered into China and domestic applications, as shown in Fig. 4. As can be seen from the application trend curve, the number of domestic applications account for more than 90% of the total number of patents accepted in China, while domestic applications in this field mostly involves the technology of beidou, therefore, the above data shows that since the end of the 20th century, beidou technology had developed rapidly and its technical strength and intellectual property level had been continuously improved.

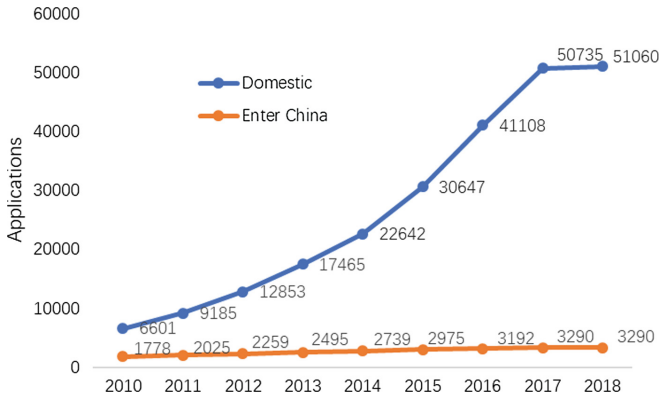

Fig. 4. Patent application trend in China satellite navigation

3.2 Regional Distribution Analysis of China Satellite Navigation

In this paper, the main application regions of satellite navigation patents in China are statistically analyzed, as shown in Fig. 5.

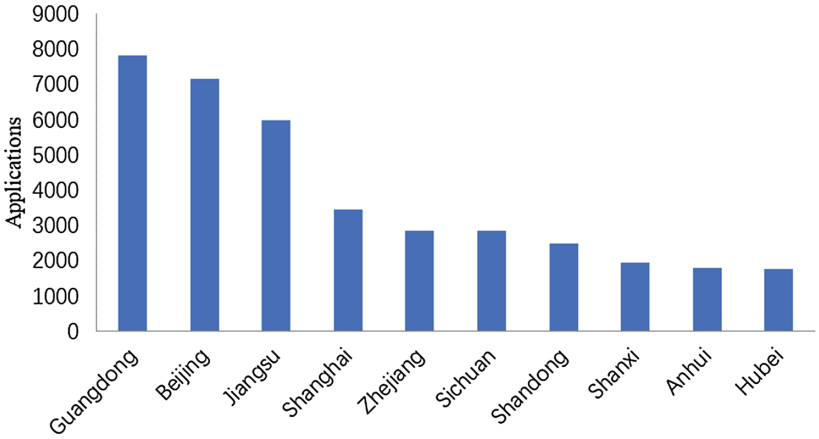

Fig. 5. The main application regions of satellite navigation patents in China

The top three regions in terms of patent application are guangdong, Beijing and jiangsu. With the development of beidou technology, the emerging enterprises in the above-mentioned regions have rapidly risen and applied for a large number of patents. In general, the number of patent applications in each region is basically equivalent to

the level of the local satellite navigation industry, which indicates that economically developed regions play a crucial role in promoting the development of beidou satellite navigation industry.

3.3 Application Distribution Analysis of Beidou Industry

This paper further discusses the application of beidou industry, and studies its development and patent layout characteristics.

Industry applications include: science and technology applications, personal applications, social applications, transportation applications, agricultural, forestry and fishery applications and environmental applications.

In which:

The application fields of science and technology include geographical mapping, monitoring of bridges, landslides and dams, management of smart cities and crustal deformation etc.

Personal application fields include real-time positioning terminals for the elderly or children, shared bicycles etc.

Social applications include disaster early warning or management, medical services, rescue and timing services;

Traffic applications include navigation or monitoring of roads or vehicles, traffic control, tracking and driving tests, etc.

Agricultural, forestry and fishery applications include information connectivity and sharing between agricultural, forestry and fishery enterprises and administrative departments, also include port operations, agriculture, tillage, soil sampling, equipment navigation, etc.

Environmental applications include automatic monitoring of the environment through positioning and navigation, especially in environmental emergency monitoring, fire and earthquake monitoring etc.

Through the above division method to confirm the patent search strategy, the application distribution trend of beidou industry is obtained as shown in Fig. 6. As can be seen from Fig. 6, the key industrial application fields of beidou industry are science and technology application field and personal application field. The corresponding patent applications are 4277 and 3841, accounting for 30.30% and 26.97% respectively. In addition, the number of applications in the above two industries have been increasing year by year, with broad application prospects and bright market prospects.

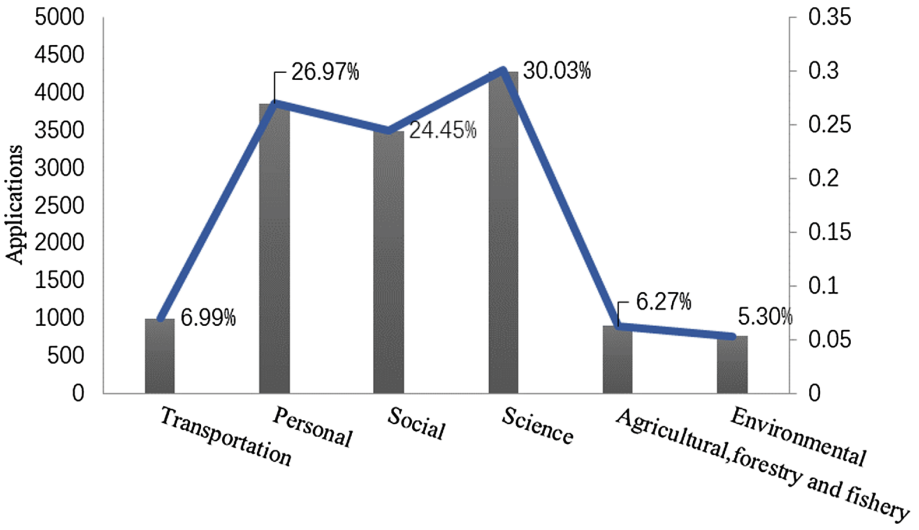

Fig. 6. Application distribution of beidou industry

Although the number of patent applications for transportation applications, agricultural, forestry and fishery applications, environmental applications are not high, but applications involving national security and infrastructure such as road traffic, disaster monitoring, agriculture, forestry and fisheries are also particularly important. The application of beidou system in the above fields cannot be ignored.

In a word, satellite navigation has been widely used at present. The beidou system has achieved cross-border integration in many areas of people's livelihood and penetrated into all aspects of our lives.

4 Discussion on Patent Layout of Qualcomm Inc.

It can be seen from the above analysis that in the field of satellite navigation, Qualcomm inc. of the United States has absolute technical advantages and patent layout advantages both in America or the other countries, is the leading enterprise in satellite navigation field. Therefore, Qualcomm inc. was selected as the representative of innovative subjects, its market layout and intellectual property development strategy are analyzed in detail for reference or risk prevention of beidou enterprises in China.

Figure 7 shows the application amount and layout country of Qualcomm, as can be seen from the trend of the application, before 1995, Qualcomm applied for few patents in the field of satellite navigation, which was in the embryonic stage of technology, technologies of this time mainly focused on radio transmission and positioning technologies. During the period from 1996 to 2014, Qualcomm's patent application in this field grew rapidly and reached its peak in 2014. The number of applications in 2014 was almost 25 times higher than that in 1996.

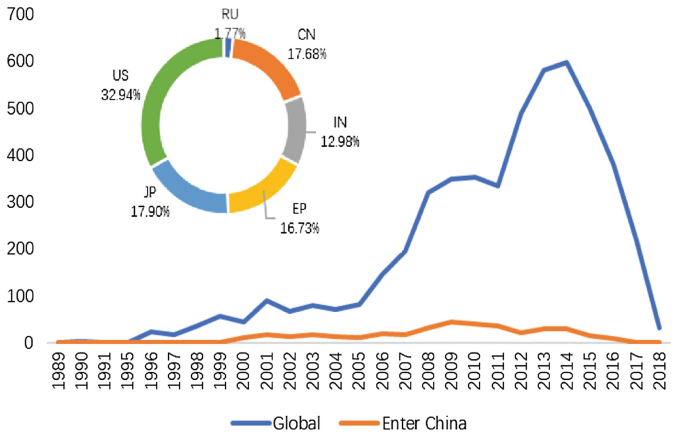

Fig. 7. Qualcomm's application and patent layout

The rapid patent accumulation during this period was related to Qualcomm's launch of two types of 64-bit mobile system chips – Snapdragon 610 and 615 in 2014. Snapdragon 610 and 615 are highly recognized and welcomed by consumers, which showed significant advantages in both product development and market occupancy. In addition, Qualcomm acquired Atheros Communications in 2011, completed 2,400 patent transactions with HP in 2014, and conducted investment and acquisition negotiations with Israeli chip manufacturers in 2014, all of this accelerated Qualcomm's rapid technology accumulation and patent accumulation in the field of satellite navigation and formed a solid patent barrier. Qualcomm's leading position in the industry thus formed.

Since 2015, Qualcomm has entered the adjustment period after a substantial increase in the early stage, and the annual application volume shows a downward trend. The reasons are analyzed as follows: first, Qualcomm has finished a large number of patent layouts for core technologies; second, Qualcomm's massive layoffs and response to a number of lawsuits during this period have also affected the company's accumulation of patent applications. It can also be seen from the figure that the number of Qualcomm's patent applications in China has been steadily increasing since 2005, the number of Qualcomm's patent applications in China accounts for 17.68% of its total patent applications, only less than the United States and Japan, so China is the main market that Qualcomm has focus on in recent years.

In addition, this paper further analyzes IPC (International Patent Classification) and key technologies of Qualcomm patents in the field of satellite navigation, and obtained Table 1.

Table 1 shows the ranking of IPC classification of Qualcomm's relevant patent. According to the ipc ranking, patent class of G01S, H04L, H04W, H04B and G06F are the main classification. These main classification mainly involve radio direction, navigation, digital transmission, communication network and data processing, etc.

Table 1. IPC of Qualcomm's patent in satellite navigation

IPC	The IPC instructions
G01S	Radio orientation; radio navigation; using radio wave ranging or velocity measurement; similar devices for other waves are used
H04L	The transmission of digital information, as by telegraph
H04W	Wireless communication network
H04B	Transmission
G06F	Electrical digital data processing

Through the selection and analysis of Qualcomm's core patents, it is found that this company's patents in the field of satellite navigation are mostly concentrated on receiver structure, auxiliary system and RF front-end, which is due to Qualcomm itself is a radio communication technology research and development company. The above key research directions are the company's mainstream business directions, and also the key layout directions of the patents.

Through the above analysis of Qualcomm, it can be seen that this company has the largest number of patent applications in the field of satellite navigation in the world, with prominent key technical fields. It had made patent layout in all major countries, had obvious market advantages and formed certain patent barriers. Innovation subjects in China should pay full attention to its core technologies and avoid intellectual property risks when making patent layout in related technical directions.

5 Intellectual Property Warning Advice of Beidou Industry

Based on the macro analysis of satellite navigation and the micro analysis of qualcomm inc., this paper will propose the following measures and suggestions for the risk avoidance and early warning of beidou enterprises:

5.1 Continue Patent Layout and Increase the Number of Core Patents

Due to the risks such as lower proportion of effective patents and insufficient core patent technology in China, it is urgent to develop the cultivation and layout of beidou high-value patents and form a high-value core patents pool. It not only pays attention to the number of patent applications, but also focus on the operation and transformation of patents after granted, speeds up the industrialization of core technologies, avoid the intellectual property risks of beidou navigation technology export, truly implements the strategy of "technology export, patent first", reduces the risk of patent litigation, and provides intellectual property protection and core technology reserve for beidou system to participate in global competition.

5.2 Give Full Play to the Unique Advantages of Beidou System and Continuously Carry Out Independent Research and Development

At the end of 2011 to early 2013, a patent dispute surrounding satellite navigation signal broke out between Britain and the United States, in the end, the two countries issued a joint statement. In order to avoid risks, BDS must be avoid the British and American patent layout in navigation signal, give full play to the unique advantages, eliminate potential threat on technology and implement independent intellectual property protection as soon as possible.

5.3 Introduce New Rules of International Competition for Beidou Enterprise

In view of the intellectual property risks faced by beidou enterprises "going out" and foreign enterprises "coming in", through domestic media, intellectual property public service platform, industry associations and other channels, and by means of intellectual property publicity week, international conference BBS, industry training activities, white paper publishing, BDS will promote China's satellite navigation experience and achievements of intellectual property protection, guide enterprises to carry out targeted improvements.

At the same time, enterprises should be guided to master basic intellectual property risk avoidance and coping strategies, strengthen risk prevention awareness.

The basic process of intellectual property risk avoidance and response is shown in Fig. 8:

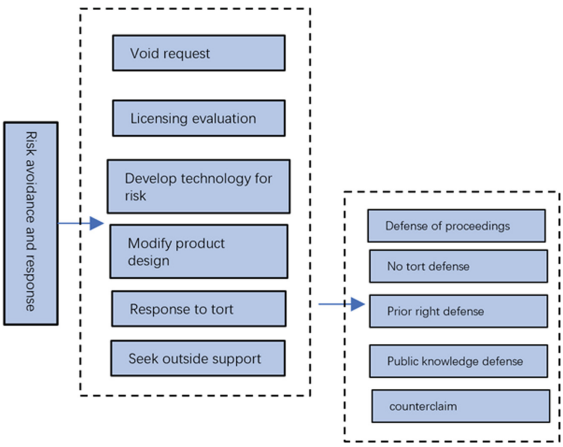

Fig. 8. Risk avoidance and response of intellectual property

5.4 Track Core Technology, Grasy the Dynamics of Competitors in Real-Time

On the one hand, we can track the countries/regions, litigation-related companies, or potential litigation-related patents by means of patent analysis, make intellectual property warning, avoid risks in advance, and minimize the risks of intellectual property in the areas where enterprises have advantages. On the other hand, beidou enterprises in China should track and investigate the application status, legal status and litigation status of basic patents with infringement risks, analyze and determine the protection scope of the granted patent claims in detail, and grasp the development trend of competitors in real time.

5.5 Improve the Intellectual Property Practical Ability of Beidou's Innovative Applicants

Beidou intellectual property cultivation is still in the primary stage, focusing on the patent front end of patent mining and patent applications, with the need of "going out", beidou system is urgent to enhance the capabilities on international layout, operating, risk warning and conflict management.

6 Conclusion

At present, beidou industry is on a scale. The sales of the core foundation products of autonomous intellectual property reached a hundred million, such as core chips and modules, etc. High-precision products of beidou have been exported to more than 70 countries and regions in the world. As a basic system for protecting innovation and regulating order, intellectual property is an important guarantee for China's beidou system to go global and the beidou industry to improve its competitiveness. This paper discussed the general situation and specific cases of satellite navigation, and on this basis, put forward to some early warning suggestions as a reference for the independent and international development of China's satellite navigation.

Reference

1. Quan Y, Lau L, Roberts GW, Meng X (2015) Measurement signal quality assessment on all available and new signals of multi-GNSS (GPS, GLONASS, Galileo, BDS, and QZSS) with real data

Author Index

J. Sun et al. (Eds.): CSNC 2019, LNEE 563, pp. 673–675, 2019.
https://doi.org/10.1007/978-981-13-7759-4